

**SYNTHESIS AND CHARACTERIZATION OF 3d-METAL  
NANOPARTICLES IMMOBILIZED ONTO GRAPHENE  
OXIDE NANOCOMPOSITE FOR ITS APPLICATIONS IN  
ADSORPTION AND CATALYSIS**

**Thesis**

Submitted in partial fulfilment of the requirements for the degree of

**DOCTOR OF PHILOSOPHY**

by

**ANUMA SAROJA**

**(Reg. No. 148003CY14F03)**



**DEPARTMENT OF CHEMISTRY  
NATIONAL INSTITUTE OF TECHNOLOGY KARNATAKA  
SURATHKAL, MANGALORE -575025**

**MAY, 2022**

## DECLARATION

I hereby *declare* that the Research Thesis entitled "**Synthesis and Characterization of 3d-Metal Nanoparticles immobilized onto Graphene Oxide Nanocomposite for its Applications in Adsorption and Catalysis**" which is being submitted to the **National Institute of Technology Karnataka, Surathkal** in partial fulfilment of the requirements for the award of the degree of **Doctor of Philosophy** in **Chemistry** is a *bonafide report of the research work carried out by me*. The material contained in this Research Thesis has not been submitted to any University or Institution for the award of any degree.

*A. Saroja*

**ANUMA SAROJA**  
Reg. No. 148003CY14F03  
Department of Chemistry

Place: NITK, Surathkal  
Date: 24-05-2022

# CERTIFICATE

This is to *certify* that the Research Thesis entitled **Synthesis and Characterization of 3d-Metal Nanoparticles immobilized onto Graphene Oxide Nanocomposite for its Applications in Adsorption and Catalysis** submitted by **Anuma Saroja (Register Number: 148003CY14F03)** as the record of the research work carried out by her, is *accepted as the Research Thesis submission* in partial fulfilment of the requirements for the award of degree of **Doctor of Philosophy**.

  
24.05.2022  
Research Guide


**Dr. B. RAMACHANDRA BHAT**

Professor

Department of Chemistry

National Institute of Technology Karnataka

Surathkal, Srinivasnagar, MANGALORE - 575 025

  
24/05/2022  
HEAD, DEPARTMENT OF CHEMISTRY  
National Institute of Technology Karnataka  
Surathkal, Srinivasnagar  
MANGALORE- 575 025, D.K.

## ACKNOWLEDGEMENT

This journey to realize a life-long dream of obtaining Ph.D. degree would not have been possible without the support of many individuals who have been there in my thick and thin. In that sense, this journey has also been theirs as it is mine. In this short space, I wish to acknowledge that support which made this dream possible for me.

As it is said that a great teacher makes good student. The role of a research supervisor is of paramount importance for shaping the Ph.D. degree. Therefore, it is my duty to acknowledge the ever supporting and generous Prof. Badekai Ramachandra Bhat for being a constant source of everlasting support and inspiration. His insightfulness, guidance, patience and thoughtfulness have always been conveyed and included positively by our research group. It has been a fortune to have him as an advisor and to have freedom to explore and evaluate the ideas. I have great admiration towards him for being a wonderful teacher and above all a great human being.

I am grateful to my RPAC members Prof. D. Krishna Bhat, Dept of Chemistry and Prof. S. M. Kulkarni, Dept of Mechanical Engineering. Their encouragement, perceptive comments and fruitful discussions throughout the progress of my research work have been success driving factors towards accomplishment of my objectives.

I would like to thank Prof. D. Uday Kumar, Prof. A. M. Isloor, Prof. D. Krishna Bhat and Prof. B. Ramachandra Bhat who have extended administrative facility for my Ph.D. work in their tenure as the Head of the Department of Chemistry. I would like to thank Prof. M. Govinda Raj, Dept. of Mining Engineering and Prof. Katta Venkataramana, Dept of Civil Engineering for their extensive support and suggestions throughout the journey of my Ph.D. I am thankful to the Prof. Swapan Bhattacharya, Former Director of NITK in this Ph.D. journey. I am thankful to the National Institute of Technology Karnataka, Surathkal for providing an opportunity to conduct my research work and faculty members of the chemistry department for their good wishes.

I am thankful to the kind assistance of Scientium Analyze Solutions Jaipur, MRC MNIT Jaipur, SAIF/CRNTS IIT Bombay, AMRC IIT Mandi, ACNSMM Amrita Vishwa Vidyapeetham, STIC CUSAT Kochi, Dept. of Metallurgy and Materials Engg., Dept. of Chemical Engg. NITK Surathkal, for extending their sophisticated experimental and characterization facilities.

I am grateful to all the non-teaching staff of the Dept. of Chemistry, NITK Surathkal for extending their kind assistance and made the time spent in the department comfortable. I wish

to state special gratitude to Mrs. Sharmila Nandini & Mr. Prashanth for his care and help in all the official matter without fail.

The research tenure can be hectic if not for the enthusiastic team of lab mates to cheer you up. I would acknowledge a very supportive team of fellow research scholars, Dr. Pooja Bhat, Dr. Raghavendra Prasad, Dr. Lolakshi Mahesh Kumar, Dr. Ansari Rashida Bano Maqbool Hasan, Dr. Praveen Mishra, Mr. Madhu N. Nimbalkar, Miss Lavanya rao, Miss Fiona and Miss Vishrutha KS and Mr. Shreeganesh Hedge for their company during my Ph.D. tenure and being steady support throughout the course of Ph.D. I cannot leave to thank my supportive friends within and outside the department, and few more for being there as constant source of joy and support.

I would like to express an extreme sense of gratefulness to my family members, especially my parents, my brother , my cousin Babu and my grandparents.

Finally, I conclude with an abundance of thanks to all those who have helped me directly or indirectly in making this dissertation a possibility.

## ABSTRACT

The thesis titled “*Synthesis and Characterization of 3d-Metal Nanoparticles immobilized onto Graphene Oxide Nanocomposite for its Applications in Adsorption and Catalysis*” encompass the work on 2D graphene oxide metal nanocomposites, particularly the metal nanoparticles/complexes to the ferrites for the prospective use as materials for adsorption and catalytic applications. A new route to obtain the mixed ferrite by binary solvent system is discussed in the adsorption applications. The graphene nanocomposites in their native state were found to be highly useful for the removal of cationic and anionic pollutants such as MB, RB, CR, Pb(II) & Cd(II). The removal rate of 95.1% for the pollutant MB after 5<sup>th</sup> consecutive cycles by GO-Fe/CPTMS-SiO<sub>2</sub>@MF adsorbent under the optimized conditions. The removal rate of MB dye from the real wastewater is around 90.1%. But the maximum adsorption capacity ( $q_e$ ) for the desorption studies on the GO-Fe/CPTMS-SiO<sub>2</sub>@MF adsorbent for MB dye on simulated wastewater is 1794.34 mg g<sup>-1</sup> and for metal ion Pb(II) is 1806.45 mg g<sup>-1</sup> is highest among the other dyes and metal ions. Due to the spinel structure of mixed ferrite nanoparticle in the GO-Fe/CPTMS-SiO<sub>2</sub>@MF adsorbent with high surface area and superparamagnetic nature helps in the effective removal of pollutants from the simulated and real wastewater. The catalyst CoASGO has been used in the Suzuki cross-coupling reaction with a maximum yield of 97.4%. It can be recycled up to 6 regenerative cycles effectively and hence it can be used as an excellent catalyst for the cross-coupling reactions. The work presented in this thesis demonstrates that these nanocomposites found to be effective in the adsorption and catalytic applications.

**Keywords:** Graphene oxide, Adsorbent, Catalyst, Cross-coupling, Adsorption capacity.

# TABLE OF CONTENTS

LIST OF FIGURES .....	viii
LIST OF TABLES .....	xvii
LIST OF ABBREVIATIONS .....	xx
CHAPTER-1.....	1
INTRODUCTION.....	1
1.1 NANOMATERIALS.....	2
1.1.1 Nanoparticle Synthesis .....	3
1.2 GRAPHENE.....	4
1.2.1 Introduction.....	4
1.2.2 Properties of graphene.....	6
1.2.3 Potential applications of Graphene .....	7
1.2.4 Synthesis of graphene .....	7
1.2.4.1 Mechanical Exfoliation of Graphite (Scotch-tape method).....	7
1.2.4.2 Liquid phase Exfoliation .....	8
1.2.4.3 Epitaxial Growth.....	8
1.2.4.4 Chemical Synthesis .....	8
1.3 TRANSITION METALS NANOPARTICLES.....	9
1.3.1 Schiff Base Metal Complexes .....	9
1.3.2 Basic properties of transition metal complexes .....	10
1.3.3 Nanoparticles.....	10
1.4 SILANE COUPLING GROUPS.....	11
1.5 APPLICATIONS OF NANOCOMPOSITES IN CATALYSIS .....	12
1.5.1 Introduction to catalysis .....	12
1.5.2 History.....	12
1.5.3 Technical perspective.....	13
1.5.4 Classification of Catalysis.....	13
1.5.5 Characteristics of catalytic reactions .....	15
1.5.6 Types of catalysts .....	17
1.5.5.1 Homogeneous catalysts.....	18
1.5.5.2 Biocatalysts .....	19
1.5.5.3 Heterogeneous catalysts.....	21
1.5.5.4 Comparison of Heterogeneous catalysis over homogeneous catalysis.....	22
1.5.6 Catalyst Deactivation.....	22

1.5.7 Catalytic application in Coupling reactions .....	22
1.5.7.1 Suzuki cross-coupling .....	22
1.6 ADSORPTION.....	24
1.6.1 Water pollution and sewage treatment .....	24
1.6.2 Types of Dyes.....	26
1.6.3 Effects of dyes .....	27
1.7 ADSORPTION MODELS.....	33
1.7.1 Adsorption Isotherms .....	33
1.7.2 Thermodynamic Studies.....	35
1.7.3 Adsorption Kinetic Studies .....	35
1.8 VISION .....	36
CHAPTER-2.....	38
STATE OF THE WORK .....	38
2.1 LITERATURE SURVEY.....	39
2.1.1 History of Suzuki cross-coupling reaction .....	39
2.1.2 Emergence of other transition metals as catalysts for Suzuki cross-coupling reactions .....	40
2.1.3 Graphene as supportive materials for nanoparticles in Suzuki cross-coupling reactions .....	41
2.1.4 Graphene oxide metal nanoparticles as adsorbent in the removal of organic and inorganic pollutants .....	45
2.1.6 Ferrites as an adsorbent .....	48
2.2 SUMMARY OF LITERATURE REVIEW.....	51
2.3 PROPOSED WORK.....	51
2.3.1 Scope of the work .....	51
2.3.2 Motivation.....	53
2.4 OBJECTIVES .....	54
CHAPTER-3.....	56
Synthesis of copper complex immobilized on to graphene nanosheet as a heterogeneous catalyst for Suzuki cross-coupling reaction .....	56
3.1. INTRODUCTION.....	57
3.2. EXPERIMENTAL .....	59
3.2.1 Chemicals required .....	59
3.2.2 Synthesis of 3-aminopropyl trimethoxysilane functionalized-graphene oxide (AGO) .....	59
3.2.3 Synthesis of Cu-Schiff base complex (CuL).....	59
3.2.4 Synthesis of Cu-Schiff base immobilized Graphene oxide (CAGO).....	60
3.2.5 Suzuki coupling reaction and yield.....	60



3.2.6 Characterization Techniques .....	60
<b>3.3. RESULTS AND DISCUSSION .....</b>	<b>61</b>
3.3.1 Vibrational Spectroscopy (FTIR) .....	61
3.3.2 UV-Vis Spectroscopy (UV) .....	62
3.3.3 X-ray Diffraction (XRD) .....	63
3.3.4 SEM & EDS (Scanning Electron Microscopy & Energy Dispersive X-ray Spectroscopy).....	64
3.3.5 Transmission Electron Microscopy (TEM & HR-TEM).....	66
3.3.6 X-ray photoelectron spectroscopy (XPS).....	67
3.3.7 Thermal Analysis (TGA) .....	69
3.3.8 Suzuki cross-coupling reaction .....	70
<b>3.4 CONCLUSIONS .....</b>	<b>75</b>
<b>CHAPTER-4.....</b>	<b>77</b>
<b>Synthesis of Cobalt Schiff base Graphene nanocomposite for the effective catalytic applications in Suzuki cross-coupling reactions .....</b>	<b>77</b>
<b>4.1 INTRODUCTION.....</b>	<b>78</b>
<b>4.2 EXPERIMENTAL SECTION .....</b>	<b>80</b>
4.2.1 Chemicals required .....	80
4.2.2 Synthesis of Graphene oxide (GO) .....	80
4.2.3 Synthesis of 3-aminopropyl trimethoxysilane functionalized-GO (ASGO).....	80
4.2.4 Synthesis of Cobalt oxide particles .....	80
4.2.5 Synthesis of graphene oxide immobilized cobalt Schiff base complexes (CoASGO) ...	81
4.2.6 Experimental procedure.....	81
4.2.7 Characterization Techniques .....	82
<b>4.3 RESULTS AND DISCUSSION .....</b>	<b>82</b>
4.3.1 Vibrational Spectroscopy (FTIR) .....	82
4.3.2 X-ray Diffraction (XRD) .....	84
4.3.3 SEM & EDS (Scanning Electron Microscopy & Energy Dispersive X-ray Spectroscopy).....	85
4.3.4 Transmission Electron Microscopy (TEM) .....	87
4.3.5 X-ray photoelectron spectroscopy (XPS).....	89
4.3.6 Thermal analysis .....	90
4.3.6.1 Thermogravimetric analysis (TGA) .....	90
4.3.6.2 ICP-AES Analysis .....	91
4.3.7 Suzuki cross-coupling reaction .....	91
<b>4.4 CONCLUSIONS .....</b>	<b>96</b>
<b>CHAPTER-5.....</b>	<b>98</b>

<b>Synthesis of Cobalt oxide-polypyrrole polymer and functionalized onto Graphene oxide for the efficient removal of dyes and heavy metal pollutants from aqueous effluents .....</b>	<b>98</b>
<b>5.1. INTRODUCTION.....</b>	<b>99</b>
<b>5.2. EXPERIMENTAL SECTION .....</b>	<b>102</b>
5.2.1 Chemical Required .....	102
5.2.2 Synthesis of Graphene Oxide (GO) .....	102
5.2.3 Synthesis of Co <sub>3</sub> O <sub>4</sub> nanoparticle (CO).....	102
5.2.4 Synthesis of Cobalt Oxide-Polypyrrole (COPY) .....	103
5.2.5 Synthesis of Cobalt Oxide-Polypyrrole/GO Composite (COPYGO) .....	103
5.2.6 Batch adsorption experiment.....	104
5.2.7 Isotherms Experiment .....	105
5.2.8 Kinetic Studies.....	105
5.2.9 Adsorption and recycling performances of COPYGO in model (actual) wastewater.....	106
5.2.10 Characterization Techniques .....	106
<b>5.3 RESULTS AND DISCUSSIONS .....</b>	<b>107</b>
5.3.1 Vibrational Spectroscopy (FTIR) .....	107
5.3.2 X-ray diffraction (XRD) .....	108
5.3.3 Scanning Electron Microscopy (FE-SEM).....	109
5.3.4 Transmission Electron Microscopy (TEM & HR-TEM).....	111
5.3.5 Thermogravimetric analysis (TGA) .....	112
5.3.6 Zeta potential.....	113
5.3.7 Vibrating-sample Magnetometry (VSM).....	114
5.3.8 X-ray photoelectron spectroscopy (XPS).....	115
5.3.9 N <sub>2</sub> Adsorption-Desorption Isotherms (BET) .....	117
5.3.10 Raman Spectroscopy.....	119
5.3.11 Effect of initial concentration on adsorption capacity .....	120
5.3.12 Effect of pH on adsorption capacity .....	120
5.3.13 Effect of adsorbent dosage on adsorption capacity.....	122
5.3.14 Effect of contact time on adsorption.....	123
5.3.15 Adsorption Isotherm studies .....	124
5.3.16 Van't Hoff plot (Thermodynamic studies).....	131
5.3.17 Adsorption Kinetic Studies .....	133
5.3.18 Activation energy (E <sub>a</sub> ).....	139
5.3.19 Cycle regeneration .....	139
5.3.20 XPS Analysis & FTIR Spectra of COPYGO after adsorption of Pb(II) & Cd(II) .....	141

5.3.21 TEM Analysis of COPYGO after uptake of MB and CR .....	144
5.3.22 Recycling evaluation of COPYGO in model(actual) wastewater .....	146
5.3.23 Adsorption of real wastewater on COPYGO .....	147
5.3.24 Recyclability studies of the real wastewater .....	149
5.4 CONCLUSIONS .....	150
CHAPTER-6.....	152
Synthesis of GO-CeO <sub>2</sub> @CoFe <sub>2</sub> O <sub>4</sub> nanocomposite by hydrothermal method for the effective adsorption of cationic and anionic pollutants from textile wastewater.....	152
6.1 INTRODUCTION.....	153
6.2 EXPERIMENTAL SECTION .....	154
6.2.1 Chemicals required.....	154
6.2.2 Synthesis of Graphene oxide (GO) .....	154
6.2.3 Synthesis of Nanoceria (CeO <sub>2</sub> ).....	154
6.2.4 Synthesis of Cobalt ferrite Nanoparticle (CoFe <sub>2</sub> O <sub>4</sub> ) .....	155
6.2.5 Synthesis of Graphene oxide-nanoceria composite (GO-CeO <sub>2</sub> ).....	155
6.2.6 Synthesis of Graphene oxide nanoceria cobalt ferrite composite (GO-CeO <sub>2</sub> @CoFe <sub>2</sub> O <sub>4</sub> ) .....	155
6.2.7 Adsorption experiments .....	156
6.2.8 Stability and regeneration tests .....	156
6.2.9 Adsorption and recycling performances of GO-CeO <sub>2</sub> @CoFe <sub>2</sub> O <sub>4</sub> in model waste water .....	157
6.2.10 Characterization Techniques .....	157
6.3 RESULTS AND DISCUSSION .....	158
6.3.1 Vibrational Spectroscopy (FTIR) .....	158
6.3.2 X-ray Diffraction (XRD) .....	159
6.3.3 Raman Spectroscopy.....	160
6.3.4 Thermogravimetric Analysis (TGA) .....	161
6.3.5 Morphology Studies (FE-SEM & EDS) .....	162
6.3.6 Transmission Electron Microscopy (TEM) .....	164
6.3.7 Vibrating-sample Magnetometry (VSM).....	167
6.3.8 N <sub>2</sub> Adsorption-Desorption Isotherms (BET) .....	168
6.3.9 Zeta potential.....	170
6.3.10 X-ray Electron Spectroscopy (XPS) .....	171
6.3.11 Effect of pH of pollutants on adsorption.....	173
6.3.12 Effect of initial concentration of adsorbent on adsorption capacity .....	175
6.3.13 Effect of time on adsorption.....	177
6.3.14 Effect of adsorbent dosage on adsorption capacity.....	177

6.3.15 Effect of Ionic strength .....	178
6.3.16 Adsorption Isotherm Studies .....	180
6.3.17 Van't Hoff plot (Thermodynamic studies).....	190
6.3.18 Adsorption Kinetic Studies .....	194
6.3.19 Activation energy of adsorption.....	201
6.3.20 Stability and reusability of adsorbent .....	202
6.3.21 Recycled studies.....	206
6.3.22 Proposed mechanism for adsorption.....	214
6.3.23 Adsorption and recycling performances of GO-CeO <sub>2</sub> @CoFe <sub>2</sub> O <sub>4</sub> in model wastewater .....	216
6.3.24 Adsorption of real wastewater on GO-CeO <sub>2</sub> @CoFe <sub>2</sub> O <sub>4</sub> .....	216
6.3.25 Recyclability studies of the real wastewater .....	219
<b>6.4 CONCLUSIONS .....</b>	<b>220</b>
<b>CHAPTER-7.....</b>	<b>221</b>
<b>Synthesis of novel, magnetic GO-Fe/CPTMS-SiO<sub>2</sub>@MF composite for the removal of dyes and heavy metal ions .....</b>	<b>221</b>
<b>7.1 INTRODUCTION.....</b>	<b>222</b>
<b>7.2 EXPERIMENTAL SECTION .....</b>	<b>223</b>
7.2.1 Chemicals required .....	223
7.2.2 Synthesis of Graphene oxide (GO) .....	223
7.2.3 Synthesis of Iron oxide Nanoparticle (Fe).....	223
7.2.3 Synthesis of Mixed Ferrite nanoparticle (MF) .....	224
7.2.5 Synthesis of Graphene-Iron oxide composite (GO-Fe).....	224
7.2.6 Synthesis of Mixed Ferrite-Tetraethyl Orthosilicate (SiO <sub>2</sub> @MF).....	224
7.2.7 Synthesis of Mixed Ferrite-Tetraethyl Orthosilicate and 3-Chloropropyltrimethoxy silane (CPTMS-SiO <sub>2</sub> @MF) .....	224
7.2.8 Synthesis of Mixed Ferrite Nanocomposites (GO-Fe/CPTMS-SiO <sub>2</sub> @MF) .....	225
7.2.9 Adsorption experiments .....	225
7.2.10 Stability and reusability tests .....	226
7.2.10 Adsorption and recycling performances of GO-Fe/CPTMS-SiO <sub>2</sub> @MF in model waste water .....	227
7.2.11 Characterization Techniques .....	227
<b>7.3 RESULTS AND DISCUSSION .....</b>	<b>227</b>
7.3.1 Vibrational Spectroscopy (FTIR) .....	227
7.3.2 X-ray Diffraction (XRD) .....	230
7.3.3 Raman Spectroscopy.....	231
7.3.4 Thermal Analysis (TGA).....	233

7.3.5 Scanning Electron Microscopy and Energy Dispersive X-ray Spectroscopy (FE-SEM & EDS) .....	233
7.3.6 Transmission Electron Microscopy (TEM) .....	236
7.3.7 Vibrating-sample Magnetometry (VSM).....	238
7.3.8 N <sub>2</sub> adsorption–desorption studies .....	239
7.3.9 Zeta potential.....	241
7.3.10 X-ray photoelectron Spectroscopy (XPS) .....	242
7.3.11 Effect of initial solution pH of pollutants on adsorption .....	246
7.3.12 Effect of adsorbent dosage on adsorption .....	248
7.3.13 Effect of capacity of adsorbate on adsorption capacity .....	250
7.3.14 Effect of contact time on adsorption.....	251
7.3.15 Effect of Ionic strength .....	251
7.3.16 Adsorption Isotherm Studies .....	253
7.3.17 Van't Hoff plot (Thermodynamic studies).....	261
7.3.18 Adsorption Kinetic Studies .....	265
7.3.19 Activation energy of adsorption.....	272
7.3.20 Stability and reusability of adsorbent .....	273
7.3.21 Recycled graphs.....	276
7.3.22 Proposed mechanism for adsorption.....	285
7.3.23 Adsorption and recycling performances of GO-Fe/CPTMS-SiO <sub>2</sub> @MF in model waste water .....	287
7.3.24 Adsorption of real wastewater on GO-Fe/CPTMS-SiO <sub>2</sub> @MF .....	288
7.3.25 Regeneration studies .....	290
<b>7.4 CONCLUSIONS .....</b>	<b>291</b>
<b>CHAPTER-8.....</b>	<b>293</b>
<b>CONCLUSIONS .....</b>	<b>293</b>
<b>8.1 SUMMARY OF RESEARCH WORK .....</b>	<b>294</b>
<b>8.2 CONCLUSIONS .....</b>	<b>303</b>
<b>8.3 FUTURE WORK.....</b>	<b>304</b>
<b>REFERENCES: .....</b>	<b>305</b>
<b>LIST OF PUBLICATIONS .....</b>	<b>349</b>
<b>LISTS OF CONFERENCES .....</b>	<b>349</b>
<b>LIST OF WORKSHOPS.....</b>	<b>351</b>
<b>CURRICULUM VITAE.....</b>	<b>352</b>

# LIST OF FIGURES

## CHAPTER-1

Figure 1.1. Two technological approaches employed in the nanoworld.....	4
Figure 1.2. Carbon materials as fullerenes, carbon nanotubes (CNTs) and graphite (0D), 1D and 3D respectively can be derived from single layer graphene (2D).....	5
Figure 1.3. General Scheme of Schiff base.....	10
Figure 1.4. Diagram of the potential energy of catalyzed and uncatalyzed reactions.....	17
Figure 1.5. Pictorial representation of the types of catalysts.....	18
Figure 1.6. General reaction mechanism of Suzuki coupling reaction.....	24
Figure 1.7. Diagrammatic representation of industrial wastewater affecting the entire ecosystem.....	26
Figure 1.8. Schematic representation of Dyes classification.....	26
Figure 1.9. Nature of effects of Textile wastewater in our food chain.....	28
Figure 1.10. Various techniques for the treatment of wastewater.....	32

## CHAPTER-3

Scheme 3.1. Synthesis of CAGO catalyst.....	60
Figure 3.1. FTIR spectra of a) GO, b) AGO and c) CAGO.....	62
Figure 3.2. UV spectra of a) GO, b) AGO, and c) CAGO.....	63
Figure 3.3. XRD graph of GO, AGO, and CAGO complex.....	64
Figure 3.4. SEM of a) GO, b) AGO, c) CAGO.....	65
Figure 3.5. EDS of a) GO, b) AGO and c) CAGO.....	66
Figure 3.6. TEM images of a) GO, b) AGO, c) SAED of AGO, d) CAGO, e) HR-TEM of CAGO and f) SAED of CAGO.....	67
Figure 3.7. XPS analysis of CAGO composite with a) elemental survey, b) C 1s scan, c) Si 2p scan, d) N 1s scan, e) Cu 2p scan and f) O 1s scan.....	69
Figure 3.8. TGA of the a) GO, and b) CAGO.....	70
Figure 3.9. The effect of (a) catalyst amount and (b) reaction time on the GC yield of Suzuki coupling reaction.....	74
Figure 3.10. Recycling ability of CAGO as catalyst for Suzuki coupling reactions.....	75
Figure 3.11. TEM images of fresh and used catalyst after 5th cycle a) fresh catalyst b) used catalyst.....	75

## CHAPTER-4

Scheme 4.1. Schematic representation for the synthesis of CoASGO complex.....	81
Figure 4.1. FTIR spectra of CoASGO complex with GO.....	83
Figure 4.2. FTIR Spectra of amino functionalized GO (ASGO).....	84
Figure 4.3. XRD graph of a) CoASGO complex and b) Cobalt oxide particles .....	85
Figure 4.4. SEM of a) GO, b) ASGO, c,d) CoASGO, and e) EDS image of CoASGO.....	86
Figure 4.5. TEM images of a) GO, b) ASGO, c) SAED of ASGO, d) CoASGO, e) SAED of CoASGO, f) average size of TEM image of CoASGO, g) HR-TEM of CoASGO, h) SAED of HR-TEM of CoASGO and i) average size of HR-TEM image of CoASGO.....	89
Figure 4.6. XPS analysis of CoASGO composite with a) elemental survey, b) C 1s scan, c) N 1s scan, d) O 1s scan, e) Si 2p scan and f) Co 2p scan.....	90
Figure 4.7. TGA graph shows the a) GO and b) the synthesized catalyst.....	91
Figure 4.8. The effect of (a) catalyst amount and (b) reaction time on the GC yield of Suzuki coupling reaction.....	94
Figure 4.9. Recycling ability of CoASGO as catalyst for Suzuki coupling reactions.....	96
Figure 4.10. TEM images of Fresh and used catalyst after 5 <sup>th</sup> cycle a) Fresh catalyst b) used catalyst.....	96

## CHAPTER-5

Scheme 5.1. Synthesis of COPYGO.....	104
Figure 5.1. FTIR spectra of Co <sub>3</sub> O <sub>4</sub> nanoparticle, COPY & COPYGO.....	108
Figure 5.2. XRD pattern for the Co <sub>3</sub> O <sub>4</sub> nanoparticle, COPY and COPYGO.....	109
Figure 5.3. FE-SEM images of a, b) CO c, d) COPY and e, f) COPYGO.....	110
Figure 5.4. TEM images of CO (a,b,c,d), COPYGO (e,f,g) & SAED pattern of COPYGO (f).....	112
Figure 5.5. TGA of GO & COPYGO.....	113
Figure 5.6. Zeta potential of COPYGO at different pH.....	114
Figure 5.7. Applied magnetic field plot of Co <sub>3</sub> O <sub>4</sub> nanoparticles (CO) and COPYGO.....	115
Figure 5.8. XPS Spectrum of a) Elemental survey of COPYGO b) C 1s, c) Co 2p, d) N 1s and e) O 1s.....	117
Figure 5.9a. N <sub>2</sub> adsorption-desorption isotherms of COPYGO.....	118
Figure 5.9b. Pore size distribution curves of COPYGO.....	118

Figure 5.10. Raman spectra of both GO and COPYGO.....	119
Figure 5.11. Adsorption of a) MB b) CR c) Pb(II) & d) Cd(II) as a function of concentration at various temperature.....	120
Figure 5.12. Removal rate of the MB, CR, Pb(II) and Cd(II) at various pH.....	122
Figure 5.13. Proposed mechanism of the metal ions: Pb(II) & Cd(II).....	122
Figure 5.14. Different adsorbent doses with the adsorption capacity $q_e$ a) MB, b) CR, c) Pb(II) and d) Cd(II).....	123
Figure 5.15. Effect of time (t) with the adsorption capacity ( $q_t$ ).....	124
Figure 5.16. Adsorption isotherms at four different temperatures for MB: a) 308.5 K b) 313.5 K c) 318.5 K & d) 323.5 K.....	127
Figure 5.17. Adsorption isotherms at four different temperatures for CR: a) 308.5 K b) 313.5 K c) 318.5 K & d) 323.5 K.....	128
Figure 5.18. Adsorption isotherms at four different temperatures for Pb(II): a) 308.5 K b) 313.5 K c) 318.5 K & d) 323.5 K.....	128
Figure 5.19. Adsorption isotherms at four different temperatures for Cd(II): a) 308.5 K b) 313.5 K c) 318.5 K & d) 323.5 K.....	129
Figure 5.20. Van't Hoff plots for the four adsorbates a) MB, b) CR, c) Pb(II) & d) Cd(II)...	132
Figure 5.21. Pseudo first order kinetics for the four adsorbates: a) MB, b) CR, c) Pb(II) & d) Cd(II).....	132
Figure 5.22. Pseudo second order kinetics for the four adsorbates: a) MB, b) CR, c) Pb(II) & d) Cd(II).....	136
Figure 5.23. Intraparticle diffusion for the four adsorbates: a) MB, b) CR, c) Pb(II) & d) Cd(II).....	137
Figure 5.24. Pseudo second order at 318.5 K for the four adsorbates: MB, CR, Pb(II) & Cd(II).....	137
Figure 5.25. Arrhenius plot for the four adsorbates at different temperatures.....	139
Figure 5.26. Regenerative capacity of the COPYGO for four adsorbates: MB, CR, Pb(II) & Cd(II).....	140
Figure 5.27. Proposed mechanism for the pollutants (MB, CR, Pb(II) & Cd(II) adsorption on the COPYGO.....	141
Figure 5.28. XPS spectra of COPYGO with the after the Pb(II) adsorption: a) elemental survey of COPYGO after Pb(II) adsorption, b) Pb 4f, c) C 1s, d) Co 2p, e) O 1s & f) N 1s.....	143
Figure 5.29. XPS of COPYGO with the Cd(II) adsorption: a) elemental survey of COPYGO after Cd(II) adsorption & b) Cd 3d, c) C 1s, d) Co 2p, e) O 1s & f) N 1s.....	144



Figure 5.30. FTIR spectra of COPYGO after adsorption of Pb(II) and Cd(II).....	144
Figure 5.31. Recycled HR-TEM images of a,b) MB reused COPYGO, c) SAED of MB reused COPYGO & d,e) CR reused COPYGO, f) SAED of CR reused COPYGO.....	145
Figure 5.32. Adsorption and recycling performance of COPYGO in model wastewater.....	147
Figure 5.33. Regenerative capacity of the real wastewater for the pollutants: MB, CR, Pb(II) & Cd(II).....	150

## CHAPTER-6

Scheme 6.1. Synthesis of GO-CeO <sub>2</sub> @CoFe <sub>2</sub> O <sub>4</sub> .....	154
Figure 6.1. FTIR spectra of CoFe <sub>2</sub> O <sub>4</sub> nanoparticle, GO-CeO <sub>2</sub> & GO-CeO <sub>2</sub> @CoFe <sub>2</sub> O <sub>4</sub> .....	158
Figure 6.2. FTIR spectra of GO-CeO <sub>2</sub> & Nanoceria (CeO <sub>2</sub> ).....	159
Figure 6.3. XRD pattern for the CoFe <sub>2</sub> O <sub>4</sub> nanoparticle, CeO <sub>2</sub> , GO-CeO <sub>2</sub> & GO-CeO <sub>2</sub> @CoFe <sub>2</sub> O <sub>4</sub> .....	160
Figure 6.4. Raman spectra of GO and GO-CeO <sub>2</sub> @CoFe <sub>2</sub> O <sub>4</sub> .....	161
Figure 6.5. TGA of GO & GO-CeO <sub>2</sub> @CoFe <sub>2</sub> O <sub>4</sub> .....	162
Figure 6.6. FE-SEM images of (a) CoFe <sub>2</sub> O <sub>4</sub> , (b)CeO <sub>2</sub> , (c)GO-CeO <sub>2</sub> & (d) GO-CeO <sub>2</sub> @CoFe <sub>2</sub> O <sub>4</sub> .....	163
Figure 6.7. EDS analysis of (a) CoFe <sub>2</sub> O <sub>4</sub> , (b)CeO <sub>2</sub> , (c)GO-CeO <sub>2</sub> & (d) GO-CeO <sub>2</sub> @CoFe <sub>2</sub> O <sub>4</sub> .....	164
Figure 6.8. TEM images of CoFe <sub>2</sub> O <sub>4</sub> (a) TEM, (b) HR-TEM & (e) SAED pattern and GO-CeO <sub>2</sub> @CoFe <sub>2</sub> O <sub>4</sub> (c) TEM, (d) HR-TEM & (f) SAED pattern.....	166
Figure 6.9. Applied magnetic field plot of CoFe <sub>2</sub> O <sub>4</sub> and GO-CeO <sub>2</sub> @CoFe <sub>2</sub> O <sub>4</sub> .....	168
Figure 6.10. N <sub>2</sub> adsorption-desorption isotherms of CoFe <sub>2</sub> O <sub>4</sub> , GO-CeO <sub>2</sub> & GO-CeO <sub>2</sub> @CoFe <sub>2</sub> O <sub>4</sub> .....	170
Figure 6.11. Pore size distribution curves of a) CoFe <sub>2</sub> O <sub>4</sub> , b) GO-CeO <sub>2</sub> & c) GO-CeO <sub>2</sub> @CoFe <sub>2</sub> O <sub>4</sub> com.....	170
Figure 6.12. Zeta potential of GO-CeO <sub>2</sub> @CoFe <sub>2</sub> O <sub>4</sub> at different pH.....	171
Figure 6.13. XPS spectra of GO-CeO <sub>2</sub> @CoFe <sub>2</sub> O <sub>4</sub> : (a) Elemental survey, (b) C 1s, (c) Ce 3d, (d) O 1s, (e) Co 2p & (f) Fe 2p.....	173
Figure 6.14. Adsorption of a) MB b) RB c) CR d) Pb(II) & e) Cd(II) as a function of concentration at various temperature.....	175
Figure 6.15. Proposed mechanism of the metal ions: Pb(II) & Cd(II).....	175

Figure 6.16. Adsorption of a) MB b) RB c) CR d) Pb(II) & e) Cd(II) as a function of initial concentration of adsorbate on adsorption capacity.....	176
Figure 6.17. Effect of time (t) with the adsorption capacity (qt).....	177
Figure 6.18. Different adsorbent doses with the adsorption capacity $q_e$ a) MB, b) RB, c) CR, d) Pb(II) and e) Cd(II).....	178
Figure 6.19. Effect of ionic strength with the removal rate of dyes a) MB, b) RB & c) CR.....	179
Figure 6.20. Effect of ionic strength with the removal rate of metal ions a) Pb(II) and b) Cd(II).....	180
Figure 6.21. Adsorption isotherms at five different temperatures for MB: a) 308.5 K b) 313.5 K c) 318.5 K d) 323.5 K & e) 328.5 K.....	182
Figure 6.22. Adsorption isotherms at five different temperatures for RB: a) 308.5 K b) 313.5 K c) 318.5 K d) 323.5 K & e) 328.5 K.....	183
Figure 6.23. Adsorption isotherms at five different temperatures for CR: a) 308.5 K b) 313.5 K c) 318.5 K d) 323.5 K & e) 328.5 K.....	184
Figure 6.24. Adsorption isotherms at five different temperatures for Pb(II): a) 308.5 K b) 313.5 K c) 318.5 K d) 323.5 K & e) 328.5 K.....	185
Figure 6.25. Adsorption isotherms at five different temperatures for Cd(II): a) 308.5 K b) 313.5 K c) 318.5 K d) 323.5 K & e) 328.5 K.....	186
Figure 6.26. Separation factor $R_L$ values for the adsorbates a) MB, b) RB, c) CR, d) Pb(II) & e) Cd(II).....	190
Figure 6.27. Van't Hoff plots for the adsorbates a) MB, b) RB, c) CR, d) Pb(II) & e) Cd(II).....	192
Figure 6.28. Pseudo first order kinetics for the five adsorbates: a) MB, b) RB, c) CR, d) Pb(II) & e) Cd(II).....	195
Figure 6.29. Pseudo second order kinetics for the five adsorbates: a) MB, b) RB, c) CR, d) Pb(II) & e) Cd(II).....	196
Figure 6.30. Intraparticle diffusion for the five adsorbates: a) MB, b) RB, c) CR, d) Pb(II) & e) Cd(II).....	199
Figure 6.31. Arrhenius plot for the five adsorbates at different temperatures.....	202
Figure 6.32. Stability of GO-CeO <sub>2</sub> @CoFe <sub>2</sub> O <sub>4</sub> at different pH.....	203
Figure 6.33. Regenerative capacity of the GO-CeO <sub>2</sub> @CoFe <sub>2</sub> O <sub>4</sub> for five adsorbates: MB, RB, CR, Pb(II) & Cd(II).....	204
Figure 6.34. Desorption studies of synthetic wastewater with GO-CeO <sub>2</sub> @CoFe <sub>2</sub> O <sub>4</sub> .....	205

Figure 6.35. Desorption studies of synthetic wastewater with adsorption capacity $q_e$ of regeneration cycles: a) MB, b) RB, c) CR, d) Pb(II) & e) Cd(II).....	206
Figure 6.36. XPS spectra of Pb(II) adsorbed GO-CeO <sub>2</sub> @CoFe <sub>2</sub> O <sub>4</sub> : a) elemental survey, b) C 1s, c) Ce 3d, d) O 1s, e) Co 2p, f) Fe 2p & g) Pb 4f.....	209
Figure 6.37. XPS spectra of Cd(II) adsorbed GO-CeO <sub>2</sub> @CoFe <sub>2</sub> O <sub>4</sub> : a) elemental survey, b) C 1s, c) Ce 3d, d) O 1s, e) Co 2p, f) Fe 2p & g) Pb 4f.....	211
Figure 6.38. FTIR Spectra of GO-CeO <sub>2</sub> @CoFe <sub>2</sub> O <sub>4</sub> , Pb(II) adsorbed & Cd(II) adsorbed.....	211
Figure 6.39. FTIR Spectra of GO-CeO <sub>2</sub> @CoFe <sub>2</sub> O <sub>4</sub> , MB dye adsorbed, RB dye adsorbed & CR dye adsorbed.....	212
Figure 6.40. TEM images of dyes adsorbed GO-CeO <sub>2</sub> @CoFe <sub>2</sub> O <sub>4</sub> : (a, b) MB dye, (g) SAED of MB adsorbed, (c, d) RB dye, (h) SAED of RB adsorbed (e, f) CR dye & (i) SAED of RB adsorbed.....	214
Figure 6.41. Proposed mechanism for the pollutants (MB, RB & CR) adsorption on the GO-CeO <sub>2</sub> @CoFe <sub>2</sub> O <sub>4</sub> composite.....	215
Figure 6.42. Adsorption and recycling performance of GO-CeO <sub>2</sub> @CoFe <sub>2</sub> O <sub>4</sub> in model wastewater.....	216
Figure 6.43. Regenerative capacity of the real wastewater for the pollutants: MB, RB, CR, Pb(II) & Cd(II).....	219

## CHAPTER-7

Scheme 7.1. Synthesis of GO-Fe/CPTMS-SiO <sub>2</sub> @MF.....	225
Figure 7.1. FTIR Spectra of MF, SiO <sub>2</sub> @MF, CPTMS-SiO <sub>2</sub> @MF & Composite (GO-Fe/CPTMS-SiO <sub>2</sub> @MF) .....	229
Figure 7.2. FTIR Spectra of GO-Fe & Fe.....	229
Figure 7.3. XRD pattern for the MF, CPTMS-SiO <sub>2</sub> @MF & GO-Fe/CPTMS-SiO <sub>2</sub> @MF Composite.....	230
Figure 7.4. XRD pattern for the GO-Fe & GO.....	231
Figure 7.5. Raman spectra of both GO & Composite (GO-Fe/CPTMS-SiO <sub>2</sub> @MF).....	232
Figure 7.6. TGA of GO & Composite (GO-Fe/CPTMS-SiO <sub>2</sub> @MF) .....	233
Figure 7.7. FE-SEM image of the: a) Fe <sub>3</sub> O <sub>4</sub> , b) GO-Fe, c) MF, d) SiO <sub>2</sub> @MF, e) CPTMS-SiO <sub>2</sub> @MF & f) GO-Fe/CPTMS-SiO <sub>2</sub> @MF.....	235
Figure 7.8. EDX analysis of the: a) Fe <sub>3</sub> O <sub>4</sub> , b) GO-Fe, c) MF, d) SiO <sub>2</sub> @MF, e) CPTMS-SiO <sub>2</sub> @MF & f) GO-Fe/CPTMS-SiO <sub>2</sub> @MF.....	236

Figure 7.9. TEM images of the a,b) MF, e) SAED pattern of MF, c,d) Composite & f) SAED pattern of Composite.....	237
Figure 7.10. Applied magnetic field plot of MF & Composite (GO-Fe/CPTMS-SiO <sub>2</sub> @MF) .....	239
Figure 7.11. N <sub>2</sub> adsorption-desorption isotherms of MF, GO-Fe & Composite (GO-Fe/CPTMS-SiO <sub>2</sub> @MF) .....	240
Figure 7.12. Pore size distribution of a) GO-Fe/CPTMS-SiO <sub>2</sub> @MF, b) GO-Fe & c) MF....	241
Figure 7.13. Zeta potential values of MF and Composite (GO-Fe/CPTMS-SiO <sub>2</sub> @MF) at different pH.....	242
Figure 7.14. XPS Spectrum of MF a) Elemental survey, b) C 1s, c) Co 2p, d) Fe 2p, e) Ni 2p, f) O 1s & g) Zn 2p.....	244
Figure 7.15. XPS spectrum of Composite(GO-Fe/CPTMS-SiO <sub>2</sub> @MF): a) Elemental survey, b) C 1s, c) Co 2p, d) Fe 2p, e) Ni 2p, f) O 1s, g) Si 2p & h) Zn 2p.....	246
Figure 7.16. Effect of pH on the adsorption of the pollutants: MB, RB, CR, Pb(II) & Cd(II) .....	248
Figure 7.17. Proposed mechanism for the metal ions Pb(II) & Cd(II) ions.....	248
Figure 7.18. Effect on adsorbent dosage on adsorption capacity upon pollutants a) MB, b) RB, c) CR, d) Pb(II) & e) Cd(II) .....	248
Figure 7.19. Adsorbent dosage on the adsorption of pollutants: a) MB, b) RB, c) CR, d) Pb(II) & e) Cd(II).....	250
Figure 7.20. Effect of time on the adsorption of pollutants on adsorbent.....	251
Figure 7.21. Ionic strength of dye adsorbed composite in synthetic wastewater.....	252
Figure 7.22. Ionic strength of metal adsorbed composite in synthetic wastewater.....	252
Figure 7.23. MB adsorption values for the four isotherms: a) Langmuir b) Freundlich c) DR & d) Temkin.....	255
Figure 7.24. RB adsorption values for the four isotherms: a) Langmuir b) Freundlich c) DR & d) Temkin.....	256
Figure 7.25. CR adsorption values for the four isotherms: a) Langmuir b) Freundlich c) DR & d) Temkin.....	256
Figure 7.26. Pb(II) adsorption values for the four isotherms: a) Langmuir b) Freundlich c) DR & d) Temkin.....	257
Figure 7.27. Cd(II) adsorption values for the four isotherms: a) Langmuir b) Freundlich c) DR & d) Temkin.....	258
Figure 7.28. R <sub>L</sub> values for the pollutants adsorption: a) MB, b) RB, c) CR, d) Pb(II) &	

e) Cd(II).....	261
Figure 7.29. Van't hoff plot for the pollutants adsorption: a) MB, b) RB, c) CR, d) Pb(II) & e) Cd(II).....	263
Figure 7.30. Pseudo first order values for the pollutants: a) MB, b) RB, c) CR, d) Pb(II) & e) Cd(II).....	266
Figure 7.31. Pseudo second order values for the pollutants: a) MB, b) RB, c) CR, d) Pb(II) & e) Cd(II).....	267
Figure 7.32. Intraparticle diffusion values for the pollutants: a) MB, b) RB, c) CR, d) Pb(II) & e) Cd(II).....	270
Figure 7.33. Activation energy of the pollutants adsorbed on composite (GO-Fe/CPTMS-SiO <sub>2</sub> @MF) .....	272
Figure 7.34. Stability of Fe's leaching on Fe <sub>3</sub> O <sub>4</sub> and GO-Fe/CPTMS-SiO <sub>2</sub> @MF Composite .....	273
Figure. 7.35. Recyclability studies of synthetic wastewater with GO-Fe/CPTMS-SiO <sub>2</sub> @MF.....	275
Figure. 7.36. Desorption studies of synthetic wastewater with GO-Fe/CPTMS-SiO <sub>2</sub> @MF.....	275
Figure. 7.37. Desorption studies of synthetic wastewater with adsorption capacity q <sub>e</sub> of regeneration cycles: a) MB, b) RB, c) CR, d) Pb(II) & e) Cd(II).....	276
Figure 7.38. XPS Spectrum of Pb(II) adsorbed composite: a) Elemental survey, b) C 1s, c) Co 2p, d) Fe 2p, e) Ni 2p, f) O 1s g) Pb 4f, h) Si 2p & i) Zn 2p.....	280
Figure 7.39. XPS Spectrum of Cd(II) adsorbed composite: a) Elemental Survey, b) C 1s, c) Co 2p, d) Fe 2p, e) Ni 2p, f) O 1s, g) Cd 3d, h) Si 2p & i) Zn 2p.....	282
Figure 7.40. FTIR Spectra of Composite & dye adsorbed composite: MB, RB & CR.....	282
Figure 7.41. FTIR Spectra of Composite & metal adsorbed composite: Pb(II) & Cd(II).....	283
Figure 7.42. TEM images of dye adsorbed composite: a,b) MB, g) SAED pattern of MB c,d) RB, h) SAED pattern of RB & e,f) CR & i) SAED pattern of CR.....	285
Figure 7.43. Proposed mechanism for the dyes MB, RB & CR.....	287
Figure 7.44. Recycling performances of GO-Fe/CPTMS-SiO <sub>2</sub> @MF in model wastewater...288	
Figure 7.45. Recyclability studies of real wastewater with GO-Fe/CPTMS-SiO <sub>2</sub> @MF.....	291

## CHAPTER-8

Figure 8.1. A plausible mechanism of CoASGO catalyst in Suzuki cross-coupling

reaction.....	296
Figure 8.2. The recyclability studies of Suzuki cross-coupling reaction of CoASGO and CAGO.....	297
Figure 8.3. The recyclability studies of pollutants in simulated wastewater on adsorbents a) COPYGO, b) GO- GO-CeO <sub>2</sub> @CoFe <sub>2</sub> O <sub>4</sub> & c) GO-Fe/CPTMS-SiO <sub>2</sub> @MF.....	298
Figure 8.4. Removal rate of model wastewater in adsorbent dosages, a) 10 mg and b) 20 mg.....	299
Figure 8.5. The recyclability studies of pollutants in real wastewater on adsorbents (a) COPYGO, (b) GO-CeO <sub>2</sub> @CoFe <sub>2</sub> O <sub>4</sub> & (c) GO-Fe/CPTMS-SiO <sub>2</sub> @MF.....	301

# LIST OF TABLES

## CHAPTER-1

Table 1.1: Different synthetic methods of Graphene.....	9
---	---

## CHAPTER-3

Table 3.1: Effect of various solvents and bases on yield at temp 80 °C.....	70
Table 3.2: GC yield of the products of various aryl halide and arylboronic acids at 80 °C.....	70
Table 3.3: Comparison catalytic yield of CAGO with control catalyst GO+CuL and only CuL complex.....	72

## CHAPTER-4

Table 4.1. Effect of various solvents and bases on yield at temp 80 °C.....	91
Table 4.2. GC yield of products at 80 °C.....	91

## CHAPTER-5

Table 5.1: The $M_s$ and $H_c$ values of CO nanoparticle & COPYGO.....	114
Table 5.2: Langmuir and Freundlich Isotherm for the COPYGO.....	129
Table 5.3: DR and Temkin Isotherm for the COPYGO.....	130
Table 5.4: Thermodynamics of the adsorbent COPYGO.....	133
Table 5.5: Kinetic parameters for Lagergren models for COPYGO.....	138
Table 5.6: Intraparticle diffusion model for COPYGO.....	139
Table 5.7: Analysis of the real wastewater sample.....	148
Table 5.8: Langmuir and Freundlich isotherms of real wastewater on COPYGO.....	149
Table 5.9: DR and Temkin isotherms of real wastewater on COPYGO.....	150
Table 5.10: Kinetic studies of real wastewater on COPYGO.....	150
Table 5.11: Recyclability studies of pollutants in real wastewater on COPYGO.....	151

## CHAPTER-6

Table 6.1: The $M_s$ and $H_c$ values of $CoFe_2O_4$ and $GO-CeO_2@CoFe_2O_4$ .....	168
Table 6.2: Pore characteristics of $CoFe_2O_4$ , $GO-CeO_2$ & $GO-CeO_2@CoFe_2O_4$ .....	170
Table 6.3: Langmuir and Freundlich Isotherm for the $GO-CeO_2@CoFe_2O_4$ .....	187
Table 6.4: DR and Temkin Isotherm for the $GO-CeO_2@CoFe_2O_4$ .....	188

Table 6.5: Thermodynamics of the adsorbent GO-CeO <sub>2</sub> @CoFe <sub>2</sub> O <sub>4</sub> .....	193
Table 6.6: Kinetic parameters for Lagergren models for GO-CeO <sub>2</sub> @CoFe <sub>2</sub> O <sub>4</sub> .....	197
Table 6.7: Intraparticle diffusion model for GO-CeO <sub>2</sub> @CoFe <sub>2</sub> O <sub>4</sub> .....	200
Table 6.8a: Percentage desorption efficiency of dyes over adsorbent using different Eluents.....	203
Table 6.8b: Percentage desorption efficiency of metal ions over adsorbent using different eluents.....	204
Table 6.9: Analysis of the real wastewater sample.....	216
Table 6.10: The adsorption isotherms of real wastewater on GO-CeO <sub>2</sub> @CoFe <sub>2</sub> O <sub>4</sub> .....	217
Table 6.11: DR and Temkin isotherms of real wastewater on GO-CeO <sub>2</sub> @CoFe <sub>2</sub> O <sub>4</sub> .....	217
Table 6.12: Kinetic studies of real wastewater on GO-CeO <sub>2</sub> @CoFe <sub>2</sub> O <sub>4</sub> .....	218
Table 6.13: The recyclability studies of pollutants such as MB, RB, CR, Pb(II) & Cd(II) over GO-CeO <sub>2</sub> @CoFe <sub>2</sub> O <sub>4</sub> .....	219

## CHAPTER-7

Table 7.1: M <sub>s</sub> and H <sub>c</sub> values of MF & GO-Fe/CPTMS-SiO <sub>2</sub> @MF.....	239
Table 7.2: Pore characteristics for the GO-Fe/CPTMS-SiO <sub>2</sub> @MF, MF and GO-Fe.....	241
Table 7.3: Langmuir & Freundlich Isotherm values for the pollutants adsorption: a) MB, b) RB, c) CR, d) Pb(II) & e) Cd(II).....	259
Table 7.4: DR & Temkin Isotherm values for the pollutants adsorption: a) MB, b) RB, c) CR, d) Pb(II) & e) Cd(II).....	260
Table 7.5: Thermodynamic studies for the pollutants adsorption: a) MB, b) RB, c) CR, d) Pb(II) & e) Cd(II).....	264
Table 7.6: Kinetic studies values for the pollutants adsorption: a) MB, b) RB, c) CR, d) Pb(II) & e) Cd(II).....	268
Table 7.7: Intraparticle diffusion values for the pollutants adsorption on the GO-Fe/CPTMS-SiO <sub>2</sub> @MF .....	271
Table 7.8a: Percentage desorption efficiency of dyes over adsorbent using different HCl concentrations.....	274
Table 7.8b: Percentage desorption efficiency of metal ions over adsorbent using different eluents.....	274
Table 7.9: Analysis of the real wastewater sample.....	288



Table 7.10: Langmuir and Freundlich Isotherms of real wastewater on GO-Fe/CPTMS-SiO <sub>2</sub> @MF .....	289
Table 7.11: DR and Temkin Isotherms of real wastewater on GO-Fe/CPTMS-SiO <sub>2</sub> @MF.....	289
Table 7.12: Kinetic studies of real wastewater on GO-Fe/CPTMS-SiO <sub>2</sub> @MF.....	290
Table 7.13: The recyclability studies of pollutants such as MB, RB, CR, Pb(II) & Cd(II) over GO-Fe/CPTMS-SiO <sub>2</sub> @MF.....	291

## CHAPTER-8

Table 8.1: Types of metal nanoparticles synthesized and their functionalization on GO support.....	295
Table 8.2: Maximum product yield obtained for the synthesized nanocomposites.....	295
Table 8.3: Removal rate of model wastewater of all pollutants in various adsorbents dosages.....	300
Table 8.4: The recyclability studies of pollutants such as MB, CR, Pb(II) & Cd(II) over COPYGO.....	301
Table 8.5: The recyclability studies of pollutants such as MB, RB, CR, Pb(II) & Cd(II) over GO-CeO <sub>2</sub> @CoFe <sub>2</sub> O <sub>4</sub> .....	302
Table 8.6: The recyclability studies of pollutants such as MB, RB, CR, Pb(II) & Cd(II) over GO-Fe/CPTMS-SiO <sub>2</sub> @MF.....	302

## LIST OF ABBREVIATIONS

APTMS	: 3-aminopropyl trimethoxy silane
AFM	: Atomic Force Microscopy
AAS	: Atomic Absorption Spectroscopy
BOD	: Biological Oxygen Demand
BET	: Brunauer-Emmett-Tellar surface area
BIS	: Bureau of Indian Standards
Bipy	: 2,2'- Bipyridine
COD	: Chemical Oxygen Demand
CDG	: Chemically Derived Graphene
CPTMS	: 3- chloropropyl trimethoxy silane
CR	: Congo red
CC	: Column Chromatography
CS	: Chitosan
CVD	: Chemical Vapor Deposition
CNTs	: Carbon Nanotubes
Cd(II)	: Cadmium nitrate
DMF	: Dimethylformamide
DR	: Dubinin-Radushkevich isotherm
EDX	: Energy Dispersive X-ray Analysis
EXP	: Expansion
EPR	: Electron Paramagnetic Resonance Spectroscopy
EPA	: Environment Protection Agency
EG	: Ethylene glycol
$E_a$	: Activation Energy
$E_R$	: Average Energies of the reactants
$E_P$	: Average Energies of the products
EU	: European Union
FTIR	: Fourier Transform Infrared Spectroscopy
FC	: Flash Chromatography
GC	: Gas Chromatography
GC-MS	: Gas Chromatography Mass Spectrometry

GO	: Graphene Oxide
GDP	: Gross Domestic Product
GICs	: Graphite Intercalation compounds
GPa	: Gigapascal
$\Delta G$	: Gibbs Free energy
HPLC	: High Pressure Liquid Chromatography
HOPG	: Highly Ordered Pyrolytic Graphene
HR-TEM	: High Resolution-Transmission Electron Microscopy
ICP-AES	: Inductively coupled plasma atomic emission spectroscopy
L-dopa	: L-3,4-dihydroxy phenyl alanine
MB	: Methylene Blue
MLD	: Million litres per day
mTEG	: mono-methyltriethylene glycol
NMs	: Nanomaterials
Nps	: Nanoparticles
N(Et) <sub>3</sub>	: Triethyl amine
NMR	: Nuclear Magnetic Resonance Spectroscopy
NMP	: N-methyl pyrrolidone
Pb(II)	: Lead nitrate
PVP	: Polyvinylpyrrolidone
PEG	: Polyethylene glycol
Ppm	: parts per million
Pd	: Palladium
Pt	: Platinum
PVA	: Polyvinyl alcohol
RB	: Rhodamine B
rGO	: Reduced Graphene oxide
RBC	: Red blood cells
SC-XRD	: Single Cell X-ray Diffraction
SS-NMR	: Solid State-Nuclear Magnetic Resonance Spectroscopy
Sphos	: 2-dicyclohexyl phosphino-2',6'-dimethoxy biphenyl
SEM	: Scanning Electron Microscopy
SDS	: Sodium Dodecyl Sulfate
SiC	: Silicon Carbide

TEM	: Transmission Electron Microscopy
TGA	: Thermogravimetric Analysis
TEOS	: Tetraethyl Orthosilicate
TLC	: Thin Layer Chromatography
TON	: Turn over Number
TOF	: Turn over Frequency
TMEDA	: Tetramethylethylene diamine
TPa	: Terapascal
UV-Vis	: Ultra Violet -Visible Spectroscopy
VSM	: Vibrating-sample magnetometry
WHO	: World Health Organization
XPS	: X-ray Photoelectron Spectroscopy
XRD	: X-ray Diffraction

**CHAPTER-1**  
**INTRODUCTION**

**Abstract:** This chapter provide a brief introduction of carbon nanomaterials and their applications in adsorption and catalysis

## 1.1 NANOMATERIALS

The term nanomaterials (NMs) refers to the particles with varied measurements or internal anatomy which were calibrated in nanoscale displaying outstanding properties. The unique properties include optical, mechanical, chemical, magnetic and conductivity etc. These materials paved a route to create best new composites which have a possibility to boost the quality of life. These materials slowly started to develop in order to commercialize as well as commodities to transfer innovative technological applications. The term nanoparticle refers to a nano-sized substance in a three dimensional structure on a nanometer scale range possibly (1-100nm) (ISO 2008). Nanocomposite refers to the polyphase form with one of the phases possessing one dimensional structure in a nanoscale. The story of nanomaterials started with the synthesis of gold nanoparticles named “activated gold” discovered by Michael Faraday and published in the first scientific reports in 1857. This remarkable discovery made by Faraday led to the scattering of light using colloidal nanoparticles termed to be Tyndall effect. Feynman stated that “*there is a plenty of room at the bottom*” which were concealed in the tiniest dimension of matter. This lecture became the birth time for Nanotechnological era (Feynman 1959).

To understand and know the diversity in nanomaterials, these are synthesized through cutting, ball milling, chipping, pounding, bottom-up (Magasinski et al. 2010) and top-down approaches (Sabatier 1986). According to Gleiter (1995) based on chemical composition and crystallinity of nanomaterials, these are organized into 4 types: (1) carbon based NMs, (2) organic based NMs, (3) inorganic based NMs & (4) composite based NMs (Buzea et al. 2007). Carbon based NMs mostly consist of carbon, 15<sup>th</sup> most abundant element in earth crust along with 4<sup>th</sup> abundant element in the universe. It is a unique and diverse element in periodic table which have structural forms includes diamond, graphene sheets, CNTS (Kong 2003) and fullerenes (Yan et al. 2016) respectively. The nickname given to graphene as a “miracle material” which mean substance with outstanding properties. It is a quasi 2D structure having sp<sup>2</sup> hybridized carbon possessing the crystalline morphology. Graphene’s 2D atomic structure and honeycomb lattice makes the electrons in a material move at a speed of 300 times lower when compared with speed of light in vacuum (Meyer et al. 2008). This remarkable properties such as physical, mechanical, chemical and optical nature makes the Graphene to have

applications in composite materials (Stankovich et al. 2006), water treatment (Safarpour and Khataee 2019), thermal (Liu et al. 2012), hydrogen storage (Elias et al. 2009; Sofo et al. 2007) and catalysis (Yam et al. 2020). Organic based NMs consist of organic compounds which includes lipid, carbohydrate or any polymeric substance which ranges within 10nm-1 $\mu$ m (Kreuter 2014). Most of the polymers have been synthesized due to their huge structural integrity and stability which are useful in applications like drug delivery system (Kumar and Lal 2014). Inorganic based NMs composed of metal and their oxides and ceramic based exhibiting interesting optical and electronic properties (Asta et al. 2007). Technically engineered inorganic NMs such as metal oxide and metals gained attention due to their contrasting agent property which are helpful for the semiconductor quantum dots (Gao et al. 2005). These can be widely used to diagnose and therapeutic tool in vitro and in vivo detections (Bailey et al. 2004). Composite based NMs utilized two or more varied substances which got blended or even mixed to form desired structures. Nanocomposite which acts as building blocks between the nanoparticles and hosting matrix to develop a novel substances with unpredictable elasticity and enhancement in the overall properties (Wang and Huang 2014). These composites possess enhanced mechanical (Okamoto and Ray 2004), high thermal stability (Yano et al. 1993) and flame retardant properties (Gilman 1999).

The classification of nanomaterials done by Pokropivyn and Skorokhod based on dimensionality and divided into 0-dimensional (0D), 1-dimensional (1D), 2-dimensional (2D) & 3-dimensional (3D) (Pokropivny and Skorokhod 2007). Out of all dimensions, 2D NMs gained attention within a large aspect to space ratio in nanoscale properties (Lee et al. 2016). The differences between composite materials and nanocomposites were due to their large surface to volume ratio with their nanofillers or matrix interface as a third phase different from that of matrix.

### **1.1.1 Nanoparticle Synthesis**

Various methods are there for the synthesis of Nanoparticles with two approaches(Read et al. 2014):

(1) Top-down approach

(2) Bottom-up approach

(1) Top-down approach:

This mechanism was based on the assembly of structures by altering components of bulk material, which are divided into smaller pieces via mechanical, chemical and other process by destructive method to form efficient nanostructures. This method is useful for the synthesis of electronic device by the deposition technology and lithographic techniques (Read et al. 2014).

(2) Bottom-up approach:

This mechanism is a building up method, in which atoms, molecules and machines from the basic building blocks to synthesize nanomaterials or nanodevices for the development of macroscopic concepts at the molecular level (Kuhlbusch et al. 2011). This method is of interest to all researchers in the areas of nanotechnology which includes sol gel, chemical synthesis, spinning and self-assembly method. The variations in the metastable phase led to the presence of small quantities of new phase reaches the critical size, which led to the lower free energy. This resulted in the generation of nanoparticles with a well-controlled size distribution.

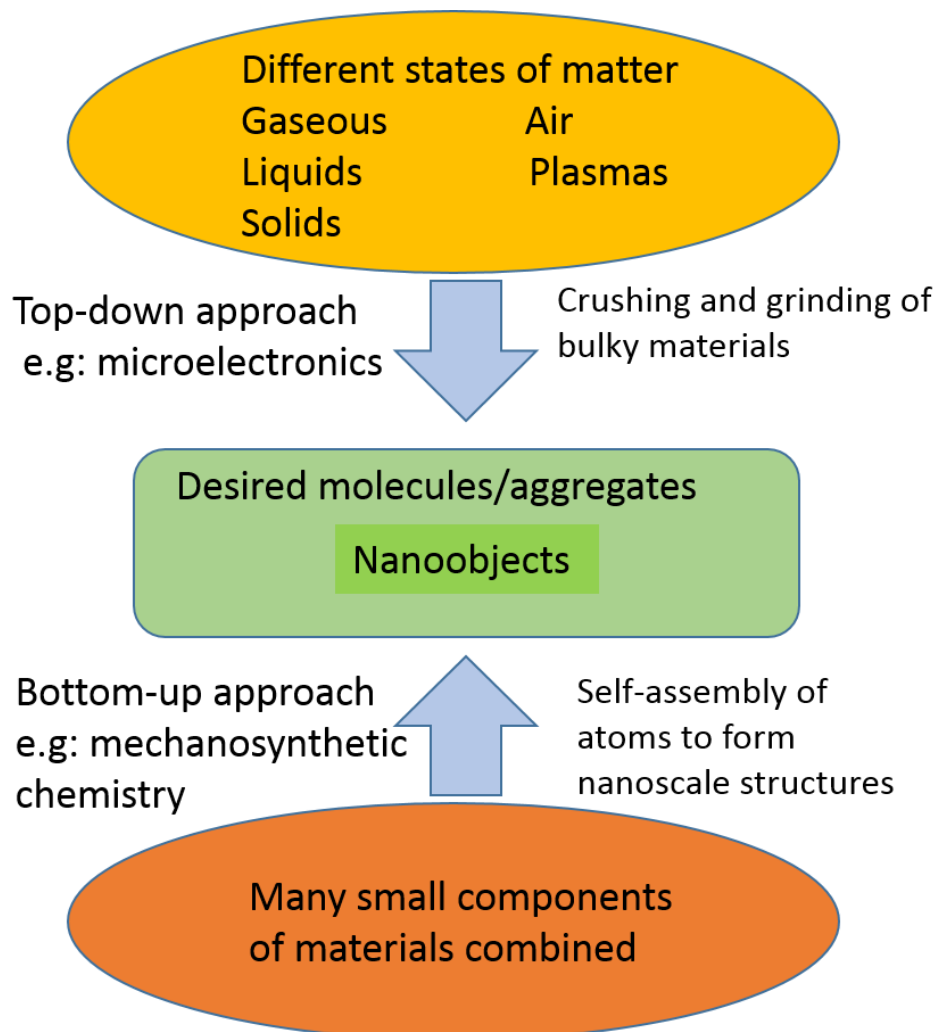


Figure 1.1. Two technological approaches employed in the nanoworld

## 1.2 GRAPHENE

### 1.2.1 Introduction

The term 'Graphite', is deduced from a Greek terminology "graphein" which consist of arrangement of planar carbon atoms in a honeycomb structure (Kim 2015). The distance



between planes is 0.335nm and the difference between the carbon atoms in the lattice is 0.142nm in a graphite structure (Kharisov and Kharissova 2019). In a graphite, the monolayer is consisting of  $sp^2$  hybridized carbon atoms known as graphene. The term ‘graphene’ emerged as a mixture of graphite and suffix–ene i.e., for the formation of aromatic hydrocarbons with polycyclic morphology (Boehm et al. 1986). The feasibility of covering of graphene into 0D fullerenes, rotating further to form 1D carbon nanotubes(CNTs) and later stacked to form 3D graphite making it as a basic building unit for all graphitic materials as shown in figure 1.2 (Geim and Novoselov 2010)

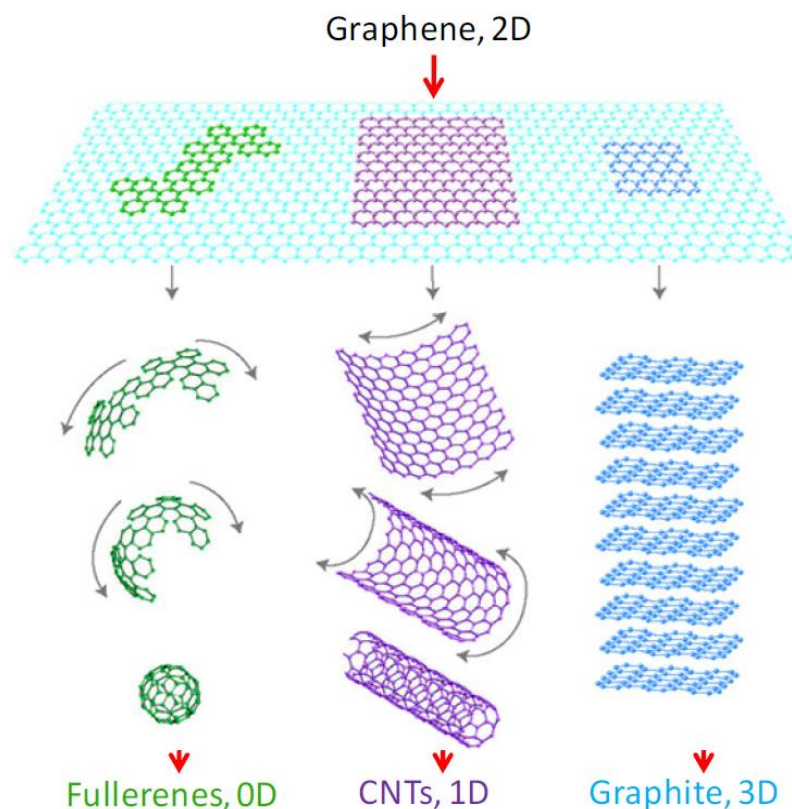


Figure 1.2. Carbon materials as fullerenes, carbon nanotubes (CNTs) and graphite (0D), 1D and 3D respectively can be derived from single layer graphene (2D)

After the fullerene discovered, by Kroto, Curl and Smalley (Kroto et al. 1991), CNTs by Iijima (Iijima 1991) and further graphene studied theoretically by P. R. Wallace (Wallace 1947), J. W. McClure (McClure 1956) and G. W. Semenoff (Semenoff 1984). Later A.K. Geim and K. Novoselov from Manchester University in 2004 segregated the graphene by adhesive Scotch tape method to characterize it (Novoselov et al. 2004). They received Nobel Prize in 2010 for the “ground breaking experiments with respect to two-dimensional material graphene”(Geim 2009).

From the past, graphene derivatives such as graphite intercalation compounds (GICs), graphene oxide (GO) and reduced graphene oxide (rGO) were reported by Schafhaeuti (Schafhaeuti 1840), by using acidic or basic medium to intercalate the carbon lamellae and further exfoliated with sulfuric and nitric acids. Later Brodie, Staudenmaier and Hummers also exfoliated the graphitic surface using high oxidation reagents (Brodie 1859; Hummers Jr and Offeman 1958; Staudenmaier 1898). However, in 1962 Boehm invented the word “graphene” and in 1986 he along with his co-workers reported that the lamellar carbon possessed oxygen and hydrogen in a smaller proportion due to the chemical reduction of GO in dilute basic media such as  $N_2H_4$ ,  $H_2S$  or iron (II) salts (DE LA CRUZ and COWLEY 1962). This is the first time, Boehm and team reported rGO or chemically derived graphene (CDG) and not pristine graphene. The formation of pristine graphene was reported by Kurtz’s group using a Scotch tape method in 2004 to form ultra-thin graphitic films. The visualization of few nanometer thick graphite from a highly ordered pyrolytic carbon (HOPG) investigated in 1995 using Atomic Force Microscopy (AFM) (Ebbesen and Hiura 1995) and Scanning Electron Microscopy (SEM) (Lu et al. 1999). The electrical property were analyzed for the graphitic carbon thickness up to 60 layer from 1997-2001 (Dujardin et al. 2001; Ohashi et al. 1997, 2000).

### **1.2.2 Properties of graphene**

The 2D honeycomb lattice structure of graphene arranged with  $sp^2$  carbon atoms forms sigma bond with their neighbouring atoms and the 4<sup>th</sup> electron occupied the  $\pi p_z$  orbital which is perpendicular to the plane to form highly delocalized  $\pi$  bonds. It has zero band gap with a very tiny effective mass due to which the carrier capacity as high as  $2,00,000 \text{ cm}^2 \text{ V}^{-1} \text{ S}^{-1}$  with a density of  $10^{12} \text{ cm}^{-2}$  (Du et al. 2008). This effect makes the electron to flow easily in graphene when compared to copper. The edges in graphene termed as armchair or zig-zag because of the lattice design at the atomic level.

Graphene is considered as strongest materials with a high mechanical strength having a Young’s modulus of 1.0 TPa and the fracture strength of 130 GPa more than CNTs (Lee et al. 2008; Van Lier et al. 2000). Due to this properties, it is tougher than diamond and by 300 times sturdy than steel when measured with same thickness (Lee et al. 2008). Graphene possess high conductance ( $>5000 \text{ W/m K}$ ) (Chen et al. 2012) with a surface area of  $2600 \text{ m}^2/\text{g}$  (Stankovich et al. 2007). It can be oxidized to form graphene oxide, a functional derivative of graphene such as hydroxyl, alkoxy, epoxy and carboxyl groups (Marcano et al. 2010). Later, the reduction by thermally or chemically yields to form CDG or rGO (Stankovich et al. 2007).

### 1.2.3 Potential applications of Graphene

Graphene and their derivatives have been widely useful in numerous applications:

a) It offers high physicochemical properties which includes high surface area, electrical and thermal conductivity with a huge potential for adsorption capacity due to the 2D nanostructure and having high crystallinity over its surface led to the elimination of organic and inorganic pollutants from the textile wastewater.

b) These functionalized graphene derivatives have extensive applications in solar energy related conversion and electrochemical energy techniques:

i) Due to its excellent optical and electronic properties, it is used in photovoltaic and photoelectrochemical devices.

ii) These nanocomposites have potentials in artificial photosynthesis such as photochemical and photoelectrochemical water splitting due to its ability to be an electron acceptor and charge transferring agent. These can replace with noble metals like Pt likely to be used in semiconductor and photochemical water splitting.

c) Due to its light mass and a large surface area created a platform for its application in lithium ion batteries. The long cycle stability of graphene and the outstanding electronic properties led to the enhancement in the electrochemical stability of Supercapacitor field.

d) The hexagonal lattice with  $sp^2$  carbon atom favours the excellent conductivity for the mobility of electrons with the unique large surface area and chemical interactions enhances the catalytic activity.

### 1.2.4 Synthesis of graphene

There are 4 main methods for the synthesis of graphene. They are

Mechanical Exfoliation

Liquid phase Exfoliation

Epitaxial growth

Chemical synthesis methods.

#### 1.2.4.1 Mechanical Exfoliation of Graphite (Scotch-tape method)

This technique was given by Heinrich Kurz et al. (1990). It involves the HOPG which got stuck to the adhesive tape and thereafter folding the two ends using a tiny crystal when the tapes pulled apart, flakes gets cleaved to form thin individual slices (Seibert et al. 1990). The particles that got adhered on to the silicon wafer within the  $SiO_2$  coating and when it is dragged apart. Now, the graphene can be seen by naked eye due to its contrast. However, the synthesis and identification of single layer graphene was first reported by Novoselov and Geim using this

method (Novoselov et al. 2004). This method cannot be used for the bulk production of graphene sheets (Chen et al. 2012).

#### **1.2.4.2 Liquid phase Exfoliation**

The graphite dispersion takes place in N-methyl pyrrolidone (NMP) and ultrasonicated to generate non-exfoliated graphene which was reported by Hernandez et al. to achieve the graphene dispersion of  $0.01\text{mg mL}^{-1}$  (Hernandez et al. 2008). Further, the exfoliation of graphene in NMP was improved by Mariani et al. upto  $2.1\text{ mg mL}^{-1}$  in polymer-graphene composite (Alzari et al. 2011) and  $5\text{ mg mL}^{-1}$  by exfoliation of graphite in ionic liquids (Nuvoli et al. 2011). The main advantage of this technique is less cost and scalable.

#### **1.2.4.3 Epitaxial Growth**

##### **a) Epitaxial Growth from SiC**

The epitaxial growth of graphene using SiC was developed by Walt da Heer and his co-workers (Berger et al. 2004). It starts with the thermal desorption of Si above  $1250\text{ }^{\circ}\text{C}$  and pressure of  $\sim 10^{-6}$  Torr resulted in the generation of carbon rich islands. It was analyzed using the Scanning Tunnelling microscope and found that graphene possessed low level of defects within a long-range order which were grown on SiC (Hass et al. 2008).

Using this technique, only single to few layers of graphene can be obtained and these are used in making of electronic devices. It can be controllable and scalable because of the high cost of SiC substrate which led to the huge expense. Compared with exfoliation method, it helps in the synthesis of brittle and defective graphene because of their high lattice conflicts in between SiC and the graphene.

##### **b) Epitaxial Growth on transition metals or transition metal deposited substrates**

The controllable growth of graphitic films is done by Chemical Vapor Deposition (CVD) in which hydrocarbons were catalyzed by metal substrates such as Ru, Rh and Ni at high temperatures by Blakely et al in 1970 (Blakely et al. 1970; Grant and Haas 1970; McConville et al. 1986; Rosei et al. 1983). In this method, the graphene formed via cooling step due to the segregation-precipitation of carbon on a metastable carbon-metal solid solution. The amount of graphene formed is dependent on the carbon solubility over the metal and the CVD growth capacity which was proved by the isotopic labelling (Mattevi et al. 2011). The advantage of this method is to extend to large surface substrates.

#### **1.2.4.4 Chemical Synthesis**

The bulk quantity of graphene defective can be synthesized only by this technique. It involves both the oxidation and reduction methods. In this typical procedure, graphite in the presence of strong oxidizing agents such as  $\text{KClO}_3$ ,  $\text{HNO}_3$ ,  $\text{H}_2\text{SO}_4$ ,  $\text{H}_3\text{PO}_4$  and  $\text{KMnO}_4$  is converted to

GO. These oxidation process enhances the distance due to the addition of various functional groups in the intersheet carbon layers. If the oxidation rate increases, the probability of high-quality graphene oxide sheet can be enhanced and further reduces to form rGO. The oxidation process can be improved from Brodie's to Staudenmaier's, Hummers', modified Hummers' and currently Tour's method. The high-quality graphene oxide with an intersheet spacing of 9.5 Å obtained by Tours method. Table 1.1 below gives the representation of various preparation methods for the formation of chemically derived graphene (Compton and Nguyen 2010).

Table 1.1: Different synthetic methods of Graphene

	Brodie	Staudenmaier	Hummers	Modified Hummers		Tour
Year	1859	1898	1958	1999	2004	2010
Oxidants	KClO <sub>3</sub> , HNO <sub>3</sub>	KClO <sub>3</sub> or NaClO <sub>3</sub> HNO <sub>3</sub> H <sub>2</sub> SO <sub>4</sub>	NaNO <sub>3</sub> , KMnO <sub>4</sub> , H <sub>2</sub> SO <sub>4</sub>	K <sub>2</sub> S <sub>2</sub> O <sub>8</sub> , P <sub>2</sub> O <sub>5</sub> , KMnO <sub>4</sub> , H <sub>2</sub> SO <sub>4</sub>	NaNO <sub>3</sub> , KMnO <sub>4</sub> , H <sub>2</sub> SO <sub>4</sub>	H <sub>2</sub> SO <sub>4</sub> , H <sub>3</sub> PO <sub>4</sub> , KMnO <sub>4</sub>
C:O ratio	2.28	1.85	2.25	1.3	1.8	--
Reaction time	3-4days	1-2days	2-10h	8h	5days	12h
Intersheet spacing (Å)	5.95	6.23	6.67	6.9	8.3	9.5

The hydrophilic character of GO is due to the presence of polar oxygen functional moieties which helps in dispersing polar solvents, especially in water. These functional groups in GO weakens the van der Waals interactions which resulted in the incomplete degradation of sp<sup>2</sup> lattice into a C=C sheet of graphene with limited  $\pi$ - $\pi$  stacking ability. It attains non-conducting behavior due to the absence of conducting graphitic framework. The formation of CDG by the reducing process of GO through annealing process at 1000 °C under Ar flow restores the conductivity of graphitic framework by the reduction of all functional groups (Stankovich et al. 2007). From the above methods, we can conclude that CVD can give large amount of pristine graphene useful for design of electronics, whereas the chemical method is used to synthesize in large scale of graphene.

## 1.3 TRANSITION METALS NANOPARTICLES

### 1.3.1 Schiff Base Metal Complexes

#### Schiff Base

Schiff base was first reported by a German chemist, Nobel prize winner, Hugo Schiff in 1841 (McNaught and Wilkinson 1997; Schiff 1866). Schiff bases are the condensation products of aldehyde and primary amines. Structurally, Schiff base is an equivalent of a keto or formyl groups in which carbonyl group is displaced by an imine or azomethine group.

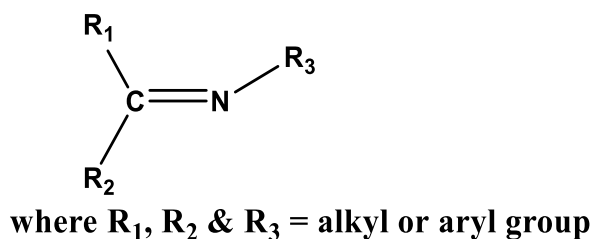


Figure 1.3. General Scheme of Schiff base

Schiff base is synthesized by the condensation of carbonyl group with amine in presence of various solvents as well as various conditions with the removal of water molecule. The existence of a dehydrating agent benefits the synthesis of Schiff base. The azomethine group which contains sp<sup>2</sup> hybridized nitrogen atom possess lone pair of electrons combined with one or more donor atoms contributes to the excellent chelating ability. This chelation behavior is useful in Coordination chemistry to form stable metal complexes. Over a wide range of Schiff base metal complexes were screened to be effective for the catalysis (homo and hetero) at various temperatures.

### 1.3.2 Basic properties of transition metal complexes

The d-orbitals of a transition metal atoms or ions possess degenerate orbitals. These transition metal developed the coordination complexes due to the interaction of metal d-orbitals with the electron flock of the ligand. The d-orbitals splits into various energy levels due to the significant geometric planes of the complex. This Crystal field theory is investigated to foresee the energy levels of d-orbitals of a transition metal which are distributed and the transfer of electron from low energy to high energy via the photon of electromagnetic radiation.

Transition metal complexes which possess ligands got coordinated with chelation property to attain thermal stability. These complexes are stable to air and moisture ensuring the high durability of catalyst and broad scope in this field.

### 1.3.3 Nanoparticles

Nanoparticles (Nps) have gained considerate attention with diverse applications. The electronic energy levels of Nps reveal the nature of property such as conducting, magnetic and metallic character. The unique physico-chemical properties are related to the density and limited size of these Nps surface along with corners as well as edges. Magnetic Nps have gained their interest

due to their size, shape and easy recovery after the reaction. From the earlier years, metallic and metal oxides Nps became an interesting material for the elimination of organic and inorganic pollutants in wastewater. With the easy tendency of bare Nps to agglomerate because of the instability, the isolation of metallic Nps from wastewater is a confusing process. The metallic Nps i.e., Fe<sup>0</sup> is very significant due to their high stability, more surface area, non-toxic and reduction property. These are very less toxic and eco-friendly compared to the metallic Nps.

The word ferrite obtained from latin word 'Ferrum' which mean iron. The properties of ferrite which includes chemical composition, structural properties, particle size and the particles interaction with encircling matrix (Hilpert 1909). Ferrite Nps constitutes the high surface area and the existence of unstable forces at its surface which are perfect for the adsorption of pollutants in wastewater (Tadjarodi et al. 2015). Further coating of these Nps with silane groups and surfactants along with composites makes them stable aggregation, which increase physico-chemical stability to perform functionalized composites. Compared to metal oxides, ferrites help in synergistic adsorption and elimination of organic pollutants. These are classified into normal spinels and inverse spinels. Transition metal acts as cations which got fixed into the interstitial sites along with "d" energy levels from d<sup>0</sup> to d<sup>10</sup>. The difference in energy levels of electron family may be tetrahedral (T<sub>d</sub>) and octahedral (O<sub>h</sub>) sites and their corresponding interactions at the electronic levels of metal cations resulted in the magnetic property of spinel ferrites. Based on the structural arrangement of metal cations, size and charge neutrality, spinels were categorized as:

Normal spinels A[B<sub>2</sub>O<sub>4</sub>] with A<sup>2+</sup> ions occupy T<sub>d</sub> sites and B<sup>3+</sup> ions occupy O<sub>h</sub> sites. Eg: ZnFe<sub>2</sub>O<sub>4</sub> & CdFe<sub>2</sub>O<sub>4</sub>.

Inverse spinels B[ABO<sub>4</sub>] with A<sup>2+</sup> ions occupy O<sub>h</sub> sites and B<sup>3+</sup> ions occupy both O<sub>h</sub> and T<sub>d</sub> sites. Eg: NiFe<sub>2</sub>O<sub>4</sub>, MgFe<sub>2</sub>O<sub>4</sub> & CoFe<sub>2</sub>O<sub>4</sub>.

Mixed spinels which include A<sup>2+</sup> and B<sup>3+</sup> ions occupied both O<sub>h</sub> and T<sub>d</sub> sites A<sub>x</sub>B<sub>y</sub>[A<sub>1-x</sub> B<sub>2-y</sub>O<sub>4</sub>] Eg: MnFe<sub>2</sub>O<sub>4</sub>.

## 1.4 SILANE COUPLING GROUPS

Silane coupling groups are a prominent class in the synthesis of nanocomposites derived from organic polymers and inorganic filling agents. The general formula is (RO)<sub>3</sub>-Si-R'-X where X refers to organofunctional group, R' is the alkylene chain and OR termed to be any hydroxyl group such as alkoxy groups.

The silanols easily combine with the hydroxyl groups on metal atom within the inorganic surface to form an oxane bond through the removal of water molecules. Compared to monoalkoxysilanes, trialkoxysilanes are in tenfold equilibrium constant towards the bonding of inorganic substances. Once the inorganic surface is treated with silane coupling groups, the treated surface exhibited more surface energy and become reactive due to the presence of organofunctional group of silane moiety. This way, the surface of an inorganic composite can be modified to get the desired the transformation which allow the optimization during the synthesis. Magnetic Nps belong to an advanced category in Nanotechnology constitute the main advantages such as magnetic separation for the easy removal of pollutants. Compared to non-magnetic nanoparticles, the magnetic Nps have high surface area, chemically inert, less toxic, biocompatible and easy dispersiveness. Further, functionalization of Nps provide complex formation, chemical binding to the ligand formation with regards to electrostatic and van der waals interactions. The effective functionalization enlarged the charged functional groups alter the charges on the nanocomposite surface, resulted in the enhancement of electrostatic interactions between the composite and the pollutants. Further, the functionalization justified the surface and the geometry array of coated moiety depend on the global size, and the surface area of magnetic Nps.

## **1.5 APPLICATIONS OF NANOCOMPOSITES IN CATALYSIS**

### **1.5.1 Introduction to catalysis**

The word “Catalysis” was given by Berzelius for the first time in 1836 to analyze the new entity able to promote the development of a chemical reaction by a “catalytic contact”. A “catalyst” is any substance or material capable of changing the speed of a reaction without being used up in the reaction.

### **1.5.2 History**

The term “catalyst” is derived from the greek word of which ‘catal’ means to annul o untie from the Dybkaer, IUPAC Technical report 2001 which are accelerated by materials which remain unaltered during the reaction. Humphry Davy (1820) discovered the platinum usage in catalysis and Wilhelm Ostwald (1880) Leipzig University proceeded the systematic investigation which catalyzed the acids and bases along with the chemical reactions to determine the strength of both acid and base. For this work, Ostwald received the Nobel Prize (1909) in chemistry.



### 1.5.3 Technical perspective

The total energy in a reaction for the conversion of reactants to products does not change in presence of a catalyst and lower free energy was gained to attain the transition state. It can engage in many organic reactions and its effect vary due to the existence of other materials known to be inhibitors or poisons. The substances which increases the activity are known as promoters.

The catalyzed reactions possess lower activation energy compared to the uncatalyzed reactions due to high reaction rate with a constant temperature and concentration. It may alter the reaction system to bind the reagents in order to polarize the bonds

Eg: Acid catalyst such as osmate esters in OsO<sub>4</sub> catalyzed the alkenes dihydroxylation.

The catalytic systems kinetically represented the chemical reactions which depends on the frequency of reactant species participating in a rate-limiting step. It is a slowest step and affected by its activity. In heterogeneous catalysis, the reagents diffusion on its surface can be rate-determining step. The catalyst which was dissolved into solution in a solid-liquid system.

### 1.5.4 Classification of Catalysis

Catalytic reactions are of 4 types

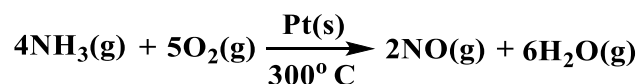
- a) Positive catalysis
- b) Negative catalysis
- c) Auto-catalysis
- d) Induced catalysis

#### a) Positive Catalysis

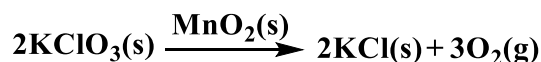
The speed of a chemical reaction is accelerated by a catalyst termed to be positive catalyst and the method is called as positive catalysis. This activation energy is reduced by a smaller path due to a catalyst, further the rate of reaction also increased.

Examples:

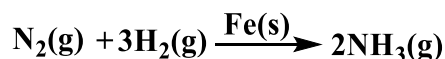
- i) The oxidation of ammonia in presence of platinum gauze.



- ii) The decomposition of potassium chlorate is lethargic even at high temperature, due to the addition of small amount of manganese dioxide enhances the decomposition rate to a larger extent and it remains unaltered during the reaction.



- iii) Synthesis of NH<sub>3</sub> by Haber's process in the presence of Fe, \.

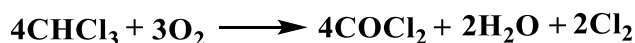


### b) Negative Catalysis

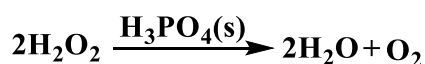
The speed of a reaction is retarded by a foreign substance termed as negative catalyst and the method is said to be negative catalysis. These are the examples of negative catalysts.

Examples:

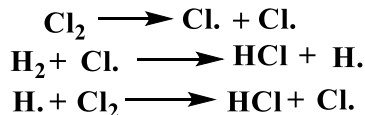
i) Chloroform is oxidized in air to form toxic  $\text{COCl}_2$ . When 2% ethanol is added to chloroform, its oxidation is stopped, hence ethanol acts as catalytic poison or negative catalyst.



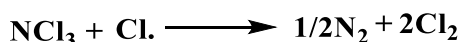
ii) These negative catalyst works by poisoning a catalyst earlier subsided in the reaction mixture. However, if the small quantity of alkali dissolved which gets catalyzed the decomposition of  $\text{H}_2\text{O}_2$ , and further adding the phosphoric acid could destruct the alkali catalysts and prevents decomposition.



iii) Negative catalysts have been operated to break the chain reactions. For example, the  $\text{H}_2$  and  $\text{Cl}_2$  gas combustion led to a chain reaction which is negatively charged by nitrogen trichloride.



$\text{NCl}_3$  shattered the chain of reactions by absorbing  $\text{Cl}\cdot$  and the reaction stops.



iv) Sodium sulphite gets oxidized in air which can be retarded by alcohol. Hence, alcohol acts as a negative catalyst.



### c) Auto-Catalysis

The product which was produced in the reaction acts as catalyst to initiate the further reaction, the substance termed to be auto-catalyst and the method said to be auto-catalysis.

Examples:

i) Ethyl acetate is hydrolysed by water molecule which acts as an auto-catalytic reaction, since acetic acid released into the reaction behaves as a catalyst.



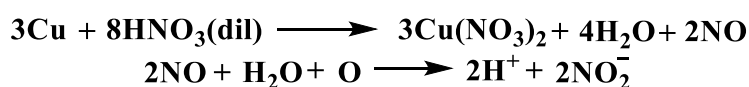
ii) The oxidation of oxalic acid by acidic  $\text{KMnO}_4$  is catalyzed due to the  $\text{Mn}^{2+}$  ion generated in the reaction. At first, the color of  $\text{KMnO}_4$  fades slowly, but the  $\text{Mn}^{2+}$  ion developed in the solution, the color releases rapidly; then  $\text{Mn}^{2+}$  ions behave as an auto-catalyst.



iii) The free arsenic formed by the decomposition of arsine ( $\text{AsH}_3$ ) autocatalyzes the reaction.



iv) When nitric oxide is dropped onto copper metal, the reactions is very sluggish at the initial stage, but gradually the reactions becomes faster due to the production of nitrous oxide in the reaction which is known as an auto-catalyst.

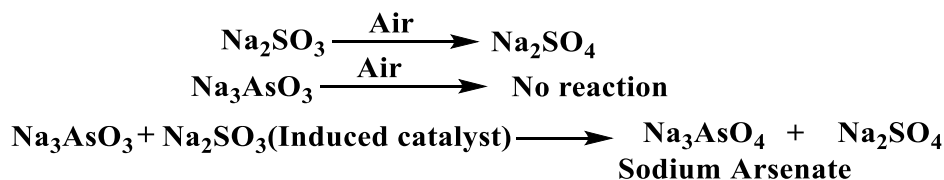


#### d) Induced Catalysis

When any reaction governs the speed of other reaction, not feasible under ordinary conditions, this method is termed as induced catalysis.

Example:

i) Sodium arsenite is not oxidizable in air. If the air is penetrated through a mixture of sodium arsenite and sodium sulphite, it resulted in simultaneous oxidation. The sodium sulphite oxidation activates the oxidation of sodium arsenite.



### 1.5.5 Characteristics of catalytic reactions

Among the different catalytic reactions, the characteristics are given to the criteria of catalysis is as follows:

(1) The mass and chemical composition of catalyst remains unaltered till the completion of the reaction. The analysis of both qualitative and quantitative phenomena proved the same and usually the catalyst undergoes a physical change during the reaction.

(2) A small amount of catalyst is required to perform the unlimited reactions. Usually, a trace amount of metal catalyst enough to carry out a very large amounts of reactants.

3) For a reaction to start, generally catalysts are not necessary. It only enhances the speed of a reaction which are already in progress itself. But in certain conditions like a mixture of hydrogen and oxygen remains neutral at room temperature and due to the introduction of

platinum which acts as catalyst to initiate the reaction. From the above line, the analysis can be reacting molecules doesn't have minimum kinetic energy to initiate the collision between the molecules in the absence of catalyst, they tend to rebound back.

4) It is effective when it is finely tuned. For example, in heterogeneous catalysis, the solid catalyst such as finely divided nickel acts as a better catalyst than solid nickel which signifies its high surface area due to its controlled structure.

5) It is specific for a reaction and produces different reactions with the different catalysts with the same starting material. In case of formic acid in presence of hot copper produces  $\text{CO}_2$  and  $\text{H}_2$  and in presence of hot aluminium oxide, it produces  $\text{CO}$  and  $\text{H}_2\text{O}$ .

6) The rate of a reaction also depends on the temperature factor and it is studied under Le-Chatelier's principle. The rise in temperature alters the activity of the catalyst and it may lead to the decrease in rate of a reaction. For example, platinum with the increase in temperature, it coagulates. The temperature at which the maximum rate of a reaction taken place is called as optimum temperature.

7) It does not change the finishing stage of equilibrium but it only reduces the time necessary for a reaction to happen. In a reversible reaction, it helps to initiate both forward and backward reaction at a same stand to attain equilibrium.

8) **Catalytic promoters:** A material not a catalyst, but promotes the catalytic activity is termed to be which, a promoter or an activator.

9) **Catalytic poisoning:** A substance that destruct the performance of a catalyst to initiate a reaction is termed to be catalytic poison and the process is known as catalytic poisoning.

Examples:

(i) The platinum catalyst is poisoned by carbon monoxide in the oxidation reaction of  $\text{H}_2$ .

(ii) The platinum catalyst utilized in the oxidation of  $\text{SO}_2$  (contact process) is poisoned by arsenic oxide ( $\text{As}_2\text{O}_3$ ).

(iii) In the Haber's process of  $\text{NH}_3$  ammonia, the catalyst  $\text{Fe}$  is poisoned by  $\text{H}_2\text{S}$

10) A positive catalyst reduces the activation energy.

(i) From the collision theory, if any reaction needs to happen, a number of effective collisions were required in between the reactant molecules.

(ii) The reacting molecules should possess minimum energy termed as  $E_a$  for the effective collisions.

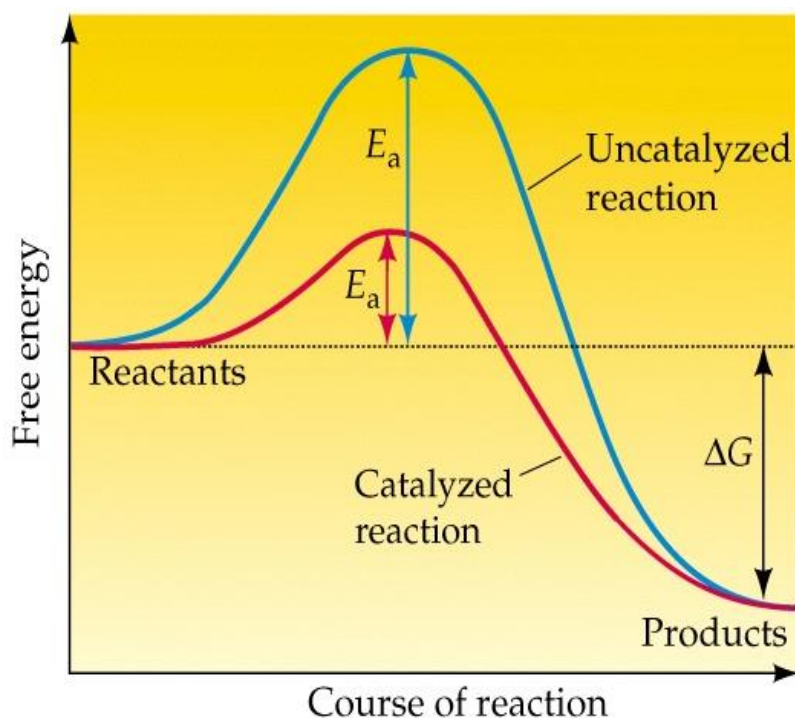


Figure 1.4. Diagram of the potential energy of catalyzed and uncatalyzed reactions (Sinauer Associates 2001)

(iii) Once the collision, the reactants form an activated complex which yields to form products

(iv) A catalyst enroute a new path with the utilization of minimum activation energy. Therefore, the number of collisions in presence of catalyst were higher than in absence of catalyst

(v) Figure 1.4 represented that the  $E_a$  without any catalyst is greater than the  $E_a$  with the catalyst.

(vi) The difference in average energies of reactants and products gives the  $\Delta G$  value, i.e.,  $\Delta G = E_R - E_P$ .

### 1.5.6 Types of catalysts

Depending on whether a catalyst exists in a single or multi phases as that of the substrate, catalysts are classified into three main types – homogeneous, heterogeneous and biocatalysts. Figure 1.5 shows the types of catalysts in pictorial representation.

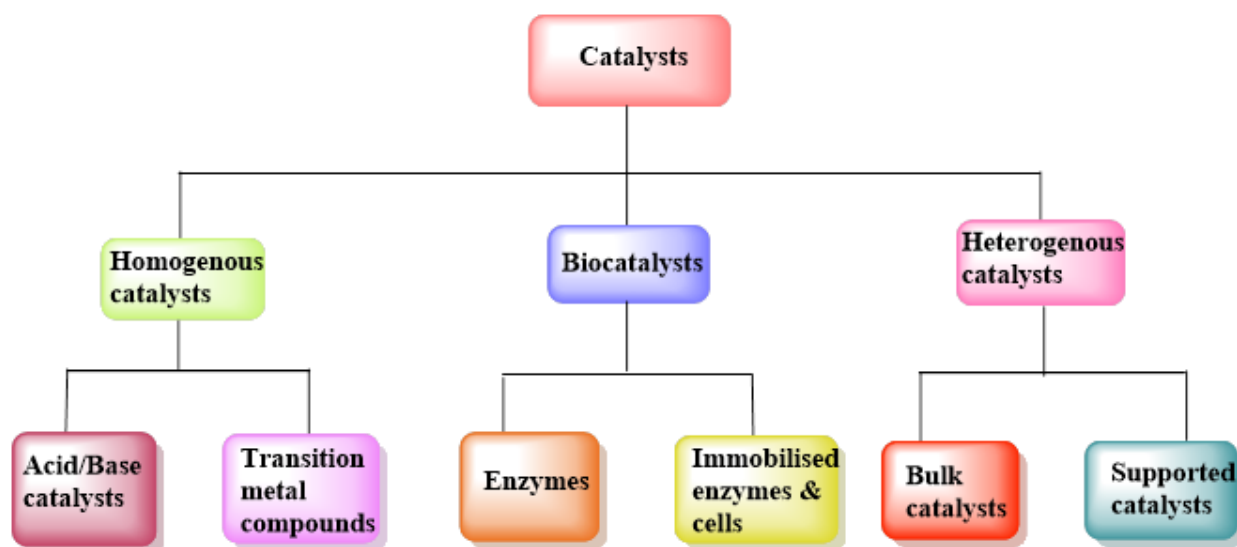


Figure 1.5. Pictorial representation of the types of catalysts

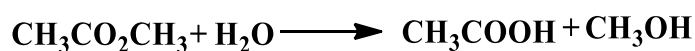
### 1.5.5.1 Homogeneous catalysts

When the catalyst is in the same phase with that of the reactants, the phenomena is said to be homogeneous catalysis and the catalysts are called as homogeneous catalysts. In this type, the reactant solution is solubilized by a soluble catalyst only. This is applicable to the gas and even solids also. This phenomenon refers to the catalysis of organometallic compounds which have high practical significance.

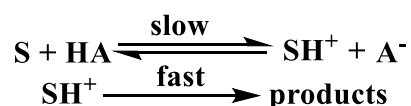
Examples of Homogeneous catalysts:

Acid/base catalysts:

Water generates protons with the dissociation of water acts as a homogeneous catalyst accelerates the ester hydrolysis.



Usually, esters don't hydrolyze at higher rates in absence of acids. Both acid and base acts as catalyst in acid catalysis and the proton is utilized for the catalysis and the rate of reaction depends on pH mainly due to the  $\text{H}^+$  and  $\text{OH}^-$  ions. The transfer of proton is the rate-limiting step and these substrates fastly give rise to products.



### Organometallic compounds/Transition metal compounds

These are one of the class in homogeneous catalysis which consist of organometallic compounds. These include hydroformylation, transfer hydrogenation along with Ziegler-Natta polymerization, Wacker process, Monsanto process and Cativa process.

### Disadvantages of Homogeneous catalysis

- These catalysts are not stable under harsh environments which limit their usage.
- The catalysts are completely in dispersed phase with that of the reaction mixture which becomes difficult to recover the catalyst after the reaction.

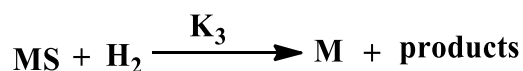
### Theory of homogeneous catalysis

The catalyst initially forms an intermediate complex with the reactant. This reactant with which combines is often termed as 'substrate'.



Where 'S' is substrate, M is catalyst and MS is the intermediate compound.

Then MS reacts with other reactant molecule ( $\text{H}_2$ ) to form the product and catalyst.



This reaction is slow and is the rate determining step.

The catalyst M is regenerated in the last step. Thus, the rate of homogeneous catalytic reactions depends upon the concentration of catalyst M.

#### 1.5.5.2 Biocatalysts

Biocatalysis is a chemical process through which enzymes or other biological catalysts initiate the reactions between organic components and the catalysts involved in this process are known as biocatalysts. During the world war-II, the production of penicillin by using microbial resource is the most significant Biocatalysis process. Biocatalysis also initiated in the production of alcohol by fermentation process in presence of yeast under anaerobic conditions. The term biocatalysis is also referred in the application of enzymes in chemistry (Bommarius and Riebel 2005).

Biocatalysts have advantages like high stereo-, regio-, chemo selectivity, less requirements of tedious protection and deprotecting agents in synthetic chemistry, low incidence of by-products, mild reaction conditions, efficient catalysts for both simple and complex organic transformations and biodegradable.

The disadvantages are low stability than conventional catalysts, development of industrial catalysts takes longer time to establish, less availability of commercial biocatalysts, requirements of microbiological sources if the biocatalyst is not commercial enzyme.

### Enzymes

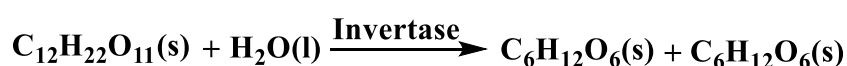
Enzymes are also known as biomolecules which only speed up the reactions without consuming or altering themselves until the completion of chemical reactions. These are proteins or protein-

based molecules which have unique catalytic properties and possess more advantages compared to chemical catalysts. They are biocompatible, biodegradable, highly selective and efficient, and are specific in nature. These properties find applications in biomedical, pharmaceutical and food industries.

Enzymes get denatured due to environmental factors (temperature, pH and salt concentration) and other physical and chemical factors. Because of denaturation, they may lose catalytic activity temporarily or permanently due to the change in structure of bond pattern distribution. Traditionally, the enzyme catalysis is carried out in aqueous buffer solutions; where the industrial catalysis may not always be.

Examples:

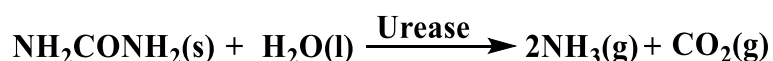
i) Inversion of cane sugar: The invertase enzyme converts cane sugar into glucose and fructose.



ii) Conversion of glucose into ethyl alcohol: The zymase enzyme converts glucose into ethyl alcohol and carbon dioxide.



iii) Decomposition of urea into ammonia and carbon dioxide: The urease enzyme decomposes urea into ammonia and carbon dioxide.



### **Immobilized enzymes/cells**

Immobilization is defined as the attachment of cell or enzyme to an inert, distinct insoluble support or matrix. This support or matrix on which the enzymes are immobilized allows the exchange of medium including substrate or effector or inhibitor molecules. Therefore, it can provide the increased resistance to the changes in conditions such as pH and temperature. The first immobilized enzyme was amino acylase of *Aspergillus oryzae* for the production of amino acids in Japan (Basso and Serban 2019).

Hence some mobilization methods have been developed like physical adsorption, entrapment, encapsulation of porous structure of support via covalent binding and cross linking of the ligands on the materials. Upon immobilization, enzymes attain better stability which makes easily recoverable and reusable continuously. Enzymes are immobilized on gold particles, polymers, magnetic particles and CNTs.



The advantages are increase functional efficiency of enzyme, reusability, stability, less labor input in the process, less costly, less reaction time, improved process control and high enzyme substrate ratio. The disadvantages are catalytic activity lost during immobilization, difficulty in purification and isolation of enzyme.

Examples:

i) Cross Linked enzyme aggregates of Penicillin G amylase is an active and highly stable biocatalyst for the deacetylation of penicillin-G to form 6-aminopenicillanic acid, which in turn reacts with amino acid side chain to form ampicillin (Cao et al. 2000).

ii) (R)-Phenyl ethanol was produced with 95% yield and >99% ee through dynamic kinetic resolution of 1-phenyl ethanol using *Candida Antarctica* Lipase B(CALB) as a resolution catalyst and Ruthenium complex as racemization catalyst (Bogár et al. 2007).

### 1.5.5.3 Heterogeneous catalysts

When both the catalyst and the reactants are in different phase in a reaction, the catalysis is known to be heterogeneous catalysis. These are solids which act on substrates in liquid or gaseous mixtures. Different mechanisms were proposed depending on the surface where the adsorption proceeds such as Langmuir, Eley-Rideal and Mars-van Krevelen (A.O et al. 2012; Eriksson et al. 1997; Redlich and Peterson 1959). But the total surface area remains significant due to their small size of the catalyst having the higher surface area to the given amount of reactant molecules.

These catalysts have active sites and depends on the mechanism, they can be in planar metal surface or crystal edge with metal valences or a combination of both. However, to find out the nature of active site on a catalytic surface is challenging research. The research findings for the catalysis using metal is as follows: (i) In Haber's process, the synthesis of  $\text{NH}_3$  from  $\text{N}_2$  and  $\text{H}_2$  in presence of finely divided Fe as catalyst. These reactant gases adsorb onto the active surface of Fe and after they are physisorbed, the reagents undergo chemisorption resulting the dissociation of adsorbed species and the formation of new fragments with close proximity. The triple bond in  $\text{N}_2$  molecule is broken which is difficult in gaseous phase due to high  $E_a$  but in presence of Fe catalyst, the  $E_a$  got reduced and the rate of reaction enhanced. (ii) The oxidation of  $\text{SO}_2$  over  $\text{V}_2\text{O}_5$  catalyst for the synthesis of sulfuric acid.

These catalysts act as good supportive materials in order to increase the rate of a reaction and to minimize the cost. Support usually prevents the agglomeration, sintering of the small catalytic materials and enhances the surface area for the reaction. These support materials can be porous with high surface area, zeolites or activated carbon,  $\text{SiO}_2$ , titanium dioxide, calcium carbonate, and barium sulphate.

#### **1.5.5.4 Comparison of Heterogeneous catalysis over homogeneous catalysis**

In a heterogeneous catalysis, the reactants diffuse to the catalytic surface and adsorb onto it, and the reactions were performed at a very high temperatures and are often accompanied by low specificities. But these catalysts are difficult to study as the reaction mechanism is unknown. However, the recovery of the catalysts is easy in case of heterogeneous catalysts. On the other hand, homogeneous catalysts can be tailored by ligand variation and every single catalytic site act as an active site which makes intrinsically more active and selective towards the reaction. At low temperatures, the reactions were performed with a high specificity with respect to the catalyst utilized. The mechanism of homogenous catalysis can be developed easily when compared with the heterogeneous catalytic activity.

#### **1.5.6 Catalyst Deactivation**

The loss of catalytic activity or selectivity as the reaction proceeds over a period is known as catalyst deactivation. However, as the catalyst deactivates, the reaction pathway deviates from the “ideal rate law”. The catalyst decay can be due to poisoning, fouling, thermal degradation, vapor compound formation or leaching, vapor-solid or solid-solid reactions and attrition or crushing etc.

#### **1.5.7 Catalytic application in Coupling reactions**

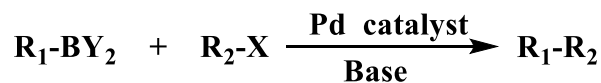
When the two hydrocarbon fragments are joined together in presence of a metal catalyst to form a new covalent bond is known as coupling reaction. Here, the important compound includes the type RM where R refers to organic fragment and M refers to the main group center which reacts with organic halide type R'X to form new carbon-carbon bond R-R' as a product. Richard F. Heck, Ei-ichi Negishi and Akira Suzuki were awarded the Nobel Prize in Chemistry (2010) for developing the palladium catalyzed cross-coupling reactions. Two types of coupling reactions are there i.e.,

1. Heterocouplings: The coupling in between two different groups, for example, the Heck reaction of an alkene ( $RC=CH$ ) and an alkyl halide ( $R'-H$ ) to give a substituted Alkene ( $RC=CR'$ ).
2. Homocouplings: The coupling between two same groups, for example, the Glaser coupling of two acetylide ( $RC\equiv CH$ ) to form a dialkyne ( $RC\equiv C-C\equiv CR$ ).

##### **1.5.7.1 Suzuki cross-coupling**

The organic reaction in which the coupling groups are boronic acid with an organic halide in presence of palladium (0) complex is known as Suzuki cross-coupling reaction. It was first reported by Akira Suzuki(1979) and later developed by Richard F. Heck and Ei-ichi

Negishi (2010). This coupling is useful to produce polyolefins, styrenes and substituted biphenyls. The general scheme for the coupling is given below



Where  $R_1-BY_2$  refers to organoboron species and  $R_2-X$  refers to organohalide species

### **Reaction mechanism**

The generalized mechanism for the Suzuki cross-coupling is the usage of palladium catalyst which is a significant step in the reaction. The first step includes the addition of palladium species (1) to the organohalide group (2) which is an oxidative addition. The formation of organopalladium species (3) takes place and then it reacts with base to give intermediate (4). This intermediate upon transmetallation with boron-ate complex (6) (formed by the reaction of boronic acid (5) with base) to produce the organopalladium species (8). The last step is the reductive elimination of palladium (II) complex to form the desired product (9) which completes the catalytic cycle. The role of base in the cross-coupling was never fully understood. It was first considered to form a trialkyl borate ( $R_3B-OR$ ) by the reaction of trialkyl borane ( $BR_3$ ) with alkoxide ( $RO^-$ ), as the formed borate species is more nucleophilic and highly reactive towards the palladium complex in the transmetallation step. Later Duc and co-workers explained the role of base in three steps: (i) Formation of palladium complex (ii) formation of trialkyl borate & (iii) the acceleration of the reductive elimination due to the reaction between alkoxide and palladium complex. The reaction mechanism is given below:

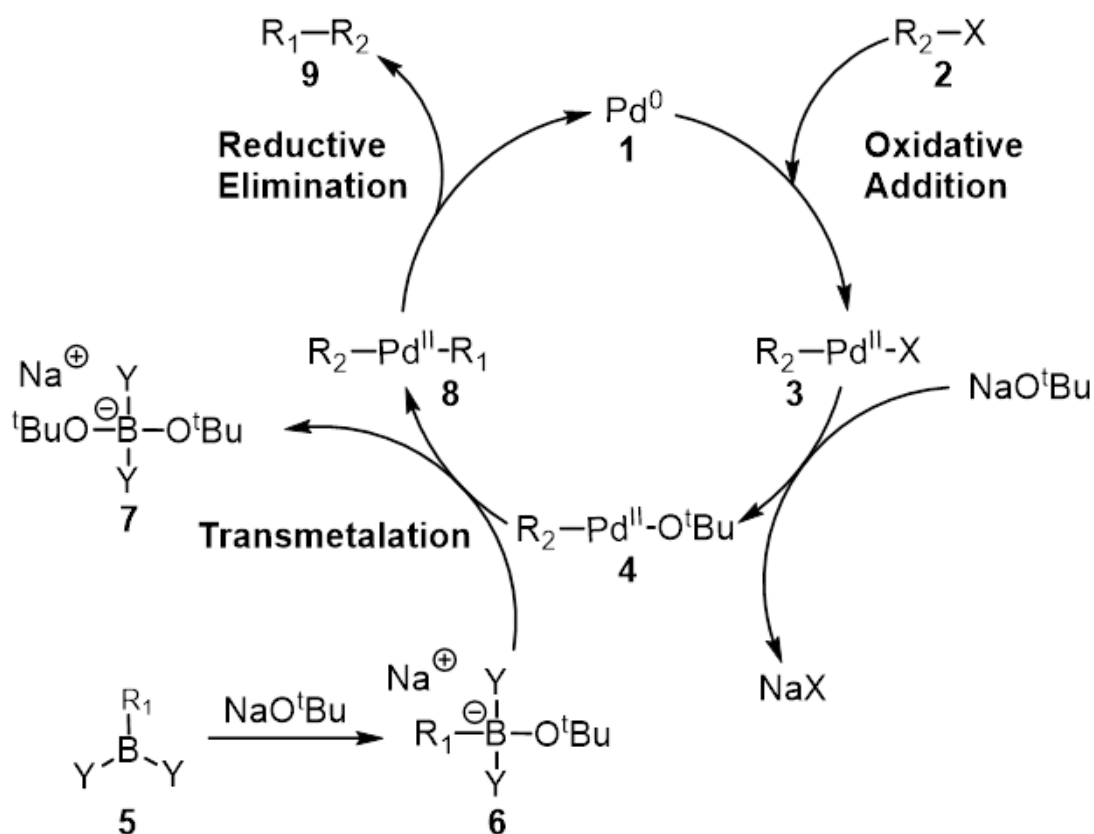


Figure 1.6. General reaction mechanism of Suzuki coupling reaction

## 1.6 ADSORPTION

### 1.6.1 Water pollution and sewage treatment

Due to the rapid industrialization and urbanization, human population started to have huge burden on the usage of water and its pollution, created a high demand for the clean water. Water pollution attained significance due to its ability to absorb any substance other than any liquid. Due to this, all the water bodies such as rivers, reservoirs, lakes and our ocean drowned with chemical waste, plastics and other toxic pollutants. Because of this, the number of individuals with water scarcity will increase to 3.9 billion by 2030 as according to the World Water Council (Xu et al. 2018). The existing and upcoming water scarcity demanded the need for wastewater treatment for the household utilization, industries and agricultural needs. Textile industry is a large global manufacture that creates a huge amount of wastewater and became a threat to the water resources and for a growing economy. Wastewater treatment and the potable water purification are an emergency to have sustained human society and mitigate the pollution problems and health issues. There are an estimated 38354 million litres of water per day (MLD) is produced only in India's major cities, but the sewage treatment done at 11786 MLD only.

However, environmental field in India is expanding quickly to provide the viable opportunities for abating the water pollution using innovative technologies. Of which, the United nations (2015:6.3) has specified for the improvement to “water quality by reducing pollution, eliminating dumping and minimizing release of hazardous chemicals and materials, having the proportion of untreated wastewater and substantially increasing recycling and safe reuse globally” by 2030 (C. H. Woo 2018; Lee et al. 2016).

Wastewater treatment had become a topmost priority due to the discharge of various pollutants into natural water bodies which contribute to the industries such as textile industry 54%, paper and pulp industry 10%, dye industry 21%, tannery as well as paint industry 8%, dye manufacturing industries 7%, pharmaceutical industry and craft bleaching industry (Gisi et al. 2016). These generates a massive impact on our ecosystem which accounts for 10,000 different textiles dyes of which ~700,000 tons of dye production have been done worldwide (Moussavi and Mahmoudi 2009). India is one of the largest producers of textiles which contribute to the 5% of GDP, 14% of industrial production and 45 million population are employed in this sector (Velusamy et al. 2021). About 1.6 MLD to produce 8000 kg/day of fabric, out of which 8% of water utilized for printing and 16 % of water in dyeing process (Kant 2012).

During the fabric manufacturing process, a lot of mechanical and chemical process are involved which include desizing, scoring, bleaching, dyeing, printing and finishing ect. During this process, a lot of effluents which contains a significant amount of COD, BOD, suspended solids, organic nitrogen, traces of heavy metals, dispersants, acids, alkalis and various dyes. These stated pollutants discharge degraded the water quality, spreads toxicity and severely affecting the photosynthesis. It creates a huge blow to the aquatic life because of low light penetration and inadequate oxygen consumption. The huge amount of dyes imparted during the dyeing remained unfixed in textile effluents and they became toxic, carcinogenic and mutagens to all living beings. Dyes which posses thick color to water and causes severe health problems like haemorrhage, ulceration of skin, nausea, irritation to skin and dermatitis. These dye containg wastewater are nonbiodegradable causing huge effect to environment (RAI et al. 2005). These textile effluents contains dyes, heavy metals and micro organisms which are very harmful to mankind and ecosystem.

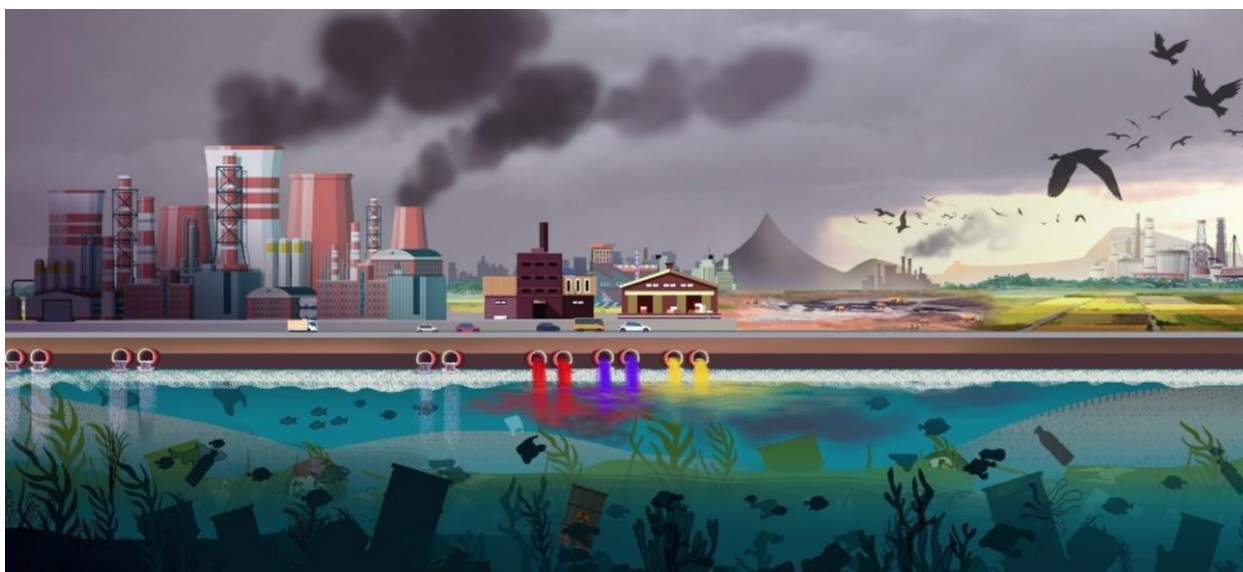


Figure 1.7. Diagrammatic representation of industrial wastewater affecting the entire ecosystem (Velusamy et al. 2021)

### 1.6.2 Types of Dyes

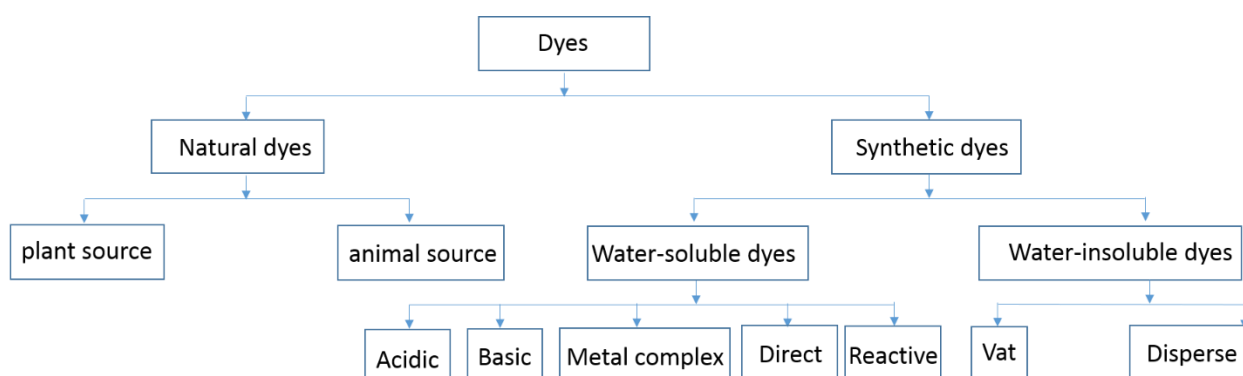


Figure 1.8. Schematic representation of Dyes classification

Dyes are soluble compounds that can absorb the light radiation within the visible range along with reflecting or scattering phenomena in a sustainable approach. Dyes contain auxochrome and chromophore possessing aromatic structure which enhances color and bond between the fiber during dyeing and printing process. Based on solubility, dyes are classified into two subdivisions i.e., water-soluble and water insoluble dyes.

#### **Water-soluble dyes:**

It includes basic, acidic, metal complex, direct and reactive dyes

#### **Acidic dyes:**

These are water-soluble anionic dyes which contain chromophore namely: azo, quinolone, xanthane and azine groups etc.

Eg: Acid orange, acid violet.

#### **Basic dyes:**

These are water soluble cationic dyes, perfect synthetic dyes which contain chromophores namely diphenylmethane, azine, thiazine and xanthene etc.

Eg: Basic blue, Rhodamine b, methylene blue.

#### **Metal complex dyes:**

These are mordant and pre-metallized dyes which showed high affinity towards protein fibers to form a coordinate bond with a metal ion through covalent bond formation.

Eg: Reactive black, brilliant green.

#### **Direct dyes:**

These are water soluble anionic dyes containing sulphonic acid groups to stabilize water solubility. Eg: Congo red.

#### **Reactive dyes:**

These are water-soluble anionic dyes which contain azo and anthraquinone based reactive dyes for proteins and polyamide fibres.

Eg: Reactive blue.

#### **Vat dyes:**

These are insoluble dyes, chemically complex solubilized on a alkaline reduction used for dyeing of cotton and other cellulose fibres along with mordant. They contain impurities like Cu, Fe, Pb, Cd, Ba and Mn during the production process.

Eg: Synthetic alizarin, Alizarin yellow.

#### **Disperse dyes:**

Disperse dyes are water insoluble, low molecular weight used for dyeing of hydrophobic fibres which contains mostly azo, anthroquinone, nitro and quinine groups.

Eg: Disperse orange 1, disperse red 60.

### **1.6.3 Effects of dyes**

In the modern world, environmental pollution became one of the vital and high priority problems across the globe. Due to the rapid development of industrial sector, water pollution has gained importance due to its close relationship with the mankind. These organic dyes and heavy metal ion contaminants which are discharged from dyes manufacturing industries, paper making industries, metallurgy and textile industries has resulted in increasing of toxic concentration in water bodies due to the heavy quantity of water used in textile industries, high amount of liquid pollutants are discharging (Li et al. 2016; Ma et al. 2017; Zhao et al. 2015). The presence of organic contaminants in industrial effluents which is a global concern to the environment because of its toxicity, carcinogenic nature and mutagenicity. These organic contaminants have low biodegradability and high stability towards photo-chemical treatments

because of their complex aromatic structure (Inyang et al. 2014). Some of the metallurgy industries are disposing heavy metals like lead and cadmium. These heavy metals are accumulating in the living organism over a period of time and causes serious diseases like memory loss, kidney problem and reproductive effect in human. To remove these pollutants from waste water, different types of techniques are developed such as biological water decontamination process, chemical precipitation and adsorption (Arami et al. 2005; Rahsepar et al. 2012).

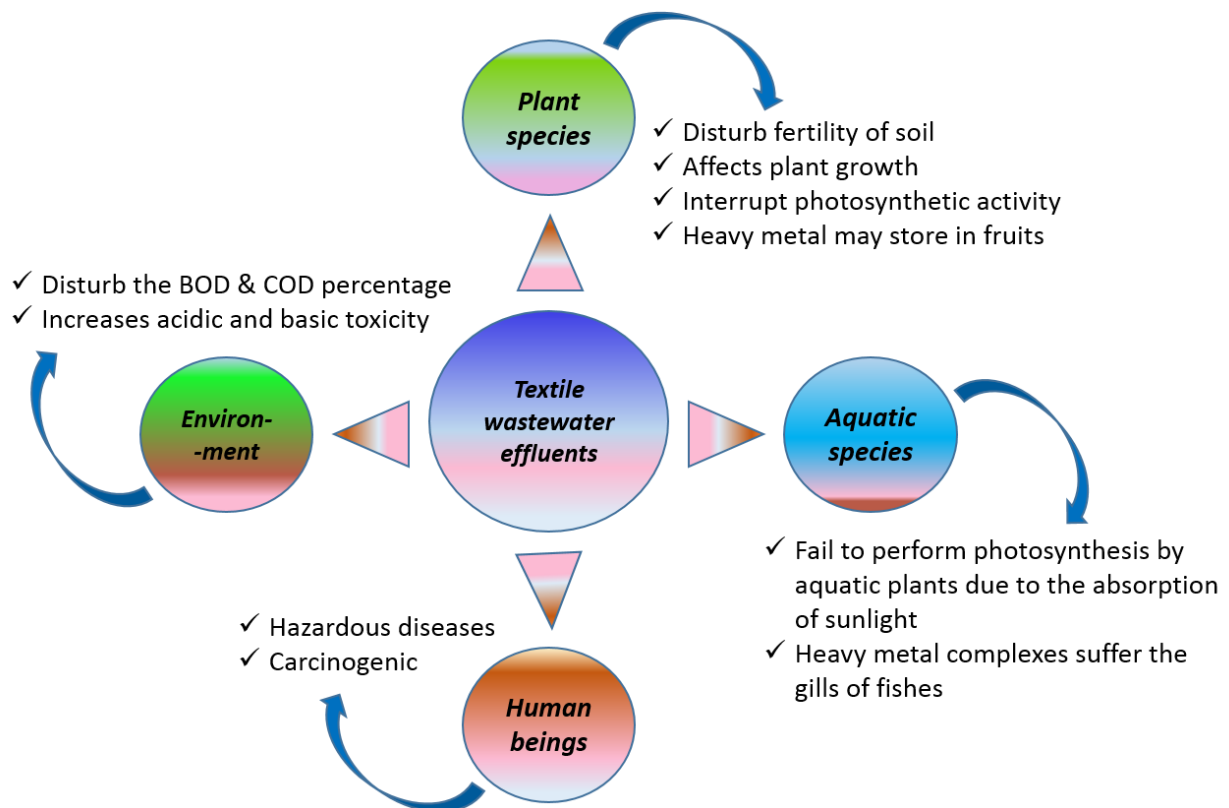


Figure 1.9. Nature of effects of Textile wastewater in our food chain

The cationic dyes used are Methylene blue (MB) and Rhodamine B (RB) are utilized for the dyeing of fabric in textile industry. Due to this, an excessive amount of MB released during this chemical process causes a wide range of environmental pollution. Annually a wide range of  $\sim 7 \times 10^5$  tons produced for commercial utilization of dyes are discharged into the water resources affecting the aquatic ecosystem. It causes carcinogenic and mutagenic effects in the living beings and the existence of dye in water hinder the penetration of sunlight in aquatic life leading to lack of photosynthesis thus affecting the food chain. RB is a brilliant red fluorescent dye, used as coloring agent in various industries and as biological stainer and tracer in biotechnology area. Its high solubility and inexpensive nature make it to use extensively in various fields. Beyond 10 ppm, it is highly poisonous to aquatic life and it is mutagenic and



carcinogenic in nature. In human, it causes skin irritation, respiratory infection, haemolysis of RBC, degenerative effects in liver, kidney etc.

An anionic dye named Congo red (CR) with a diazo group with symmetric aromatic groups is stable to thermal and optical activity due to its high resistance with respect to light and biodegradation property. It is carcinogenic and mutagenic to human population and aquatic life causing effects like respiratory problems, skin disorders and allergic reactions. Heavy metals were emerged due to pretreatment process such as dyeing, painting, and finishing steps due to the continuous usage of metal containing chemicals and complexes. According to the WHO and EPA the maximum permissible limit set for Pb(II) is  $6.0 \times 10^{-3} \text{ mg L}^{-1}$ . The effects of Pb(II) include digestive problems, neurological disorders, high blood pressure, reproductive health problems, kidney disfunction, muscle and joint pain, fertility problems. In case of infants it lead to the damage of developing brains. The maximum acceptable limit of Cd(II) according to BIS is  $0.003 \text{ mg L}^{-1}$  and with regards to EU the environmental quality it is  $10 \mu\text{g L}^{-1}$ . Cadmium which is a heavy metal used in industries such as plating, battery, phosphate fertilizers, stabilizers and alloys. It causes "Itai-Itai" disease in mankind due to its accumulation in the rivers which resulted in the softening of the bones and fractures (Bhatnagar and Sillanpää 2009). Even at a very low concentration, it causes hepatic toxicity, lung cancer, and diseases related to respiratory system, kidney and reproductive system (Demim et al. 2013; Filipič 2012).

The disposal of organic pollutants, dyes and heavy metals in wastewater was controlled by several protocols. Due to the existence of many inhibitory by-products, a high efficient enforcement method is required to remove pollutants from wastewater. In order to protect the environment and living organism, several treatment methods have been developed. Many conventional treatment methods such as coagulation-flocculation, ion exchange, membrane separation, ion exchange, chemical precipitation, reverse osmosis, electrochemical treatment, adsorption etc. In these methods, they have huge limitations such as high operational cost, rise in capital investment, and the dispose of secondary toxic pollutants.

### **Coagulation/Flocculation:**

Coagulants are used to enhance the density of colloidal solution and it depends on its solution type, pH, temperature, alkaline nature and mixing conditions. Commonly used coagulants are  $\text{Al}_2(\text{SO}_4)_3$ ,  $\text{Fe}_2(\text{SO}_4)_3$  etc. Although this method is effective for the removal of heavy metals but the main disadvantage is generation of secondary pollutants which are harmful to ecosystem. It also produces enormous sludge by the utilization of chemicals.

**Membrane filtration:**

It is the pressure driven separation technique in the treatment of wastewater. These porous membranes can foul easily with hydrophobic nature. Although, it has high removal efficiency for heavy metals, less space requirement and easy operation but the main disadvantage is rejection handling, membrane fouling and high-power cost. It involves many processes such as ultrafiltration, microfiltration and reverse osmosis. Clogging occurs in the microfiltration membrane which is the main defect of this membrane. In case of ultrafiltration, the polymers get adhered to the metal ions to form macromolecules and the membrane size is smaller than the macromolecules which get retained. However, the concentration of flux depends on PVA dosage, and it did not change the mercury elimination. Reverse osmosis which include semi-permeable membrane depends on size and charge exclusion. The main disadvantage is fouling of the membrane.

**Biological treatment:**

It involves microorganism in the biosorption process for the removal of heavy metal ions. The main disadvantage includes microorganisms and pre-treatment such as physicochemical treatment and creation of biological sludge and uncontrollable degrading products.

**Oxidation process:**

It is of many categories for the treatment of wastewater which include

**Fenton's process:**

Fenton oxidation involves the presence of UV light,  $H_2O_2$  is hydrolysed into the  $OH^\circ$  formation. So, the main disadvantage includes the formation of high amounts of anions in the treated wastewater and the generation of high amounts of Ferrous iron sludge.

**O<sub>3</sub> process:**

Ozonation process involves the synthesis of  $O_3$  using the oxygen molecules in presence of any energy source to form oxygen atoms to form an unstable ozone gas. This will get decomposed to elemental form over a short period by the reaction of radical by-products. The main disadvantages include more complex technique, high cost and huge amounts of suspended solids, BOD and COD etc.

**Adsorption:**

Adsorption is a surface frontier phenomenon where the aggregation of species/ materials onto a solution or solid phase from the abundant matter. Ion-exchange is a separation technique which substitutes the ions with another from sewage effluents with high removal efficiency of metal ions. Ion exchange resins which include natural and synthetic and they are cross-linked, long chain organic polymer, microporous and exchangeable ions. The main disadvantage of

this process is the fouling effect of the matrix formed when used in high heavy metal concentration. This process is expensive because a huge amount of synthetic resin is required for the large quantity of wastewater.

From the available literatures, adsorption process is a surface phenomena which operates in low cost expenses and a highly advantageous method for removing the various harmful dyes and heavy metal ions from the industrial toxic wastetwater. It operates in simple operation, high efficiency and feasibility in economy. Most of the researchers are interested to find the laser treatment technology which have achieved and explored efficient adsorbents to improve the efficacy in adsorption. From th above research, the carbonaceous materials proved to be effective adsorbents to remove pollutants because of their high internal pore structure, high surface area and a bulk range of functional groups.

Carbon based porous materials which possess highly attractive features with varied allotropic forms, micro structure and morphologies consist of carbon nanotubes, graphene, graphdiyne, activated carbon, mesoporous carbon, carbon nanospheres, amorphous carbon etc., having huge applications in environment and energy storage (Ahmad et al. 2018; He et al. 2018; Kuang et al. 2018; Liu et al. 2018; Qin et al. 2019; Wang et al. 2018; d; Xu et al. 2017). Out of the multifarious carbon allotropes, graphene derivatives gained attention due to its more oxygenated groups on its surface. Graphene, which is a one atom thick 2D layer of  $sp^2$  hybridized carbon atoms, was studied extensively, due to its exceptional electrical, mechanical, optical and chemical behavior. It has been known for the outstanding nano adsorbent due to its high surface area ( $\sim 2620 \text{ m}^2 \text{ g}^{-1}$ ) (Khurana et al. 2017; Novoselov et al. 2004, 2012). Graphene oxide is one among the carbon family which consists of unique characteristics such as numerous oxygen-containing functional groups i.e., hydroxyl, carbonyl, carboxyl as well as epoxy groups at its surface and edges. Graphene oxide have been extensively studied in the areas like photocatalysis, sensors, electrocatalysis and adsorption phenomena (Xu et al. 2018; Zhao et al. 2017; Zou et al. 2018). Although graphene oxide holds as a good adsorbent capability to the various pollutants, but the detachment of GO from the aqueous solution is a risky and challenging task because of the good hydrophilicity and effective dispersion of GO in the water. It needs energetic centrifugation or filtration, and these approaches further leads to the secondary pollution. In order to overcome this problem, magnetic separation became as an alternative technique by integrating magnetic nanoparticles onto GO to synthesize magnetic graphene nanocomposites have gained greater attention.

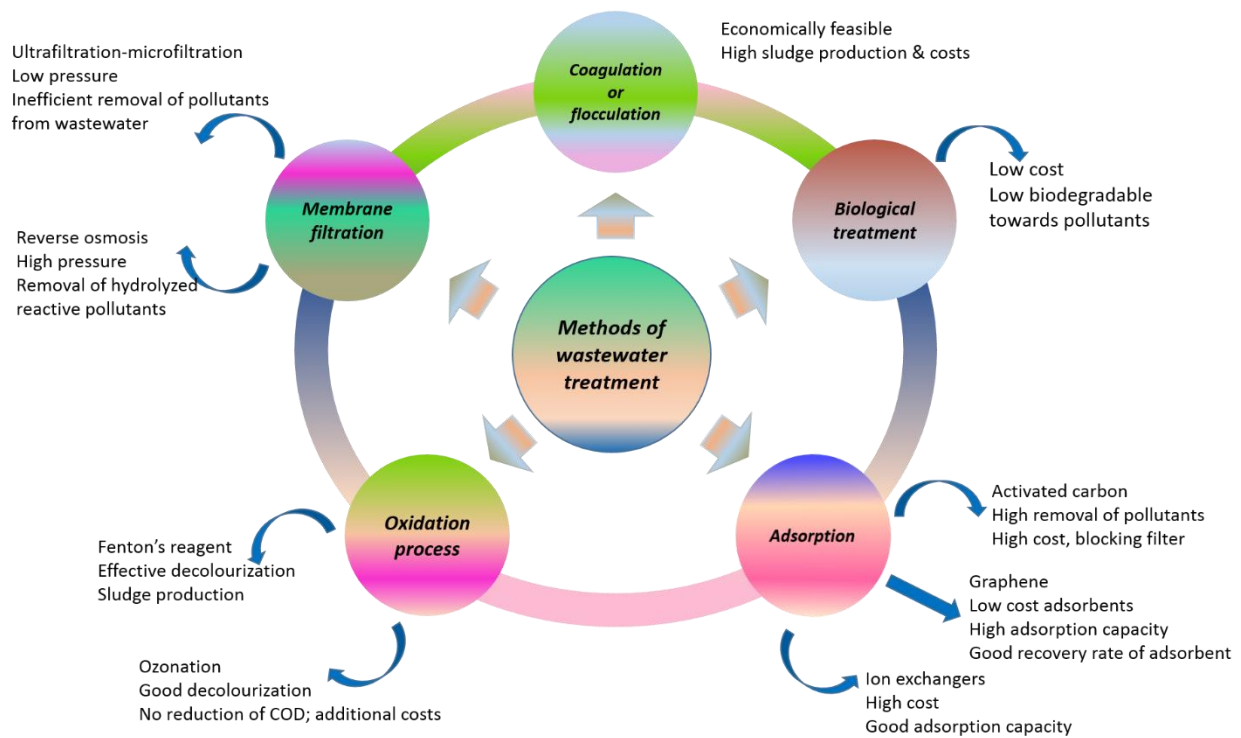


Figure 1.10. Various techniques for the treatment of wastewater

Adsorption is a surface frontier phenomenon where the aggregation of species/ materials onto a solution or solid phase from the abundant matter. This phenomenon has recognized from the archaic period. From the literature sources in 1773 where Scheele executed adsorption phenomenon for the gas uptake using solid supports such as charcoal and clay (Dąbrowski 2001). This research area i.e., adsorption gained more interest in its scope and significant improvements with the advancement of various isotherm models by Langmuir (Langmuir 1916) and Freundlich (Freundlich 1907) and the kinetic models envisioned by Lagergren (Lagergren 1898).

The usage of magnetic nature in the water purification is an antique concept. The predated text preceded the magnetism usage in wastewater treatment from 1873. Therefore, the usage of magnetism have engaged in diverse water treatments i.e., anti-scaling techniques and pipelines in industries (Coey and Cass 2000), coagulation (Singer and Bilyk 2002), biological processes (Ni et al. 2013). The usage of magnetism in this adsorption phenomena, which is a fascinated approach gained interest across the world. Magnetic adsorbents are a special type of adsorbents in which base material is ingrained with magnetic particles in the form of metal oxides such as Fe, Co, Ni and Cu (Philippova et al. 2011). With the usage of an external magnetic field, the magnetic adsorbent easily gets separated and quickly from wastewater due to the presence of metal component within the adsorbent. Since then, the magnetic nanoparticles modified with polymers (Albornoz et al. 2004; Philippova et al. 2011), CNTs (Hu et al. 2010) and graphite

materials (Park et al. 2019) have been developed and commercially utilized in the elimination of contaminants. An absolute adsorbent for the commercial use should possess factors such as (i) high activity (ii) fast adsorption rate (iii) cost-effective (iv) environmental friendly (v) reusability and (vi) easy separation of the adsorbent.

With the latest generation adsorbent substances evolved so far, magnetic nanoadsorbent possessed high surface area, tunable morphology, ease of separation and high efficiency are the most promising path. During the recent times, spinel ferrites became the fundamental choice for the removal of organic and inorganic contaminants for the treatment of water applications because of the presence of nanometer-sized, superparamagnetic properties and a high surface to volume ratio. Spinel ferrites ( $MFe_2O_4$ ) are magnetic materials where the M(II) and Fe (III) cations occupy both tetrahedral as well as octahedral sites respectively whereas inverse spinel ferrites half of the Fe (III) occupy tetrahedral site. The spinel ferrites designed on the graphene oxide nanosheets can avoid agglomeration, apart from its graphene which inhibited the leaching the pollutants thereby increasing the efficiency in adsorption process.

## 1.7 ADSORPTION MODELS

### 1.7.1 Adsorption Isotherms

Heterogeneous nanocomposite has been applied extensively for the adsorption of dyes and heavy metals. For this adsorption study, a constant adsorbate concentration can reach equilibrium at a specified temperature. However, the term sorption isotherm denotes to the distribution of concentration of adsorbate and adsorbent in an aqueous solution. The parameters obtained from the sorption isotherms can be applied to know the surface properties of adsorbents and other properties such as particle size, metal ion and pH of the solution. For fitting a nonlinear isotherm model, the dependent and independent variables are transformed and evaluated by different error equations.

Four models have been proposed to compare the isotherm data obtained from adsorption study for the dyes and metal ions.

Langmuir Isotherm:

$$q_e = \frac{Q_m K_a C_e}{1 + K_a C_e} \quad (1.1)$$

Freundlich Isotherm:

$$q_e = K_f C_e^{1/n} \quad (1.2)$$

DR Isotherm:

$$q_e = \frac{RT}{b_T} \ln A_T C_e \quad (1.3)$$

Temkin Isotherm:

$$q_e = (q_s) \exp(-K_{DR} \varepsilon^2) \quad (1.4)$$

Where  $Q_m$  ( $\text{mg g}^{-1}$ ) represented to the maximum adsorption equilibrium of adsorbent was explained using monolayer with the pollutants per unit mass.  $K_L$  is known as Langmuir adsorption coefficient ( $\text{L mg}^{-1}$ ) which explained the energy of adsorption.  $K_f$  is an approximation constant and the factor  $1/n$  described as function of adsorption strength.  $1/n$  factor value higher than one which corresponds to the cooperative adsorption on its nanocomposite surface. The  $K_f$ , value enhances with the increases in adsorption capacity. From Temkin model, where  $R$  corresponded to the Universal gas constant ( $8.314 \text{ J/mol/K}$ ),  $A_T$  as the maximum binding constant ( $\text{L g}^{-1}$ ) and  $b_T$  refers to the heat of adsorption ( $\text{J mol}^{-1}$ ).  $q_s$  ( $\text{mol g}^{-1}$ ) termed to be maximum adsorption capacity of D-R model which is used to know the porosity of adsorbent with the energy of adsorption ( $E$ ),  $K_{DR}$  ( $\text{mol}^2/\text{k/J}^2$ ) is the D-R isotherm constant, which is linked to the free energy required for adsorption per unit mass of the adsorbate,  $\varepsilon$  corresponds to the Polanyi potential using the following expression:

$$\varepsilon = RT \ln \left( 1 + \frac{1}{C_e} \right) \quad (1.5)$$

To calibrate the mean free energy for the adsorbent we calculated by using the following equations:

$$E = \frac{1}{(2B_D)^{1/2}} \quad (1.6)$$

All the isotherm models were calibrated and optimized with the experimental data to measure the (COD), coefficient of determination  $r^2$  using the following expression with the graphs plotted in non-linear pattern in origin software.

$$r^2 = \frac{(q_m - \bar{q}_e)^2}{(q_m - \bar{q}_e)^2 + (q_m - q_e)^2} \quad (1.7)$$

The term  $R_L$  known to be dimensional separation factor was calibrated to know the relationship between adsorbent and the adsorbate group which is given by the expression.

$$R_L = \frac{1}{1 + K_a \times C_o} \quad (1.8)$$

### 1.7.2 Thermodynamic Studies

Among the isotherm models, Langmuir found to be best model for calculating the thermodynamic factor at various temperatures.  $K_a$  value is made dimensionless and the parameter like Gibbs free energy ( $\Delta G^\circ$ , KJ mol<sup>-1</sup>), change on enthalpy ( $\Delta H^\circ$ , KJ mol<sup>-1</sup>) and change in entropy ( $\Delta S^\circ$ , J/mol/K) were measured via equations and plotted in table. Here, it is unimolecular adsorption and the calculated values for the equilibrium constant  $K_e$  is given below eq.

$$K_e = \frac{1000 \times K_a \times M}{\gamma} \quad (1.9)$$

$$K_e = \frac{1000 \times K_a \times \text{mol. wt. of adsorbate} \times \text{standard conc. of adsorbate}}{\text{activity coefficient of adsorbate}}$$

$$\Delta G^\circ = -RT \ln(K_e) \quad (1.10)$$

The equation calculated with the help of thermodynamics 3<sup>rd</sup> law

$$\Delta G^\circ = \Delta H^\circ - T \Delta S \quad (1.11)$$

Van't Hoff's Equation calculated by fitting the curve from the equation (12) and (13) (Lima et al. 2015, 2019; Liu 2009; Xu and Liu 2008)

$$\ln K_e = \frac{\Delta S^\circ}{R} - \frac{\Delta H^\circ}{RT} \quad (1.12)$$

The term  $K_e$  corresponds to the equilibrium constant for adsorption,  $M$  (g/mol) refers to the pollutant molar mass,  $\gamma$  known as the activity coefficient (dimensionless),  $R$  referred to the gas constant,  $T$  is the temperature (K). The graph between  $\ln K_e$  and  $1/T$  gave the slope and intercept for the calculation of  $\Delta H^\circ$  as well as  $\Delta S^\circ$  (Panagopoulos et al. 2017).

### 1.7.3 Adsorption Kinetic Studies

To investigate the mechanism for the pollutants adsorption study, various theoretical models have been studies on the reaction rate data, these are

- 1) Pseudo first order
- 2) Pseudo second order
- 3) Intraparticle diffusion

Pseudo first order Kinetic model:

The linear form of PFO equation is as follows:

$$\ln(q_e - q_t) = \ln q_e - k_1 t \quad (1.13)$$

Pseudo second order Kinetic model:

The linear form of PFO equation is as follows:

$$\frac{t}{q_t} = \frac{1}{k_2 q_e^2} + \frac{1}{q_e} \quad (1.14)$$

Where  $k_1$  ( $\text{min}^{-1}$ ) referred to the pseudo 1<sup>st</sup> order rate constant and  $k_2$  ( $\text{g/mg/min}$ ) corresponds to the pseudo 2<sup>nd</sup> order rate constant;  $q_t$  &  $q_e$  are the adsorption capacities of the adsorbent at any time  $t$  and equilibrium respectively.

PFO model assumes that it is physisorptive in nature whereas PSO model assumes that the adsorption is chemisorptive in nature where the rate of adsorption is controlled by the sorption kinetics.

Intraparticle diffusion model:

To evaluate the diffusion process upon the substrate, an intraparticle diffusion model proposed by Weber and Morris by the following equation:

$$q_t = k_p t^{1/2} + x_i \quad (1.15)$$

This mechanism gave the equation where the uptake of pollutant at regular time interval ( $q_t$ ) vs time  $t$ , where  $k_p$  ( $(\text{mg/g}) \text{min}^{1/2}$ ) is a intraparticle diffusion rate constant (Weber and Morris 1963). Where  $x_i$  represented the boundary layer thickness (Kavitha and Namasivayam 2007). The plots between  $q_t$  and  $t^{1/2}$  indicated the intercept positive values i.e.,  $x_i \neq 0$ . If  $x_i = 0$ , the way, adsorption phenomena is monitored by this method (Wu et al. 2009), the positive value of intercept explained the spontaneous type that took at time  $t = 0$  initially through film diffusion.

Activation energy:

$$\ln k_2 = -\frac{E_a}{2.303RT} + \text{constant} \quad (1.16)$$

The graphs plotted between  $\ln k_2$  vs  $1/T$  taken for examining the data of rate constants of pseudo second order ( $k_2$ ) at various temperatures to calculate the activation energy ( $E_a$ ) values.

## 1.8 VISION

Carbon is among the most abundant material found around us. Carbon nanostructure have been present with us since the time we learnt to make fire and its real potential have been unearthed only in couple of decades. Their properties and ease of modification to support nanoparticles makes them as an ideal choice for wide range of applications such as catalysis, environment and energy storage devices etc. Along with carbon support, nanoparticles started to play a prominent role in shaping the design of nanocomposites. Various literature reports have emphasized the compatibility of these materials towards these applications.



With each progressive step taken in science and technology, we are also risking our environment with a variety of pollutants and hazardous materials. This makes the importance of nanoadsorbents for the removal of organic and inorganic pollutants even more evident. Today, due to the rapid industrialization and heavy usage of dyes and metals ions in textile industries, we are surrounded with hazardous organic and inorganic pollutants like heavy metals, cationic and anionic dyes, toxic gases, biological parasites to name a few. The removal of harmful pollutants from various water bodies is vital to the entire ecosystem. The process of removal of these pollutants should be a lead cause for the generation of secondary pollutants along with heavy sludge formation. These 2D carbon nanostructures with the impregnation of nanoparticles in itself to form nanocomposites excelled in this field, of all the above-mentioned targeted groups. Their high surface area and excellent adsorption performances enables them to be used for removal of these pollutants with exceptional adsorption capacity.

Progress in medicinal chemistry also means we need more alternatives catalysts to sustain our future challenges. Although various homogenous catalysts were present for the synthesis of various organic compounds which require intensive work and high cost along with labour in industries. The introduction of heterogeneous catalysts with the applications of nanotechnology helps us to deal with the challenging organic reactions in the nearby future. In this field, again the use of 2D carbon nanomaterials is at the forefront in terms of research pertaining to catalytic reactions. With the finding of GO supported metal oxides as catalysts which is also a possibility for exploring the various cross-coupling reactions. Much research has been done since 2009 to see the GO supported metal oxides as catalysts for the cross-coupling reactions. Therefore, the properties of graphene oxide nanocomposites towards the adsorption and catalytic application are explored.

**CHAPTER-2**  
**STATE OF THE WORK**

**Abstract:** *This chapter summarizes the current state of research pertaining to the synthesis of graphene nanocomposites for their intended usage in adsorption and catalytic applications.*

## **2.1 LITERATURE SURVEY**

Graphene and their nanocomposites gained significant attention for the synthesis of metal catalysed carbon-carbon bond formation and the adsorption of various pollutants from the textile industry wastewater. The development of coupling reactions for the formation of carbon-carbon formation started in the earlier 1970s attained a lot of attention in synthetic organic chemistry. Compound containing carbon-carbon bond have found applications in diverse areas including pharmaceuticals, natural products, optical materials, liquid crystals, conductive polymers etc. These metals involved coupling reactions became a major choice for the biaryl synthesis which has the more synthetic advantage such as high selectivity, broad substrate scope and mild reaction condition.

### **2.1.1 History of Suzuki cross-coupling reaction**

The formation of carbon-carbon bond in synthetic organic chemistry has been developed in 1970's using the transition metals as catalysts is of utmost importance due to its diverse applications such as pharmaceuticals, natural products, optical materials, liquid crystals and conductive polymers etc. The synthesis of biaryl compounds in the presence of transition metals catalysis is the main choice due to its advantages such as high selectivity, broad substrate, scope and mild reaction conditions.

The first catalytic reaction which is a stereospecific cross-coupling catalysed in the presence of  $\text{Pd}(\text{PPh}_3)_4$  catalyst with the alkenyl boranes and alkenyl or alkynyl halides to form trans dienes with high stereo and regio product with good yields. (Miyaura et al. 1979). Later, the  $\text{Pd}(\text{PPh}_3)_4$  catalysed the various aromatic halides with aryl boronic acids with aqueous  $\text{Na}_2\text{CO}_3$  base under  $\text{N}_2$  atmosphere and the products were analyzed by Gas Chromatography (GC) (Miyaura et al. 1981). The cross-coupling reactions were done in presence of water soluble  $\text{Pd}(0)$  catalyst using an organic base to yield 60-90% yield (Miyaura et al. 1989).

The Pd catalysts  $\text{Pd}(\text{OAc})_2$ , in presence of (N, N-dimethylamino-1'-dicyclohexyl phosphino) biphenyl ligand for the effective cross-coupling of aromatic chlorides which are electron rich as well as electron deficient at room temperature and  $\text{K}_3\text{PO}_4$  as base (Wolfe and Buchwald 1999). The doping of Pd on  $\text{KF}/\text{Al}_2\text{O}_3$  as an effective catalyst for the cross-coupling

of aromatic halides and boronic acids without any solvent for 4h to give biaryl products (Kabalka et al. 1999).

The complexes synthesized such as Pd-imidazol-2-ylidene which catalysed the coupling of chlorides with boronic acids in presence of  $\text{Cs}_2\text{CO}_3$  base, dioxane solvent for 1.5h. The products were confirmed by Thin Layer Chromatography (TLC) and isolated by Column Chromatography (CC) (Zhang et al. 1999). The Pd nps which were optimized by PVP were effective for catalysing the reaction of 2-thiophene boronic acid with iodides (Li et al. 2000). A new class heterogeneous support such as perovskites with palladium as stable catalysts for catalyzing the halides with boronic acids and  $\text{K}_2\text{CO}_3$  base at 80 °C to give 95% yield (Smith et al. 2003). The deposition of  $\text{Pd}(\text{OH})_2$  onto the carbon support known as Pearman's catalyst found to be highly effective in catalyzing the Suzuki cross-coupling reactions of boronic acids with 1-bromo-4-nitrobenzene in presence of aqueous  $\text{Na}_2\text{CO}_3$  at 80 °C to give biaryls as products (Mori and Seki 2003).

The synthesis of ligand series such as 2-aryl-2-oxazoline ligands with Pd for catalyzing the bromides with boronic acids in  $\text{Cs}_2\text{CO}_3$  base and dioxane solvent at 80 °C to form biaryl products (Tao and Boykin 2002).  $\text{Ni}(\text{COD})_2/\text{PCy}_3$  catalysts catalysed the cross-coupling of aromatic arenesulfonate with borates at room temperature using  $\text{K}_2\text{CO}_3$  base and THF solvent for 8h gives biaryl product with a good yield (Tang and Hu 2004).

### **2.1.2 Emergence of other transition metals as catalysts for Suzuki cross-coupling reactions**

For the first time, the synthesis of bimetallic cluster such as Pd/Ni nanocluster catalysts were controlled by PVP or tetraalkyl ammonium salts were effective for the cross-coupling of reaction partners such as iodo, bromo or activated chloroaromatics (Reetz and Westermann 2000). The introduction of copper/Pd bimetallic nanoclusters as clusters emerged as a new trend in the usage of 3d transition metals and investigated by Thathagar et. al. The catalysts were analysed by XRD and the size of the metal clusters found to be 1.0 and 2.5 nm with a distribution of  $\pm 0.1$  nm (Thathagar et al. 2003). Ni complexes which are phosphine free i.e.,  $\text{NiCl}_2(\text{NET}_3)_2$  and  $\text{NiCl}_2(\text{bipy})$  were synthesized and first reported the catalytic activity. It is found that the Ni catalysts were highly active for these reactions (Leadbeater and Marco 2003). The Pd nanoparticle size of around 1-5 nm were stabilized by poly(N,N-dialkyl carbodiimide) ligand and the catalytic reactions were carried with halides and boronic acids to get a maximum yield of 97% and a TON of 1600 (Liu et al. 2004).

A new, air stable palladium catalyst (DAPCy) which was synthesized from Pd(OAc)<sub>2</sub> and dicyclohexylamine for the effective catalysis of bromides with boronic acids at room temperature under normal conditions. The crystal was analyzed by SC-XRD (Tao and Boykin 2004). The synthesis of Pd-SH-FSM catalyst through the mesoporous silica FSM-16 which was supported by mercaptosilane Pd complexes which is a heterogeneous catalyst for determining the catalytic activity of 4-bromo anisole and boronic acids, K<sub>2</sub>CO<sub>3</sub> base, benzonitrile as internal standard with DMF solvent at 130 °C under N<sub>2</sub> atmosphere. The catalyst gave a TON of 73,000 and TOF is 36,000 h<sup>-1</sup> (Shimizu et al. 2004).

A mixed oxide named Pd/MgLa was investigated to know the catalytic activity of chlorides and bromides with boronic acids. The catalyst advantages are easily separated, regeneration capacity and doesn't need any inert conditions (Cwik et al. 2005). The synthesis of poly(2-oxazoline) ligand and functionalization by using Pd carbene complex to form polymer induced catalyst with a TOF of 5,200 h<sup>-1</sup> and TON of 2700 for the cross-coupling of iodides with boronic acids (Schönfelder et al. 2005).

### **2.1.3 Graphene as supportive materials for nanoparticles in Suzuki cross-coupling reactions**

The synthesis of Fe<sub>2</sub>O<sub>3</sub> nanoparticles which were supported on Pd-NHC complex for catalyzing the aryl halides with boronic acids and the products recovered using FC and analysed by NMR and mass spectral studies. It can be easily separated using permanent magnet externally (Stevens et al. 2005). The polymer catalyst which is phosphine free named carbapalladacycle supported on PEG (MW 6000 Da) network was an effective and reusable catalyst up to 10 consecutive cycles with a high TON (Corma et al. 2006). A novel air-stable PdCl<sub>2</sub>{P<sup>t</sup>Bu<sub>2</sub>(p-R-Ph)}<sub>2</sub> (R=H, NMe<sub>2</sub>, CF<sub>3</sub>) complex which served as a catalyst in the coupling of halides which includes 5 or 6 membered ring structures with a broad range of borates. The product yield is from 89-99% with a TON up to 10,000 (Guram et al. 2006).

The complex that is formed by the coating of PEG over mesoporous silica upon Pd for the catalytic reactions in H<sub>2</sub>O. The complex catalyst SBA-Si-PEG-Pd(PPh<sub>3</sub>)<sub>n</sub> is stable in air for weeks and the reactions were done in normal conditions to give maximum yield of 98% without any Pd Leaching (determined by ICP) (Yang et al. 2006). A heterogeneous and ligand free Pd on carbon support as a catalyst for the catalytic reaction of 4-bromonitrobenzene with arylboronic acid to form biaryl products in aqueous media (Maegawa et al. 2007).

The synthesis of chiral catalyst which is binap stabilized by Pd nanoparticles with a size of 1.2-1.7 nm for the catalytic reactions of naphthyl halides with naphthyl boronic acid to form stereospecific chiral naphthalene's as products (Sawai et al. 2008).

The usage of triazolyl dendrimers for stabilizing the Pd nanoparticles termed as "Click chemistry" which is a stable catalyst can effectively catalyze the reaction with a low amount of Pd (0.01mol%). The catalyst is analysed using TEM and UV spectroscopy (Ornelas et al. 2008). A versatile catalyst (tert-butylphenylphosphinomethyl) polystyrene with Pd nanoparticles for catalyzing the Suzuki cross-coupling reactions of aryl chlorides. The Pd amount is as low as 4 milliequiv and it can reusable up to 7 cycles with a less leaching of < 0.1% of initial amount (Schweizer et al. 2010).

The synthesis of uniform sized nanorods Pd around 200 to 300 nm using copper acetate for catalyzing the aryl iodides with boronic acids for 4h in EtOH:H<sub>2</sub>O (4:1). The product is extracted using dichloromethane with the help of GC-MS (Chen et al. 2009). The synthesis of palladium nanoparticle immobilized on various graphite substrates such as graphite oxide Pd<sup>+2</sup>-GO, chemically reduced graphene oxide Pd<sup>0</sup>-CDG and Pd<sup>0</sup>-CDG-H<sub>2</sub> and Pd<sup>0</sup>-CDG-N<sub>2</sub>H<sub>4</sub> and Pd<sup>0</sup>-CDG-EXP and characterized using SS-NMR, X-ray scattering(WAXS), BET, FE-SEM and TEM analysis. These Pd catalysts catalyzes different aryl bromides with boronic acids in presence of EtOH:H<sub>2</sub>O (1:1) ratio as solvent at 80 °C and the products were analysed by HPLC analysis. It has a TON up to 6700 and the higher TOF exceeding 39,000 h<sup>-1</sup> which is highest for heterogeneous catalyst in this reaction. The palladium leaching is (<1ppm) which is done by AAS (Scheuermann et al. 2009).

The formation of Pd nanoparticles by reducing Na<sub>2</sub>PdCl<sub>4</sub> using SDS and EG and their deposition on CNTs for the cross-coupling of 4-iodoacetophenone with boronic acids in 30min to give 100% yield without any deterioration of catalytic activity after repeated cycles. The TOF up to 1520 h<sup>-1</sup> (Chen et al. 2008). For the first time, the synthesis of CuO and 2,2-diamino-6,6-dimethylbiphenyl ligand for the effective catalyses of iodides/bromides with boronic acids in presence of K<sub>2</sub>CO<sub>3</sub> base and DMF as solvent (Ye et al. 2010). The synthesis of Pd nanoparticles on rGO by the irradiation of GO with Pd ions in aqueous solution. The catalyst exhibits exceptional catalytic activity with a high TON of 7800 and TOF of 2,30,000 h<sup>-1</sup> (Siamaki et al. 2011).

The synthesis of Ni/Pd core/shell nanoparticles up on graphene which possessed high surface area with a high stability. It is effective in the coupling of boronic acids with aryl halides at 110 °C with a high conversion rate of 98% with the consecutive 5<sup>th</sup> run. The catalyst size is 10 nm (Metin et al. 2013). A novel Pd catalysts supported on fibrous

nanosilica KCC-1 functionalized with amino groups was synthesized and characterized by SS-NMR and TEM. The catalyst catalyses the aryl halides, arylboronic acid and  $K_3PO_4$  were heated in 3:2 ratio of  $H_2O$  and EtOH at  $100\text{ }^\circ C$  for 4h to give 97% yield through GC analysis (Fihri et al. 2012). The synthesis of heterogeneous catalyst (Pd-Ni/rGO) fabricated due to the interaction of nickel oxide around the Pd/GO with a size of  $2.5\pm 1\text{ nm}$ . The TOF is  $38,750\text{ h}^{-1}$  for Suzuki cross-coupling reaction with a maximum yield of 96% (Nie et al. 2014).

The synthesis of Pd nanoparticles and their immobilization of phosphine functionalized graphene (phosphorus ligand  $PPh_2$  groups grafted on the surface of graphene). The catalytic reactions were performed by using PFG-Pd(1.2mol% Pd),  $K_2CO_3$ ,  $H_2O:EtOH(1:1)$  for 12h at  $80\text{ }^\circ C$  to give maximum yield of 93% (Fareghi-Alamdari et al. 2016). The formation of graphene supported bimetallic nanoparticles species (Pd-Co) by chemical reduction method of varied composition and investigated by various analysis like XPS, TEM, XRD and Raman spectra. The Metal nanoparticles Pd, Co (1:1) on graphene is an effective catalyst for the Suzuki cross-coupling reaction. The enhances activity of the catalyst is due to the graphene's high surface area and promotional effect of Co dopants which increases the reactivity of Pd sites (Feng et al. 2014).

The design of copper salen complex on GO support through immobilization and further analysed by XPS, Raman Spectra, SEM, TEM and EPR (Zhao et al. 2014). Later, the synthesis of graphene immobilized MTO-Schiff base complex using methyltrioxorhenium (MTO). The composite formed is analysed by FTIR, TGA and elemental analysis (Khatri et al. 2014). The immobilization of oxo-vanadium Schiff base up on GO by using APTMS as a coupler. The synthesized vanadyl Schiff base analysed by FTIR, TGA, XRD and ICP-AES (Verma et al. 2014). A new and heterogeneous catalyst synthesized by the covalent linkage of copper(II) complex of 1,2-bis(4-aminophenylthio)ethane up on GO and it is analysed by XRD, TEM, FE-SEM and ICP-AES analysis (Zarnegaryan et al. 2016).

The synthesis of [(TMEDA)Ni(o-tlyl)Cl] using TMEDA ligand along with diamine and phosphate-ligated Ni and Pd complexes and analysed by SC-XRD studies. The nickel complexes catalyses  $sp^2-sp^3$  Suzuki cross-coupling with various aryl halides substrates and the maximum yield is 98% with a selectivity of 87% (Shields et al. 2015). The synthesis of Fe-ppm Pd nanoparticles using pure  $FeCl_3$  doped with 320ppm of Pd using 0.005M  $Pd(OAc)_2$  solution in dry  $CH_2Cl_2$ . The reactions were carried out using halides with boronic acids using 5mol% pure  $FeCl_3$ ,  $Pd(OAc)_2$  (320ppm), Sphos (5mol%) Nps under Argon atmosphere for 24h at  $45\text{ }^\circ C$  to yield 95%. The filtrate is augmented with TPGS-750-M therefore no wastage after

the reaction workup is done. The environmental factor (E factor) “a metric of greenness” is applied to micellar catalysis is very low (E factor=3) (Handa et al. 2015).

The formation of Nickel diglyme in presence of glycerol as solvent for the coupling of diazonium salts. Usually diazonium salts are well known for various couplings of C-N, C-O, C-S organic transformation. The reactions of various substituted diazonium salts with boronic acids done under optimized conditions to give a higher yield of unsymmetrical biaryl products. Here the base free conditions and glycerol as solvent which makes the reaction environmentally benign in nature (Bhojane et al. 2016). The synthesis of cationic Ni pincer complexes using the 2, 4-diaminotriazine scaffold and analysed by SC-XRD. The complexes were air stable, thermally robust and the catalyst catalyses the several  $sp^2$  and  $sp^3$  halides and pseudo halides with various boronic acids. The products were isolated using CC and maximum yield is 98% (Mastalir et al. 2016).

The novel ionic liquid catalyst i.e., Pd supported ionic liquid (Pd-SILP) which is an amino functionalized imidazolium was immobilized up on Merrifield resin (Pd-SILP-PS). The weakly binded amine group makes the facile ligand exchange and also broader scope of  $\sigma$ -donation. However, the SILP catalyst is stable and effective for the coupling of 4-halobenzophenone and boronic acids in presence of EtOH at room temperature within 10 min to give good yields with both iodo and bromo substituents (More et al. 2017). The synthesis of GO framework with encapsulating with Pd nanoparticles to know the catalytic activity both in protic and aprotic solvents (Tran et al. 2018). A facile synthetic method to form triple hollow carbon spheres using hydrothermal method in a one pot mechanism. Here, the synthesis of  $CuNiFe_2O_4$  ferrites synthesized by mixing Fe, Cu, Ni salts with glucose and heated at 180 °C. The coupling between the iodides and bromides with boronic acids to give biphenyl product with good yield for Suzuki cross-coupling. The complex catalyst possesses more active sites, high surface area and easy recovery (Rajabzadeh et al. 2018).

The synthesis of magnetically separable sporopollenin-based Pd catalysts which is bio-based and catalysed the various aryl halides with phenylboronic acids to give biaryl products. The prepared catalyst was magnetically recoverable and retained its catalytic activity up to 10<sup>th</sup> cycle for biphenyl yields i.e., 93 % with a remarkable TOF (Baran et al. 2018a). A series of Pd catalysts on hydrogen nanotubes by impregnating method of different loadings. The synthesized catalyst catalysed the cross-coupling of 4-bromobenzaldehyde with phenylboronic acid and 4-hydroxy phenylboronic acid which gave good results. The catalyst was reusable upto 5<sup>th</sup> cycle and further deactivation of the catalyst attributed to the Pd leaching during filtration as well as the presence of inorganic and organic ion species on the catalytic



surface and the agglomeration of pd nanoparticle on its reactive sites (Martínez-Klimov et al. 2018). A hydrophilic heterogeneous cobalt catalyst was synthesized using chitosan, mTEG-CS-Co-Schiff base for the catalytic activity in water as solvent. The maximum yield for the biphenyl product is 93% at 90 °C (Sobhani et al. 2020).

The synthesis of Iron oxide-boehmite composite using the cobalt nanoparticles on amino functionalized boehmite with Iron oxide for the evaluation of its catalytic activity. The maximum yield obtained is 95 % using water solvent and KOH base at 80 °C (Mohammadinezhad and Akhlaghinia 2017). The synthesis of magnetic starch which is functionalized with 2,2'-furil with amine functionality composed of apple seeds for the immobilization of cobalt. The maximum product formed is 95% using EtOH:H<sub>2</sub>O (1:1) solvent mixture, K<sub>2</sub>CO<sub>3</sub> base at 80 °C (Arghan et al. 2019). The synthesis of L-dopa ligand and their functionalization on GO supported Co@Fe<sub>3</sub>O<sub>4</sub> for investigating the cross-coupling of aryl halides with boronic acids. The maximum yield is 80 % with K<sub>2</sub>CO<sub>3</sub> base and water solvent at 100 °C (Sharma et al. 2019). The design of sulfonated salicylidene thiadiazole complexes with Co(II) as the catalyst for determining the catalytic activity. The maximum product formed is 80 % using K<sub>2</sub>CO<sub>3</sub> base and EtOH solvent at 100 °C (Abd El-Lateef et al. 2019).

#### **2.1.4 Graphene oxide metal nanoparticles as adsorbent in the removal of organic and inorganic pollutants**

Various adsorbents has been investigated for the elimination of organic and inorganic contaminants in water using activated carbon (Li et al. 2014; Natale et al. 2013; Tang et al. 2007), silica gel (Kumar et al. 2007; Yin et al. 2009), zeolite (Chaouati et al. 2013; Kong et al. 2014; Rida et al. 2013), clay minerals (Mouzdahir et al. 2010; Zhang et al. 2011). In spite of heavy generating expenses, most of the scientists moved their target from dead biomass and waste material such as peanut shell (Witek-Krowiak et al. 2011), saw dust (Kalavathy and Miranda 2010; S and A-H 2012), sunflower leaves (Benaïssa and Elouchdi 2007), guava leaf (Ponnusami et al. 2008) for the elimination of various pollutants from industrial effluents. Furthermore, these adsorbents found to have more efficient in the elimination of various pollutants from wastewater and they have single innate detriment which is crucial to separate them. Due to this, studies were investigated to examine the usage of magnetism as a beneficial strategy to separate the floating adsorbents in wastewater.

Cobalt oxide (Co<sub>3</sub>O<sub>4</sub>) nanoparticles being inorganic metal substituents which gained significant importance due to cubic spinel crystals in chemistry field. Although Co<sub>3</sub>O<sub>4</sub> have prominent applications in various fields, but its usage as adsorbent for the removal

of harmful contaminants from the textile wastewater in recent times (Al Nafiey et al. 2017; Deng et al. 2016; Shahabuddin et al. 2016; Song et al. 2016). In short,  $\text{Co}_3\text{O}_4$  application is new in the environmental research area. Although, metal oxide nanoparticles are best for the removal of pollutants, but the agglomeration of nanoparticles makes it impossible to get the regenerative cycles. Hence, these metal oxides were surrounded by polypyrrole which then later immobilized onto graphene oxide heterogenous support. The formation of P25 which is a self-prepared  $\text{TiO}_2$  surrounded with polypyrrole (PPy/P25 or PPy/ $\text{TiO}_2$ ) nanocomposite in the elimination of cationic methylene blue (MB) was investigated by Feng et al. The results proved that it observed Langmuir adsorption and Pseudo second order which explained its role of adsorption behavior in the nanocomposite. (Li et al. 2013). The synthesis of PPy and their coordinated metal oxides (PPy/ $\text{Al}_2\text{O}_3$ ) with different groups by oxidative polymerization to know the effect of adsorption property of metal oxide and their respective removal of cationic contaminants such as MB. The removal of MB on  $\text{Al}_2\text{O}_3$  surface is higher than  $\text{SiO}_2$  and  $\text{Fe}_3\text{O}_4$  (Chen et al. 2016). Further, the fabrication of PPy up on the PVF nanofibers via core-shell shape using polydopamine. The  $q_{\text{max}}$  of MB and CR were 370.4 and 384.6 mg/g and it is dependent on the solution pH (Ma et al. 2018). The introduction of NiFe LDHs with 3D GO through a sandwich model reported in hydrothermal technique. It showed high adsorption for the anionic pollutants like CR, methyl orange and hexavalent chromium ions (Zheng et al. 2019).

The formation of magnetic lignin type adsorbent ( $\text{Fe}_3\text{O}_4/\text{C-ALCLS}$ ) for the adsorption studies of azo group having dyes such as CR, Titan yellow and Eriochrome blue black R. It followed the pseudo first, second orders along with Elovich and Intraparticle diffusion model (Jiang et al. 2019). The synthesis of  $\text{Co}_3\text{O}_4/\text{rGO}$  composite through easiest way for the removal of Cr(VI) and RB (Al Nafiey et al. 2017). Kunde et.al investigated the synthesis of multiwalled CNTs/Alumina (RMAC) nodules through sol-gel route. The factors influencing the adsorption of cationic MB dye was examined by varying the amount of composite from 1wt % to 5wt % (Kunde et al. 2019). The development of 3D regenerated cellulose up on GO composite which is an aerogel through a simple and freeze-drying method and it showed outstanding dye removal efficiency for the removal of MB (Ren et al. 2018). The novel layered adsorbent (CTAB-Chitosan@ $\text{Al}_2\text{O}_3$ ) through a surface modification which showed excellent adsorption performance for the CR dye (Cai et al. 2020). The development of ecofriendly composite from seagrass *Posidonia oceanica* which got activated by  $\text{CH}_3\text{COOH}$  for the adsorption of MB and Pb(II) reported the synthesis of eco-friendly adsorbent from dried leaves of seagrass *Posidonia oceanica* were activated using acetic acid for the removal of MB

and Pb(II) ion from the aqueous solutions (Elmorsi et al. 2019). The synthesis of green adsorbent biochar with Fe<sub>2</sub>O<sub>3</sub> from banana bark extract along with ferrous sulphate for the adsorption of cationic MB dye over a varied range of pH values (Zhang et al. 2020).

Mohamed et. al reported the amino functional group i.e., 3-aminopropyltrimethoxy silane for supporting the MOF structure(nFe<sub>3</sub>O<sub>4</sub>@MIL-88A(Fe)/APTMS) through microwave technique. It removes all the pollutants like Cd(II), Pb(II) and anionic Cr(VI) ions and suited with a maximum of 6 adsorption models (Mahmoud et al. 2020). The development of toxic glutaraldehyde and epichlorohydrin free magnetic adsorbent CHT/ALG/Fe<sub>3</sub>O<sub>4</sub>@SiO<sub>2</sub> which is an chitosan as well as alginate source for the adsorption of Pb(II) from textile wastewater (Facchi et al. 2018). The introduction of magnetic GO by different generation of dendrimers and they are proved to be effective for the adsorption of Cd(II) and Pb(II) metal ions from the aqueous medium using batch system (Einollahi Peer et al. 2018).

The formation of one pot magnetic GO through the usage of silane groups such as n-Propyl trimethoxy silane along with Fe<sub>3</sub>O<sub>4</sub>/SiO<sub>2</sub>. The q<sub>max</sub> for the Cd(II) and Pb(II) metal ions are 128.2 and 385.1 mg/g under neutral pH and the effect of Na<sup>+</sup> and K<sup>+</sup> ions have been discussed over the adsorption efficiency. The fabrication of iron nanoparticles with activated carbon (IONPACs) by the impregnation method which explained the adsorption behavior along the coordinating surface along with the pH of the solution. The synthesis of magnetic ZnO nanoparticles supported on GO through hydrothermal method to remove tetracycline antibiotic. They explained the various interactions for the adsorption phenomena which made the GO as a framework and the ZnO found to be photocatalyst.

Niladri Sarkar et al. reported the quick synthesis of graphene quantum dots adorned with magnetic GO via ethanol:HCl mixture solvent. The as-synthesized nanohybrid incorporated via in-situ methodology with the porous carboxymethyl cellulose with PVA using PEG-1500 as pore forming agent. The swelling behavior of the nanocomposite hydrogel due to change in pH observed to the adsorption of contaminants MB & RB dyes within the defined range of temperature and time period. The synthesis of magnetic GO in order to enhance the surface area, number of active sites, high stability and excellent magnetic characteristics. These are effective for the adsorption of different heavy metals, radionucleides along with various dyes from the wastewater. Shariq et. al., synthesized the activated carbon obtained from phosphoric acid by chemical activation of heavy oil fly ash. The concentration of Rhodamine B was monitored by adsorption process until its equilibrium is achieved for several days. The results showed that there is a huge removal of RB dye from synthetic wastewater (Muhammad Shariq Vohra,Dhahran (SA) 2016). Saini et. al invented the Fe<sub>3</sub>O<sub>4</sub>magnetic nanoparticles

decorated activated carbon nanocomposite as adsorbent in a triple walled reactor cooled to -2 °C by polymerizing with various oxidants. The synthesized adsorbent is tested for the dyes MB and methyl orange as model impurity (Parveen Saini et al. 2016).

Debora et. al synthesized the fabrication of polyvinyl-N-carbazole-graphene oxide (PVK-GO) nanocomposite and GO-EDTA nanomaterial modified membrane filters for the adsorption of antibacterial and heavy metal ions removal. The adsorption capacity of metallic species raises with the increase in pH of its solution. Further, the decrease in pH led to the neutralization of the surface charge and the cationic metal ions adsorption decreases. The rise in solution pH converts the –COOH and –OH groups to –COO<sup>-</sup> and –O<sup>-</sup> groups respectively which provided the electrostatic interactions favouring the adsorption of Pb(II) ions and other cationic species.

### **2.1.6 Ferrites as an adsorbent**

With the development of new generation of materials so far, the emerging trend remain to concentrate towards the important features such as high surface area, tuning morphology, easily separable separation and high efficacy which became as the most promising path for the applications in catalysis and adsorption. During the recent times, spinel ferrites became the fundamental choice for the adsorption of organic and inorganic pollutants for the treatment of water applications because of the presence of nanometer-sized, superparamagnetic nature and a high surface to volume ratio. Spinel ferrites (MFe<sub>2</sub>O<sub>4</sub>) are magnetic materials where the M(II) and Fe(III) cations occupy both tetrahedral as well as octahedral sites respectively whereas inverse spinel ferrites half of the Fe(III) occupy tetrahedral site. The spinel ferrites formed on the graphene oxide nanosheets avoided the agglomeration, apart from it graphene which inhibited the leaching of the pollutants thereby increasing the efficiency in adsorption process. Ferrites with a hexagonal plane when loaded with Cobalt which can ease magnetization direction on a planar surface allowed to maintain the relative high permeability upto GHz region (Harris 2012; Pullar 2012; Stergiou 2017). It has a positive effect on the ferrite anisotropy which resulted in the unquenched orbital moment in octahedral sites.

Kashinath et. al fabricated the cerium oxide-graphene oxide hybrid nanocomposite under microwave irradiation without any surfactant and organic solvents for the removal of chromium ions using the photocatalytic activity (Kashinath et al. 2019). Wang et al (2020) prepared Biochar-loaded Ce<sup>3+</sup> loaded ultra-fine ceria nanoparticles by precipitation and pyrolysis method to remove the phosphate from water. Here, Ce<sup>+3</sup> ions of ceria played a vital role for the removal of (PO<sub>4</sub>)<sup>3-</sup> and the formation of cerium phosphate crystals taken place in

10 min (Wang et al. 2020). Yang et. al synthesized a porous 3D rGO/ZIF-67 which gave adsorption for the cationic and anionic dyes such as crystal violet and methyl orange with a  $q_{\max}$  of 1714.5 mg g<sup>-1</sup> and 426.3 mg g<sup>-1</sup> respectively (Yang et al. 2018). Cai et. al reported the synthesis of phytic acid modified CoFe<sub>2</sub>O<sub>4</sub> magnetic composite by a microwave hydrothermal method. The magnetic composite exhibited good adsorption for the MB & CR dyes and metal ion Pb<sup>2+</sup> of which Pb<sup>2+</sup> showing high  $q_{\max}$  of 833.8 mg g<sup>-1</sup> (Cai et al. 2017). Farghali et. al synthesized multi-walled carbon nanotubes decorated with CoFe<sub>2</sub>O<sub>4</sub> nanoparticles for the adsorption of MB. The  $q_{\max}$  for MB is 11.95 mg g<sup>-1</sup> at 323 K (Farghali et al. 2013). Wang et al reported a novel PPD rGO/NiFe<sub>2</sub>O<sub>4</sub> magnetic composite by hydrothermal method and insitu oxidative polymerization. The adsorption capacity for the MB & CR is maximum at pH-3 (Wang et al. 2017). Peng et al synthesized humic acid modified Fe<sub>3</sub>O<sub>4</sub> nanoparticles by coprecipitation method for the adsorption of RB dye from wastewater and the  $q_{\max}$  is 161.8 mg g<sup>-1</sup> with a removal rate of 98.5% (Peng et al. 2012). Alwan et al reported the synthesis of cobalt oxide nanoparticles on rGO for the removal of RB dyes with a  $q_{\max}$  of 434.782 mg g<sup>-1</sup> (Alwan et al. 2018). Zhang et al synthesized magnetic  $\gamma$ -Fe<sub>2</sub>O<sub>3</sub>-ZnO biochar nanocomposite by thermal decomposition for the removal of RB dye using photocatalytic method (Zhang et al. 2020).

Hou et al. reported the sponge like porous MnFe<sub>2</sub>O<sub>4</sub> formed by sol-gel method with egg white. The  $q_{\max}$  for MB is 20.67 mg g<sup>-1</sup> with seven regeneration cycles with a high activity of 96% (Hou et al. 2010). Hou et al. synthesized 3D NiFe<sub>2</sub>O<sub>4</sub> in presence of egg white using the sol-gel method. The porous NiFe<sub>2</sub>O<sub>4</sub> structure possess  $q_{\max}$  for MB is 138.50 mg g<sup>-1</sup> with a high removal efficiency >97% (Hou et al. 2011). Wang et al. synthesized varied MFe<sub>2</sub>O<sub>4</sub> (M=Mn, Fe, Co, Ni) ferrites nanocrystals using the hydrothermal method for the removal of anionic CR dye. The  $q_{\max}$  of CoFe<sub>2</sub>O<sub>4</sub> for CR is 244.5 mg g<sup>-1</sup> (Wang et al. 2012). Peng et al. investigated the formation of humic acid modified Fe<sub>3</sub>O<sub>4</sub> (Fe<sub>3</sub>O<sub>4</sub>/HA) by coprecipitation method for the adsorption of cationic dye RB from the waste effluents. The  $q_{\max}$  of RB is 161.8 mg g<sup>-1</sup> with an equilibrium time of less than 15 min (Peng et al. 2012). The synthesis of magnetic NiZnFe<sub>2</sub>O<sub>4</sub> nanoparticle onto the alginate composite from single and binary systems with the dyes i.e., Basic Blue 9, Basic Blue 41 & Basic Red 18 with their  $q_{\max}$  of 106 mg g<sup>-1</sup>, 25 mg g<sup>-1</sup> & 56 mg g<sup>-1</sup> (Mahmoodi 2013). The synthesis of CoFe<sub>2-x</sub>Gd<sub>x</sub>O<sub>4</sub> through the doping of Gd<sup>3+</sup> ions via hydrothermal method led to an increase in adsorption capability for the CR from aqueous solution. Due to the doping of Gd<sup>3+</sup>, the  $q_{\max}$  for CR increased from 131.1 to 161.1 mg g<sup>-1</sup>. The CR dye highest adsorption efficiency was 263.2 mg g<sup>-1</sup> for x=0.07

(Zhao et al. 2014). Zhang et al. investigated the synthesis of magnetic  $\text{CoFe}_2\text{O}_4$  on rGO nanocomposite for the removal of heavy metal ions  $\text{Pb(II)}$  from the wastewater. The  $q_{\text{max}}$  for  $\text{Pb(II)}$  is  $299.4 \text{ mg g}^{-1}$  at pH 5.3 (Zhang et al. 2014). Yang et al. synthesized magnetic  $\text{MnFe}_2\text{O}_4$  pore flake structure adsorbent for the adsorption of MB & CR in mono and binary systems. The interaction is synergistic which showed the CR adsorption increased within the order of CR (binary dye :  $32.21 \text{ mg g}^{-1}$ ) compared to CR (single dye :  $25.78 \text{ mg g}^{-1}$ ), the cationic dye MB is hindered due to the competitive adsorptive process on multiple solute systems (Yang et al. 2014). Akkaya Saygili et al. reported a new biomagnetic composite ( $\text{MnFe}_2\text{O}_4/\text{PW}$ ) for the adsorption of CR from wastewater with an  $q_{\text{max}}$  of  $86.96 \text{ mg g}^{-1}$  (Saygili 2015). Santhosh et al. explained the preparation method of magnetic  $\text{CoFe}_2\text{O}_4$  &  $\text{NiFe}_2\text{O}_4$  with graphene nanocomposites through solvothermal method for the adsorption of  $\text{Pb(II)}$  &  $\text{Cd(II)}$  from the aqueous effluents. The  $q_{\text{max}}$  of  $\text{CoFe}_2\text{O}_4\text{-G}$  for  $\text{Pb(II)}$  at pH-5 &  $\text{Cd(II)}$  at pH-7 is  $142.8 \text{ mg g}^{-1}$  &  $105.26 \text{ mg g}^{-1}$  respectively (Santhosh et al. 2015). Wang et al. prepared PAA/ $\text{MnFe}_2\text{O}_4$  nanocomposites by hydrothermal method with a removal efficiency of 96.3% (Wang et al. 2015). Lu et al. reported a novel hierarchical porous  $\text{MgFe}_2\text{O}_4/\gamma\text{-Fe}_2\text{O}_3$  microspheres for the removal of CR dye and minocycline from wastewater. The  $q_{\text{max}}$  for CR and minocycline is  $259.1 \text{ mg g}^{-1}$  and  $200.8 \text{ mg g}^{-1}$  respectively (Lu et al. 2016). Wang et al. synthesized a new magnetic adsorbent PmPD/rGO/NFO through the hydrothermal methods as well as insitu oxidative polymerization. The  $q_{\text{max}}$  for  $\text{Cr(VI)}$  is up to  $502.5 \text{ mg g}^{-1}$  at pH-3 (Wang et al. 2017). Sabarish et al. reported the hierarchical silicate-1 using tetrapropylammonium hydroxide sodium alginate by hydrothermal method, which followed Freundlich isotherm and PSO kinetic model (Sabarish and Unnikrishnan 2018). Zhirui Niu et al. reported a synthesis of new Mn-Zn ferrite/biochar composite using bioleaching as well as hydrothermal methodology with the help of battery waste as well as sawdust of pine trees. The  $q_{\text{max}}$  for  $\text{Pb(II)}$  was  $99.5 \text{ mg g}^{-1}$  at 298 K and it followed pseudo second order (Niu et al. 2020). Bintu Thomas et al. synthesized super-paramagnetic  $\text{NiFe}_2\text{O}_4\text{-Pd}$  (NFO-Pd) nanohybrid by solvothermal coupled with chemical reduction method using APTMS. The removal efficiency of  $\text{NiFe}_2\text{O}_4\text{-Pd}$  nanohybrid for the  $\text{Pb(II)}$  &  $\text{Cd(II)}$  ions are 98% & 97% respectively (Thomas and Alexander 2020). Zhang et al. synthesized the  $\gamma\text{-Fe}_2\text{O}_3\text{-ZnO}$ -biochar nanocomposite in triethylene glycol through thermal decomposition in the presence of  $\text{N}_2$  atmosphere for the removal of RB in wastewater (Zhang et al. 2020).

## **2.2 SUMMARY OF LITERATURE REVIEW**

Graphene oxide nanocomposites which consist of metal oxides to ferrites have shown voluminous advances in the field of adsorption and catalytic applications.

Carbon supports like graphene and graphene oxide have been recently used as supporting material for the Suzuki cross-coupling reaction due to their high thermal stability, huge loading capacity of metal nanoparticles and other excellent properties. The usage of expensive metals like palladium, platinum and rhodium as catalysts in the cross-coupling reactions led to the high cost and metal leaching during the metal recovery. This problem made to investigate the alternative metals such as 3d transition metals like Iron, Copper, Cobalt and Nickel which are having similar physical properties. These 3d transition group metals became an alternate pathway in the selection of metal catalysts in heterogeneous catalysis due to their high chemical stability, electronic and magnetic properties.

As discussed in the above section, graphene oxide possesses excellent supporting materials due to varied properties. Due to the various oxygen functional groups and high chemical stability in graphene oxide which led to the high adsorption capacity of dyes and heavy metal ions from the textile effluents. The synthesis of various nanoparticles like metal oxide to the metal ferrites which is a latest generation adsorbent having a very high surface area, tunable morphology and superparamagnetic nature. The spinel ferrites formed on the graphene oxide nanosheets avoided the agglomeration, apart from graphene oxide which inhibited the leaching of the pollutants thereby increasing the efficiency in adsorption process. These designed graphene adsorbents can avoid agglomeration, prevents the leaching of pollutants further enhancing the adsorption process.

## **2.3 PROPOSED WORK**

### **2.3.1 Scope of the work**

The synthesis of transition metal nanoparticle is a powerful methodology in nanotechnology which finds as a catalyst in organic synthesis and as a nanoadsorbent in the adsorption phenomena. The synthesis of biaryl compounds is of great interest in pharmaceutical industry and conjugated organic materials. The wide scope of applications for these compounds through organic transformation needs an efficient method for their preparation. Hence, the complexes of different ligands possess with metals possess distinct structure which can be active catalysts for C-C coupling reactions. Due to the rapid industrialization and urbanization, the need for clean water has been increased due to the heavy usage for the household utilities, industries

and agricultural needs. According to the report of World Water Council by 2030, the number of individuals for water scarcity will be increased by 3.9 billion. Wastewater treatment as well as water purification became an emergency to have sustainable human society and the mitigation of environmental pollution in the ecosystem. India is one of the leading producers of textiles which accounts for 5% of its GDP. There is an estimated amount of 38354 million litres per day (MLD) is generated in India's major cities, but the sewage wastewater treatment is done at 11786 MLD only. During the fabric manufacturing, a lot of chemical processes and mechanical techniques are involved which include bleaching, desizing, dyeing, printing and finishing etc. Due to this process, a lot of effluents which contains a large number of COD, BOD, suspended solids, organic nitrogen, heavy metals, alkalis and various dyes. Many conventional treatments such as coagulation-flocculation, ion-exchange, membrane filtration, electrochemical treatment, adsorption have been developed. But there are huge limitations such as high operating cost, more capital investment and the generation of secondary pollutants along with sludge formation. The literature reports states that adsorption is a surface phenomenon which operates in low cost and highly advantageous method for the removal of dyes and metal ions from the wastewater. The surface functionalization of metal oxide and ferrites nanoparticles in the nanocomposite resulted in the enhancement of adsorption performance since most of the nanoparticles tend to agglomerate and reduce the surface area. Hence, the modification of surface metal nanoparticles with surfactant such as silane groups have been emerged to be successful strategy for the improvement of adsorption capacity of nanoadsorbent.

From the literature survey, carbonaceous materials proved to be effective adsorbents to remove pollutants from wastewater due to their high internal pore structure, high surface area and a bulk range of functional groups. Various reports confirmed that a carbon surface oxidation process increases the functional groups constituting the oxygen groups with a high adsorption capacity of pollutants due to hydrophilic nature. A large number of adsorbents such as carbon nanotubes, activated carbon, clay minerals, microorganisms, plants and agricultural wastes of which graphene oxide has become a centre of attraction due to its 2D dimensional structure and high surface area ( $\sim 2600 \text{ m}^2 \text{ g}^{-1}$ ) due to which graphene became an incomparable perfect materials for the adsorption of pollutants. GO could be a promising heterogeneous support for the removal of dyes and heavy metal ions in the wastewater

Graphene derivatives finds applications as supporting materials for the synthesis of heterogeneous catalysts and adsorbents. These graphene derivatives can be modified with



different functional groups which allows the properties of graphene for specific applications. Graphene oxide is one such derivative with rich oxygen-containing functional groups such as hydroxyl, epoxy, carbonyl and carboxyl groups which are inexpensive. These materials are used to prepare graphene-based nanomaterials, due to their remarkable electronic, mechanical and chemical properties. Due to the 2D nature of this substrate and its surface area, it is possible to immobilize metal nanoparticles on the surface for application as catalyst in organic transformations. Therefore, the surface of graphene is modified with organic or inorganic materials in order to improve the catalytic ability of these catalysts in organic transformations and removal of pollutants in textile wastewater.

The presence of functional groups on graphene oxide surface enables immobilization of metal Schiff base complexes. The nano palladium, nickel-copper mixed metal oxides and palladium Schiff base complexes immobilized on graphene have been extensively studied as the catalysts for Suzuki cross-coupling reactions. A greener, eco-friendly metals like cobalt and copper immobilized on graphene oxide were synthesized, studied and its catalytic activity in Suzuki coupling reaction applications. With this aim, the use of inexpensive metals like cobalt and copper for the synthesis of graphene supported metal complexes and its applications in C-C coupling reactions requires an investigation and complete studies. Here, the synthesis of cobalt oxide nanoparticles, cobalt ferrite and mixed ferrites and their functionalization with different surfactants such as silane groups, polypyrrole and nanoceria (cerium oxide) with the graphene oxide nanocomposite for the effective removal of dyes and metals ions in the textile wastewater.

### **2.3.2 Motivation**

Graphene nanocomposites are an exciting class of materials and warrants more insight to understand their properties. They are fairly new in the game and this excites the curiosity to explore the material for their properties and varied potential applications. This material properties make them widely used for a variety of purposes, among them catalysis and adsorption application are at the fore front. During the recent times, the usage of graphene oxide as a heterogeneous support have shown profound applications as catalysts and adsorbents in cross-coupling reactions and removal of pollutants. The synthesis of nanoparticles using hydrothermal method and their subsequent complex formation followed by immobilization on graphene oxide in Suzuki cross-coupling reaction became very specific towards the active sites on reactants surface with oxidation-reductive process to yield high product formation. This served as the effective catalyst in this cross-coupling reaction. In the removal of both cationic

and anionic pollutants i.e., dyes and heavy metal ions, the pH dependence factor played a key role in the synthesis of adsorbents. The synthesis of metal oxide nanoparticles to the nano ferrites which have magical properties like high surface area and superparamagnetic behavior enhances the removal rate of dyes and heavy metal ions which later proved to be applicable for the industrial wastewater. This shows promising potential for these materials to be employed as a choicest material for aforementioned applications.

## 2.4 OBJECTIVES

The aim of this research work is to develop a highly active catalyst for the cross-coupling reaction using graphene supported metal complexes for conjugated organic materials and pharmaceutical industry. In case of wastewater treatment, the development of nanobullets such as metal oxides to ferrites which were incorporated onto functionalized graphene oxide for the effective removal of dyes and metal ions from the wastewater. Graphene oxide termed to be magic material which is an ideal support for metal nanoparticles and its complexes due to its high specific surface area with intrinsic low mass, ample oxygen carrying functionalities and excellent mechanical strength.

The main objectives of the proposed research plan are as follows

- To synthesize graphene immobilized nano metal/metal complexes from Copper and Cobalt transitions metals using silane coupling agents.
- To synthesize COPY, CPTMS-SiO<sub>2</sub>-MF, CoFe<sub>2</sub>O<sub>4</sub>-CeO<sub>2</sub> and incorporated onto graphene oxide and functionalized to form nanocomposite for adsorption studies.
- To characterize the above materials using UV-Vis, FT-IR, powder X-ray diffraction, Thermogravimetric analysis, VSM, TEM, SEM etc.
- To study the catalytic activity of the graphene immobilized nano metal/metal complexes in Suzuki cross-coupling reaction and extending the scope catalytic system with different organic substrates and the effect of substituents in the activities of catalyst.
- To study the adsorption capacity of nanoadsorbents for the textile effluents which include cationic pollutants such as Methylene blue, Rhodamine B, Lead nitrate, Cadmium nitrate and anionic pollutants such as Congo red.
- To study the various pollutants with respect to isotherms and kinetic studies both in simulated wastewater and real wastewater.

- To study the regeneration capacity of nanoadsorbent in the simulated and real wastewater.

## **CHAPTER-3**

**Synthesis of copper complex immobilized on to graphene nanosheet as a heterogeneous catalyst for Suzuki cross-coupling reaction**

**Abstract:** *This chapter discuss a straight forward synthesis of a heterogeneous catalyst by covalently immobilizing copper Schiff base complex on the surface of amino functionalized graphene oxide (AGO) for the Suzuki cross-coupling of substituted aryl halides with arylboronic acids. The as-synthesized complex and subsequent catalyst were characterized for their structural features using suitable techniques.*

### 3.1. INTRODUCTION

Transition metal catalyzed cross-coupling reactions are an influential method for the synthesis of biaryl compounds (Miyaura and Suzuki 1995). Their applications include a broad range of synthetic target intermediates in manufacture of materials for the synthesis of natural products in the field of medicinal chemistry and pharmaceutical industries (Bahrami et al. 2017). An advantage of Suzuki Coupling reaction over other cross-coupling reactions is its wide accessibility of organoboron compounds i.e., a broad functional group variation and are considerably stable as well as environmentally benign (Mirabedini et al. 2015). From its discovery 1989, till now the Suzuki–Miyaura cross-coupling involving the coupling of an organoboron reagent and organic halides or pseudo halides became one among the important methods in the formation of carbon-carbon bonds and also suitable synthetic procedure in organic chemistry, because of the starting materials stability, resistance to various functional groups and suitable to a wide range of solvents (Bahrami et al. 2017; Shang et al. 2013).

Among the various comprehensively well-studied approaches, in order to yield a maximum product with aryl bromides to form carbon-carbon bond, with the improvement of transition metal complexes onto different supports, a viable approach is heterogenization of various carbon supports such as carbon nanotube, graphite and fullerenes (F. Machado and Serp 2012; Rodriguez-Reinoso 1998). Graphene, a novel member to graphitic carbon family which consist of 2D nanosheets of  $sp^2$  hybridized carbon atoms and possess fascinating properties such as high thermal and mechanical stability as well as optical properties with an excellent surface area of  $2630 \text{ m}^2/\text{g}$  to become a promising candidate as an catalyst or catalyst support (Chae et al. 2004).

During the previous years, metal grafted on heterogeneous support has an extensive progress than the homogeneous catalysts due to its reusability, stability and selectivity (Bell 2003; Xie and Tang 1990). Copper is a 3d group element which has variable oxidation potential and possess unique properties that helps in tuning the size of cu nanoparticles (Gawande et al. 2016; Sun et al. 2013). Bahrami et al. reported that Graphene or Graphene oxide (GO) as a

solid support for N-heterocyclic-carbene palladium complex as an efficient catalyst for Suzuki coupling reaction (Bahrami and Kamrani 2018). Scheuermann et al. reported the palladium nanoparticle preparation by in-situ strategy and supported onto graphite oxide and chemically derived graphene derivatives (Scheuermann et al. 2009). They studied the catalytic activity along with the morphology of catalytic surface during the Suzuki coupling reaction and a low leaching of palladium. Rothenberg Thathagar and his co-workers first reported that the bimetallic clusters Cu/Pd catalyzed the Suzuki coupling reaction of aryl halides and phenylboronic acids with a high product yield (Thathagar et al. 2002). They investigated that the copper-based catalysts enhanced the catalytic activity and these are environmentally friendly and less costly which can be an alternative to precious metals. Mao et al. reported that the copper powder in presence of PEG-400 and  $K_2CO_3$  base as an effective catalyst for Suzuki coupling with a high yield for aryl iodides (Mao et al. 2008). They performed the catalytic reactions in presence of Iodine as co-catalyst to get moderate yield for aryl bromides. Deng et al. reported the copper oxide effectively co-catalyzed the coupling of arylboronic acids with ethyl bromoacetate in presence of palladium species as catalyst to give good yields without using any poisonous base thallium carbonate (Liu and Deng 2002). Li et.al and Su et. al reported the synthesis of copper and other metals which are immobilized graphene oxide for the styrene epoxidation catalytic studies (Li et al. 2013; Su et al. 2014).

Graphene oxide (GO) which possess large surface area having many oxygen functional groups along with distinct 2D nanostructure are helpful in amalgamation with various metal salts and polymers (Compton and Nguyen 2010). Due to its unique nanostructure, it has applications in the areas such as composites, sensors, solar cells, heterogeneous catalysis and gas storage devices (Wang et al. 2012). The hybrid materials possessing both the amino binding group and graphene oxide as an added benefit for the strong bonding of copper other than unfunctionalized GO (Huang et al. 2014). The modification in functionalized GO boosts the catalytic performance along with more dispersion (Astruc et al. 2005). Furthermore, these functionalized GO retains binding capability by enhancing the active sites on the catalytic surface (Fan et al. 2015). The leaching of metal does not occur during the reaction because of the metal remains intact firmly with the functionalized GO (Astruc et al. 2005). These groups make the GO maintain its acidic, basic and oxidative properties without any destruction of its chemical and catalytic performance (Mirabedini et al. 2015).

GO nanosheets which are formed from graphite using improved Hummers method were bestowed with many oxygen functionalities (Marcano et al. 2010). GO surface is covalently modified using silane coupling agent 3-aminopropyl trimethoxysilane (APTMS) has an amino

group which enhances the chemical modification of GO hydroxyl groups through silylation (B. Bhat and Ramachandra Bhat 2015).

In present work, we report an in-situ synthesis of copper Schiff base complex grafted onto graphene oxide. The chemical modification of GO is to support the imino(methyl)benzaldehyde ligands, i.e., condensation of 2-amino phenol with terephthalaldehyde. The amino silane functionalized GO reacted with copper complexes simultaneously to form metal chelates. It is anticipated that the barrier effect of CAGO complex combination along with its catalytic activity lead to the increase in the formation carbon-carbon bond using aryl halides in Suzuki coupling reaction and the stability of the prepared nanocomposite which helps in recyclability of the catalyst.

## **3.2. EXPERIMENTAL**

### **3.2.1 Chemicals required**

Graphite, 3-aminopropyl trimethoxy silane (APTMS),  $\text{Cu}(\text{CH}_3\text{COO})_2 \cdot 3\text{H}_2\text{O}$ , terephthalaldehyde and 2-aminophenol, arylboronic acids and aryl halides were purchased from sigma-Aldrich. Ethanol, toluene, acetonitrile, DMSO, hydrogen peroxide, sulphuric acid, and phosphoric acid were obtained from Finar chemicals limited. Caesium carbonate, potassium carbonate, sodium hydroxide, potassium hydroxide, sodium nitrate, sodium carbonate and potassium permanganate are obtained from Lobo chemie limited.

### **3.2.2 Synthesis of 3-aminopropyl trimethoxysilane functionalized-graphene oxide (AGO)**

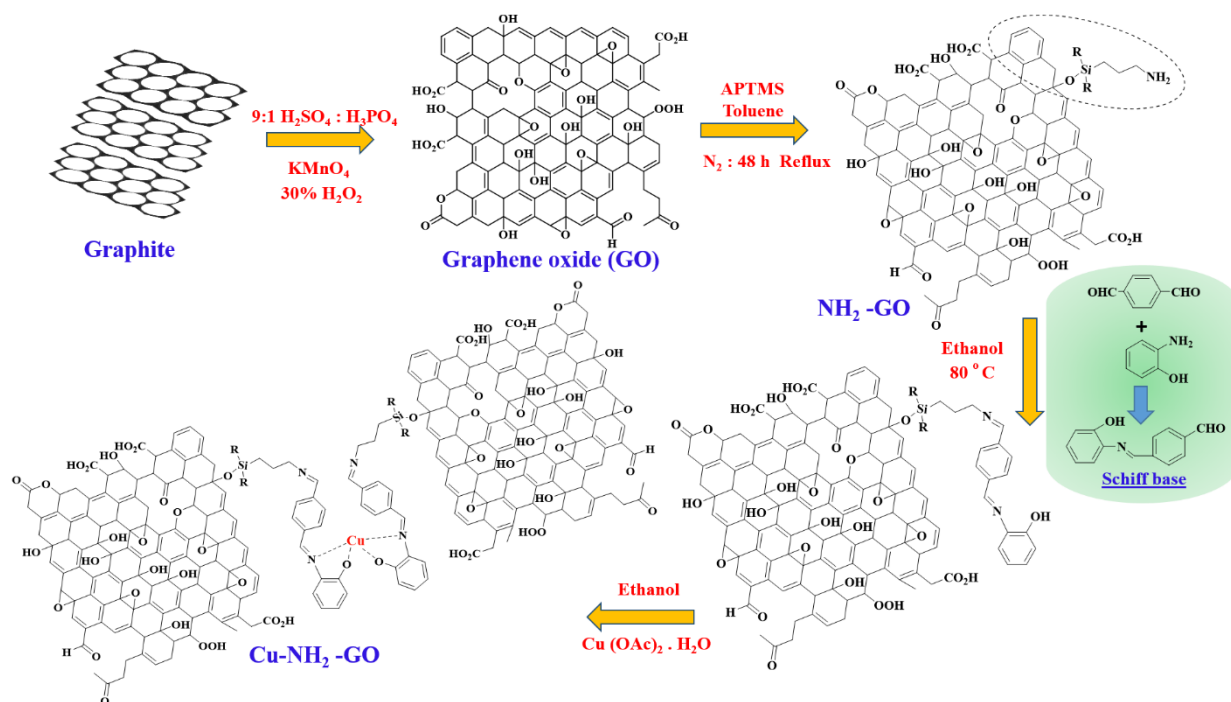
GO was prepared according to the improved Hummers method (Marcano et al. 2010b). 1000 mg GO was suspended in 50 mL of dry toluene using ultrasonic bath and refluxed with 4 mL APTMS in  $\text{N}_2$  for 24h (Mungse et al. 2012). The black product was filtered and washed with dry toluene and ethanol to remove any residual APTMS. The sample was dried in vacuum oven around 90 °C for 6h.

### **3.2.3 Synthesis of Cu-Schiff base complex (CuL)**

The Schiff base (L) was synthesized by refluxing 470 mg terephthalaldehyde (1.0mmol) and 229 mg 2-amino phenol (0.6mmol) dissolved in 20 mL ethanol. The product was filtered and washed with ethanol before drying in an oven (Yield: 86.2%). Further, Schiff base 500 mg and 500 mg  $\text{Cu}(\text{Ac})_2 \cdot \text{H}_2\text{O}$  were dissolved in ethanol and stirred at room temperature for 24h. The product was filtered and washed with ethanol several times before drying (Yield: 82%).

### 3.2.4 Synthesis of Cu-Schiff base immobilized Graphene oxide (CAGO)

500 mg CuL complex was added to the suspension amino functionalized GO (500 mg, 0.05 mmol) in 60 mL ethanol, and refluxed for 24h at 60 °C. The product brought to room temperature followed by filtration and ethanol wash. The filtered CAGO then dried in an oven at 50 °C.



Scheme 3.1. Synthesis of CAGO catalyst

### 3.2.5 Suzuki coupling reaction and yield

Aryl halide (1 mmol) and phenylboronic acid (1.5 mmol) taken in a flask along with the catalyst (0.36 mol%) and base K<sub>2</sub>CO<sub>3</sub> (3mmol) in ethyl alcohol (5 mL), and refluxed at 80 °C for 12h. The product was analyzed using Gas Chromatography (GC) (Shimadzu 2014, Japan) fitted with siloxane Restek capillary column (30 m length and 0.25 mm diameter) and flame ionization Detector (FID).

### 3.2.6 Characterization Techniques

Prepared materials were characterized using ICP-AES, FTIR, DR-UV, TGA, XRD, SEM, EDS, TEM and XPS to understand their structure, composition and stability. The FTIR spectra were recorded on a Bruker-Alpha ECO-ATR FTIR in the range 500-4000 cm<sup>-1</sup> using KBr method. UV-Vis spectra were recorded from 200-800 nm on Analytik Jena SPECORD S600. XRD measurements were carried out using Cu K $\alpha$  radiation on a Rigaku 600 diffractometer Miniflex equipped with Ni-filtered CuK $\alpha$  radiation (40 kV, 30 mA, and  $\lambda$  = 1.54056 nm), within diffraction angles of 5° - 80° at the scanning speed of 2° per minute. The



surface morphology of the synthesized materials was studied on Zeiss Sigma SEM with oxford EDS. HR-TEM Analysis were taken on a FIE Tecnie-F20 with an acceleration voltage of 200kV. X-Ray photoelectron spectroscopy (XPS) was measured on a Kratos XSAM800 X-ray electron photometer using Al K $\alpha$  radiation. TG analysis was carried out on a Hitachi DTA-6300 working in a N<sub>2</sub> stream with a heating rate of 5 °C per min in the range of 25-800 °C. The samples were heated at a constant rate of 10 °C/min under N<sub>2</sub> flow from 200-800 °C. Metal content was estimated by inductively coupled plasma atomic emission spectroscopy (ICP-AES) analysis on an Agilent 5100 Synchronous Vertical Dual View ICP-AES with Dichroic Spectral Combiner (DSC) Technology.

### **3.3. RESULTS AND DISCUSSION**

#### **3.3.1 Vibrational Spectroscopy (FTIR)**

Figure 3.1 show the FTIR spectra of the pure GO, AGO and CAGO. GO exhibit characteristic strong band at 3394 cm<sup>-1</sup> and 1725 cm<sup>-1</sup> representing -OH and C=O bonds of hydroxyl, carbonyl and carboxylic acid groups along with the bands at 1058, 1220, and 1621 cm<sup>-1</sup> indicating the epoxy (C-O), phenol, C=C bonds in their scaffold (Mungse et al. 2012; Nasserri et al. 2014). AGO presents a doublet band at 2850 and 2917 cm<sup>-1</sup> exhibiting the presence of symmetric and asymmetric stretching vibrations of the methyl and methylene alkyl chains. The bands at 1121.5, 1034, and 1620 cm<sup>-1</sup> justify the Si-O-Si, Si-O-C, and C-N vibrations due to the grafting of APTMS onto GO (Mungse et al. 2012; Wang et al. 2016). In contrast, CAGO shows a sharp peak at 1438 cm<sup>-1</sup> for CO which confirmed the binding of copper with acetate groups (Anuradha et al. 2015; Kumari et al. 2016). Additionally, band at 674 cm<sup>-1</sup> signifies the Cu-N bond stretching due to the coordination of copper with N, O sites on the catalytic surface (Li et al. 2013).

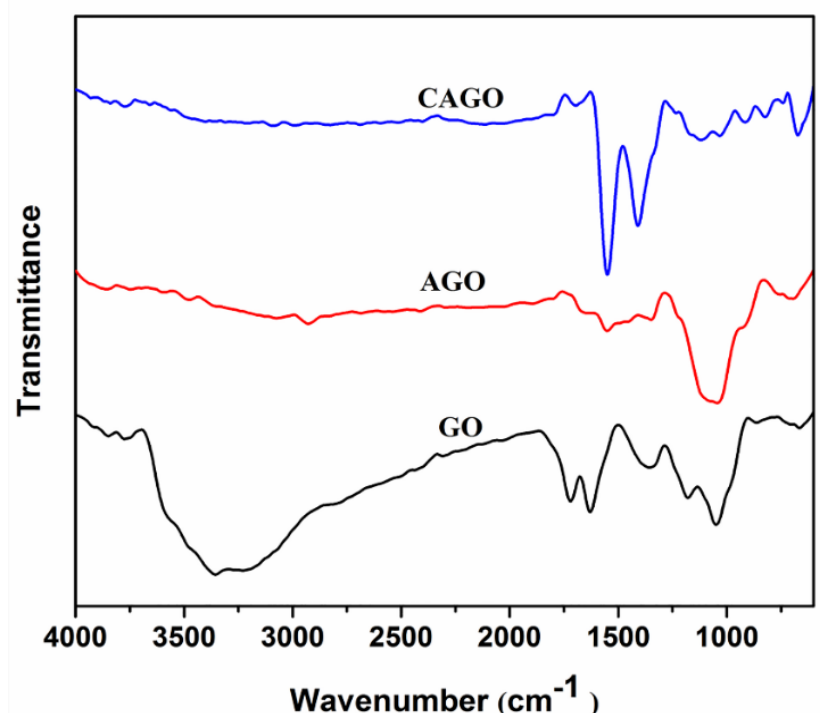


Figure 3.1. FTIR spectra of a) GO, b) AGO and c) CAGO

### 3.3.2 UV-Vis Spectroscopy (UV)

The UV-Vis spectra of the pure GO, AGO and CAGO has absorption bands around 232 nm and 300nm, indicating the transitions of both  $\pi$ - $\pi^*$  and  $n$ - $\pi^*$  on C=C and C=O (Figure 3.2). The absorption bands from 260-430 nm indicated the ligand to metal charge transfer (MLCT) and the ligand charge transfer around  $\pi$  bond electron and the non-bonded electrons in the catalyst (Li et al. 2013). The band at 320 nm in AGO is due to the amino functionalization of GO surface. Additionally, a weak band around 630 nm in CAGO represents to the d-d transitions of the central copper ion, confirmed the incorporation of metal ion that the transition metal complexes have been successfully anchored on GO (Li et al. 2013).

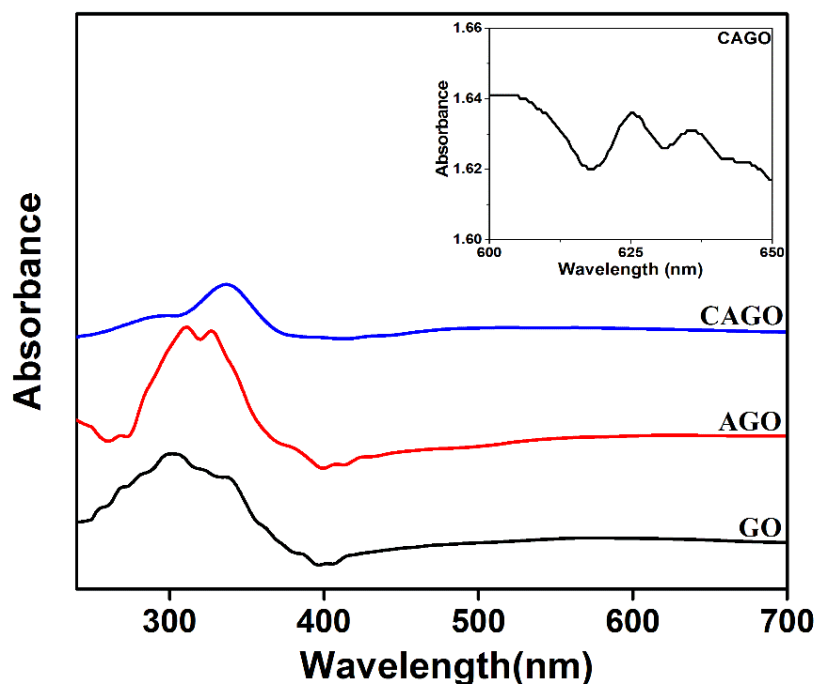


Figure 3.2. UV spectra of a) GO, b) AGO, and c) CAGO

### 3.3.3 X-ray Diffraction (XRD)

The XRD spectra (Figure 3.3) of GO, AGO and CAGO shows a broad peak at 10.91 for the (001) reflection of GO (Scheuermann et al. 2009). The reminiscence of this peak for AGO and GO states that the presence of GO in both forms. Additionally, AGO and CAGO exhibit a broad peak at 22.24 due to the amino functionalization of GO (Nasseri et al. 2014). The GO peak around 10.9 becomes weak after the introduction of organometallic species which confirms the formation of CAGO (Su et al. 2014). The broad diffraction peaks indicate amorphous nature of the catalyst.

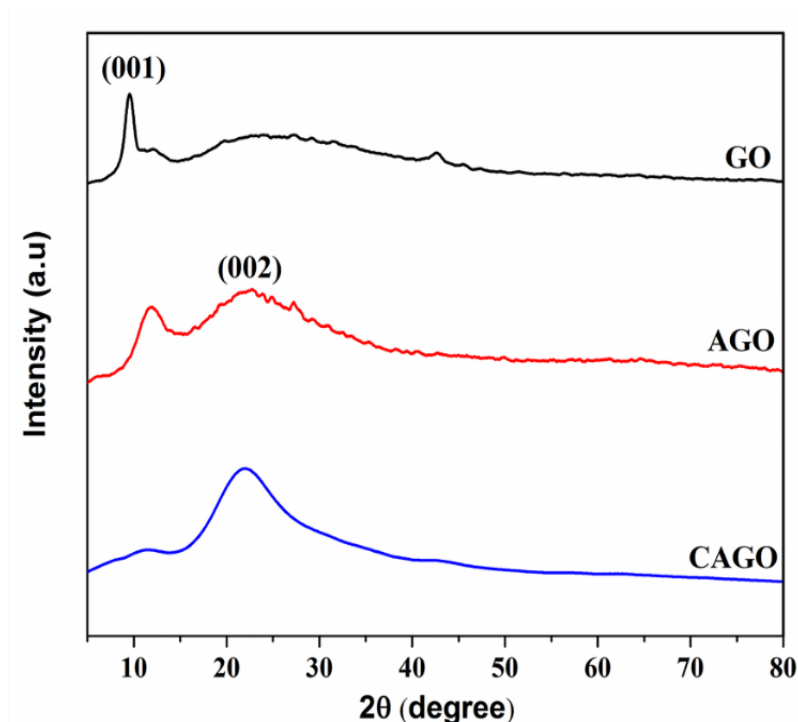


Figure 3.3. XRD graph of GO, AGO, and CAGO complex

### 3.3.4 SEM & EDS (Scanning Electron Microscopy & Energy Dispersive X-ray Spectroscopy)

The surface morphology and microstructural features of GO, AGO, and CAGO were analyzed using SEM and EDS (Figure 3.4 & 3.5). GO and the CAGO exhibited twists in nanosheets which are not in an ordered phase with crumpled features. The  $sp^2$  hybridized carbon of GO possess folded edges and protrusions (Mungse et al. 2012) which facilitates the immobilization of CuL. These reactive areas act as idealistic patterns which help the reactant substrates to form their target modification of GO. The amino functionalized GO surface had network like structures which is the result of solvents used for covalent functionalization. However, the stacking of CAGO was much greater than that of GO was due to the interaction of amino groups at the surface or in the basal planes of GO (Zhao et al. 2014). The EDS analysis of CAGO exhibited the presence of Cu (Figure 3.5(c)) which was absent in AGO (Figure 3.5(b)). This further emphasis successful immobilization of Cu-Schiff base complex on AGO. Figure 3.5 provides different elemental composition (in atomic %) of GO, AGO and CAGO as measured in EDS. The composition of Cu element was found to be 0.34 mmol/g in CAGO from ICP-AES analysis. These results suggest that the metal complex supported on GO.

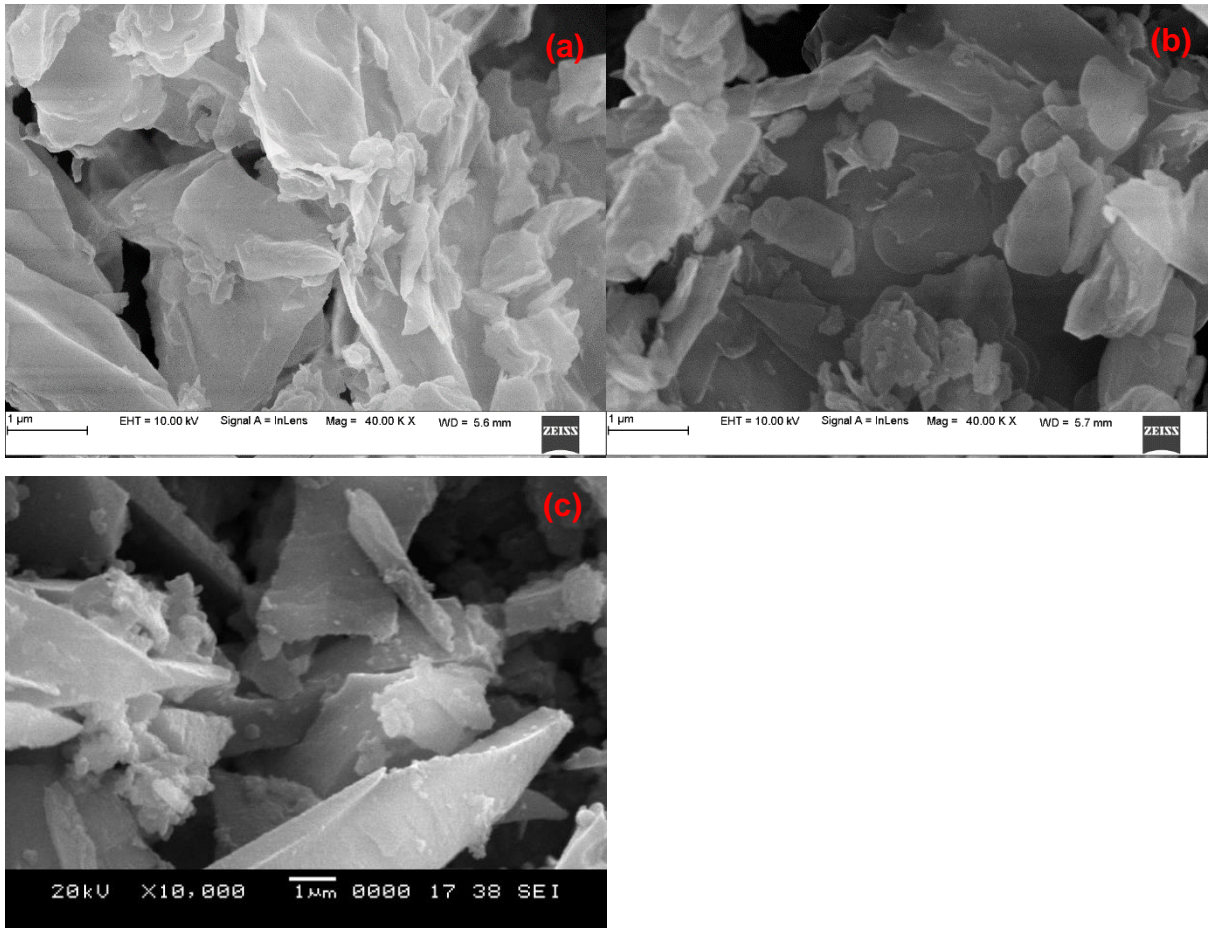
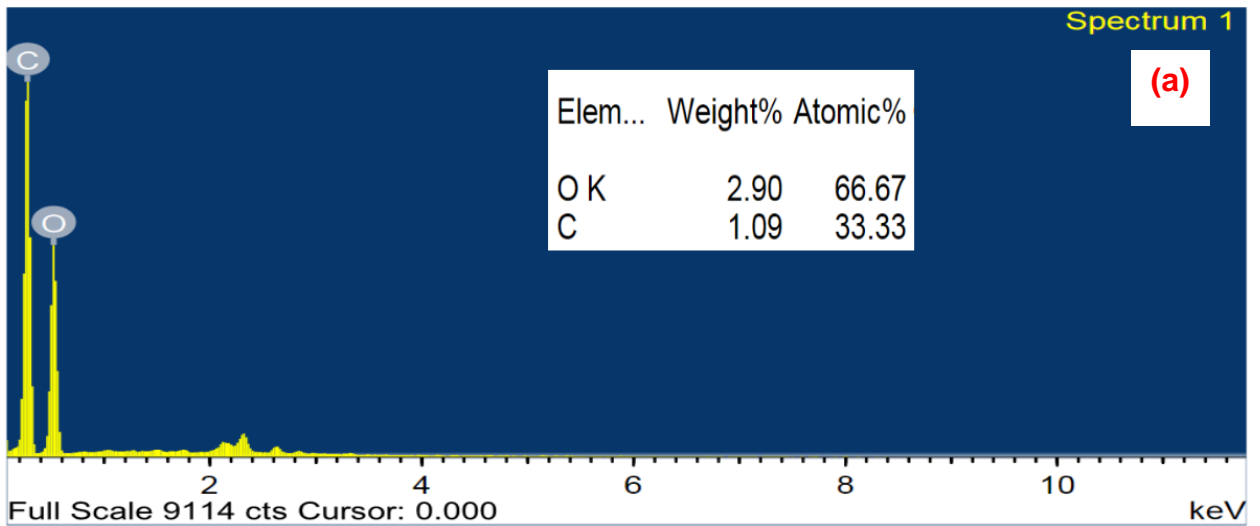


Figure 3.4. SEM of a) GO, b) AGO & c) CAGO



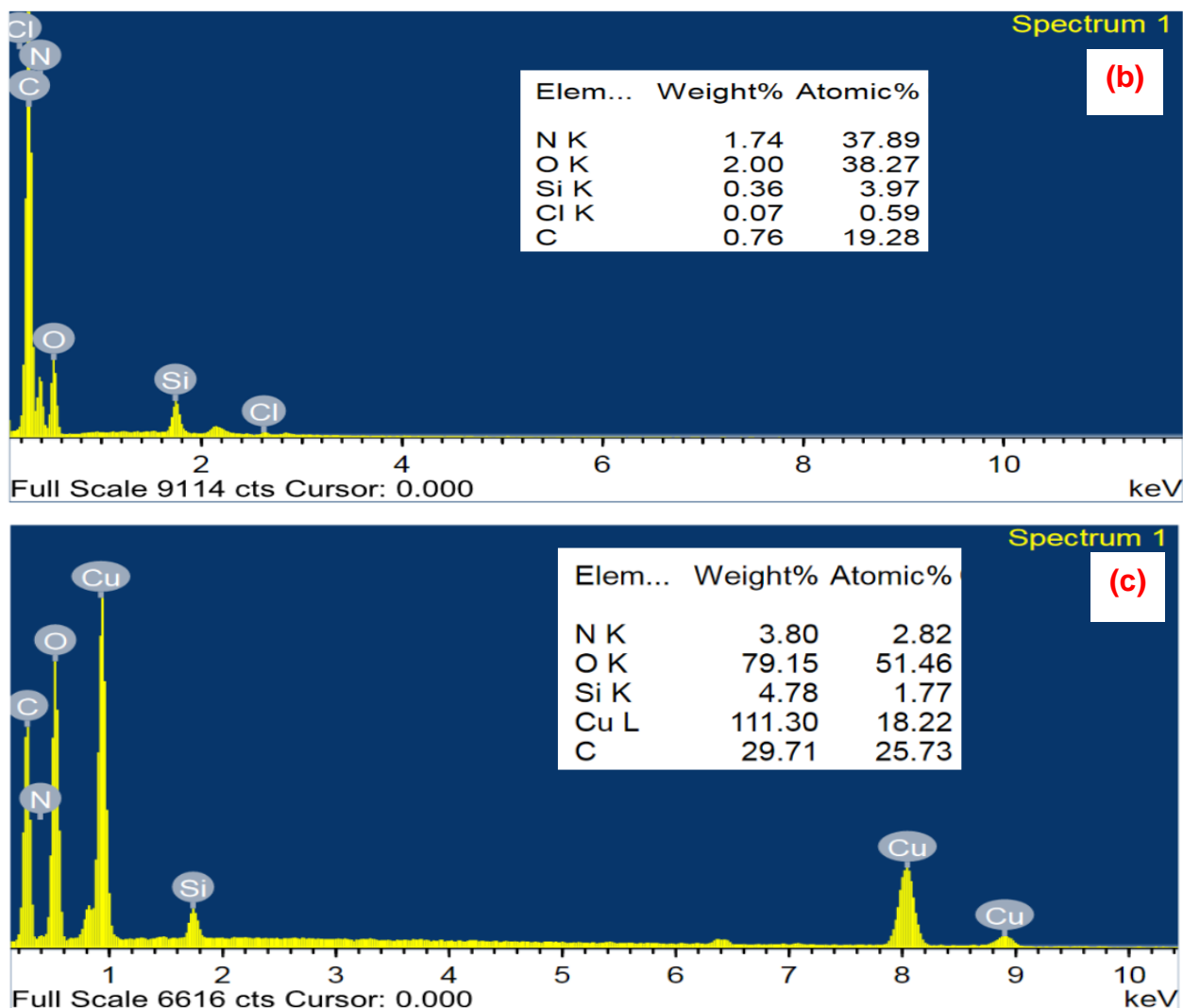


Figure 3.5. EDS of a) GO, b) AGO and c) CAGO

### 3.3.5 Transmission Electron Microscopy (TEM & HR-TEM)

TEM of GO shows typical few layer nanoscopic feature (Figure 3.6(a)) (Zhu et al. 2010). The amino functionalization of GO in AGO (Figure 3.6(b)) resulted in a layered morphology due to the presence of silane group on its surface and its SAED pattern given in figure 3.6(c). The TEM of CAGO (Figure 3.6(d, e)) depicts the retained layered feature with crumpling feature thus suggesting the agglomeration. The SAED pattern (Figure 3.6(f)) confirmed the same.

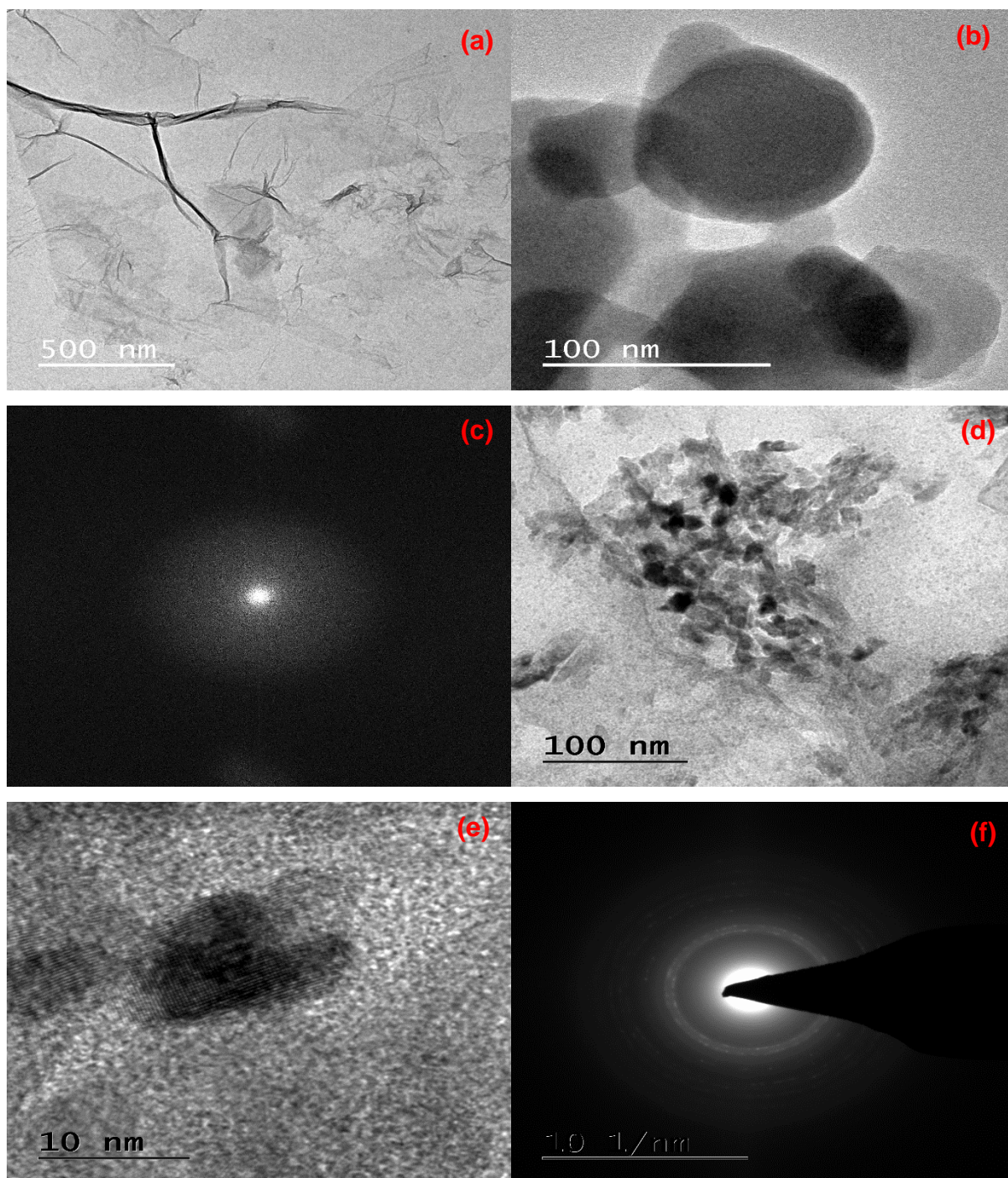
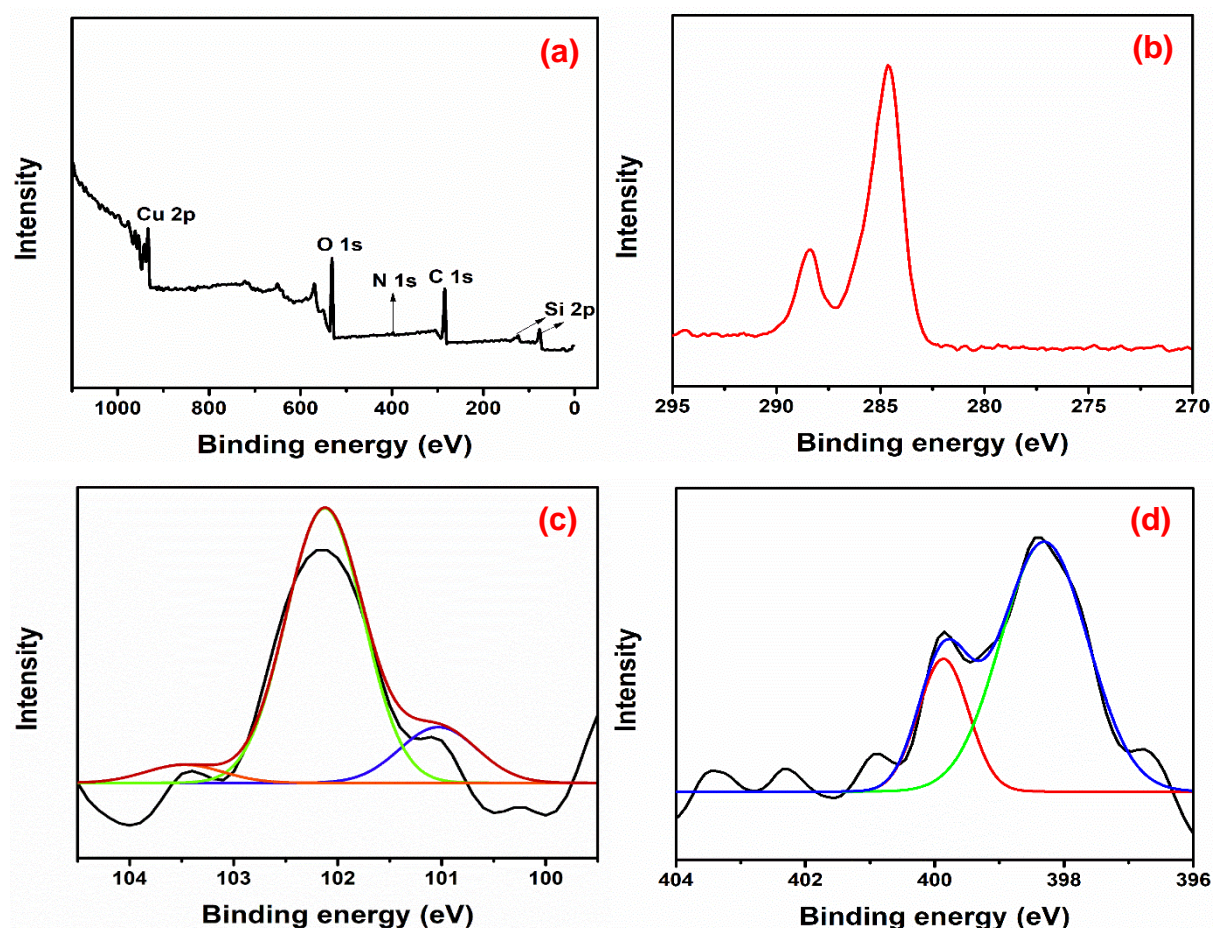


Figure 3.6. TEM images of a) GO, b) AGO, c) SAED of AGO, d) CAGO, e) HR-TEM of CAGO and f) SAED of CAGO

### 3.3.6 X-ray photoelectron spectroscopy (XPS)

XPS of CAGO was obtained to further understand the nature of binding of C, Si, N and Cu and O in the composite. C1s scan (Figure 3.7(b)) shows typical peaks at 284.8 eV for C-C and C-O-C, and 289 eV for O-C=O binding which is mainly due to the GO support which is further supported by O1s scan with peak at 532.5 eV for C-O binding (Li et al. 2013). The Si

2p and N 1s scan (Figure 3.7(c, d)) represents the silylation between APTMS with the surface hydroxyl groups on the GO support. The prominent peak at 102.25 eV in Si 2p scan corresponds to the SiO linkage while the shoulder at 101 eV is from N-Si linkage. This N-Si linkage can be confirmed by the presence of a doublet corresponding to 398 eV and 400 eV which are due to N-Si<sub>3</sub> and N-Si<sub>2</sub>O linkage respectively. The Cu 2p spectra (Figure 3.7(e)) shows two typical bands at 933.9 which is indicative of Cu-O bond whereas 953.8 eV represents Cu-N bond of Cu(II) ions. Additionally, a Cu 2p<sub>3/2</sub> satellite peak at 943.0 eV is observed which is a result of the electrostatic interaction between the ligand and the copper metal ion (Anuradha et al. 2015; Zhu et al. 2010). Figure 3.7(a) gives the specific binding energy of Cu, N, O, C and Si elements in the CAGO. These observations support the predicted binding of various elements in the prepared complex.





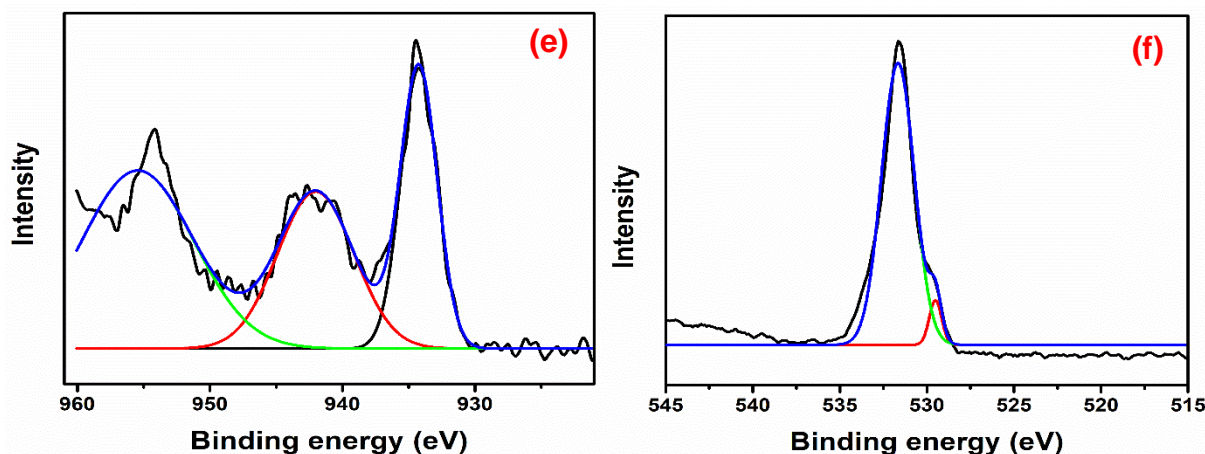


Figure 3.7. XPS analysis of CAGO composite with a) elemental survey, b) C 1s scan, c) Si 2p scan, d) N 1s scan, e) Cu 2p scan and f) O 1s scan

### 3.3.7 Thermal Analysis (TGA)

TGA of GO (Figure 3.8(a)) depicts two degradation steps in GO. The loss within 170-250 °C is attributed to the loss in H<sub>2</sub>O and CO<sub>2</sub> due to the removal of OH and C-O-C functional groups which is usually the case in thermal reduction of GO. The gradual loss in the region from 280-600 °C presumably due to the degradation of the left over C-O and C-H moieties (Dikin et al. 2007; Zhou et al. 2010). The weight loss in the CAGO is observed in three steps (Figure 3.8(b)). First, a loss of 4.59% at 90-190 °C represented the removal of physically adsorbed water. Another weight loss of 33% around 250-450 °C corresponds to the thermal decomposition of undigested functionalities of oxygen along with unreacted APTMS (Gemeay et al. 2017). This suggest that CAGO can be utilized as a heterogenous catalyst up to 250 °C without undergoing degradation. Final, the weight loss region corresponds to the degradation of GO.

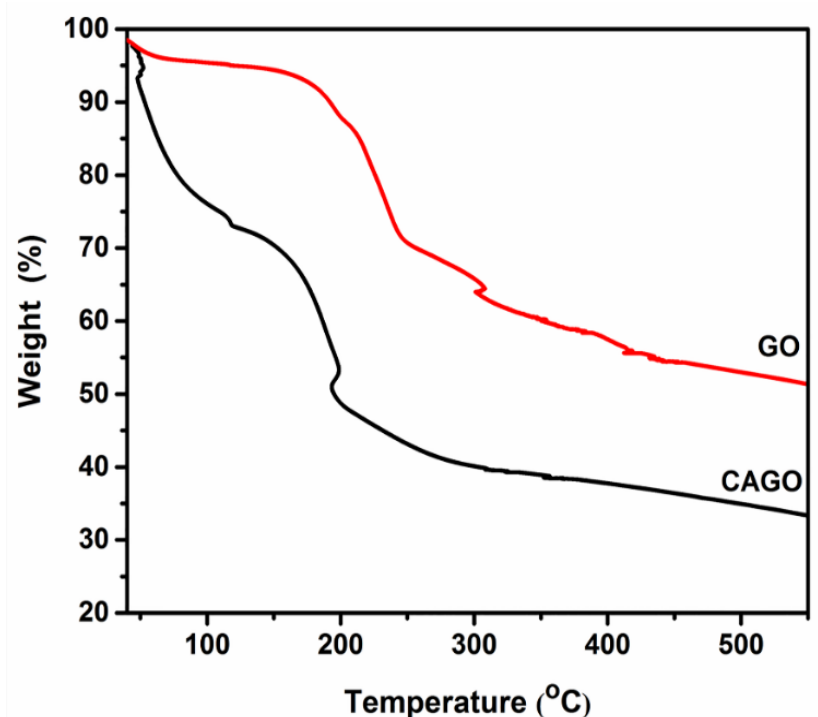


Figure 3.8. TGA of the a) GO and b) CAGO

### 3.3.8 Suzuki cross-coupling reaction

The catalytic performance of the synthesized catalyst was explored using the Suzuki coupling of certain phenylboronic acid and phenyl iodide as the model reaction. The summary of CAGO catalyzed reactions with different solvents and base are given as Table 3.1. EtOH and  $K_2CO_3$  were found to be the best solvent and base pair for the reaction with GC yield of 94%. Further, the effect of catalyst on the yield of reaction for different substituted aryl halides and phenylboronic acids are given as Table 3.2. The results suggest that the amount and time taken for the product formation for CAGO catalyzed reaction depends on the nature of substituent group. Aryl bromides having donor moieties require a long time to complete their reaction because of the polarity in molecule which is due to the transfer of electron through  $\pi$ -bond on aryl bromides. In fact, the product formation is less for aryl chlorides because of the high bond dissociation energy of the C-Cl bond (96 kcal/mol) (McGivern et al. 2000). Henceforth, the reaction between phenyl iodide and phenyl boronic acid was monitored to study the performance of CAGO as catalyst.

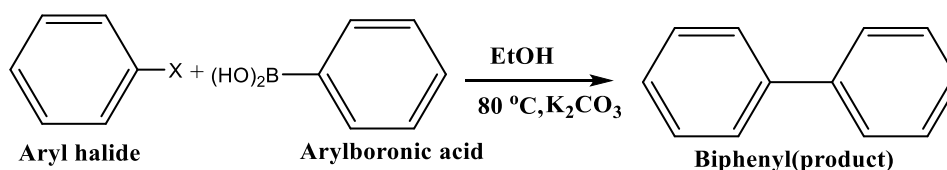
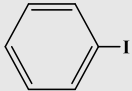
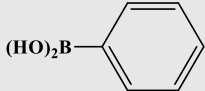
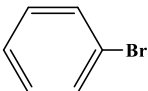
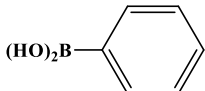
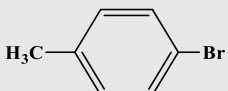
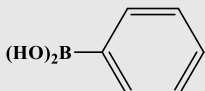
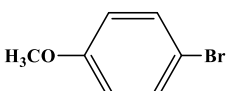
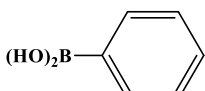
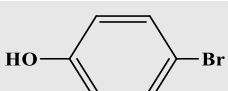
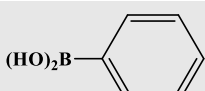
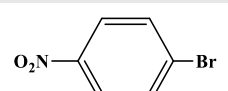
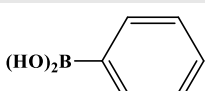
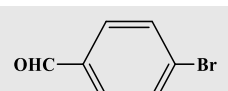
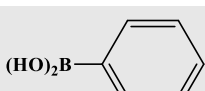
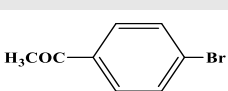
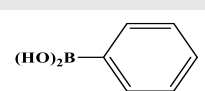
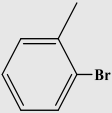
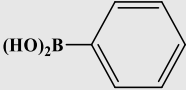
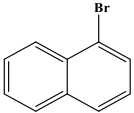
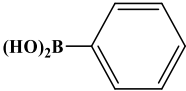
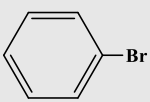
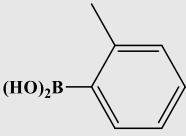
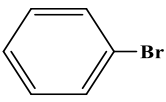
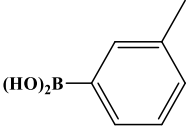
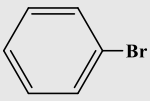
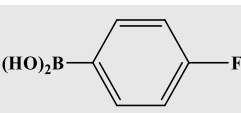
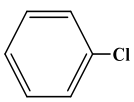
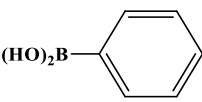
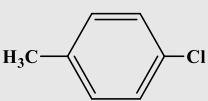
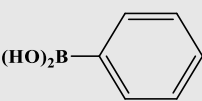


Table 3.1: Effect of various solvents and bases on yield at temp 80 °C

Sl. No.	Solvent	Base	Temperature	Catalyst (mol%)	Yield (%)
1	EtOH	K <sub>2</sub> CO <sub>3</sub>	80	0.36	94
2	EtOH	Na <sub>2</sub> CO <sub>3</sub>	80	0.36	88
3	EtOH	Et <sub>3</sub> N	80	0.36	53.9
4	EtOH	KOH	80	0.36	65
5	EtOH	NaOH	80	0.36	57.9
6	Acetonitrile	K <sub>2</sub> CO <sub>3</sub>	80	0.50	75
7	Dimethyl sulfoxide	K <sub>2</sub> CO <sub>3</sub>	80	0.50	71
8	Tetrahydrofuran	K <sub>2</sub> CO <sub>3</sub>	80	0.50	60.5
9	Toluene	K <sub>2</sub> CO <sub>3</sub>	80	0.50	52

Table 3.2: GC yield of the products of various aryl halide and arylboronic acids at 80 °C

Sl. No.	Aryl halides	Arylboronic acids	Time(h)	Yield (%)
1			8	94
2			12	91.9
3			24	80
4			24	75
5			24	72
6			12	88.9
7			12	87
8			12	83.9

9			24	80
10			24	73.9
11			24	64
12			24	69
13			24	87.9
14			24	17.9
15			24	22

**Reaction Content:** EtOH (5 mL), Aryl halides (1.0 mol), arylboronic acids (1.5 mol),  $K_2CO_3$  (2 mol), and CAGO Catalyst (0.36 mol%)

Table 3.3 represents the comparison of catalytic yield of CAGO with GO+CuL as control catalyst. As observed from the percentage yield, it can be seen that CAGO provides highest yield among all the three catalyst which is due to the absorptive nature of the catalyst. In case of GO+CuL catalyst, the yield was found to be very low which can be attributed to the fact that CuL is not bound to GO therefore it goes into liquid phase whereas the reactants get adsorbed on GO thereby limiting the yield. This can be further ascertained by the use of only Cu-Schiff base complex as catalyst which showed improvement over the GO+CuL catalyst because the reactant and catalyst were in same phase. Therefore, from this experiment it can be seen that, CuL is active catalyst for the Suzuki cross-coupling reaction, and when it is bound to AGO, the synergistic effect of catalytic activity and adsorption increase the overall reaction yield.

Table 3.3: Comparison catalytic yield of CAGO with control catalyst GO+CuL and only CuL complex

Sl. No	Catalyst	Amount of catalyst (mol%)	Yield (%)
1	CAGO	0.36	94
2	CAGO	0.72	94
3	CAGO	0.18	80
4	CAGO	0.09	62
5	GO+CuL	0.36	5
6	GO+CuL	0.72	13
7	GO+CuL	1.00	13
8	CuL	0.18	32
9	CuL	0.36	46
10	CuL	0.72	65
11	CuL	1.00	65
12	CuL	2.00	65

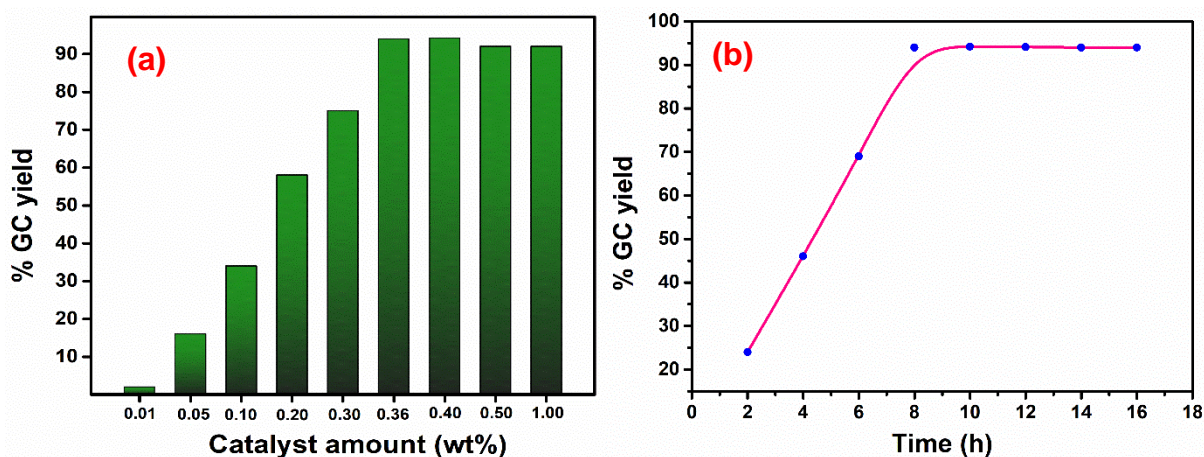


Figure 3.9. The effect of (a) catalyst amount and (b) reaction time on the GC yield of Suzuki coupling reaction

The influence of the amount of catalyst was investigated, and it was found that the biphenyl product formation enhanced from 2% to 94% when the catalytic amount of catalyst gradually raised from 0.01 mol% to 0.36 mol% under the optimal reaction conditions (Figure 3.9(a)). Further increase in the amount of catalyst showed no significant improvement in yield. Additionally, the catalyzed reaction was observed to give highest yield for 8h of reaction after which there was no further improvement (Figure 3.9(b)).

The effectiveness of a heterogenous catalyst in nanocatalysis depends on its particle size, irrespective of the coupling reaction mechanism. The smaller the nanoparticle is, better will be its catalytic activity. Therefore, CAGO displays more catalytic activity due to the good dispersion and small size of the CuL nanoparticles. GO which possess rich oxygen functional groups, aids in tuning the surface of CuL nanoparticles without aggregating and maintained catalyst performance throughout the reaction.

The catalyst recyclability studies (Figure 3.10) were further done to prove the reusability of the heterogeneous catalyst found to be beneficial for reliable practical applications. 0.36 mol% of CAGO catalyst was used for this reaction. The study suggests that CAGO catalyst can be reused for 4 times without any significant loss of its catalytic activity. However, a gradual decrease in the product yield was observed in subsequent reactions. The catalyst metal leaching during the reaction was studied using ICP analysis. The concentration of copper metal in CAGO catalyst and the recovered catalyst was found to be 0.28 mmol/g which confirmed that copper leaching of the catalyst was very less. The TEM image of the fresh catalysts and the used catalyst (Figure 3.11(a, b)) proved that the metal leaching is less during the coupling reaction. The results proved that CAGO complex is stable which prevents the copper leaching.

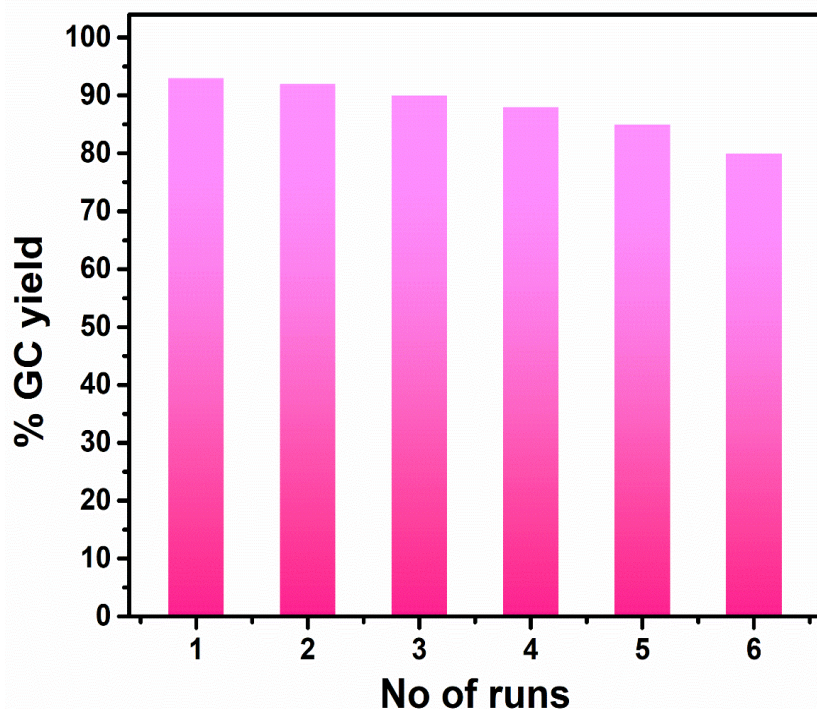


Figure 3.10. Recycling ability of CAGO as catalyst for Suzuki coupling reactions

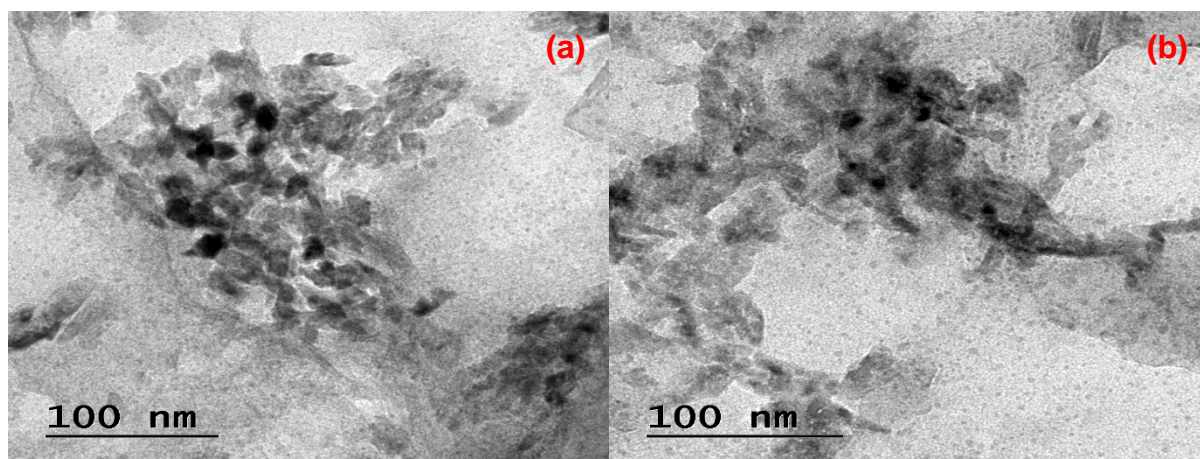


Figure 3.11. TEM images of fresh and used catalyst after 5<sup>th</sup> cycle a) fresh catalyst b) used catalyst

### 3.4 CONCLUSIONS

An in-situ strategy has been developed for the synthesis of a copper Schiff base complex and simultaneously grafted on GO support through a surface modification. The as-prepared catalyst was found to be an efficient catalyst for the synthesis of biphenyl as products from the Suzuki cross-coupling reaction (C-C bond) of substituted aryl halides and phenylboronic acid. The 2D structure of GO support which owe to its excellent performance possessing outstanding properties and the robust synthetic methodology. Therefore, GO acts

as good supporting material having its unique properties and a powerful supporting agent for homogeneous metal complexes for their practical applications. Heterogeneous nanocatalysts is highly active, possesses high surface area, and its thermal and chemical stabilities were confirmed using various characterization technique through spectroscopic methods and surface analysis. This recoverable and reusable catalyst is benign, low cost and be handled easily. More wide and in-depth analysis in heterogeneous coordination catalysis were done to further studies in various organic reactions were anticipated.



## **CHAPTER-4**

**Synthesis of Cobalt Schiff base Graphene nanocomposite for the effective catalytic applications in Suzuki cross-coupling reactions**

**Abstract:** *This chapter reports a simple and direct pathway to synthesize heterogeneous catalyst (CoASGO) by covalently immobilizing cobalt Schiff base complex onto the surface of amino functionalized graphene oxide (ASGO) for the cross-coupling of aryl halides and arylboronic acids to form biaryl as product is reported. High product yield, environmentally benign, easy workup, easy filtration of catalyst and mild reaction conditions are the main facets of this catalyst.*

## 4.1 INTRODUCTION

Nowadays, Graphene and its materials emerged as an interesting moiety having impeccable properties such as high surface area, defective lattice sites with adjustable tuning properties and high thermal and electronic properties (Bai and Shen 2012; F. Machado and Serp 2012). Nevertheless, graphene based materials are helpful in controlling the growth of size of metal nanoparticles (NPs) with adjustable tuning properties which makes them known to be heterogeneous catalysts (F. Machado and Serp 2012). In order to overcome the present demand for the design of heterogeneous catalyst, numerous methodologies were developed in carbon based materials, graphene oxide with varied oxygen containing functional moieties capable for anchoring the metal NPs making them as nanocomposites (Fan et al. 2015; Wang and Astruc 2018). These nanocomposites acts as promising material in catalysis, energy storage devices electronics and sensor applications (Hancock 2011). Various techniques have been monitored to synthesize graphene-metal nanoparticle composites and the simplest method is the incorporation of metal precursors on to the surface of GO using noncovalent interactions at an elevated temperatures (Kuila et al. 2012; Mkhoyan et al. 2009).

Suzuki-Miyaura cross-coupling reaction is extensively known method for the carbon-carbon bond formation in organic synthesis which includes from the manufacture i.e., small complex intermediates to the industrially viable active pharmaceutical ingredients (APIs) (Miyaura and Suzuki 1995). Of all the various transition metals, palladium is predominantly used for this (Bahrami and Kamrani 2018; Baran et al. 2018; Xiao et al. 2015). However, palladium being a precious metal, high cost volatility prohibits its usage in huge quantities. Due to the search for alternative catalytic methodology, which employs a suitable transition metal 1<sup>st</sup> row element such as cobalt and iron transition metals which is an important approach due to its sustainability in its eco-friendly nature (Cahiez and Moyeux 2010; Dey et al. 2018; Gosmini et al. 2008; Marinescu et al. 2018; Xu et al. 2017).

For this heterogenization of homogeneous catalysts which contributes to the increase in the efficiency of the catalysts due to its more reactive sites on its surface which further expand its use in industrial application (Li et al. 2013; Su et al. 2014). Schiff base first reported by Hugo Schiff and when they coordinated with metals such as Co, Cu, Ni etc., to form metal complexes (Abu-Dief and Mohamed 2015; Anuradha, Shweta Kumari, Devendra D. Pathak 2015; Mukherjee et al. 2018; Yorimitsu and Oshima 2006). However these complexes finds its applicability in various oxidative-reduction reactions (Xu et al. 2017). Due to the lack of catalyst efficiency as well as stability and recovery is the major issue (Molnár and Papp 2017). Herein, we synthesized Schiff base metal complexes immobilized to the graphene oxide as catalysts for Suzuki coupling reactions. Immobilization phenomena onto solid support is better than impregnation technique which leads to minimize metal leaching as well as improving the long-stability of catalyst.

Scheuermann et al reported the palladium supported graphene oxide and chemically derived graphene (CDGs) with a high catalytic activity and also they stated the morphology of carbon support along with functionalization (Scheuermann et al. 2009). Feng et al reported the Pd-Co bimetallic nanoparticle (1:1) ratio supported on graphene by chemical reduction method for the coupling of phenyl acetylene and aryl halide in THF/water mixture using triethylamine as base at 80 °C (Feng et al. 2014). The catalyst retained satisfied catalytic activity after 5<sup>th</sup> successive runs along with stability. Alamdari reported a phosphine group functionalized graphene along with palladium nanoparticles and the catalyst were active till 5<sup>th</sup> successive cycles for Suzuki, Heck and N-arylation reactions (Fareghi-Alamdari et al. 2016). Shang et al reported a novel catalyst i.e., palladium supported on an ionic liquid modified graphene (GO-NHC-Pd<sup>2+</sup>) for catalyzing the Suzuki coupling reaction with at least 6<sup>th</sup> consecutive cycles retained its activity (Shang et al. 2013). Martinez-Klimov et al reported the palladium species supported on hydrogen titanate nanotubes by impregnation method and tested its activity in Suzuki coupling with 10% decrease in catalytic activity after five cycles (Martínez-Klimov et al. 2018). Jinhui Tong et al reported the synthesise of Cu-Pd ferrites on mesoporous SBA-15 and MCM-41 molecular sieves and retained its activity after 10 consecutive cycles (Tong et al. 2016). Nesreen Ahmed et al (2017) reported the CuAl and CoAl double layered hydroxides (LDHs) onto graphene oxide and the catalytic activity in Ullmann reaction is 91% and 98% in 25min (Ahmed et al. 2017). Phuong Tran et al (2018) reported the graphene oxide framework with encapsulated with palladium species and the catalytic activity in Suzuki coupling reaction using both protic and aprotic solvents with good yield (Tran et al. 2018).

In this work, we synthesized a cobalt Schiff base immobilized onto graphene oxide using APTMS as a coupling agent for the formation of carbon-carbon bond and varying the catalytic activity in Suzuki cross-coupling reaction. Herein we synthesized the GO and later it is amino functionalized and then Co Schiff base is immobilized on to amino functionalized GO.

## **4.2 EXPERIMENTAL SECTION**

### **4.2.1 Chemicals required**

Graphite powder, 3-aminopropyl trimethoxy silane (APTMS), 2-aminoethanol, arylboronic acids, terephthalaldehyde and various aryl halides were purchased from sigma Aldrich. All the solvents like ethanol, toluene, acetonitrile, DMSO, hydrogen peroxide and along with sulphuric acid, phosphoric acid are obtained from Finar chemicals limited. Caesium carbonate, potassium carbonate, sodium hydroxide, potassium hydroxide, SDS (sodium dodecyl sulphate), sodium nitrate, sodium carbonate, Cobalt nitrate hexahydrate ( $\text{CoNO}_3 \cdot 6\text{H}_2\text{O}$ ) and potassium permanganate are obtained from lobo chemie limited.

### **4.2.2 Synthesis of Graphene oxide (GO)**

GO was prepared according to the improved Hummers method (Marcano et al. 2010). 5g of graphite and 2.5g of  $\text{NaNO}_3$  were mixed with 108 mL of  $\text{H}_2\text{SO}_4$  and 12 mL of  $\text{H}_3\text{PO}_4$  and later maintained in an ice bath along with stirring for 10 min. After that, 15g of  $\text{KMnO}_4$  were added slowly by adjusting the temperature at 5 °C. Then it was stirred for 2h in an ice bath and after that the temperature of the reaction was raised to 45 °C for 30 min. Later, the mixture is adjusted to 98 °C for 12h and then deionized water dropped slowly to this mixture to get its volume to 400 mL. After that 15 mL  $\text{H}_2\text{O}_2$  was added after 5 min and stirred vigorously using glass rod. The collected product was centrifuged, washed several times with deionized water and 5% HCl solution and later it is dried, kept in oven at 50 °C.

### **4.2.3 Synthesis of 3-aminopropyl trimethoxysilane functionalized-GO (ASGO)**

The as prepared 1000 mg GO was immersed in 50 mL of toluene using ultrasonic bath and was refluxed with 2 mL of APTMS under a nitrogen atmosphere for 24h around 110 °C (Li et al. 2013). After that, the black powder obtained was filtered, washed with toluene for several times, and later washed using absolute EtOH to remove any physisorbed traces of APTMS. The sample was dried in vacuum oven around 90 °C for 6h.

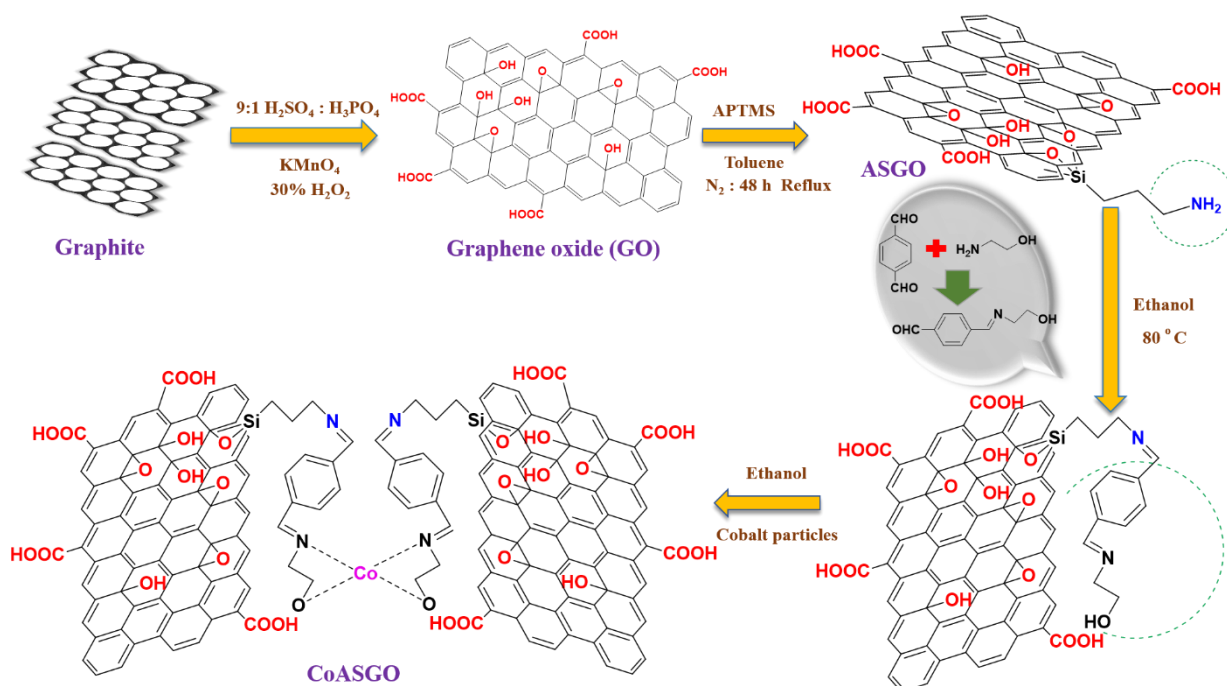
### **4.2.4 Synthesis of Cobalt oxide particles**

0.2162g of SDS in 50 mL of distilled water along with 0.8731g of  $\text{CoNO}_3 \cdot 6\text{H}_2\text{O}$  in 10 mL of distilled water were prepared separately. Later, the cobalt solution is stirred by adding SDS

solution dropwise and kept constant stirring at room temperature. Next, 0.3603g of urea is dissolved in distilled water and the entire mixture were added together and stirred for 2h. After that the solution is transferred to Teflon lined autoclave for 2h at 140 °C. The final product obtained is filtered, washed repeatedly with ethanol and dried in an oven at 80 °C for 12h. Then, it is annealed at 400 °C for 2h in vacuum oven and then the black-colored powder is obtained.

#### 4.2.5 Synthesis of graphene oxide immobilized cobalt Schiff base complexes (CoASGO)

The terephthalaldehyde amount (470 mg, 1.0 mmol) and 2-amino ethanol (229 mg, 0.6 mmol) along with few drops of acetic acid were added to the mixture and refluxed for 24h. The formed solid product is filtered and washed several times with ethanol. Later the (500 mg, 0.05 mmol) amino functionalized GO was dispersed in 60 mL of absolute ethanol and then the (100 mg, 0.01 mmol) of Schiff base is added to the mixture and refluxed for 24h. After refluxing, the product cooled down to room temperature and achieved the solid product by filtering and washed with ethanol twice. Finally, the obtained product was mixed with Co oxide particles (488.1 mg, 2.0 mmol) in ethanol and reacted for 24h room temperature. The product was filtered and washed with ethanol, and dried in an oven at 50 °C.



Scheme 4.1. The synthesis of CoASGO complex

#### 4.2.6 Experimental procedure

Aryl halide (1 mmol) and arylboronic acid (1.5 mmol) taken in a flask along with the catalyst (0.32 mol%) and base  $\text{Cs}_2\text{CO}_3$  (3 mmol) in ethyl alcohol (5 mL). The flask was charged in a parallel synthesizer Talboys at 80 °C under reflux conditions up to 12h. Once the reaction is

completed (monitored by using thin layer chromatography) the product was analyzed using Gas Chromatography (GC) (Shimadzu 2014, Japan), siloxane Restek capillary column (30m length and 0.25mm diameter) and flame Ionization Detector (FID).

#### **4.2.7 Characterization Techniques**

In this work, the CoASGO catalyst shows improved reactivity due to the covalent interaction of amino functionalized GO with cobalt Schiff base complex. Herein, we reported a series of physicochemical characterizations such as ICP-AES, FTIR, TGA, PXRD, SEM, EDX, TEM and XPS were conducted on the catalyst to understand the structure and composition as well as to identify an efficient means to enhance the stability of the catalyst. The infrared spectra were recorded using KBr disks in a Bruker-Alpha ECO-ATR FTIR in the range 500-4000 $\text{cm}^{-1}$ . PXRD measurements were carried out using Cu K $\alpha$  radiation on a Rigaku 600 diffractometer Miniflex. Diffractions were carried out in the ranges ( $2\theta$ ) of 5-80° at the scanning speed of 2° per minute for the XRD patterns of GO and their covalently attached amino functionalized Schiff base metal complex catalysts. HR-TEM Analysis were taken on a FIE Tecnie-F20 with an acceleration voltage of 200kV. X-Ray photoelectron spectroscopy (XPS) was measured on a Kratos XSAM800 X-ray electron photometer using Al K radiation. TG analysis performed on a Hitachi DTA-6300 in N $_2$  stream with a heating rate of 5 °C per minute in the range of 25-800 °C. The samples were heated at a constant rate of 10 °C/min under N $_2$  flow from 200-800 °C. Metal content was calculated by inductively coupled plasma atomic emission spectroscopy (ICP-AES) analysis on a Agilent 5100 Synchronous vertical Dual view ICP-AES with Dichroic Spectral Combiner (DSC) Technology.

### **4.3 RESULTS AND DISCUSSION**

#### **4.3.1 Vibrational Spectroscopy (FTIR)**

FT-IR spectra of the pure GO and CoASGO shown in Figure 4.1. In GO, a strong band is around 1710  $\text{cm}^{-1}$  (C=O) represented the carboxylic acid and they were bands at 1058, 1220 and 1621  $\text{cm}^{-1}$  represented the epoxy(C-O), phenol, C=C etc., in their scaffold (Dikin et al. 2007; Kuila et al. 2012; Marcano et al. 2010; Mkhoyan et al. 2009). The hydroxyl groups in GO around 3394  $\text{cm}^{-1}$  which indicated the stretching mode of O-H bonds. In ASGO, there is a doublet band around 2850 and 2917  $\text{cm}^{-1}$  exhibited the symmetric and asymmetric stretching vibrations of methyl and methylene alkyl groups in ASGO (Gemeay et al. 2017; Pandey et al. 2016). Further, the other bands in ASGO around 1121.5, 1029 and 1629  $\text{cm}^{-1}$  intended to be Si-O-Si, Si-O-C linkages and bending N-H vibrations which indicated that the grafting of APTMS

onto GO by chemical bonding have taken place. Two bands around 3423.7 and 1629  $\text{cm}^{-1}$  i.e., N-H group which confirmed that the amino functionalization successfully taken place on its surface i.e., ASGO shown in figure 4.2 (Pandey et al. 2016). A band around 692  $\text{cm}^{-1}$  proved that the silylation process taken place on GO shown in figure 4.2. The band around 1629  $\text{cm}^{-1}$ , in amino functionalized GO disappeared and moved to lower frequency (C=N  $\text{cm}^{-1}$ ) at 1610  $\text{cm}^{-1}$  confirmed that the  $-\text{NH}_2$  groups in ASGO undergone condensation reaction with the other side carbonyl group of terephthalaldehyde to form C=N bond on the heterogeneous support which confirmed the binding of amino functionalized GO surface with the organic Schiff base moiety. A peak around 660  $\text{cm}^{-1}$  confirmed the presence of cobalt moiety on the heterogeneous catalyst shown in figure 4.1 (Song et al. 2018). There is a band around 598  $\text{cm}^{-1}$  which signified the stretching of Co-N bond and it proved the coordination of cobalt with N, O sites on the catalytic surface of the heterogeneous catalyst shown in figure 4.1 (Li et al. 2013).

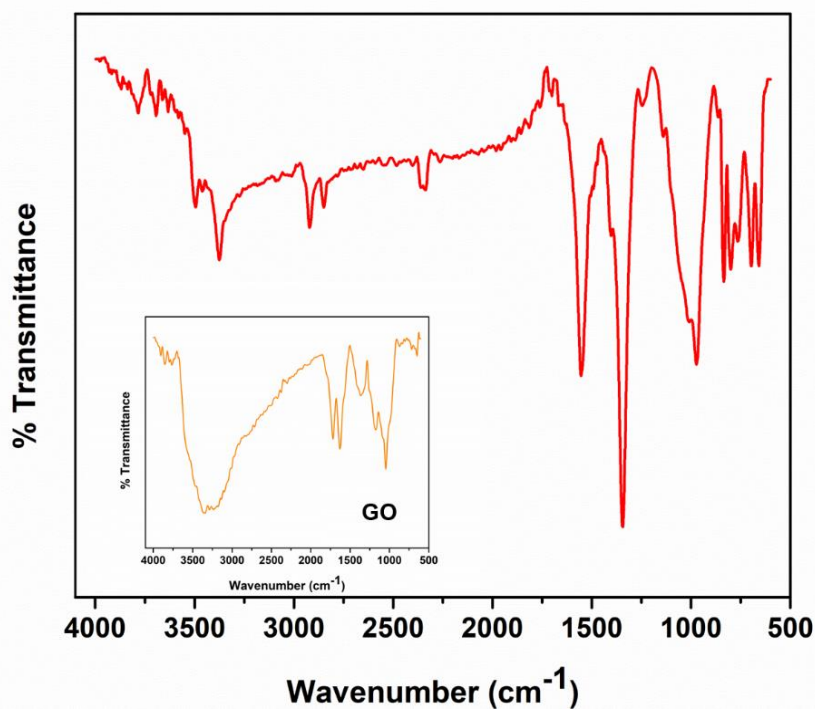


Figure 4.1. FTIR spectra of CoASGO complex with GO

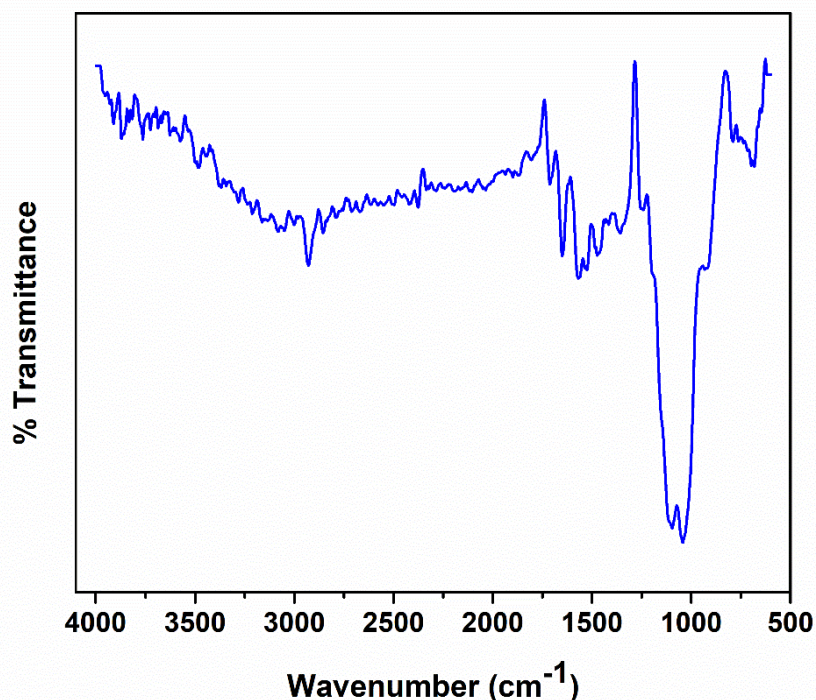


Figure 4.2. FTIR Spectra of amino functionalized GO (ASGO)

#### 4.3.2 X-ray Diffraction (XRD)

In GO, a broad peak around  $2\theta = 10.91$  confirmed that the graphene oxide has been formed with oxygen moieties which got amalgamated on the basal planes of graphitic layers having hydroxyl groups which increase the interlayer distance between the graphitic sheets shown in supplementary information (figure 4.3) (Dikin et al. 2007; Marcano et al. 2010). In ASGO, the diffraction peak around  $2\theta = 10.9$  represented that graphene oxide chemical morphology not damaged due to the amino functionalization of GO (Gemeay et al. 2017; Pandey et al. 2016). Due to the functionalization of GO with APTMS, the peak intensity reduces and a new broad peak appears around  $20.1^\circ$  respectively shown in figure 4.3. The peak weakening is due to the saturation of spaces between interlayer exhibiting amorphous morphology (Pandey et al. 2016). However, due to the shattering of varied range of stacking equal to GO nanosheet exfoliation and the newly protruded peaks nearest to the reduced GO confirmed that some of the oxygen moieties possessing hydroxyl group in GO have been successfully functionalized. A broad peak around  $2\theta = 22.24$  confirmed the oxygen groups on graphene oxide surface have been successfully functionalized due to the amino functionalization and which in turn lead to encapsulation of metal complex. The cobalt crystallites peaks in cobalt oxide particles were around 18.9, 32.3, 36.7, 42.7, 56.2 shown in figure 4.3(b) (Dey et al. 2018). The peaks in synthesized catalyst CoASGO around 18.9, 31.2, 37.4, 44.7, 59.2 and 65.2 respectively shown



in figure 4.3(a). The intensity of a weak peak indicates the cobalt oxide molecules were in smaller in size (Dey et al. 2018; Song et al. 2018). A weak peak around 10.9 represented that the immobilization had taken place with the simultaneous introduction of organometallic species which resembles the complex prepared successfully (Su et al. 2014). However, the broader peaks of diffraction pattern explained that the synthesized catalysts is amorphous in nature.

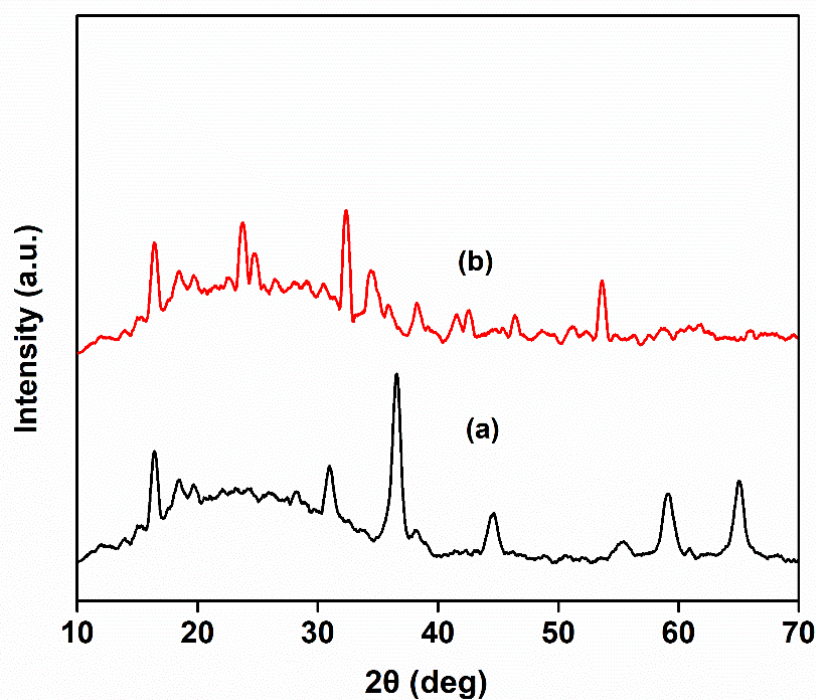


Figure 4.3. XRD graph of a) CoASGO complex and b) Cobalt oxide particles

#### 4.3.3 SEM & EDS (Scanning Electron Microscopy & Energy Dispersive X-ray Spectroscopy)

The morphology and structural features of GO, catalyst CoASGO and ASGO were analyzed using FE-SEM analysis and EDS analysis. In GO, the 2D structure represented twist in its nanosheets which resemble to be not in ordered phase with a lot of crumpling feature shown in figure 4.4(a) (Dikin et al. 2007). The carbon in GO is  $sp^2$  hybridized with a lot of protrusion and folded edges enabling the Co Schiff base complexes to get immobilized onto the graphitic surface. The reactive sites on these heterogeneous support acts as idealistic patterns which in turn enables the reactant moieties undergo target-oriented modification on GO. Therefore the stacking phenomena which is more in synthesized catalyst due to the amino modification using APTMS shown in figure 4.4(b) along with organometallic species introduction compared to

the basal planes of pure GO shown in figure 4.4(c,d) (Dey et al. 2018; Gemeay et al. 2017; Pandey et al. 2016; Xu et al. 2017).

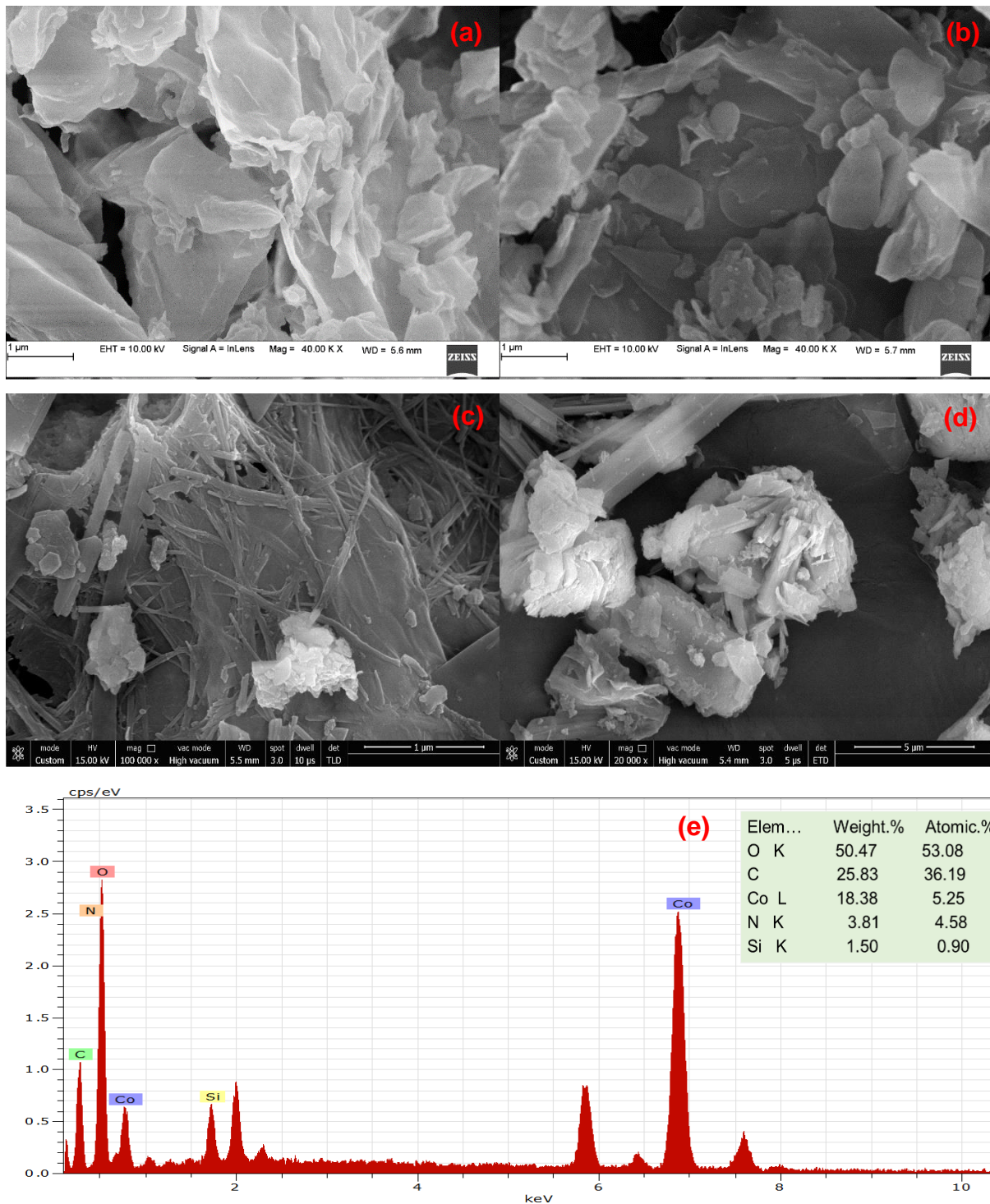


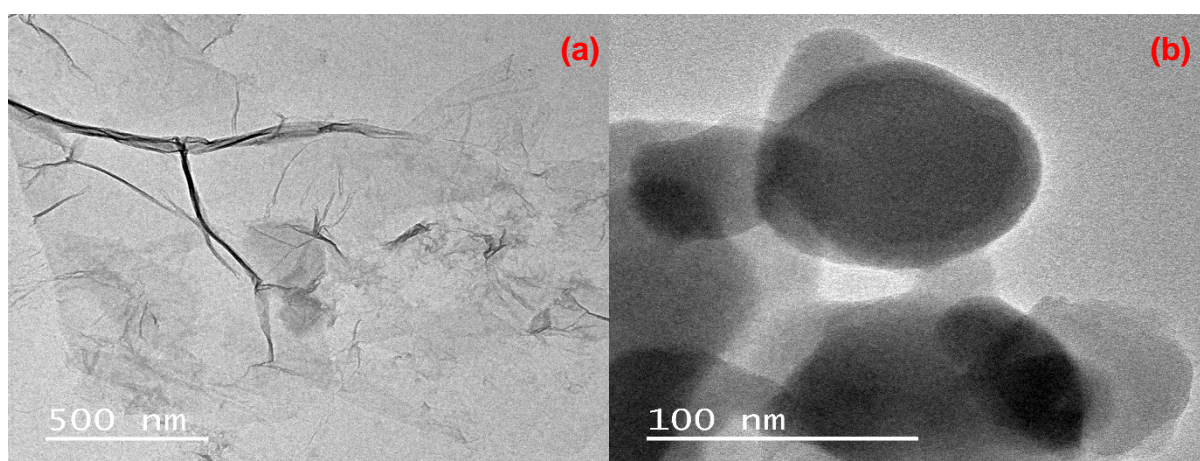
Figure 4.4. SEM of a) GO, b) ASGO, c,d) CoASGO, and e) EDS image of CoASGO

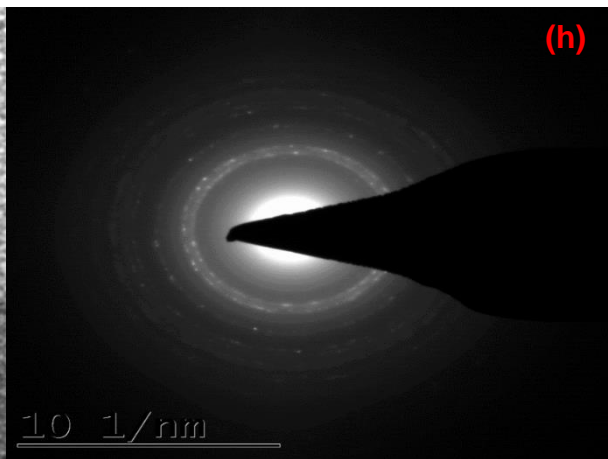
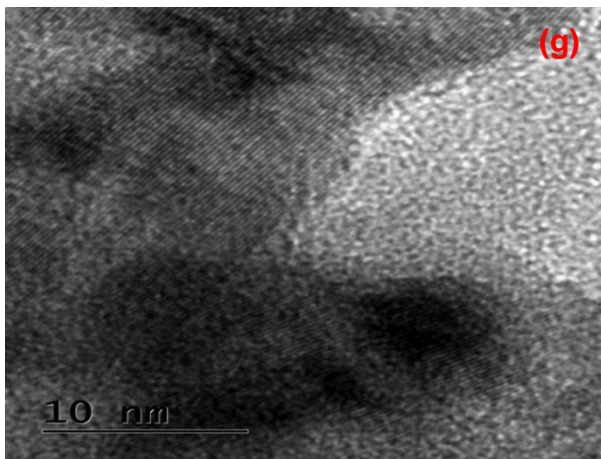
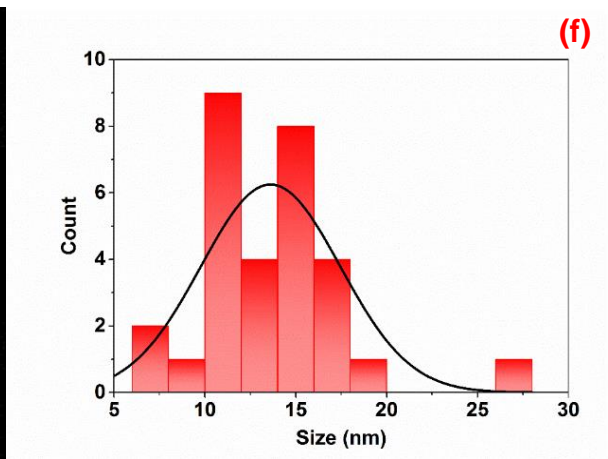
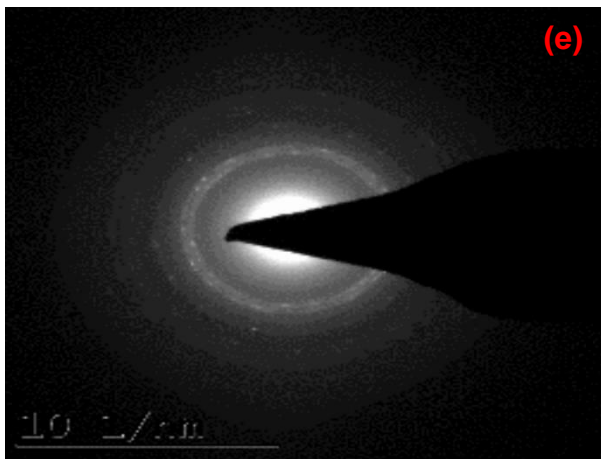
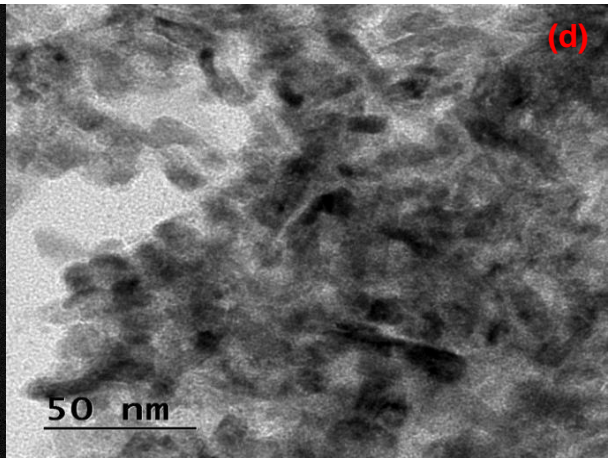
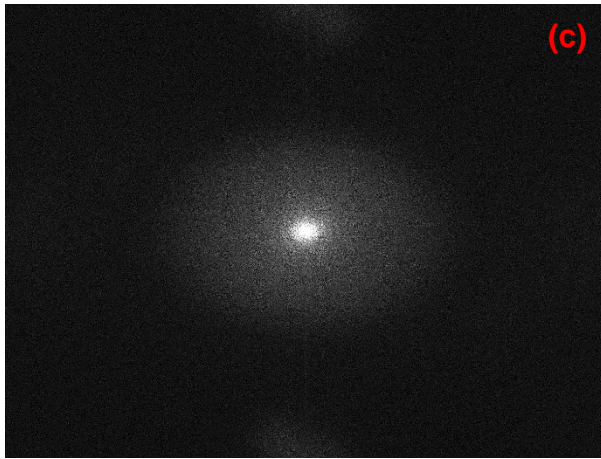
EDS analysis showed the atomic wt% of the GO, ASGO are given in chapter-1 and CoASGO given in figure 4.4(e). In GO, it is a cluster of both carbon and oxygen moieties with different functional groups shown in figure 3.5(a). In amino functionalized Graphene oxide ASGO, the elemental mapping showed the composition of elements such as carbon, oxygen,

silicon and nitrogen which confirmed that APTMS successfully loaded onto the surface of GO given in figure 3.5(b). The elemental composition of the synthesized catalyst showed the composition of various elements like cobalt, nitrogen, oxygen, carbon and silicon with different atomic wt% ratio shown in figure 4.4(e). However, the presence of various elements confirmed the loading of Co Schiff base onto amino functionalized GO surface. The results from EDS mapping depicted that the homogeneous distribution of Co, N and Si on the GO support.

#### 4.3.4 Transmission Electron Microscopy (TEM)

TEM sample preparation was done by fixing some pieces of composite on a carbon coated copper grid by gentle pressing and making them to adhere to their surface firmly. The figure 4.5(a) showed that the synthesized GO with a nanoscopic morphology having wrinkled structures with a few layers or sheets (Scheuermann et al. 2009). After the amino functionalization on GO (ASGO), the figure 4.5(b) showed the layered morphology is due to the binding of silane groups onto the GO surface. It also confirmed that the GO nanosheets structure not damaged during the amino functionalization. Figure 4.5(c, d) indicates the Selective area diffraction pattern (SAED) that the catalyst is polycrystalline phase. Numerous crumpling feature with a layered fashion in nanosheets which justified the cobalt schiff base is immobilized onto amino functionalized GO shown in figure 4.5(c). The average size of CoASGO in HR-TEM image confirmed that it is 6 nm in its size and the TEM image of the catalyst CoASGO it is 15 nm in its size shown in figure 4.5(d, e).





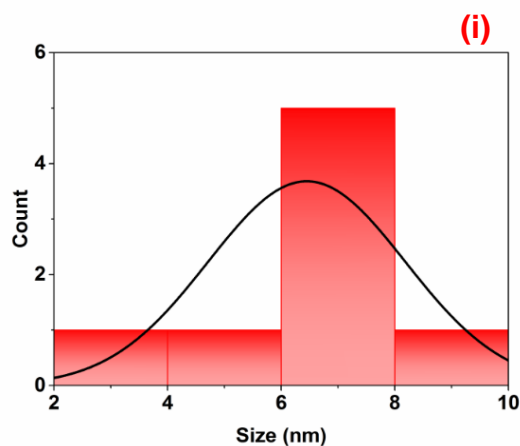


Figure 4.5. TEM images of a) GO, b) ASGO, c) SAED of ASGO, d) CoASGO, e) SAED of CoASGO, f) average size of TEM image of CoASGO, g) HR-TEM of CoASGO, h) SAED of HR-TEM of CoASGO and i) average size of HR-TEM image of CoASGO

#### 4.3.5 X-ray photoelectron spectroscopy (XPS)

The binding energies of synthesized catalyst CoASGO were 284.5 eV and 531.5 eV which were shown in the deconvoluted XPS spectra of C 1s and O 1s in figure 4.6 (Xu et al. 2017). In deconvoluted C 1s XPS spectra there are four peaks around 284.3, 285.4, 287.4, 289.1 eV which represented the C=C, C-OH, C-O-C and COO<sup>-</sup> groups respectively (Marinescu et al. 2018; Song et al. 2018). A band around 102.6 eV confirmed that the silicon is bonded to oxygen in Si 2p spectra (Su et al. 2014). And further it had confirmed that the silylation reaction taken place on the hydroxyl group of GO surface with APTMS as a coupling agent. The silylation process also explained the presence of Si and N atom along with Cobalt signal in the wide spectra of synthesized catalyst. In N 1s XPS spectra, there is a signal around 399.75 eV which confirmed that the N-H group converted to C=N is due to the Schiff base formation i.e., involves the condensation of terephthalaldehyde and 2-aminoethanol. Further, there is a shift at 399.75 eV because of the electron pair effect of nitrogen atoms and central cobalt ions. The satellite peak of Co 2p<sub>1/2</sub> and Co 2p<sub>3/2</sub> spectra of synthesized complex shows two typical bands at 795.6 and 779.3 eV confirmed the binding energy of Cobalt atom with Co<sup>3+</sup> ion and the coordination of cobalt metal with the nitrogen and oxygen groups (Song et al. 2018). There is a satellite peak around 795.6.0 eV i.e., Co 2p<sub>3/2</sub> which confirmed the electrostatic interaction with the ligand and cobalt metal. Finally, the wide survey of XPS spectra confirms that all elements Co, Si, N, C and O atoms are present on the synthesized catalyst.

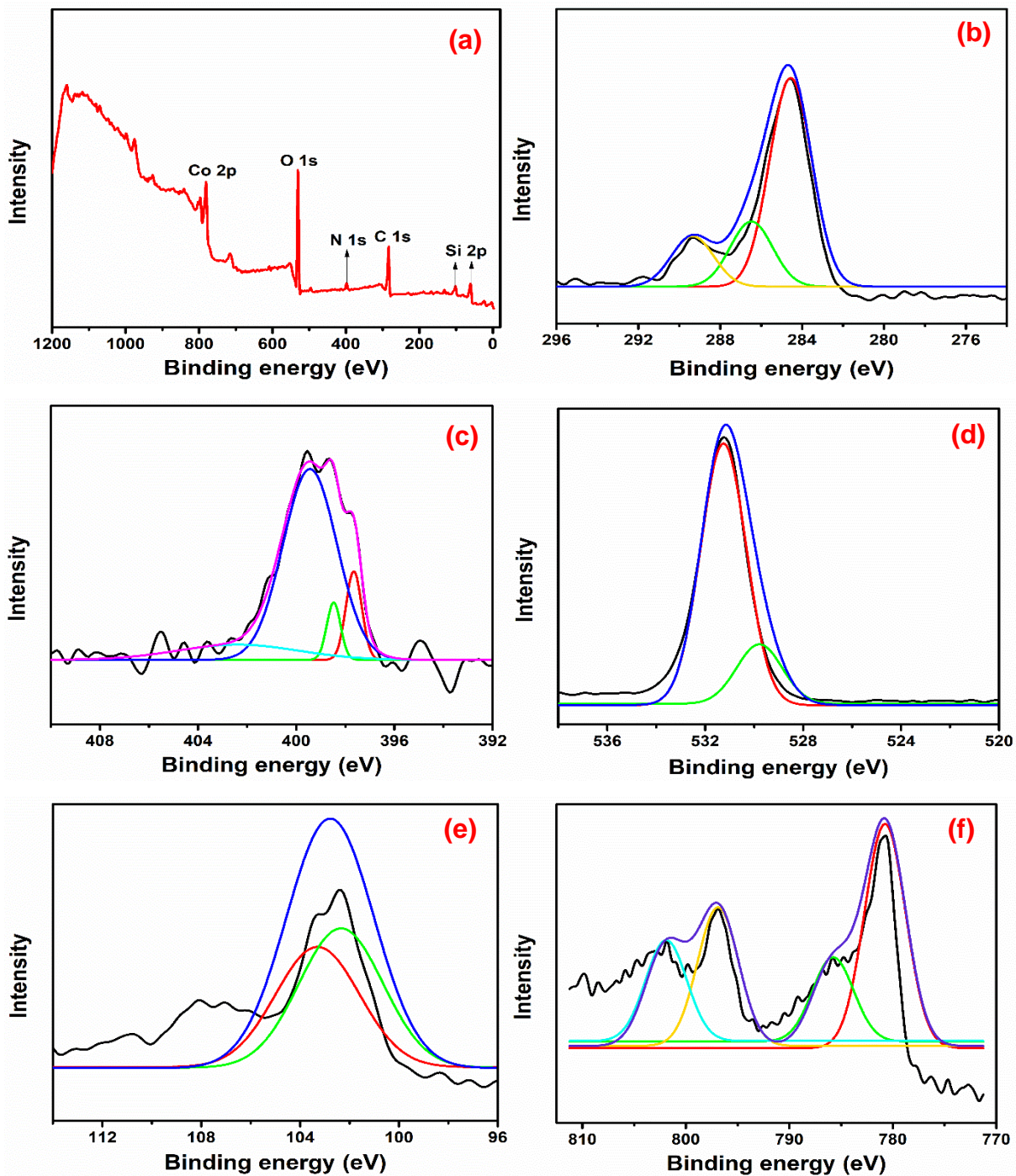


Figure 4.6. XPS analysis of CoASGO composite with a) elemental survey, b) C 1s scan, c) N 1s scan, d) O 1s scan, e) Si 2p scan and f) Co 2p scan

### 4.3.6 Thermal analysis

#### 4.3.6.1 Thermogravimetric analysis (TGA)

Figure 4.7 showed the weight loss in GO is in two degradation step i.e., at first 90-190 °C which is due to the removal of physisorbed water trapped in the GO as well as C-O-C functional groups which remained in the water molecules (Su et al. 2014). The second step is 220-600 °C

explained the removal of all the remaining oxygen groups along the destruction of carbon ring. Further, the synthesized catalyst CoASGO observed in three steps shown in figure 4.7: at first, there is a loss observed around 4.59% at 90-190 °C represented physisorbed hydroxyl groups and second weight loss is 33% around 250-450 °C confirmed the removal of undigested oxygen functionalities along with unreacted APTMS. Final weight loss is 42.5% around 320-600 °C represented the gradual degradation of the synthesized catalyst CoASGO in figure 4.8(b).

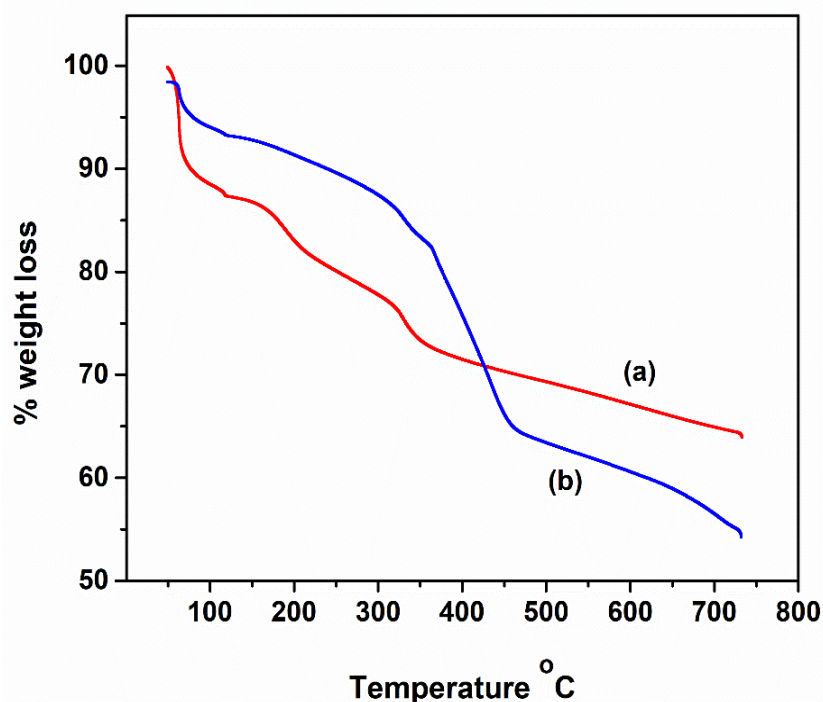


Figure 4.7. TGA graph shows the a) GO and b) the synthesized catalyst

#### 4.3.6.2 ICP-AES Analysis

Before the measurements were done, the catalyst was digested in concentrated nitric acid which were diluted to volume and mixed. The Co complex is 0.31mmol/g represented the weight loss during the immobilization of Co Schiff base complex onto amino functionalized GO surface. Here, the ligand to metal molar ratio is 1:1 during the synthesis of catalyst and then the molar ratio calculated from ICP analysis is 0.34mmol/g respectively. The results suggests that the metal complex successfully supported onto GO.

#### 4.3.7 Suzuki cross-coupling reaction

The synthesized catalyst CoASGO explored and tested for the Suzuki cross-coupling of some arylboronic acids with various substituted aryl halides as a model reaction for determining the catalytic performance (Miyaura and Suzuki 1995). Here the activity of the catalyst

substantiated using the coupling reactions by following some of the suitable variations in base, solvents, catalyst amount as well as reactants variations. The cross-coupling reaction which involves the substituted aryl halides and arylboronic acids with the catalyst amount along with EtOH as solvent and Cs<sub>2</sub>CO<sub>3</sub> base at a specified temperature at 80 °C is given in table 4.1.

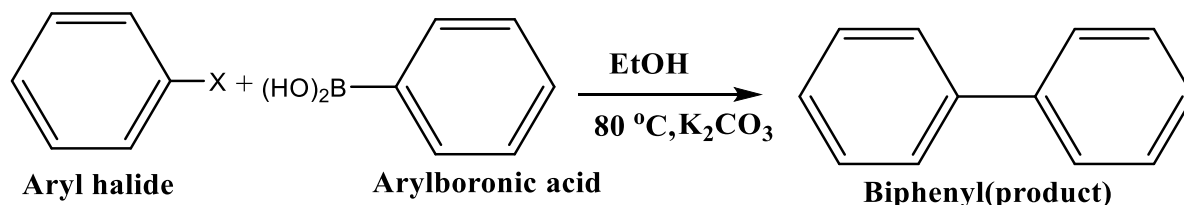


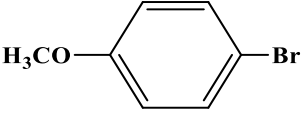
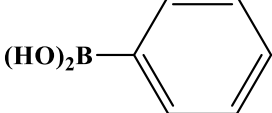
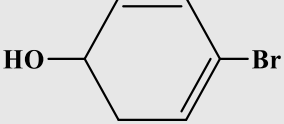
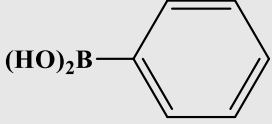
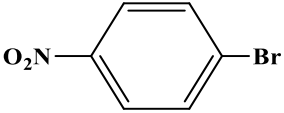
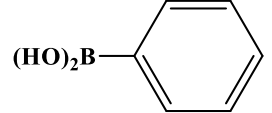
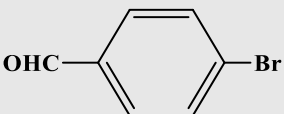
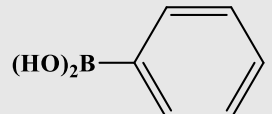
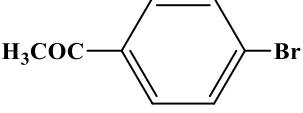
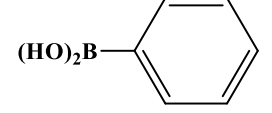
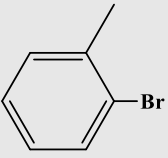
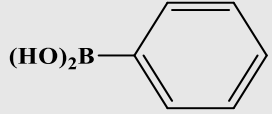
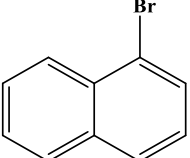
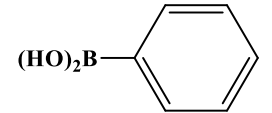
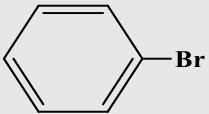
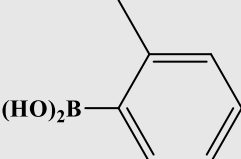
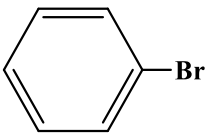
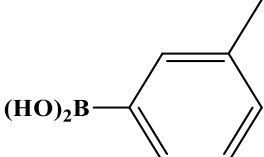
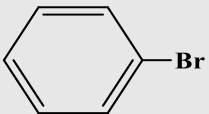
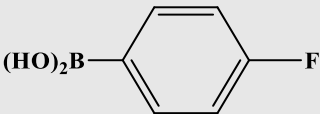
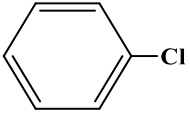
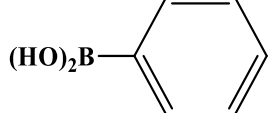
Table 4.1. Effect of various solvents and bases on yield at temp 80 °C

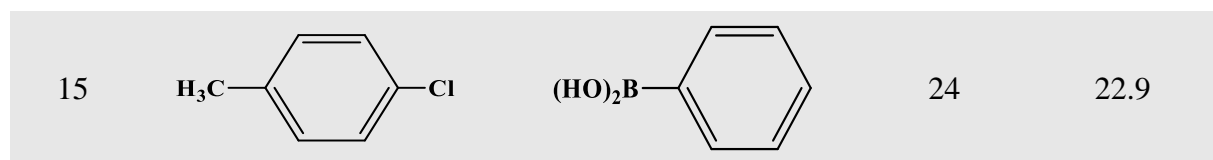
Sl. No.	Solvent	Base	Temperature	Catalyst (mol%)	Yield (%)
1	EtOH	Cs <sub>2</sub> CO <sub>3</sub>	80	0.32	96.5
2	EtOH	K <sub>2</sub> CO <sub>3</sub>	80	0.32	78.9
3	EtOH	Et <sub>3</sub> N	80	0.32	55
4	EtOH	KOH	80	0.32	12
5	EtOH	NaOH	80	0.32	34.9
6	Acetonitrile	Cs <sub>2</sub> CO <sub>3</sub>	80	0.50	74.9
7	Dimethyl sulfoxide	Cs <sub>2</sub> CO <sub>3</sub>	80	0.50	71
8	Tetrahydrofuran	Cs <sub>2</sub> CO <sub>3</sub>	80	0.50	60.5
9	Toluene	Cs <sub>2</sub> CO <sub>3</sub>	80	0.50	52

Table 4.2. GC yield of products at 80 °C

Sl. No.	Aryl halides	Aryl boronic acids	Time(h)	Yield (%)
1			8	97
2			12	96.5
3			24	64.7



4			24	52.7
5			24	65
6			12	89
7			12	86.9
8			12	84.7
9			24	58.9
10			24	68
11			24	53
12			24	44.9
13			24	55
14			24	17.9



**Reaction Content:** EtOH(5 mL), Aryl halides(1.0 mol), aryl boronic acids(1.5 mol), Cs<sub>2</sub>CO<sub>3</sub>(2 mol), and CoASGO Catalyst (0.32 mol%)

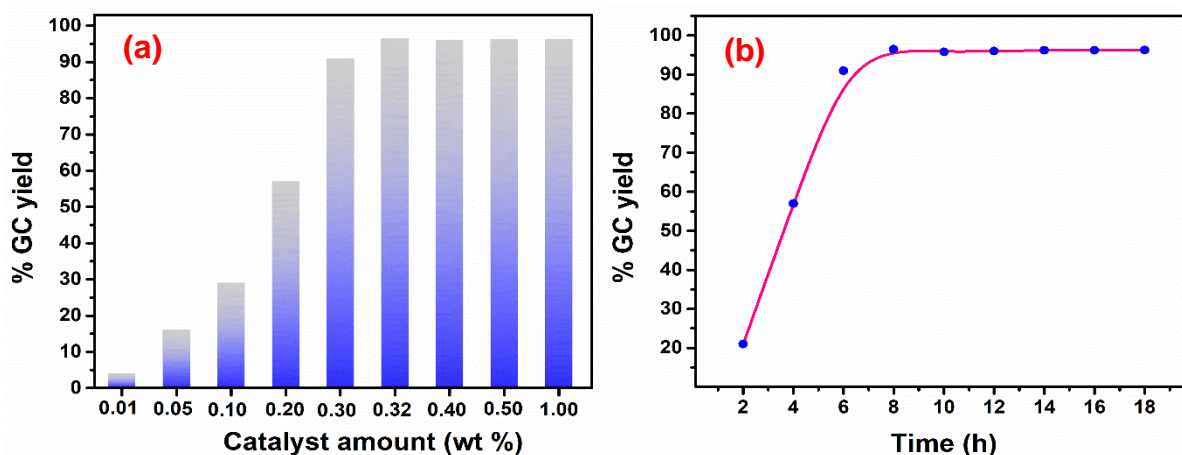


Figure 4.8. The effect of (a) catalyst amount and (b) reaction time on the GC yield of Suzuki coupling reaction

In case of aryl halides such as iodo and bromo substituents, the yield of the products is 96.5% with phenylboronic acid using ethanol as solvent and a specified temperature around 80 °C using caesium carbonate as base with a reaction time of 6.5h showing in table 4.1. The results from the table 4.2 stated the rate of reaction with variation to product formation taken place with a time of 1h to 24h and also depends on the type of substrates either electron donating or withdrawing group. Here the model reactions were done using coupling of bromobenzene with phenylboronic acid with different solvents and time variation along with base studies. Six bases have been tested with yield as follows: KOH (12%), K<sub>2</sub>CO<sub>3</sub> (79%), Et<sub>3</sub>N (55%), NaOH (35%) and Cs<sub>2</sub>CO<sub>3</sub> (96.5%). From the base variation, the better base is Cs<sub>2</sub>CO<sub>3</sub> which gave good yield and abundantly available in nature. Here, we studied the time variation from 1h to 24h and recorded as follows; 1h (11%), 2h (21%), 4h (57%), 6h (91%), 10h (95.8%), 12h (96.2%) and 24h (96.3%) and the best time period is 6.5h with 96.5% for bromobenzene shown in figure 4.8(b). However, the product yield for iodobenzene is 97.4% at 6.5h at 80 °C. And the solvents variation shown in the table 4.1 which confirmed that EtOH is best solvent for the reaction. On the other hand, the catalyst loading is 0.01 mol% to 1.00 mol% in the experiments and the maximum yield is obtained at 0.32 mol% catalyst loading shown in figure 4.8(a). In determining the catalytic behavior of the catalyst under certain optimized conditions, the biphenyl product gave maximum yield with iodobenzene and bromobenzene i.e., 97.4% and

96.5%. Electron withdrawing groups such as NO<sub>2</sub> and CHO gave 89% and 87% higher biphenyl yield. Aryl bromides having donor groups takes long time to form biphenyl product which is due to the migration of electron through  $\pi$  bond on aryl bromides. Since the aryl chlorides are more attractive substrates, due to its low cost and availability but its poor reactivity and high bond dissociation energy C-Cl bond (96 kcal/mol) is a major problem restricting it in industrial application (Sun et al. 2013). Hence, a lot of attempts can be made which can fulfil the gap in future work in this area. Apart from the coupling reaction mechanism, with respect to certain evaluation the efficiency of a heterogeneous catalyst in nanocatalysis depends on its size (Kuila et al. 2012). However, the smaller the size of particle is, greater will be its catalytic activity (Lamei et al. 2017). But due to the good dispersion and cobalt nanoparticles formation without any aggregation along with GO meant for tuning the surface of cobalt nanoparticle improved the catalytic performance throughout the reaction (Marinescu et al. 2018). The high product formation is due to the cobalt oxide average particle size which is confirmed from the HR-TEM image of the CoASGO complex found to be 6 nm and the heterogeneous support being GO enhances the surface area of the catalyst which leads to the more reactive sites on its surface.

Recyclability studies were done to prove the reusability of the heterogeneous catalyst which may be beneficial for reliable application (Molnár and Papp 2017). The model reactions done using bromobenzene and phenylboronic acid with 0.32 mol% catalyst under the optimized conditions. Once the reaction is done, the catalyst is filtered using simple filtration and washed twice with acetonitrile (2\*10 mL) and stirred in ethanol for 30 min at room temperature finally dried in an oven at 60 °C. The catalyst shown in figure 4.9, can be reused for 5times without any significant loss of its catalytic activity. After that, there is a decrease in product yield. Further analysis, i.e., the catalyst studies done using ICP-AES analysis. For fresh catalyst, the concentration of Co metal is 1.24 wt% and the catalyst after 6<sup>th</sup> cycle is 1.20 wt% confirmed that the metal leaching was very less in the consecutive cycles. Later, the next 6<sup>th</sup>, 7<sup>th</sup>, 8<sup>th</sup> cycles the catalyst metal leaching increased by 10% i.e., 1.116%. However, till the 5<sup>th</sup> consecutive cycles the catalyst supporting material played a key role, hence carbon supported material especially graphene which enhances the thermal stability of the catalytic system as well as functional groups on these heterogeneous supports to prevent further leaching of metal ions. The catalyst deactivation can be explained to some extent with the loss of Co metal ion in the reaction process. The other cause is due to the recycling reactions which results in the decrease in catalytic activity because of the agglomeration of Co nanoparticle. The TEM analysis of the fresh catalyst and the 5<sup>th</sup> cycle catalyst confirmed that the metal leaching during the coupling

reaction is less shown in figure 4.10. The results justified that the complex catalyst remains stable without any metal leaching.

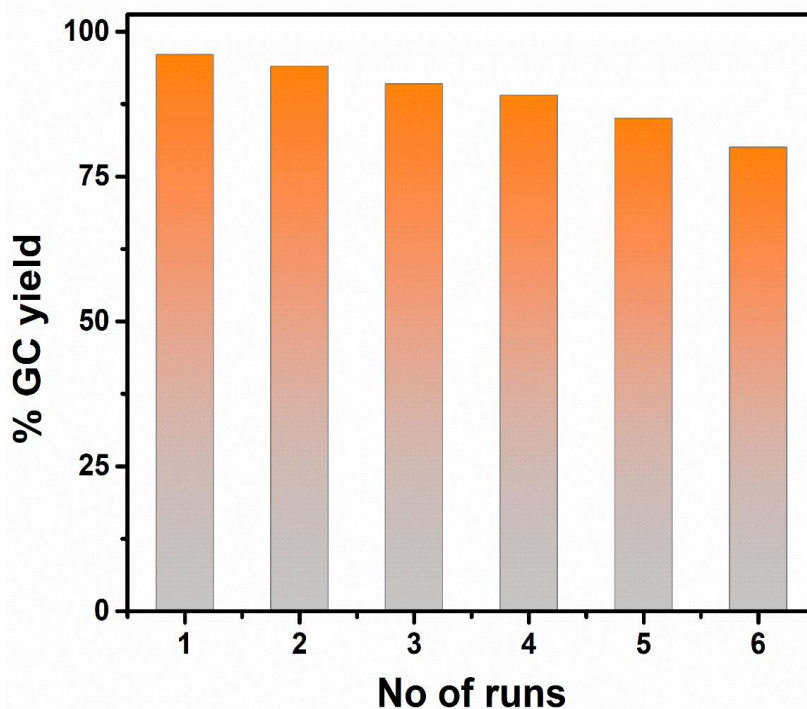


Figure 4.9. Recycling ability of CoASGO as catalyst for Suzuki coupling reactions

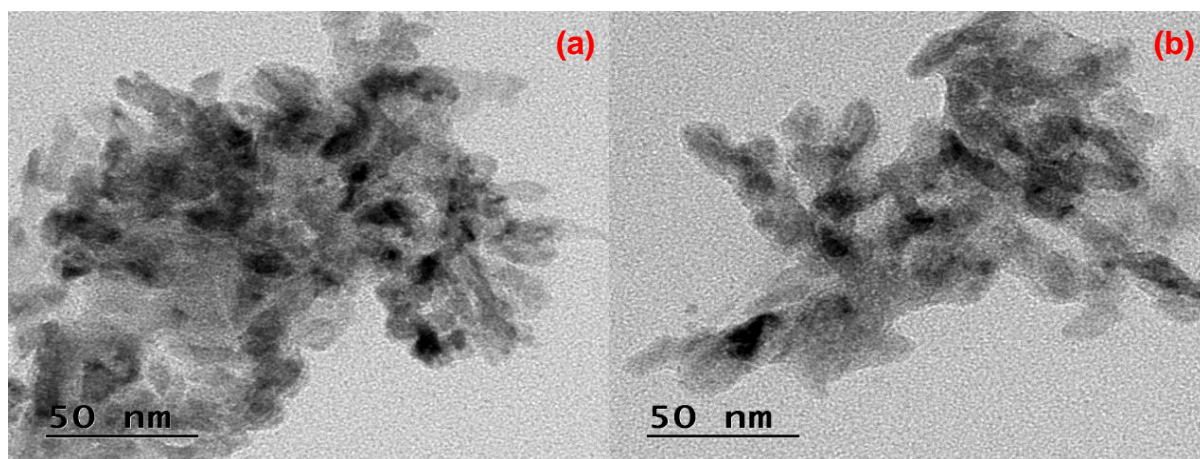


Figure 4.10. TEM images of Fresh and used catalyst after 5<sup>th</sup> cycle a) Fresh catalyst b) used catalyst

#### 4.4 CONCLUSIONS

In conclusion, an effective in-situ strategy has been developed to synthesize the CoASGO nanocomposite by the usage of cobalt oxide nanoparticles. The synthesized composite can yield up to a maximum of 97.4% using phenyl iodides which proves that it is effective for the Suzuki

cross-coupling reaction. The heterogenous support GO possess outstanding properties with 2D structure which makes it a robustious supporting material for the wrapping of homogeneous complexes to attain their practical applications. The catalyst has high surface area, effective thermal and chemical stability. The catalyst is easily recoverable, reusable, benign and can be handled easily. Further, an in-depth and effective studies need to be carried out in coordination catalysis in order to attain the maintain the catalyst stability for a longer period of time.

## **CHAPTER-5**

**Synthesis of Cobalt oxide-polypyrrole polymer and functionalized onto Graphene oxide for the efficient removal of dyes and heavy metal pollutants from aqueous effluents**

**Abstract:** *Water pollution attained significant interest due to rapid industrialization which created a huge demand for clean water. Textile and paint industries became global manufacturer which generated a large quantity of wastewater and it is a threat to the water resources. This chapter explains the synthesis of a conjugated polymer polypyrrole and their functionalization with cobalt oxide nanoparticles. Further, it is immobilized on GO to form COPYGO for the effective removal of dyes and metals ions from aqueous effluents.*

## 5.1. INTRODUCTION

Environmental pollution is of paramount concern which is increasingly preponderate because of the very rapid industrialization across the globe (Masindi and Muedi 2018). These environmental effects challenge the entire human life due to the increase in water pollution causing an adverse impact upon the availability of fresh water (González et al. 2015; Kafshgari et al. 2017). Due to the problems of environmental pollution such as dyes and heavy metal ions in waste water which is more harmful to the entire ecosystem have not completely solved till now (Martin and Johnson 2012). The synthetic dyes are one of the major pollutants released from various industries and its improper disposal enhances the water crisis. These organic dyes can abate the incident sunlight and disturb the photosynthesis of aquatic plants. These phenomena effectively influence the aquatic life environment. These synthetic organic dyes are harmful to aquatic organisms and human life due to their innate toxicity, mutagenesis and carcinogenic effects (Adhikari et al. 2017; Jha et al. 2016; Kong et al. 2016; Lei et al. 2018). They were highly stable and very rarely can be biodegradable. Often, the biodegradation fade the color of water, but the cleaved molecule along with aromatic NH<sub>2</sub> groups remain toxic to human health (Chung 2016; Lei et al. 2016; Vahidhabanu et al. 2017).

Methylene blue (MB) is a frequently used cationic dye for coloring of fabrics. Due to the excessive quantity of MB found in the industrial wastes which leads to a wide range of environmental pollution (Konicki et al. 2018; Yao et al. 2012). A wide range of  $\sim 7 \times 10^5$  tons (annually produced) of commercially utilized dyes are discharged into the water bodies thus causing harm to aquatic life (Bensalah et al. 2009; Gosetti et al. 2004; Turhan and Turgut 2009). Along with carcinogenic and mutagenic affects, the existence of these pollutants in water hinder the penetration of light, results in the lack of photosynthetic activity which affects the food chain (Ai et al. 2011; Waranusantigul et al. 2003).

Congo red (CR) is an anionic dye with diazo group having symmetric aromatic nature that exhibited thermal and optical stability which offered resistance towards light as well as

biodegradable phenomenon (Budiman et al. 2016; Chen et al. 2018; Santhosh et al. 2017; Yang et al. 2013). Mutagens and carcinogens present in CR is harmful to mankind and aquatic organisms causing various harmful effects such as respiratory disorders, skin irritation and allergic reactions (Sham and Notley 2018; Wang and Wang 2008). The synthesis of surfactant based montmorillonites (MMT) with OTAB, DTAB & CTAB material for the adsorption of CR dye (Santhosh et al. 2017). The CR removal capacity is high for MMT with CTAB (2.0) adsorbent. The magnetic nanoparticle  $\text{SiO}_2@\text{CoFe}_2\text{O}_4$  on graphene oxide nanocomposite was reported for the removal of anionic dye acid black I and Cr(VI) ions from aqueous solution (Chen et al. 2018). CR adsorption capacity of  $366 \text{ mg g}^{-1}$  was achieved with chest husk-like hollow microsphere nickel cobaltite ( $\text{NiCo}_2\text{O}_4$ ) material under neutral pH (Wang and Wang 2008).

Along with the dyes, inorganic toxic, heavy metal pollutants such as Lead (Pb) and Cadmium (Cd), ions led to significant problem. Usually biological, physical and chemical methods have been widely used for the treatment of organic pollutants, unlike them, inorganic pollutants possess characteristics features such as solubility, oxidation-reduction properties and complex formation along with their decomposition becomes a major concern for the environment. Heavy metals in water bodies leads to the death of aquatic life, oxygen deficiency as well as algal blooms. These heavy metals when discharged into the aquatic system gets converted into hydrated ion. These hydrated ions disrupt the enzymatic process and it gets absorbed faster into the cell organism. The removal of pollutants in wastewater are controlled by various methods. But due to the presence of inhibitory properties, a high removal enforcement method should be developed for the hazardous pollutants (Qu et al. 2013). World Health Organization (WHO) and Environmental Protection Agency (EPA) found that a low level ( $5 \mu\text{g dL}^{-1}$ ) of Pb(II) exposure in children have led to the damage of central and peripheral nervous system (Carolin et al. 2017). The rapid growth in industrialization and mining activities results in a higher level of Pb(II) which may increase the risk of cardiovascular diseases and weight loss leading to death (Acharya et al. 2009; Mahmoud et al. 2020). Therefore, EPA confirms that the maximum Pb(II) level in drinking water should not exceed 15 ppb. Cadmium, which is a heavy metal used in plating, battery, phosphate fertilizers, stabilizers and alloy industries. Cadmium metal causes “Itai-Itai” disease in humans which results in softening of bones which causes fractures (Bhatnagar and Sillanpää 2009). Even at a very low concentration, it causes hepatic toxicity, lung cancer and diseases related to respiratory system, kidney and reproductive system (Demim et al. 2013; Filipič 2012).



To solve this problem, a broad area of research has been explored and a great number of techniques has been developed such as adsorption, coagulation, ion-exchange, reverse osmosis and precipitation (Cui et al. 2018; Ghaemi and Safari 2018; Wang et al. 2018; Xie et al. 2014). Out of all the techniques, adsorption known to be attractive and eco-friendly phenomena for both the organic and the inorganic contaminants in water (Magdy and Altaher 2018; Satilmis and Budd 2017).

Polypyrrole which is a conjugated polymer, has many favorable properties such as easy to synthesize, good redox potential, tunable electric conductivity, biocompatible and environmental stability (Boyle et al. 1989; Liu et al. 2015; Ma et al. 2018; Wan et al. 2017; Wei et al. 2015; Wu et al. 2015). The presence of positively charged nitrogen atoms in polypyrrole is a best prospect for its applications in adsorption and filtration separation (Zhang and Bai 2003).

Carbon based porous materials which possess highly attractive features with varied allotropic forms, micro structure and morphologies consist of carbon nanotubes, graphene, graphdiyne, activated carbon, mesoporous carbon, carbon nanospheres, amorphous carbon etc., having huge applications in environment and energy storage (Ahmad et al. 2018; He et al. 2018; Kuang et al. 2018; Liu et al. 2018; Qin et al. 2019; Wang et al. 2018; Xu et al. 2017). Out of the multifarious carbon allotropes, graphene derivatives gained attention due to its more oxygenated groups on its surface. Graphene oxide have been extensively studied in the areas like photocatalysis, sensors, electrocatalysis and adsorption phenomena (Xu et al. 2018; Zhao et al. 2017; Zou et al. 2018). Although graphene oxide has good adsorbent capability to various pollutants, but the detachment of GO from the aqueous solution is a risky and challenging task because of the good hydrophilicity and effective dispersion of GO in water. It needs energetic centrifugation or filtration, and these approaches further leads to the secondary pollution. In order to overcome this problem, magnetic separation involving technique by integrating magnetic nanoparticles onto GO to synthesize magnetic graphene nanocomposites gained attention (Sivashankar et al. 2014).

Various metal oxides have been synthesized and applied in the elimination of pollutants from waste water due of their greater pore size distribution and low toxicity (Anastopoulos et al. 2018). Advancement in the synthetic mechanism of metal oxide nanoparticles is a part of today's research. Cobalt oxide ( $\text{Co}_3\text{O}_4$ ) nanoparticles are the inorganic metal oxides that possess cubic spinel crystal structures (Bhatnagar and Sillanpää 2009). Although  $\text{Co}_3\text{O}_4$  has key applications in different areas, but began to be useful for the removal of hazardous

pollutants from the aqueous medium not long ago (Al Nafiey et al. 2017; Deng et al. 2016; Shahabuddin et al. 2016; Song et al. 2016).

The aim of this study is to synthesize a novel graphene oxide based magnetic  $\text{Co}_3\text{O}_4$  nanoparticles decorated with polypyrrole conducting polymer for augmenting the water stability and facilitating the removal of pollutants from wastewater. The designed materials is aimed to improve the overall adsorption of CR dye as well as Pb(II) and Cd(II) metal ions in acidic simulated solution and MB dye in basic simulated solution.

## **5.2. EXPERIMENTAL SECTION**

### **5.2.1 Chemical Required**

Natural graphite flakes, potassium permanganate ( $\text{KMnO}_4$ ), hydrogen peroxide (30%), pyrrole, ferric chloride, cobalt sulphate heptahydrate, and hydrazine hydrate were procured from Sigma Aldrich and used as they were obtained. Sulfuric acid ( $\text{H}_2\text{SO}_4$ , 98%) was purchased from Merck. Sodium hydroxide, glycine, ethanol, acetone, Conc. HCl, Methylene blue, and Congo red were obtained from Lobo Chemie Limited.  $\text{Pb}(\text{NO}_3)_2$  and  $\text{Cd}(\text{NO}_3)_2 \cdot 4\text{H}_2\text{O}$  obtained from Alfa Aesar.

### **5.2.2 Synthesis of Graphene Oxide (GO)**

Graphene oxide was synthesized by Improved Hummer's method (Marcano et al. 2018). 1.5 g of graphite flakes and 3 g of  $\text{KMnO}_4$  were mixed with 200 mL mixture of sulfuric acid and phosphoric acid (9:1). The reaction mixture was stirred for 12h at 50 °C. The reaction mixture allowed to cool in room temperature and adding into ice approximately 400 mL slowly with stirring. Hydrogen peroxide 30% (8-10 mL) added into the solution with vigorous stirring. The color of the solution changed from brown to bright yellow. The obtained mixture was filtered and centrifuged. The product obtained after decantation was washed with distilled water and absolute ethanol several times. The resultant graphene oxide dried at 60 °C for 24 h.

### **5.2.3 Synthesis of $\text{Co}_3\text{O}_4$ nanoparticle (CO)**

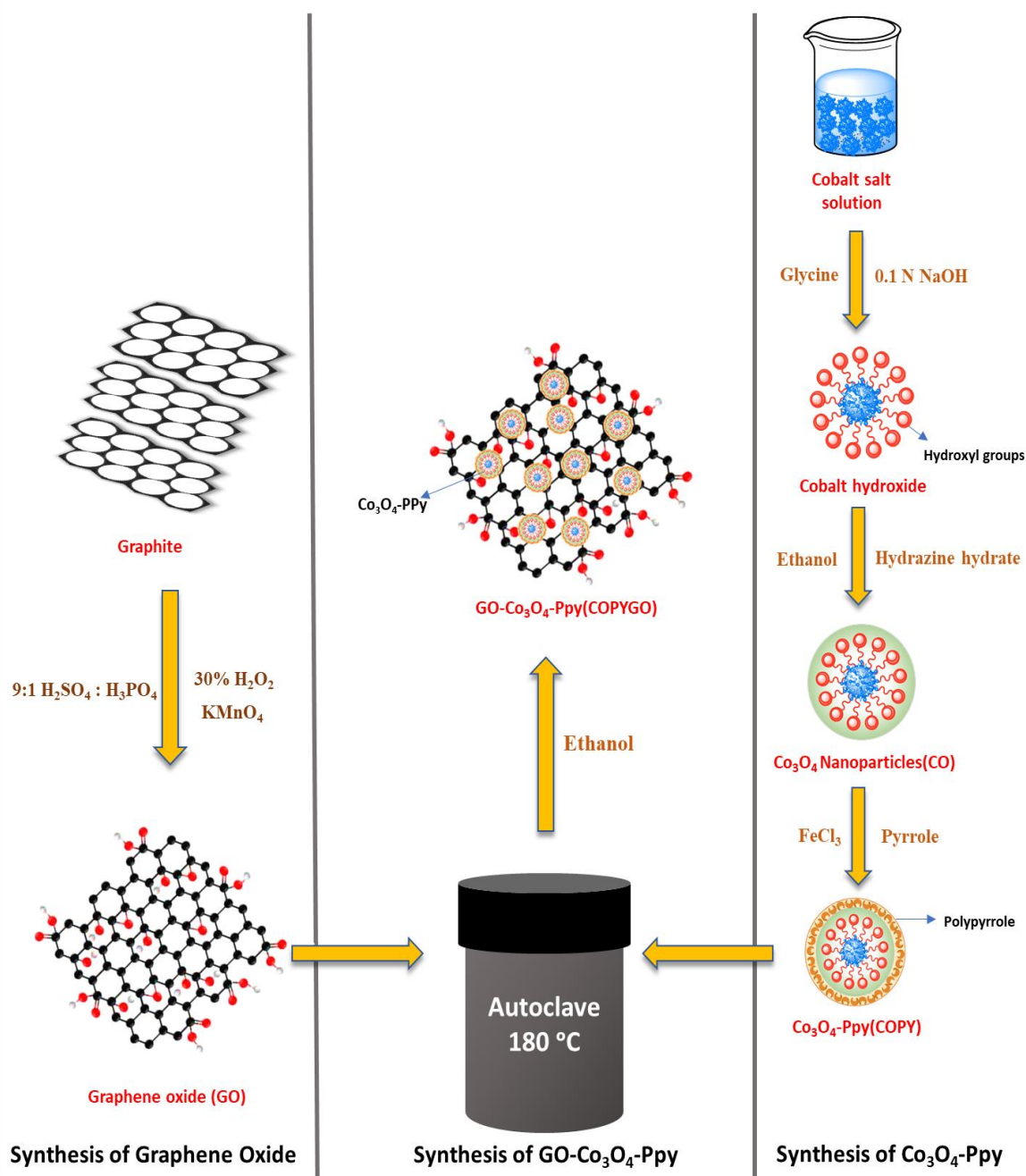
A pure magnetic cobalt oxide nanoparticle (CO) has been successfully synthesized by simple hydrothermal method with glycine as complexing agent. The CO was prepared by dissolving 5.3 mM of cobalt sulphate heptahydrate in 80 mL distilled water at pH 9.0. 2 eq. of glycine and 4.5 mL of hydrazine hydrate were added to the above solution and stirred for 1h. The solution was autoclaved at 180 °C for 12h. The product CO nanoparticle washed several times with distilled water and dried at 60 °C.

#### **5.2.4 Synthesis of Cobalt Oxide-Polypyrrole (COPY)**

0.4 mL of pyrrole monomer is dispersed in 40 mL of deionized water and stirred for 1h. To the above solution, FeCl<sub>3</sub> (2.125 g in 40 mL of distilled water) was added dropwise solution. 50 mg of cobalt oxide nanoparticle was added to the same solution. The temperature of the solution was maintained at 0-5 °C and stirred for 12h. The crude product washed several times with ethanol for removing impurities and a final wash with acetone followed by washing with distilled water and filtered, dried in an oven at 60 °C for overnight.

#### **5.2.5 Synthesis of Cobalt Oxide-Polypyrrole/GO Composite (COPYGO)**

GO (500 mg) was dispersed in ethanol (50 mL). 100 mg COPY was added to a solution containing 500 mg GO in 50 mL ethanol. The mixture was stirred for 1h. Later, autoclaved at 120 °C for 3h. The obtained solid product (COPYGO) was filtered and washed several times with ethanol as well as acetone and dried at 60 °C.



Scheme 5.1. Synthesis of COPYGO

### 5.2.6 Batch adsorption experiment

The COPYGO was studied for the adsorption of cationic dye Methylene Blue, anionic dye Congo red, heavy metal ions such as Lead and Cadmium from wastewater. The adsorption performance of the adsorbent was quantified for a period of 1-15 h for the different adsorbates. The pH of the adsorbate solution was adjusted in presence of 0.1 M HCl and 0.05 M NaOH solutions. The temperature was varied from 308.5-323.5 K for various adsorbates. In case of dyes, after the adsorption of the dye solution, the adsorbent was filtered off. In case of dye

adsorption, the adsorbent was filtered off and the supernatant solution is analyzed using UV spectrometer. In case of heavy metal ions, the adsorbent is filtered off, the supernatant solution is estimated by ICP-AES analysis to know the amount of metal ion.

The adsorption of MB was studied by taking wastewater sample of 25 mL with MB concentration ranges from 20-600 mg L<sup>-1</sup> onto 0.01 g of COPYGO in a series stirred at 200 rpm at different pH and temperatures. The adsorption of anionic dye CR by taking wastewater sample of 30 mL with CR concentration ranges from 20-300 mg L<sup>-1</sup> onto 0.012 g of adsorbent in a series at different pH and temperatures. The adsorption studies of Pb(II) was carried out by taking 30 mL of wastewater containing 20-500 mg L<sup>-1</sup> Pb(II) onto 0.01 g of adsorbent at different pH and temperature. 30 mL of wastewater containing 20-400 mg L<sup>-1</sup> Cd(II) was added to 0.01 g of COPYGO at different pH and temperature to study the adsorption phenomena.

### 5.2.7 Isotherms Experiment

The adsorption isotherm experiments were done at different concentration for each adsorbate i.e., MB from 30-400 mg L<sup>-1</sup> at a pH of 7.2, CR for 25-200 mg L<sup>-1</sup> at a pH of 5.0, Pb(II) for 20-400 mg L<sup>-1</sup> at a pH of 5.5 and Cd(II) for 25-200 mg L<sup>-1</sup> at a pH of 6.1. The temperature chosen 308.5 K, 313.5 K, 318.5 K and 323.5 K for all the four adsorbates. Further, the temperature resulted in the gradual decrease in the adsorption capacity of each adsorbate.

The mass balancing relationship applied to evaluate the quantity of adsorbate adsorbed ( $q_e$  mg g<sup>-1</sup>) of COPYGO was given by the equation (5.1):

$$q_e = \frac{(C_o - C_e)V}{m} \quad (5.1)$$

where,  $q_e$  is the adsorption capacity of the adsorbent (COPYGO) (mg g<sup>-1</sup>),  $C_o$  and  $C_e$  are the initial and final concentrations of the adsorbate at equilibrium state (mg L<sup>-1</sup>),  $V$  is the volume of the adsorbate solution (L) and  $m$  is the mass of the adsorbent (g).

### 5.2.8 Kinetic Studies

Kinetic studies were done using different concentration along with different time period to attain equilibrium state for the four adsorbate i.e., MB at 150 mg L<sup>-1</sup> for 300 mins, CR at 100 mg L<sup>-1</sup> for 400 mins, Pb(II) at 150 mg L<sup>-1</sup> for 400 mins and Cd(II) at 150 mg L<sup>-1</sup> for 400 mins. The adsorption experiments were done at four different temperature (308.5- 323.5K) for all four adsorbates and at different optimized pH for each adsorbate. The adsorption capacity at any time 't' ( $q_t$  mg g<sup>-1</sup>) was calculated using the equation (5.2):

$$q_t = \frac{(C_o - C_t)V}{m} \quad (5.2)$$

where  $C_o$  and  $C_t$  are the initial and final concentration at time 't' ( $\text{mg L}^{-1}$ ); V is the volume of the adsorbate solution (L) and m is the mass of the adsorbent (g).

The removal efficiency or rate of the adsorbate solution (% adsorption) is given by the following equation (5.3):

$$\% \text{ removal rate} = \frac{C_e - C_o}{C_o} \times 100 \quad (5.3)$$

All the adsorption experiments were carried out within the average of replicates, which is mentioned here for a mono adsorption data. For the rate of removal of adsorption, same set of experiments were done to determine the efficacy of adsorbent. The experimental data of four adsorbates onto COPYGO was investigated using Non-linear isotherms namely Langmuir, Freundlich, D-R and Temkin isotherms. The origin pro 2018 was used to get the best fit for the non-linear curve fitting graph.

### **5.2.9 Adsorption and recycling performances of COPYGO in model (actual) wastewater**

A synthetic model wastewater was prepared based on the OECD guideline for the testing of chemicals, and a suitable amount of biological and chemical medium which consisted of 110 mg of peptone, 80 mg of meat extract, 15 mg of urea, 20 mg of  $\text{K}_2\text{H}_2\text{PO}_4$ , 4 mg of NaCl, 1.5 mg  $\text{CaCl}_2 \cdot 2\text{H}_2\text{O}$  and 1.5 mg of  $\text{MgSO}_4 \cdot 7\text{H}_2\text{O}$  in 1 L of tap water (Guideline 2001; Zhao et al. 2015). This waste sample used as a solvent for the pollutants MB  $600 \text{ mg L}^{-1}$ , CR  $300 \text{ mg L}^{-1}$ , Pb(II)  $500 \text{ mg L}^{-1}$  & Cd(II)  $400 \text{ mg L}^{-1}$ . COPYGO (20 mg) was added into the model wastewater solution, and the adsorption tests was carried out in an orbital shaker for 12h.

### **5.2.10 Characterization Techniques**

The FTIR spectra was measured using Bruker-Alpha ECO-ATR FTIR within a range of  $4000\text{-}599 \text{ cm}^{-1}$ . Surface morphology was done using FE-SEM with EDS analysis from Zeiss Sigma SEM with oxford EDS. The internal structure of the samples was done using HR-TEM FEI Tecnai G2 20 (200 KV). The TG analysis was implemented at  $\text{N}_2$  atmosphere from  $25 \text{ }^\circ\text{C}$  to  $800 \text{ }^\circ\text{C}$  with a rate of flow heat of  $10 \text{ }^\circ\text{C}/\text{min}$  using Perkin Elmer STA 6000 thermal analyzer. Zeta potential was measured in presence of Zetasizer WT, Malvern Instruments. The phase identification and composition were carried out using X-ray diffractometer Bruker D8 advance. Raman spectrometer (STR500 Airix) was used for analysing the composition of the GO and COPYGO. The magnetic properties of the COPYGO and CO were done by VSM squid analysis. XPS analysis was performed to determine the elements and their composition using ThermoScientific, NEXSA surface analysis with a monochromatic Al-K $\alpha$  source ( $h\nu = 1486.6\text{eV}$ ). BET measurements to find out the  $\text{N}_2$  adsorption-desorption studies and to know

the pore diameter of the nano adsorbent from Nova touch LX2. The dye wastewater after the adsorption process is analyzed using UV spectrometer Analytik Jena SPECORD S600. In case of heavy metal ions, the heavy metal ion wastewater after the adsorption process is estimated by Agilent 5100 ICP-AES with Dichroic Spectral Combiner (DSC) Technology.

## 5.3 RESULTS AND DISCUSSIONS

### 5.3.1 Vibrational Spectroscopy (FTIR)

FTIR spectrum of the  $\text{Co}_3\text{O}_4$ , COPY & COPYGO are shown in Figure 5.1. The FTIR spectroscopy was investigated to know the interactions between COPYGO and the adsorbates. There is a small intense peak around 1687 and 1728  $\text{cm}^{-1}$  attributed to the C=C stretching and C=O stretching vibrations of the carboxylic group (Bao et al. 2020). The peaks at 1560  $\text{cm}^{-1}$ , 1429-1497  $\text{cm}^{-1}$  represented the anti-symmetric and symmetric C-C stretching vibrations of pyrrole ring and the frequency at 1357  $\text{cm}^{-1}$  referred to the C-N in-plane vibrations respectively. The frequency at 1286, 1236, 1151 and 1093  $\text{cm}^{-1}$  represented the mode of vibration is through C-H bending whereas 987-665  $\text{cm}^{-1}$  ascribed to the vibration of C-H out-of-plane deformation. The peak at 1560  $\text{cm}^{-1}$  broadens due to the interaction between aromatic ring of pyrrole and Graphene oxide (Qiao et al. 2020). In case of COPY, the peaks around 1560  $\text{cm}^{-1}$  is due to the interaction between Co-O nanoparticle with the C-N species of pyrrole. The peak around 661 and 573  $\text{cm}^{-1}$  attributed to the Co-O band from the cobalt oxide and the peaks around 3012-3423  $\text{cm}^{-1}$  represented the N-H stretching vibrations in the polypyrrole (Zhang et al. 2020). The cobalt oxide having peaks around 661 and 573  $\text{cm}^{-1}$  represented the peaks of Co-O bond. For the pure COPYGO, the FTIR spectrum showed a broaden peak 3343  $\text{cm}^{-1}$  and 1689  $\text{cm}^{-1}$  is ascribed to the stretching mode of the hydroxyl group and the bending mode vibrations of -OH groups on the surface of the graphene oxide nanosheets (Zhang et al. 2020).

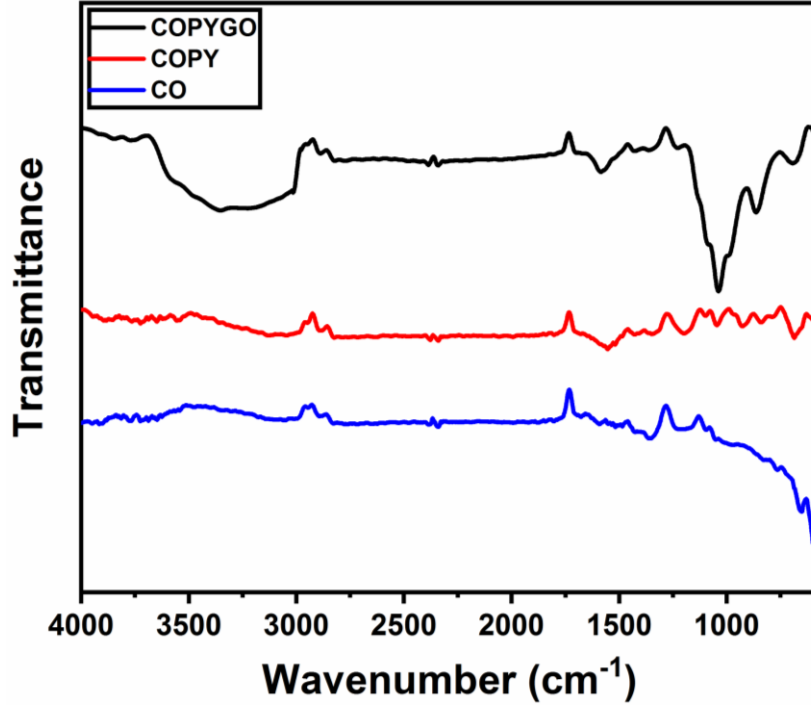


Figure 5.1. FTIR spectra of  $\text{Co}_3\text{O}_4$  nanoparticle, COPY & COPYGO

### 5.3.2 X-ray diffraction (XRD)

X-ray diffraction patterns of the  $\text{Co}_3\text{O}_4$  nanoparticle, COPY & COPYGO are shown in Figure 5.2. A broad reflection pattern in the range  $2\theta = 20\text{-}30^\circ$  reflects the amorphous nature in COPY & COPYGO (Marcano et al. 2018; Zhu et al. 2010). A peak around  $2\theta = 24^\circ$  indicated the presence of Py which is amorphous in nature and peak at 33 and 35 indicated a chain propagating in Py molecules apart from amorphous nature (Chafai et al. 2017; Xiong et al. 2009). COPYGO composites have a broad scattering peak possessing core-shell nano spherical structure, which confirmed that there is no further crystallinity order introduced into the nanocomposites. A peak at  $2\theta = 10.2^\circ$  in COPYGO confirms that the structure of GO is not destroyed on wrapping of COPY. In the COPYGO nanocomposite as well as  $\text{Co}_3\text{O}_4$  nanoparticle, the diffraction peaks at 19.50, 31.37, 37.02, 39.10, 44.97, 55.84, 59.58, 65.44 and 77.65 represented the crystalline face centered cubic phase of  $\text{Co}_3\text{O}_4$  which is in accordance with reported value (JCPDS Card No. 76-1802) (Šetka et al. 2017). XRD can be used to investigate peak broadening in determining the crystallize size. The size of CO nanoparticle was determined by the X-ray line broadening method using the Scherrer equation:

$$D_{hkl}(nm) = \frac{K\lambda_{(nm)}}{\beta_{hkl}(\text{Rad})\cos\theta} \quad (5.4)$$



Where  $K$  represented the shape factor ( $K=0.91$  for nano-spheres particles), indicates the X-rays wavelength ( $\lambda=0.154$  for Cu  $K\alpha$  radiation),  $\beta_D$  is the peak width at the half-minimum intensity and  $\theta$  shows the Bragg's diffraction angle.

The Debye-Scherrer equation was used to calculate an average crystalline size of 10.43 nm for the CO nanoparticle. The results are in consistent with TEM analysis.

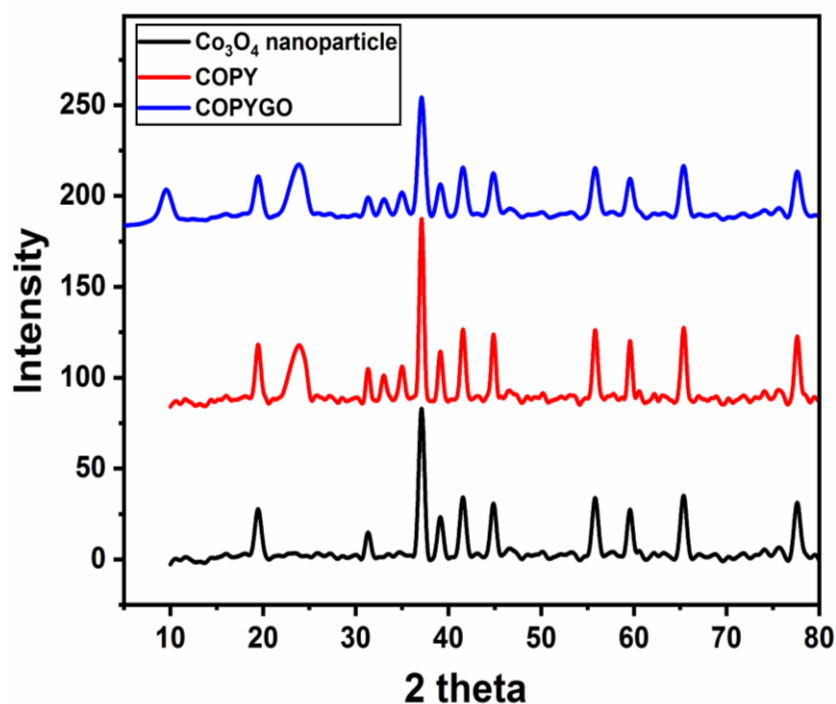


Figure 5.2. XRD pattern for the  $\text{Co}_3\text{O}_4$  nanoparticle, COPY and COPYGO

### 5.3.3 Scanning Electron Microscopy (FE-SEM)

The surface morphology of the materials is shown in Figure 5.3 of FE-SEM images of CO (a,b), COPY (c,d) and COPYGO (e,f). The COPYGO nanocomposite images show that the CO is uniformly surrounded by polypyrrole and then it is supported by GO which confirmed CO is well dispersed onto the heterogeneous support. This phenomena explains that the interaction between the polymer molecules as well as graphene oxide overcomes the Vander Waals forces between the carbon-carbon layers (Bose et al. 2010). The images of COPY and COPYGO in Figure 5.3(c-f) displayed rough and wrinkle surface in which the Py molecules are uniformly grown on  $\text{Co}_3\text{O}_4$  nanoparticles and bonded with the GO sheets by hydrogen bonding and  $\pi$ - $\pi$  interactions (Tikish et al. 2018; Wu et al. 2015). COPYGO image showed a rough surface of granular moiety of composites which can provide high surface area to enhance the adsorption properties of nano adsorbent. Increase in surface area results in storage of more charges which further help in charge transfer during the adsorption (Farhadi et al. 2016). Figure 5.3(e) showed

the graphene oxide nanosheets with wrinkle like structure whereas  $\text{Co}_3\text{O}_4$  nanoparticle have quasi-spherical shape. For the typical cobalt oxide nanoparticles, the lattice distance of 0.26 nm were observed, corresponding to the (111) crystal plane of cubic cobalt phase (Fan et al. 2014; Ramesh et al. 2017).

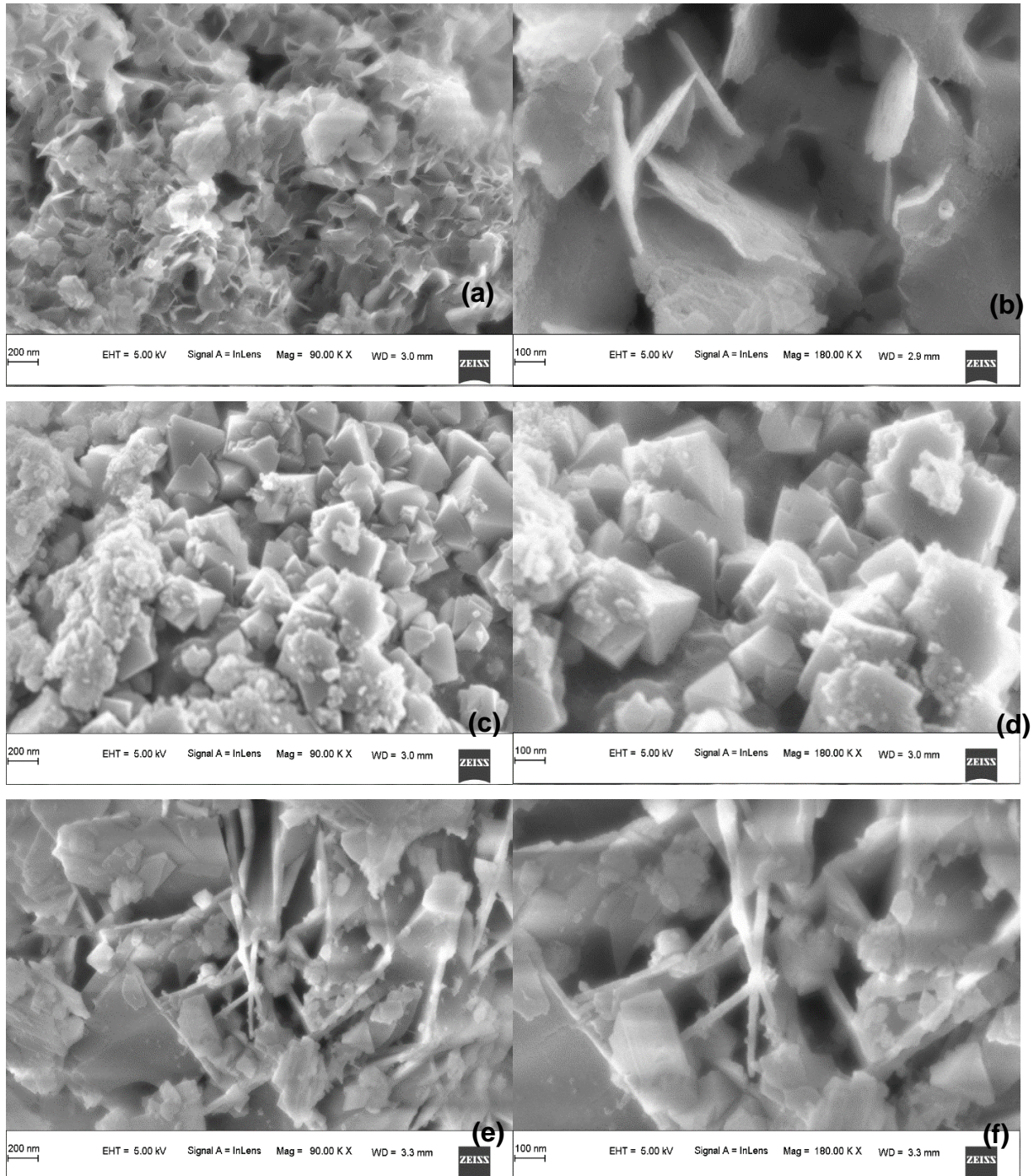
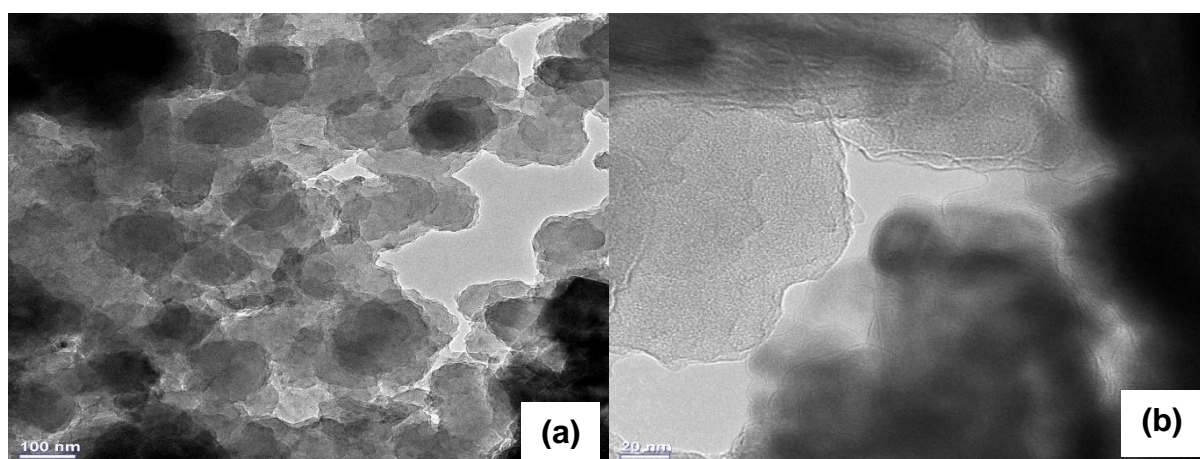


Figure 5.3. FE-SEM images of a, b) CO c, d) COPY and e, f) COPYGO

### 5.3.4 Transmission Electron Microscopy (TEM & HR-TEM)

The TEM images of CO & COPYGO are shown in Figure 5.4. In COPYGO nanocomposite shown in Figure 5.4(e-g), displayed that the cobalt nanoparticles have uniformly dispersed and decorated on both side of the graphene oxide support with a small size distribution. The magnified TEM images showed that cobalt oxide nanoparticles are in the range of 10-25 nm shown in Figure 5.4(c). The distribution and the clear structure of the  $\text{Co}_3\text{O}_4$  nanoparticle was studied using HR-TEM (Figure 5.4(d)). The micrograph confirms the presence of non-agglomerated small size nanoparticles centered around 1 nm. Further, the Fresnel fringes has measured with a diameter of about 0.5 nm of the image analysis shown in Figure 5.4(a) (Kulandaivalu et al. 2019).

The surface morphology of Graphene oxide nanosheets with COPY shows a typical crumpled and wrinkled structure. Normally, the Py with nanospheres were grown on GO nanosheets possess the similar size as that of the GO nanosheets. These smaller size  $\text{Co}_3\text{O}_4$  nanoparticles can have short diffusion path and provide more surface charge which are helpful for the removal of dye molecules. However, a little agglomerate of Py may be observed because of the interactions like  $\pi$ - $\pi$  stacking, donor-interactions and hydrogen bonding with functional groups (Yamada et al. 2019). The low aggregation of  $\text{Co}_3\text{O}_4$  nanoparticles represented that there is a good dispersion between graphene oxide and  $\text{Co}_3\text{O}_4$  nanoparticle. From the TEM images, it is clear that they exist a strong interaction between COPY and GO sheets. Further it helps in the fast electron transport from the graphene oxide support to the  $\text{Co}_3\text{O}_4$  nanoparticle which provide a better platform for the enhanced adsorption for pollutants.



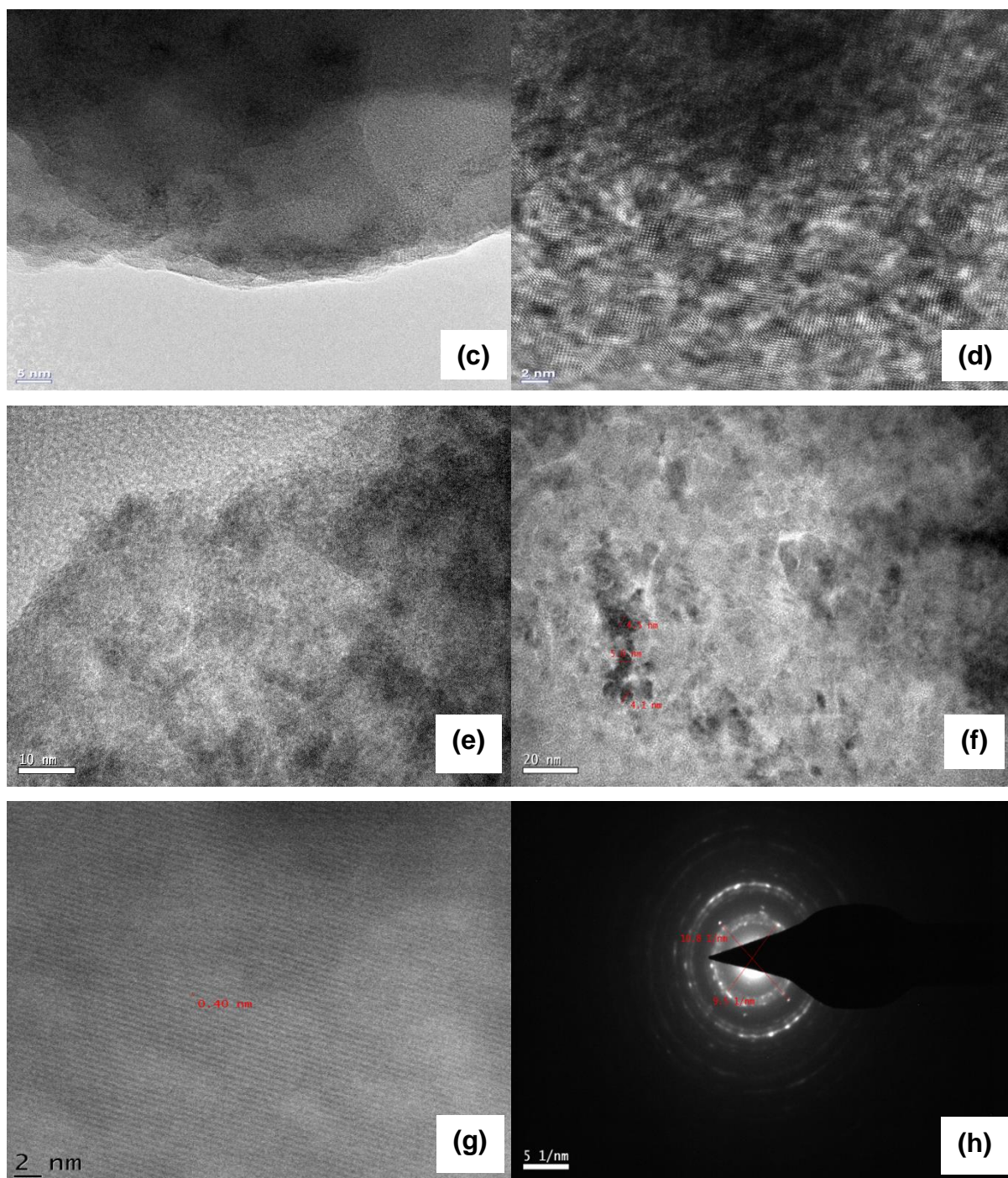


Figure 5.4. TEM images of CO (a,b,c,d), COPYGO (e,f,g) & SAED pattern of COPYGO (f)

### 5.3.5 Thermogravimetric analysis (TGA)

The TG analysis, (Figure 5.5) indicates the weight loss at different stages for both GO and COPYGO. The weight loss at different stages of the as-synthesized adsorbent is carried out in order to find out the nature of functional groups present on Graphene oxide nanosheets. However, the graphene oxide is stable up to 120 °C, and loses surface water molecules around 220 °C. The weight loss at 350-650 °C confirms that the removal of functional groups such as

hydroxyl, carboxyl, epoxy etc. Further, the weight loss around 700-800 °C, due to the removal of any organic moiety on the carbon ring and destruction of hexagonal carbon. The weight loss seen in COPYGO shown in Figure 5.5, at 80-150 °C may be due to the physisorbed water molecules. The weight loss at 220-500 °C indicates the loss of polypyrrole ring present on the graphene oxide along with the CO nanoparticle (Yussuf et al. 2018).

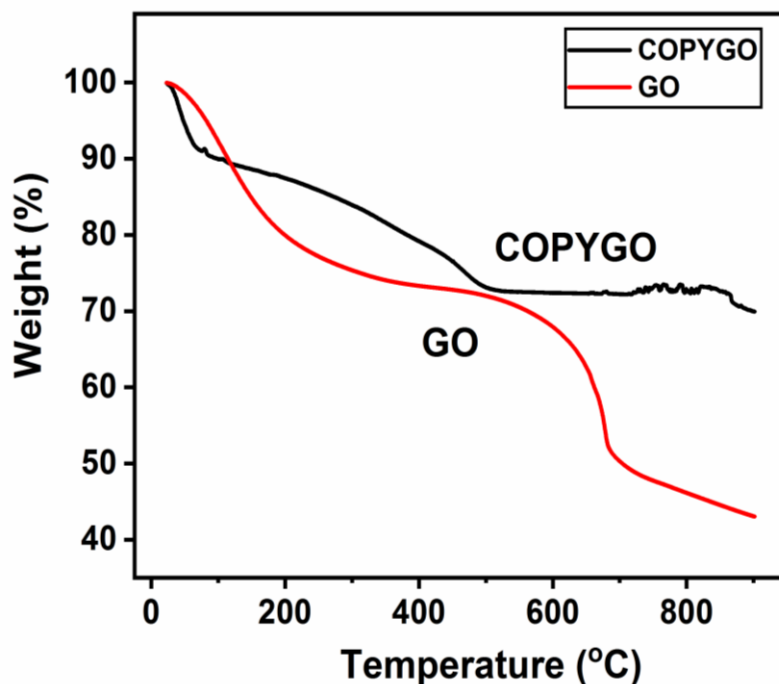


Figure 5.5. TGA of GO & COPYGO

### 5.3.6 Zeta potential

It is widely known that the pH value factor plays a prominent role in the adsorption experiments. Figure 5.6 represents the pH value versus zeta potential of the nano adsorbent species, which can determine the surface charge. The Isoelectric point (IEP) of GO was already described to be around 3-4 because of the presence of huge oxygen containing functionalities on its surface along with its edges to exhibit inclination to deprotonate the solution (Osuna et al. 1996; Ren et al. 2018). The graphene oxide will be negatively charged at pH-7 (Wang et al. 2010; Yan et al. 2010). Accordingly, COPYGO exhibited a lesser positive value, because of the negative charges on the GO surface. The IEP of COPYGO is 5.8. With the surface carrying positive charge on COPYGO, it can attract anionic species through electrostatic interactions and cationic dyes at pH 5 to 5.7 due to the presence of positive charge on the nano adsorbent species through hydrogen bonding.

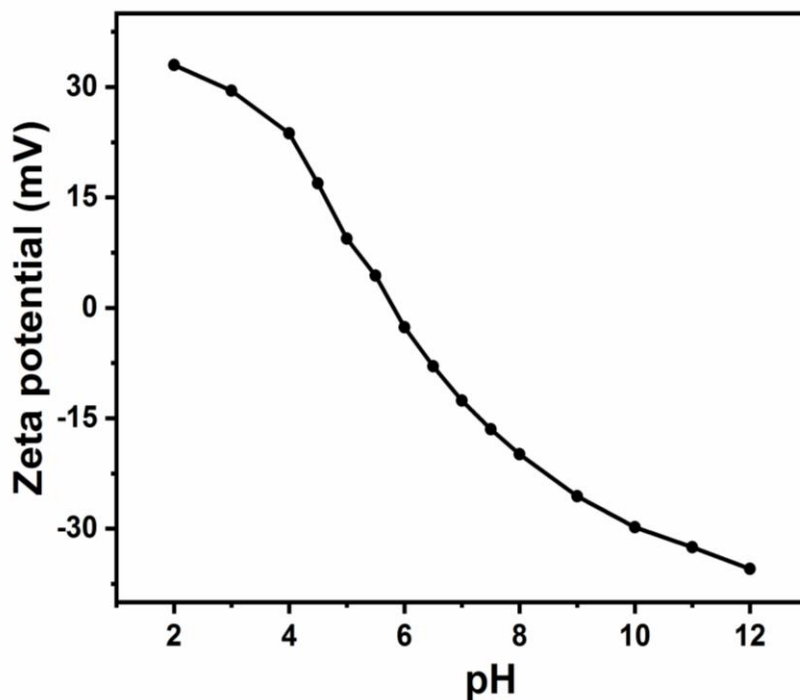


Figure 5.6. Zeta potential of COPYGO at different pH

### 5.3.7 Vibrating-sample Magnetometry (VSM)

Figure 5.7 indicated the magnetic hysteric loops of the as-synthesized COPYGO as well as  $\text{Co}_3\text{O}_4$  nanoparticle (CO) with an applied magnetic field (20 k Oe) at room temperature (300K). The field dependent value with the reported room temperature possesses super magnetic nature of  $\text{Co}_3\text{O}_4$  nanoparticle. The saturation magnetization curve of  $\text{Co}_3\text{O}_4$  nanoparticle and COPYGO were measured to be 22.23 and 44.30 emu/g indicated that both the  $\text{Co}_3\text{O}_4$  nanoparticle and COPYGO which possess a high magnetism given in Table 5.1 (Yao et al. 2013). The saturation magnetization of COPYGO has been decreased compared to CO nanoparticle due to the presence of Graphene oxide support as well as wrapping of the Py chains (Facchi et al. 2018; Lin et al. 2016). The COPYGO is easily isolated from the reaction mixture in the presence of external magnet for 30s after the completion of the reaction. The presence of hysteric loops in COPYGO and  $\text{Co}_3\text{O}_4$  nanoparticle (CO) indicated both materials possess ferromagnetic nature and these materials having  $H_c$  values less than 100 emu/g indicated that they possess soft magnetic properties (Zhu et al. 2015). Owing to the easy manner of magnetic separation methodology of nanocomposite, these nanoadsorbent can be avoided going through nature water ecosystem and abate the unknown certain damage to the environment.

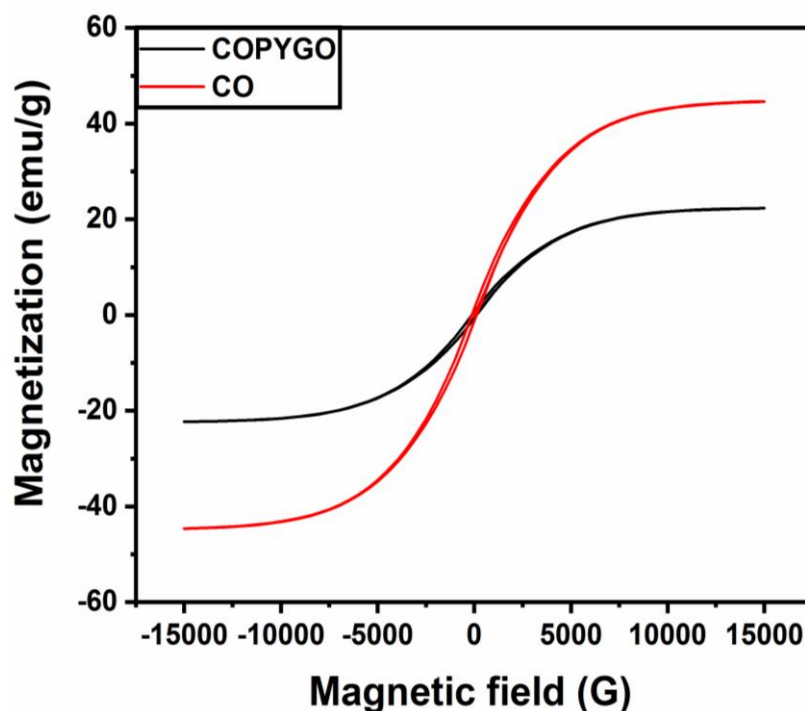


Figure 5.7. Applied magnetic field plot of  $\text{Co}_3\text{O}_4$  nanoparticles (CO) and COPYGO

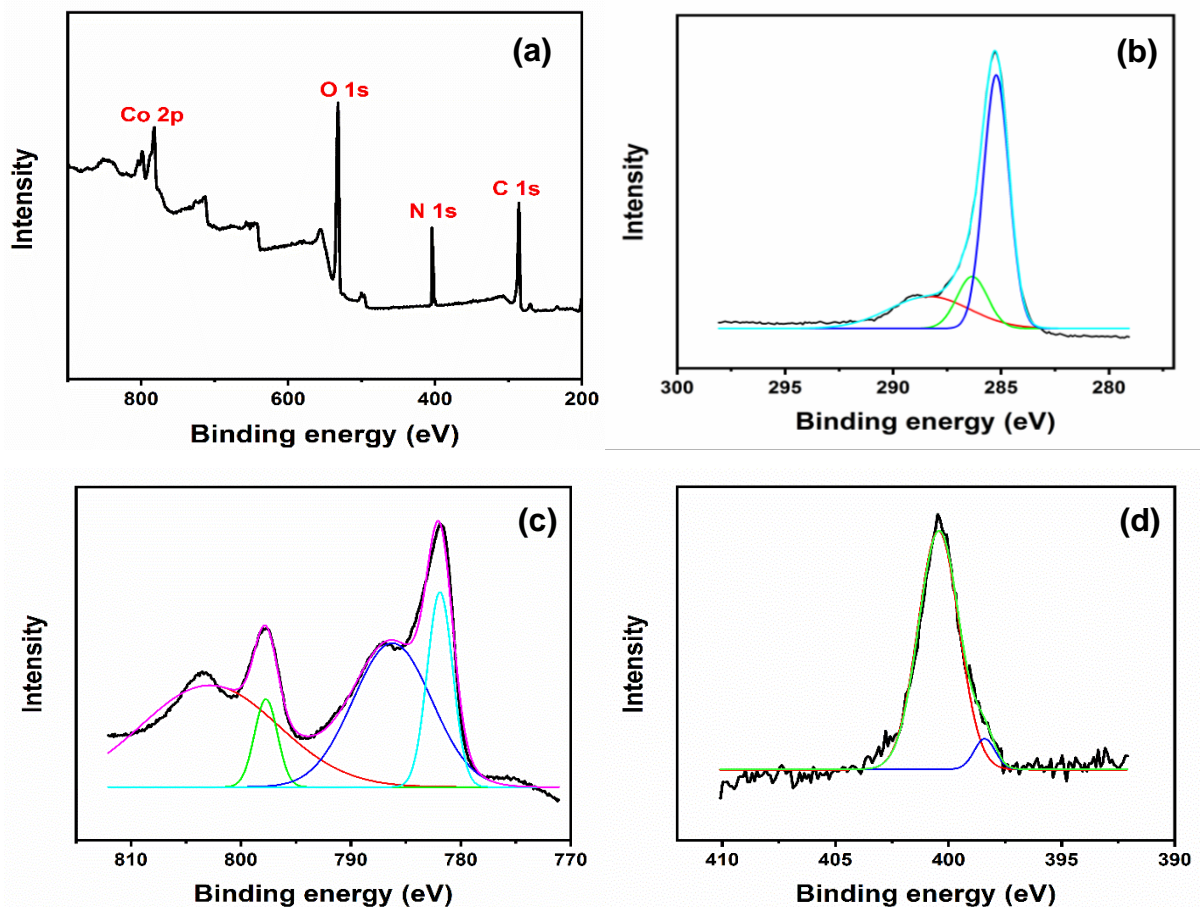
Table 5.1: The  $M_s$  and  $H_c$  values of CO nanoparticle & COPYGO

Type of Compounds	Magnetic properties	
	$M_s$	$H_c$
CO	44.30	122.00
COPYGO	22.23	103.20

### 5.3.8 X-ray photoelectron spectroscopy (XPS)

XPS spectra of COPYGO is shown in Figure 5.8. XPS survey of the COPYGO confirmed the presence of carbon, nitrogen, oxygen, cobalt which further explained that the nitrogen and cobalt have been successfully incorporated onto the graphene oxide by hydrothermal method shown in Figure 5.8(a). The peak area and intensity of cobalt oxide indicated the surface of the cobalt nanostructure with a substantial satellite peak within the 2p spectrum as shown in the Figure 5.8(c). From the XPS spectra, (Figure 5.8(a)) the elemental composition of the elements with their respective binding energies are 779.2 eV, 285 eV, 400.8 eV and 532.4 eV to the Co 2p, C 1s, N 1s and O 1s respectively. The binding energy of the Co 2p<sub>3/2</sub> and Co 2p<sub>1/2</sub> peaks around 779.2 and 795.2 eV reported the spinel structure of  $\text{Co}_3\text{O}_4$  upon nano graphene oxide support. It also confirmed that the Co has +3 and +2 oxidation states respectively (Yang et al. 2018). However, the 2p<sub>3/2</sub> peak of the cobalt oxide move towards the more binding energy side due to the highly electron correlated system with three unpaired 3d electrons (Wang et al. 2015). The slighter shift to high binding energies is due to the mechanochemical reaction of

Co 2p peaks, indicated that the defective sites which were released on its surface and further, due to the charge transfer reactions between the surface active sites as well as graphene oxide support which played a pivotal role with the removal of metal ions. The N 1s peak of the COPYGO has two components around 400.1 eV and 398.5 eV which is a characteristic peak of pyrrolic N and Co-N bonding and these Co atoms are coordinated with polypyrrole which served as an active site for the adsorption of metal ions (Deng et al. 2013). The C 1s spectrum of these nanocomposite explained that it is deconvoluted into  $sp^2$  hybridized C atom in graphene oxide (eV) and  $sp^2$  bonded with N (eV), carboxyl O-C=O (eV), carbon bonded with oxygen (Appaturi et al. 2019). The O 1s spectrum of COPYGO indicated that the binding energies at 531.3 eV and 533.0 eV corresponding to the oxygen species of metal hydroxides and hydroxyl group of water molecules on the surface of the COPYGO. The oxygen species O 1s spectrum explained that the peaks at 529.8 eV represented to the metal-oxygen bond, 531.9 eV and 532.9 eV represented the surface hydroxyl and the adsorbed water molecules respectively (Liu et al. 2017).





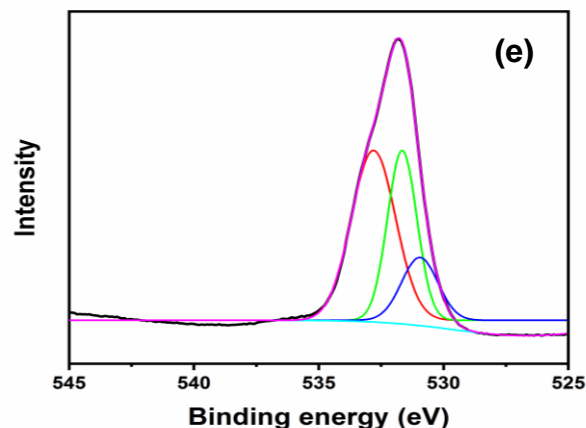


Figure 5.8. XPS Spectrum of a) Elemental survey of COPYGO b) C 1s, c) Co 2p, d) N 1s and e) O 1s

### 5.3.9 N<sub>2</sub> Adsorption-Desorption Isotherms (BET)

N<sub>2</sub> isotherms represented the porosity of synthesized sample. The isotherms were studied for knowing the total surface area of COPYGO and the nature of pore size distributions. Figure 5.9(a, b) represented the isotherms for the COPYGO samples, with their corresponding porosity curves determined by using this BJH plots. Hysteresis loops have been represented in the two isotherms, and they have specified characteristic of isotherm type IV. These indicated that the mesopores exist in the COPYGO. Further, there is a stage-wise desorption which can be observed at the desorption stage in the isotherms of COPYGO. Thus, the loops are a mixture of both H<sub>1</sub> and H<sub>2</sub> loops (Petitto and Langell 2004). From the BJH plot, at a relative pressure of 0.45-0.9, the H<sub>2</sub> loops which corresponds to the ink bottle shaped mesopores aroused from the Co<sub>3</sub>O<sub>4</sub> nanoparticles (CO) with the Graphene oxide nanosheets. The loops with a relative pressure of 0.9-1.0 represented the specific type of type H<sub>3</sub>. These results justified that the mesopores existence within a limited split width produced with the congregation of Co nanoparticles onto graphene oxide surface (Ren et al. 2015). The pore size distribution curves (Figure 5.9(b)) represented the bimodal distributions within the extent of 0.2 nm to 66.6 nm. The peak at 42.95 nm has been associated with a larger mesopores which are produced due to the self-assembly of Co nanoparticles. The peak area found at 5.4 nm and 42.95 nm indicated the bigger mesopores found in between the nanosheets interconnected graphene oxide. Thus, it exhibited hierarchic pore structure which can contribute to the effective adsorption towards the dyes and metal ions in wastewater. COPYGO exhibited slightly higher S<sub>BET</sub> (133m<sup>2</sup> g<sup>-1</sup>), d<sub>p</sub> of 0.38 and V<sub>p</sub> of 10.88 nm. Greater number of adsorption sites and higher pore size as well as volume contributed to speedy diffusion and improved adsorption capacity for the pollutants.

Therefore, the presence of GO and polypyrrole in the COPYGO enhanced the total surface area, improved pore volume as well as size are very crucial for the exemplary adsorption capacity.

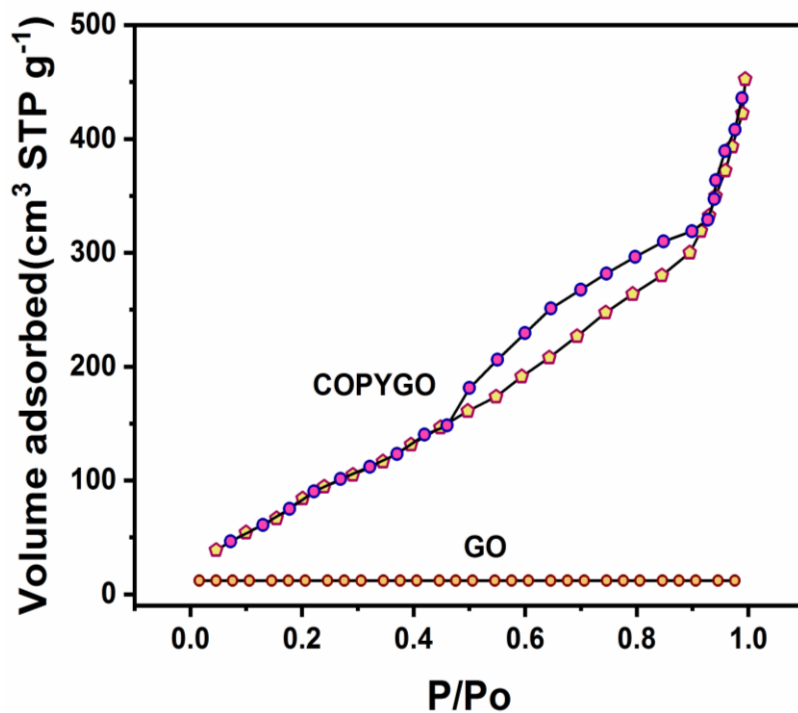


Figure 5.9a. N<sub>2</sub> adsorption-desorption isotherms of COPYGO

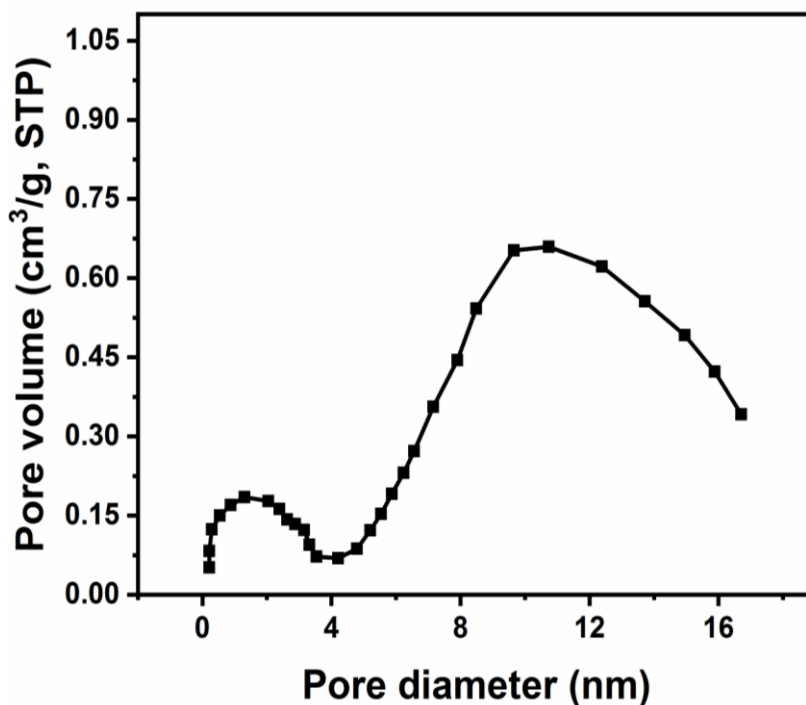


Figure 5.9b. Pore size distribution curves of COPYGO

### 5.3.10 Raman Spectroscopy

Raman spectra of the GO and COPYGO are shown in Figure 5.10. Raman spectra of the COPYGO has main peaks at 486, 633 and 702  $\text{cm}^{-1}$  which indicated the crystalline nature of the  $\text{Co}_3\text{O}_4$  namely the  $E_g$ ,  $F_{2g}$ ,  $A_{1g}$  modes respectively (Bose et al. 2010; Hu et al. 2019). In addition to this, the D and G-bands around 1344 and 1599  $\text{cm}^{-1}$  confirmed the existence of graphene oxide in nanocomposite. Usually, the D-bands represented the vibrating mode of the hexagonal carbon rings, random edge arrangements and low symmetric carbon structure and G-bands represented the first order scattering of  $\text{sp}^2$  hybridized carbon domains (Cheng et al. 2011; Liang et al. 2015; Thommes Matthias et al. 2015). The vibration bands of Py might not appear in the area 1375 and 1570  $\text{cm}^{-1}$  due to the low intensity or might be overlapped with GO (D and G-band). In GO, Raman spectra showed two peaks around 1405  $\text{cm}^{-1}$  and 1600  $\text{cm}^{-1}$ . The D-band is originated from hexagonal disordered carbon chains, due to K-points phonons of  $A_{1g}$  symmetry whereas G-band attributed to the  $E_{2g}$  phonons of  $\text{sp}^2$  hybridized carbon atoms. The intensity of D/G ratio is 0.46 where it is a measure of disorder degree as well as average size of  $\text{sp}^2$  carbon domains (Malard et al. 2009; Zhang et al. 2016) whereas for COPYGO it is 0.84.

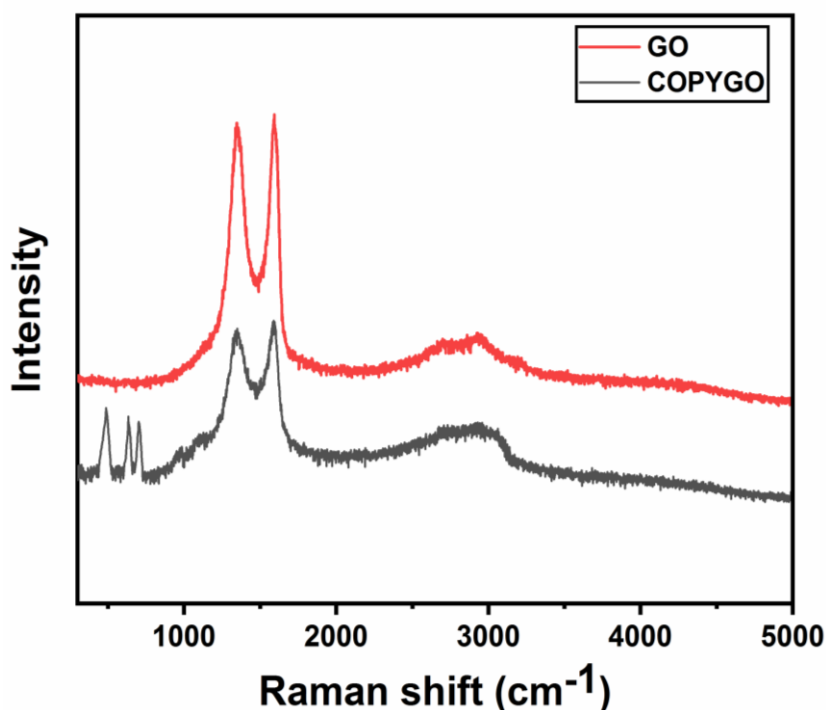


Figure 5.10. Raman spectra of both GO and COPYGO

### 5.3.11 Effect of initial concentration on adsorption capacity

The effect of initial concentration on the adsorption efficacy observed for MB, CR, Pb(II) and Cd(II) shown in Figure 5.11. However, the removal rate of MB, CR, Pb(II) and Cd(II) were decreasing accordingly along the increase in amount of initial concentration is due to the restricted amount of active sites with the rigid dosage of COPYGO. Although, there is no astounding theory, the higher is the initial concentration then the adsorption efficiency will be less.

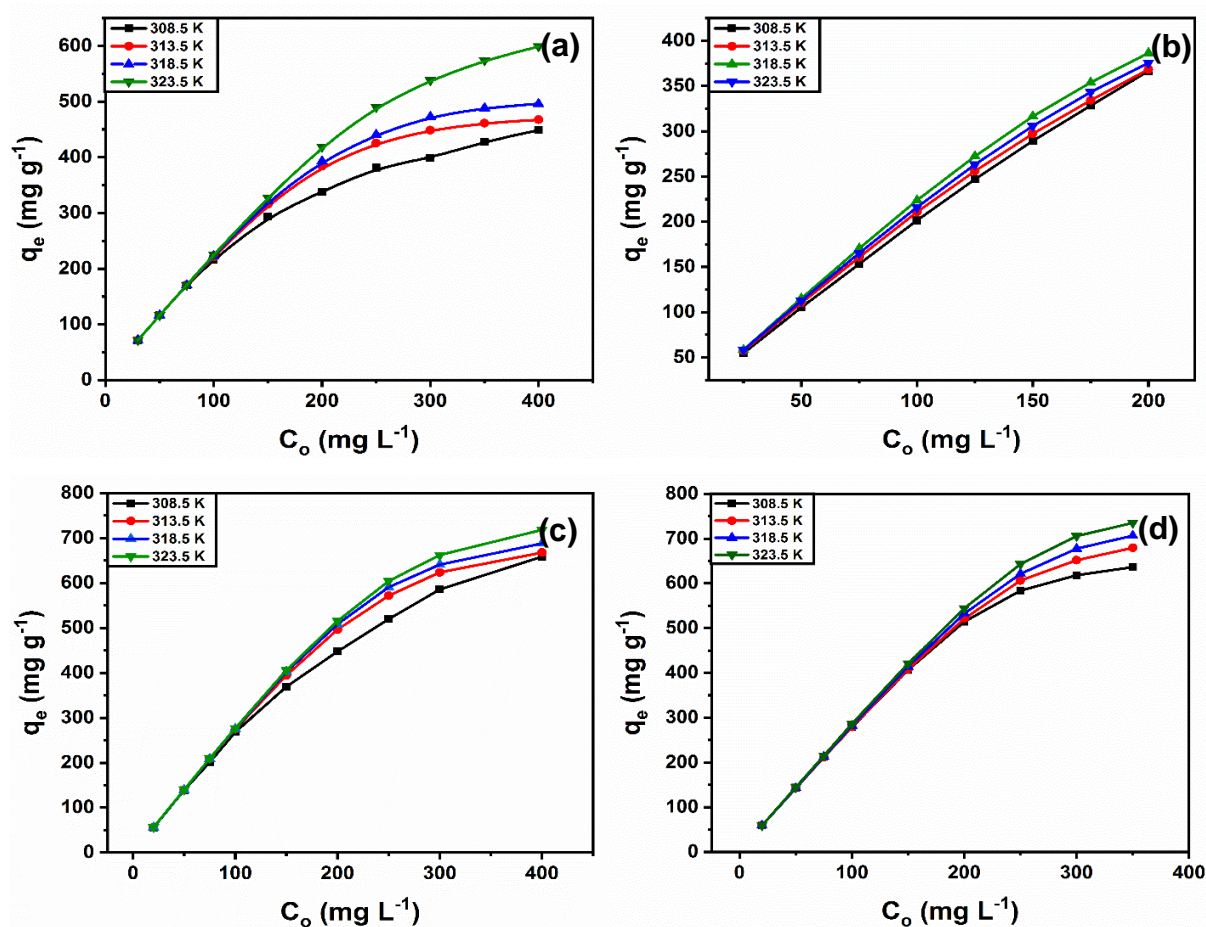


Figure 5.11. Adsorption of a) MB b) CR c) Pb(II) & d) Cd(II) as a function of concentration at various temperature

### 5.3.12 Effect of pH on adsorption capacity

The pH of the solution is very important for the adsorption of dyes and metal ions further which can greatly affect the pollutants and the distribution of surface charge on the functional groups of COPYGO. From the Figure 5.12, it was examined that the adsorption property of pollutant increases with the raise in the pH of the solution. The removal efficiency of pollutants reaches

the highest in case of MB, CR, Pb(II) and Cd(II) at pH 7.2, 5.0, 5.5 and 6.1. Further, the pH of the solution increases leads to the decrease in the adsorption capacity of dye and metal ions. It is because of the reaction of the  $H^+$  ions and  $OH^-$  ions which upon synergy between nano adsorbent and the pollutants in their respective acidic and basic environments. Usually, at low pH, the hydroxyl and carboxyl groups tend to bound with the more amount of  $H_3O^+$ , which can actively compete with the cationic dyes as well as heavy metal ions for the adsorption sites. Due to this effect, the nanocomposite becomes positive due to protonation strategy, leading to the electrostatic attraction in between the pollutants and the COPYGO. Along with this, the enhancement in adsorption efficiency with the increase in pH, because of the coordination of free lone pairs on nitrogen and oxygen atom which are found to be more suitable with the metal ions and cationic dye (Ferrari et al. 2006; Nethravathi et al. 2014). As the pH value increases, the hydroxyl and carboxyl group on the COPYGO surface gets deprotonated. The charge on its surface becomes negative, further the adsorption is controlled by using the electrostatic attractions. Further the increase in pH beyond 5.5, 6.1 and 7.2, the adsorption capacity decreases gradually because of the synthesis of hydroxyl precipitate with both metal ions shown in figure 5.13. In case of CR, an anionic dye which is acidic containing amino and sulphite groups with a low isoelectric point 3. At low pH around 1-3, CR will become cationic which results in ammonium as well as azonium rich ions leading to the azo group  $\pi$ - $\pi$  transitions (Du et al. 2014). At higher pH around 10.0, stability of the chromophoric group is lost which changes the original color dye (Fan et al. 2015). At the pH 4.0-5.5 shown in figure 5.12, the amino groups protonation on CR takes place. The percentage of removal rate of the anionic CR is observed that is increased at lower pH. This may be due to enhanced electrostatic attraction between the COPYGO and the CR dye (Yang et al. 2014).

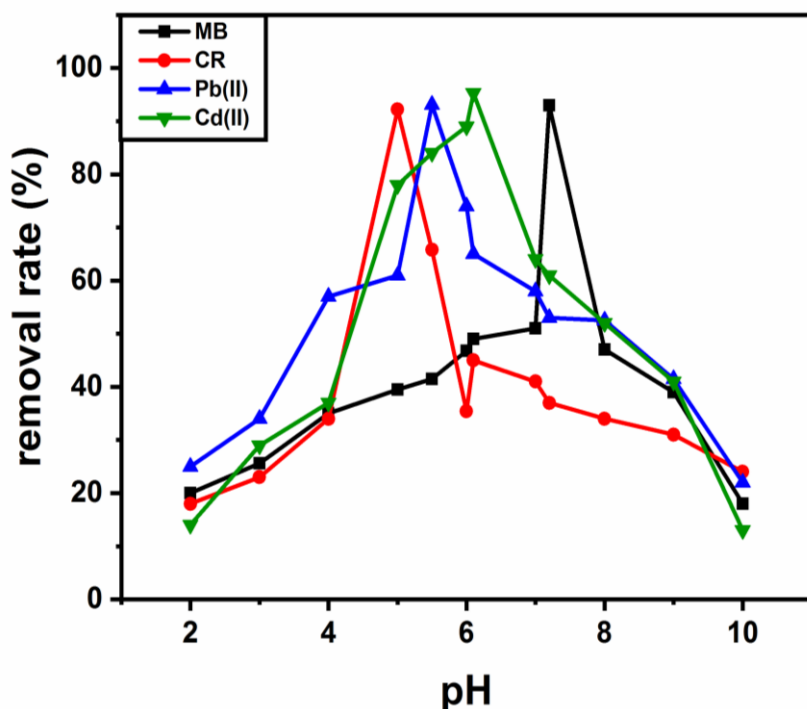


Figure 5.12. Removal rate of the MB, CR, Pb(II) and Cd(II) at various pH

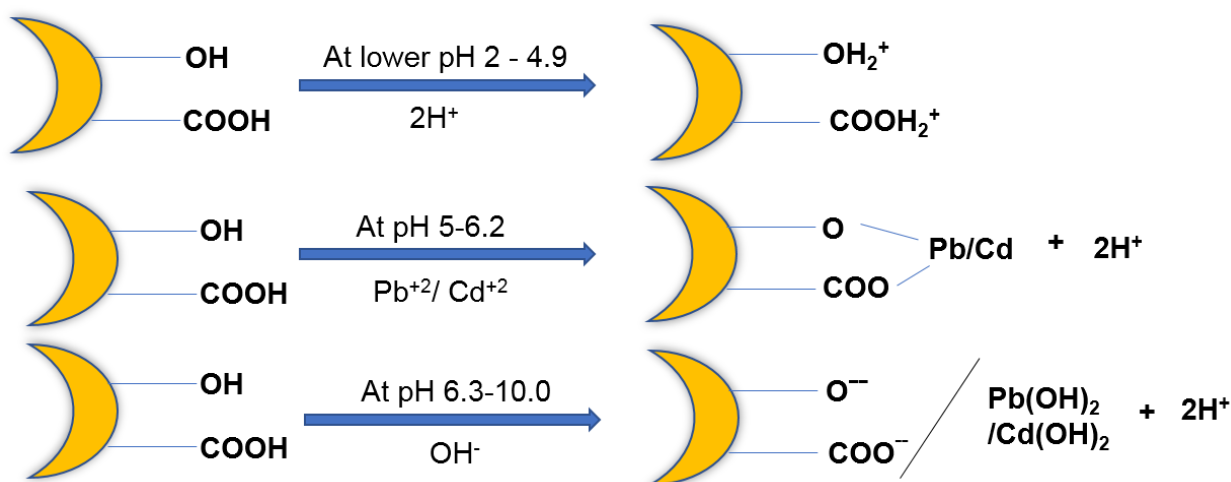


Figure 5.13. Proposed mechanism of the metal ions: Pb(II) & Cd(II)

### 5.3.13 Effect of adsorbent dosage on adsorption capacity

The results observed from the Figure 5.14 that with the increase in amount of COPYGO, the adsorption capacity of these adsorbate increases. The percentage of removal rate increases drastically and it reaches up to a maximum for all the adsorbate molecules. This is due to the concentration of adsorbate remain steady to the total amount of adsorbate stuffs, which are getting adsorbed increased due to the increase in COPYGO dosage and the percentage of removal rate also enhanced significantly. However, the adsorbate concentration remains unchanged, the amount of adsorbent increases effectively, which led to the unsaturation of

active sites on the COPYGO. As there is no enough adsorbate to mix with it, led to the decrease in adsorption efficiency of the COPYGO.

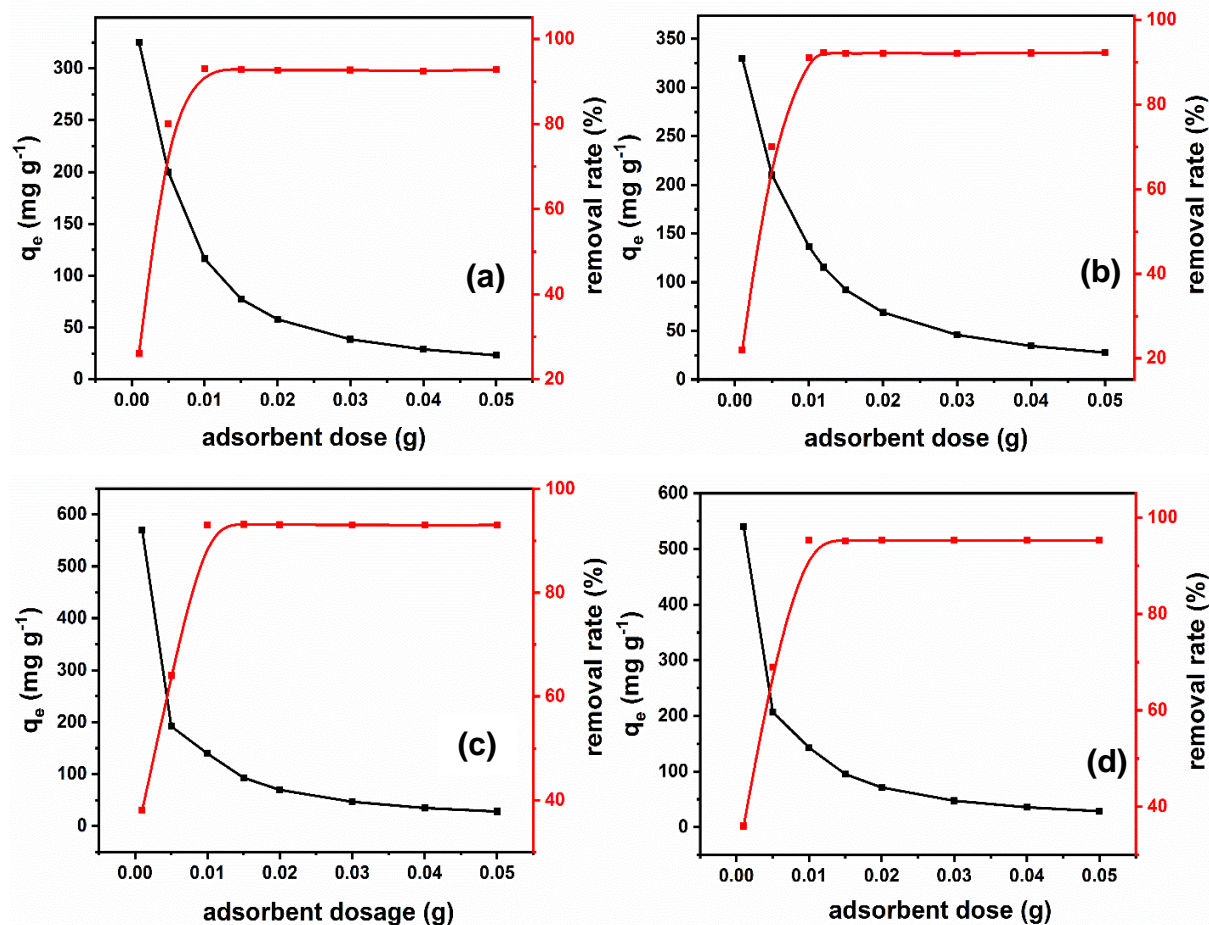


Figure 5.14. Different adsorbent doses with the adsorption capacity  $q_e$  a) MB, b) CR, c) Pb(II) and d) Cd(II)

### 5.3.14 Effect of contact time on adsorption

The effect of contact time on the adsorption property of adsorbates onto COPYGO nanocomposite was investigated throughout the adsorption experiments at various time periods for MB, CR, Pb(II) and Cd(II) is 300 min, 400 min, 400 min and 400 min respectively. Figure 5.15 shows the results of effect of contact time on the adsorption capacity of adsorbates onto nano adsorbent. During the initial stage of adsorption, for MB, CR, Pb(II) and Cd(II) (first 120 min) exhibited first increase of  $204.5 \text{ mg g}^{-1}$ ,  $199.75 \text{ mg g}^{-1}$ ,  $333.3 \text{ mg g}^{-1}$  and  $388.8 \text{ mg g}^{-1}$  respectively. Further, the adsorption capacity of the adsorbates slightly increased for all the adsorbates with the increase in contact time. The pollutant adsorption on COPYGO rapidly increased in the initial stages is due to the presence of active adsorption spots which were increasingly engaged with the pollutants led to the equilibrium state in adsorption phenomena.

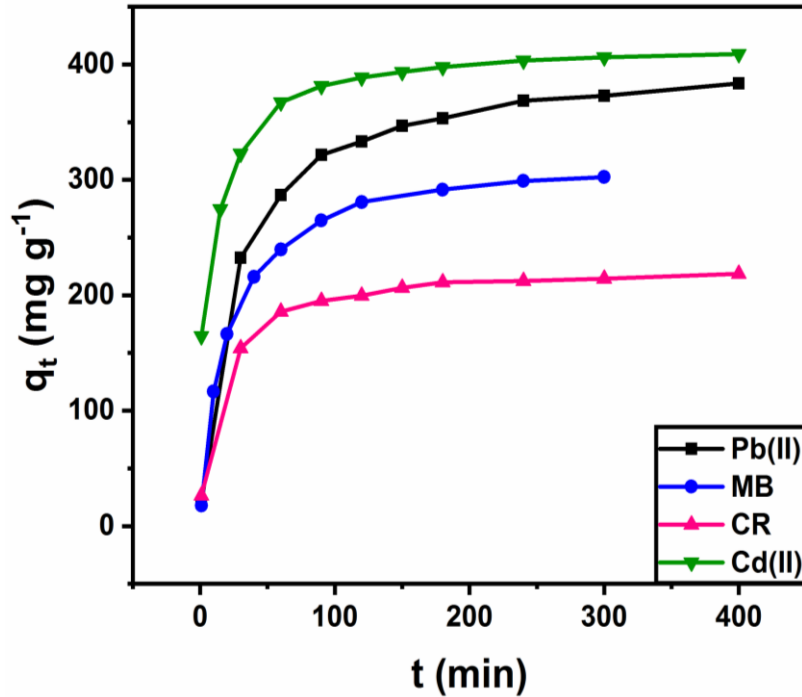


Figure 5.15. Effect of time (t) with the adsorption capacity ( $q_t$ )

### 5.3.15 Adsorption Isotherm studies

The adsorption phenomena thoroughly examined and inferred with the application of various adsorption isotherm models. The isotherms further explained that how COPYGO can interact with pollutants to get good adsorption capacity. Usually, the adsorbent surface may have monolayer or multilayers (Tran et al. 2017; Wang et al. 2018). The Langmuir adsorption isotherm explained that the COPYGO which possess a finite amount of active adsorption sites as well as solute particles adsorbed upon the COPYGO as a monolayer adsorbent as given in the Figure 5.16-5.19. The Langmuir isotherm is given in the following equation:

$$q_e = \frac{Q_m K_a C_e}{1 + K_a C_e} \quad (5.5)$$

Here in equation,  $Q_m$  ( $\text{mg g}^{-1}$ ) represented the maximum adsorption capacity of the COPYGO for building a monolayer of the pollutant per unit mass of the COPYGO whereas  $q_e$  ( $\text{mg g}^{-1}$ ) and  $C_e$  ( $\text{mg L}^{-1}$ ) are the adsorption capacity and the pollutant concentration at equilibrium respectively.  $K_a$  is termed as Langmuir constant ( $\text{L mg}^{-1}$ ) at equilibrium which normally represented the energy for adsorption.

Freundlich adsorption isotherm is validated for multi-layered one in which solute particles gets adsorbed onto the heterogeneous surface through an irregular distribution of isosteric heat in adsorption phenomena (Wu et al. 2014). This model is expressed in the following form:



$$q_e = K_f C_e^{1/n} \quad (5.6)$$

$K_f$  is a constant term which referred to an approximate factor for adsorption capacity and  $1/n$  is a function which refers to the strength of adsorption efficiency. Therefore, if the  $1/n$  is greater than one, it represents the cooperative adsorption on its surface. Higher the value of  $K_f$  which led to the increase in adsorption capacity. Freundlich constants  $K_f$  values for MB, CR, Pb(II) and Cd(II) are 163.146, 156.395, 163.815 and 182.391 respectively and the adsorption rate 'n' which have been measured from the graph are 3.383, 3.087, 3.045 and 3.115 respectively from Table 5.2. The higher values of  $K_f$  as well as the 'n' values greater than one for both dyes and metal ions represented the favorable nature of adsorption shown in Figure 5.16-5.19. Temkin Isotherm model explains the possible effects that got aroused due to the interactions of adsorbate with COPYGO shown in Figure 5.16-5.19. Temkin model justifies that the COPYGO surface covered with the adsorbate (MB, CR, Pb(II) and Cd(II)) molecules, the isosteric heat (which is a function of temperature) decreased linearly with increase in temperature instead of exhibiting logarithmic decreasing by neglecting the various concentrations of adsorbate molecules. This may be is due to the interaction of adsorbate molecules and COPYGO nano adsorbent. This isotherm assumed that there is a homogeneous distribution of pollutants in this solution. The Temkin model in the non-linear form is given in the following equation:

$$q_e = \frac{RT}{b_T} \ln A_T C_e \quad (5.7)$$

Where, R is the universal gas constant ( $8.314 \text{ J mol}^{-1} \text{ K}^{-1}$ ), T is the Temperature- Kelvin unit (K),  $A_T$  is the equilibrium binding constant ( $\text{L g}^{-1}$ ) which corresponded the maximum binding energy and  $b_T$  which represented the heat of adsorption ( $\text{J mol}^{-1}$ ).

The physical or chemical properties of the adsorption phenomena was investigated using Dubinin-Radushkevich (D-R) Isotherm shown in Figure 5.16-5.19. The D-R isotherm is expressed in the following equation:

$$q_e = (q_s) \exp(-K_{DR} \varepsilon^2) \quad (5.8)$$

$q_s$  ( $\text{mol g}^{-1}$ ) is the maximum adsorption capacity of D-R isotherm which is helpful to calculate the porosity of COPYGO, the apparent energy of adsorption (E) and K is the absolute temperature in Kelvin.  $K_{DR}$  ( $\text{mol}^2 \text{ k}^{-1} \text{ J}^{-2}$ ) is Dubinin-Radushkevich isotherm constant, which is linked to the both adsorption and absorption process (sorption) free energy per mole of the sorbate,  $\varepsilon$  is the Polanyi potential using the following equation:

$$\varepsilon = RT \ln \left( 1 + \frac{1}{C_e} \right) \quad (5.9)$$

These equations are useful to evaluate the mean free energy of adsorption.

$$E = \frac{1}{(2B_D)^{1/2}} \quad (5.10)$$

The above-mentioned models have been drawn using non-linear graph (Figure 5.16-5.19). Four models are compared and the results were optimized to determine the coefficients of determination (COD)  $r^2$  in between the results and the isotherm, using a non-linear curve.

$$r^2 = \frac{(q_m - \bar{q}_e)^2}{(q_m - \bar{q}_e)^2 + (q_m - q_e)^2} \quad (5.11)$$

The figures showing detailed data for all the four isotherm models for the pollutants MB, CR, Pb(II) and Cd(II) with their parameters and COD are shown in the table 5.2 & 5.3. Here, the graphs plotted for the adsorption capacity of MB, CR, Pb(II) and Cd(II) were termed as adsorbates which is adsorbed per unit mass of the adsorbent COPYGO,  $q_e$  with respect to the dye concentration at the equilibrium  $C_e$ . Table 5.2 & 5.3 shows the difference of  $R^2$  values for all the four isotherm models on the COPYGO. The data explained the capability for different isotherm models of MB, CR, Pb(II) and Cd(II) is in the following sequence i.e., Langmuir > Temkin > Freundlich > D-R. These isotherms with various models which are drawn for these adsorbates and their detailed information are given in Figure 5.16-5.19.

Table 5.2 & 5.3 gives information about the significant variables for all isotherm models with four variant temperatures (308.5 K, 313.5 K, 318.5 K and 323.5 K) were drawn using the non-linear curve optimization in Origin pro 2018. The selective primary values with their specifications used to get a converging fit without any modification with the experimental data which showed in the figure 5.16 all the specifications with their COD and the adjusted  $R^2$  at four different temperatures from 308.5 K to 323.5 K. In the adsorption process temperature played a key role on the adsorption capacity of each adsorbate onto nano adsorbent. The maximum adsorption capacity for MB was found to be 663.018 mg g<sup>-1</sup> at temp 323.5 K, for CR was found to be 659.056 mg g<sup>-1</sup> at temp 308.5 K, for Pb(II) was found to be 780.363 mg g<sup>-1</sup> at temp 323.5 K and for Cd(II) was found to be 794.188 mg g<sup>-1</sup> at temp 323.5 K.

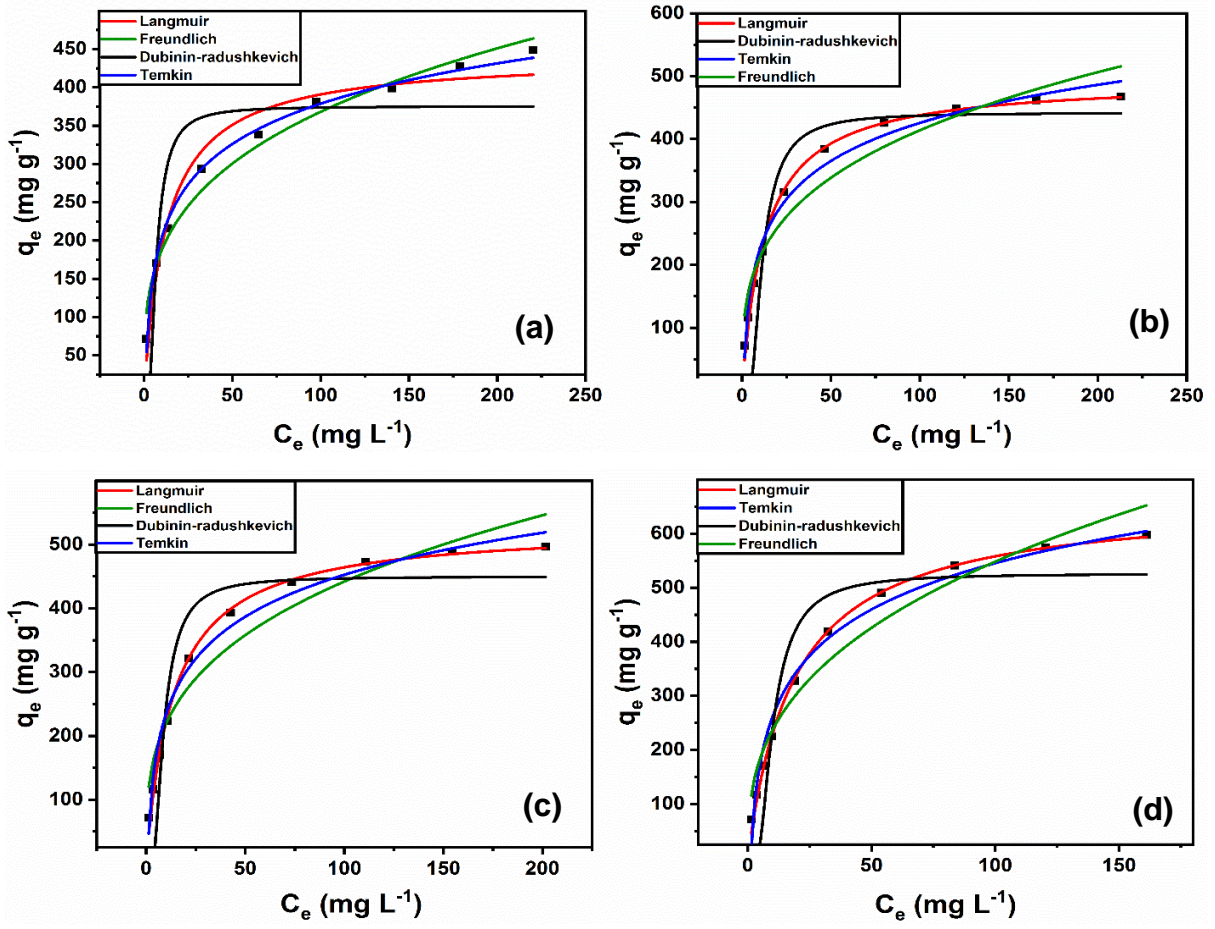
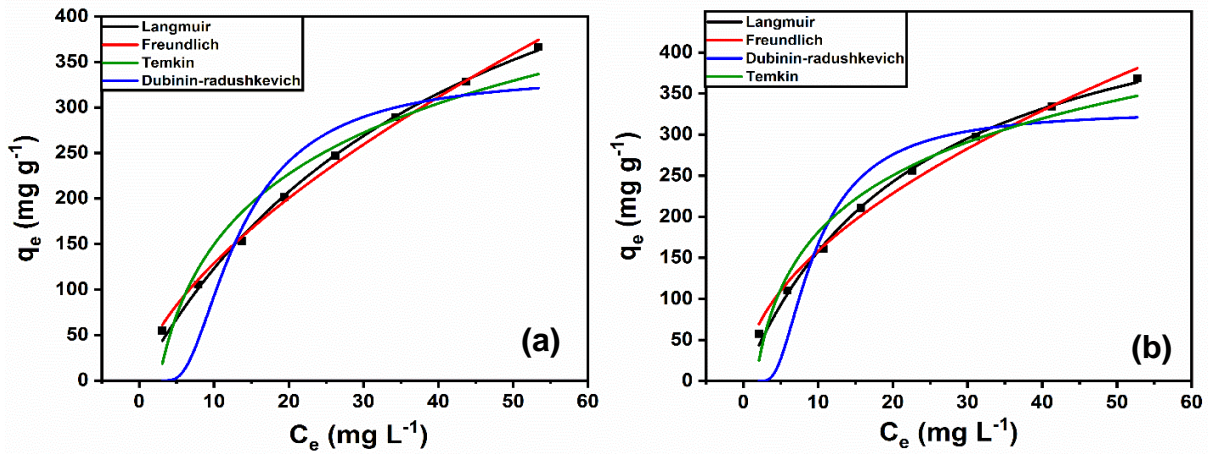


Figure 5.16. Adsorption isotherms at four different temperatures for MB: a) 308.5 K b) 313.5 K c) 318.5 K & d) 323.5 K



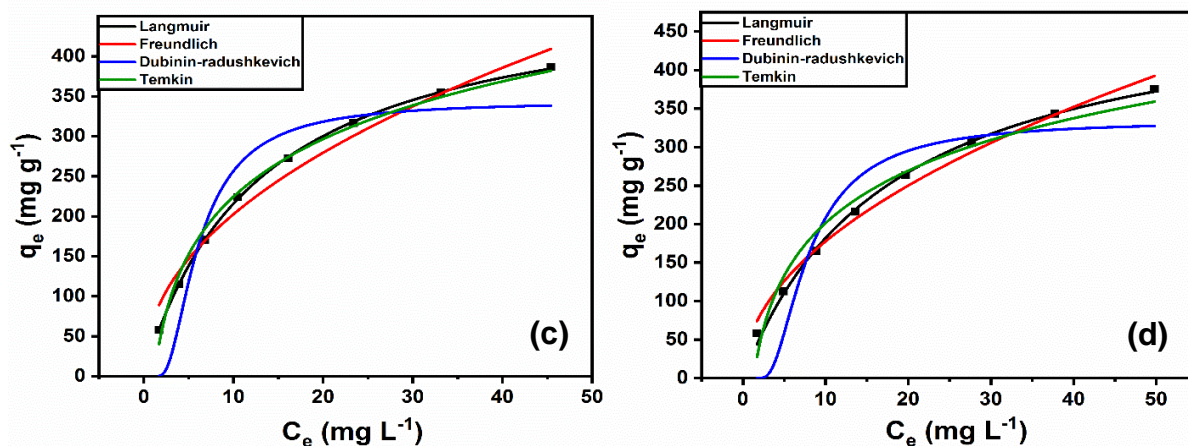


Figure 5.17. Adsorption isotherms at four different temperatures for CR: a) 308.5 K b) 313.5 K c) 318.5 K & d) 323.5 K

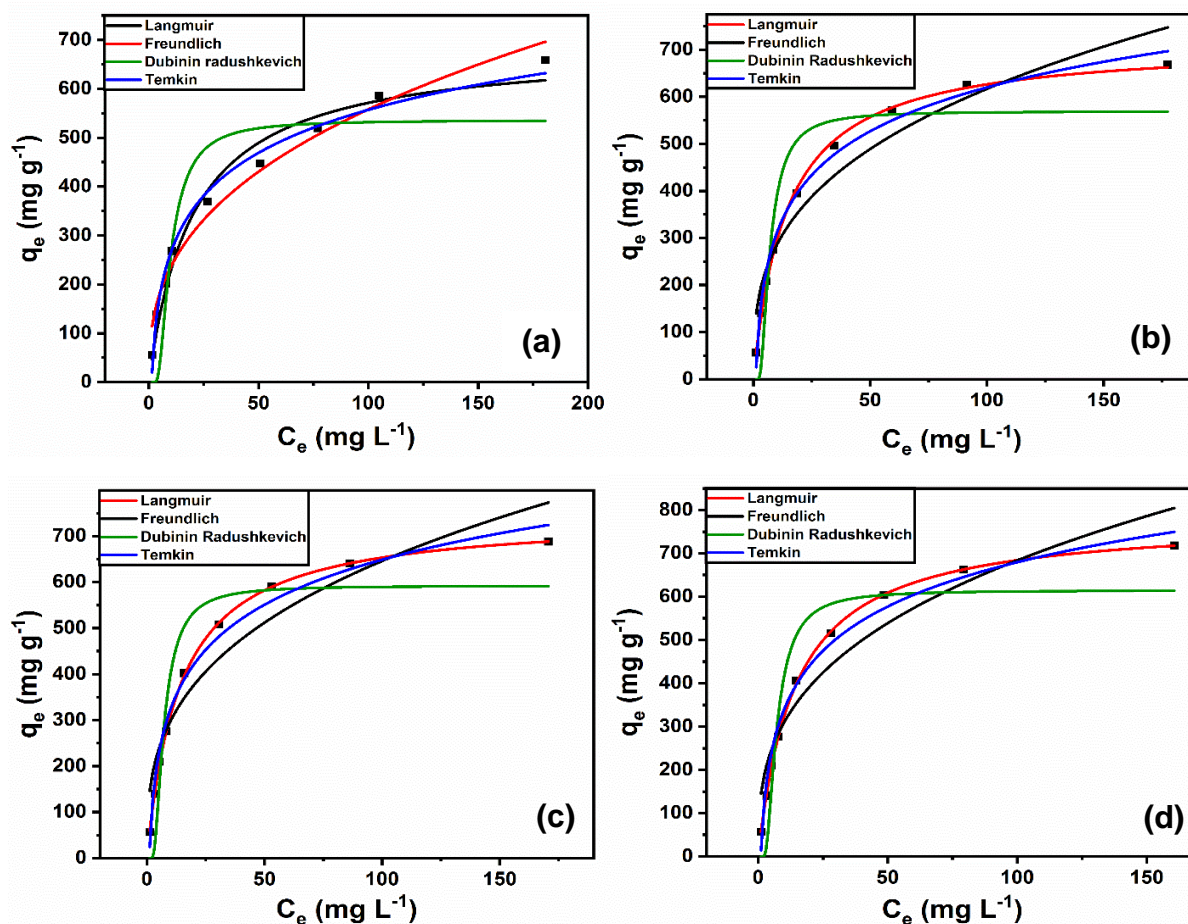


Figure 5.18. Adsorption isotherms at four different temperatures for Pb(II): a) 308.5 K b) 313.5 K c) 318.5 K & d) 323.5 K

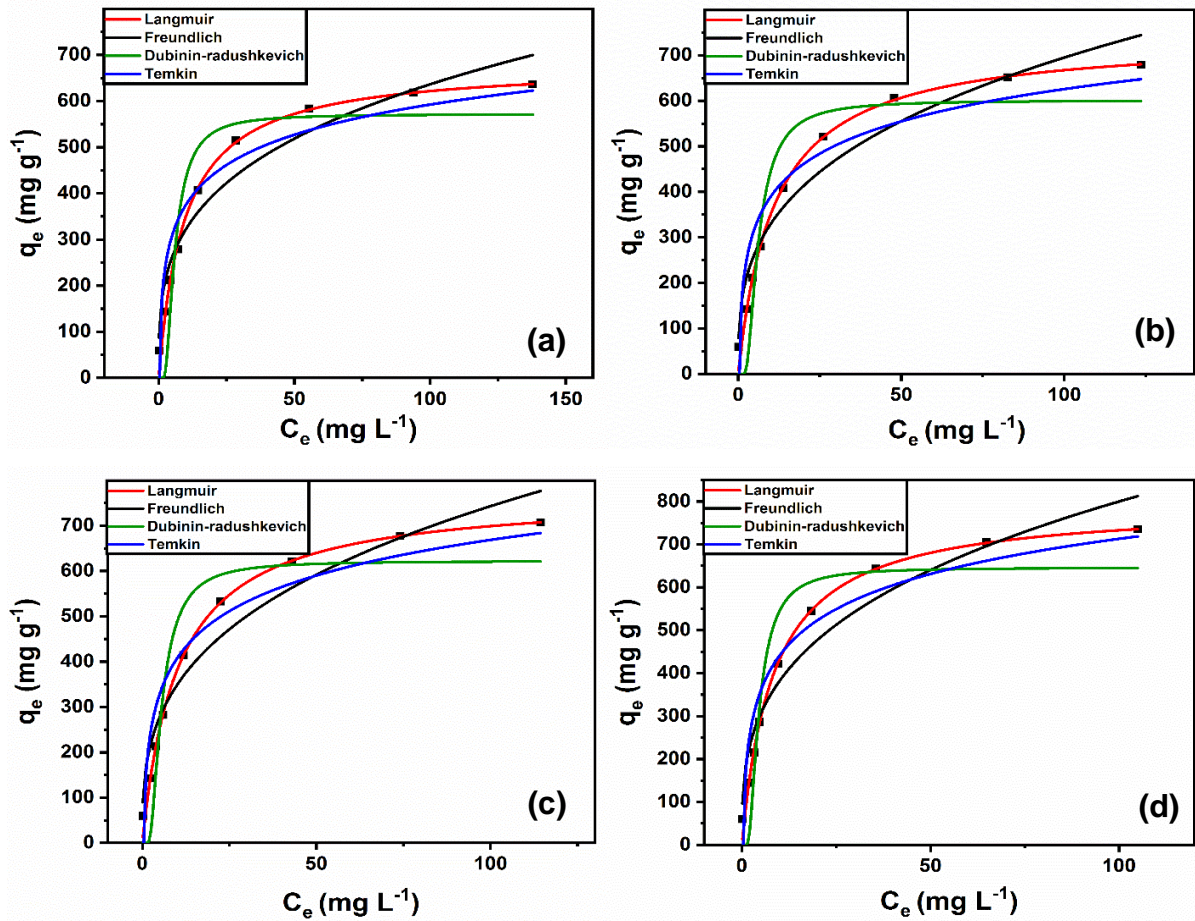


Figure 5.19. Adsorption isotherms at four different temperatures for Cd(II): a) 308.5 K b) 313.5 K c) 318.5 K & d) 323.5 K

Table 5.2: Langmuir and Freundlich Isotherm for the COPYGO

Pollutants	Temp(K)	Langmuir				Freundlich			
		$Q_{max}$ $mg\ g^{-1}$	$K_a$ $L\ mg^{-1}$	Adj. $R^2$	$R^2$ (COD)	n	$K_F$ $(mg\ g^{-1})(L\ mg^{-1})^{1/n}$	Adj. $R^2$	$R^2$ (COD)
MB	308.5	440.81187	0.053179759	0.99542	0.99593	3.44442	108.74396	0.92867	0.93660
	313.5	494.97342	0.061236772	0.96928	0.97269	3.41441	95.59103	0.97673	0.97932
	318.5	528.41217	0.096605747	0.99638	0.99678	3.28321	108.68627	0.93279	0.94025
	323.5	663.41217	0.078339180	0.99718	0.99749	2.74499	102.40228	0.94937	0.95500
CR	308.5	493.59772	0.022969910	0.99755	0.99790	1.57223	29.81450	0.99572	0.99633
	313.5	504.69405	0.035328335	0.99636	0.99688	1.89582	47.03778	0.98971	0.99118
	318.5	523.48168	0.053047903	0.99980	0.99982	2.15168	69.44250	0.96810	0.97265
	323.5	659.05602	0.077629331	0.99667	0.99715	2.02575	56.98535	0.98489	0.98705

Pb	308.5	686.01789	0.049760000	0.97666	0.97958	2.67056	99.48767	0.97444	0.97764
	313.5	715.53601	0.070120000	0.99863	0.99880	2.98526	131.84422	0.92142	0.93124
	318.5	744.33691	0.071830000	0.99965	0.99969	2.98064	137.81409	0.90654	0.91822
	323.5	780.36384	0.071050000	0.99955	0.99961	2.90958	140.45018	0.91067	0.92184
0Cd	308.5	680.55032	0.081316000	0.99043	0.99163	3.38286	163.14646	0.93846	0.94615
	313.5	741.44476	0.091959000	0.99272	0.99363	3.08750	156.39483	0.94286	0.95000
	318.5	770.30676	0.104307400	0.99442	0.99512	3.04561	163.81566	0.93917	0.94677
	323.5	794.18818	0.119264400	0.99490	0.99554	3.11513	182.39056	0.93508	0.94319

Table 5.3: DR and Temkin Isotherm for the COPYGO

Pollutants	Temp(K)	Dubinin-Radushkevich				Temkin			
		$q_s$	$K_{DR}$	Adj.	$R^2$	$A_T$	$B_T$	Adj.	$R^2$
		( $\text{mol g}^{-1}$ )	( $\text{mol}^2 \text{k}^{-1} \text{J}^{-2}$ )	$R^2$	(COD)	( $\text{L g}^{-1}$ )	( $\text{J mol}^{-1}$ )	$R^2$	(COD)
MB	308.5	375.3462	0.01680	0.75785	0.78476	1.46752	33.72045	0.99505	0.99560
	313.5	425.0933	0.02392	0.83449	0.85288	1.31127	29.80416	0.98225	0.98423
	318.5	449.7844	0.02548	0.85004	0.86670	1.17056	27.82590	0.98293	0.98483
	323.5	526.2449	0.03244	0.85864	0.87435	0.82401	21.72105	0.97702	0.97957
CR	308.5	337.4199	0.05541	0.84394	0.86623	0.38083	22.90259	0.94039	0.94891
	313.5	329.5792	0.02884	0.83432	0.85799	0.61320	26.05398	0.95906	0.96491
	318.5	343.5804	0.01216	0.85607	0.87664	0.86509	25.42102	0.99079	0.99211
	323.5	334.2266	0.01940	0.83495	0.85853	0.77763	27.35584	0.96577	0.97066
Pb	308.5	535.8752	0.03109	0.80813	0.83212	0.80829	20.19144	0.98479	0.98669
	313.5	563.9882	0.01630	0.86314	0.88024	1.00955	19.37788	0.98746	0.98903
	318.5	592.2232	0.01635	0.87907	0.89419	0.99074	18.72743	0.98252	0.98471
	323.5	614.6232	0.01593	0.87953	0.89459	0.99881	18.19184	0.98092	0.98330
Cd	308.5	571.7651	0.01200	0.80212	0.83212	5.29801	27.10768	0.89828	0.91099
	313.5	600.9540	0.01265	0.87275	0.88866	4.49990	25.40614	0.87162	0.88767
	318.5	622.3296	0.01012	0.88083	0.89572	3.63525	23.30990	0.89472	0.90788

### 5.3.16 Van't Hoff plot (Thermodynamic studies)

Temperature is one of the important parameters for the adsorption phenomena. Normally pollutants were released into the waste sludges at high temperatures from textile industry. Out of the four models, Langmuir adsorption isotherm observed to be best fit for all pollutants, the thermodynamic parameters can be evaluated from the Langmuir equilibrium constant ( $K_a$ ) from table 5.2 by applying the non-linear strategy whereas values of  $K_a$  are made initially dimensionless. This adsorption is a single molecule chemisorption and these values were applied to get the formula for  $K_e$  as given below:

$$K_e = \frac{1000 \times K_a \times M}{\gamma} \quad (5.12)$$

$$K_e = \frac{1000 \times K_a \times \text{mol. wt. of adsorbate} \times \text{standard conc. of adsorbate}}{\text{activity coefficient of adsorbate}}$$

By fitting the curve with formula (5.12) & (5.13) and the relevant thermodynamic parameters,  $\Delta G$ ,  $\Delta S$  and  $\Delta H$  has been calculated and the respective parameters are listed in table 5.4.

$$\Delta G = -RT \ln(K_e) \quad (5.13)$$

According to the 3<sup>rd</sup> law of thermodynamics, we get

$$\Delta G = \Delta H - T\Delta S \quad (5.14)$$

By combining eq 5.13 & 5.14, Van't Hoff equation is obtained.

$$\ln K_e = \frac{\Delta S}{R} - \frac{\Delta H}{RT} \quad (5.15)$$

Where  $K_e$  is the adsorption equilibrium constant,  $M$  ( $\text{g mol}^{-1}$ ) is Molar mass of dye molecule,  $\gamma$  is the coefficient of activity (dimensionless),  $R$  is Molar gas constant,  $T$ (K) is the reaction temperature. A plot between  $\ln K_e$  verses  $1/T$  to determine the enthalpy ( $\Delta H$ ) and entropy ( $\Delta S$ ) from the graphs both slope and intercept. Figure 5.20(a-d) gives the Van't Hoff plot for the pollutants using the adsorption process.

The thermodynamic studies evaluated using the above equations are given in the table 5.4.

The  $\Delta G$  negative values ascribed that this adsorption phenomena is spontaneous in nature. The values of  $\Delta H$  as  $21.0004 \text{ kJ mol}^{-1}$  for MB,  $67.1738 \text{ kJ mol}^{-1}$  for CR,  $19.001 \text{ kJ mol}^{-1}$  for Pb(II) and  $21.0823 \text{ kJ mol}^{-1}$  for Cd(II), which confirms that it is endothermic and chemisorption in nature. In view of the presence of hydroxyl, carboxyl functional groups which successively

assumed to develop secondary bonds which leads to the increase in adsorption rate. The  $\Delta S$  positive values resulted in the increased randomness of adsorbate molecules which can enhance the liquid-solid interface in the adsorption phenomena. The positive values claimed that the attainable structural modifications in both pollutant and COPYGO in the adsorption phenomena. The  $R^2$  values observed from the graph are near to unity confirmed the accuracy of the obtained  $\Delta H$  and  $\Delta S$  values. Finally, the increase in temperature favors the adsorption of pollutant onto COPYGO.

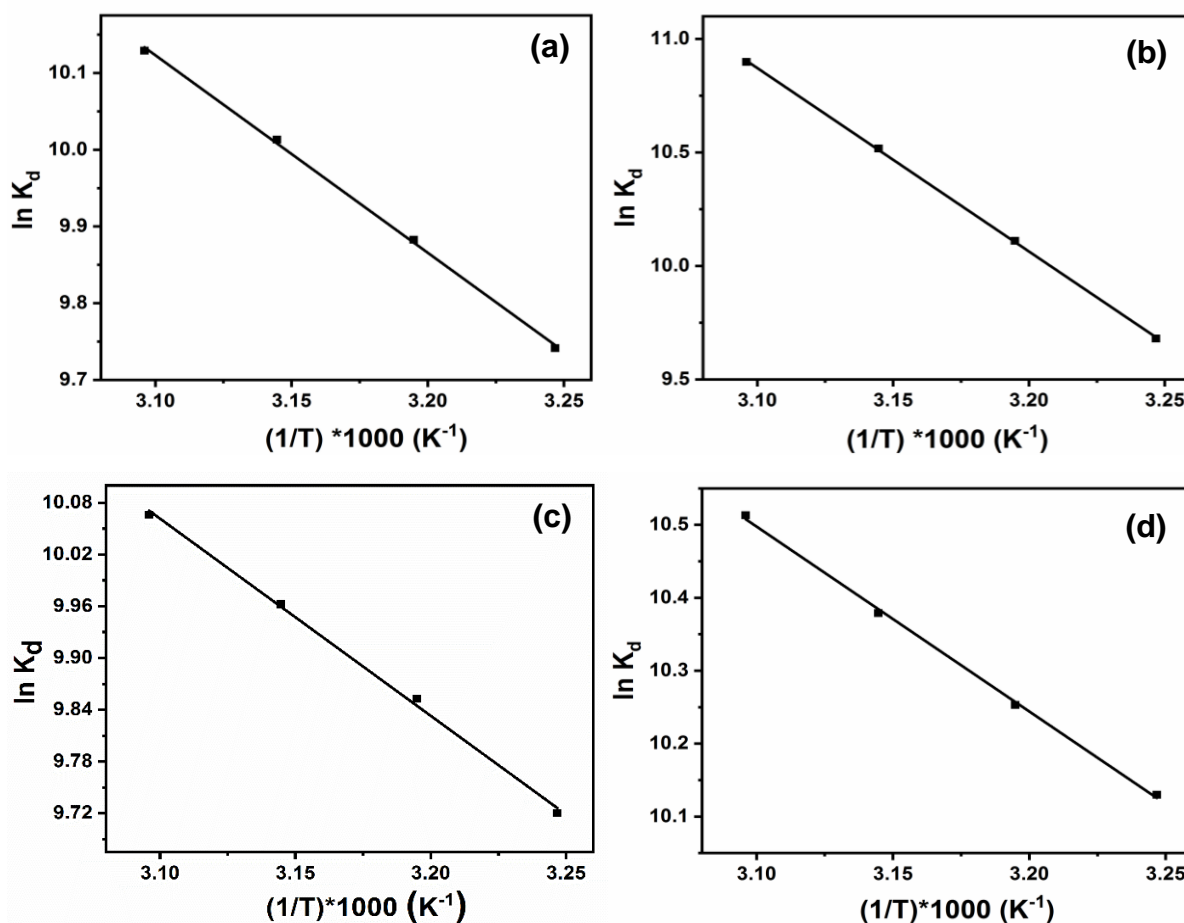


Figure 5.20. Van't Hoff plots for the four adsorbates a) MB, b) CR, c) Pb(II) & d) Cd(II)

Table 5.4: Thermodynamics of the adsorbent COPYGO

Thermodynamics parameters					
Pollutants	Temp(K)	$\Delta G$ (kJ mol <sup>-1</sup> )	$\Delta H$ (kJ mol <sup>-1</sup> )	$\Delta S$ (JK <sup>-1</sup> mol <sup>-1</sup> )	$R^2$
MB	308.5	24.98570	21.0004	150.47442	0.99913
	313.5	25.75830			
	318.5	26.51980			



	323.5	27.24240			
CR	308.5	24.82918	67.1738	298.62840	0.99982
	313.5	26.35360			
	318.5	27.85040			
	323.5	29.31170			
Pb	308.5	24.93030	19.0010	142.55500	0.99794
	313.5	25.68100			
	318.5	26.38020			
	323.5	27.07350			
Cd	308.5	25.98210	21.0823	152.63310	0.99887
	313.5	26.72380			
	318.5	27.48360			
	323.5	28.27550			

---

### 5.3.17 Adsorption Kinetic Studies

It has been observed from the Figure 5.21-5.22, that with increase in time period adsorption capacity increases rapidly up to 20 min, and then they will be a steady increase till it reaches the equilibrium. In order to determine the effectiveness of the adsorption rate, the following kinetic models were used for the adsorption study i.e., Lagergren pseudo first order, Lagergren pseudo second order and intra particle diffusion model (Salleh et al. 2011).

The equation for pseudo first order kinetic model is given below:

$$\ln(q_e - q_t) = \ln q_e - k_1 t \quad (5.16)$$

The equation for pseudo second order kinetic model is expressed as follows:

$$\frac{t}{q_t} = \frac{1}{k_2 q_e^2} + \frac{1}{q_e} \quad (5.17)$$

The equation for intraparticle diffusion model is given below:

$$q_t = k_p t^{1/2} + x_i \quad (5.18)$$

where,  $q_e$  ( $\text{mg g}^{-1}$ ) is the adsorption capacity until it reached equilibrium,  $q_t$  ( $\text{mg g}^{-1}$ ) is the adsorption capacity at regular time intervals 't', t is time for adsorption,  $x_i$  is the constant related to the thickness and shape of the boundary layer,  $k_1$  ( $\text{min}^{-1}$ ) is the pseudo first order rate constant

and  $k_2$  ( $\text{g mg}^{-1} \text{min}^{-1}$ ) is the pseudo second order rate constant respectively. Here,  $K_p$  ( $\text{mmol g}^{-1} \text{min}^{-1/2}$ ) refers to the intraparticle diffusion rate constants.

The first kinetic model presumed that the adsorption phenomena is predominated using the diffusion path. The second kinetic model presumed that the adsorption capacity will be monitored by chemisorption. This chemisorption explains about the deactivation of electron, the adsorption as well as desorption of active sites on COPYGO surface.

The methodology adopted by Intraparticle diffusion model mechanism involve the uptake of adsorbate solution by COPYGO includes three successive steps namely i) film diffusion ii) intraparticle diffusion path and iii) mass action. For this model, here it is intraparticle diffusion in which  $q_t$  is in linear relationship with the  $t^{1/2}$  and then the straight line which passes through the origin, then the rate limiting step is governed using the intraparticle diffusion. If not, then it is governed by internal diffusion manner. If  $x_i = 0$ , it referred to the adsorption being monitored by intraparticle diffusion path, the intercept positive values (Table 5.6) suggests that it is a spontaneous adsorption, at  $t = 0$  with the film diffusion.

$R_i$  is termed to be initial adsorption rate which is calculated from the following equation:

$$R_i = 1 - \frac{x_i}{q_e} \quad (5.19)$$

From table 5.5, it is confirmed that the adsorption phenomena of the adsorbate molecules followed the pseudo second order kinetic model with the correlation coefficient  $R^2$  near to 1, further justified that it is a chemisorption mechanism. Here, the  $q_e$  calculated value and the  $q_e$  experimental value almost equal which resembled the applicability of second kinetic model. The  $R^2$  values with respect to first kinetic model is not fitted properly with the experimental value and there is a significant low value of  $q_e$ , which has been calculated with this model. This reason highlights the inapplicability of the model.

In case of Intra particle diffusion, it is calculated from the fitting parameters, the relationship between  $t^{1/2}$  and  $q_t$  which is not a straight line from the graph shown in Figure 5.23. The Figure 5.23(a-d) justifies that the adsorption mechanism is monitored by three stages. The first stage indicates the initiation of adsorption process, where the adsorption increased with an increase in  $t^{1/2}$  value confirmed that the diffusion stage of different adsorbates within the boundary layer. Once the reaction has been proceeded, the adsorption capacity further enhances into the second stage with the increase in  $t^{1/2}$  value, when compared to the previous stage, the slope of the graph reduced and further increased the speed of adsorption capacity calms down. It is because it followed an intraparticle diffusion in this stage and it is a rate limiting step with variable adsorption through diffusion process into the mesopores. In the final stage, the line tries to

align with the abscissa, represented by the equilibrium stage with the completion of the adsorption process. ( $K_p$ ) Intraparticle rate constant is measured using the slope of the secondary linear fraction given in table 5.6. The multiple linearity in the graph indicates that there were more than one processes proceeded during the adsorption phenomena.

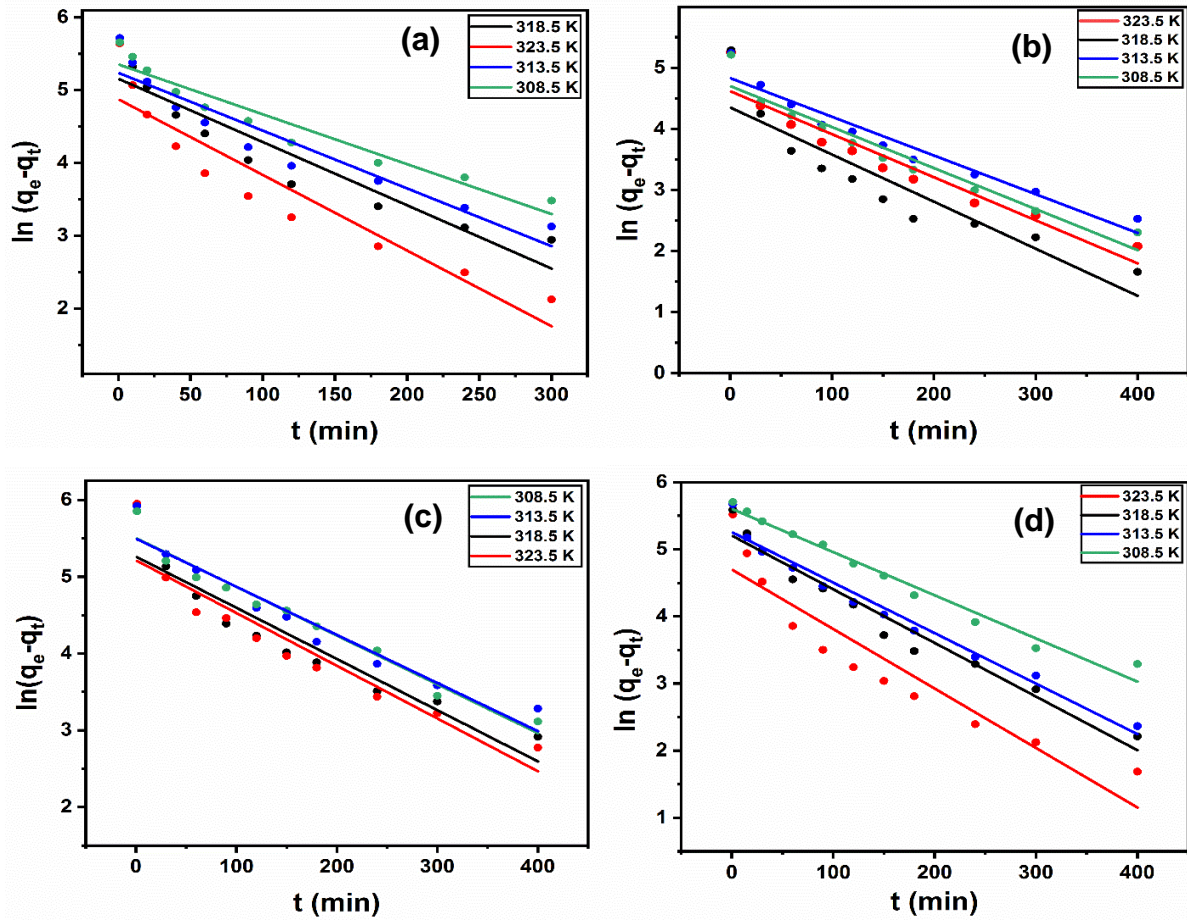
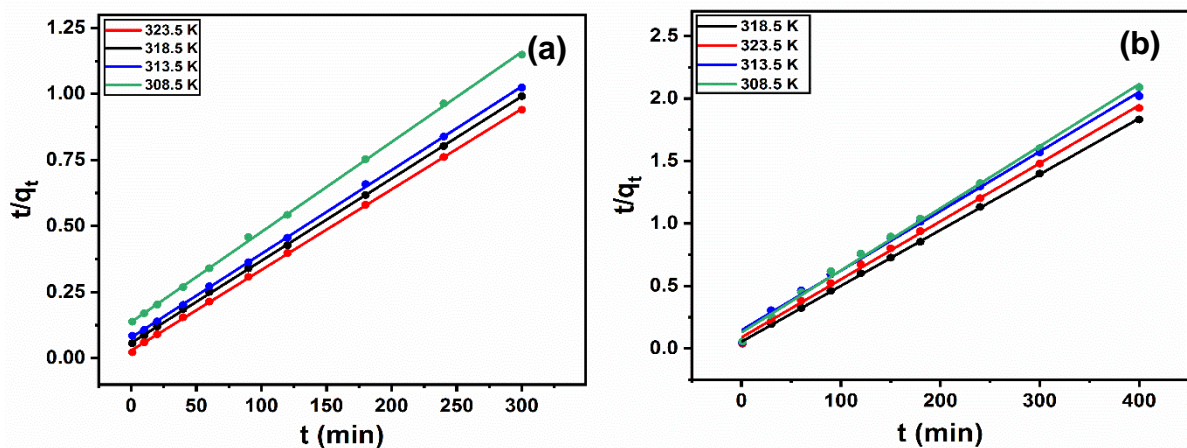


Figure 5.21. Pseudo first order kinetics for the four adsorbates: a) MB, b) CR, c) Pb(II) & d) Cd(II)



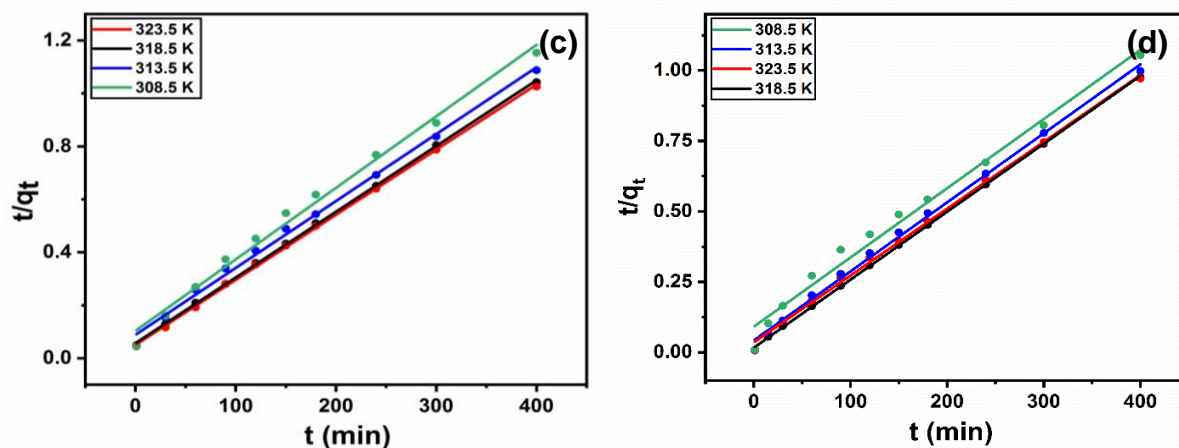


Figure 5.22. Pseudo second order kinetics for the four adsorbates: a) MB, b) CR, c) Pb(II) & d) Cd(II)

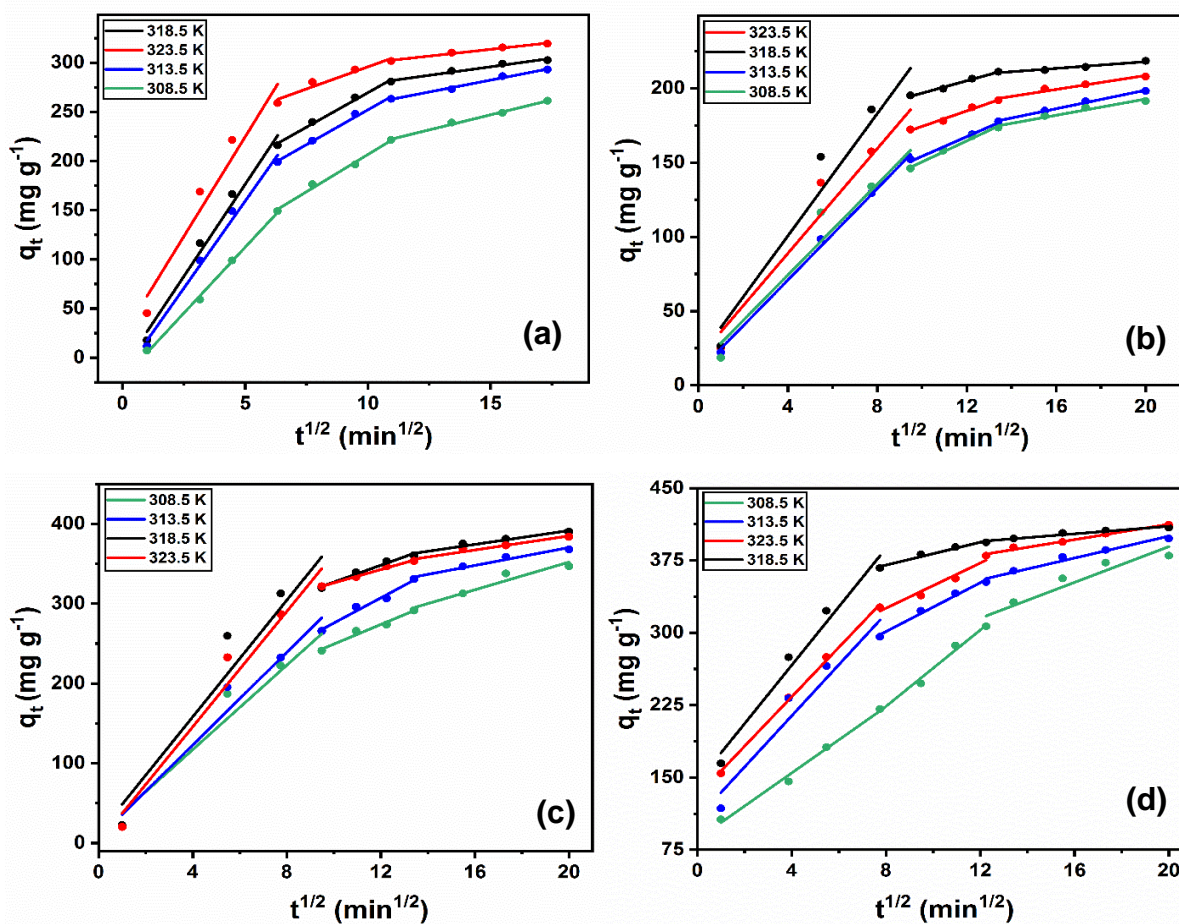


Figure 5.23. Intraparticle diffusion for the four adsorbates: a) MB, b) CR, c) Pb(II) & d) Cd(II)

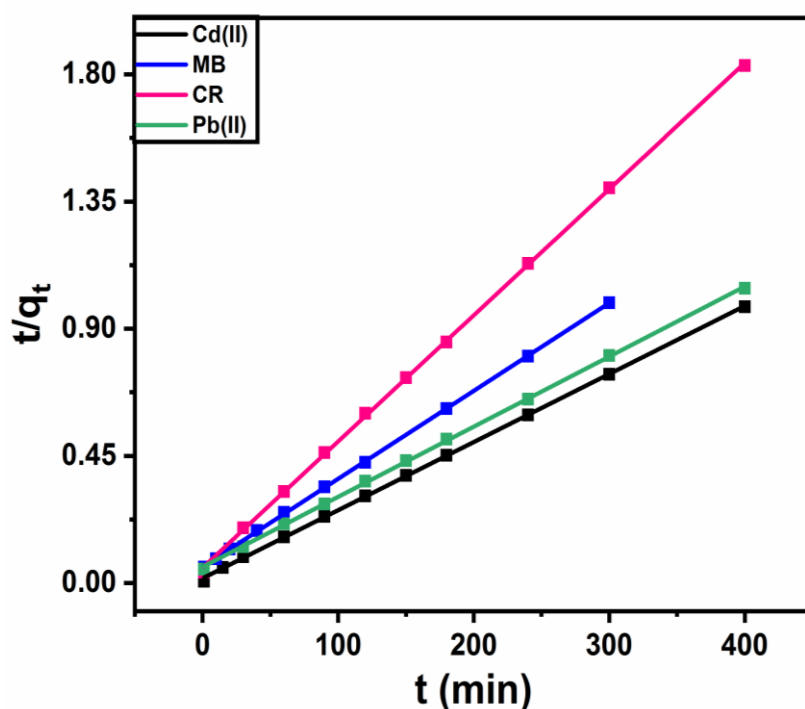


Figure 5.24. Pseudo second order at 318.5 K for the four adsorbates: MB, CR, Pb(II) & Cd(II)

Table 5.5: Kinetic parameters for Lagergren models for COPYGO

Pollutants	Temp (K)	Pseudo-first-order				Pseudo-second-order			
		$q_{e(\text{exp})}$	$q_{e(\text{calc})}$	$k_1$	$R^2$	$q_{e(\text{calc})}$	$k_2$	$R^2$	$E_a$
		( $\text{mg g}^{-1}$ )	( $\text{mg g}^{-1}$ )	( $\text{min}^{-1}$ )		( $\text{g mg}^{-1}$ )	( $\text{min}^{-1}$ )		( $\text{kJ mol}^{-1}$ )
MB	308.5	293.75	211.622	0.00686	0.93420	293.255	0.00323003	0.99957	26.27
	313.5	315.75	188.527	0.00794	0.90503	315.457	0.00456769	0.99980	
	318.5	321.50	173.804	0.00870	0.88511	321.543	0.00644807	0.99990	
	323.5	327.60	131.138	0.01040	0.88313	327.869	0.00930250	0.99982	
CR	308.5	201.50	109.984	0.00671	0.93511	201.207	0.00123752	0.99670	42.14
	313.5	210.75	125.335	0.00634	0.94253	209.644	0.00224831	0.99501	
	318.5	223.75	141.186	0.00771	0.83916	223.714	0.00383511	0.99972	
	323.5	216.00	101.154	0.00704	0.91448	215.517	0.00699013	0.99834	
Pb	308.5	369.33	245.417	0.00635	0.96345	370.370	0.00040099	0.99078	26.65
	313.5	394.50	243.613	0.00626	0.93750	395.257	0.00083454	0.99578	

	318.5	402.15	192.865	0.00667	0.88149	403.226	0.00169433	0.99971	
	323.5	406.05	183.797	0.00687	0.88604	406.504	0.00323615	0.99944	
Cd	308.5	406.65	271.073	0.00643	0.97856	406.500	6.6553E-05	0.98530	25.80
	313.5	408.45	191.909	0.00752	0.97002	408.163	0.00014137	0.99671	
	318.5	414.45	181.950	0.00799	0.95958	414.937	0.00034613	0.99976	
	323.5	421.05	109.893	0.00886	0.87765	421.941	0.00083461	0.99796	

Table 5.6: Intraparticle diffusion model for COPYGO

Intraparticle diffusion						
Pollutants	Temp (K)	$K_p$	$x_i$	$q_e$	$R_i$	$R^2$
		$\text{mmol g}^{-1} \text{min}^{-1/2}$	$(\text{mmol g}^{-1})$	$(\text{mmol g}^{-1})$		
MB	308.5	16.022610	62.929910	293.75	0.78577	0.99452
	313.5	18.131996	100.919260	315.75	0.68038	0.99130
	318.5	18.325200	199.606980	321.50	0.37913	0.98426
	323.5	17.421250	166.806750	327.60	0.49082	0.96316
CR	308.5	8.377160	76.946456	201.50	0.61813	0.96170
	313.5	8.386880	77.870170	210.75	0.63051	0.99092
	318.5	8.631970	122.947580	223.75	0.45051	0.96200
	323.5	8.410266	100.683200	216.00	0.53387	0.96396
Pb	308.5	15.793770	105.523400	369.33	0.71428	0.95086
	313.5	16.799760	127.676100	394.50	0.67636	0.96818
	318.5	17.141700	179.458870	402.15	0.55371	0.95247
	323.5	16.288290	180.232000	406.05	0.55613	0.97008
Cd	308.5	15.403510	118.490220	406.65	0.70862	0.95941
	313.5	14.945700	198.211030	408.45	0.51726	0.96401
	318.5	13.776030	231.920750	414.45	0.44041	0.97937
	323.5	12.717630	279.838427	421.05	0.33538	0.96230

### 5.3.18 Activation energy ( $E_a$ )

The graph of  $\ln k_2$  versus  $1/T$  were plotted with the values of second order rate constant ( $k_2$ ) at four different temperatures are given in Figure 5.25. According to Arrhenius equation 5.20, activation energy ( $E_a$ ) values evaluated for the adsorption phenomena of various adsorbates MB, CR, Pb(II) and Cd(II) were obtained from the graph are  $26.27 \text{ kJ mol}^{-1}$ ,  $42.14 \text{ kJ mol}^{-1}$ ,  $26.25 \text{ kJ mol}^{-1}$  and  $25.80 \text{ kJ mol}^{-1}$  respectively from Table 5.5. The obtained  $E_a$  values justified that it is a chemisorption process.

$$\ln k_2 = -\frac{E_a}{2.303RT} + \text{constant} \quad (5.20)$$

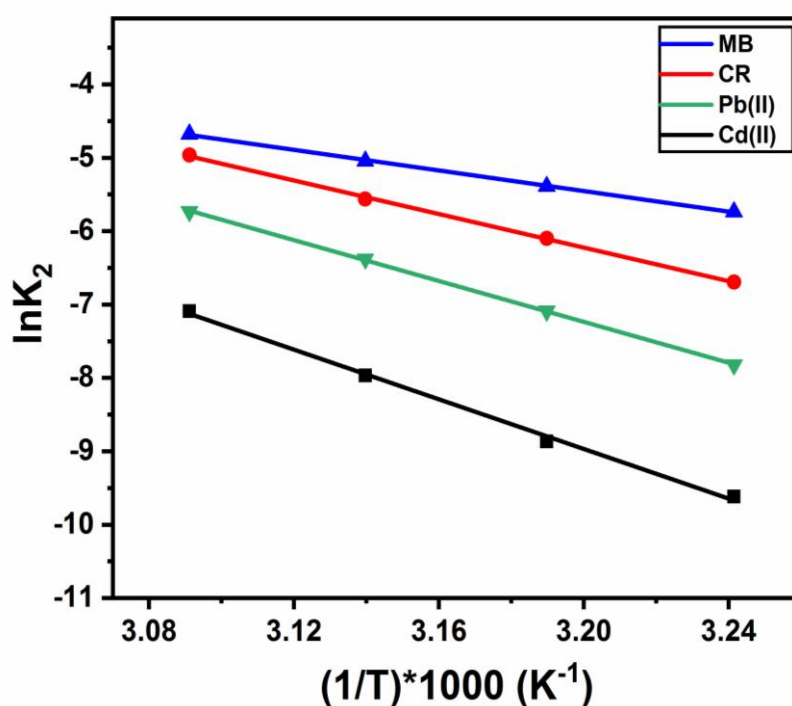


Figure 5.25. Arrhenius plot for the four adsorbates at different temperatures

### 5.3.19 Cycle regeneration

The regeneration cycles of the MB, CR, Pb(II) and Cd(II) being adsorbed onto COPYGO adsorbent are shown in Figure 5.26. The values obtained from the figure 5.26 with a regeneration efficiency of MB, CR, Pb(II) and Cd(II) is 89, 90.1, 91.2, 93.4 respectively after five regenerative cycles and the loss of adsorbent is in mid-teens which represented that the adsorbent can be recycled. It is indicated that the adsorbent COPYGO has good stability towards regenerative cycles. The pollutant adsorption phenomena can be proceeded in a step-wise manner. Initially, the pollutants diffuse from the liquid phase to the boundary line where

the interactions take place and the adsorption capacity rapidly increases along with time. Next, after a particular time the disorderness of the solid-liquid interfaces enhances i.e.,  $\Delta S > 0$ . In the next stage, the adsorbate gets diffused into the COPYGO particles, and the adsorption capacity starts to decrease further leading to the lack of adsorbent sites for adsorption. The electrostatic attraction between the particles leads to decrease in rate of adsorption. At the end, the equilibrium stage is attained and the adsorption capacity remains unaffected. Due to the increase in temperature which enhances the adsorption process on COPYGO contributing to the adsorption phenomena and are in consistent with  $\Delta H$  values. Therefore, the adsorption is endothermic process. The process of adsorption of adsorbate is a chemisorption, and hence that the desorption process from COPYGO is not a opposite phenomenon of adsorption. Usually, an acid or base used for the desorption of the adsorbate. In this process, the adsorbent washed with ethanol and later treated with 0.5 M NaOH solution. The desorption process enhances with increase in temperature. Since in this process,  $\Delta H < 0$ , very high temperature is not favorable for adsorption or desorption process. Here,  $\Delta S > 0$ , the reaction of the adsorbate investigated that the Gibbs free energy  $\Delta G < 0$ , where it is spontaneous reaction. Specifically, the desorption observed here is a reversible process, which led to the decrease in efficiency of COPYGO as the number of cycles increases.

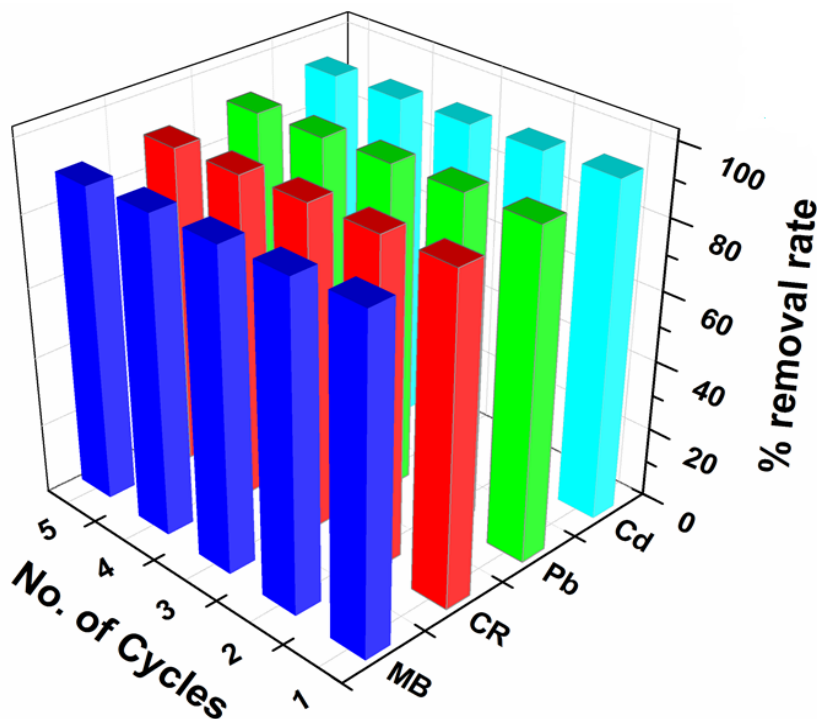


Figure 5.26. Regenerative capacity of the COPYGO for four adsorbates: MB, CR, Pb(II) & Cd(II)



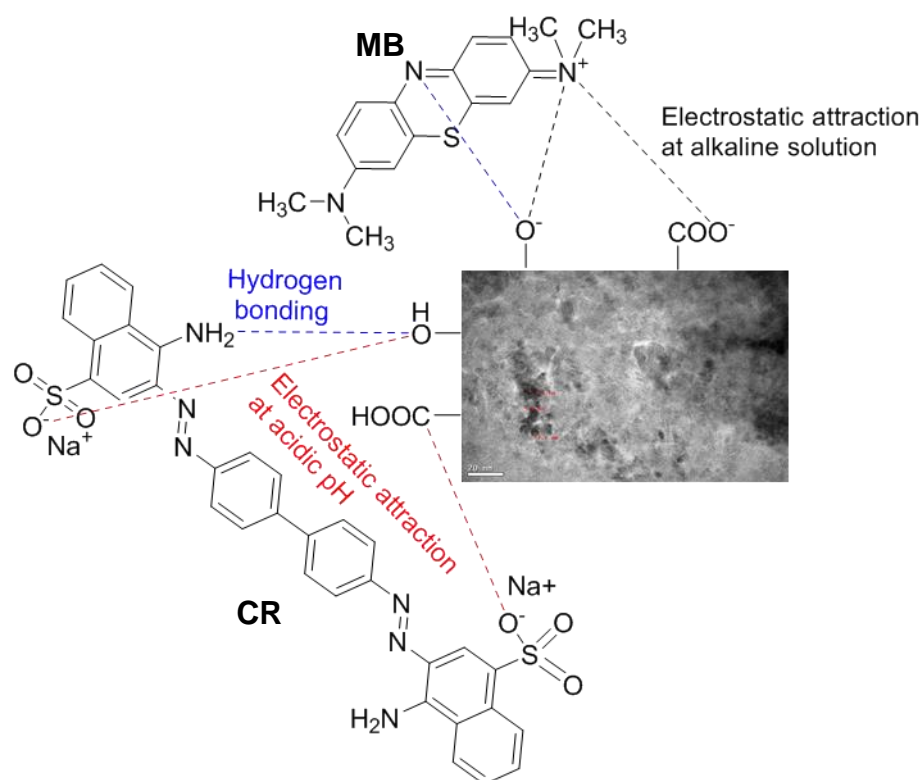
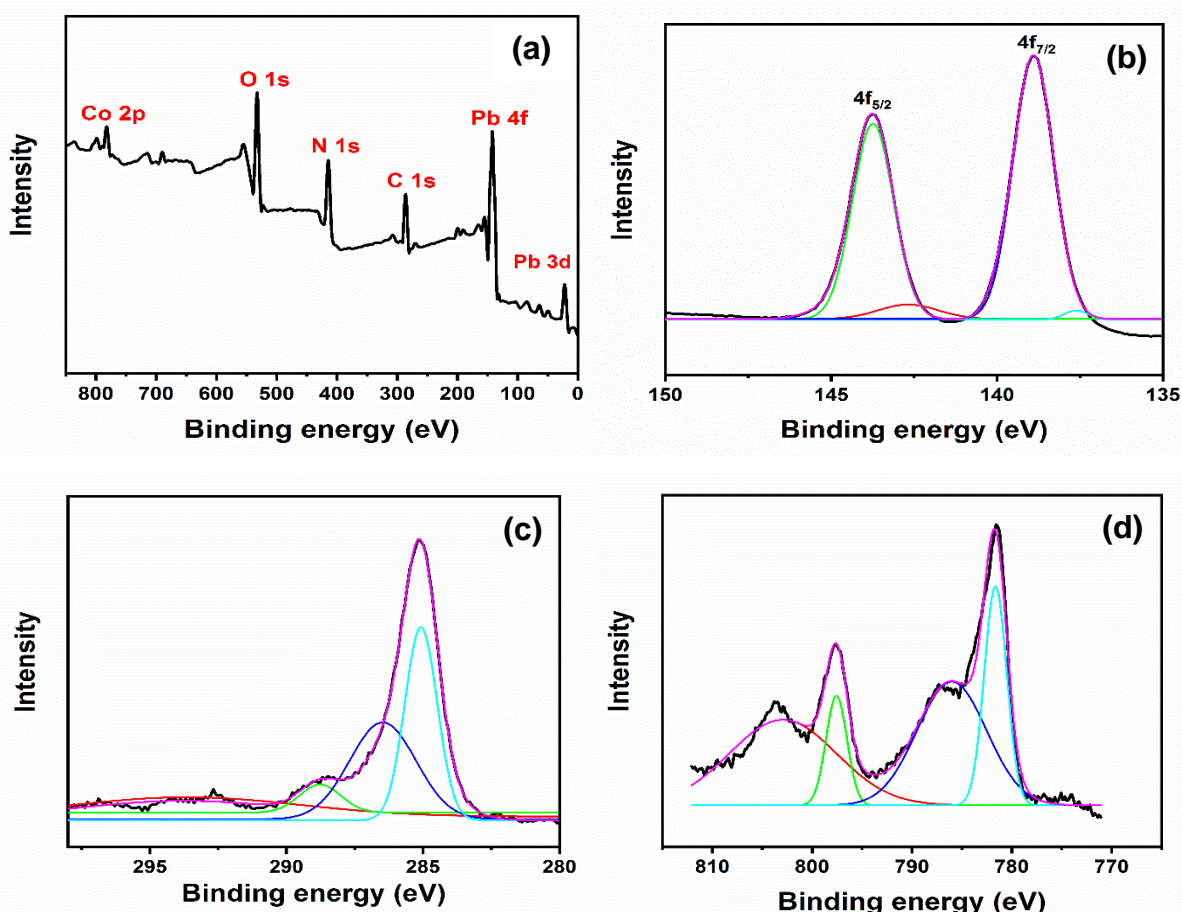


Figure 5.27. Proposed mechanism for the pollutants (MB, CR, Pb(II) & Cd(II)) adsorption on the COPYGO

### 5.3.20 XPS Analysis & FTIR Spectra of COPYGO after adsorption of Pb(II) & Cd(II)

XPS spectrum of COPYGO before and after adsorption revealed that the presence of peaks with a binding energy of 283.6, 285.5 and 287.0 eV were attributed to the C-C, C-OH and O-C-O after the adsorption these three peaks changed and the peaks associated with C-OH adsorption decreased along with its intensity given in Figure 5.28(c). XPS survey of Pb(II) adsorption with the binding energies of 138.5 eV and 143.5 attributed to the Pb 4f<sub>7/2</sub> and Pb 4f<sub>5/2</sub> confirmed the Pb(II) uptake in Figure 5.28(a). Therefore, the adsorption of Pb(II) has been explained with respect to hydroxyl groups shown in Figure 5.28. The presence of -OH group in carboxyl group which is highly stable than that of hydroxyl group, therefore, Pb(II) as a choice tries to attack hydroxyl group and hence the C-OH is reduced heavily (Langmuir 1916; Xu et al. 2018). XPS of the spectra COPYGO after Cd(II) adsorption showed the presence of new bands with binding energy values of 405.5 eV and 412.25 eV corresponded to the Cd 3d<sub>5/2</sub> and Cd 3d<sub>3/2</sub> of Cd-O and Cd-OH which confirmed the uptake of Cd(II) onto COPYGO surface given in Figure 5.29(a). The N 1s spectra of Pb(II) and Cd(II) uptake on COPYGO with binding energy values of 415.4 eV and 405.2 eV respectively confirms the increase in peak values of COPYGO (Figure 5.28(f) & 5.29(f)). It is due to the formation of N-H interactions of

COPYGO with metal ions during the adsorption phenomena which include  $\pi$ - $\pi$  interactions. However, the O 1s spectra of Cd(II) uptake increased to 532.5 eV and 533.1 eV and for Pb(II) uptake and it is 532.8 eV and 532.4 eV for Cd(II) upon adsorption proved that most of the interactions with Cd(II) compared to the Pb(II) uptake. FTIR spectra of the COPYGO before and after uptake of Cd(II) and Pb(II) were compared to elucidate the interactive mechanism between COPYGO and the Cd(II) and Pb(II) given in Figure 5.30. The peak at  $958\text{ cm}^{-1}$  is shifted to  $1080\text{ cm}^{-1}$  for cadmium and  $1120\text{ cm}^{-1}$  for lead which indicated the hydrogen bonding, whereas the spectra around  $1689\text{ cm}^{-1}$  is shifted to  $1524\text{ cm}^{-1}$  for Pb(II) and  $1634\text{ cm}^{-1}$  for Cd(II) due to the interaction of hydroxyl group of COPYGO with the adsorbates. The peak at  $1357\text{ cm}^{-1}$  is shifted to the higher wave number  $1404\text{ cm}^{-1}$  and  $1395\text{ cm}^{-1}$  due to the chelating interaction between N-H interactions in pyrrole on the COPYGO surface and the metal ions. All these results elucidated that the hydroxyl group and the carboxyl group occurred due to chelation or ion exchange interface with the metal ions.



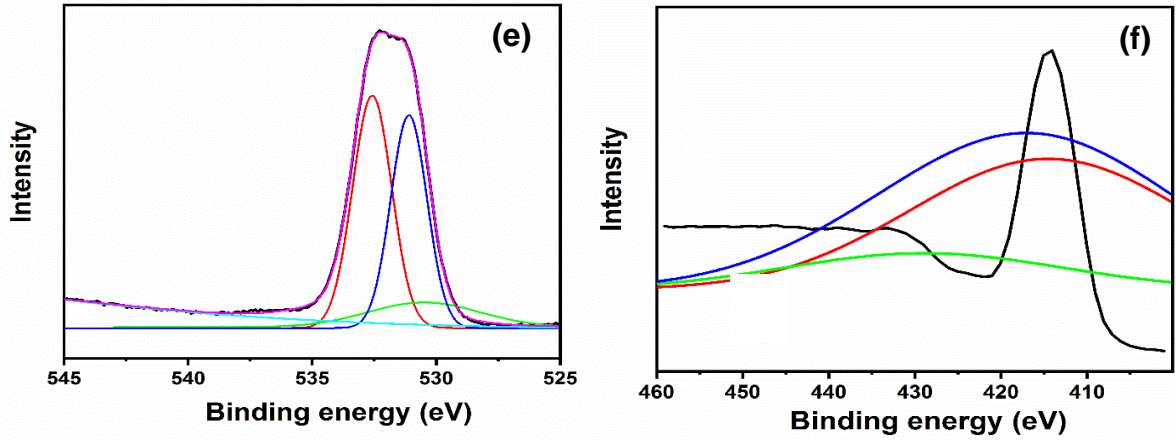
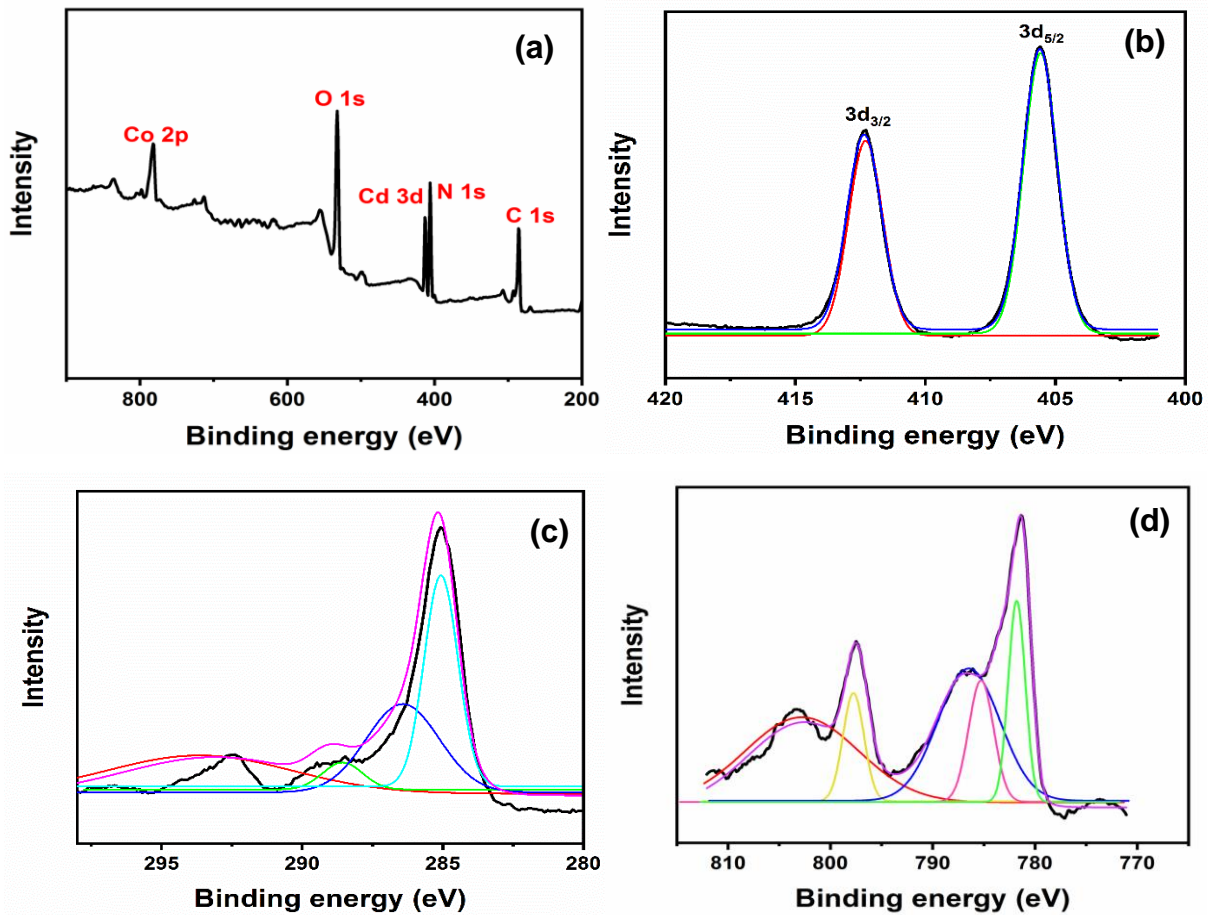


Figure 5.28. XPS spectra of COPYGO with the after the Pb(II) adsorption: a) elemental survey of COPYGO after Pb(II) adsorption, b) Pb 4f, c) C 1s, d) Co 2p, e) O 1s & f) N 1s



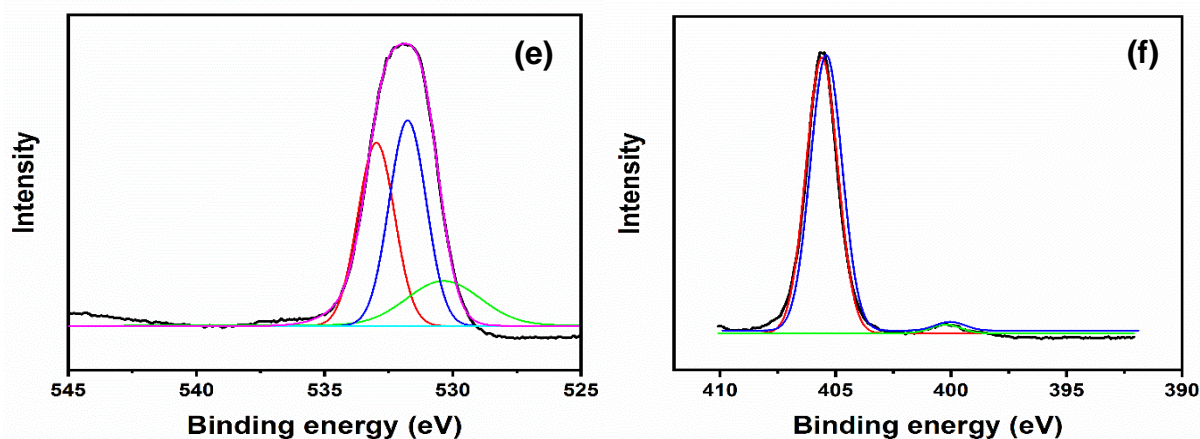


Figure 5.29. XPS of COPYGO with the Cd(II) adsorption: a) elemental survey of COPYGO after Cd(II) adsorption & b) Cd 3d, c) C 1s, d) Co 2p, e) O 1s & f) N 1s

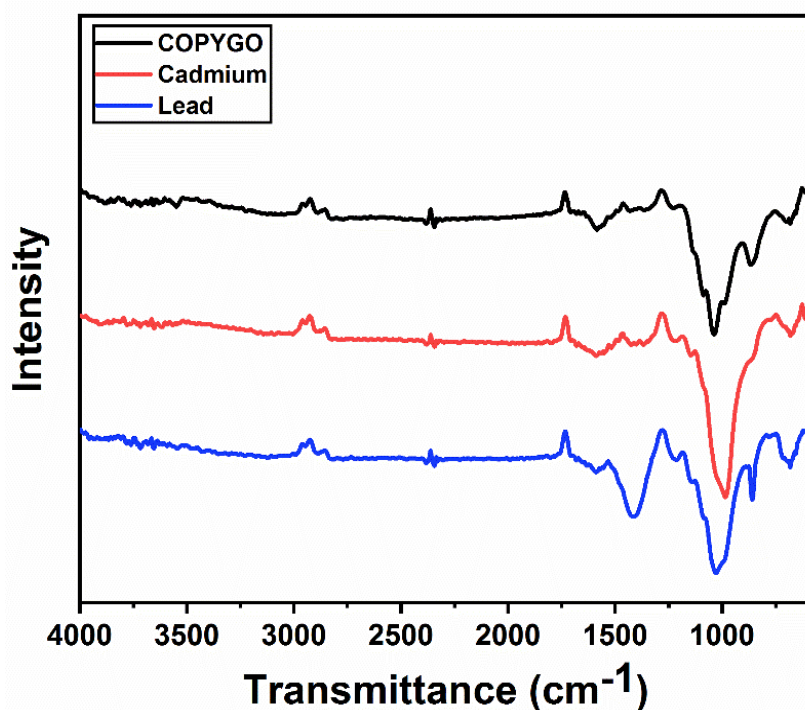


Figure 5.30. FTIR spectra of COPYGO after adsorption of Pb(II) and Cd(II)

### 5.3.21 TEM Analysis of COPYGO after uptake of MB and CR

TEM analysis of the pure COPYGO and after adsorption of MB and CR shown in Figure 5.4(e-h) and 5.31(a-g). The particle size of the COPYGO before adsorption is 4.10 nm which is given in Figure 5.4(h). After adsorption of MB and CR, the particle size of the COPYGO is 3.50 nm and 4.46 nm respectively which resembled the differences due to the variation in the sizes of adsorbate. However, from the HR-TEM of pure COPYGO, the size is found to be 0.40 nm. The size of the COPYGO after uptake of MB & CR are 0.41 nm and 0.44 nm respectively. The

SAED pattern of COPYGO is polycrystalline and smaller in size whereas after the five cycles of adsorption in the COPYGO, the crystallinity is lost due to the interaction of dyes with the COPYGO and they appeared as monocrystalline in nature. These effected the adsorption efficiency of the MB and CR dyes due to decay.

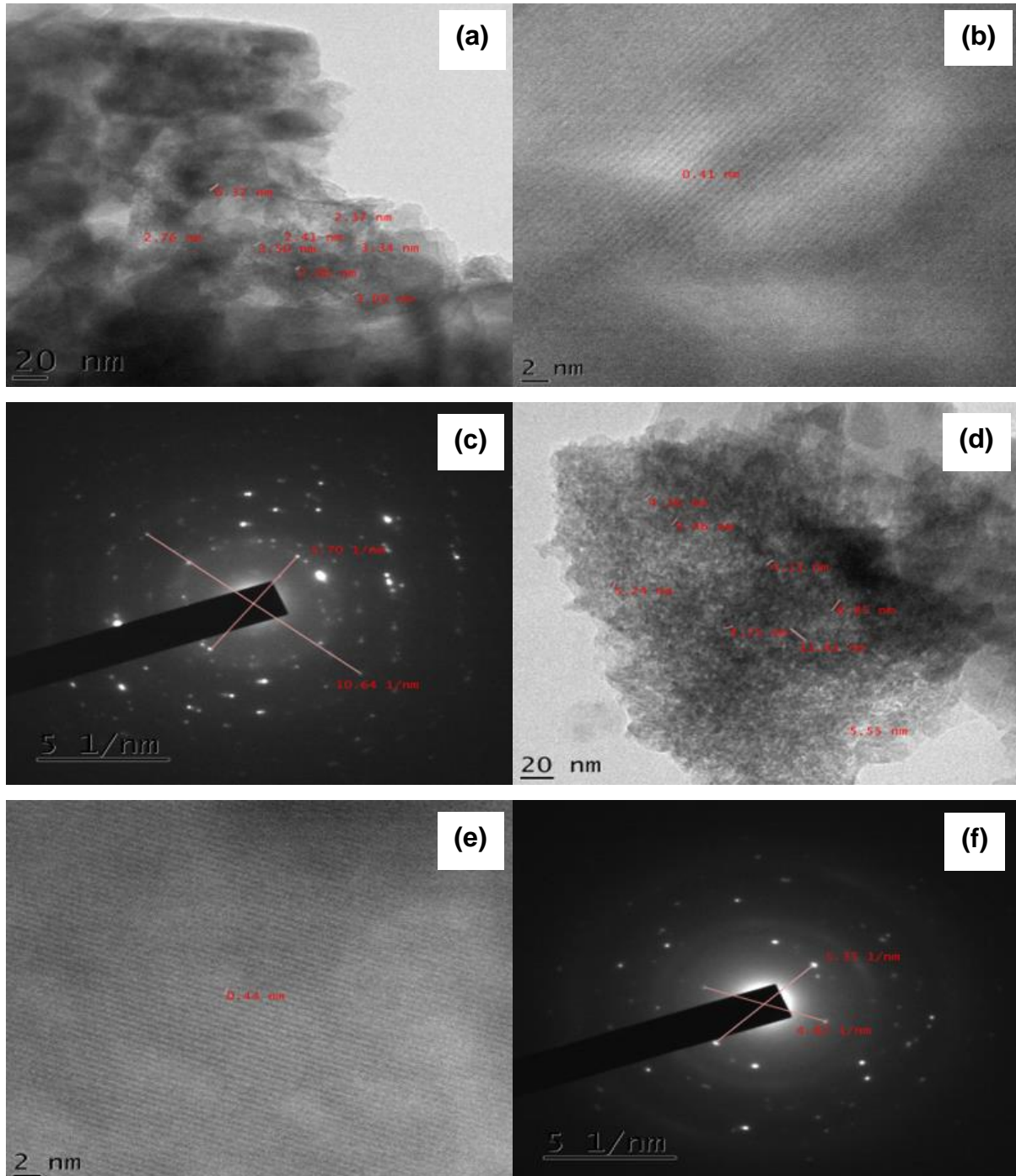


Figure 5.31. Recycled HR-TEM images of a,b) MB reused COPYGO, c) SAED of MB reused COPYGO & d,e) CR reused COPYGO, f) SAED of CR reused COPYGO

From the above analysis, the predicted adsorption mechanism includes complexation adsorption as well as electrostatic adsorption shown in Figure 5.27. The graphene oxide support

not only increased the effective specific area, but it also provided two to three layers for the effective adsorption leading to the highest adsorption capacity for all the adsorbates in the process. The plausible mechanism for these dyes can be described as below, 1) large surface area and mesoporous feature which have improved the efficiency of adsorption 2) Surface modification of polypyrrole improved the stability and effectiveness of magnetic nanoparticles. The large quantity of oxygen groups especially hydroxyl as well as carboxyl surface functional groups of graphene oxide support explained that the chelation effect of toxic metals which enhances the high metal removal efficiency. Further, the existence of  $\text{Co}_3\text{O}_4$  nanoparticles on its nanocomposite surface increases the surface area thereby enhancing the adsorption of the pollutant. The adsorption capacity depends on the surface area along with its porosity. Due to the synergistic effect of COPY with GO which has been remarkably enhanced the adsorption on the COPYGO nanocomposite when compared to the plane  $\text{Co}_3\text{O}_4$  nanoparticle (A.O et al. 2012; H. M. F. Freundlich 1906). Adsorption process might have taken place between the heterogeneous surface carbon support and the hydrophilic interactions which include both organic and inorganic pollutants more efficiently participated in adsorption phenomena, which led to the increase in adsorption efficiency.

### **5.3.22 Recycling evaluation of COPYGO in model(actual) wastewater**

To evaluate the prospect of adsorbent in real life application, its adsorption and recycling performances towards MB, CR, Pb(II) & Cd(II) were tested in model wastewater. The removal rates of MB, CR, Pb(II) & Cd(II) at a adsorbent dosage of  $20 \text{ mg L}^{-1}$  in model wastewater were 91.4, 87.9 90.9 & 93.8 respectively. These data are little closer to the removal rates obtained in synthetic wastewater from figure 5.26 which indicates that the presence of chemical and biological medium such as dissolved organic nitrogen has less significant effect on adsorption processes of pollutants. Notably, after regeneration, a small decrease in the removal rates were observed for all the pollutants, which demonstrated that COPYGO has a good stability and reusability in model wastewater. The above observation has been presented in the figure 5.32. From the above discussion, COPYGO could be an effective adsorbent candidate in actual wastewater treatment.

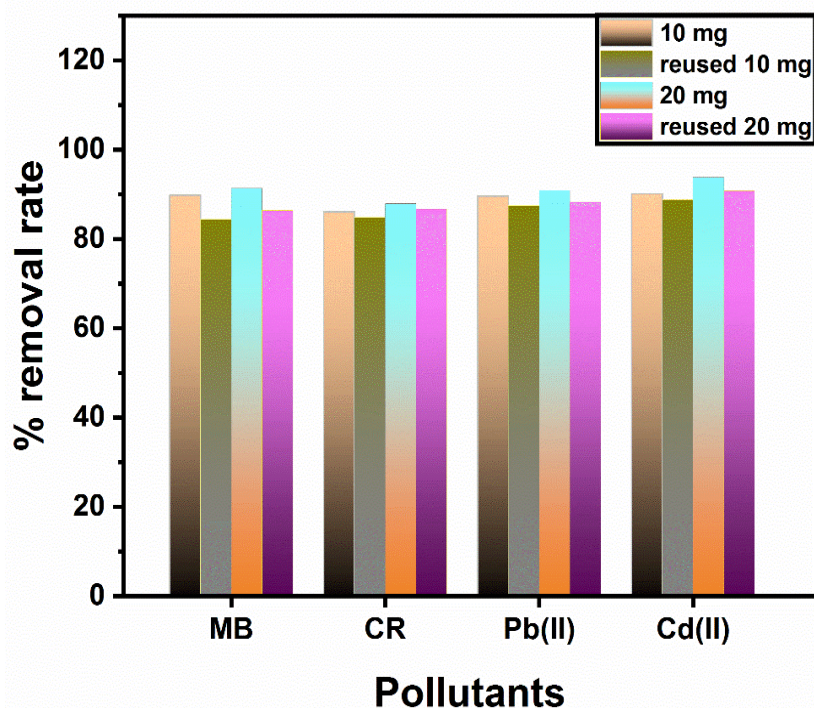


Figure 5.32. Adsorption and recycling performance of COPYGO in model wastewater

### 5.3.23 Adsorption of real wastewater on COPYGO

For the valorization of COPYGO studies, the adsorption of real textile industry effluent and industrial wastes containing pollutants which include MB & CR dyes as well as Pb(II) & Cd(II) metal ions were investigated to check the effectiveness of the adsorbent. The effluents were analyzed for COD, turbidity and its values with respect to the adsorbent COPYGO are given in table 7. The adsorption studies were conducted at 318.5 K and 323.5 K for all the pollutants MB, CR, Pb(II) and Cd(II) and the amount of adsorbent and adsorption procedure is similar to that of the simulated effluents.

In case of real wastewater, the COD was performed using the USEPA method (USEPA 2013) and using a Digital Reactor Block DRB 2000 (HACH, Germany). Standard digital turbidimeter from Bante instruments was used to measure the Turbidity. The pollutant structure and chemistry in the real wastewater sample and their disclosure of any identification or structural analysis was strictly prohibited by the supplier.

Table 5.7: Analysis of the real wastewater sample

Type of test	COD (mg L <sup>-1</sup> )	TOC	Turbidity	Temperature	Color
Value	703	237	27.4	25	Black

From the analysis, it showed that the adsorption of real wastewater is less when compared to the simulated wastewater may be due to the presence of various impurities and organic moieties in the adsorbate. The adsorption analysis data is given in the following tables 8, 9 & 10.

Table 5.8: The adsorption isotherms of real wastewater on COPYGO

Pollutants	Temp(K)	Langmuir				Freundlich			
		$Q_{max}$	$K_a$	Adj.	$R^2$	n	$K_F$	Adj.	$R^2$
		$mg\ g^{-1}$	$L\ mg^{-1}$	$R^2$	(COD)		$(mg\ g^{-1})(L\ mg^{-1})^{1/n}$	$R^2$	(COD)
MB	318.5	468.8448	0.06724	0.99624	0.99666	3.35423	96.62478	0.92669	0.93483
	323.5	667.0235	0.03461	0.99374	0.99444	2.4826	77.78853	0.95127	0.95669
CR	318.5	371.17522	0.10271	0.9968	0.99726	2.80545	77.28312	0.92954	0.93961
	323.5	314.17956	0.08434	0.99517	0.99586	2.93646	64.53037	0.93744	0.94637
Pb	318.5	696.58439	0.05269	0.99402	0.99476	2.83732	111.03236	0.91662	0.92705
	323.5	650.58082	0.04395	0.99449	0.99518	2.78635	96.00903	0.91851	0.9287
Cd	318.5	740.89324	0.07507	0.99462	0.99529	2.86979	135.83991	0.94024	0.94771
	323.5	668.82249	0.04974	0.99207	0.99306	2.75073	103.12456	0.96583	0.9701

Table 5.9: The adsorption isotherms of real wastewater on COPYGO

Pollutants	Temp(K)	Dubinin-Radushkevich				Temkin			
		$q_s$	$K_{DR}$	Adj.	$R^2$	$A_T$	$B_T$	Adj.	$R^2$
		$(mol\ g^{-1})$	$(mol^2\ k^{-1}\ J^{-2})$	$R^2$	(COD)	$(L\ g^{-1})$	$(J\ mol^{-1})$	$R^2$	(COD)
MB	318.5	398.9989	0.02474	0.88011	0.89343	1.00123	30.83201	0.98186	0.98388
	323.5	513.8844	0.08041	0.8614	0.8768	0.52415	21.26762	0.96377	0.9678
CR	318.5	290.6932	0.01067	0.82583	0.85071	1.16602	34.58305	0.98875	0.99035
	323.5	253.8099	0.01991	0.82699	0.85171	1.08090	43.01383	0.98493	0.98708
Pb	318.5	560.9088	0.04220	0.85757	0.87537	0.71317	19.71646	0.98177	0.98405
	323.5	516.4362	0.05456	0.85060	0.86928	0.59153	21.28865	0.97927	0.98186
Cd	318.5	590.4631	0.01609	0.88412	0.89860	1.76261	21.59838	0.93083	0.93947
	323.5	524.0998	0.03522	0.8572	0.87505	1.61099	26.08811	0.90728	0.91887



### Kinetic Studies:

Table 5.10: Kinetic studies of real wastewater on COPYGO

Pollutants	Temp (K)	Pseudo-first-order				Pseudo-second-order		
		$q_{e(\text{exp})}$ ( $\text{mg g}^{-1}$ )	$q_{e(\text{calc})}$ ( $\text{mg g}^{-1}$ )	$k_1$ ( $\text{min}^{-1}$ )	$R^2$	$q_{e(\text{calc})}$ ( $\text{mg g}^{-1}$ )	$k_2$ ( $\text{g mg}^{-1} \text{min}^{-1}$ )	$R^2$
MB	318.5	303.25	188.6021	0.000783	0.93030	302.1148	0.0024401	0.99929
	323.5	312.575	164.4571	0.00106	0.89152	310.5590	0.0040343	0.99976
CR	318.5	217.25	99.9260	0.000917	0.87148	217.1913	0.003661	0.99968
	323.5	199.00	94.0381	0.000929	0.83295	196.0784	0.008968	0.99993
Pb	318.5	387.63	231.6737	0.000666	0.89448	385.1051	0.001471	0.99937
	323.5	368.28	240.5120	0.000644	0.90499	367.0037	0.001404	0.99923
Cd	318.5	405.75	152.4398	0.00111	0.81475	403.2258	0.000185	0.99993
	323.5	370.56	190.2159	0.000734	0.91148	369.7472	0.000122	0.99937

#### 5.3.24 Recyclability studies of the real wastewater

The recyclability studies on the COPYGO adsorbent revealed that the real wastewater removal rate is less compared to the simulated wastewater under the same parameters as shown in figure 5.33 and the table is given in table 5.11.

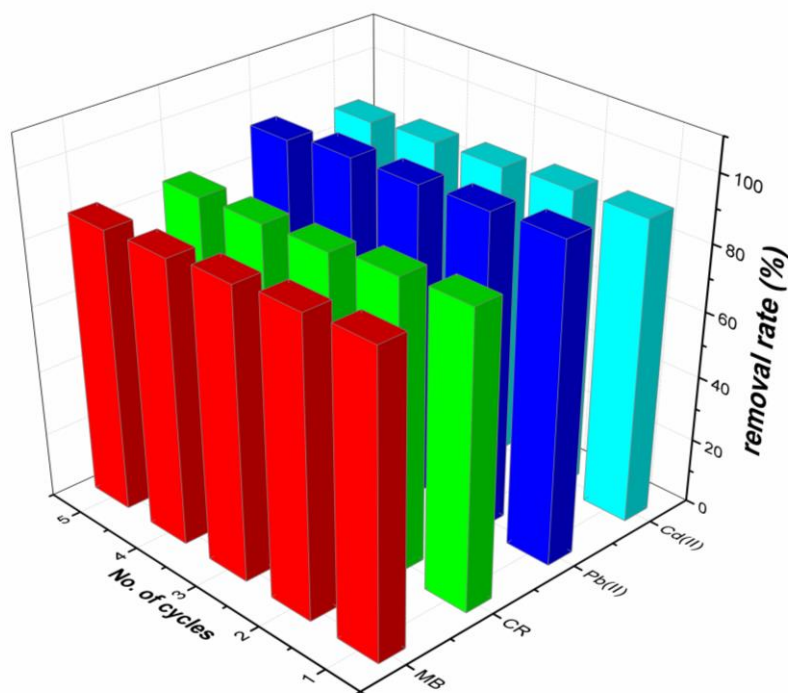


Figure 5.33. Regenerative capacity of the real wastewater for the pollutants: MB, CR, Pb(II) & Cd(II)

Table 5.11: Recyclability studies of pollutants in real wastewater on COPYGO

No. of cycles	Removal rate of pollutants in real wastewater (%)			
	MB	CR	Pb(II)	Cd(II)
1	91.6	89.9	96.96	92.07
2	90.4	88.8	95.9	91.7
3	88.6	86.5	95.1	90.3
4	86.7	85.8	94.8	89.8
5	85.9	85.1	92.2	88.4

## 5.4 CONCLUSIONS

In this study, a nanohybrid composite, COPYGO was successfully synthesized using hydrothermal methodology. The as-synthesized adsorbent possessed a large surface area with uniformity in wrinkle like morphology. COPYGO effectively removes dyes like MB, CR and metal ions Pb(II), Cd(II) in wastewater. COPYGO being magnetic in nature which can be efficiently separated using a magnet is an advantage of this adsorbent. As the pH increases, the maximum adsorption ability increases for the pollutants. These hybrid composite finds its applications as a suitable adsorbent material in the wide range of pH 2.0-10.0. The adsorbent can be easily regenerated and recycled. The analysis of real wastewater showed that the adsorption capacity of COPYGO reduced due to the presence of various impurities in the real wastewater compared to the simulated effluents. The results on COPYGO proved to be a

promising candidate for the removal of pollutants like MB, CR, Pb(II) & Cd(II) from the real wastewater.

## **CHAPTER-6**

**Synthesis of GO-CeO<sub>2</sub>@CoFe<sub>2</sub>O<sub>4</sub> nanocomposite by hydrothermal method for the effective adsorption of cationic and anionic pollutants from textile wastewater**

***Abstract:** This chapter discusses the synthesis of nanoceria which possess abundant oxygen vacancies can be used as a good doping agent for the  $\text{CoFe}_2\text{O}_4$  nanoparticle. These nanoparticles along with nanoceria were further immobilized on GO for controlling the particle aggregation due to its small size and to attain stability.*

## **6.1 INTRODUCTION**

Due to the rapid industrialization and urbanization, human population started to have huge burden on the usage of water and its pollution which created a high ultimatum for the clean water. Water pollution is more significant due to its ability to absorb/dissolve any substances compared to other liquid. Due to this, all the water bodies such as rivers, reservoirs, lakes and our ocean drowned with chemical waste, plastics and other toxic pollutants. Because of this, the amount of population with water scarcity would increase to 3.9 billion by 2030 according to the World Water Council (Xu et al. 2018). The existing and upcoming water scarcity demanded the requirement for wastewater treatment for the household utilization, industries and agricultural needs. Textile industry is a large global manufacturer that creates a huge amount of wastewater and became a menace to the water bodies and for a developing economy. Wastewater treatment and the potable water purification are an emergency to have a sustained human life and mitigate the pollution problems and health issues. There is an estimated 38,354 MLD is produced only in major cities of India, but its sewage treatment done at 11,786 MLD only. However, environmental field in India is expanding quickly to provide the viable opportunities for abating the water pollution using innovative technologies. Of which, the United nations (2015:6.3) has specified for the improvement to “water quality by reducing pollution, eliminating dumping and minimizing release of hazardous chemicals and materials, having the proportion of untreated wastewater and substantially increasing recycling and safe reuse globally” by 2030 (C. H. Woo 2018; Lee et al. 2016).

Cerium being an abundant rare-earth element gained attention due to its unique properties like biocompatibility, redox and transport properties, thermal stability and oxygen storage capacity. The surface structure of ceria ( $\text{CeO}_2$ ) resulted in the formation of mobile oxygen vacancies and a high movement in oxygen groups due to its storage capacity. The unique properties of ceria can be improved by doping with other metal ions to form new stable materials with new physical and chemical properties.

Cobalt ferrite ( $\text{CoFe}_2\text{O}_4$ ) gained greater attention due to its minimum magnetic saturation, easy and effective separation. Further, the plain nanoparticles tend to agglomerate due to its small

size as well as easily accumulation takes place in any acidic medium and hence, the nanoparticle surface need to be modified or supported on any heterogeneous groups to sustain stability. Hence, nanoceria incorporated GO nanocomposite is used as a support for the  $\text{CoFe}_2\text{O}_4$  nanoparticles which can effectively remove the pollutants from the wastewater and attains stability in acidic medium without any accumulation.

## **6.2 EXPERIMENTAL SECTION**

### **6.2.1 Chemicals required**

Graphite, Potassium Permanganate ( $\text{KMnO}_4$ ), Sulfuric Acid ( $\text{H}_2\text{SO}_4$ ), Phosphoric Acid ( $\text{H}_3\text{PO}_4$ ), Hydrogen Peroxide ( $\text{H}_2\text{O}_2$ ), Ethanol ( $\text{C}_2\text{H}_5\text{OH}$ ), Acetone ( $\text{C}_3\text{H}_6\text{O}$ ) and Toluene ( $\text{C}_7\text{H}_8$ ) are from Lobo chemie Limited. Cobalt Nitrate Hexahydrate  $\text{Co}(\text{NO}_3)_2 \cdot \text{H}_2\text{O}$ , Ferric Nitrate Nonahydrate  $\text{Fe}(\text{NO}_3)_3 \cdot 9\text{H}_2\text{O}$ , Cerium nitrate. hexahydrate, urea, Sodium Hydroxide ( $\text{NaOH}$ ), ethylene glycol, PVP, Methylene blue(MB) , Rhodamine-B(RB), Congo red(CR), are from Sigma Aldrich Limited.

### **6.2.2 Synthesis of Graphene oxide (GO)**

Graphene oxide nanosheets were synthesized by Improved Hummer's method. 1.5g of graphite flakes and 3g of  $\text{KMnO}_4$  were mixed with a 200 mL acid mixture of sulfuric acid and phosphoric acid (9:1). The reaction mixture was stirred for 12h by keeping the temperature at 50 °C. The reaction mixture allowed to cool in room temperature and transferred in to ice approximately 400 mL slowly with stirring. Hydrogen peroxide 30% (8-10 mL) transferred in to the solution with vigorous stirring. The color of the mixture turned from brown to bright yellow. The obtained mixture was filtered through a Sieve tub and the filtrate is centrifuge it. After decantation, the product washed with distilled water and absolute ethanol several times and a final acetone wash. The resultant graphene oxide dried at 60 °C for 24h.

### **6.2.3 Synthesis of Nanoceria ( $\text{CeO}_2$ )**

Cerium nitrate. hexahydrate (1eq) and urea (1eq) were dissolved in 35 mL of distilled water and stirred for 30 min. Later, 1M sodium hydroxide solution is prepared and mixed with the above solution using burette drop by drop in order to maintain of pH-9. The mixture was transferred to Teflon lined autoclave for 3h at 200 °C. Wash the mixture several times with distilled water and dried in an oven. Later, the mixture is transferred into tubular furnace and calcined at 500 °C for 2h. The product nanoceria is formed.

#### 6.2.4 Synthesis of Cobalt ferrite Nanoparticle ( $\text{CoFe}_2\text{O}_4$ )

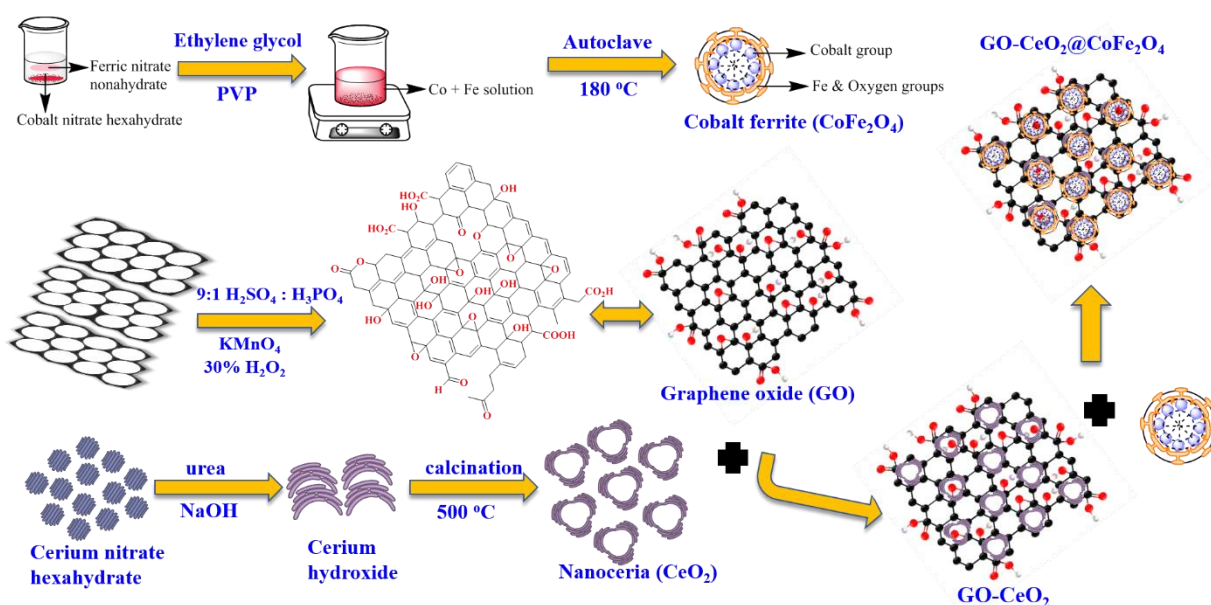
About 1.2369g of Cobalt nitrate hexahydrate and 3.434g of Iron nitrate nonahydrate is taken in beaker and dissolved with 25 mL of distilled water. 50 mL of Ethylene glycol was added slowly to the above solution maintained at 45 °C with stirring. Later 0.03g of Poly vinyl pyrrolidone (PVP) is added with stirring for 2h. Adjust the pH to 7 by adding NaOH solution at room temperature. The solution is autoclaved at 180 °C for 18h. The reaction mixture was cooled, washed with ethanol and dried at 80 °C for 5h.

#### 6.2.5 Synthesis of Graphene oxide-nanoceria composite ( $\text{GO-CeO}_2$ )

100 mg of graphene oxide were dispersed in 50 mL ethanol under ultrasonication for 30 min. 500 mg of nanoceria calcined at 500 °C is added to the above solution with stirring for 3h to get homogeneous suspension. The solution is autoclaved at 130 °C for 12h. The reaction mixture was filtered off and washed with distilled water and ethanol several times to remove unreacted nanoceria. The product was dried at 80 °C.

#### 6.2.6 Synthesis of Graphene oxide nanoceria cobalt ferrite composite ( $\text{GO-CeO}_2@ \text{CoFe}_2\text{O}_4$ )

100 mg of  $\text{GO-CeO}_2$  composite is dispersed in 50 mL ethanol solution and ultrasonicated for 30 min. 500 mg of  $\text{CoFe}_2\text{O}_4$  is added under constant stirring at 80 °C for 12h. The product is separated using external magnetic field and washed several times with ethanol, 2-propanol and dried at 60 °C for 12h. The complete synthesis of  $\text{GO-CeO}_2@ \text{CoFe}_2\text{O}_4$  composite is given in the scheme 6.1.



Scheme 6.1. Synthesis of  $\text{GO-CeO}_2@ \text{CoFe}_2\text{O}_4$

### 6.2.7 Adsorption experiments

The simulated wastewater treatment using the dyes such as MB, RB, CR as well as heavy metal ions Pb(II), Cd(II) in mono systems prepared using the salts  $\text{Pb}(\text{NO}_3)_2$ ,  $\text{Cd}(\text{NO}_3)_2 \cdot 6\text{H}_2\text{O}$  in aqueous solution. Isotherm and kinetic studies along with pH of the solution, ionic strength and adsorbent dosage capacity adjusted using 1 M HCl and 1 M NaOH solution as well as the solid sodium salt (NaCl) respectively as in the case of real wastewater which contains many salts along with impurities. The reaction mixture was kept in an Orbital Shaker at 200 rpm at fixed temperature.

To investigate the adsorption performances using different factors such as pH, Isotherm models, dosage capacities and the thermodynamic studies using 10 mg  $\text{GO-CeO}_2@\text{CoFe}_2\text{O}_4$  was consumed in 50 mL of distilled water. The kinetic experiments were conducted for 6h to govern the potency of the equilibrium effect. 10 mg of nanocomposite is used for each 50 mL pollutant. Then, the pollutants MB, RB, CR, Pb(II) & Cd(II) with a measured initial concentration of  $400 \text{ mg L}^{-1}$ ,  $200 \text{ mg L}^{-1}$ ,  $200 \text{ mg L}^{-1}$ ,  $200 \text{ mg L}^{-1}$  &  $200 \text{ mg L}^{-1}$  respectively. After the reaction time, the adsorbent was separated by magnet and the concentration of the pollutant in the remaining wastewater determined by UV spectroscopy. The adsorption equilibrium, rate of removal and the differential kinetic parameters computed using the equations are given below:

$$q_e = \frac{(C_o - C_e)V}{m} \quad (6.1)$$

$$q_t = \frac{(C_o - C_t)V}{m} \quad (6.2)$$

$$\% \text{ removal rate} = \frac{C_o - C_e}{C_o} \times 100 \quad (6.3)$$

Where  $C_o$  ( $\text{mg L}^{-1}$ ) is initial pollutant concentration;  $C_e$  ( $\text{mg L}^{-1}$ ) is the final pollutant concentration in the adsorption equilibrium and  $C_t$  ( $\text{mg L}^{-1}$ ) is the final concentration at a specific time interval in the wastewater,  $V$  (L) is the initial amount of wastewater and  $m$  is the mass of the  $\text{GO-CeO}_2@\text{CoFe}_2\text{O}_4$ .

### 6.2.8 Stability and regeneration tests

The stability of  $\text{GO-CeO}_2@\text{CoFe}_2\text{O}_4$  and  $\text{CoFe}_2\text{O}_4$  is studied by carrying out the Fe leaching at pH range 1-10 using ICP-AES analysis. 10 mg of each  $\text{GO-CeO}_2@\text{CoFe}_2\text{O}_4$  and  $\text{CoFe}_2\text{O}_4$  were dispersed in 25 mL of distilled water and the pH is adjusted using 1M HCl/1M NaOH. The reaction mixture was kept in orbital shaker for 24h and the supernatant collected and measured.



The regeneration tests were carried out by treating the first used adsorbent with 50 mL of desorbing agents at 50 °C for a period of 12h with 200 rpm shaking speed. After the desorption process, the recovered adsorbent isolated using magnet and washed with ethanol and 0.01 M NaOH solution. Finally, the adsorbent was washed several times with distilled water and dried for the next adsorption process. The desorbing agents are HCl (1.0 M or 0.1 M or 0.01 M) or 0.1 M H<sub>2</sub>SO<sub>4</sub> for the cationic and anionic dyes and HCl (1 M or 0.1 M) or 0.01 M EDTA for the heavy metal ions.

### **6.2.9 Adsorption and recycling performances of GO-CeO<sub>2</sub>@CoFe<sub>2</sub>O<sub>4</sub> in model waste water**

The model wastewater prepared using the OECD guidelines in the presence of biological and chemical medium composed of 160 mg of peptone, 110 mg of meat extract, 30 mg of urea, 30 mg of K<sub>2</sub>H<sub>2</sub>PO<sub>4</sub>, 8 mg of NaCl, 3 mg CaCl<sub>2</sub> · 2H<sub>2</sub>O and 2 mg of MgSO<sub>4</sub> · 7H<sub>2</sub>O were mixed and prepared a clear aqueous solution in 1L tap water (Guideline 2001; Zhao et al. 2015). The model wastewater which was synthesized and utilized as a aqueous medium for the pollutants 1000 mg L<sup>-1</sup> of each MB, CR, Pb(II), Cd(II) 600 mg L<sup>-1</sup> & RB 400 mg L<sup>-1</sup>. To this solution, 20 mg of fresh adsorbent was added and performed the adsorption process for 10h in a shaker. The reusability tests were done using the desorbing agent 1.0 M HCl solution for the saturated nanocomposite.

### **6.2.10 Characterization Techniques**

FTIR spectra was measured using Bruker-Alpha ECO-ATR FTIR within a range of 4000-599 cm<sup>-1</sup>. Surface morphology was done using FE-SEM with EDS analysis from Zeiss Sigma SEM with oxford EDS. The internal structure of the samples was done using HR-TEM FEI Tecnai G2 20 (200 KV). The TG analysis was implemented at N<sub>2</sub> atmosphere from 25 °C to 800 °C with a rate of flow heat of 10 °C/ min using Perkin Elmer STA 6000 thermal analyzer. Zeta potential was measured in presence of Zetasizer WT, Malvern Instruments. The phase identification and composition were carried out using X-ray diffractometer Bruker D8 advance. Raman spectrometer (STR500 Airix) was used for analysing the composition of the GO and GO- CeO<sub>2</sub>@CoFe<sub>2</sub>O<sub>4</sub>. The magnetic properties of the GO- CeO<sub>2</sub>@CoFe<sub>2</sub>O<sub>4</sub> and CoFe<sub>2</sub>O<sub>4</sub> were done by VSM squid analysis. XPS analysis was performed to determine the elements and their composition using ThermoScientific, NEXSA surface analysis with a monochromatic Al-K $\alpha$  source (h $\nu$  =1486.6eV). BET measurements to find out the N<sub>2</sub> adsorption-desorption studies and to know the pore diameter of the nanoadsorbent from Nova touch LX2.

## 6.3 RESULTS AND DISCUSSION

### 6.3.1 Vibrational Spectroscopy (FTIR)

Fourier transform infrared (FTIR) analysis of  $\text{CoFe}_2\text{O}_4$ ,  $\text{GO-CeO}_2$  and  $\text{GO-CeO}_2@\text{CoFe}_2\text{O}_4$  were performed in the range of  $400\text{-}4000\text{ cm}^{-1}$ . Figure 6.1 shows that the peaks at  $932\text{ cm}^{-1}$  and  $588\text{ cm}^{-1}$  confirmed to the Co-O and Fe-O vibrations of  $\text{CoFe}_2\text{O}_4$  and  $\text{GO-CeO}_2@\text{CoFe}_2\text{O}_4$  respectively. The absorption peaks at  $476$  and  $588\text{ cm}^{-1}$  is due to the O- $M_{\text{oct}}$ -O at octahedral sites and O- $M_{\text{tet}}$ -O at tetrahedral sites on  $\text{CoFe}_2\text{O}_4$  (Pradeep et al. 2008; Shobana et al. 2007). The broad peaks at  $3390$ ,  $1562$  and  $1635\text{ cm}^{-1}$  attributed to the stretching and bending vibrations of OH groups which are present on the surface of  $\text{CoFe}_2\text{O}_4$  and the presence of hydroxyl groups in both  $\text{GO-CeO}_2$  and  $\text{GO-CeO}_2@\text{CoFe}_2\text{O}_4$ . GO exhibits the characteristic strong band around  $3394\text{ cm}^{-1}$  and  $1660\text{ cm}^{-1}$  corresponded to the -OH and C=O bonds of hydroxyl, carbonyl and carboxylic acid groups (Lv et al. 2020; Mungse et al. 2012). The bands present around  $1058$ ,  $1220$ , and  $1621\text{ cm}^{-1}$  indicated the epoxy (C-O), phenol, C=C bonds respectively as shown in the figure 6.2. The peak for the characteristic absorption band for  $\text{CeO}_2$  nanoparticle which appeared at  $462\text{ cm}^{-1}$  in  $\text{GO-CeO}_2$  attributed to the Ce-O stretching vibration of  $\text{CeO}_2$  shown in figure 6.2 (Bai et al. 2014; Parwaiz et al. 2017). Further incorporation of  $\text{CoFe}_2\text{O}_4$  nanoparticle onto  $\text{GO-CeO}_2$  surface triggered minor changes in the stretching vibrations but no ancillary peaks were observed.

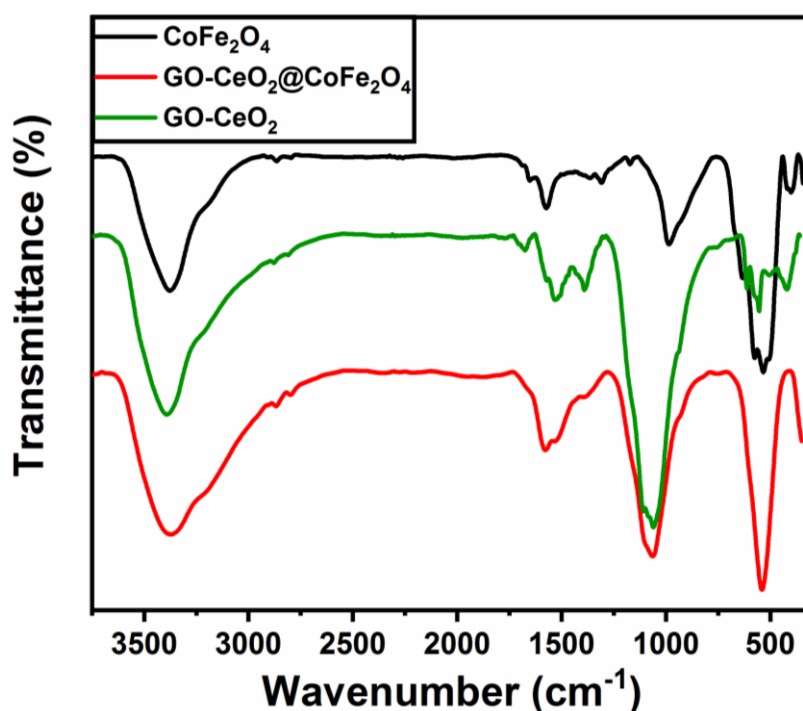


Figure 6.1. FTIR spectra of  $\text{CoFe}_2\text{O}_4$  nanoparticle,  $\text{GO-CeO}_2$  &  $\text{GO-CeO}_2@\text{CoFe}_2\text{O}_4$

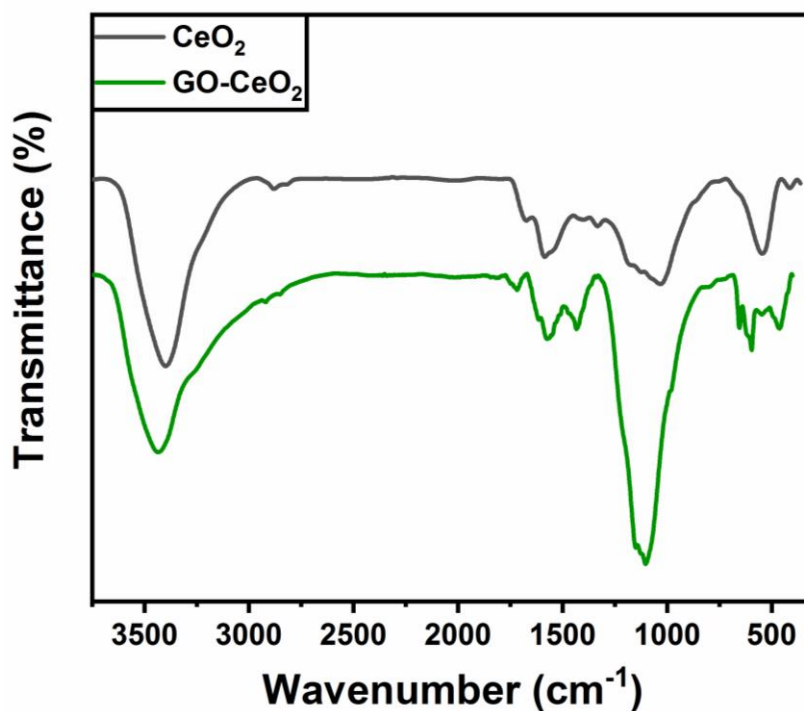


Figure 6.2. FTIR spectra of GO-CeO<sub>2</sub> & Nanoceria (CeO<sub>2</sub>)

### 6.3.2 X-ray Diffraction (XRD)

To determine the crystalline phase and structure of the as-prepared samples, XRD measurements were done as given in figure 6.3. The diffraction peaks of CoFe<sub>2</sub>O<sub>4</sub> are in good accordance with the standard XRD of cubic spinel ferrite lattice (JCPDS no. 22-1086). The diffraction peaks of CoFe<sub>2</sub>O<sub>4</sub> and GO-CeO<sub>2</sub>@CoFe<sub>2</sub>O<sub>4</sub> are at 18.40, 30.39, 35.61, 43.37, 53.82, 57.19, 62.75 and 74.38 attributed to the crystal planes of (111), (220), (311), (400), (422), (511), (440) and (533) respectively (Cai et al. 2017; Ren et al. 2016; Santhosh et al. 2017). The diffraction patterns for ceria are at 28.5, 33.2, 47.7, 56.6, 58.9, 69.4, 76.8 and 79.0 indexed to the (111), (200), (220), (311), (222), (400), (331) and (420) planes represented the cubic CeO<sub>2</sub> in accordance with JCPDS No. 34-0394 (CAO et al. 2017). In GO-CeO<sub>2</sub> and GO-CeO<sub>2</sub>@CoFe<sub>2</sub>O<sub>4</sub>, there is an additional peak at  $2\theta = 10.87$  i.e., (002) plane, which confirmed the structure of GO is retained after the deposition of nanoceria onto the graphene oxide (Du et al. 2017; Jiang et al. 2012; Yang et al. 2013). Figure 6.3 shows that the GO-CeO<sub>2</sub>@CoFe<sub>2</sub>O<sub>4</sub> have diffraction peaks at 10.89, 29.41, 34.54, 42.84, 47.7, 57.21, 62.87, 74.45 and 79.0 corresponding to the crystalline planes of (002), (111), (200), (311), (220), (511), (440), (533) and (420) respectively which confirmed that the structure of cobalt ferrite structure is not destroyed during the formation of nanocomposite. The peaks at 30.39 and 35.61 in CoFe<sub>2</sub>O<sub>4</sub>

were merged with the nanoceria diffraction peaks at 28.5 and 33.2 during the synthesis of nanocomposite to form strong broad peaks where the diffraction peak values reduced.

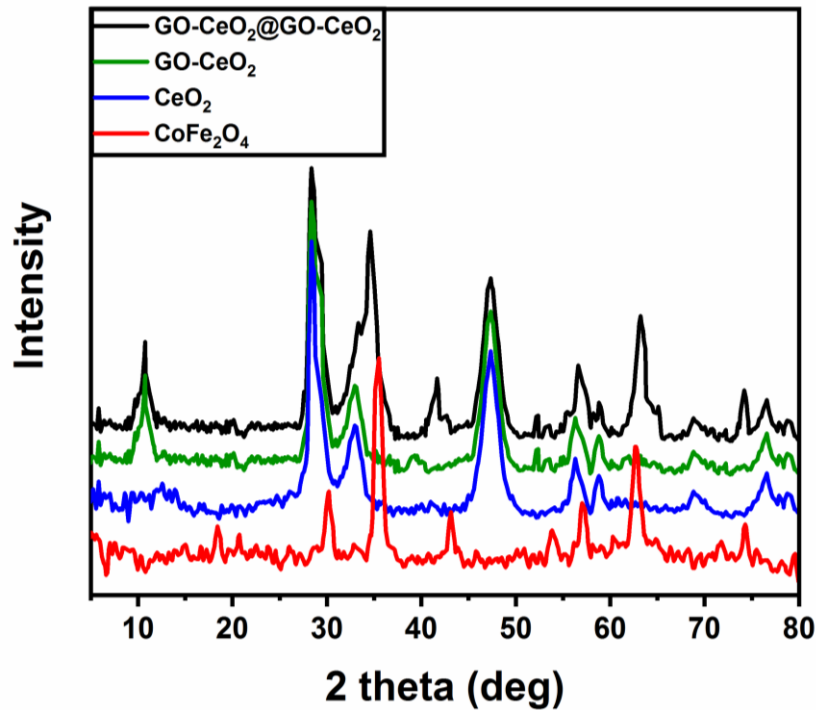


Figure 6.3. XRD pattern for the CoFe<sub>2</sub>O<sub>4</sub> nanoparticle, CeO<sub>2</sub>, GO- CeO<sub>2</sub> & GO-CeO<sub>2</sub>@CoFe<sub>2</sub>O<sub>4</sub>

To know the broadening of peaks in the XRD graph, the crystalline size of the CoFe<sub>2</sub>O<sub>4</sub> nanoparticle was measured using the X-ray broadening method with the help of Scherrer equation:

$$D_{hkl}(nm) = \frac{K\lambda_{(nm)}}{\beta_{hkl}(Rad)\cos\theta} \quad (6.4)$$

Here, K termed as the shape factor (K=0.9 for octahedral shapes),  $\lambda$  represents the wavelength of X-ray radiation ( $\lambda=0.154$  for Cu K $\alpha$  radiation),  $\beta_D$  is the width of peak with an intensity at half-minimum and the term  $\theta$  represents the Bragg's diffraction angle.

From the above equation the average crystal size of CoFe<sub>2</sub>O<sub>4</sub> particle was calculated to be 17.34 nm which is nearly resembling with TEM analysis.

### 6.3.3 Raman Spectroscopy

Raman spectra of GO and GO-CeO<sub>2</sub>@CoFe<sub>2</sub>O<sub>4</sub> is given in figure 6.4. GO indicated two prominent peaks at 1353 cm<sup>-1</sup> and 1588 cm<sup>-1</sup> assigned as D and G bands respectively. The D-band which emerged due to disorderness in sp<sup>3</sup> carbon atoms and G-band appeared because of the vibration of graphitic sp<sup>2</sup> carbon atoms. The shift around 473 cm<sup>-1</sup> confirmed to be F<sub>2g</sub>

symmetry stretching vibrations of Ce-O bond and the oxygen vacancies in the CeO<sub>2</sub> shown in figure 6.4 (Du et al. 2017; Kumar et al. 2016; Parwaiz et al. 2017; Zamaro et al. 2012). This confirmed the presence of CeO<sub>2</sub> in the nanocomposite shown in figure 6.4. The two important peaks at 470 cm<sup>-1</sup> and 690 cm<sup>-1</sup> attributed to the octahedral site sublattice and tetrahedral site sublattice vibration modes respectively. Five phonon modes, which are Raman active especially A<sub>1g</sub>, E<sub>g</sub> & 3T<sub>2g</sub>. In this spectrum, the Raman mode above 600 cm<sup>-1</sup> (i.e., 616 and 690 cm<sup>-1</sup>) corresponding to the symmetric stretching of oxygen atom with respect to the metal atom in tetrahedral void and represented as A<sub>1g</sub>. The other frequency modes below 600 cm<sup>-1</sup> are 207, 303, 360, 470 and 572 cm<sup>-1</sup> corresponded to the symmetric and asymmetric bending of the oxygen atom in metal-ion (M-O) bonds at the octahedral sites and it is represented as E<sub>g</sub> and 3T<sub>2g</sub> (Chandramohan et al. 2011; Fan et al. 2010; Sánchez-Arenillas et al. 2019). From the Raman spectra, we confirmed that the Co<sup>2+</sup> ions ratio at the tetrahedral and octahedral voids confirmed to be 616 cm<sup>-1</sup> and 470 cm<sup>-1</sup>.

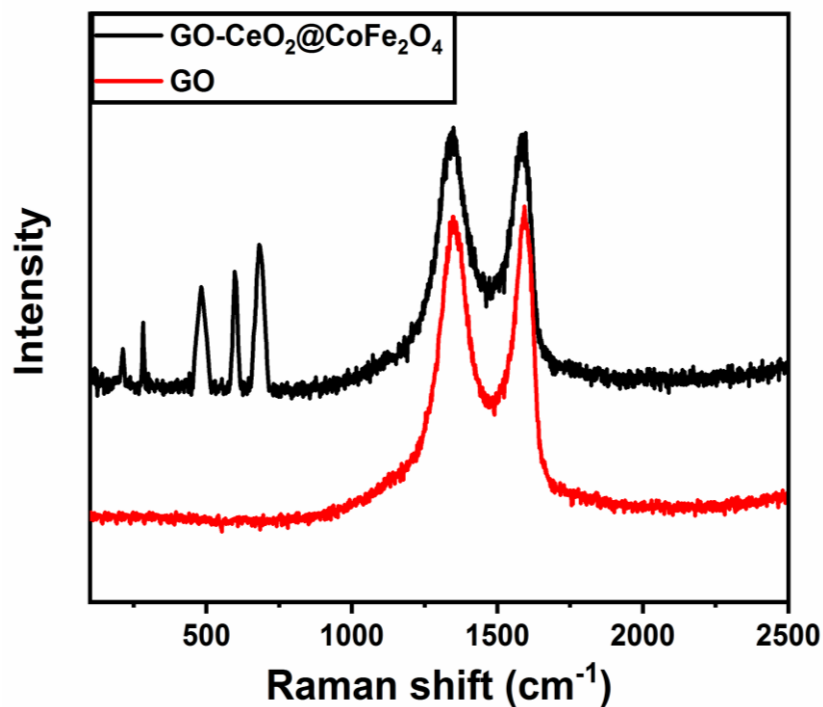


Figure 6.4. Raman spectra of GO and GO-CeO<sub>2</sub>@CoFe<sub>2</sub>O<sub>4</sub>

### 6.3.4 Thermogravimetric Analysis (TGA)

Figure 6.5 represents the TG curves of GO & GO-CeO<sub>2</sub>@CoFe<sub>2</sub>O<sub>4</sub>. In case of nanocomposite, the weight loss is observed at three stages, the first stage (90 °C-120 °C) for the evaporation of excess water molecules within the hydrophilic groups of graphene oxide nanocomposite and the second stage (250 °C-480 °C) was due to the decomposition of functional groups along with

the nanoparticles on the composite. The third stage (610 °C-790 °C) confirmed that the destruction of carbon rings takes place. However, in case of GO shown in figure 6.5, the weight loss occurred in three stages: the first stage (90 °C-210 °C) confirmed the removal of physisorbed water molecules onto the GO surface, the second stage (211 °C-420 °C), confirmed through the destruction of functional groups such as hydroxyl, carboxyl and epoxy takes place. Further, the temperature around 420 °C-800 °C, confirmed to the degradation of organic species and the destruction of hexagonal ring of carbon atoms.

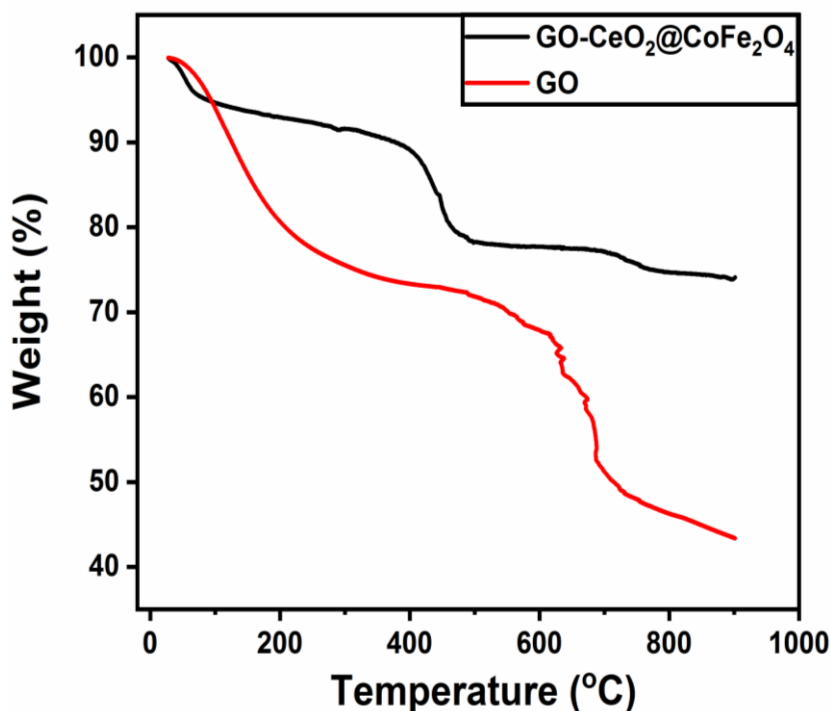


Figure 6.5. TGA of GO & GO-CeO<sub>2</sub>@CoFe<sub>2</sub>O<sub>4</sub>

### 6.3.5 Morphology Studies (FE-SEM & EDS)

Figure 6.6 shows the FE-SEM image of CoFe<sub>2</sub>O<sub>4</sub>, CeO<sub>2</sub>, GO-CeO<sub>2</sub> & GO-CeO<sub>2</sub>@CoFe<sub>2</sub>O<sub>4</sub>. Figure 6.6(a) shows the presence of spherical shaped nanoparticles which are uniform all over its surface in the range of 100-200 nm. The image of CeO<sub>2</sub> in figure 6.6(b) shows the clusters of nanoceria owing to the integration of these components. The GO-CeO<sub>2</sub> (Figure 6.6(c)) showed that the rippled silk veil layers with the GO stacking that exhibited the doping of nano CeO<sub>2</sub> onto the GO surface. GO-CeO<sub>2</sub> micrographs suggested that they are aggregations in quasi-nanospheres assembly due to the nucleation process of GO with CeO<sub>2</sub> (Vanitha et al. 2015). Figure 6.6(d) confirms the homogeneous distribution of CoFe<sub>2</sub>O<sub>4</sub> nanoparticle on to GO-CeO<sub>2</sub>@CoFe<sub>2</sub>O<sub>4</sub> composite.

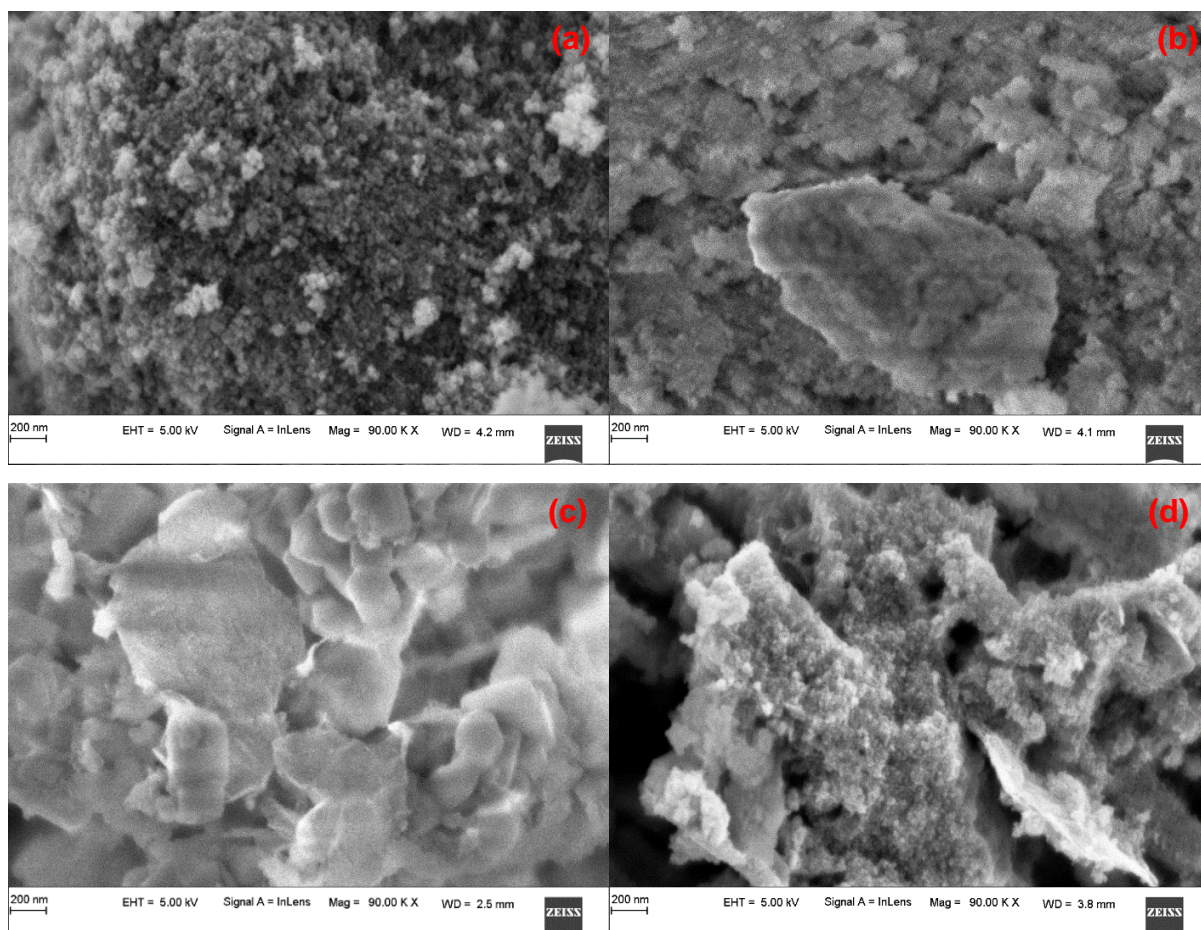


Figure 6.6. FE-SEM images of (a)  $\text{CoFe}_2\text{O}_4$ , (b)  $\text{CeO}_2$ , (c)  $\text{GO-CeO}_2$  & (d)  $\text{GO-CeO}_2@CoFe_2O_4$

The EDS analysis of  $\text{GO-CeO}_2@CoFe_2O_4$ ,  $\text{CoFe}_2O_4$ ,  $\text{GO-CeO}_2$ ,  $\text{CeO}_2$  and  $\text{GO}$  were given in figure 6.7(a-d). The  $\text{GO-CeO}_2$ ,  $\text{CoFe}_2O_4$  and  $\text{CeO}_2$  substrates are in close proximity with the synthesized nanocomposite  $\text{GO-CeO}_2@CoFe_2O_4$  and its methodology with respect to the elemental composition and atomic wt. ratios. The elemental composition in  $\text{CoFe}_2O_4$  are Fe, O & Co,  $\text{CeO}_2$  or  $\text{GO-CeO}_2$  C, O & Ce. are Ce, C & O and finally C, Co, Fe, O & Ce are in  $\text{GO-CeO}_2@CoFe_2O_4$  composite.

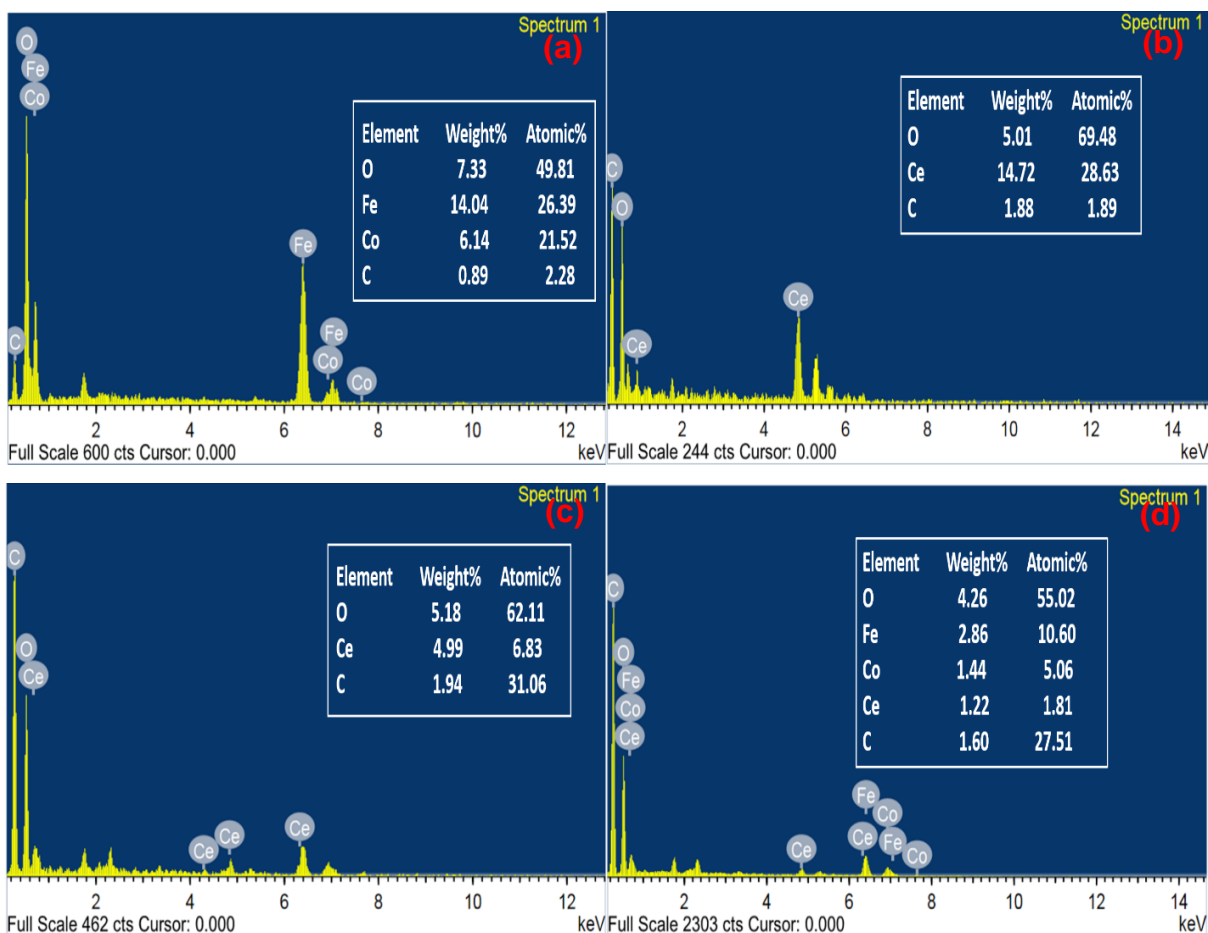


Figure 6.7. EDS analysis of (a) CoFe<sub>2</sub>O<sub>4</sub>, (b) CeO<sub>2</sub>, (c) GO-CeO<sub>2</sub> & (d) GO-CeO<sub>2</sub>@CoFe<sub>2</sub>O<sub>4</sub>

### 6.3.6 Transmission Electron Microscopy (TEM)

The morphology of the synthesized nanocomposite GO-CeO<sub>2</sub>@CoFe<sub>2</sub>O<sub>4</sub> and the CoFe<sub>2</sub>O<sub>4</sub> nanoparticles are given in the figure 6.8(a-f). The wrinkles on the surface possess spacers in the nanocomposite, constrain the aggregation of GO nanosheets increases the surface area and boosted its capacitive performance for the adsorption. The random distribution of quasispherical CeO<sub>2</sub> nanoparticles over the surface of GO nanosheets and no much aggregation is shown in the nanocomposite. CoFe<sub>2</sub>O<sub>4</sub> nanoparticles are homogenously distributed without aggregation on to the GO nanocomposite which confirmed the successful synthesis of nanocomposite GO-CeO<sub>2</sub>@CoFe<sub>2</sub>O<sub>4</sub>. CoFe<sub>2</sub>O<sub>4</sub> nanoparticle are the aggregation of a huge group of smaller nanoparticles with porous structure shown in Figure 6.8(d). TEM images 6.8(d-f) of the synthesized GO-CeO<sub>2</sub>@CoFe<sub>2</sub>O<sub>4</sub> nanocomposite showed the reduction in particle size by the addition of GO and nanoceria around the nanoparticle which surrounded it to form multiple particle shapes. The formation of multiple morphology in the nanocomposite such as flake and coralloid structures is due to the constrain in the growth of particles owing to



the GO and nanoceria addition which is in accordance with the XRD patterns. The complicated particle shape is advantageous which further enhanced the removal rate of dyes and metal ions during the adsorption process. The presence of complicated structure morphology such as coraloid and porous structures resulted in the action of capillary force leading to the improvement in specific surface area which promoted the adsorption performance of the nanocomposite (Zhang et al. 2017). The SAED patterns shows that it is more crystalline in  $\text{CoFe}_2\text{O}_4$  nanoparticle compared to the SAED pattern of nanocomposite.

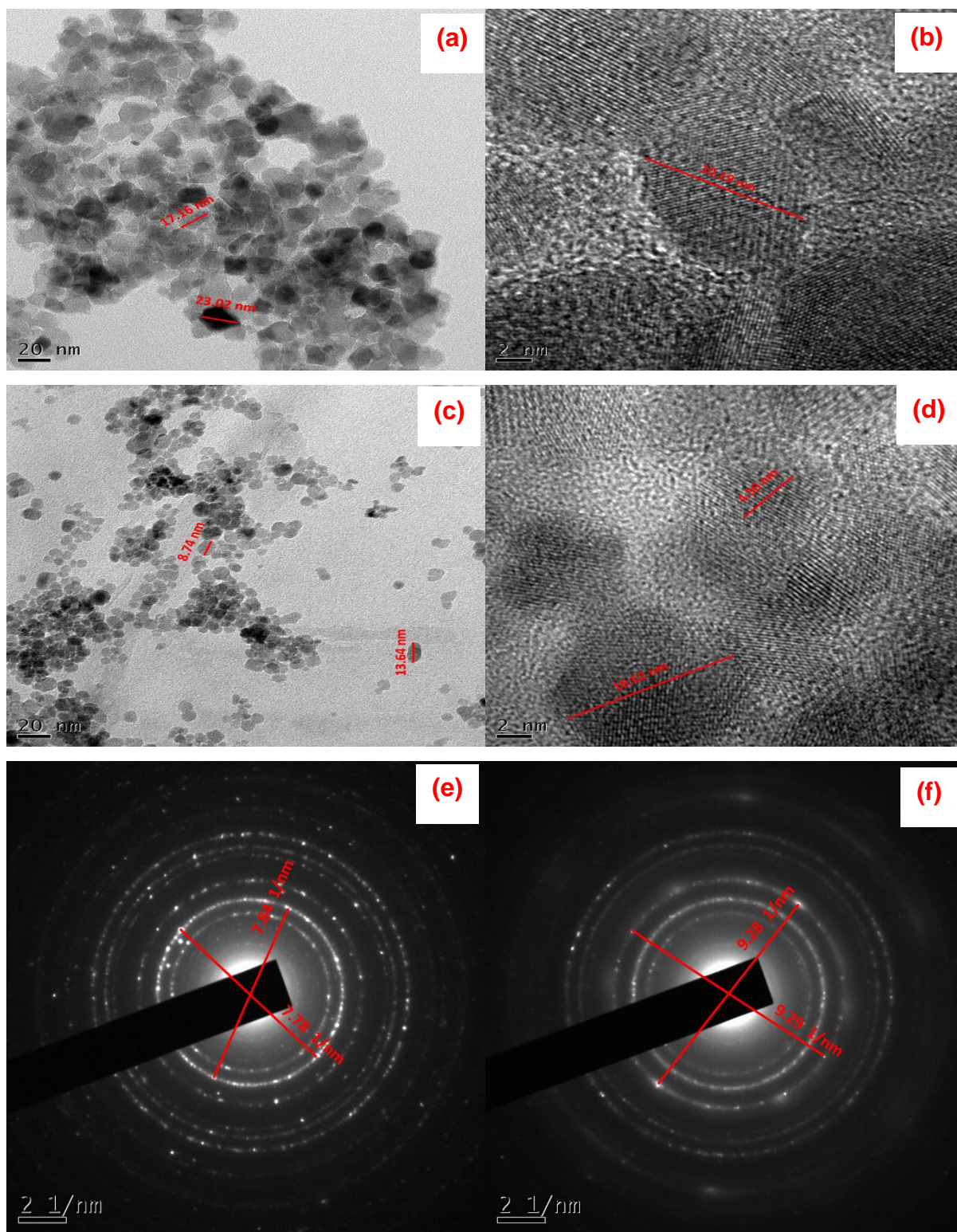


Figure 6.8. TEM images of  $\text{CoFe}_2\text{O}_4$  (a) TEM, (b) HR-TEM & (e) SAED and  $\text{GO-CoFe}_2\text{O}_4$  (c) TEM, (d) HR-TEM & (f) SAED pattern

### 6.3.7 Vibrating-sample Magnetometry (VSM)

The magnetic properties of  $\text{CoFe}_2\text{O}_4$  and  $\text{GO-CeO}_2@\text{CoFe}_2\text{O}_4$  calculated at room temperature with an applied magnetic field to the saturation magnetization shown in figure 6.9. A decrease in  $M_s$  is observed due to the addition of  $\text{GO-CeO}_2$ . The  $M_s$  of GO is found to be 0.37 emu/g with a  $H_c$  of 82 Oe which represented as weak ferromagnetic due to the presence of unsaturated groups on its edges leading to a spin reorientation with an enhanced field strength further denoted to be antiferromagnetic like behavior. The reason behind this feature in GO is due to the defects aroused within the graphitic sheets. The binding sites of oxygen atoms in the graphitic carbon framework generated the magnetic moment, but the oxygen atoms within the epoxy functional group with two carbon atoms present in sub-lattices of GO framework. With respect to Lieb's theorem proved that the epoxy group cannot exert the magnetic moment. But the oxygen atoms of hydroxyl group which is attached to the carbon atom on one-side possess magnetic moment and this led to the GO magnetic nature. If these magnetic moments were not coupled, then weak paramagnetism can be induced and when they are coupled, the interactions can be ferromagnetic, antiferromagnetic or superparamagnetic can be seen in GO framework. Further, the weak ferromagnetic nature of GO and the strong ferromagnetic nature of  $\text{CoFe}_2\text{O}_4$  nanoparticle leads to the superparamagnetic property with a good saturation magnetization of 59.5 emu/g. Table 6.1 represented the hysteresis loop of the  $\text{CoFe}_2\text{O}_4$  and  $\text{GO-CeO}_2@\text{CoFe}_2\text{O}_4$  with the saturation magnetization ( $M_s$ ) are 74.9 and 59.5 emu/g respectively. The introduction of  $\text{GO-CeO}_2$  support to the  $\text{CoFe}_2\text{O}_4$  nanoparticle could form the single domain sheets in order to create superparamagnetic behavior. The surface phenomena of GO support enhance the surface charge of carriers helps in reducing the magneto-static energy of the  $\text{CoFe}_2\text{O}_4$  nanoparticle. This leads to the superparamagnetic activity on the composite. The appreciable  $M_s$  value and low  $H_c$  value of nanocomposite makes them as soft magnet materials which allows the magnetization at a faster rate on the nanocomposite with a low applied field. According to the formula,  $M_s = \Phi m_s$ , where  $\Phi$  is the volume fraction of the magnetic particles and  $m_s$  is the saturating moment of a single particle in a compound (Cai et al. 2017; Gandhi et al. 2011). The surface interactions between the cobalt ferrite nanoparticles in the nanocomposite are less compared to the pure  $\text{CoFe}_2\text{O}_4$  nanoparticle which also contributes to the lower value of  $M_s$ . This attraction and re-dispersion properties have been managed in presence of external magnetic field which showed a good water dispersibility and magnetic separation from the sewage aqueous waste.

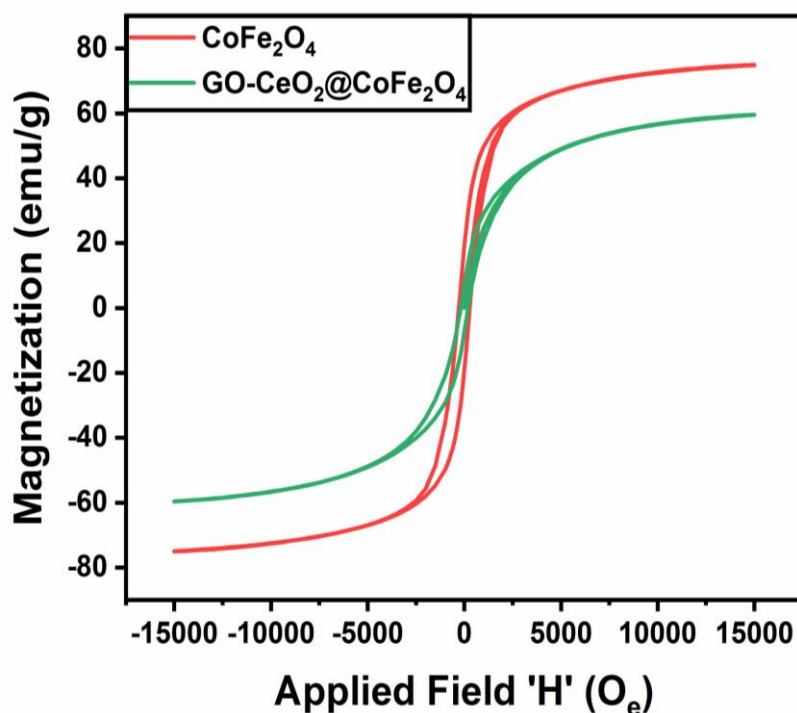


Figure 6.9. Applied magnetic field plot of  $\text{CoFe}_2\text{O}_4$  and  $\text{GO-CeO}_2@\text{CoFe}_2\text{O}_4$

Table 6.1: The  $M_s$  and  $H_c$  values of  $\text{CoFe}_2\text{O}_4$  and  $\text{GO-CeO}_2@\text{CoFe}_2\text{O}_4$

Type of Compounds	Magnetic properties	
	$M_s$	$H_c$
$\text{CoFe}_2\text{O}_4$	74.91	303.00
$\text{GO-CeO}_2@\text{CoFe}_2\text{O}_4$	59.54	201.10

### 6.3.8 $\text{N}_2$ Adsorption-Desorption Isotherms (BET)

The BET surface area was examined using the experimental values with relative pressure ( $P/P_0$ ) and the total pore volume measured from the  $\text{N}_2$  amount absorbed at the ( $P/P_0$ ) and the average pore size distribution of the mesopores evaluated using the Barret–Joyner–Halenda (BJH) methods from the desorption isotherm. The composite, ceria and nanoparticle exhibited the type-IV  $\text{N}_2$  adsorption and desorption isotherm with type H3 hysteresis loop which is a characteristic feature of mesoporous nature (Sing 1982; Wu et al. 2019; Xiang et al. 2017). The BET surface area of the  $\text{CoFe}_2\text{O}_4$ ,  $\text{GO-CeO}_2$  &  $\text{GO-CeO}_2@\text{CoFe}_2\text{O}_4$  are given in figure 6.10 and 6.11. The  $\text{N}_2$  absorption measurements investigated that the BET surface area of the composite is considerably higher than the nanoparticle and the nanoceria even affecting the pore volume of the samples which is shown in the table 6.2. Due to the introduction of  $\text{GO-CeO}_2$  layer on to the surface of Cobalt ferrite nanoparticle which have increased the surface area of nanoparticle by several times shown in figure 6.10. For the pore size distribution, the

average pore diameter of nanoparticle, ceria and composite are 4.8 nm, 5.2 nm & 9.8 nm respectively, indicating mesoporous characteristics of these samples. This may be due to the polymerization of nanoparticle which have increased the size of mesopore which has an impact on pore size and volume. Finally, the synthesized materials showed the presence of mesoporous nature which further assisted for the diffusion of pollutants through this porous material as well as facilitating the high removal rate for the removal of toxic dyes and metal ions from the environment.

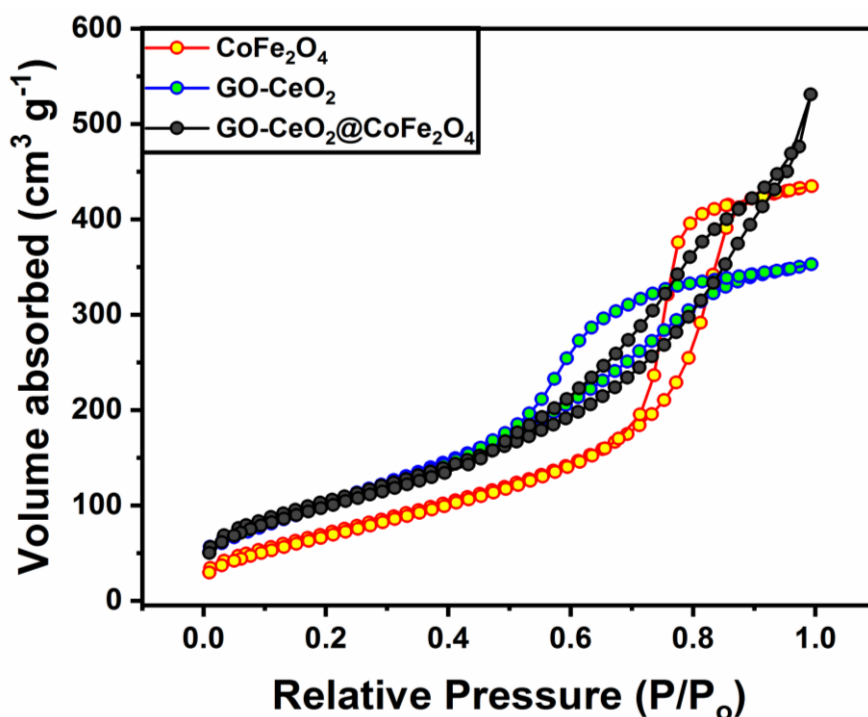
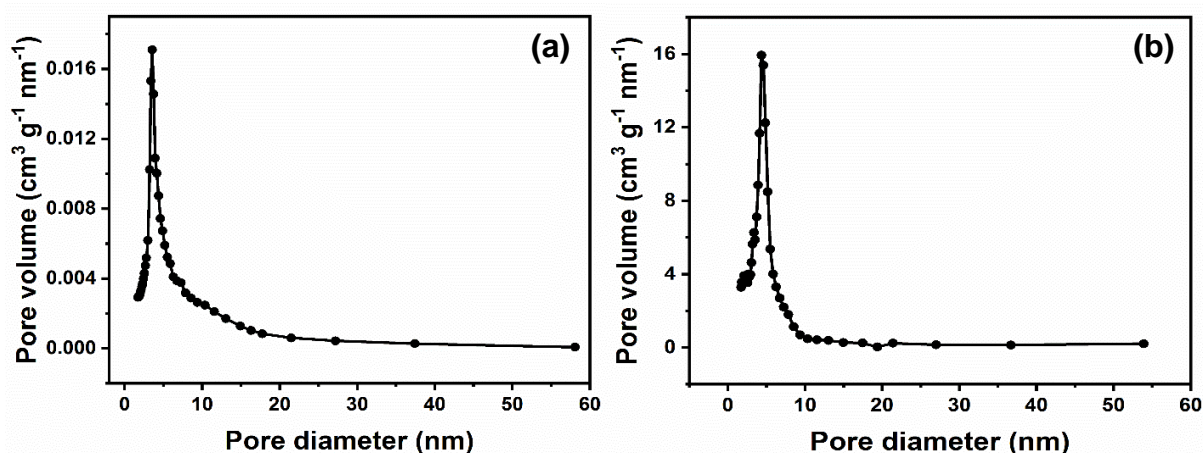


Figure 6.10. N<sub>2</sub> adsorption-desorption isotherms of CoFe<sub>2</sub>O<sub>4</sub>, GO-CeO<sub>2</sub> & GO-CeO<sub>2</sub>@CoFe<sub>2</sub>O<sub>4</sub>



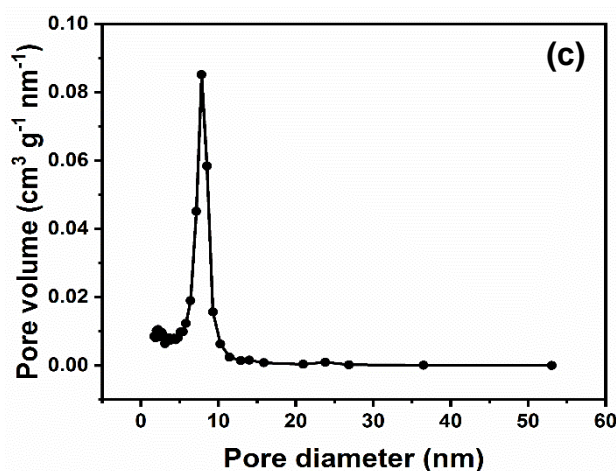


Figure 6.11. Pore size distribution curves of a)  $\text{CoFe}_2\text{O}_4$ , b)  $\text{GO-CeO}_2$  & c)  $\text{GO-CeO}_2@\text{CoFe}_2\text{O}_4$

Table 6.2: Pore characteristics of  $\text{CoFe}_2\text{O}_4$ ,  $\text{GO-CeO}_2$  &  $\text{GO-CeO}_2@\text{CoFe}_2\text{O}_4$

Samples	$S_{\text{BET}}$ ( $\text{m}^2 \text{g}^{-1}$ )	$V_p$ ( $\text{cm}^3 \text{g}^{-1}$ )	$d_p$ (nm)
$\text{GO-CeO}_2$	<b>168.7</b>	<b>0.48</b>	<b>5.2</b>
$\text{CoFe}_2\text{O}_4$	<b>160.1</b>	<b>0.71</b>	<b>4.8</b>
$\text{GO-CeO}_2@\text{CoFe}_2\text{O}_4$	<b>178.2</b>	<b>0.52</b>	<b>9.8</b>

### 6.3.9 Zeta potential

Zeta potential measurements have investigated to know the electronic interactive mechanism of the pollutants and the adsorbent in a solution. Normally, the isoelectric point (IEP) of GO is reported as 3-4, due to the availability of abundant oxygen functional groups on its surface and the edges exhibit predilection to deprotonate; further the surface of GO would be negatively charged around pH- 5.5 (Arbabi et al. 2015). Therefore, the zeta potential of the composite showed the 28.24 to - 35.64 mV in the pH range 2-12 which confirmed that the surface of  $\text{GO-CeO}_2@\text{CoFe}_2\text{O}_4$  is positively charged in acidic solution and it is negatively charged in alkaline condition. Due to the presence of  $\text{CoFe}_2\text{O}_4$  which is slightly positively charged than the GO, the composite showed IEP of pH-5.4. Further, increase in pH i.e., in alkaline medium, makes the surface of  $\text{GO-CeO}_2@\text{CoFe}_2\text{O}_4$  negatively charged facilitated the dissociation or deprotonation of  $\text{GO-CeO}_2@\text{CoFe}_2\text{O}_4$  which resulted in electrostatic interactions between  $\text{GO-CeO}_2@\text{CoFe}_2\text{O}_4$  composites and the cationic pollutants such as MB, RB,  $\text{Pb(II)}$  and  $\text{Cd(II)}$  ions. In order to confirm the electrostatic interactions between the  $\text{GO-CeO}_2@\text{CoFe}_2\text{O}_4$  and the cationic pollutants especially MB, the effect of solution pH on the adsorption performance was evaluated. Figure 6.12 shows that the  $\text{GO-CeO}_2@\text{CoFe}_2\text{O}_4$  adsorbed the MB faster at a higher pH is ascribed to the strong electrostatic interactions which have been confirmed by zeta

potential measurements due to its more negative charge at high pH values. Due to the surface possessing net positive charge at lower pH, GO-CeO<sub>2</sub>@CoFe<sub>2</sub>O<sub>4</sub> composite attract anionic species through electrostatic interactions which remain conducive for the adsorption of anionic pollutants.

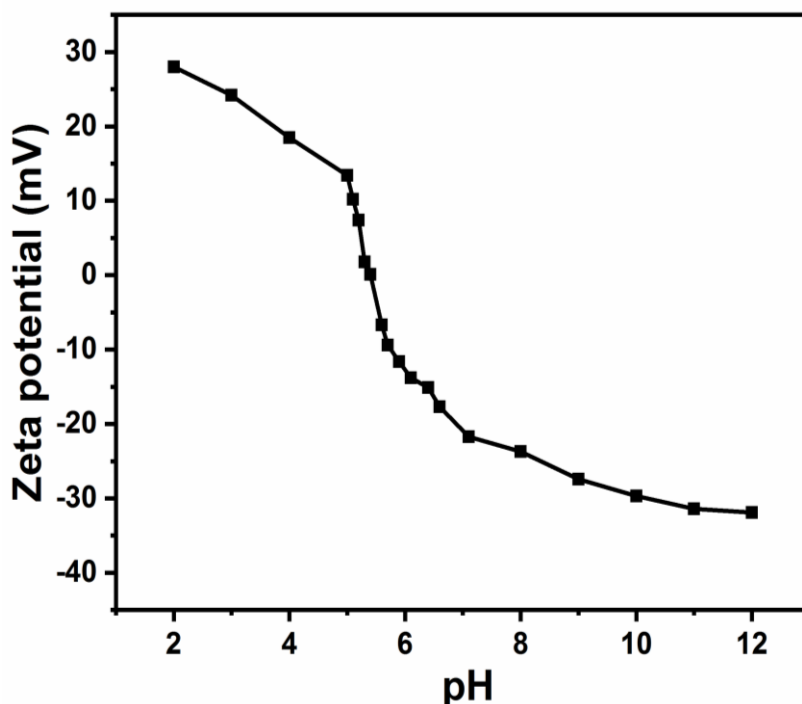
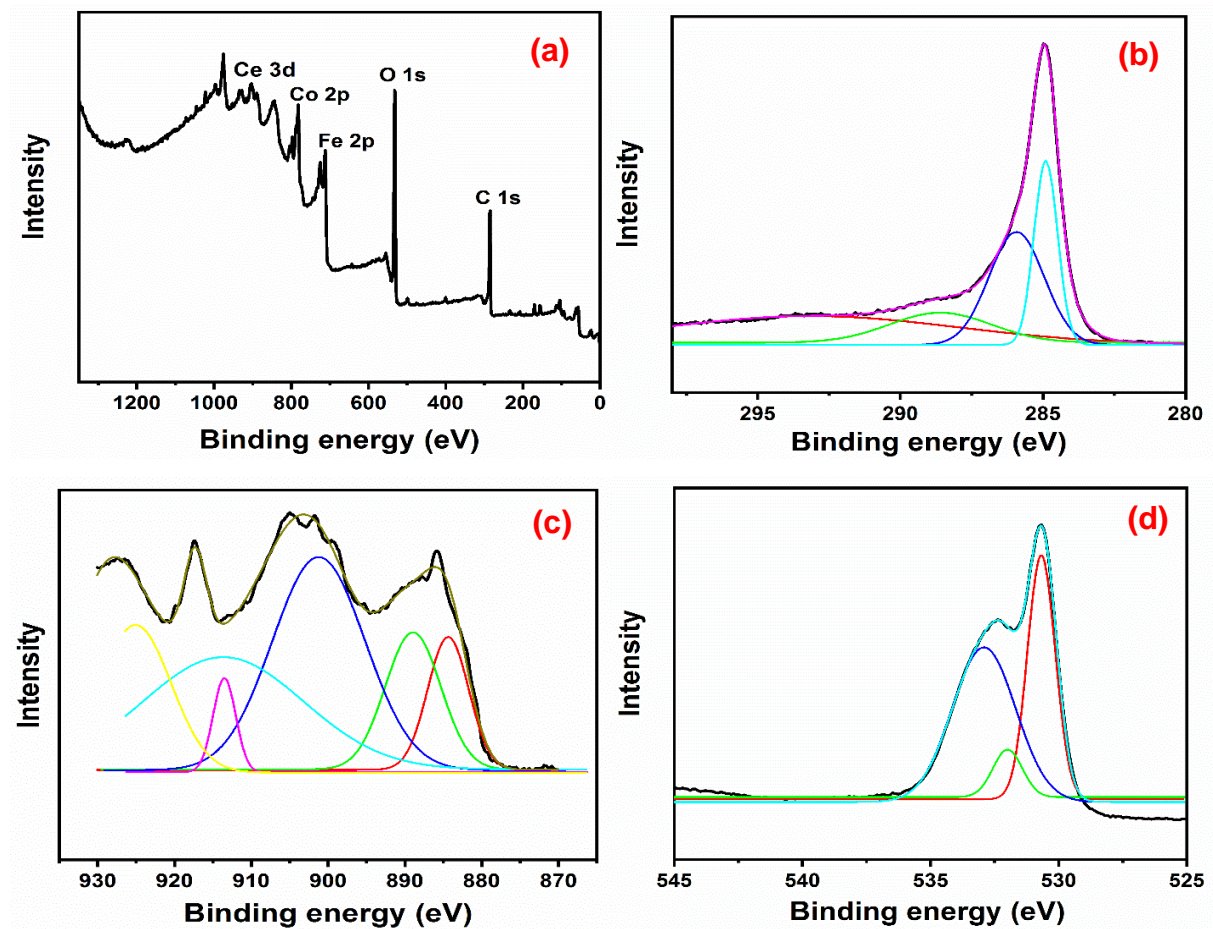


Figure 6.12. Zeta potential of GO-CeO<sub>2</sub>@CoFe<sub>2</sub>O<sub>4</sub> at different pH

### 6.3.10 X-ray Electron Spectroscopy (XPS)

Figure 6.13(a-f) shows the XPS surface analysis of GO-CeO<sub>2</sub>@CoFe<sub>2</sub>O<sub>4</sub> nanocomposite. The chemical composition with their respective binding energies are Co, Fe, O, C and Ce respectively. In the deconvoluted spectrum, the Gaussian peaks of C 1s spectra were at 284.6, 285.7, 286.8 and 287 eV attributed to the C-C bond (sp<sup>2</sup>) of graphene, C-OH group, C-O bond and the C=O bond respectively (Chandra et al. 2010; Wu et al. 2011). Figure 6.14(d) represented the O 1s spectra with three peaks; the peak at 530.4 eV binding energy value is a characteristic peak of the lattice oxide; that is the oxygen group of the metal oxides such as Fe-O and Co-O of CoFe<sub>2</sub>O<sub>4</sub> along with the other two peaks around 531.9 eV and 534.7 eV corresponded to the surface adsorbed oxygen possessing moiety such as M-OH or water molecules (Brundle et al. 1977; Xia et al. 2007). The binding energy values at 779.43 eV and 792 eV corresponds to Co 2p<sub>3/2</sub> and Co 2p<sub>1/2</sub> which occupied octahedral and tetrahedral lattice sites for Co<sup>2+</sup> ions. Figure 6.13(f) shows the two peaks at 710.1 eV and 727 eV corresponded to the Fe 2p<sub>3/2</sub> on octahedral sites and Fe 2p<sub>1/2</sub> on tetrahedral sites on Fe<sup>3+</sup> ions. The distribution

of Fe 2p peaks is about 70% on the octahedral sites and around 30% on tetrahedral sites which is in close agreement with  $\text{CoFe}_2\text{O}_4$ . It also confirmed that the  $\text{CoFe}_2\text{O}_4$  nanoparticle deformation have not taken place during the synthesis of nanocomposite (Chen et al. 2016). Figure 6.13(c) shows the Ce 3d peaks which showed that the  $3d_{5/2}$  and  $3d_{3/2}$  spin orbital components respectively. The  $\text{Ce}^{4+}$  peaks corresponded to  $u'''= 916.5$  eV,  $u''= 907.2$  eV,  $u= 900.8$  eV,  $v'''= 898.2$  eV,  $v''= 888.5$  eV and  $v= 882.2$  eV whereas the  $\text{Ce}^{3+}$  peaks appeared only at  $u'= 903.6$  eV and  $v'= 885.6$  eV respectively (Wu et al. 2019). This confirmed that the Ce 3d is mostly tetravalent and also presence of high amounts of oxygen vacancies on the ceria (Burroughs et al. 1976).





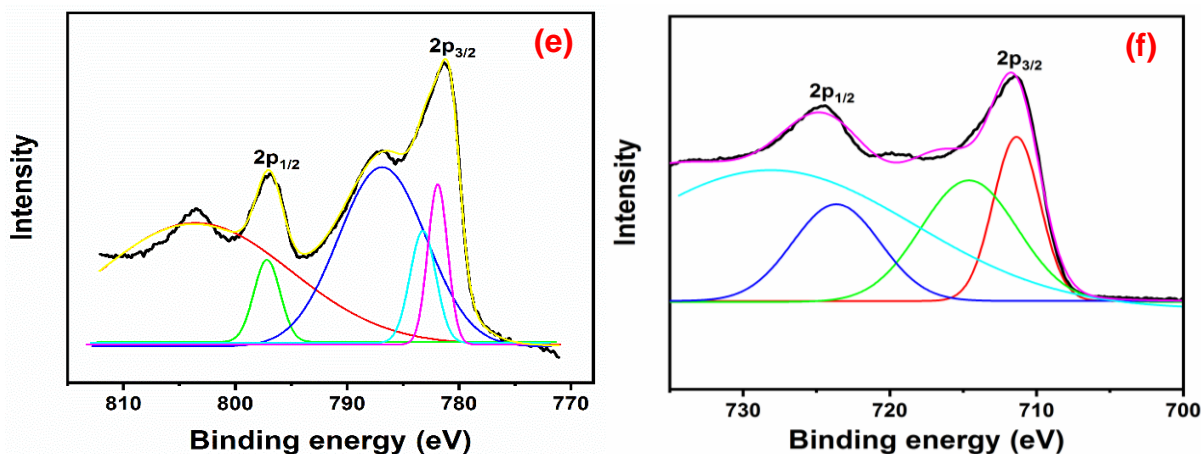


Figure 6.13. XPS spectra of GO-CeO<sub>2</sub>@CoFe<sub>2</sub>O<sub>4</sub>: (a) Elemental survey, (b) C 1s, (c) Ce 3d, (d) O 1s, (e) Co 2p & (f) Fe 2p.

### 6.3.11 Effect of pH of pollutants on adsorption

Initial solution pH plays a prominent role in determining the protonation or deprotonation of functional groups, competing ability between different groups, their solubility and existence of dyes in monomer or dimeric forms can be explained through this adsorption phenomenon. The adsorption efficiency in nanocomposite is determined for all the 5 pollutants in a batchwise manner at varied pH conditions. The pH range of 2-10 examined to know the maximum adsorption rate, which is useful to remove harmful pollutants from the wastewater shown in figure 6.14. Due to the availability of various hydroxyl groups and carboxyl groups on the adsorbent, it helps in binding the adsorbates through hydrogen bonding and chelation effects. For cationic dyes and metal ions, at lower pH (< 3.5), the rate of adsorption is very low and it can be explained by: i) proton donor functional groups such as OH & COOH groups made the sites for adsorption as less and inactive, making the low affinity between the adsorbent and cationic pollutant. ii) the surface complexation theory to determine the H<sup>+</sup> ions which hampered the active sites for adsorption. CR is an anionic dye, which contains both amino and sulphite groups leading to be acidic with an isoelectric point of approx. 3. At low pH, due to the availability of more H<sup>+</sup> ions in the system and the GO-CeO<sub>2</sub>@CoFe<sub>2</sub>O<sub>4</sub> surface acquires net positive charge by the intake of H<sup>+</sup> ions and the adsorption of CR dye takes place. At this pH, CR acquires cationic form that resulted in ammonium and azonium rich tautomeric forms which led to the π-π\* transition of the azo group. The weak adsorption of CR at basic pH is due to the availability of excess OH<sup>-</sup> ions which gets competed with CR dye anions approaching towards the adsorbent surface. CR loses the stability of chromophoric group at higher pH in alkaline condition leading to the change in color to red and it is different from original red color

(CR dye color). Further, the percentage removal of CR increased at lower pH due to the good electrostatic attractions in between the adsorbent and CR dye.

In the cationic dyes like MB & RB, the rate of adsorption enhanced due to the increase in pH of solution as well as the rise in deprotonation resulting in the decrease of competing  $H^+$  ions. For MB dye, at lower pH, the cations of MB compete with  $H^+$  ions which reduces the adsorption sites. In case of RB dye at lower pH, the amino group gets converted into tertiary ammonium cation leaving the COOH group in neutral condition to form cationic and monomeric form. At higher pH ( $>4.2$ ), RB dye existed in zwitter ionic form due to the electrostatic attractions between xanthene and carboxyl group of monomers into dimer form and the rate of adsorption increased by 81 to 94% and further it became stable.

The effect of pH on the heavy metal ions in wastewater is studied by maintaining the pH from 2-8 for 6h. This is important because the pH affects the chemistry of adsorbent, binding region and the chemical interaction which mobilizes the ionization state of various functional groups on adsorbent surface shown in figure 6.15. At lower pH, both the metal ions removal rate was very less due to the production of large quantities of  $H^+$  ions in the aqueous waste. Because of this, functional group protonation which takes place over the surface of nanoadsorbent, competed with metal ions led to the creation of coulombic repulsion/electrostatic interactions which significantly reduces the adsorption process. Further increase in the pH of the solution reduced the amount of  $H^+$  ions in to the aqueous solution and the amount of metal ions adsorbed on its surface have enhanced. The pH of the metal ions solution is explained by pH drift method (Haddad et al. 2013). If the  $pH < pH_{PZC}$ , the surface of nanoadsorbent is positively charged thereby increased the electrostatic repulsions with the positively charged metal ions and during this time period, all the  $H^+$  ions competed with the active sites of nanoadsorbent leading to the inhibition of metal ions adsorption. Again, at  $pH > 8$ , the adsorption of metal ions reduced through the aggregation of metal ions with the hydroxyl groups to form precipitates. These conclusions clearly indicates the removal rate of Pb(II) & Cd(II) enhanced within the pH range of 2-8 and thereafter reduced beyond 8. The adsorption of heavy metal ions Pb(II) & Cd(II) at extreme basic pH conditions is explained by the precipitate formation which resulted in the reduction of metal ions in solution. According to Chen et.al, the initial pH of solution greatly affected the metal adsorption mechanism by GO-CeO<sub>2</sub>@CoFe<sub>2</sub>O<sub>4</sub> nanocomposite resulted in the formation of changes of metal-adsorbent complex during the adsorption (Chen et al. 1997). From the above explanation, figure 6.14 adsorption of pollutants at the pH are 7.1, 6.4, 5.2, 6.1 & 5.8 for the cationic MB, RB dyes, anionic CR and heavy metal ions Pb(II), Cd(II) respectively.

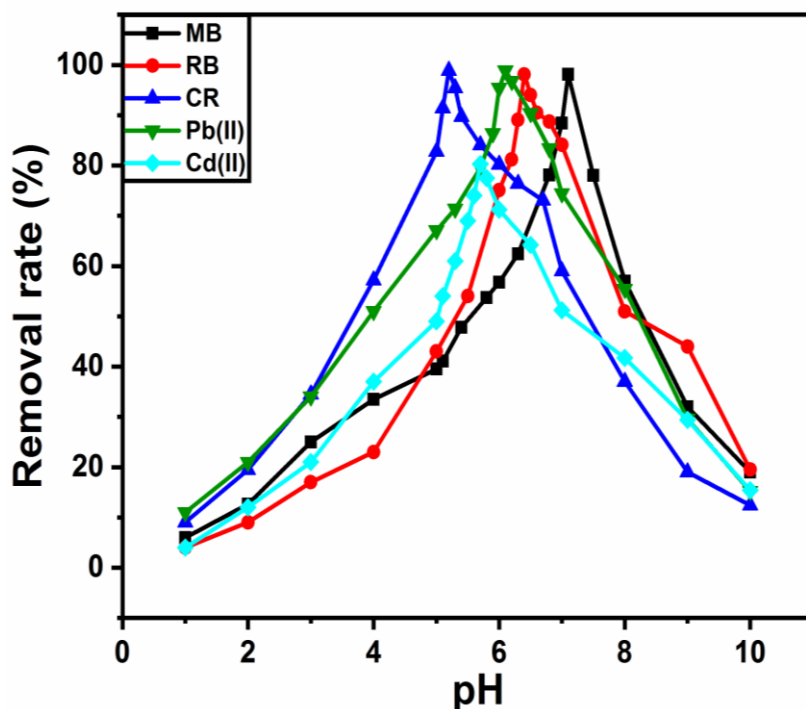


Figure 6.14. Adsorption of a) MB b) RB c) CR d) Pb(II) & e) Cd(II) as a function of concentration at various temperature

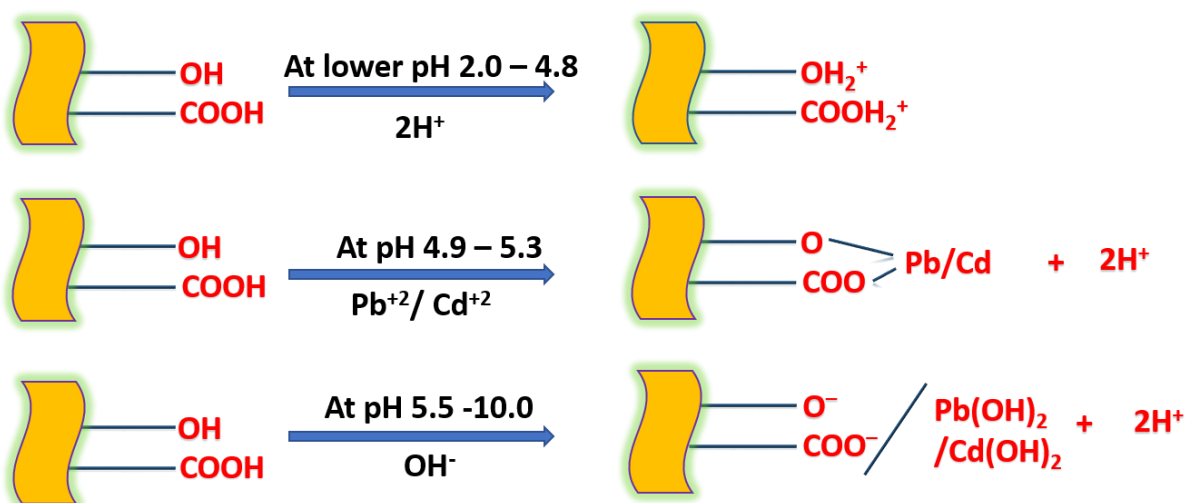


Figure 6.15. Proposed mechanism of the metal ions: Pb(II) & Cd(II)

### 6.3.12 Effect of initial concentration of adsorbent on adsorption capacity

The adsorption capacity of the adsorbent was examined by varying the concentration range from  $0.001\text{ g L}^{-1}$  to  $1\text{ g L}^{-1}$  at a specific. The adsorption rate increased with the increase in dosage capacity of adsorbent as shown in figure 6.16(a-e). The adsorption of RB marked a relative increase from 23% to 98.12%, MB with an increase of 33.5% to 98.16%, CR with an increase of 19.5% to 98.86%, Pb(II) with a maximum adsorption of 98.87%, and Cd(II) with a steadily

increase up to 80.27% was observed. The overall increase in the removal rate of pollutants is due to the presence of large number of active sites and further increase in dosage of adsorbent created a collision rate between the composite and the adsorbate in the aqueous solution. It led to the aggregation of effective adsorbing sites on the surface resulting in the reduction of adsorption efficiency.

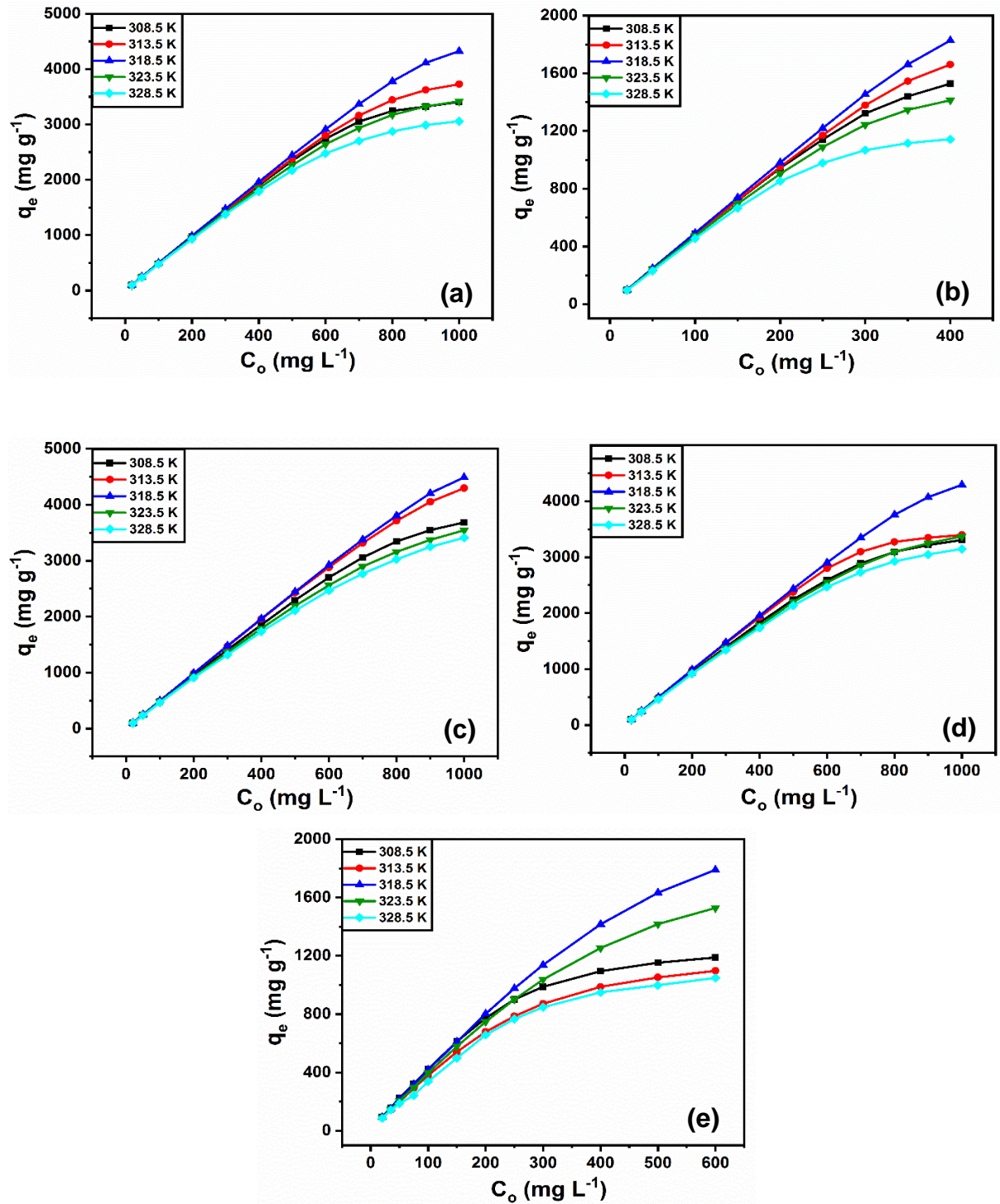


Figure 6.16. Adsorption of a) MB b) RB c) CR d) Pb(II) & e) Cd(II) as a function of initial concentration of adsorbate on adsorption capacity

### 6.3.13 Effect of time on adsorption

The kinetic studies stabilized using the effect of time intervals with respect to the amount of adsorption takes place on adsorbent surface are shown in figure 6.17. During the initial phase of adsorption, the adsorption rate is faster for CR, RB and Pb(II) when compared to the other pollutants. The period of time for adsorption during the initial phase is higher, i.e., the availability of large number of active sites on the nanoadsorbent surface which in turn maintained the stability of the process.

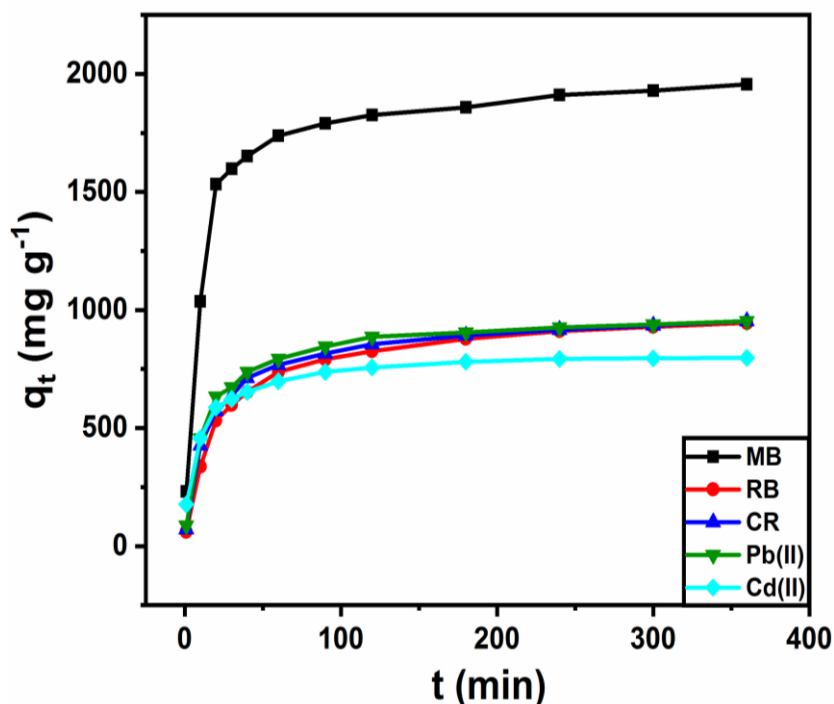


Figure 6.17. Effect of time (t) with the adsorption capacity ( $q_t$ )

### 6.3.14 Effect of adsorbent dosage on adsorption capacity

From the figure 6.18(a-e), due to the increase in adsorbent amount  $0.0005 \text{ g L}^{-1}$  to  $0.05 \text{ g L}^{-1}$ , the capacity to get adsorbed on its surface increases gradually. This results in the increase in removal efficiency of adsorbent and it attains a highest peak in rate of adsorption for all the pollutants. It is due to the presence of steady amount of adsorbate solution remained in the aqueous wastewater which remained constant during the entire time for adsorption and as the result, the increase in adsorbent molecules which generated a large number of active sites on the surface for the effective adsorption process. However, there is a further increase in adsorbent dosage with constant adsorbate concentration led to the unsaturated active sites upon the surface of  $\text{GO-CeO}_2@ \text{CoFe}_2\text{O}_4$ . Due to the lack of proper amount of adsorbate in wastewater, the adsorption efficiency gradually decreases on the adsorbent.

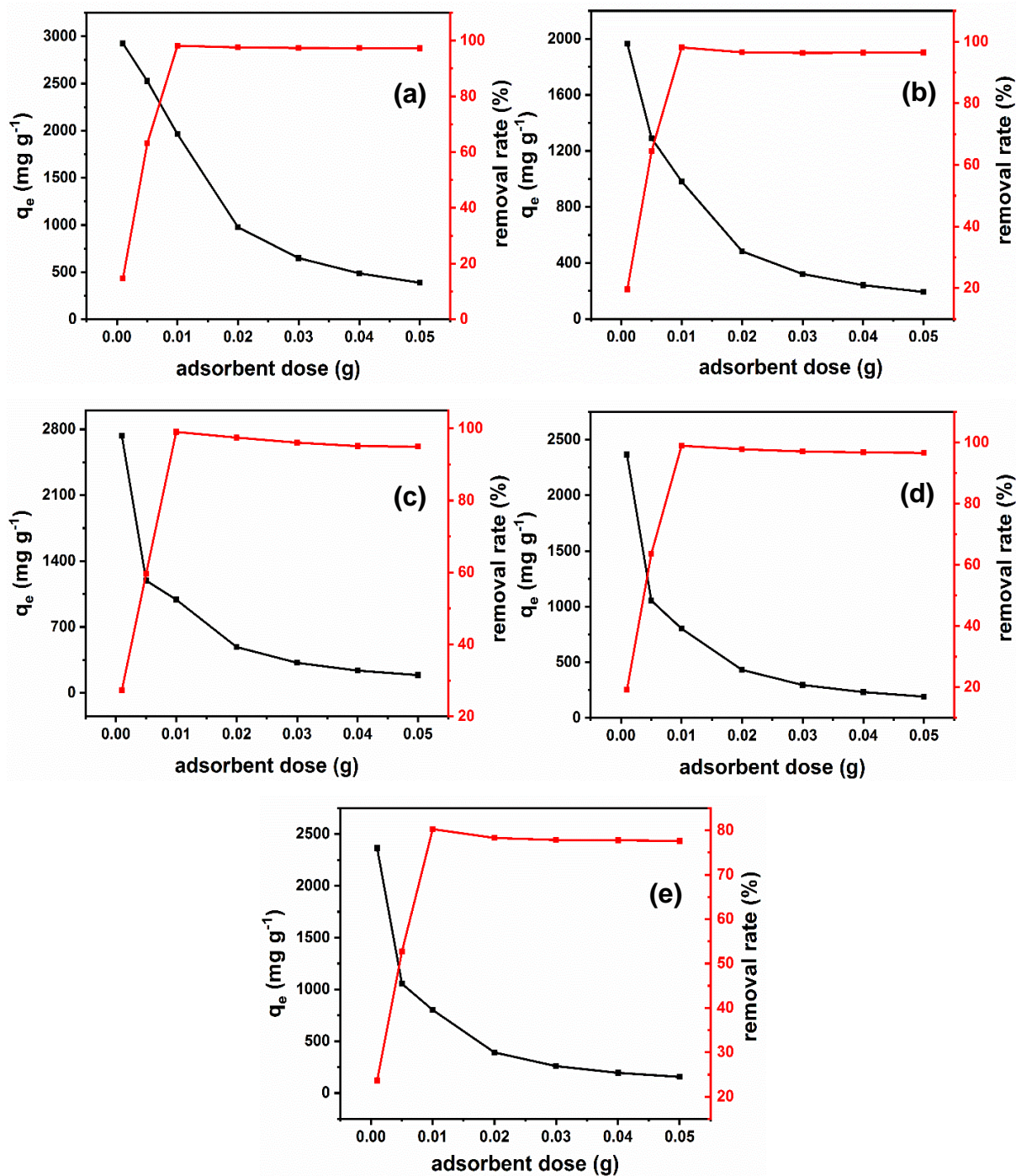


Figure 6.18. Different adsorbent doses with the adsorption capacity  $q_e$  a) MB, b) Rb, c) CR, d) Pb(II) and d) Cd(II)

### 6.3.15 Effect of Ionic strength

Studies on the ionic strength is performed to know the effect of adsorption for various pollutants. The ionic strength when we considered in mainstream sewage system, they are various contaminants along with the dyes and metal ions shown in figure 6.19 and 6.20. Among them, NaCl is present as a natural pollutant and easily gets mixed with the existing simulated

wastewater before the adsorption phenomena is followed. The presence of sodium ions in the aqueous wastewater enhances the ionic strength and reduced the electrostatic attraction between the adsorbates and the GO-CeO<sub>2</sub>@CoFe<sub>2</sub>O<sub>4</sub> and also reduced the surface charge on the nanoadsorbent. Further, the Na<sup>+</sup> ions which are preoccupied on the active sites reduced the adsorption efficacy. However, the addition of NaCl is 10 times to that of the pollutants, the removal rate of adsorbates are decreased by MB 10.4%, RB 16.1%, CR 12.1%, Pb(II) 14.3% & Cd(II) 15.9%. The presence of impurities in lower proportion in real wastewater along with pollutants is justified to be an efficient combination for the removal of pollutants in practical usage.

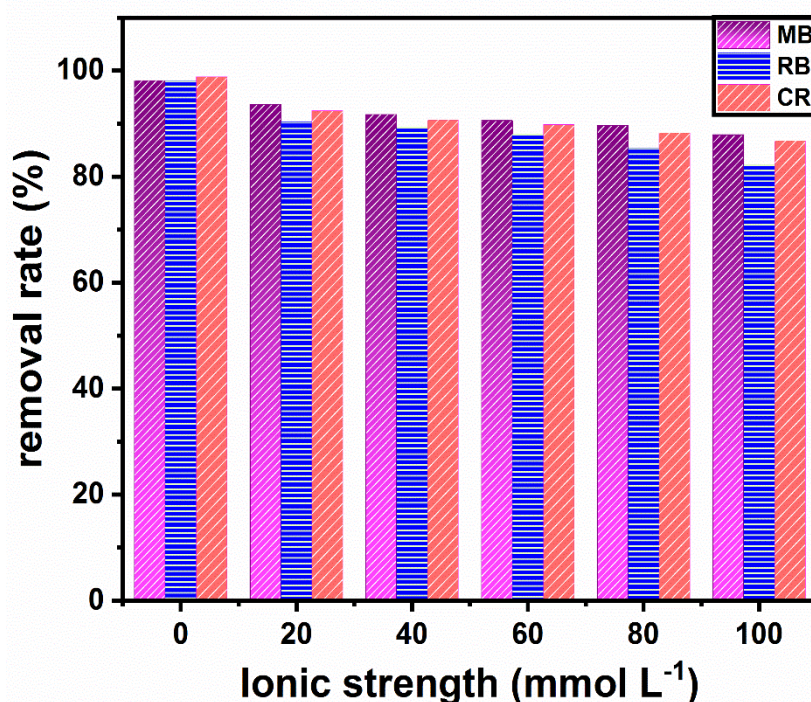


Figure 6.19. Effect of ionic strength with the removal rate of dyes a) MB, b) RB & c) CR

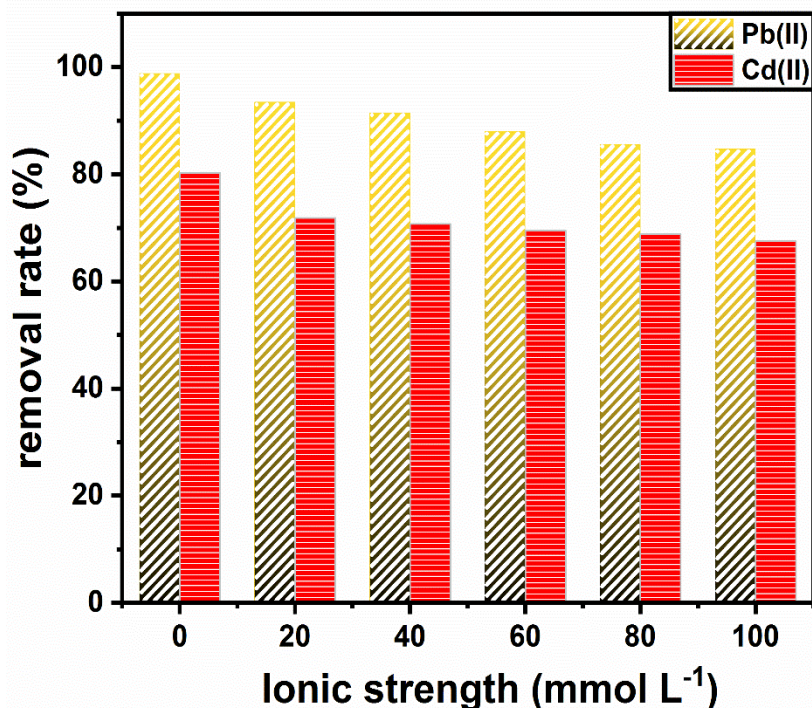


Figure 6.20. Effect of ionic strength with the removal rate of metal ions a) Pb(II) and b) Cd(II)

### 6.3.16 Adsorption Isotherm Studies

Isotherm studies which reflected the adsorption tests and their mechanism involved in the process of interaction between the pollutants and the adsorbent GO-CeO<sub>2</sub>@CoFe<sub>2</sub>O<sub>4</sub>. The adsorption tests performed at five different temperature (i.e., 308.5 K, 312.5 K, 318.5 K, 323.5 K & 328.5 K) for the adsorbates i.e., dyes and metal ions MB, CR, Pb(II) each 0-1000 mg L<sup>-1</sup>, Cd(II) 0-600 mg L<sup>-1</sup> & RB 0-400 mg L<sup>-1</sup> respectively shown in figure 6.21-6.25. The models of isotherm studies i) Langmuir isotherm model stated that the GO-CeO<sub>2</sub>@CoFe<sub>2</sub>O<sub>4</sub> as an adsorbent where its active sites are at equilibrium with monolayer adsorption upon homogeneity nature on its surface with the pollutant moieties; ii) Freundlich isotherm model is a multi-layered upon a heterogenetic surface through a non-uniformity in heat distribution on its surface of adsorbent; iii) D-R isotherm model justified the physico-chemical mechanisms predicted by using the formula; iv) Temkin model justified the rise in possible forces for the dyes and metal ions upon the nanoadsorbent along with effect of temperature which have been calculated by the linear relationship between the heat of adsorption and the measured values. All these isotherms predicted the uniformity in adsorption of pollutant and the interpreted data calculated from the experimentally obtained data and plotted their graph in non-linear method using the equations 6.5-6.8.



$$q_e = \frac{Q_m K_L C_e}{1 + K_a C_e} \quad (6.5)$$

$$q_e = K_f C_e^{1/n} \quad (6.6)$$

$$q_e = \frac{RT}{b_T} \ln A_T C_e \quad (6.7)$$

$$q_e = (q_s) \exp(-K_{DR} \varepsilon^2) \quad (6.8)$$

From the above eq. 4.,  $Q_m$  ( $\text{mg g}^{-1}$ ) corresponded to the maximum adsorption equilibrium of GO-CeO<sub>2</sub>@CoFe<sub>2</sub>O<sub>4</sub> was explained using monolayer with the pollutants per unit mass.  $K_L$  is known as Langmuir adsorption coefficient ( $\text{L mg}^{-1}$ ) which explained the energy of adsorption.  $K_f$  is an approximation constant and the factor  $1/n$  described as function of adsorption strength.  $1/n$  factor value higher than one which corresponds to the cooperative adsorption upon nanocomposite surface.  $K_f$ , value enhances with the increases in adsorption capacity. From Temkin model, where  $R$  corresponded to the Universal gas constant ( $8.314 \text{ J/mol/K}$ ),  $A_T$  refers to the maximum binding constant ( $\text{L g}^{-1}$ ) and  $b_T$  refers to the heat of adsorption ( $\text{J mol}^{-1}$ ).  $q_s$  ( $\text{mol g}^{-1}$ ) termed to be maximum adsorption capacity of D-R model used to find the porosity of GO-CeO<sub>2</sub>@CoFe<sub>2</sub>O<sub>4</sub> with the energy of adsorption ( $E$ ),  $K_{DR}$  ( $\text{mol}^2/\text{k/J}^2$ ) refers to the D-R isotherm constant, linked to the free energy required for adsorption per unit mass of the adsorbate,  $\varepsilon$  corresponds to the Polanyi potential using the following expression:

$$\varepsilon = RT \ln \left( 1 + \frac{1}{C_e} \right) \quad (6.9)$$

To calibrate the mean free energy for the adsorbent we calculated by using the following equations:

$$E = \frac{1}{(2B_D)^{1/2}} \quad (6.10)$$

All the isotherm models were calibrated and optimized with the experimental data to measure the (COD), coefficient of determination  $r^2$  using the following expression with the graphs plotted in non-linear pattern in origin software.

$$r^2 = \frac{(q_m - \bar{q}_e)^2}{(q_m - \bar{q}_e)^2 + (q_m - q_e)^2} \quad (6.11)$$

Here, the graphs represented to the various pollutants adsorbed onto per unit weight of GO-CeO<sub>2</sub>@CoFe<sub>2</sub>O<sub>4</sub> ( $q_e$ ) to the adsorbate solution remained after the process within a specified time ( $C_e$ ) which are represented in Figure 6.21-6.25. From the Table 6.3 & 6.4, the results

revealed a designated pattern within the data obtained by comparing the adj.  $R^2$  values from the isothermal models such as Langmuir > Freundlich > Temkin > D-R.

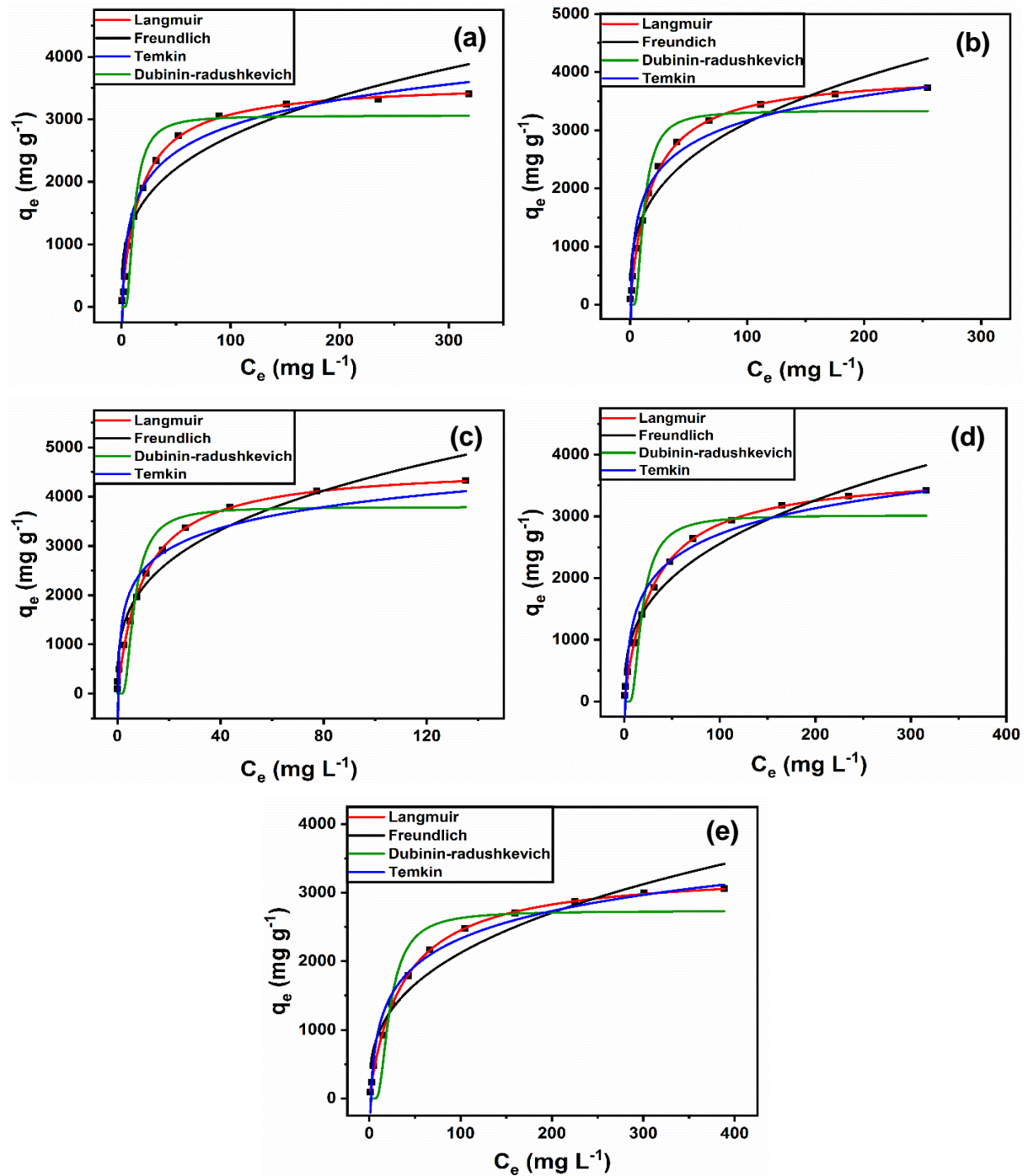


Figure 6.21. Adsorption isotherms at five different temperatures for MB: a) 308.5 K b) 313.5 K c) 318.5 K d) 323.5 K & e) 328.5 K

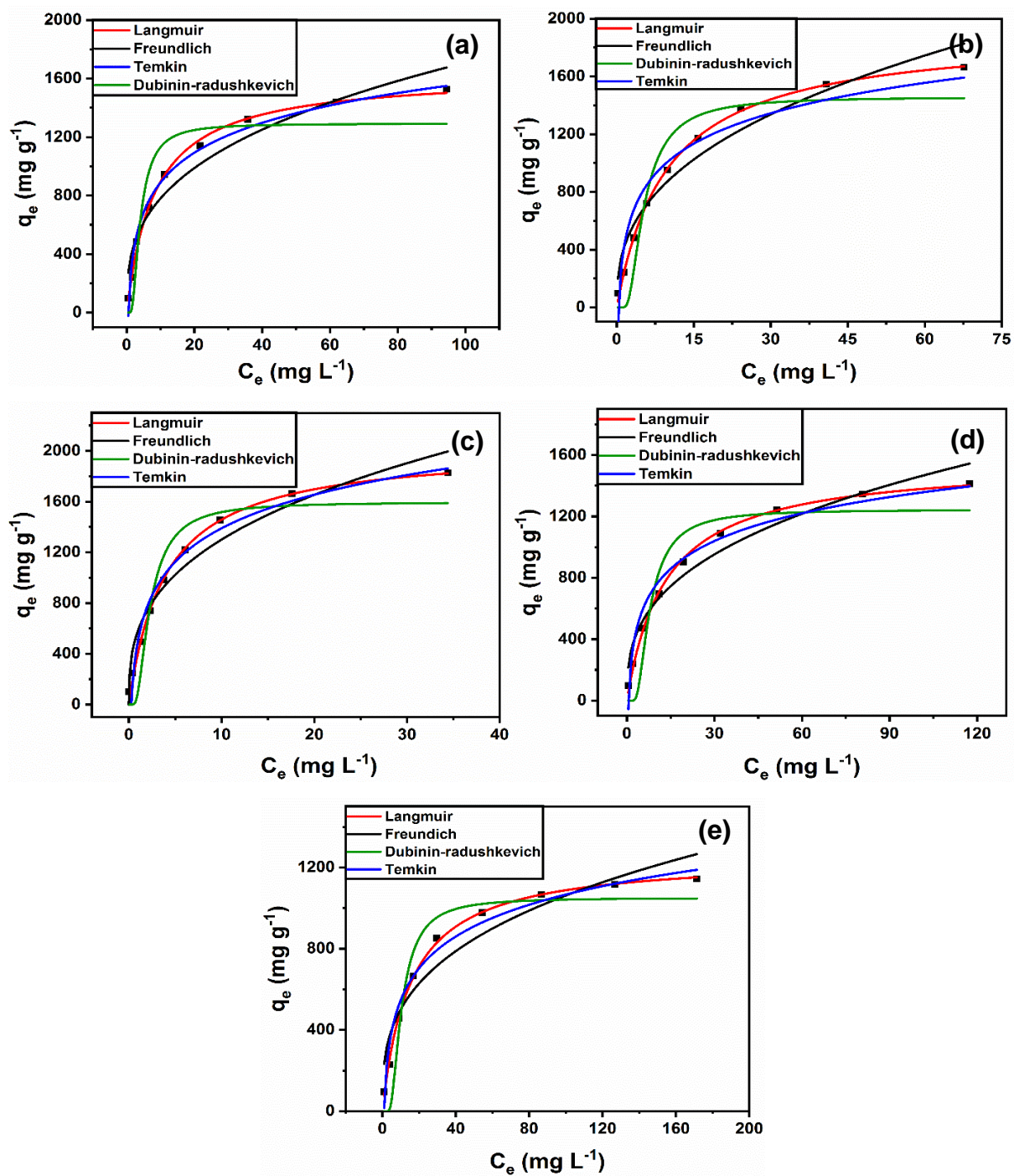


Figure 6.22. Adsorption isotherms at five different temperatures for RB: a) 308.5 K b) 313.5 K c) 318.5 K d) 323.5 K & e) 328.5 K

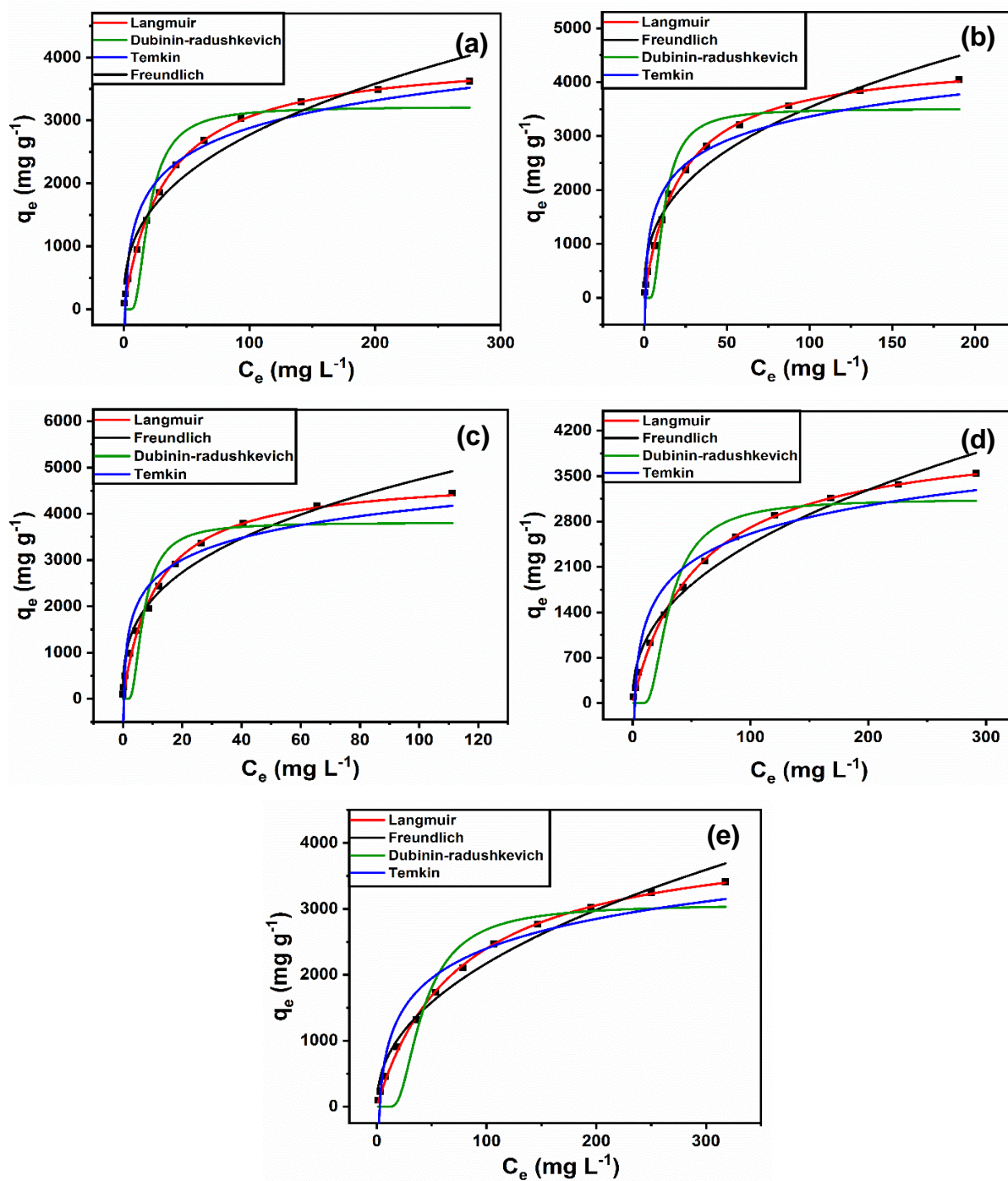


Figure 6.23. Adsorption isotherms at five different temperatures for CR: a) 308.5 K b) 313.5 K c) 318.5 K d) 323.5 K & e) 328.5 K

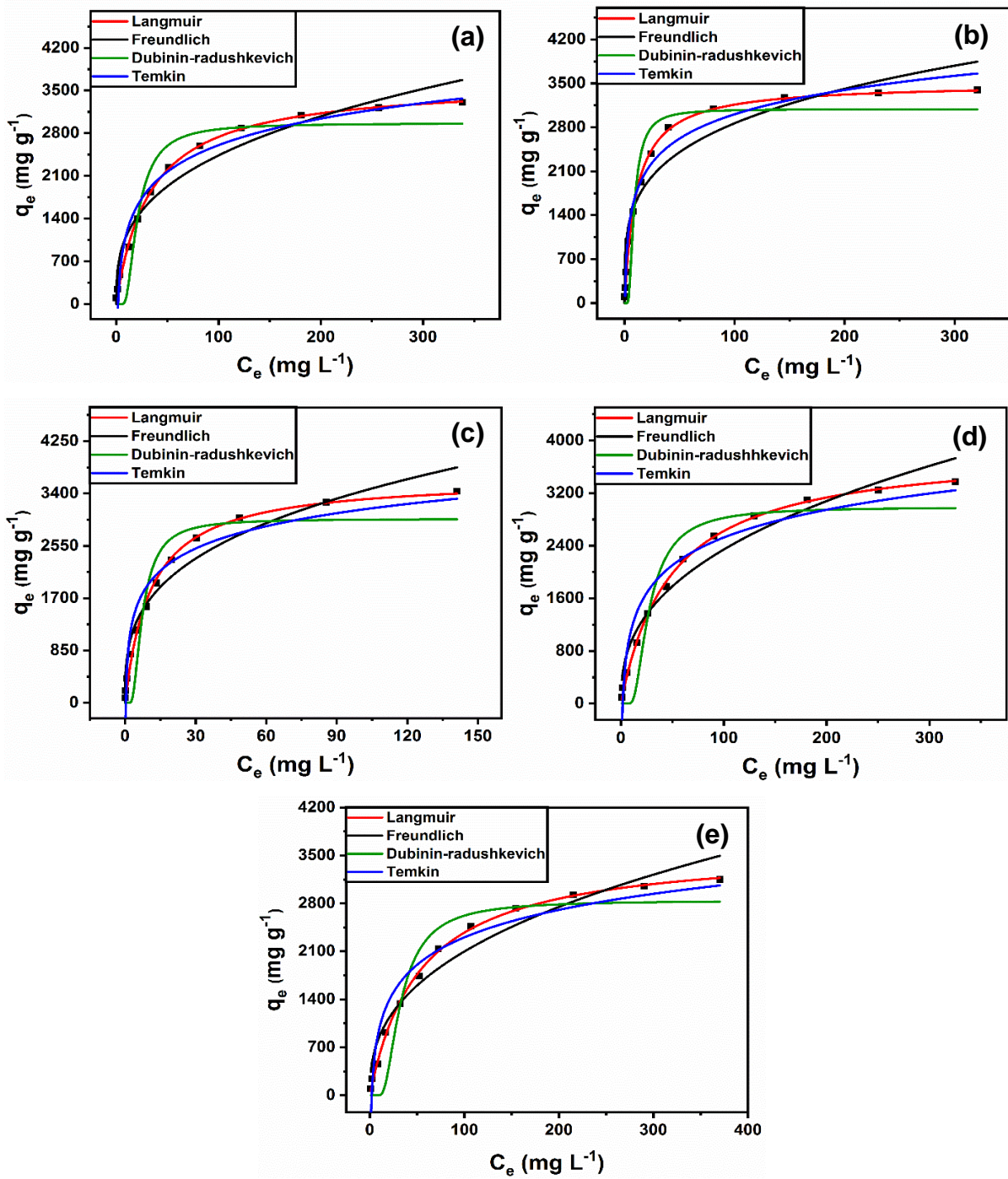


Figure 6.24. Adsorption isotherms at five different temperatures for Pb(II): a) 308.5 K b) 313.5 K c) 318.5 K d) 323.5 K & e) 328.5 K

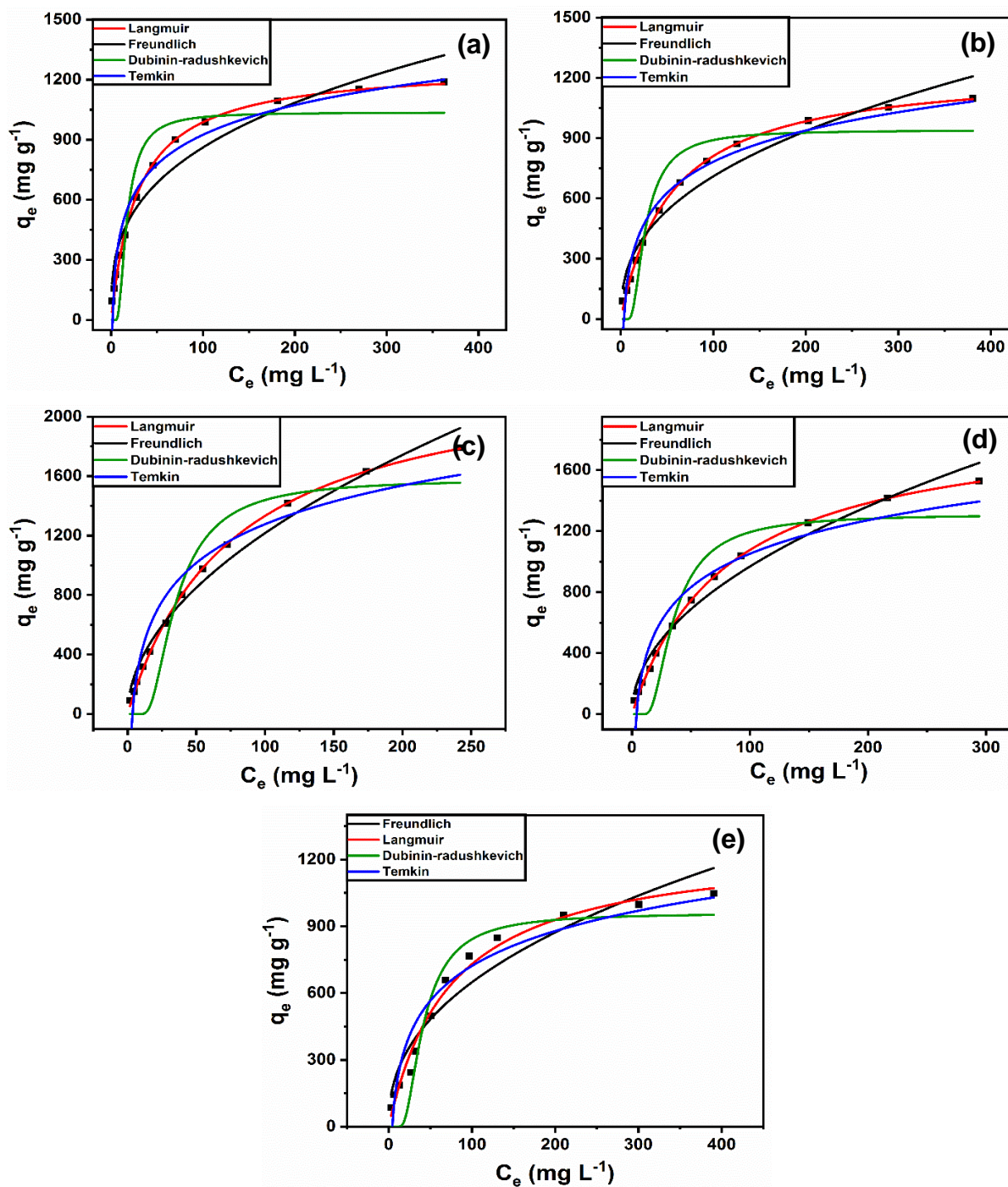


Figure 6.25. Adsorption isotherms at five different temperatures for Cd(II): a) 308.5 K b) 313.5 K c) 318.5 K d) 323.5 K & e) 328.5 K

Table 6.3: Langmuir and Freundlich Isotherm for the GO-CeO<sub>2</sub>@CoFe<sub>2</sub>O<sub>4</sub>

Pollutants	Temp(K)	Langmuir				Freundlich			
		Q <sub>max</sub>	K <sub>a</sub>	Adj.	R <sup>2</sup>	n	K <sub>F</sub>	Adj.	R <sup>2</sup>
		mg g <sup>-1</sup>	L mg <sup>-1</sup>	R <sup>2</sup>	(COD)	(mg g <sup>-1</sup> )	(L mg <sup>-1</sup> ) <sup>1/n</sup>	R <sup>2</sup>	(COD)
MB	308.5	3596.52040	0.05917	0.99799	0.99817	3.28726	672.61190	0.89182	0.90165
	313.5	4005.05090	0.07602	0.99865	0.99878	3.07417	698.57517	0.91246	0.92042
	318.5	4632.08226	0.09767	0.99541	0.99583	3.21744	1055.41119	0.94605	0.95095
	323.5	3742.05860	0.12306	0.99879	0.9989	2.84876	507.65137	0.94316	0.94833
	328.5	3338.29570	0.15762	0.99903	0.99912	2.84292	419.91717	0.93388	0.93989
RB	308.5	1632.72126	0.06595	0.99541	0.99598	2.9408	356.87650	0.92852	0.93746
	313.5	1910.05183	0.08084	0.99816	0.99839	2.60243	361.75254	0.94606	0.9528
	318.5	2030.42402	0.10079	0.99435	0.99506	2.88536	585.51855	0.94797	0.95447
	323.5	1560.10552	0.12254	0.99691	0.9973	2.82325	285.49562	0.95274	0.95864
	328.5	1252.90552	0.14987	0.99815	0.99838	3.07008	236.94900	0.91384	0.92461
CR	308.5	4059.26445	0.06055	0.99814	0.99831	2.69861	502.7055	0.94893	0.95357
	313.5	4473.09188	0.07386	0.99816	0.99833	2.69000	637.79264	0.95142	0.95583
	318.5	4847.13889	0.09073	0.99188	0.99262	2.92117	980.55134	0.96497	0.96816
	323.5	4189.1549	0.11026	0.99811	0.99828	2.35853	347.72983	0.97052	0.9732
	328.5	4197.97281	0.13333	0.99863	0.99875	2.18386	263.74864	0.97566	0.97787
Pb	308.5	3641.27112	0.0304	0.99728	0.99753	2.96952	516.71677	0.94791	0.95264
	313.5	3499.84805	0.04542	0.99679	0.99708	3.95356	893.64407	0.90969	0.9179
	318.5	4576.9013	0.06755	0.99267	0.99333	3.16231	999.36597	0.95546	0.95951
	323.5	3889.4494	0.10071	0.99826	0.99842	2.53464	380.69668	0.95618	0.96016
	328.5	3623.54534	0.15019	0.99797	0.99816	2.56616	348.67709	0.94868	0.95335
Cd	308.5	1272.94507	0.03461	0.99605	0.99641	3.00999	186.54133	0.93464	0.94058
	313.5	1250.39081	0.04844	0.99861	0.99873	2.51438	113.69173	0.95013	0.95466
	318.5	2346.42883	0.06914	0.99917	0.99924	1.9298	111.87533	0.97741	0.97946
	323.5	1938.01212	0.0955	0.99883	0.99894	2.02977	100.16908	0.97275	0.97523
	328.5	1277.48838	0.13346	0.98371	0.98519	2.33624	90.35437	0.92747	0.93406

Table 6.4: DR and Temkin Isotherm for the GO-CeO<sub>2</sub>@CoFe<sub>2</sub>O<sub>4</sub>

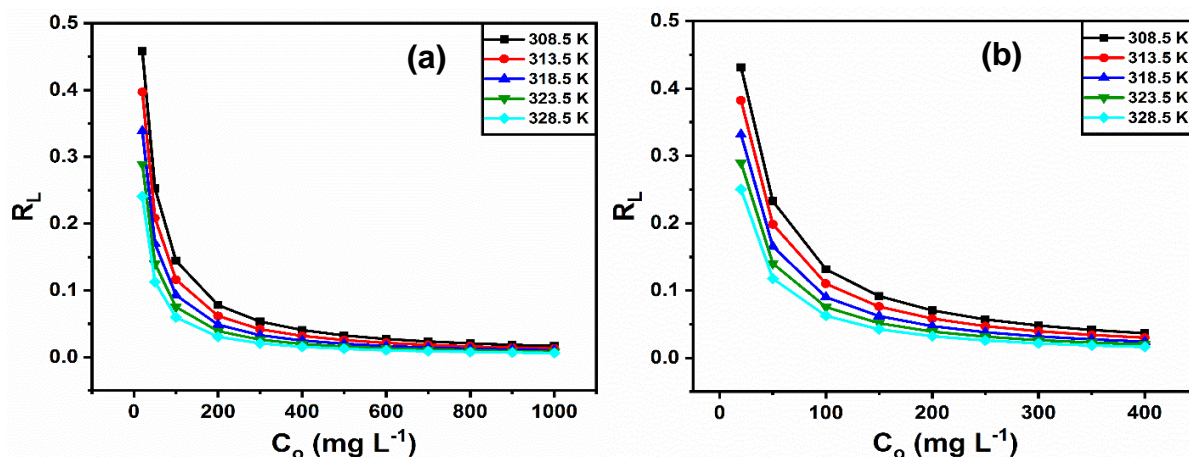
Pollutants	Temp(K)	Dubinin-Radushkevich				Temkin			
		$q_s$	$K_{DR}$	Adj.	$R^2$	$A_T$	$B_T$	Adj.	$R^2$
		(mol g <sup>-1</sup> )	(mol <sup>2</sup> k <sup>-1</sup> J <sup>-2</sup> )	$R^2$	(COD)	(L g <sup>-1</sup> )	(J mol <sup>-1</sup> )	$R^2$	(COD)
<b>MB</b>	308.5	3059.08627	0.04205	0.89608	0.90553	1.19639	4.23302	0.96626	0.96933
	313.5	3335.96355	0.04281	0.92406	0.93096	1.6759	4.21509	0.92917	0.93561
	318.5	3791.46464	0.0138	0.9047	0.91337	5.93634	4.30288	0.9038	0.91254
	323.5	3020.79144	0.10017	0.90088	0.90989	0.90846	4.46359	0.9641	0.96736
	328.5	2734.46543	0.1448	0.91968	0.92698	0.56016	4.71222	0.97947	0.98134
<b>RB</b>	308.5	1292.25087	0.00572	0.86627	0.88299	2.05977	8.71305	0.97878	0.98143
	313.5	1457.64671	0.00958	0.89187	0.90539	2.78307	8.56717	0.91794	0.9282
	318.5	1595.86479	0.00211	0.89628	0.90924	3.80205	6.92415	0.98121	0.98355
	323.5	1244.30076	0.01418	0.87393	0.88969	1.79349	10.2994	0.96264	0.96731
	328.5	1050.69635	0.0195	0.90579	0.91756	1.12823	12.08719	0.97132	0.97491
<b>CR</b>	308.5	3216.36561	0.12216	0.91247	0.92043	0.95493	4.05762	0.94742	0.9522
	313.5	3507.77133	0.04671	0.91401	0.92182	1.93399	4.07751	0.90191	0.91083
	318.5	3810.8755	0.01540	0.86879	0.88072	4.19406	3.89459	0.92635	0.93305
	323.5	3149.23946	0.28332	0.89837	0.90761	0.63827	4.27633	0.92378	0.93071
	328.5	3072.54716	0.4982	0.89749	0.90681	0.40064	4.19911	0.93004	0.9364
<b>Pb</b>	308.5	2964.32138	0.13328	0.91997	0.92724	6.44993	5.40779	0.75525	0.7775
	313.5	3089.778777	0.02372	0.88709	0.89735	2.82564	3.91782	0.9301	0.93645
	318.5	3735.42190	0.01729	0.87985	0.89078	15.14225	4.5058	0.88945	0.8995
	323.5	2989.00307	0.21564	0.90812	0.91648	1.27364	4.22811	0.95448	0.95862
	328.5	2842.69341	0.30041	0.90018	0.90925	0.65897	4.34091	0.948	0.95273
<b>Cd</b>	308.5	1036.28484	0.08977	0.87006	0.88187	0.16522	0.73546	0.96043	0.96402
	313.5	940.04973	0.21111	0.86368	0.87607	0.06276	0.73347	0.95803	0.96184
	318.5	1580.78885	0.35889	0.86785	0.87987	0.06854	0.62955	0.91925	0.92659
	323.5	1312.31895	0.35732	0.86251	0.87501	0.06681	0.76194	0.91843	0.92584
	328.5	959.77073	0.48481	0.91959	0.9269	0.06115	1.04716	0.92378	0.93071



The effect of temperature is proportional to the total adsorption capacity of GO-CeO<sub>2</sub>@CoFe<sub>2</sub>O<sub>4</sub> up to a certain time which is given in table 6.3 & 6.4 and the maximum adsorption at equilibrium for this adsorbent in case of each pollutants is as follows: at 318.5 K, MB is 4632.08 mg g<sup>-1</sup>, RB is 2030.42 mg g<sup>-1</sup>, CR is 4847.13 mg g<sup>-1</sup>, Pb(II) is 3735.42 mg g<sup>-1</sup> and Cd(II) is 1580.78 mg g<sup>-1</sup>. The adsorption of MB and CR are highest among the pollutants. The term R<sub>L</sub> known to be dimensional separation factor was calibrated to know the relationship between GO-CeO<sub>2</sub>@CoFe<sub>2</sub>O<sub>4</sub> and the adsorbate moieties which is given by the expression.

$$R_L = \frac{1}{1 + K_a \times C_o} \quad (6.12)$$

Based on the nature of R<sub>L</sub> values, it is possible to know whether the adsorption process can be favored or not. If the values of R<sub>L</sub> greater than 1 it is not favorable, if it is between 0-1 it is favored, then for zero it is irreversible and it is linear when it is equal to one.



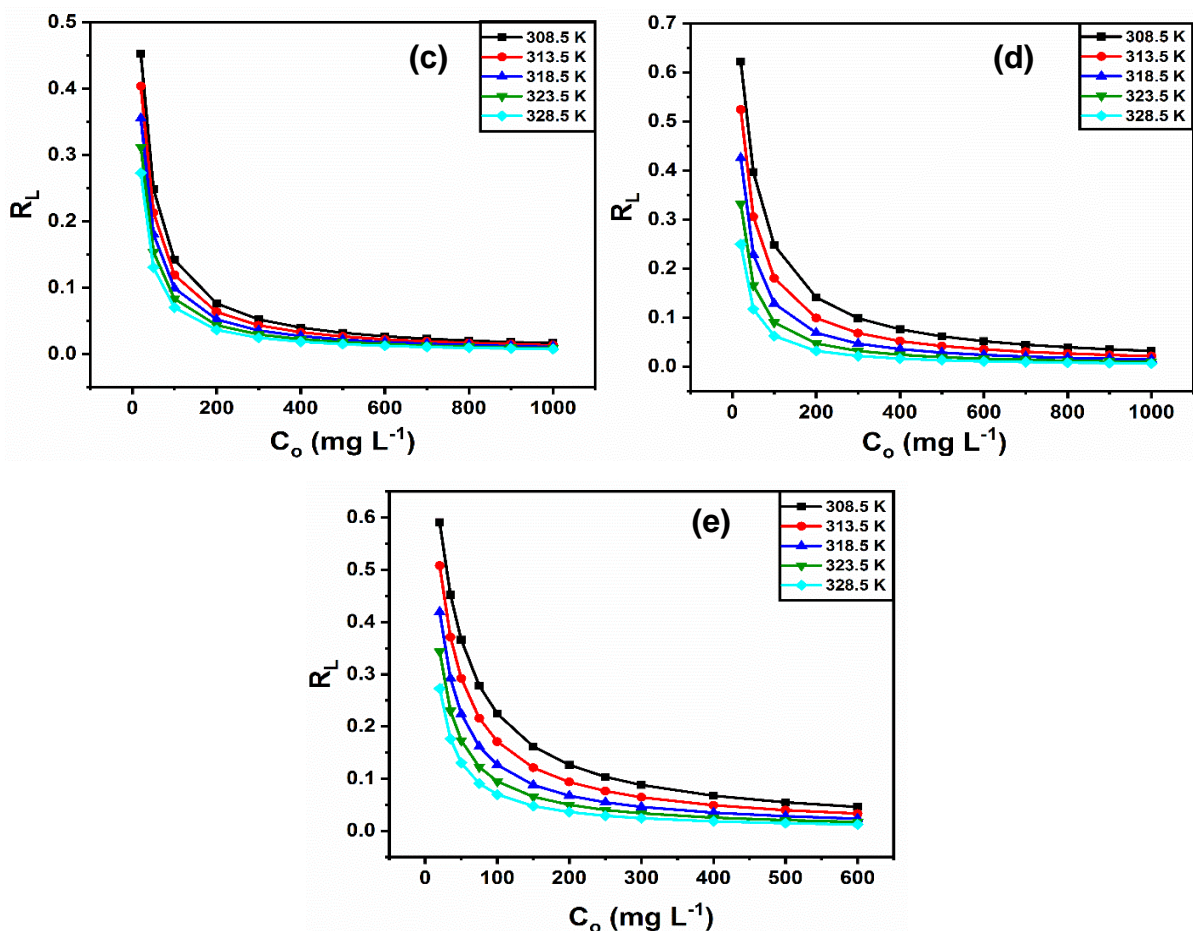


Figure 6.26. Separation factor  $R_L$  values for the adsorbates a) MB, b) RB, c) CR, d) Pb(II) & e) Cd(II)

The data from the graph plotted in Figure 6.26 is between 0-1 which represented that there are strong interactions between the nanocomposite and the adsorbates.  $K_f$  which is Freundlich constant and the data from the table 6.3 includes 1055.41 for MB, 585.51 for RB, 980.55 for CR, 999.36 for Pb(II) & 186.54 for Cd(II) where the value of  $n$  can be calculated and are 3.21, 2.88, 2.92, 3.16 & 3.00 respectively. These values represented that this model favored the adsorption process. Temkin model ascribed to the linear pattern of temperature as an adsorption function (heat of adsorption) to the logarithmic decrease without considering the concentration ranges high to low because of the changes in adsorption interactions of pollutants.

### 6.3.17 Van't Hoff plot (Thermodynamic studies)

Due to the release of high amounts of pollutants into the water bodies at a relatively high temperature from textile industry, the adsorption studies are mainly dependent on temperature parameter. Among the isotherm models, Langmuir found to be best model for calculating the

thermodynamic factor at five temperatures as shown in figure 6.21-6.25.  $K_a$  value is made dimensionless and the parameter like Gibbs free energy ( $\Delta G^\circ$ , KJ mol<sup>-1</sup>), change on enthalpy ( $\Delta H^\circ$ , KJ mol<sup>-1</sup>) and change in entropy ( $\Delta S^\circ$ , J/mol/K) were measured via equations and given in the table 5.5. Here, it is unimolecular adsorption and the calculated values for the equilibrium constant  $K_e$  as per the equation.

$$K_e = \frac{1000 \times K_a \times M}{\gamma} \quad (6.13)$$

$$K_e = \frac{1000 \times K_a \times \text{mol. wt. of adsorbate} \times \text{standard conc. of adsorbate}}{\text{activity coefficient of adsorbate}}$$

$$\Delta G = -RT \ln(K_e) \quad (6.14)$$

The equation calculated with the help of thermodynamics 3<sup>rd</sup> law

$$\Delta G = \Delta H - T\Delta S \quad (6.15)$$

Van't Hoff's Equation calculated by fitting the curve from the equation (12) and (13) (Lima et al. 2015, 2019; Liu 2009; Xu and Liu 2008)

$$\ln K_e = \frac{\Delta S}{R} - \frac{\Delta H}{RT} \quad (6.16)$$

The term  $K_e$  corresponds to the equilibrium constant for adsorption,  $M$  (g/mol) refers to the pollutant molar mass,  $\gamma$  known as the activity coefficient (dimensionless),  $R$  referred to the gas constant,  $T$  is the temperature (K). The graph plotted between  $\ln K_e$  and  $1/T$  gave the slope and intercept for the calculation of  $\Delta H$  as well as  $\Delta S$  (Panagopoulos et al. 2017). Van't Hoff's plots for the pollutants are given in figure 6.27(a-e). The thermodynamic parameters estimated from formula were given in the tabular form 6.5.

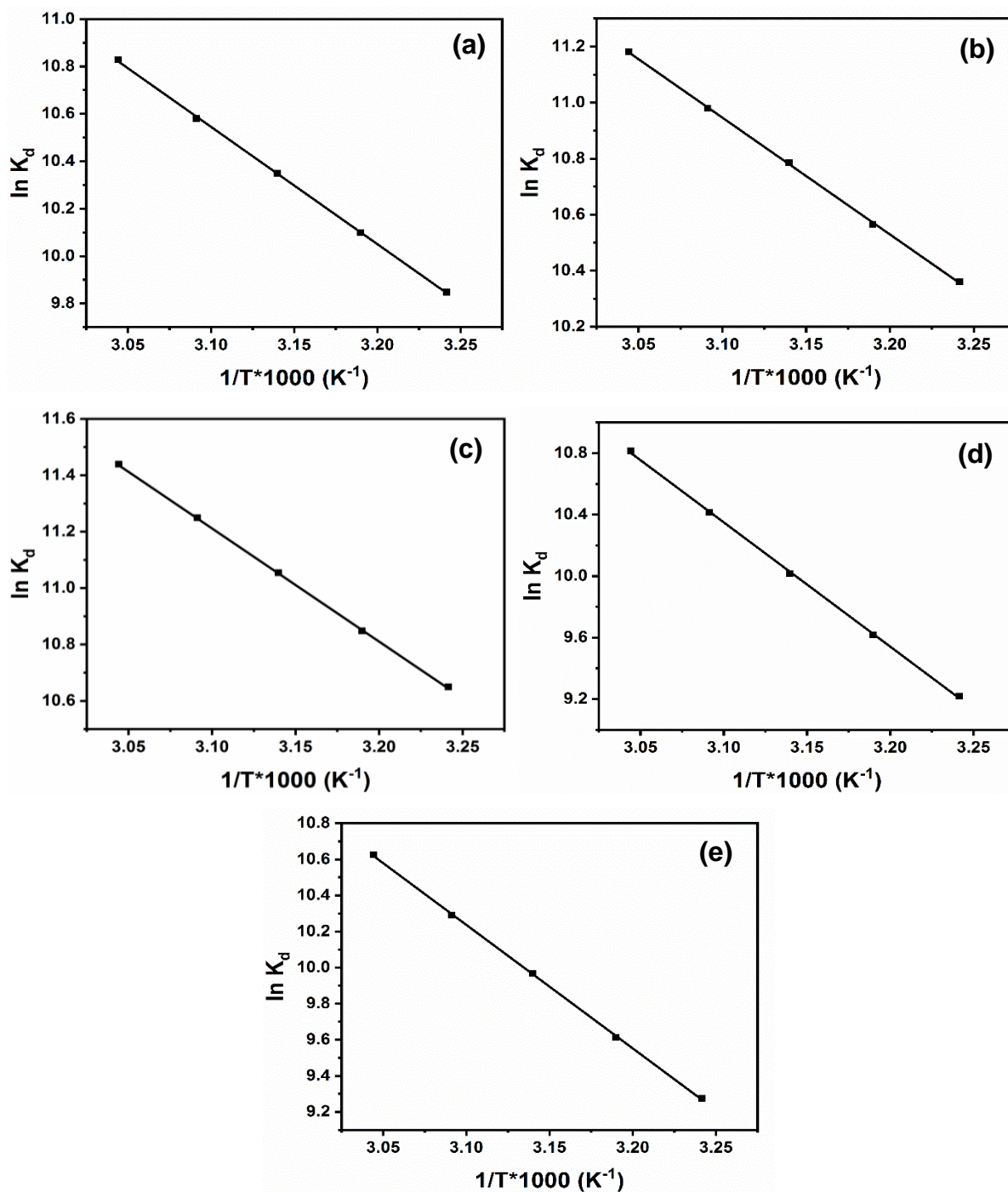


Figure 6.27. Van't Hoff plots for the adsorbates a) MB, b) RB, c) CR, d) Pb(II) & e) Cd(II)

Table 6.5: Thermodynamics of the adsorbent GO-CeO<sub>2</sub>@CoFe<sub>2</sub>O<sub>4</sub>

Thermodynamics parameters					
Pollutants	Temp(K)	$\Delta G$ (kJ mol <sup>-1</sup> )	$\Delta H$ (kJ mol <sup>-1</sup> )	$\Delta S$ (JK <sup>-1</sup> mol <sup>-1</sup> )	R <sup>2</sup>
MB	308.5	25.25951	41.1362	215.1951	0.99979
	313.5	26.32204			
	318.5	27.40544			
	323.5	28.45714			
	328.5	29.57299			
RB	308.5	26.57368	34.6758	198.5031	0.99975
	313.5	27.53498			
	318.5	28.55819			
	323.5	29.53206			
	328.5	30.53837			
CR	308.5	27.31527	33.3499	196.5969	0.99964
	313.5	28.27589			
	318.5	29.2716			
	323.5	30.25546			
	328.5	31.2419			
Pb	308.5	23.64082	67.2437	294.5051	0.99966
	313.5	25.07048			
	318.5	26.52137			
	323.5	28.01187			
	328.5	29.53634			
Cd	308.5	23.79121	56.9235	261.5725	0.99978
	313.5	25.05304			
	318.5	26.39479			
	323.5	27.67787			
	328.5	29.01971			

The  $\Delta G$  negative values from the table indicated that it is spontaneous adsorption in nature. Further, decrease in the  $\Delta G$  values with the increase of temperature justified that the adsorption process is more favored at high temperatures. The enthalpy values are 41.1362 KJ mol<sup>-1</sup> for MB, 34.6758 KJ mol<sup>-1</sup> for RB, 33.3499 KJ mol<sup>-1</sup> for CR, 67.2437 KJ mol<sup>-1</sup> for Pb(II) and 56.9235 KJ mol<sup>-1</sup> for Cd(II) which are endothermic, chemisorptive in nature, which increased the randomness in adsorbent–adsorbate interface in the aqueous wastewater. The positivity in the  $\Delta S$  values justified the randomness in the pollutants at the interface during adsorption. The calculated values gave predictions to know the structural variations during the adsorption of GO-CeO<sub>2</sub>@CoFe<sub>2</sub>O<sub>4</sub> with the adsorbate solutions. R<sup>2</sup> values near to 1 determined the accuracy in the calculated  $\Delta H$  and  $\Delta S$  values. Therefore, the increment in temperature is useful for the removal of harmful pollutants from wastewater.

### 6.3.18 Adsorption Kinetic Studies

The time dependent studies on the GO-CeO<sub>2</sub>@CoFe<sub>2</sub>O<sub>4</sub> can justify the effectiveness of adsorption process at a specified time and the rate of adsorption at different time intervals during this process.

The kinetic graphs justified the rate of uptake  $q_t$  is very high during the initial stages of adsorption because of the availability of broad range of functional groups as well as active sites up on adsorbent surface given in figure 6.28 & 6.29. Therefore, GO-CeO<sub>2</sub>@CoFe<sub>2</sub>O<sub>4</sub> found to be an efficient magnetic nanoadsorbent in wastewater treatment at a moderate time period. And these data obtained for the kinetic models (i) Lagergren pseudo first order(PFO) & (ii) pseudo second order(PSO) employed to analyze the kinetic properties of adsorption of pollutants using adsorbent. The PFO equation kinetic model is given below:

$$\ln(q_e - q_t) = \ln q_e - k_1 t \quad (6.17)$$

The PSO kinetic model equation is given below:

$$\frac{t}{q_t} = \frac{1}{k_2 q_e^2} + \frac{1}{q_e} \quad (6.18)$$

Where  $k_1$  (min<sup>-1</sup>) referred to the pseudo 1<sup>st</sup> order rate constant and  $k_2$  (g/mg/min) corresponds to the pseudo 2<sup>nd</sup> order rate constant;  $q_t$  &  $q_e$  referred to the adsorption capacities of the adsorbent at any time  $t$  and equilibrium respectively.

The PFO model is predominated by diffusion method shown in Figure 6.28 whereas the PSO models observed it is controlled by chemisorption shown in Figure 6.29 (An et al. 2019; Zhao

et al. 2019). This chemisorption results in the differential electron deactivation, adsorptive and desorptive agents possessing agile species on GO-CeO<sub>2</sub>@CoFe<sub>2</sub>O<sub>4</sub> surface.

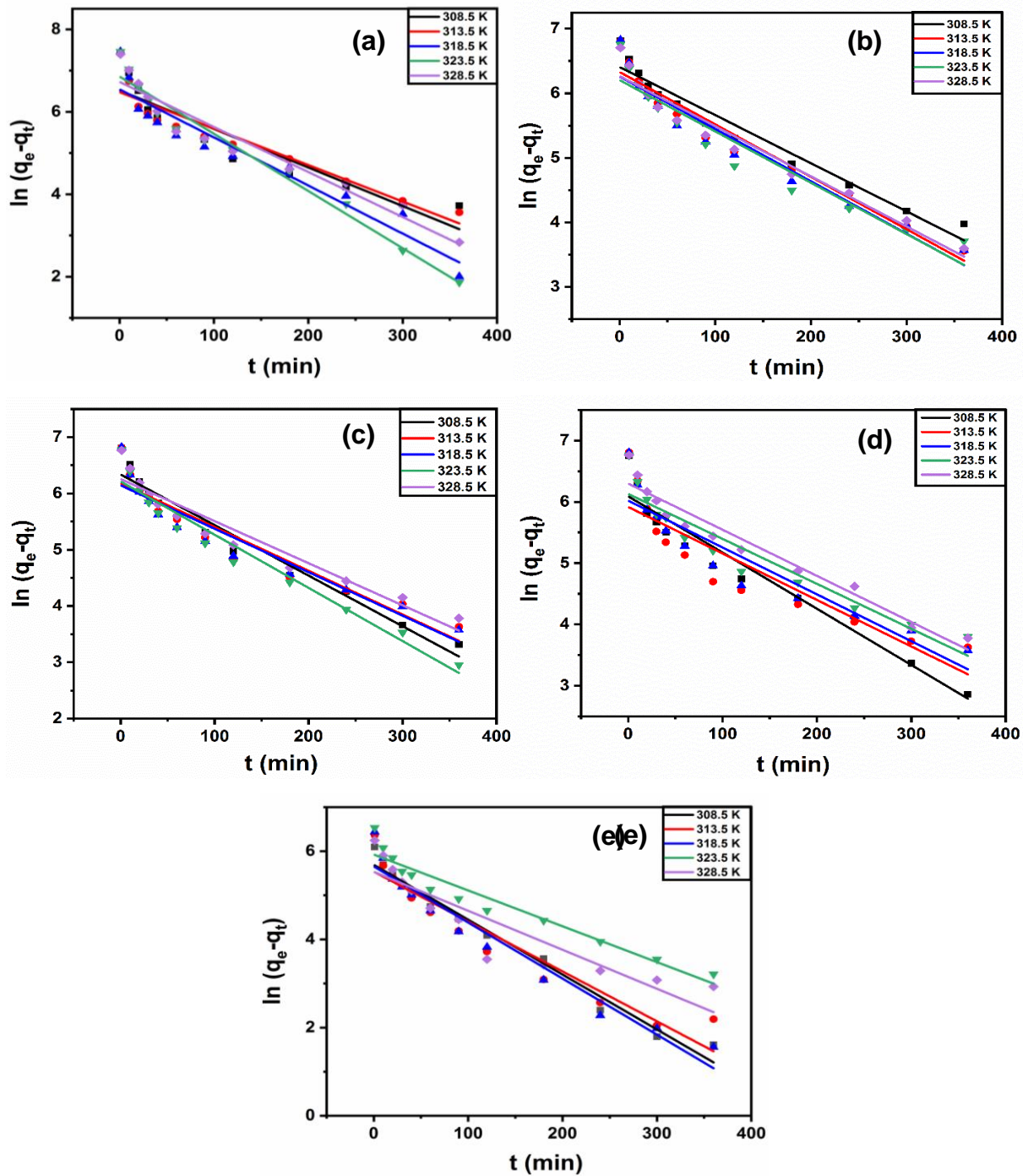


Figure 6.28. Pseudo first order kinetics for the five adsorbates: a) MB, b) RB, c) CR, d) Pb(II) & e) Cd(II)

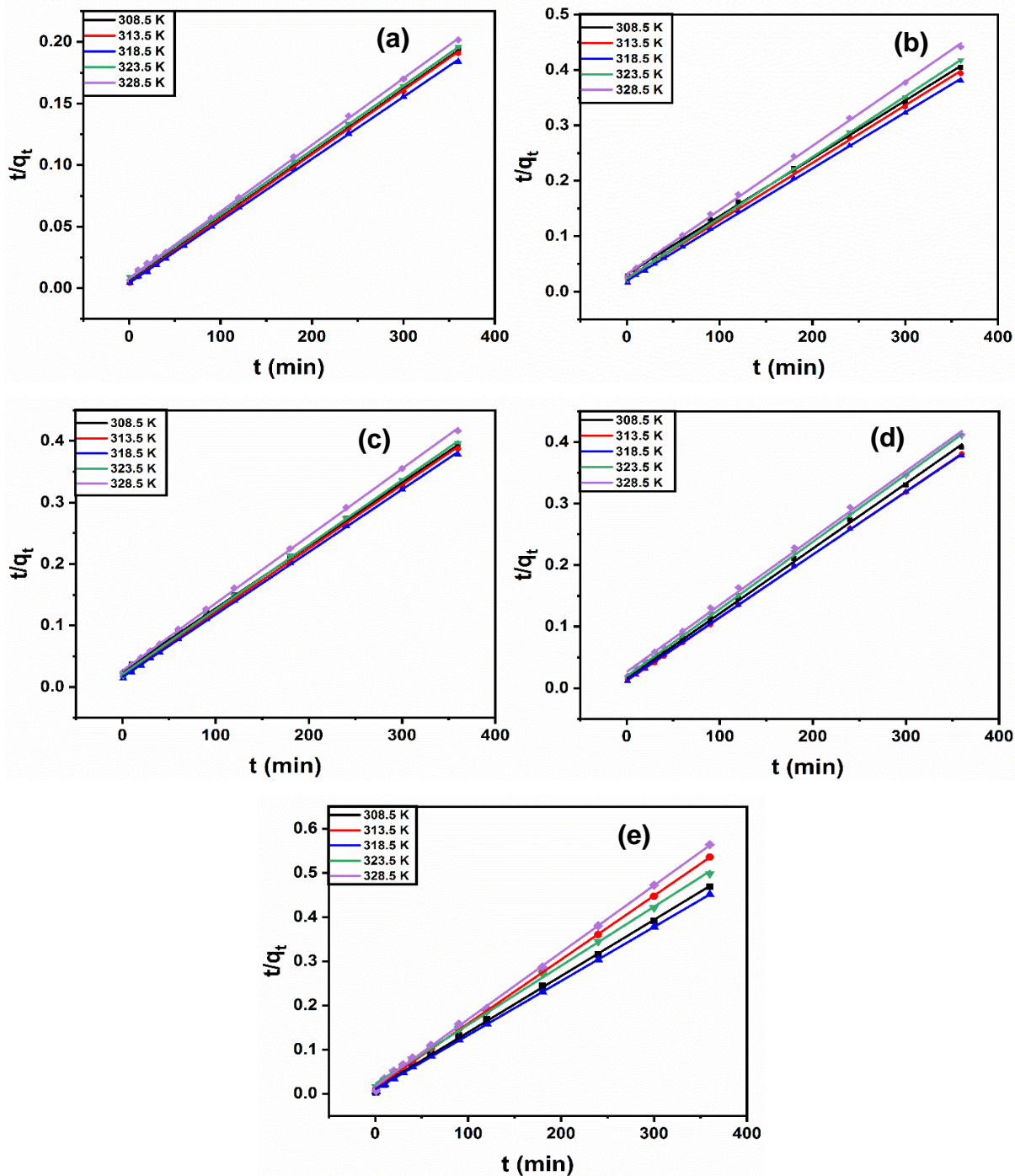


Figure 6.29. Pseudo second order kinetics for the five adsorbates: a) MB, b) RB, c) CR, d) Pb(II) & e) Cd(II)



Table 6.6: Kinetic parameters for Lagergren models for GO-CeO<sub>2</sub>@CoFe<sub>2</sub>O<sub>4</sub>

Pollutants	Temp (K)	Pseudo-first-order				Pseudo-second-order			
		$q_{e(\text{exp})}$ (mg g <sup>-1</sup> )	$q_{e(\text{calc})}$ (mg g <sup>-1</sup> )	$k_1$ (min <sup>-1</sup> )	$R^2$	$q_{e(\text{calc})}$ (mg g <sup>-1</sup> )	$k_2$ (g mg <sup>-1</sup> min <sup>-1</sup> )	$R^2$	$E_a$ (kJ mol <sup>-1</sup> )
MB	308.5	1901.60	678.7616	0.00935	0.86057	1915.4336	5.162×10 <sup>-5</sup>	0.99991	18.2283
	313.5	1920.75	649.5631	0.00884	0.89197	1919.4521	5.799×10 <sup>-5</sup>	0.99963	
	318.5	1963.20	695.5758	0.01166	0.91515	1984.9856	5.916×10 <sup>-5</sup>	0.99976	
	323.5	1844.25	948.4319	0.01388	0.96874	1913.3007	3.525×10 <sup>-5</sup>	0.99985	
	328.5	1787.70	832.6388	0.01093	0.93078	1848.3639	3.591×10 <sup>-5</sup>	0.99961	
RB	308.5	943.75	605.2672	0.00745	0.95538	961.5385	3.392×10 <sup>-5</sup>	0.99918	56.1053
	313.5	950.60	560.2651	0.00812	0.95333	952.3809	4.426×10 <sup>-5</sup>	0.99914	
	318.5	981.20	522.3145	0.00811	0.93497	990.099	5.108×10 <sup>-5</sup>	0.99955	
	323.5	903.65	494.3827	0.00795	0.9219	909.0909	5.112×10 <sup>-5</sup>	0.99978	
	328.5	852.05	525.9573	0.00776	0.95429	862.0689	4.235×10 <sup>-5</sup>	0.9992	
CR	308.5	947.75	563.4283	0.00898	0.95672	980.3922	4.129×10 <sup>-5</sup>	0.99963	66.8676
	313.5	984.10	482.2728	0.00777	0.91263	970.8738	5.784×10 <sup>-5</sup>	0.99959	
	318.5	988.60	465.5456	0.00772	0.90922	980.3922	6.527×10 <sup>-5</sup>	0.99963	
	323.5	927.15	497.8954	0.00945	0.95356	952.3809	5.389×10 <sup>-5</sup>	0.99974	
	328.5	907.95	520.4844	0.00748	0.929	909.0909	4.590×10 <sup>-5</sup>	0.99973	
Pb	308.5	937.75	441.4567	0.00916	0.93889	943.3962	7.230×10 <sup>-5</sup>	0.9993	35.1610
	313.5	982.75	371.3369	0.00758	0.82198	970.8798	9.021×10 <sup>-5</sup>	0.99991	
	318.5	988.75	411.5416	0.00764	0.87293	980.3922	8.034×10 <sup>-5</sup>	0.99982	
	323.5	922.75	458.9814	0.00733	0.90486	917.4312	6.207×10 <sup>-5</sup>	0.99955	
	328.5	917.75	543.2719	0.00752	0.94778	909.0909	4.609×10 <sup>-5</sup>	0.99822	
Cd	308.5	772.75	296.6254	0.01245	0.97817	787.4016	1.379×10 <sup>-4</sup>	0.99928	37.6507
	313.5	679.00	253.7653	0.01131	0.91483	689.6552	1.471×10 <sup>-4</sup>	0.9998	
	318.5	802.75	285.6745	0.01272	0.9474	813.0081	1.499×10 <sup>-4</sup>	0.99979	

323.5	747.75	373.6689	0.00813	0.93248	746.2687	$7.969 \times 10^{-5}$	0.99922
328.5	657.75	253.1013	0.00885	0.83798	657.8947	$1.367 \times 10^{-4}$	0.99937

Finally,  $R^2$  values obtained from the calculated values are not fitted for the PFO because of the collation of difference with experimental values which have significantly become inapplicable to this model. In case of PSO model the better regression  $R^2$  values near to 1 which found fit for this model. The  $q_{e(\text{calc})}$  values for the adsorbates MB, RB, CR, Pb(II) & Cd(II) in PSO model are 1984.98, 988.6, 980.39, 980.39, 813.00  $\text{mg g}^{-1}$  almost close to the  $q_{e(\text{exp})}$  are 1963.2, 990.09, 981.2, 988.75, 802.75  $\text{mg g}^{-1}$  respectively.

### **Intra-particle diffusion model**

To know the solution or diffusion mechanism along with rate limiting step, Intra-particle diffusion (ID) was investigated to know the uptake of pollutant in the adsorption. The pollutant uptake is classified into 3 steps: (i) film diffusion, (ii) intra-particle diffusion & (iii) mass action. This mechanism gave the equation where the uptake of pollutant at regular time interval ( $q_t$ ) vs time  $t$ , where  $k_p$  ( $(\text{mg/g}) \text{min}^{1/2}$ ) is a intraparticle diffusion rate constant (Weber and Morris 1963).

$$q_t = k_p t^{1/2} + x_i \quad (6.19)$$

Where  $x_i$  represented the boundary layer thickness (Kavitha and Namasivayam 2007). The plots between  $q_t$  and  $t^{1/2}$  indicated the intercept positive values i.e.,  $x_i \neq 0$  shown in fig. If  $x_i = 0$ , the way, adsorption phenomena is monitored by this method (Wu et al. 2009), the positive value of intercept explained the spontaneous type that took at time  $t = 0$  initially through film diffusion.

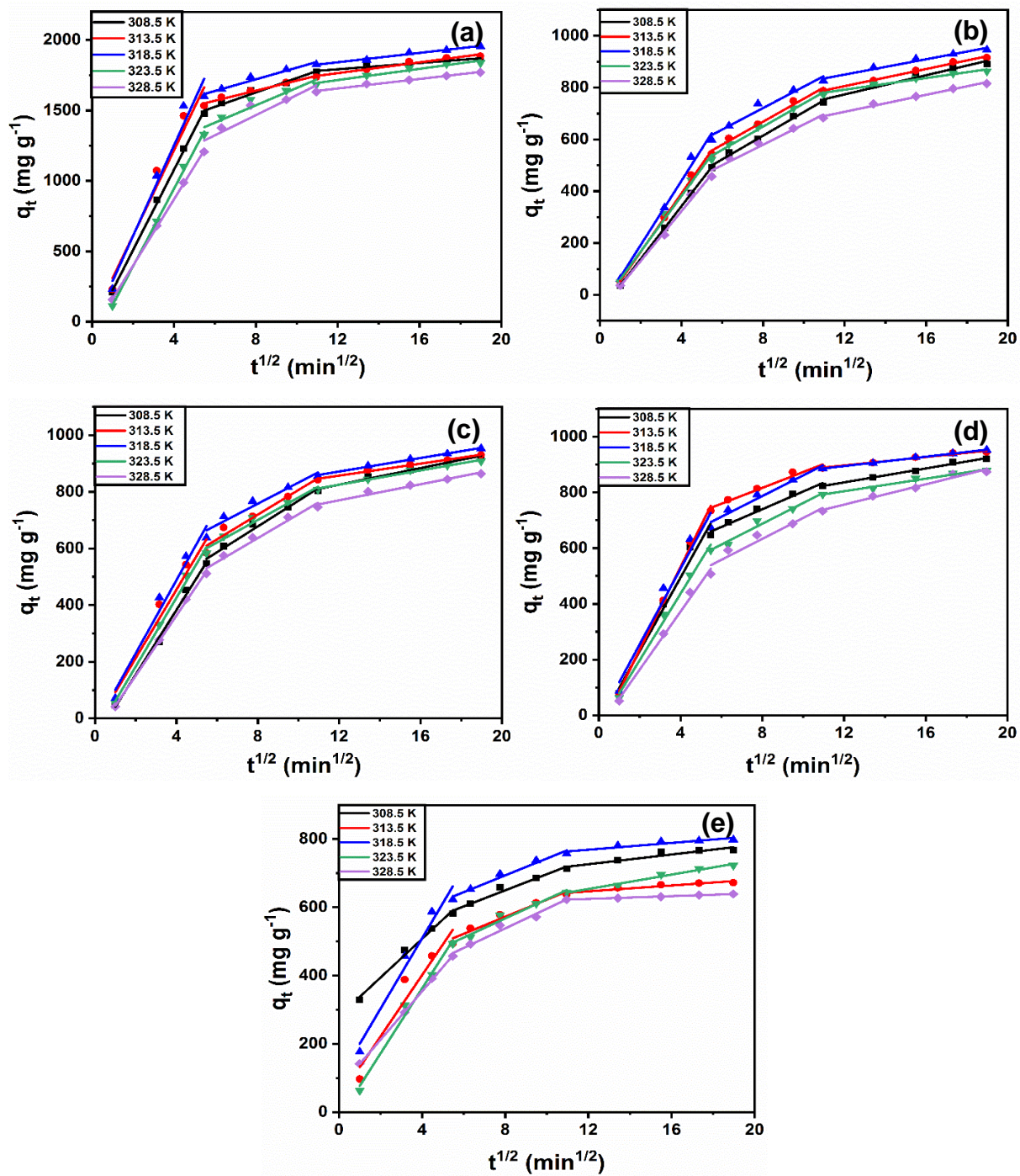


Figure 6.30. Intraparticle diffusion for the five adsorbates: a) MB, b) RB, c) CR, d) Pb(II) & e) Cd(II)

Table 6.7: Intraparticle diffusion model for GO-CeO<sub>2</sub>@CoFe<sub>2</sub>O<sub>4</sub>

Intraparticle diffusion						
Pollutants	Temp (K)	$K_p$	$x_i$	$q_e$	$R_i$	$R^2$
		mmol g <sup>-1</sup> min <sup>-1/2</sup>	(mmol g <sup>-1</sup> )	(mmol g <sup>-1</sup> )		
MB	308.5	115.8085	938.5833	1901.6	0.50642	0.97414
	313.5	119.2859	965.1234	1920.75	0.4975	0.96791
	318.5	126.2771	1000.1259	1963.20	0.49056	0.97023
	323.5	118.8834	787.8163	1844.25	0.57282	0.95301
	328.5	107.8999	758.5925	1787.70	0.57566	0.94985
RB	308.5	55.3561	245.2139	943.75	0.74017	0.98653
	313.5	57.8117	287.4635	950.60	0.69759	0.99175
	318.5	60.0435	335.82164	981.20	0.65774	0.97336
	323.5	54.4143	300.5600	903.65	0.66739	0.98224
	328.5	50.6367	237.7084	852.05	0.72101	0.98178
CR	308.5	57.9912	296.9985	947.75	0.68663	0.98521
	313.5	58.2388	357.9304	984.10	0.63629	0.9707
	318.5	59.4273	386.7389	988.60	0.6088	0.97234
	323.5	57.8157	332.7545	927.15	0.64109	0.98502
	328.5	54.1114	279.3738	907.95	0.6923	0.9825
Pb	308.5	58.8500	379.0030	937.75	0.59584	0.98199
	313.5	61.5461	444.4032	982.75	0.54779	0.98156
	318.5	60.4802	421.9784	988.75	0.57322	0.97662
	323.5	56.0146	338.9513	922.75	0.63267	0.98189
	328.5	53.3099	277.4277	917.75	0.69771	0.96655
Cd	308.5	29.1309	460.9718	772.75	0.40346	0.95452
	313.5	39.7419	336.5614	679.00	0.50433	0.92918
	318.5	44.2438	434.1921	802.75	0.45912	0.93759
	323.5	44.6071	284.1759	747.75	0.61996	0.98094
	328.5	33.9176	326.2398	657.75	0.50401	0.98895

---

The multi-linearity in the graph shown in Figure 6.30 was observed and explained the 3 steps for the adsorption. The slanting effect in this model depicted that the rate of pollutants removal is governed by only Intraparticle diffusion only (Xu et al. 2019). The initial step with the highest rate constant  $k_p$  constitutes the surface adsorption. The active sites on the GO-CeO<sub>2</sub>@CoFe<sub>2</sub>O<sub>4</sub> surface got engaged, the secondary step begins with the pollutants into pores, which led to the inner areas of adsorbent.

The tertiary step is the equilibrium phase, rate constants decreases because of the absence of free active sites and the residual concentration of pollutant (Ahmad et al. 2019). Finally, the adsorption process is governed by the quicker film and slower intra-particle diffusion for all the dyes and metal ions.

The initial adsorption factor ( $R_i$ ) gave the formula where  $R_i$  is conveyed in terms of  $x_i$  :

$$R_i = 1 - \frac{x_i}{q_e} \quad (6.20)$$

The values of  $x_i$  for MB which are higher than other pollutants proved that the film diffusion is effectively controlled by overall rate-determining step shown in table 6.7.

### 6.3.19 Activation energy of adsorption

The graphs plotted between  $\ln k_2$  vs  $1/T$  taken for examining the data of rate constants of pseudo second order ( $k_2$ ) at five distant temperatures given in figure 6.31. From the Arrhenius plot, the adsorbates (MB, RB, CR, Pb(II) & Cd(II)) having activation energy ( $E_a$ ) data was found to be 18.22 KJ mol<sup>-1</sup>, 56.10 KJ mol<sup>-1</sup>, 66.86 KJ mol<sup>-1</sup>, 35.16 KJ mol<sup>-1</sup> and 37.65 KJ mol<sup>-1</sup>. The relatively smaller  $E_a$  values resembled favored adsorption phenomena.

$$\ln k_2 = -\frac{E_a}{2.303RT} + \text{constant} \quad (6.21)$$

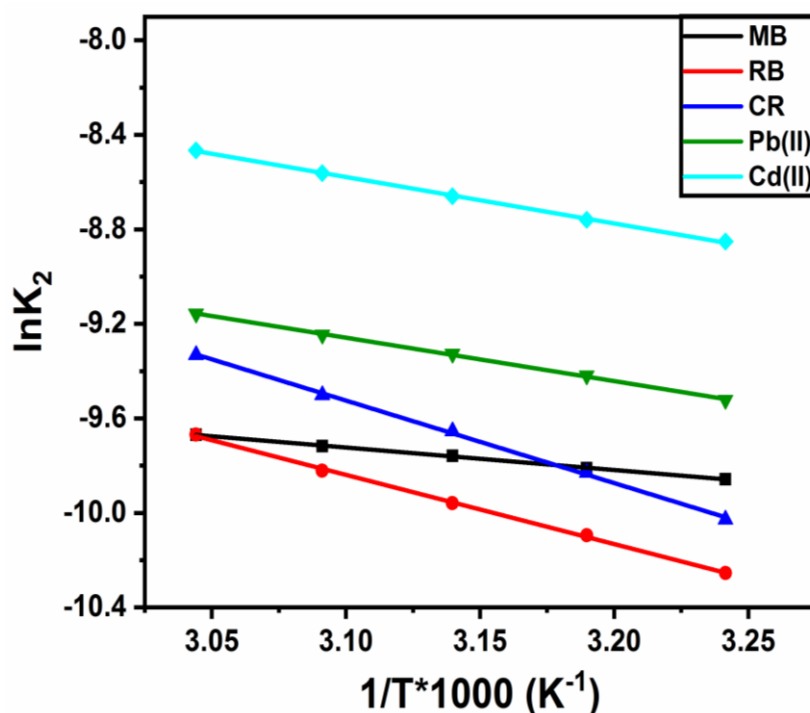


Figure 6.31. Arrhenius plot for the five adsorbates at different temperatures a) MB, b) RB, c) CR, d) Pb(II) & e) Cd(II)

Figure 6.31 indicated that the adsorption capacity  $q_e$  for all the pollutants enhances with an increment in pollutant concentration. The shift explained that it can effectively remove pollutants from water. Therefore, GO-CeO<sub>2</sub>@CoFe<sub>2</sub>O<sub>4</sub> was engaged for the elimination of dyes and heavy metal ions from the waste effluents. The nanocomposite proved to have highest removal efficacy (97%) for the pollutants except cadmium in synthetic effluents favored its advantage and a way to use in industrial wastewater treatment.

### 6.3.20 Stability and reusability of adsorbent

The stability and reusability of GO-CeO<sub>2</sub>@CoFe<sub>2</sub>O<sub>4</sub> is a determining factor for real-world applications. The stability of adsorbent has been determined to know the amount of Fe metal leached into the aqueous solution within the pH range as given in figure 6.32. The Fe metal loss is not detected even after 6 regeneration cycles which justified the CoFe<sub>2</sub>O<sub>4</sub> nanoparticle has outstanding capacity for the adsorption of pollutants and the stable nature of nanoparticle inside the nanocomposite.

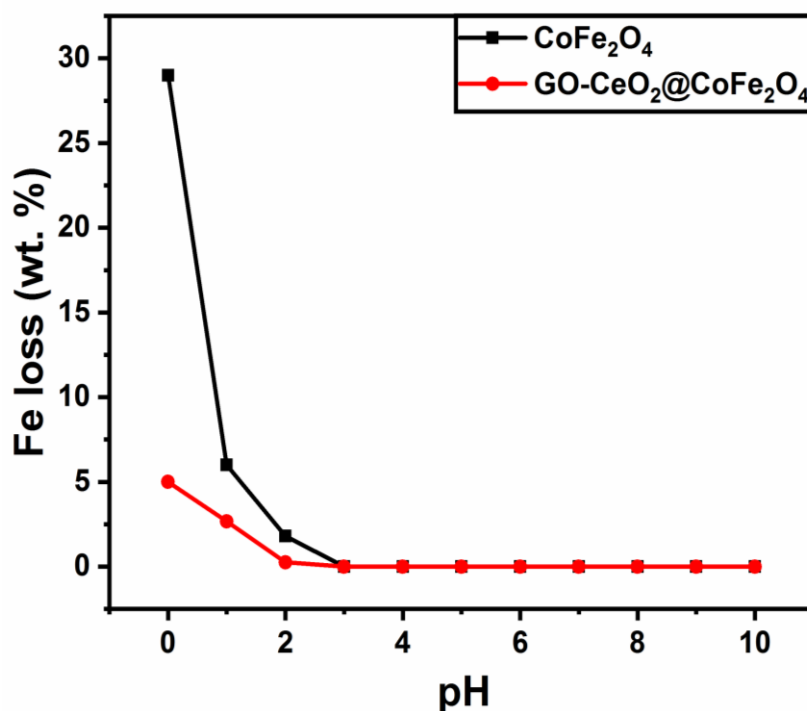


Figure 6.32. Stability of GO-CeO<sub>2</sub>@CoFe<sub>2</sub>O<sub>4</sub> at different pH.

The pollutants which got adsorbed onto GO-CeO<sub>2</sub>@CoFe<sub>2</sub>O<sub>4</sub> surface has been regenerated using some desorbing agents and their desorption values are mentioned in table 6.8a & 6.8b. For the cationic and anionic dyes, the desorbing agents used are 1.0 M HCl, 0.1 M HCl, 0.01 M HCl and 0.1 M H<sub>2</sub>SO<sub>4</sub> and for metal ions, they are 1.0 M HCl, 0.1 M HCl & 0.01 M EDTA solutions respectively. The removal rate and regeneration capacity in presence of 1.0 M HCl solution is the highest when compared to the other concentrations for the dyes given in table 6.8a. However, in heavy metal ions the regeneration capacity of 1.0 M HCl is slightly higher 3% more than 0.01 M EDTA solutions in the desorption process from table 6.8b. This is due to the formation of complexation with EDTA molecules and thus reduces the metal ions desorbed in the mesoporous nanocomposite. Further, the good performance of adsorbent in desorption process 1.0 M HCl solution is found to be better desorbing agent for all pollutants in case of simulated wastewater.

Table 6.8a: Percentage desorption efficiency of dyes over adsorbent using different eluents

Eluents	% desorption efficiency of dyes		
	MB	RB	CR
1.0 M HCl	86.33	84.08	88.20
0.1 M HCl	55.76	42.85	59.65
0.01 M HCl	31.35	12.46	35.81
0.1 M H <sub>2</sub> SO <sub>4</sub>	30.82	18.51	27.53

Table 6.8b: Percentage desorption efficiency of metal ions over adsorbent using different eluents

Eluents	% desorption efficiency of Heavy metal ions	
	Pb(II)	Cd(II)
1.0 M HCl	91.73	75.36
0.1 M HCl	51.65	38.64
0.1 M EDTA	24.89	21.65

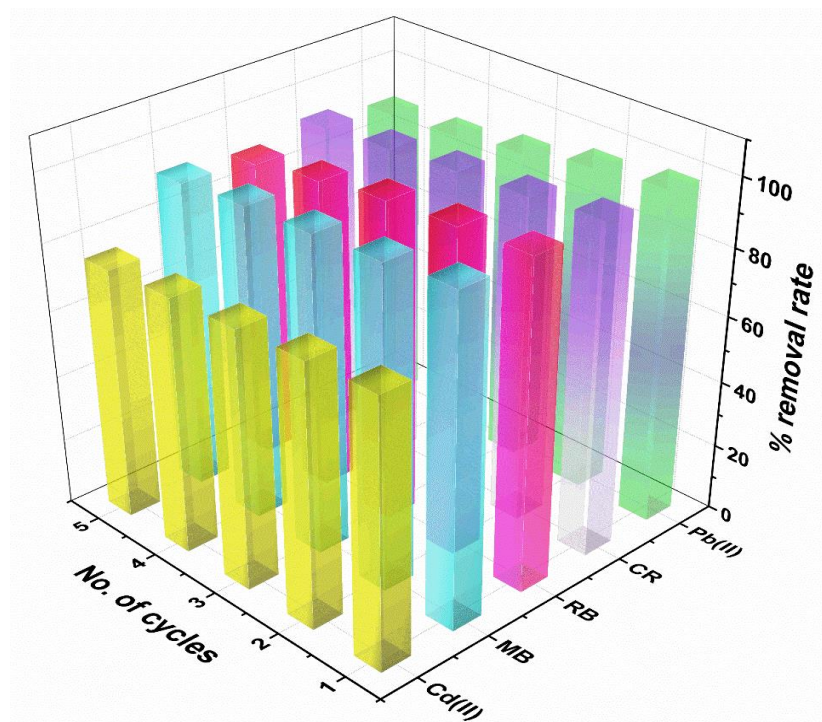


Figure 6.33. Regenerative capacity of the GO-CeO<sub>2</sub>@CoFe<sub>2</sub>O<sub>4</sub> for five adsorbates: MB, RB, CR, Pb(II) & Cd(II)

The equation 6.22 is used for calculating the desorption studies given below:

$$\% \text{ Desorption efficiency} = \frac{100 \times C_D V_D}{q_e m_D} \quad (6.22)$$



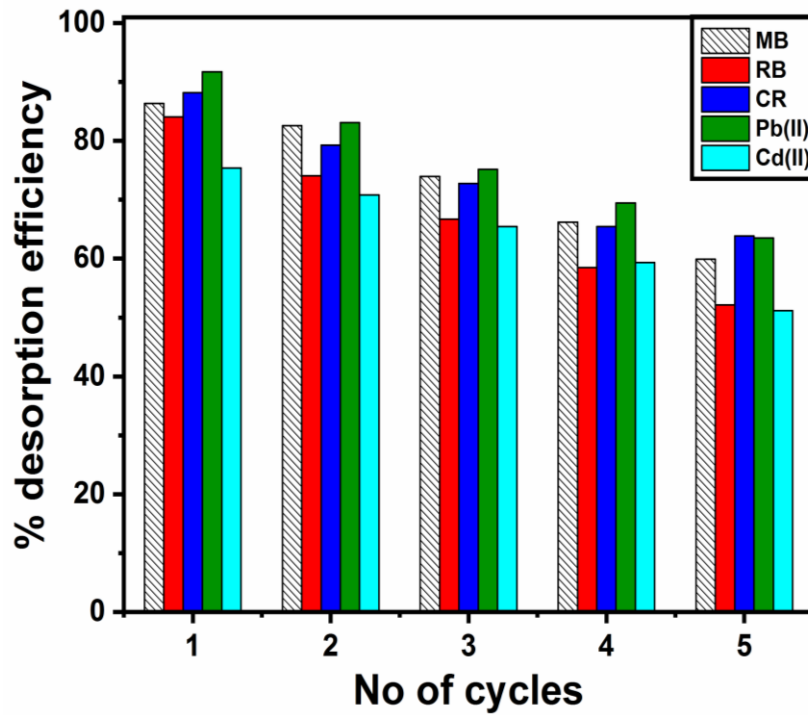
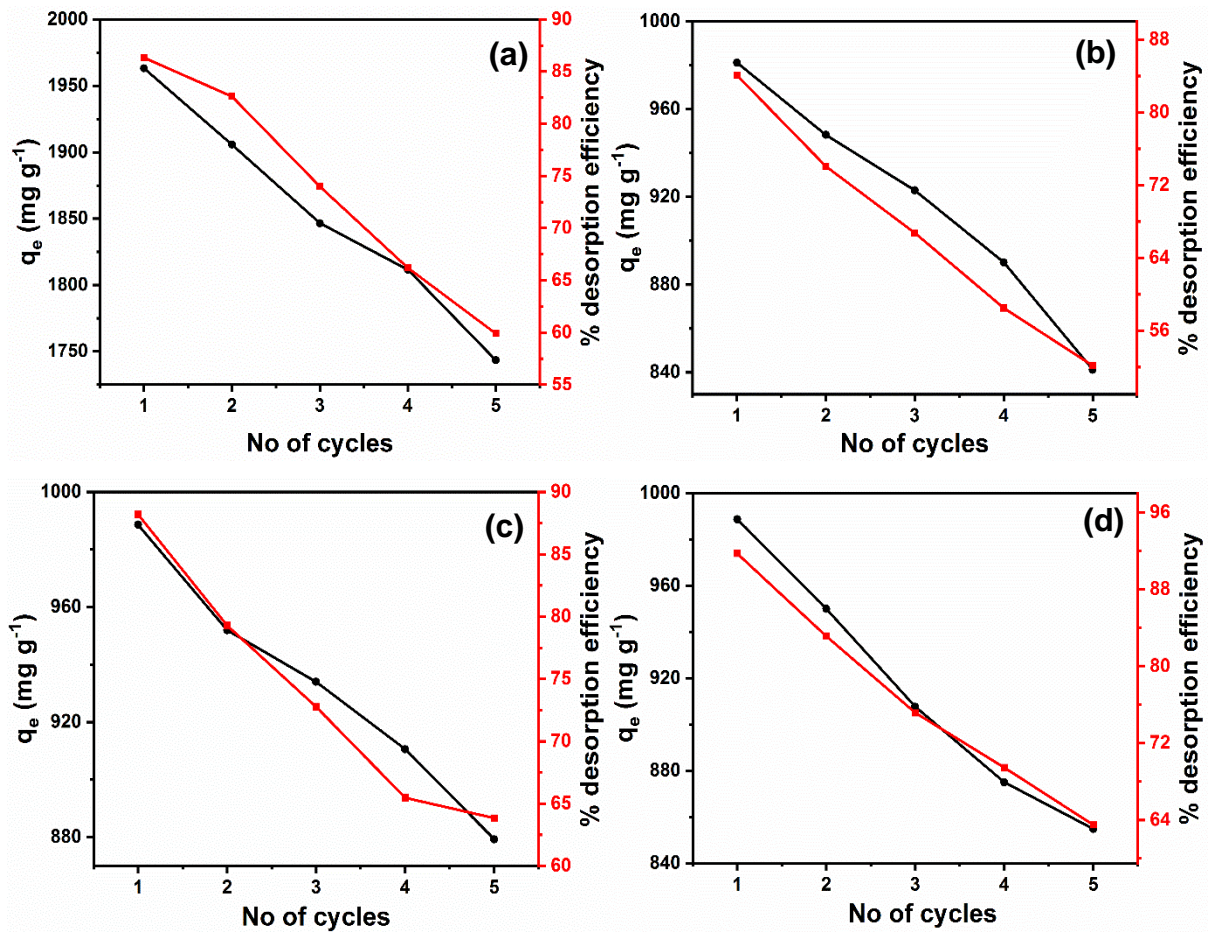


Figure 6.34. Desorption studies of synthetic wastewater with GO-CeO<sub>2</sub>@CoFe<sub>2</sub>O<sub>4</sub>



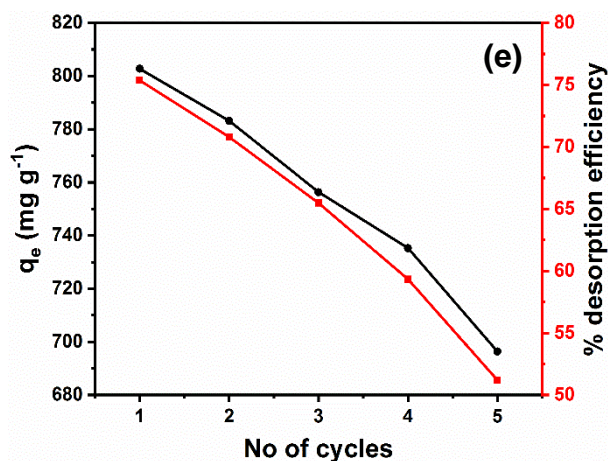


Figure 6.35. Desorption studies of synthetic wastewater with adsorption capacity  $q_e$  of regeneration cycles: a) MB, b) RB, c) CR, d) Pb(II) & e) Cd(II)

For better understanding of the nanocomposite, the recyclability cycles were done to understand the efficiency of adsorption in various cycles. Due to the better desorption performance towards all the pollutants were satisfactory, when the HCl concentration 1.0 M utilized in the 1<sup>st</sup> cycle adsorption-desorption test, and it is same for the corresponding six cycles. From the figure 6.33, a slightly decrease in recyclability capacity 90% is observed within six adsorption-desorption cycles for all pollutants except Cd(II) metal ion. It has been confirmed that the regeneration process has no effect on the structural and functional factors in GO-CeO<sub>2</sub>@CoFe<sub>2</sub>O<sub>4</sub> composite. Figure 6.34 represented the desorption studies of various pollutants with 1.0 M HCl solution as eluent and it proved that the desorption rate gradually decreased due to the consecutive cycles which is effective for CR, Pb(II) when compared to MB, RB and later it is least effective for the Cd(II). Figure 6.35 gave the adsorption capacity  $q_e$  of the recycled studies up to 5 cycles with the desorption rate.

### 6.3.21 Recycled studies

Due to the good adsorption capacity between the pollutants and GO-CeO<sub>2</sub>@CoFe<sub>2</sub>O<sub>4</sub> which explained the synthesis of CoFe<sub>2</sub>O<sub>4</sub> and incorporated into the nanoceria coated GO enhanced the surface area as well as functional groups in the nanocomposite. This increase in surface area and functional groups enhances the adsorption of pollutants.

From the results of XPS survey shown in figure 6.36 & 6.37, they are new peaks with binding energy values of Pb 4f and Cd 3d, which have appeared on nanoadsorbent, which proved that they were successfully adsorbed over the nanocomposite. The sharp peaks which appeared at Pb 4f spectra are at 138.2 eV and 143.7 eV ascribed to the Pb 4f<sub>5/2</sub> and Pb 4f<sub>7/2</sub> respectively

proved that the Pb uptake taken place after adsorption (Alqadami et al. 2020; Briggs 1981). In Cd uptake there is a strong peak around 405.6 eV and 412.7 eV congregated to the core levels of Cd 3d<sub>5/2</sub> and Cd 3d<sub>3/2</sub> after the adsorption (Maziarz et al. 2019; Wang et al. 2020). The XPS spectra which includes Pb as well as Cd, except the C-C bond which remains unchanged and the remaining groups shifted to higher binding energies values. But after the Pb adsorption, the C-OH groups intensity decreased to a higher extent which proved that the adsorption process took place on the hydroxyl groups of the adsorbent. The Ce<sup>+4</sup> spectra remains unchanged in the Cd uptake but in case of Pb uptake the binding energy values moved towards higher value. The Co 2p spectra remains unchanged after adsorption both Pb and Cd adsorption. Meanwhile, Fe-O bond in which O 1s spectra having a binding energy value 531.9 eV before adsorption shifted to 532.5 eV i.e., in case of Pb uptake and there is a slight increase in binding energy of Cd uptake around 532.8 eV after adsorption. The above interactions between the Pb/Cd with O leading to the reduction of electron cloud density and also confirmed that the Pb(II) is more adsorbed when compared to the Cd(II) on the nano adsorbent.

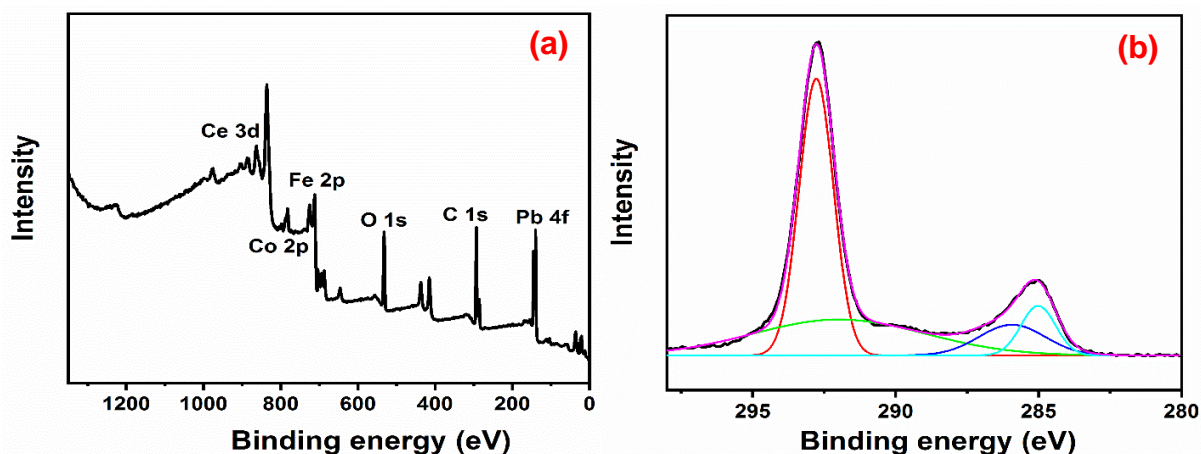
This interaction has been also confirmed by FTIR analysis in figures 6.38 & 6.39. After adsorption, the peaks around 3440 cm<sup>-1</sup> in nanocomposite are shifted to lower frequency i.e., at 3422 cm<sup>-1</sup> and 3424 cm<sup>-1</sup> for the uptake of Pb and Cd ions. A wide absorption band at 1630 cm<sup>-1</sup> is shifted to lower frequency 1620 cm<sup>-1</sup> and the intensity of the band has been reduced for both Pb and Cd uptake (Bao et al. 2020; Hu et al. 2016). This indicate clearly that the interaction of Pb(II) and Cd(II) ions with the -OH groups of the nanocomposite during the adsorption phenomena. A characteristic band was present at 1410 cm<sup>-1</sup> which represented the symmetrical stretching vibrations of -COO- groups got shifted to a lower value indicated that there is a chelation property between the metal ions (Pb and Cd) and the carboxylate groups on the adsorbent surface. This interaction justified that the XPS analysis is in correlation with FTIR spectra during the adsorption process.

The adsorption of MB dye can be enhanced with the increase in pH of the solution. Usually in the more acidic media (pH ≤ 2.5), the electrostatic repulsion between the adsorbent and the cationic MB molecules reduced the strength of adsorption capacity. When the solution pH is around 2, the removal efficiency reached up to 37%. This result is due to the MB dye and nanocomposite possessing bountiful availability of aromatic group and π-π stacking interaction occurred between the MB dye molecules and nanocomposite resulted in effective removal of MB (Ai et al. 2011; Pereira et al. 2003). This interaction is justified using the FTIR analysis (figure 6.38). The adsorption band corresponded to be the aromatic clusters in nanocomposite

which got slipped from 1660  $\text{cm}^{-1}$  (before adsorption) to 1605  $\text{cm}^{-1}$  (after adsorption of MB) through the stacking of  $\pi$ - $\pi$  interactions (Bradder et al. 2011). When the pH of solution increased to 5.9, the attractions present in between the negatively charged composite and the cationic MB molecules have been found to be electrostatic interactions resulted in the increase in adsorption efficiency of MB. The binding or attachment efficiency of RB molecules with the nanocomposite can be justified using FTIR analysis. Two possible absorption bands which are observed around 1593  $\text{cm}^{-1}$  and 1342  $\text{cm}^{-1}$  up on RB dye which got attached to the nanocomposite confirmed the adsorption of RB dye on the adsorbent surface. Here, the probable binding mechanism for adsorption is due to the H-bonding (Gangopadhyay et al. 2019; Zhang et al. 2011). The incorporation of ferrite nanoparticles onto GO-CeO<sub>2</sub> support enhanced the strength of H-bonding which confirmed the nanocomposite as a better adsorbent than the GO-CeO<sub>2</sub> support (Gangopadhyay et al. 2019).

After the CR adsorption, three new adsorption peaks observed at 1030, 1185 and 1220  $\text{cm}^{-1}$  from the CR adsorbed nanocomposite FTIR spectrum. The peak around 1070  $\text{cm}^{-1}$  resembled the SO<sub>4</sub><sup>2-</sup> originated from the stretching vibrations of S=O in the (-SO<sub>3</sub><sup>-</sup>) group. The band present at 1620  $\text{cm}^{-1}$  corresponded to the aromatic skeleton C=C vibrations and later, a band around 1577  $\text{cm}^{-1}$  confined to N=N vibrations in CR molecule (Zheng et al. 2017). A broad band around 3000-3500  $\text{cm}^{-1}$  is very strong, because of the vibrations i.e., N-H group of primary amine and O-H group of water, during the CR adsorption as well as the surface hydroxyl group on the nanocomposite (Basila 1961).

TEM images before and after adsorption of dyes took place on GO-CeO<sub>2</sub>@CoFe<sub>2</sub>O<sub>4</sub> nanocomposite in figure 6.40. The size of the nanocomposite varied in HR-TEM images before and after adsorption given in figure 6.40(a-i). The SAED pattern after the adsorption lost the crystalline nature because of repeated cycles.



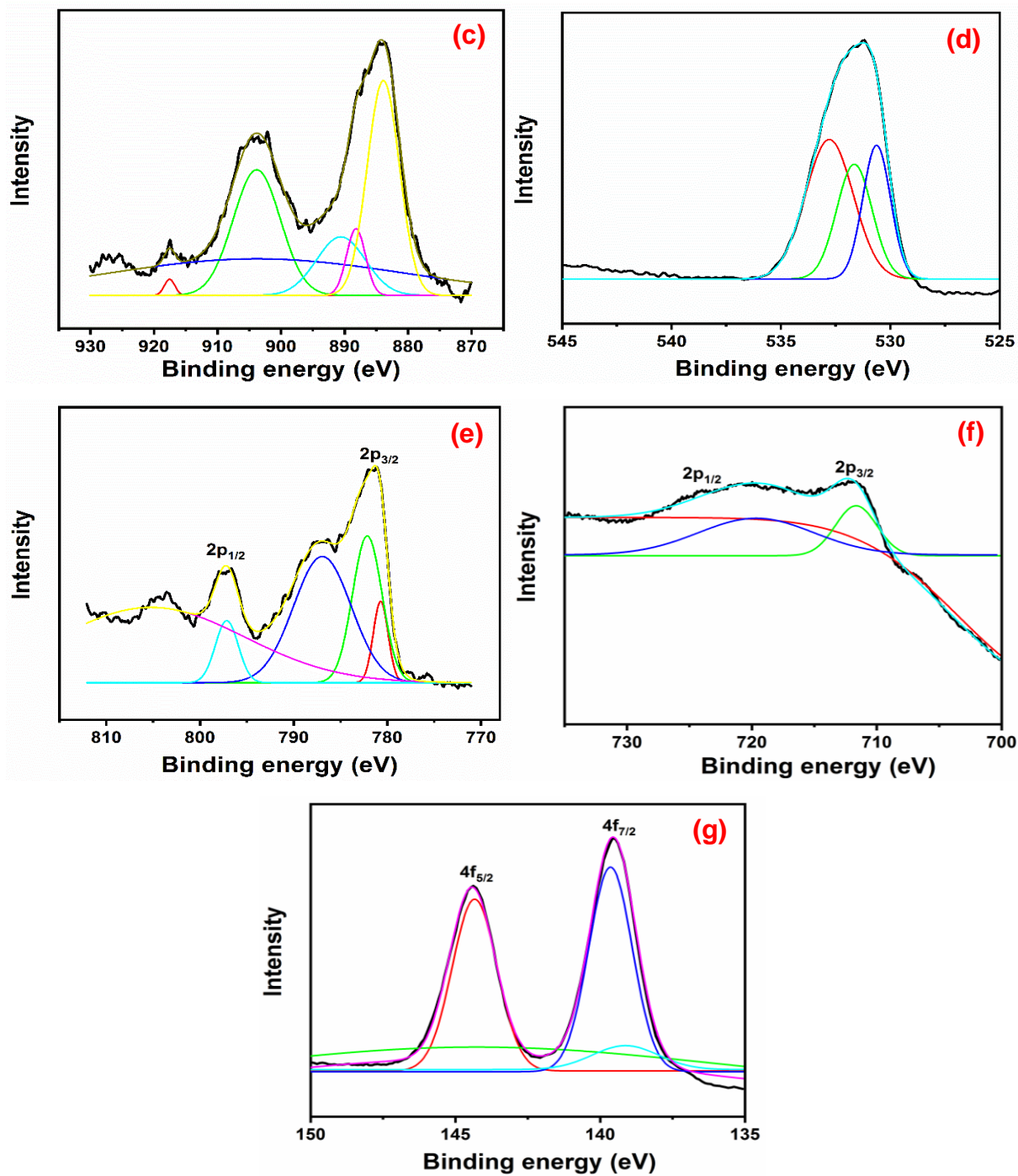
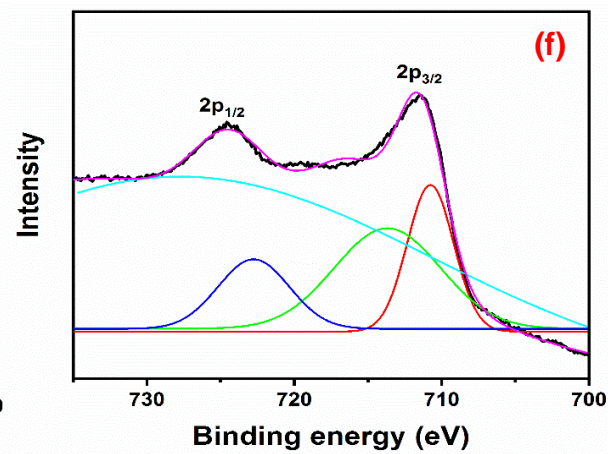
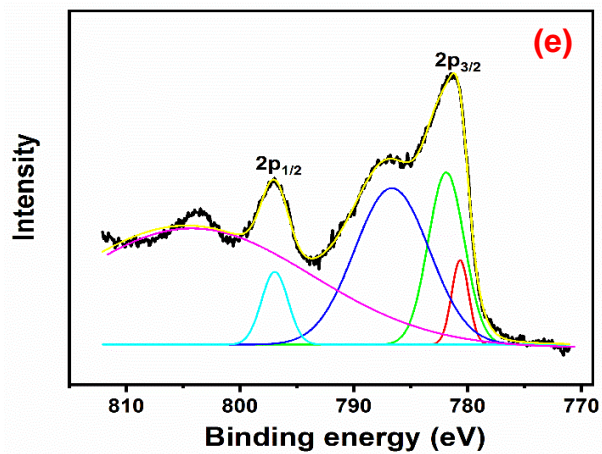
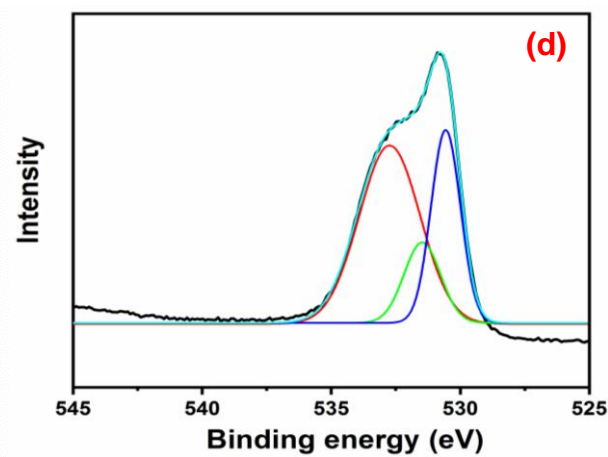
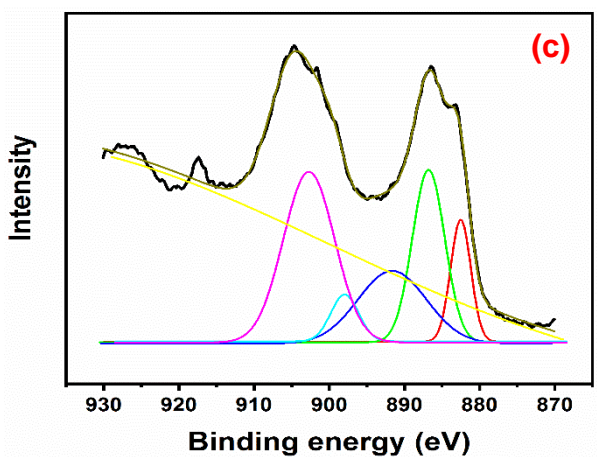
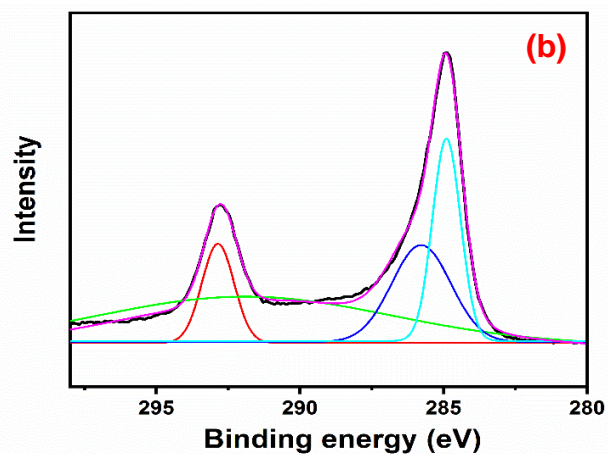
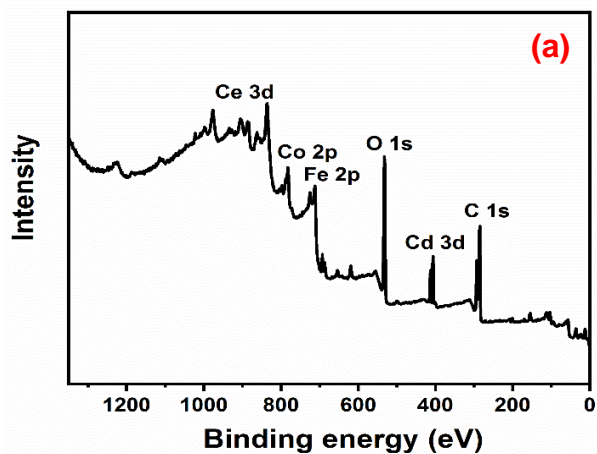


Figure 6.36. XPS spectra of Pb(II) adsorbed GO-CeO<sub>2</sub>@CoFe<sub>2</sub>O<sub>4</sub> : a) elemental survey, b) C 1s, c) Ce 3d, d) O 1s, e) Co 2p, f) Fe 2p & g) Pb 4f



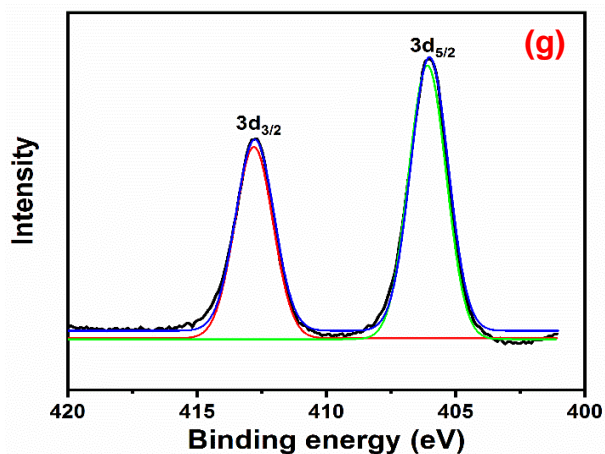


Figure 6.37. XPS spectra of Cd(II) adsorbed GO-CeO<sub>2</sub>@CoFe<sub>2</sub>O<sub>4</sub>: a) elemental survey, b) C 1s, c) Ce 3d, d) O 1s, e) Co 2p, f) Fe 2p & g) Pb 4f

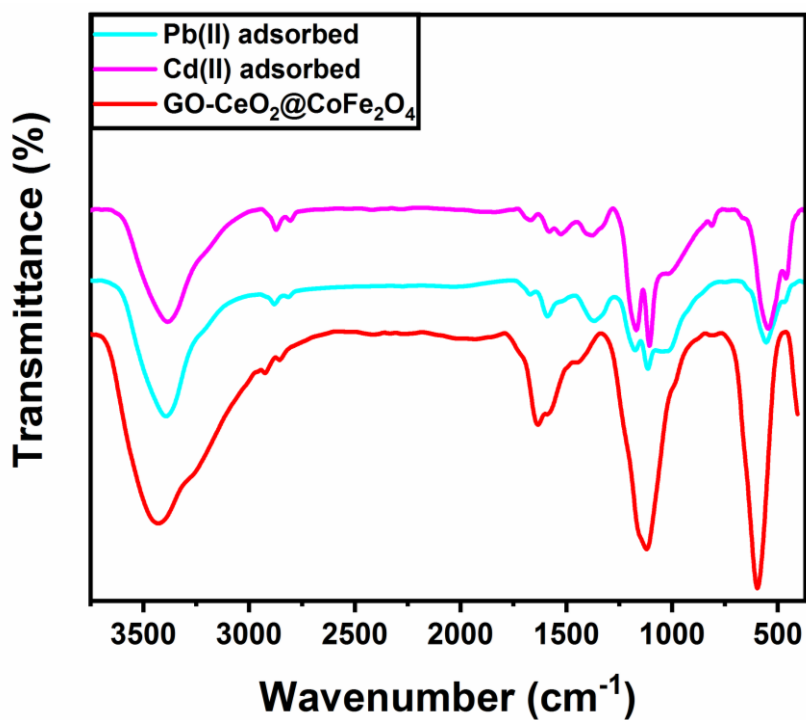


Figure 6.38. FTIR Spectra of GO-CeO<sub>2</sub>@CoFe<sub>2</sub>O<sub>4</sub>, Pb(II) adsorbed & Cd(II) adsorbed.

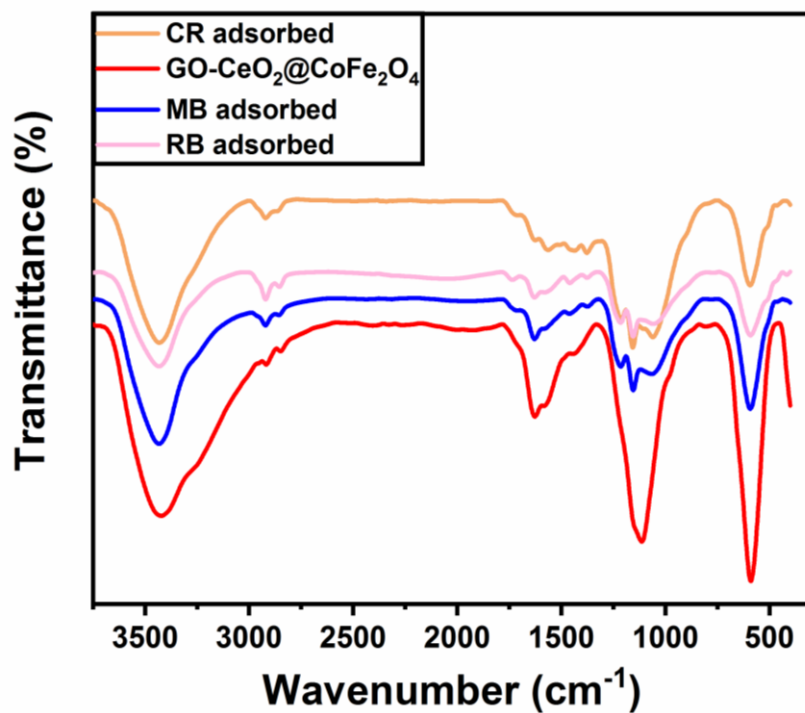
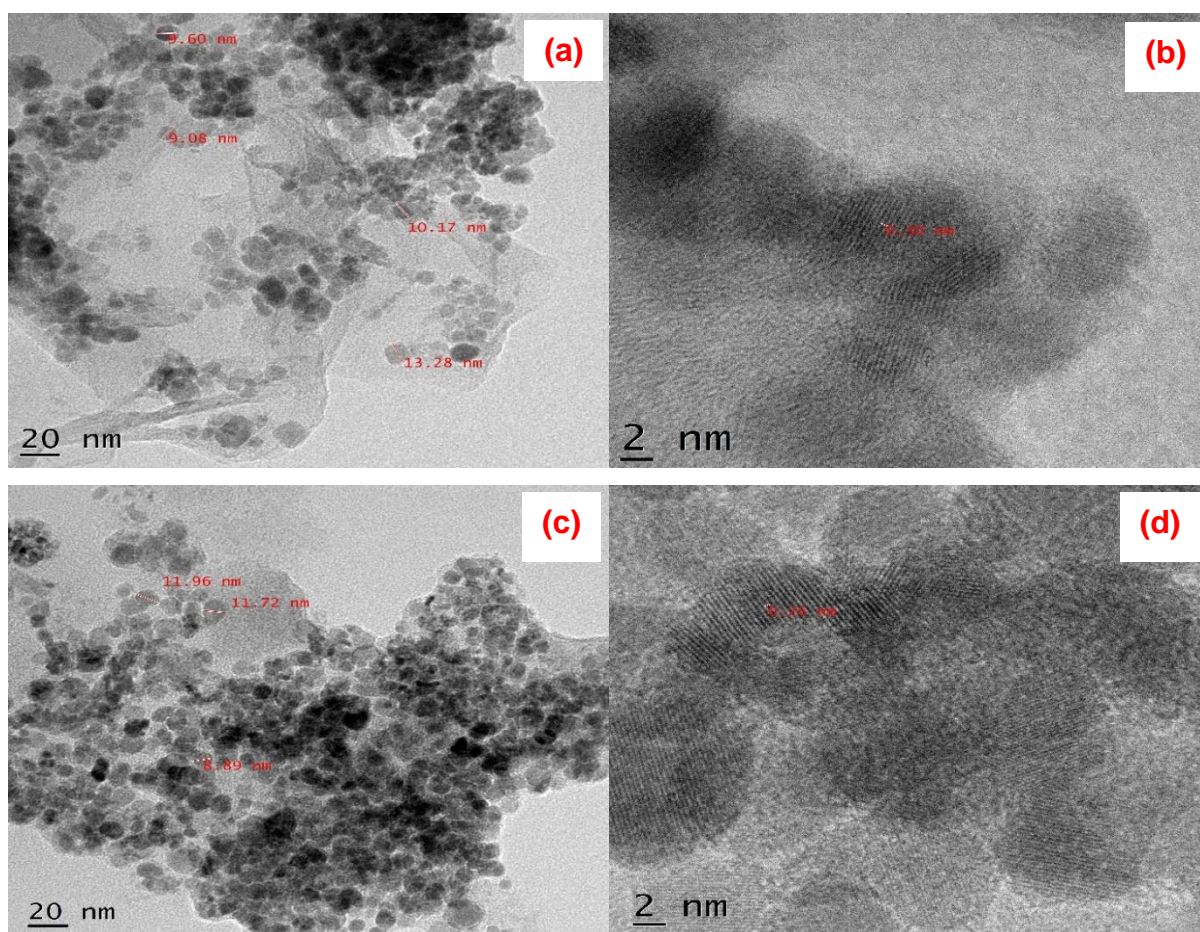


Figure 6.39. FTIR Spectra of GO-CeO<sub>2</sub>@CoFe<sub>2</sub>O<sub>4</sub>, MB dye adsorbed, RB dye adsorbed & CR dye adsorbed.





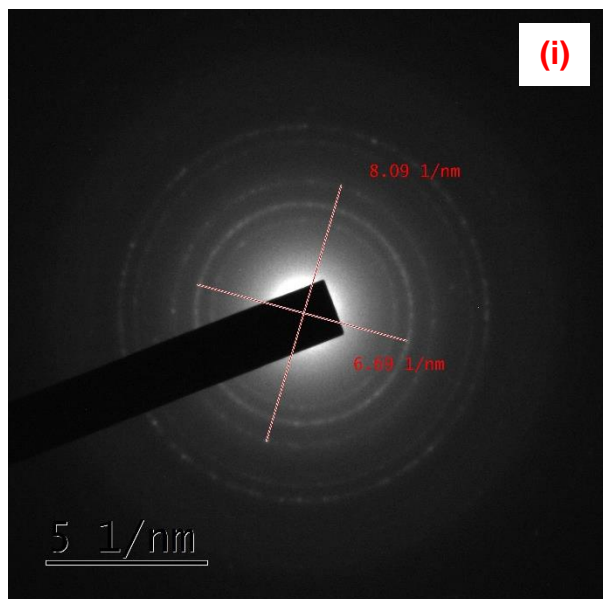
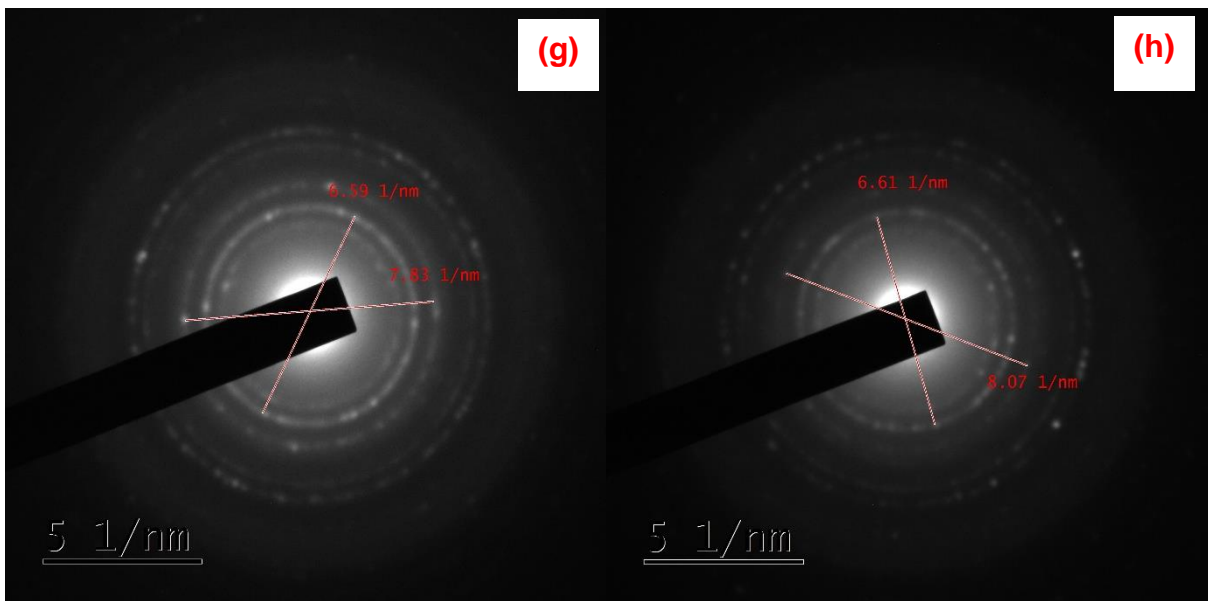
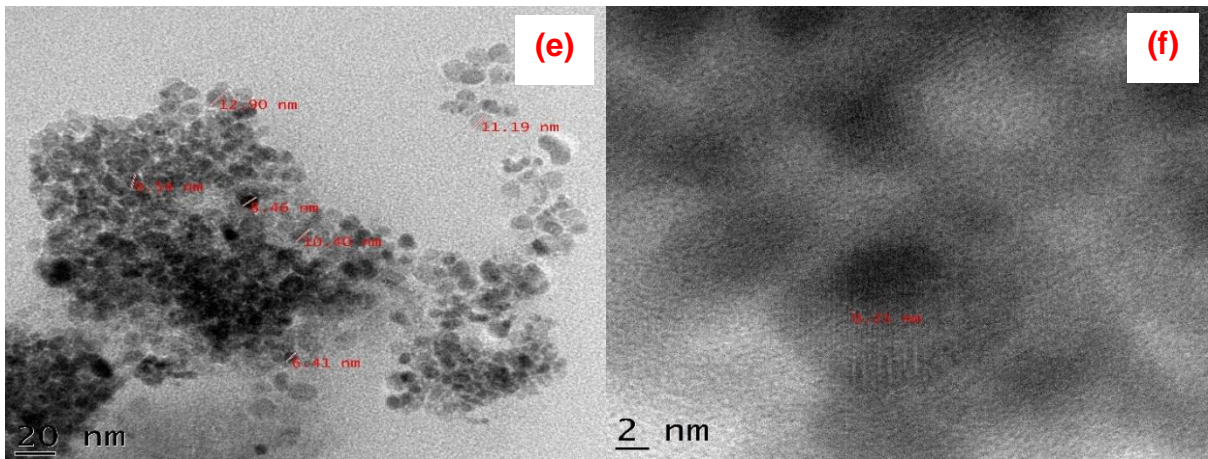


Figure 6.40. TEM images of dyes adsorbed GO-CeO<sub>2</sub>@CoFe<sub>2</sub>O<sub>4</sub>: (a, b) MB dye, (g) SAED of MB adsorbed, (c, d) RB dye, (h) SAED of RB adsorbed (e, f) CR dye & (i) SAED of CR adsorbed

### 6.3.22 Proposed mechanism for adsorption

Magnetic Spinel ferrites attained significant interest for the treatment of wastewater treatment and along with Graphene derivatives such as graphene oxide adsorb pollutants mainly due to the interactions such as Hydrogen-bonding, electrostatic and  $\pi$ - $\pi$  interactions. Cobalt ferrites have magnetic as well as porous in nature and the various hydroxyl groups which help in various interactions between the pollutants and the metal ions (M-OH/Fe-OH) which can grant variation in sorption capacity. The presence of nanoceria on the GO enhances its surface area and the GO-CeO<sub>2</sub>@CoFe<sub>2</sub>O<sub>4</sub> nanocomposite adsorption is determined by solution pH along with the surface charge in case of cationic and anionic pollutants. With a substantial increment in pH of the aqueous solution, the adsorption capacity gets reduced for all pollutants due to the presence of electrostatic interactions and the negatively charged surface on the GO-CeO<sub>2</sub>@CoFe<sub>2</sub>O<sub>4</sub> shown in figure 6.41. The adsorption of pollutants on the nanocomposite includes mechanisms like 1) Electrostatic interaction between the electron rich carboxyl groups on adsorbent and the pollutants 2) Coordination linkages between the Fe-O group as well as hydroxyl groups and the pollutant ions.

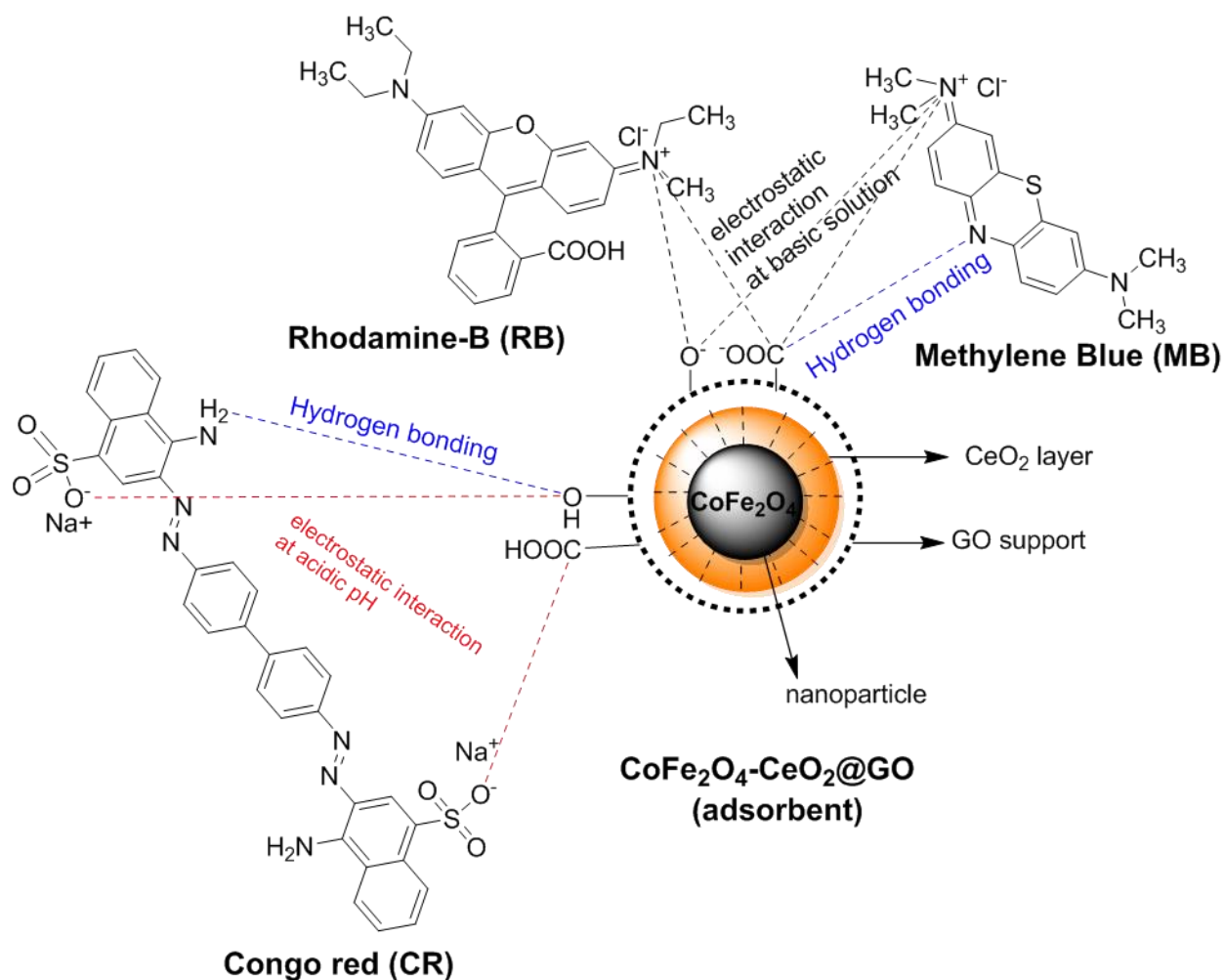


Figure 6.41. Proposed mechanism for the pollutants (MB, RB & CR) adsorption on the GO-CeO<sub>2</sub>@CoFe<sub>2</sub>O<sub>4</sub>

The adsorption mechanism has been investigated by FTIR and XPS techniques and in case of dyes, the surface of adsorbent analyzed using TEM analysis to know the pattern of crystallization after adsorption. However, the various impurities in wastewater have an effect on removal efficiency when compared to simulated effluents on GO-CeO<sub>2</sub>@CoFe<sub>2</sub>O<sub>4</sub> using (i) the strong interaction between the GO-CeO<sub>2</sub>@CoFe<sub>2</sub>O<sub>4</sub> and the pollutant upon a heterogeneous surface gave a chance of competitive ability for the impurities in wastewater which reduces the number on active sites on its surface, (ii) the high amount of impurities leads to the particle aggregation which reduces the adsorption capacity gradually, (iii) At last, it affects the activity coefficient of the adsorbates in wastewater thus limiting the transfer of pollutants in wastewater onto the GO-CeO<sub>2</sub>@CoFe<sub>2</sub>O<sub>4</sub> surface.

### 6.3.23 Adsorption and recycling performances of GO-CeO<sub>2</sub>@CoFe<sub>2</sub>O<sub>4</sub> in model wastewater

To estimate the performance of GO-CeO<sub>2</sub>@CoFe<sub>2</sub>O<sub>4</sub> in real-world applications, the adsorption process and the recyclability studies were done using the dyes and metal ions MB, RB, CR, Pb(II) & Cd(II) were tested in model wastewater shown in Figure 6.42. The removal rate of pollutants with 10 mg L<sup>-1</sup> & 20 mg L<sup>-1</sup> of adsorbent were tested. The obtained rate removal in 20 mg L<sup>-1</sup> were 96.20 (MB), 95.10 (RB), 97.46(CR), 96.82(Pb(II)) & 79.10(Cd(II)) respectively. The model wastewater data when we analyzed with that of the simulated wastewater explained in figure 6.33, the coexistence of impurities of various chemical and biological medium impurities doesn't have any impact of the pollutant's adsorption. However, a slight reduction in removal rate is observed for the nanoadsorbent which indicated that the nanocomposite has better stability and regeneration capacity in this model wastewater. From the above result, GO-CeO<sub>2</sub>@CoFe<sub>2</sub>O<sub>4</sub> can be an efficient competitor for the real wastewater treatment.

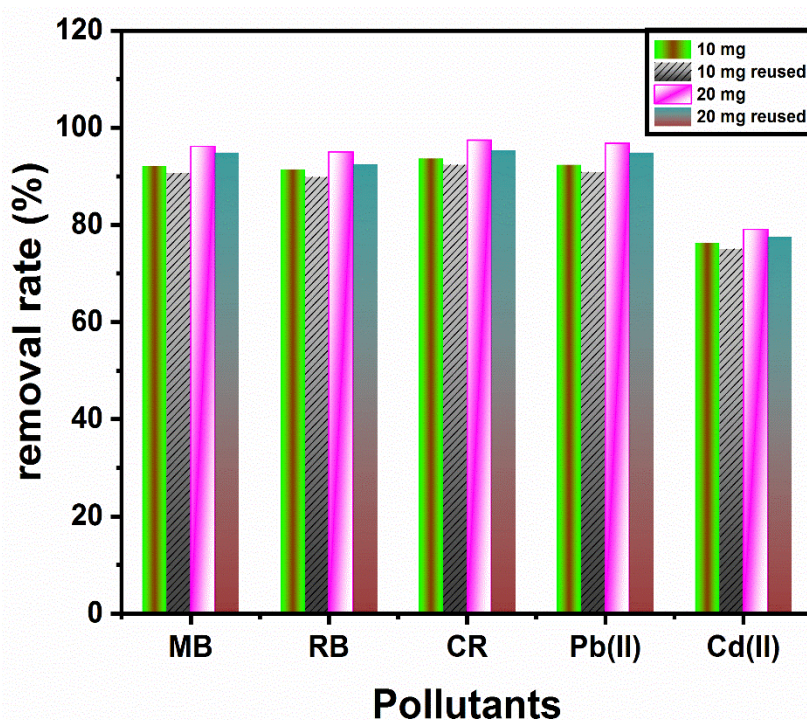


Figure 6.42. Adsorption and recycling performance of GO-CeO<sub>2</sub>@CoFe<sub>2</sub>O<sub>4</sub> in model wastewater

### 6.3.24 Adsorption of real wastewater on GO-CeO<sub>2</sub>@CoFe<sub>2</sub>O<sub>4</sub>

The real wastewater analysis has been carried out with all the adsorbates to investigate the efficacy of the nanocomposite in industrial waste effluents. The real wastewater is further

determined to find out its COD and turbidity values with reference to the nanocomposite given in table 6.9. The dye and heavy metal ion structure in the real wastewater are not known, and the declaration of any identification or structural data is stringently adhered from the purveyor. The experiments were conducted temperature 318.5 K & 323.5 K for the pollutants and the amount taken for the adsorption phenomena is same as that of the synthetic wastewater. Chemical Oxygen Demand carried out by USEPA 2013 method in presence of Digital Reactor Block 2000 (Hack, Germany). Turbidometer is used to find out turbidity in wastewater procured with Bante Instruments.

Table 6.9: Analysis of the real wastewater sample

Type of test	COD (mg L <sup>-1</sup> )	TOC	Turbidity	Temperature	Color
Value	703	237	27.4	25	Black

With respect to the above analysis, it displayed that the adsorption efficiency and adsorption capacity is less to that of the synthetic wastewater because of the existence of unlimited organic species and impurities percolated in the textile effluents. The performance of the nanocomposite and its experimental values represented in corresponding tables 6.10, 6.11 & 6.12.

Table 6.10: The adsorption isotherms of real wastewater on GO-CeO<sub>2</sub>@CoFe<sub>2</sub>O<sub>4</sub>

Pollutants	Temp(K)	Langmuir				Freundlich			
		Q <sub>max</sub>	K <sub>a</sub>	Adj.	R <sup>2</sup>	n	K <sub>F</sub>	Adj.	R <sup>2</sup>
		mg g <sup>-1</sup>	L mg <sup>-1</sup>	R <sup>2</sup>	(COD)		(mg g <sup>-1</sup> ) (L mg <sup>-1</sup> ) <sup>1/n</sup>	R <sup>2</sup>	(COD)
MB	318.5	6311.1256	0.01745	0.99202	0.99274	1.76219	294.07567	0.94784	0.95258
	323.5	3979.4626	0.01802	0.98849	0.98954	2.3554	318.48438	0.90512	0.91374
RB	318.5	2033.7687	0.25701	0.99714	0.9975	2.78197	566.26443	0.93611	0.9909
	328.5	1560.1055	0.0754	0.99691	0.9973	2.82325	285.49562	0.95274	0.95864
CR	318.5	4545.7497	0.06509	0.99039	0.99126	2.94551	825.9868	0.95495	0.95905
	323.5	4081.6721	0.01058	0.99251	0.99319	2.17296	230.46792	0.95422	0.95838
Pb	318.5	5347.1641	0.02876	0.99768	0.99789	2.13053	454.3342	0.95415	0.95832
	323.5	4022.6438	0.01621	0.995	0.99545	2.29322	295.77682	0.9317	0.93791
Cd	318.5	2490.6621	0.00998	0.99663	0.99694	1.78382	85.9565	0.96534	0.96849
	323.5	2006.7145	0.00999	0.99765	0.99786	1.88674	78.69816	0.9651	0.96827

Table 6.11: DR and Temkin adsorption isotherms of real wastewater on GO-CeO<sub>2</sub>@CoFe<sub>2</sub>O<sub>4</sub>

Pollutants	Temp(K)	Dubinin-Radushkevich				Temkin			
		$q_s$	$K_{DR}$	Adj.	$R^2$	$A_T$	$B_T$	Adj.	$R^2$
		(mol g <sup>-1</sup> )	(mol <sup>2</sup> k <sup>-1</sup> J <sup>-2</sup> )	$R^2$	(COD)	(L g <sup>-1</sup> )	(J mol <sup>-1</sup> )	$R^2$	(COD)
MB	318.5	3937.52716	0.16395	0.93237	0.93851	0.29429	2.38339	0.95226	0.95660
	323.5	3063.74410	0.31527	0.92177	0.92888	0.22803	3.37224	0.97794	0.97995
RB	318.5	1599.51312	0.00212	0.89685	0.90974	6.17182	7.90674	0.95348	0.95929
	323.5	1244.30076	0.01950	0.87393	0.88969	1.79349	10.2994	0.96264	0.96731
CR	318.5	3465.98042	0.01739	0.86891	0.88082	4.36902	4.46011	0.91226	0.92023
	323.5	2929.26733	0.71873	0.93884	0.9444	0.32625	4.32241	0.9111	0.91918
Pb	318.5	3763.09446	0.08496	0.91666	0.92423	1.02115	3.48329	0.85036	0.86396
	323.5	3005.60561	0.30179	0.93766	0.94333	0.28676	3.71791	0.9447	0.94973
Cd	318.5	1543.60699	0.41594	0.90117	0.91015	0.21815	6.74949	0.89186	0.90169
	323.5	1287.33754	0.43003	0.8906	0.90054	0.18355	7.79494	0.92774	0.93431

### Kinetic Studies:

Table 6.12: Kinetic studies of real wastewater on GO-CeO<sub>2</sub>@CoFe<sub>2</sub>O<sub>4</sub>

Pollutants	Temp (K)	Pseudo-first-order				Pseudo-second-order		
		$q_{e(exp)}$	$q_{e(calc)}$	$k_1$	$R^2$	$q_{e(calc)}$	$k_2$	$R^2$
		(mg g <sup>-1</sup> )	(mg g <sup>-1</sup> )	(min <sup>-1</sup> )		(g mg <sup>-1</sup> )	(min <sup>-1</sup> )	
MB	318.5	1873.2	732.8566	0.0085	0.88154	1871.145	4.606×10 <sup>-5</sup>	0.99945
	323.5	1763.4	806.9486	0.00757	0.85143	1761.363	3.347×10 <sup>-5</sup>	0.99937
RB	318.5	981.2	603.9793	0.00649	0.95071	934.5794	3.453×10 <sup>-5</sup>	0.9969
	323.5	903.65	539.0455	0.00691	0.95002	862.069	4.060×10 <sup>-5</sup>	0.9985
CR	318.5	979.7	497.7908	0.00757	0.91593	970.874	5.829×10 <sup>-5</sup>	0.99882
	323.5	847.3	366.8819	0.00754	0.87269	840.336	8.577×10 <sup>-5</sup>	0.99961
Pb	318.5	958.75	590.7246	0.00689	0.96386	943.3962	4.168×10 <sup>-5</sup>	0.99375

	323.5	897.9	526.1782	0.00648	0.93835	877.193	$4.801 \times 10^{-5}$	0.99766
Cd	318.5	779.2	276.9203	0.00861	0.86619	775.194	$1.373 \times 10^{-4}$	0.99984
	323.5	723.95	379.54	0.0075	0.91339	719.424	$7.408 \times 10^{-5}$	0.9991

### 6.3.25 Recyclability studies of the real wastewater

The recyclability studies on the GO-CeO<sub>2</sub>@CoFe<sub>2</sub>O<sub>4</sub> adsorbent revealed that the real wastewater removal rate is less compared to the simulated wastewater under the same parameters as shown in figure 6.43 and the table 6.13.

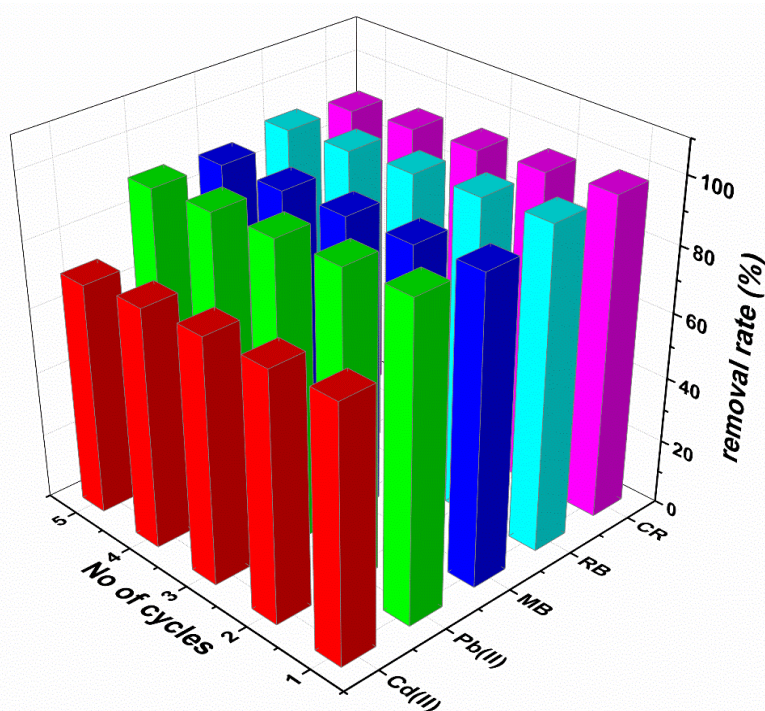


Figure 6.43. Regenerative capacity of the real wastewater for the pollutants: MB, RB, CR, Pb(II) & Cd(II)

Table 6.13: The recyclability studies of pollutants such as MB, RB, CR, Pb(II) & Cd(II) over GO-CeO<sub>2</sub>@CoFe<sub>2</sub>O<sub>4</sub>

No. of cycles	Removal rate of pollutants in real wastewater (%)				
	MB	RB	CR	Pb(II)	Cd(II)
1	93.6	98.1	97.9	95.8	77.9
2	92.1	96.9	96.1	94.7	76.4
3	91.4	95.4	94.5	93.6	75.4
4	90.4	94.1	93.1	92.4	73.8
5	89.9	92.7	91.2	90.9	71.2

## 6.4 CONCLUSIONS

In this study, GO-CeO<sub>2</sub>@CoFe<sub>2</sub>O<sub>4</sub> nanohybrid was synthesized using hydrothermal methodology has been successfully developed. The synthesized nanocomposite acquired a high surface area with wrinkled morphology. GO-CeO<sub>2</sub>@CoFe<sub>2</sub>O<sub>4</sub> efficiently removed the dyes like MB, RB, CR and the heavy metal ions Pb(II), Cd(II) in aqueous sewage effluents. GO-CeO<sub>2</sub>@CoFe<sub>2</sub>O<sub>4</sub> being magnetic in nature, gets easily separated, is a beneficial aspect of adsorbent. With the increase in pH, the maximum adsorption capacity increases for the cationic pollutants correlated with the anionic pollutants. This hybrid composite which consists of supermagnetic ferrite found effective in real wastewater for a varied pH range. It can be recycled using desorption agents like HCl and EDTA. The results determine the nanocomposite GO-CeO<sub>2</sub>@CoFe<sub>2</sub>O<sub>4</sub> as a promising material for the removal of cationic and anionic dyes along with heavy metal ions from the real-life wastewater.



## **CHAPTER-7**

**Synthesis of novel, magnetic GO-Fe/CPTMS-SiO<sub>2</sub>@MF composite for the removal of dyes and heavy metal ions**

**Abstract:** *Spinel Ferrites gained attention for the organic and inorganic pollutants due to their nanosized, superparamagnetic properties and a high surface to volume ratio. This chapter discusses about the ferrites designed on graphene nanosheets avoid the agglomeration and inhibit the leaching of pollutants to increase the efficacy of adsorption.*

## 7.1 INTRODUCTION

In the modern world, environmental pollution became one of the vital and high priority problems across the globe. Due to the rapid development of industrial sector, water pollution has gained importance due to its close relationship with the mankind. These organic dyes and heavy metal ion contaminants which are discharged from dyes manufacturing industries, paper making industries, metallurgy and textile industries has resulted in increasing of toxic concentration in water bodies due to the heavy quantity of water used in textile industries, high amount of liquid pollutants are discharging (Li et al. 2016; Ma et al. 2017; Zhao et al. 2015). The presence of organic contaminants in industrial waste is a global concern to the environment because of its toxicity, carcinogenic nature and mutagenicity. These organic contaminants possess less biodegradability and highly stable towards photo-chemical treatments because of its complex aromatic structure (Inyang et al. 2014). Some of the metallurgy industries are disposing heavy metals like lead and cadmium. These heavy metals are accumulating in the living organism over a period of time and causes serious diseases like memory loss, kidney problem and reproductive effect in human. The permissible limit created by World Health Organization (WHO) in drinking water for lead is  $0.01 \text{ mg L}^{-1}$  (Organisation mondiale de la santé et al. 2004). To remove these pollutants from waste water, different types of techniques are developed such as biological water decontamination process, chemical precipitation and adsorption (Arami et al. 2005; Rahsepar et al. 2012).

With the latest generation adsorbent substances evolved so far, magnetic nanoadsorbent possessed huge surface area, tunable morphology, easily separable and a high efficacy are the most promising path. During the recent times, spinel ferrites became the fundamental choice for the removal of organic and inorganic pollutants for the application in the treatment of wastewater because of the presence of nanometer-sized, superparamagnetic property and a huge surface to volume ratio. Spinel ferrites ( $\text{MFe}_2\text{O}_4$ ) are magnetic materials where the M(II) and Fe(III) cations occupy both tetrahedral as well as octahedral sites respectively, whereas inverse spinel ferrites occupy half of the Fe(III) occupy tetrahedral sites. These ferrites designed on the graphene oxide nanosheets can avoid agglomeration, apart from it graphene

which inhibited the leaching the pollutants thereby increasing the efficiency in adsorption process.

Here, we synthesized the highly magnetic MF nanoparticle which was supported with the Iron oxide doped graphene oxide through the cross linkage of Tetraethyl Orthosilicate for the effective functionalization on graphene oxide. These synthesized GO-Fe/CPTMS-SiO<sub>2</sub>@MF nanocomposite was effective adsorbent for the removal of cationic and anionic pollutants from the textile wastewater.

## **7.2 EXPERIMENTAL SECTION**

### **7.2.1 Chemicals required**

Graphite, Potassium Permanganate (KMnO<sub>4</sub>), Sulfuric Acid (H<sub>2</sub>SO<sub>4</sub>), Phosphoric Acid (H<sub>3</sub>PO<sub>4</sub>), Hydrogen Peroxide (H<sub>2</sub>O<sub>2</sub>), Ethanol (C<sub>2</sub>H<sub>5</sub>OH), Acetone (C<sub>3</sub>H<sub>6</sub>O) and Toluene (C<sub>7</sub>H<sub>8</sub>) are from Lobo chemie Limited. Cobalt Nitrate Hexahydrate Co(NO<sub>3</sub>)<sub>2</sub>.H<sub>2</sub>O, Ferric Nitrate Nonahydrate Fe(NO<sub>3</sub>)<sub>3</sub>.9H<sub>2</sub>O, Zinc Nitrate Hexahydrate Zn(NO<sub>3</sub>)<sub>2</sub>.6H<sub>2</sub>O, Nickel Acetate Tetrahydrate Ni(CH<sub>3</sub>CO<sub>2</sub>)<sub>4</sub>.4H<sub>2</sub>O, Sodium Hydroxide (NaOH), Hydrazine Hydrate (H<sub>6</sub>N<sub>2</sub>O), Methylene blue(MB) , Rhodamine-B(RB), Congo red(CR), 2-pentanol (C<sub>5</sub>H<sub>12</sub>O), Oleic Acid (C<sub>18</sub>H<sub>34</sub>O<sub>2</sub>), Isopropanol (C<sub>3</sub>H<sub>8</sub>O) and 3-chloropropyl trimethoxy silane are from Sigma Aldrich Limited.

### **7.2.2 Synthesis of Graphene oxide (GO)**

Graphene oxide nanosheets were synthesized by Improved Hummer's method (Marcano et al. 2018). 1.5g of flaky graphite along with 3g of KMnO<sub>4</sub> added with a 200 mL acid mixture of sulfuric acid and phosphoric acid (9:1). The reaction mixture was stirred for 12h by keeping the temperature at 50 °C. The reaction mixture allowed to cool in room temperature and transferred in to ice approximately 400 mL slowly with stirring. Hydrogen peroxide 30% (8-10 mL) transferred in to the solution with vigorous stirring. The color of the mixture turned from brown to bright yellow. The obtained mixture was filtered through a Sieve tub and the filtrate is centrifuge it. After decantation, the product washed with distilled water and absolute ethanol several times and a final acetone wash. The resultant graphene oxide dried at 60 °C for 24h.

### **7.2.3 Synthesis of Iron oxide Nanoparticle (Fe)**

1g of ferric chloride is dissolved in 50 mL of distilled water and stirred for 30 min. 300 mg of urea is dissolved in 50 mL of distilled water. The above 2 mixtures were combined together and stirred for 30 min. Further, 5 mL of hydrazine dropped into the above mixture with constant

stirring for 2h. The solution is transferred to Teflon lined autoclave for 12h at 90 °C. The obtained solid product is washed thoroughly with C<sub>2</sub>H<sub>5</sub>OH and distilled water and dried at 70 °C in an oven.

### **7.2.3 Synthesis of Mixed Ferrite nanoparticle (MF)**

291.04 mg of Cobalt nitrate hexahydrate (Co(NO<sub>3</sub>)<sub>3</sub> · 6H<sub>2</sub>O), 807.98 mg of Ferric nitrate nonahydrate (Fe(NO<sub>3</sub>)<sub>3</sub> · 6H<sub>2</sub>O), 297.49 mg of Zinc nitrate hexahydrate (Zn(NO<sub>3</sub>)<sub>2</sub> · 6H<sub>2</sub>O) and 248.8 mg of nickel acetate tetrahydrate (Ni(ac)<sub>2</sub> · 4H<sub>2</sub>O) were dissolved in 20 mL of distilled water and stirred for 2h. Later 5 mmol of sodium hydroxide was dissolved in 5 mL of distilled water and 1 mL of hydrazine hydrate is dropped slowly into this mixture with 1h constant stirring. Both the mixtures were mixed together and 12 mL of 2-pentanol and 4 mL of oleic acid is added, under rigorous stirring. Further, the reaction mixture is stirred for 30 min, and later it is transferred into Teflon lined autoclave at temperature 180 °C for 18h. The reaction mixture is cooled off and transferred into solution of n-hexane. Further, the ethanol is added to the above solution, and the nanoparticles are precipitated off. The brown shiny nanoparticles are washed off several times with C<sub>2</sub>H<sub>5</sub>OH and distilled water. Later, the nanoparticles are dried in an oven at 90 °C for 12h.

### **7.2.5 Synthesis of Graphene-Iron oxide composite (GO-Fe)**

100 mg of graphene oxide is dispersed in ethanol under ultrasonic treatment for 30 min. Later, 100 mg of Fe nanoparticle is dropped into the mixture with constant stirring for 2h. Later the mixture is maintained at pH-6 using 1N NaOH and vigorously stirred for 2h. The solution is transferred into Teflon lined autoclave at 80 °C for 6h. The product is cooled off and it is washed thoroughly with C<sub>2</sub>H<sub>5</sub>OH, and dried at 60 °C.

### **7.2.6 Synthesis of Mixed Ferrite-Tetraethyl Orthosilicate (SiO<sub>2</sub>@MF)**

The synthesis of nanocomposites which were coated with silica (SiO<sub>2</sub>) done using the sol-gel method. In brief, 0.5g of mixed ferrite nanoparticles dissolved in 50 mL of isopropanol and 10 mL of distilled water, later it is followed by ultrasonication for 30 min. after that, 4 mL of Tetraethyl Orthosilicate (TEOS) and 10 mL of NH<sub>4</sub>OH were dropped to the above solution through vigorous stirring for 12h at room temperature under N<sub>2</sub> atmosphere. At the end, the product formed is washed with ethanol, isopropanol and distilled water several times and dried at 50 °C.

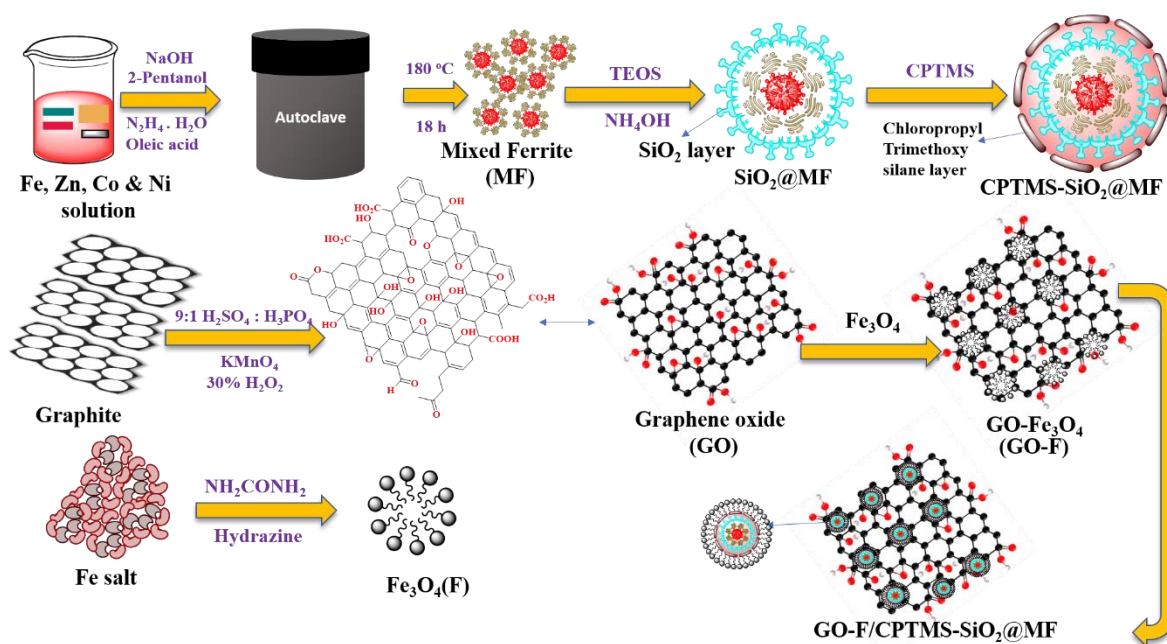
### **7.2.7 Synthesis of Mixed Ferrite-Tetraethyl Orthosilicate and 3-Chloropropyltrimethoxy silane (CPTMS-SiO<sub>2</sub>@MF)**

The formed mixed ferrite@ SiO<sub>2</sub> were functionalized with the 2 mL of 3-chloropropyltrimethoxy silane (CPTMS) as a precursor material. 0.5g of SiO<sub>2</sub>@MF

nanocomposites was added to the 40 mL of toluene and stirred vigorously. The temperature of the reaction is raised to 90 °C in reflux set up for 24h under N<sub>2</sub> atmosphere. Finally, the product formed is separated using external magnet and washed with ethanol, distilled water and dried at 60 °C.

### 7.2.8 Synthesis of Mixed Ferrite Nanocomposites (GO-Fe/CPTMS-SiO<sub>2</sub>@MF)

100 mg of GO-Fe nanocomposite is dispersed in 100 mL of ethanol solution under stirring for 30 min. Later, 500 mg of the nanocomposites added to the mixture and the reaction temperature of the reaction is raised to 75 °C with constant stirring for 12h under N<sub>2</sub> atmosphere. The product is cooled off and it is separated using external magnetic field washed several times with ethanol and distilled water. The nanocomposites dried in an oven at 60 °C for 12h.



Scheme 7.1. Synthesis of GO-Fe/CPTMS-SiO<sub>2</sub>@MF

### 7.2.9 Adsorption experiments

Synthetic waste water of dyes MB, RB, CR and heavy metal ions Pb(II), Cd(II) in single systems were respectively synthesized mixing these dyes as well as Pb(NO<sub>3</sub>)<sub>2</sub>, Cd(NO<sub>3</sub>)<sub>2</sub> · 6H<sub>2</sub>O in distilled water. The adsorbate solutions pH, ionic strength, adsorbent dosage, isotherms and kinetic studies can be adjusted by using required amount of 1.0 M HCl solution, 1.0 M NaOH solution and the solid sodium chloride respectively. Adsorption process performed at their constant temperature with a vibrating speed of 200 rpm.

The adsorption tests were performed for pH, ionic strength, isotherm models, adsorbent dosage and the thermal studies with 10 mg of GO-Fe/CPTMS-SiO<sub>2</sub>@MF was dispersed in 50

mL of synthetic wastewater. The time of reaction was maintained for 6h to assure the performance of adsorption equilibrium. In case of time studies, 10 mg of adsorbent were added to the 50 mL MB, RB, CR, Pb(II) & Cd(II) with initial concentration set at 400 mg L<sup>-1</sup>, 300 mg L<sup>-1</sup>, 400 mg L<sup>-1</sup>, 400 mg L<sup>-1</sup> & 400 mg L<sup>-1</sup>. For the isothermal and thermodynamic tests, all the adsorption tests conducted at various temperature 308.5 K, 313.5 K, 318.5 K, 323.5 K & 328.5 K.

After adsorption process, the adsorbent isolated using bar magnet. The synthetic wastewater initial and final concentrations measured with the calibrated curve between wavelength and optical density using UV spectrophotometer. The removal rate (%), adsorption capacity ( $q_e$  mg g<sup>-1</sup>) and the different time studies ( $q_t$  mg g<sup>-1</sup>) are measured using the equations respectively.

$$q_e = \frac{(C_o - C_e)V}{m} \quad (7.1)$$

$$q_t = \frac{(C_o - C_t)V}{m} \quad (7.2)$$

$$\% \text{ removal rate} = \frac{C_o - C_e}{C_o} \times 100 \quad (7.3)$$

Where  $C_o$  (mg L<sup>-1</sup>) refers to adsorbate initial concentration;  $C_e$  (mg L<sup>-1</sup>) &  $C_t$  (mg L<sup>-1</sup>) refers to the final concentrations at equipoise state and distinct time studies of the solutions,  $V$  (L) refers to capacity of adsorbate solution and the  $m$  refers to the weight in grams of the GO-Fe/CPTMS-SiO<sub>2</sub>@MF.

#### 7.2.10 Stability and reusability tests

The stability of adsorbent is determined in various pH concentration 1-10 to know the Fe's leaching using the ICP-AES analysis. 10 mg of GO-Fe/CPTMS-SiO<sub>2</sub>@MF, GO-Fe and the Fe<sub>3</sub>O<sub>4</sub> were dispersed in 25 mL of distilled water and the pH of solution maintained within a range of 0-10 using 1 M HCl /1 M NaOH. After shaking in an orbital shaker for 24h, the supernatant separated out for the measurement of concentration.

The reusability tests were tested in six adsorption-desorption cycles. 1.0 M HCl, 0.1 M HCl & 0.01 M HCl known to be desorbing groups for cation dyes, and 1.0 M HCl, 0.01 M EDTA & 0.005 M EDTA for the heavy metal ions. At first, 10 mg of composite is taken in 50 mL of wastewater, and shaken at a temperature of 318.5 K in an orbital shaker with a vibrating rate i.e., 200 rpm. The adsorbate solution initial concentration for the dyes, MB 400 mg L<sup>-1</sup>, RB 300 mg L<sup>-1</sup>, CR 400 mg L<sup>-1</sup> and metal ions Pb(II) 400 mg L<sup>-1</sup> & Cd(II) 400 mg L<sup>-1</sup> for a time of 6h. The saturated adsorbent was rejuvenated using 50 mL of desorbing agent at a similar

temperature, vibrating speed and reaction time of 12h as given above. After the reaction process is completed, the recovered adsorbent separated using magnet, washed properly with slightly basic solution and distilled water for reusage purpose.

#### **7.2.10 Adsorption and recycling performances of GO-Fe/CPTMS-SiO<sub>2</sub>@MF in model waste water**

With the OECD guideline for the testing of chemicals, the model wastewater was prepared and a suitable amount of biological and chemical medium which consisted of 160 mg of peptone, 110 mg of meat extract, 30 mg of urea, 30 mg of K<sub>2</sub>H<sub>2</sub>PO<sub>4</sub>, 8 mg of NaCl, 3 mg of CaCl<sub>2</sub> · 2H<sub>2</sub>O and 2 mg of MgSO<sub>4</sub> · 7H<sub>2</sub>O were dissolved in 1 L of tap water (Guideline 2001; Zhao et al. 2015). This wastewater used as a solvent for the contaminants such as MB, CR, Pb(II), Cd(II) 1000 mg L<sup>-1</sup> & RB 600 mg L<sup>-1</sup>. 20 mg of adsorbent was mixed with the as-synthesized adsorbate wastewater, and carried out the tests for 10 h in a orbital shaker. Further, the saturated adsorbent was reproduced in 1.0 M HCl solution and several times washed with distilled water for reusage.

#### **7.2.11 Characterization Techniques**

The FTIR spectra was measured using Bruker-Alpha ECO-ATR FTIR within a range of 4000-599 cm<sup>-1</sup>. Surface morphology was done using FE-SEM with EDS analysis from Zeiss Sigma SEM with oxford EDS. The internal structure of the samples was done using HR-TEM FEI Tecnai G2 20 (200 KV). The TG analysis was implemented at N<sub>2</sub> atmosphere from 25 °C to 800 °C with a rate of flow heat of 10 °C/ min using Perkin Elmer STA 6000 thermal analyzer. Zeta potential was measured in presence of Zetasizer WT, Malvern Instruments. The phase identification and composition were carried out using X-ray diffractometer Bruker D8 advance. Raman spectrometer (STR500 Airix) was used for analysing the composition of the GO and GO-Fe/CPTMS-SiO<sub>2</sub>@MF. The magnetic properties of the GO-Fe/CPTMS-SiO<sub>2</sub>@MF and MF were done by VSM squid analysis. XPS analysis was performed to determine the elements and their composition using ThermoScientific, NEXSA surface analysis with a monochromatic Al-Kα source (hν =1486.6eV). BET measurements to find out the N<sub>2</sub> adsorption-desorption studies and to know the pore diameter of the nano adsorbent from Nova touch LX2.

### **7.3 RESULTS AND DISCUSSION**

#### **7.3.1 Vibrational Spectroscopy (FTIR)**

FTIR spectroscopy was performed to examine the nature of interaction between the GO-Fe/CPTMS- SiO<sub>2</sub>@MF and the pollutants. Figure 7.1 & 7.2 shows the FTIR spectroscopy of

MF nanoparticle, Composite (GO-Fe/CPTMS-SiO<sub>2</sub>@MF), CPTMS-SiO<sub>2</sub>@MF, SiO<sub>2</sub>@MF, GO-Fe and Fe<sub>3</sub>O<sub>4</sub> nanoparticle. The characteristic peak around 585 cm<sup>-1</sup> attributed to the Fe-O stretching vibrations, which is observed in four stages i.e., MF, SiO<sub>2</sub>@MF, CPTMS-SiO<sub>2</sub>@MF and GO-Fe/CPTMS-SiO<sub>2</sub>@MF even after the polymer coating and chemical modification. Meanwhile, the intensity of Fe-O peaks reduced comparatively with further modification, which confirmed the successful modification of MF. The peaks around 1454 cm<sup>-1</sup> represented to the C-H bending vibrations whereas the 2856, 2911 and 2964 cm<sup>-1</sup> attributed to the C-H in CH<sub>2</sub> groups symmetrical and asymmetrical vibrations. There is a broad band around 690 cm<sup>-1</sup> designated to be C-Cl bond, and a broad band around 1180 cm<sup>-1</sup> is due to the differential spectra of Si-R, where R= alkyl group) in CPTMS-SiO<sub>2</sub>@MF, SiO<sub>2</sub>@MF and GO-Fe/CPTMS-SiO<sub>2</sub>@MF (Adam et al. 2009; Bordoloi et al. 2008). In case of CPTMS-SiO<sub>2</sub>@MF and SiO<sub>2</sub>@MF, there is a broad peak around 1100 cm<sup>-1</sup> and 800 cm<sup>-1</sup> which corresponds to the Si-O vibrations in both CPTMS-SiO<sub>2</sub>@MF and SiO<sub>2</sub>@MF (Bektar et al. 2020; Pinto et al. 2016; Sujandi et al. 2009; Wang et al. 2008). In the Figure 7.1, the peak at 460 cm<sup>-1</sup> resembled Si-O-Fe and confirmed that the CPTMS-SiO<sub>2</sub>@MF is immobilized onto GO-Fe support which had justified the nanocomposite formation (Bakhteeva et al. 2016; Lobato et al. 2019). The peak at 1030 cm<sup>-1</sup> and 1130 cm<sup>-1</sup> for Si-O-Si bonding, and the bond around 950 cm<sup>-1</sup> and 800 cm<sup>-1</sup> is related to Si-OH bond and Si-O-Si bond were investigated in CPTMS-SiO<sub>2</sub>@MF (Bakhteeva et al. 2016; Kuzminska et al. 2015; Li et al. 2010). In the FTIR spectrum, there is a peak around 590cm<sup>-1</sup> which resembled the Fe-O bond in both Fe<sub>3</sub>O<sub>4</sub> and GO-Fe compound which is shown in figure 7.2 (Kuzminska et al. 2015; Mauricio et al. 2013; Petcharoen and Sirivat 2012).



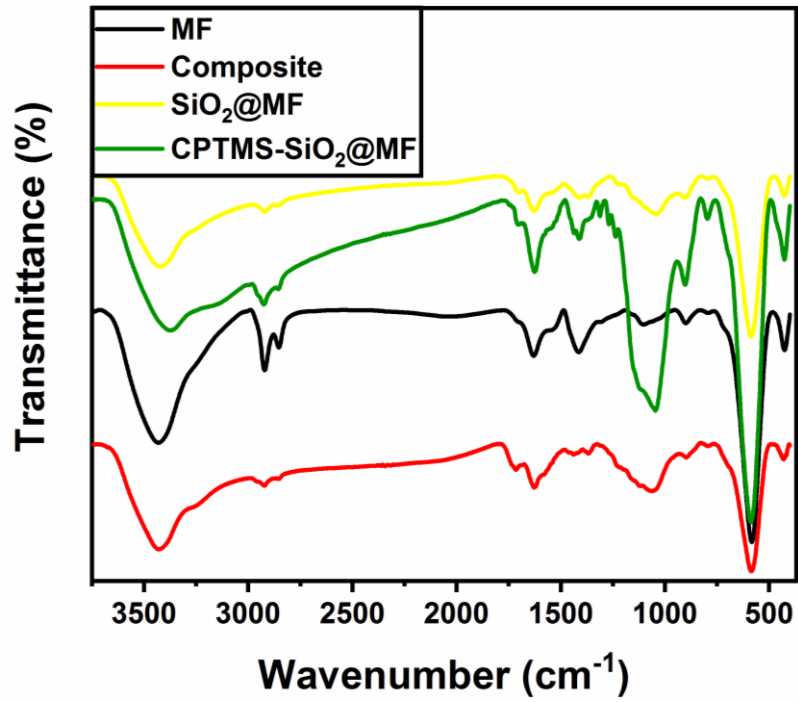


Figure 7.1. FTIR Spectra of MF, SiO<sub>2</sub>@MF, CPTMS-SiO<sub>2</sub>@MF & Composite (GO-Fe/CPTMS-SiO<sub>2</sub>@MF)

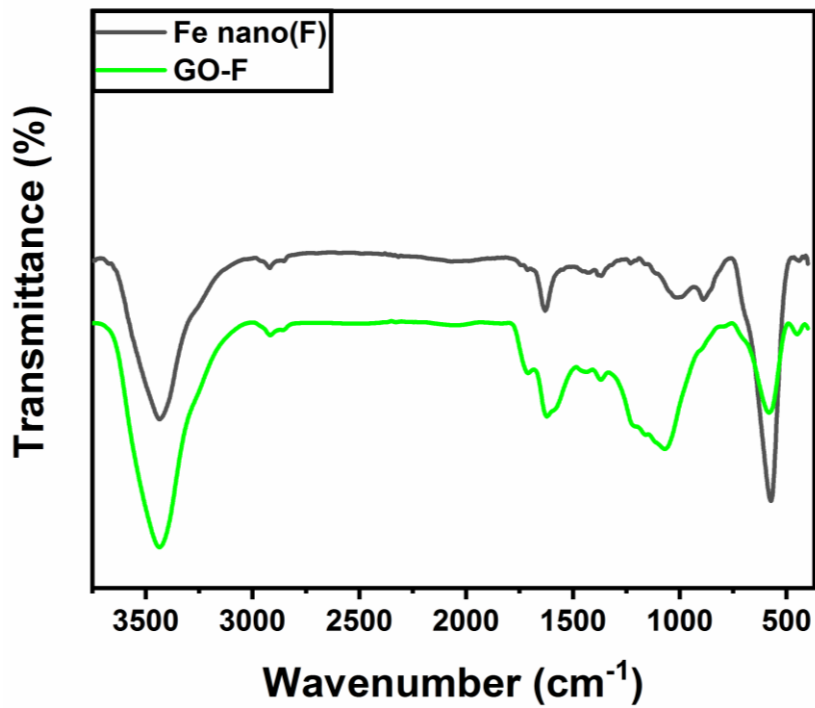


Figure 7.2. FTIR Spectra of GO-Fe & Fe

### 7.3.2 X-ray Diffraction (XRD)

To investigate the crystalline nature of MF, SiO<sub>2</sub>-MF and GO-Fe/CPTMS-SiO<sub>2</sub>@MF nanocomposite, the XRD plot in figure 7.3. The diffraction peaks at  $2\theta$  values are 18.40, 30.39, 35.61, 43.37, 53.82, 57.29, 62.75 and 74.38 corresponding to the indexed planes (111), (220), (311), (222), (422), (511), (440) and (533) with space group of Fd3m for the MF nanoparticle using Bragg's law indicated that the presence of cubic spinel structure and it has been selected for the evaluation of crystallite size (Babu et al. 2018; Cullity, B.D. 1978; Gangatharan et al. 2010; Hassan et al. 2015; Mohit et al. 2014; Raju et al. 2014; Rashad et al. 2009; Shahane et al. 2010). In case of GO & GO-Fe, there is a strong peak around  $2\theta = 10.92^\circ$  corresponded to the (002) reflection, which is persistent with a previous report (anuma et al., 2018) shown in figure 7.4. The diffraction peaks shown in figure 7.4 at  $2\theta = 10.92, 31.2, 35.4, 43.77, 53.88, 56.8$  and  $62.47$  respectively confirmed the polycrystalline Fe<sub>3</sub>O<sub>4</sub> nanoparticle deposited on the GO surface which matched the JCPDS database file (PCPDFWIN v.2.02, PDF No. 85.1436). GO having a diffraction peak around  $2\theta = 10.92$  was reduced in GO-Fe, which suggested that the stacking of GO surface layers were not destructed due to the deposition of Fe<sub>3</sub>O<sub>4</sub> (Wang et al. 2016). In both the nanocomposites, a broad peak is present at  $2\theta$  and 28 attributed to the presence of Si coating on the MF nanoparticle as well as GO-Fe/CPTMS-SiO<sub>2</sub>@MF nanocomposite (Ren et al. 2016; Santhosh et al. 2017; Shao et al. 2012).

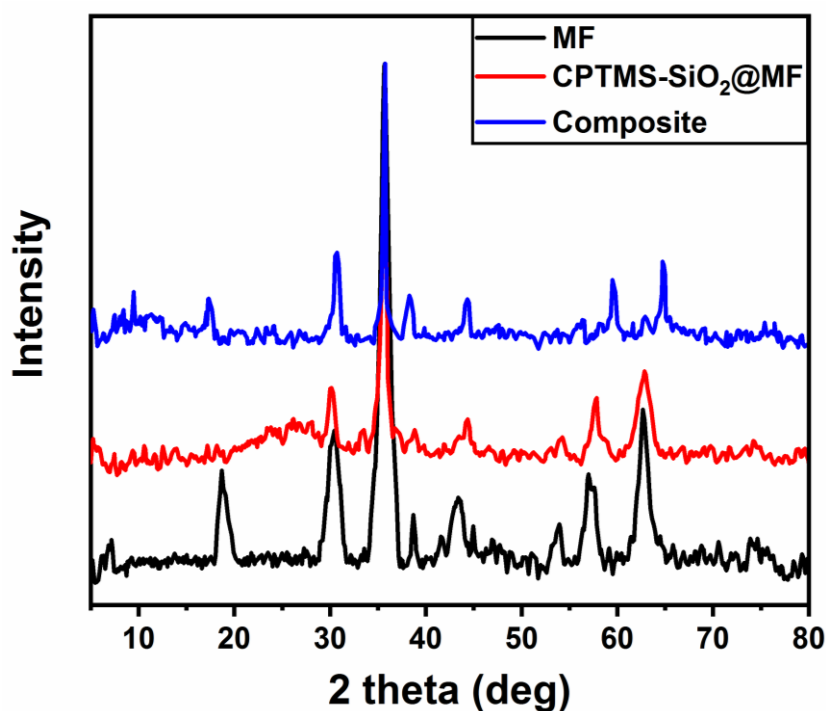


Figure 7.3. XRD pattern for the MF, CPTMS-SiO<sub>2</sub>@MF & GO-Fe/CPTMS-SiO<sub>2</sub>@MF Composite

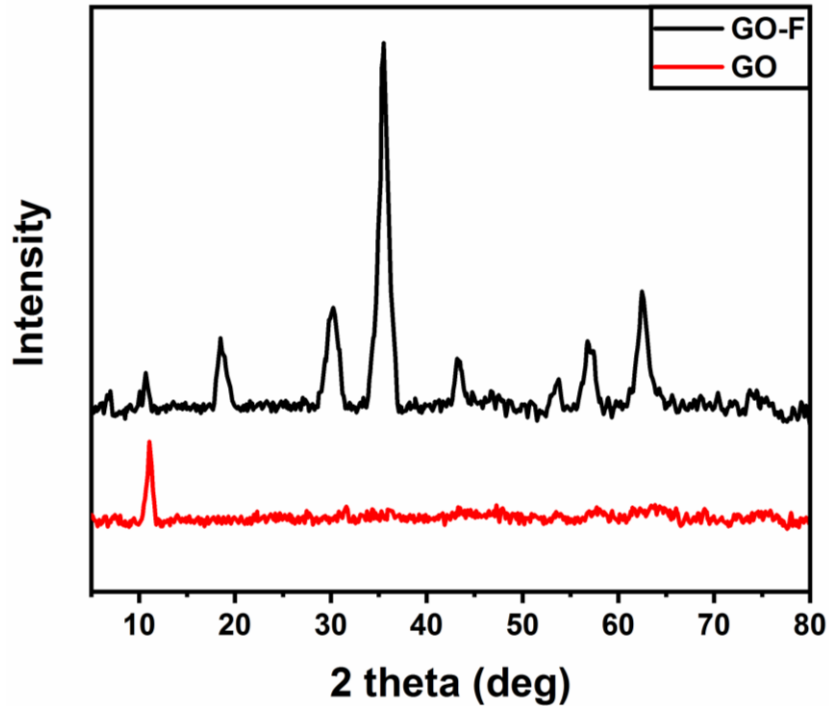


Figure 7.4. XRD pattern for the GO-Fe & GO

To know the broadening of peaks in the XRD graph, the crystalline size of the MF nanoparticle was measured using the X-ray broadening method with the help of Scherrer equation:

$$D_{hkl}(nm) = \frac{K\lambda_{(nm)}}{\beta_{hkl}(Rad)\cos\theta} \quad (7.4)$$

Here, K termed as the shape factor (K=0.9 for octahedral shapes), represents the wavelength of X-ray radiation ( $\lambda=0.154$  for Cu K $\alpha$  radiation),  $\beta_D$  termed as the width of peak with an intensity at half-minimum and the term  $\theta$  represented to the Bragg's diffraction angle.

This equation is used to know the average crystal size is 11.8 nm for the MF particle which is in resemblance with the TEM analysis.

### 7.3.3 Raman Spectroscopy

If a nanocomposite is having more than one cation, then the Raman spectra peak will be a broad one with contribution of more than one cation with the clone symmetry. These peaks were deconvoluted and their integrated intensity is a calibration of corresponding cation concentration within the unit cell. The five peaks in the various spinel ferrites spectra appeared around 150-700  $\text{cm}^{-1}$  which include  $A_{1g}$ ,  $E_g$  &  $3T_{2g}$  respectively. Usually from the figure 7.5, the  $A_{1g}$  mode (1) is the symmetric stretching of oxygen atoms with Fe/M-O group, whereas  $T_{2g}$  mode (2) represented the anti-symmetric stretching of oxygen atoms. The  $E_g$  and  $T_{2g}$  (3) attributed to the symmetric and anti-symmetric bending modes of oxygen with the metal atom

Fe respectively (Nandan et al. 2019; Shebanova and Lazor 2003). The  $T_{2g}(1)$  i.e., fifth mode confirmed to the translational movement of tetrahedron ( $MO_4$ ) which is termed as a spinel ferrite, belonging to same space group whether it can be normal, inverse or mixed having five Raman peaks. Raman spectra of the nanocomposite, which was recorded at room temperature from  $200-3000\text{ cm}^{-1}$ , were shown in figure 7.5. The appearance of multiple peaks in the Raman spectra confirmed the formation of spinel ferrites in the synthesized nanocomposite. A broad peak around  $700\text{ cm}^{-1}$  is corresponded to the  $A_{1g}$  and the remaining four peaks observed at 570, 490, 335 and  $197\text{ cm}^{-1}$  were attributed to the  $T_{2g}(3)$ ,  $T_{2g}(2)$ ,  $E_g$  and  $T_{2g}(1)$  spinel modes respectively (Chen et al. 2014; Nandan et al. 2019; Nandan and Bhatnagar 2015; Thota et al. 2016). The peak position and its intensity explained the specified characteristic feature of vibrating molecules and concentration of these cations existed in them which can lead to the changes in polarization capacity (Nandan et al. 2019; Sánchez-Arenillas et al. 2019). The characteristic  $A_{1g}$  mode represented the symmetric stretching of Fe/M-O bonds, which are in tetrahedral geometry with different cations with specified frequencies, which gives rise to broad shouldered peaks shown in figure 7.5.

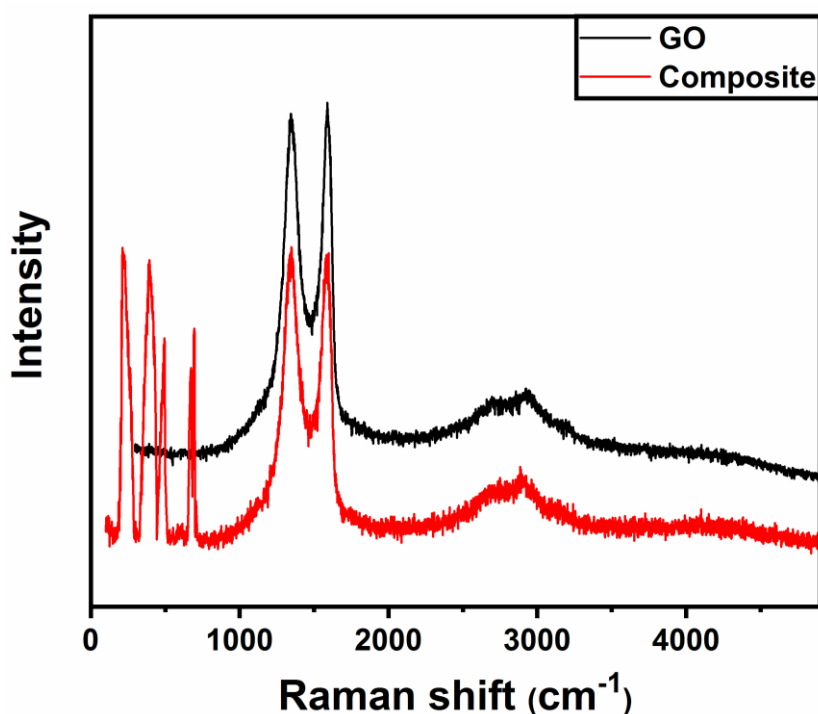


Figure 7.5. Raman spectra of both GO & Composite (GO-Fe/CPTMS-SiO<sub>2</sub>@MF)

### 7.3.4 Thermal Analysis (TGA)

Figure 7.6 represented the TG curves of GO & GO-Fe/CPTMS-SiO<sub>2</sub>@MF. For the composite, a slight weight loss was examined, indicating a higher thermal stability due to the SiO<sub>2</sub> combination with TEOS and CPTMS capping (Ma et al. 2016; Shan et al. 2015; Yang et al. 2010; Zheng et al. 2014). For the composite two stages i.e., the first stage (90 °C - 210 °C) is due to the removal of water molecules adsorbed within the hydrophilic groups and the second stage (211 °C - 450 °C) was related to the decomposition of unreacted CPTMS and other functional groups on the composite. However, in case of GO shown in figure 7.6, the weight loss occurred in three stages: the first stage (90 °C - 210 °C), is the removal of water molecules physisorbed onto the GO, the second stage (211 °C - 420 °C), confirmed the weight loss is due to the degradation of functional groups such as hydroxyl, carboxyl and epoxy groups. However, the temperature around (420 °C-800 °C), was related to the organic species degradation and annihilation of hexagonal ring of carbon atoms takes place.

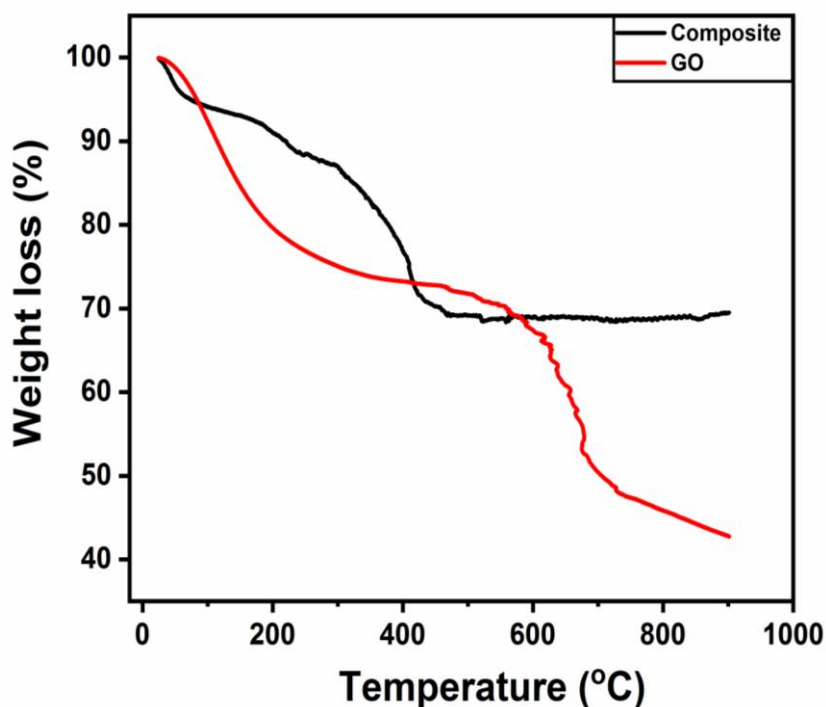
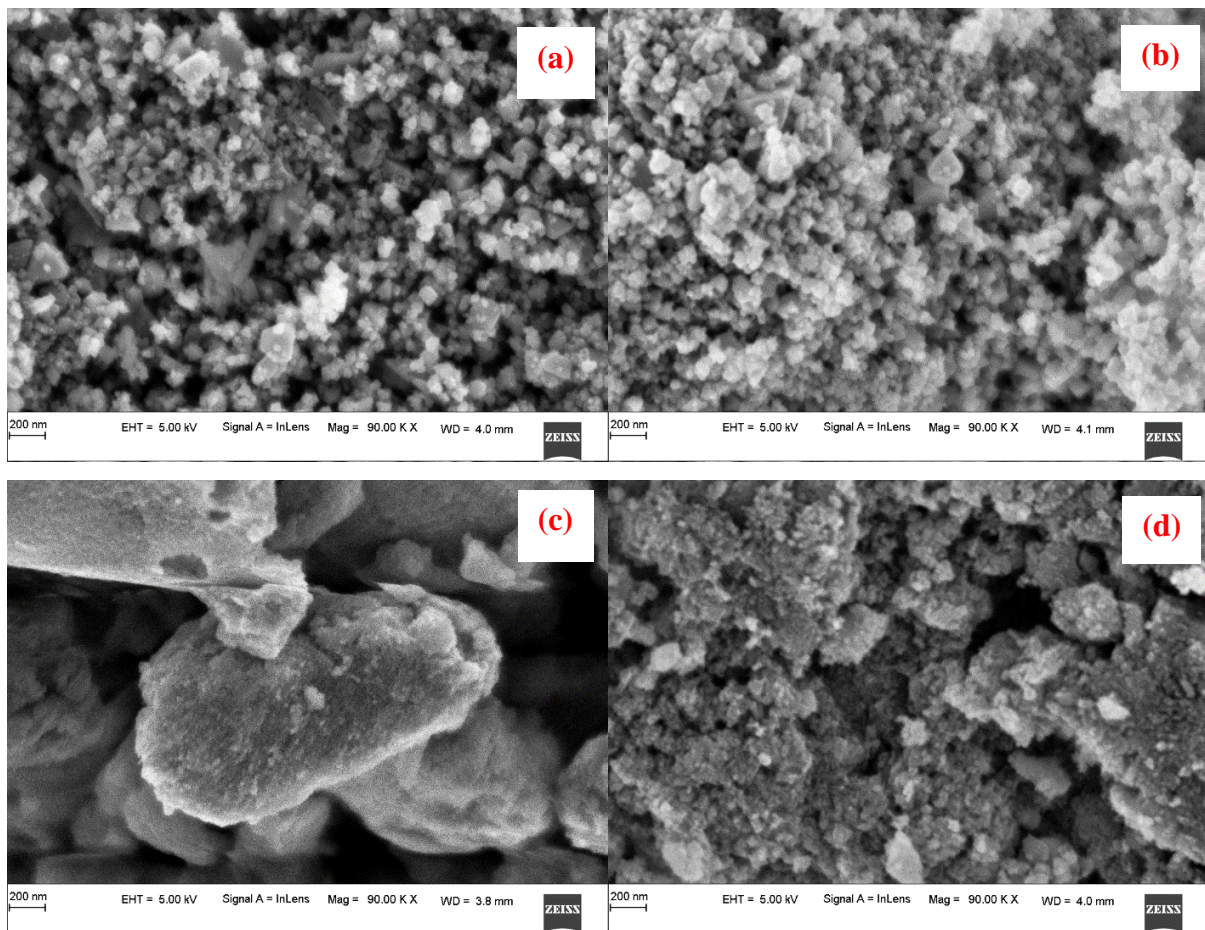


Figure 7.6. TGA of GO & Composite (GO-Fe/CPTMS-SiO<sub>2</sub>@MF)

### 7.3.5 Scanning Electron Microscopy and Energy Dispersive X-ray Spectroscopy (FE-SEM & EDS)

The SEM images of Fe<sub>3</sub>O<sub>4</sub>, GO-Fe, MF, GO-Fe/CPTMS-SiO<sub>2</sub>@MF, CPTMS-SiO<sub>2</sub>@MF and SiO<sub>2</sub>@MF were shown in the figure 7.7(a-f). The GO-Fe have more wrinkled than the pure Fe<sub>3</sub>O<sub>4</sub> shown in figure 7.7(a, b). The MF nanoparticle is spherical in shape and further

combination with SiO<sub>2</sub> and CPTMS coating made the surface as amorphous and rough texture. The composite showed slight porous network and amorphous in nature due to the magnetic nature. The EDS analysis of GO-Fe, MF, GO-Fe/CPTMS-SiO<sub>2</sub>@MF, CPTMS-SiO<sub>2</sub>@MF, SiO<sub>2</sub>@MF & Fe<sub>3</sub>O<sub>4</sub> were given in figure 7.8(a-f). The composite and the remaining substrates are in close agreement with the synthesized methodology with respect to the elemental composition and atomic wt. ratios. The elemental composition in Fe<sub>3</sub>O<sub>4</sub> are Fe, O & C and GO-Fe are C, O & Fe. The elements in MF are Fe, Co, Ni, Zn, C & O and CPTMS-SiO<sub>2</sub>@MF are Si, Co, Ni, Fe, Zn, O, C & Cl. The elements in SiO<sub>2</sub>@MF are Si, Co, Ni, Zn, Fe, O & C and GO-Fe/CPTMS-SiO<sub>2</sub>@MF are Si, Co, Ni, Fe, Zn, O & C.



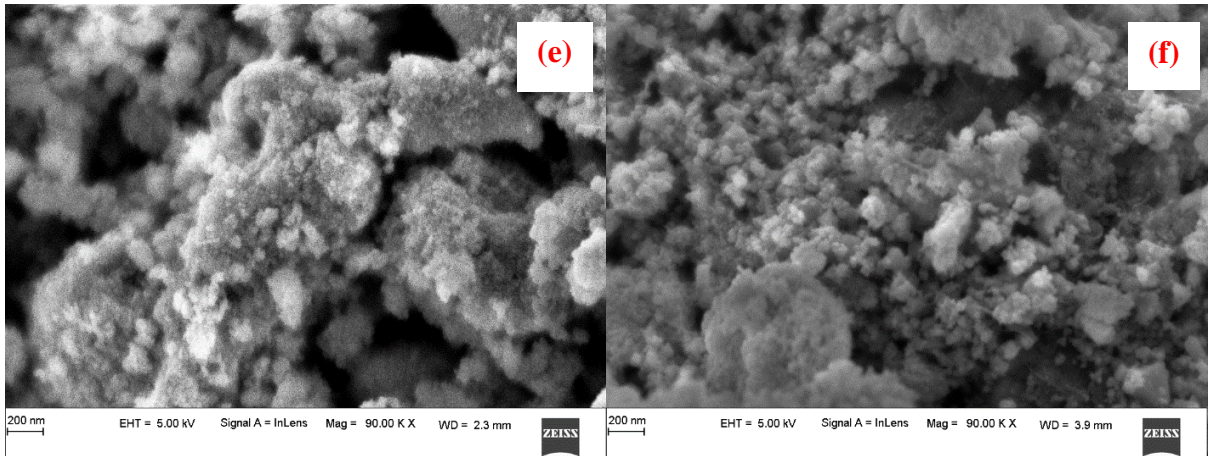
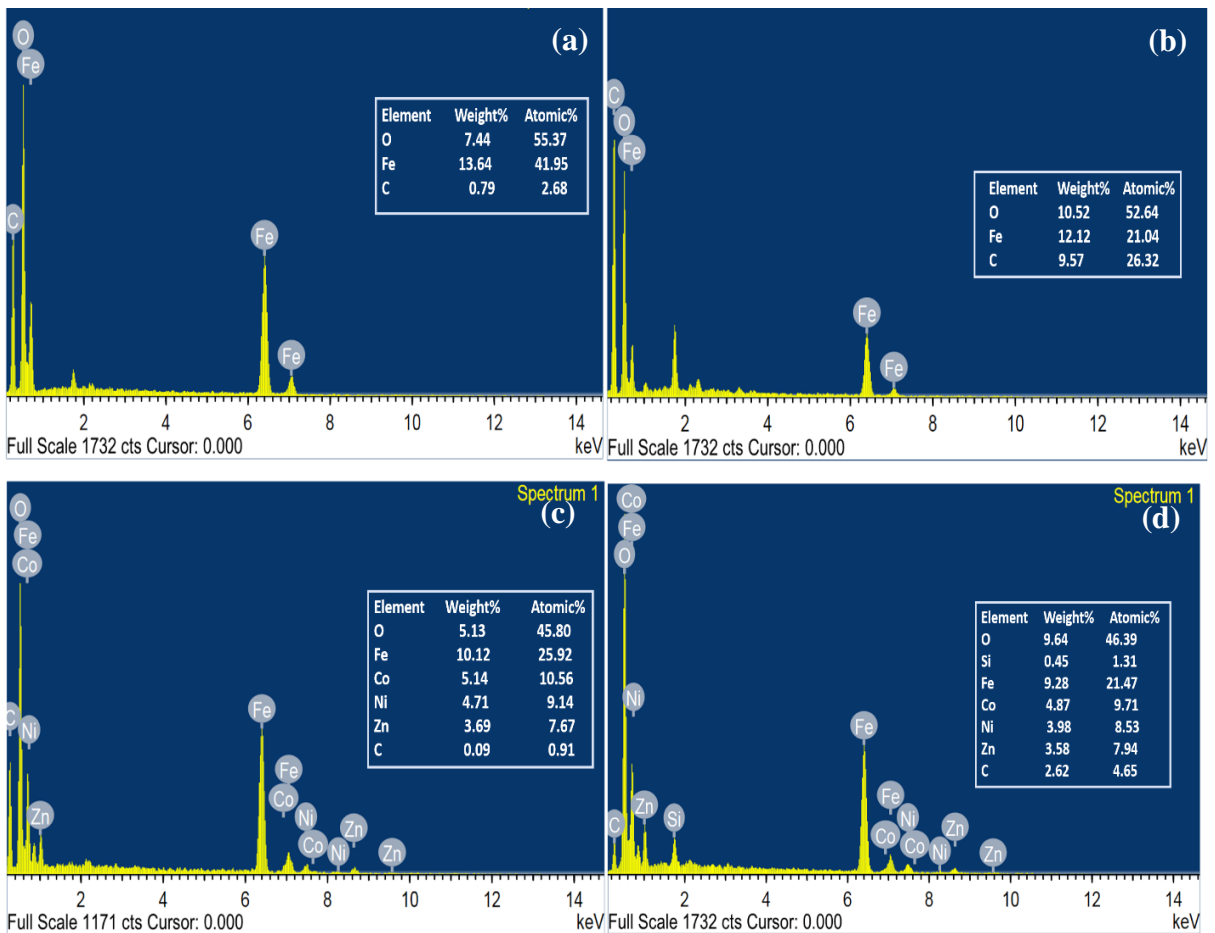


Figure 7.7. FE-SEM image of the following: a)Fe nanoparticle, b)GO-Fe, c)MF, d)SiO<sub>2</sub>@MF, e)CPTMS-SiO<sub>2</sub>@MF & f) GO-Fe/CPTMS-SiO<sub>2</sub>@MF



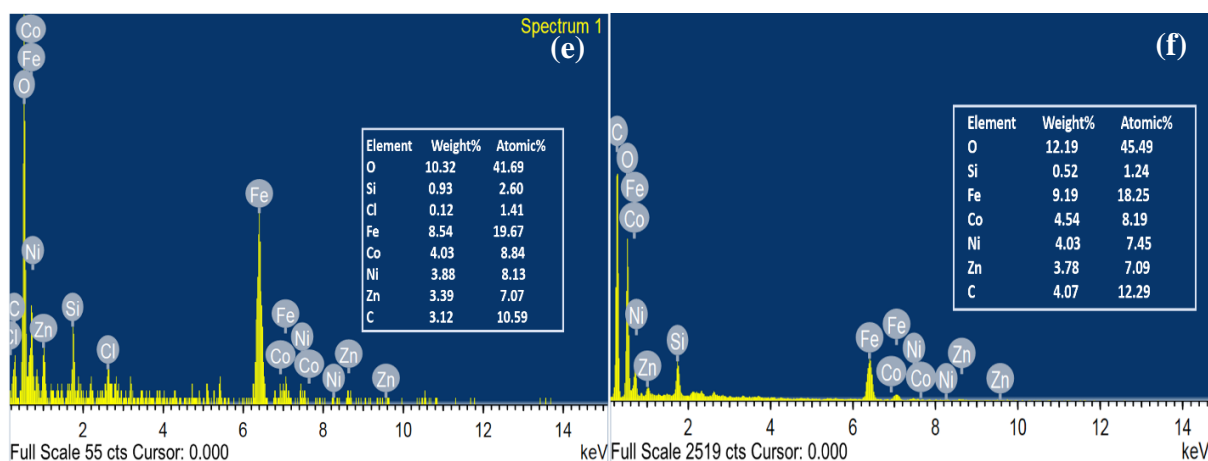


Figure 7.8. EDX analysis of the following a)Fe nanoparticle, b)GO-Fe, c)MF, d)SiO<sub>2</sub>@MF, e)CPTMS-SiO<sub>2</sub>@MF & f) GO-Fe/CPTMS-SiO<sub>2</sub>@MF

### 7.3.6 Transmission Electron Microscopy (TEM)

Figure 7.9(a-f) is the surface morphology, microstructure and particle size of GO-Fe/CPTMS-SiO<sub>2</sub>@MF and MF were characterized using TEM analysis. Figure 7.9(a) showed that the magnetic composite and MF nanoparticle is spherical shaped with an average size of 15-60 nm made up of a better amount of MF nanoballs on the composite. The nanoparticle was synthesized by solvothermal methodology in a closed system and its extraction is a novel process where the binary solvent combination is required. A clear core shell structure of GO-Fe<sub>3</sub>O<sub>4</sub> surface was observed on the magnetic composite. Due to the SiO<sub>2</sub> combination and CPTMS coating onto the composite, the surface morphology became much smoother than the MF nanoparticle and also useful for the functionalization of MF nanoparticle in order to immobilize onto GO-Fe surface (Jana et al. 2015; Zheng et al. 2019). The coating of silica layer around the MF nanoparticles resulted in the formation of superficial stabilization up on MF nanoparticles. The silica layer formed led to the synthesis of nanoaggregates which are further stabilized by CPTMS coupling agent. The SAED pattern of MF nanoparticles displayed the presence of moderate size nano crystalline particles confirmed by the rings which consist of dots. In case of composite, the SAED pattern displayed a very clear ring with bright dots which proved the crystalline nature of the nanocomposite have been enhanced due to the silylation process and the heterogenous support.



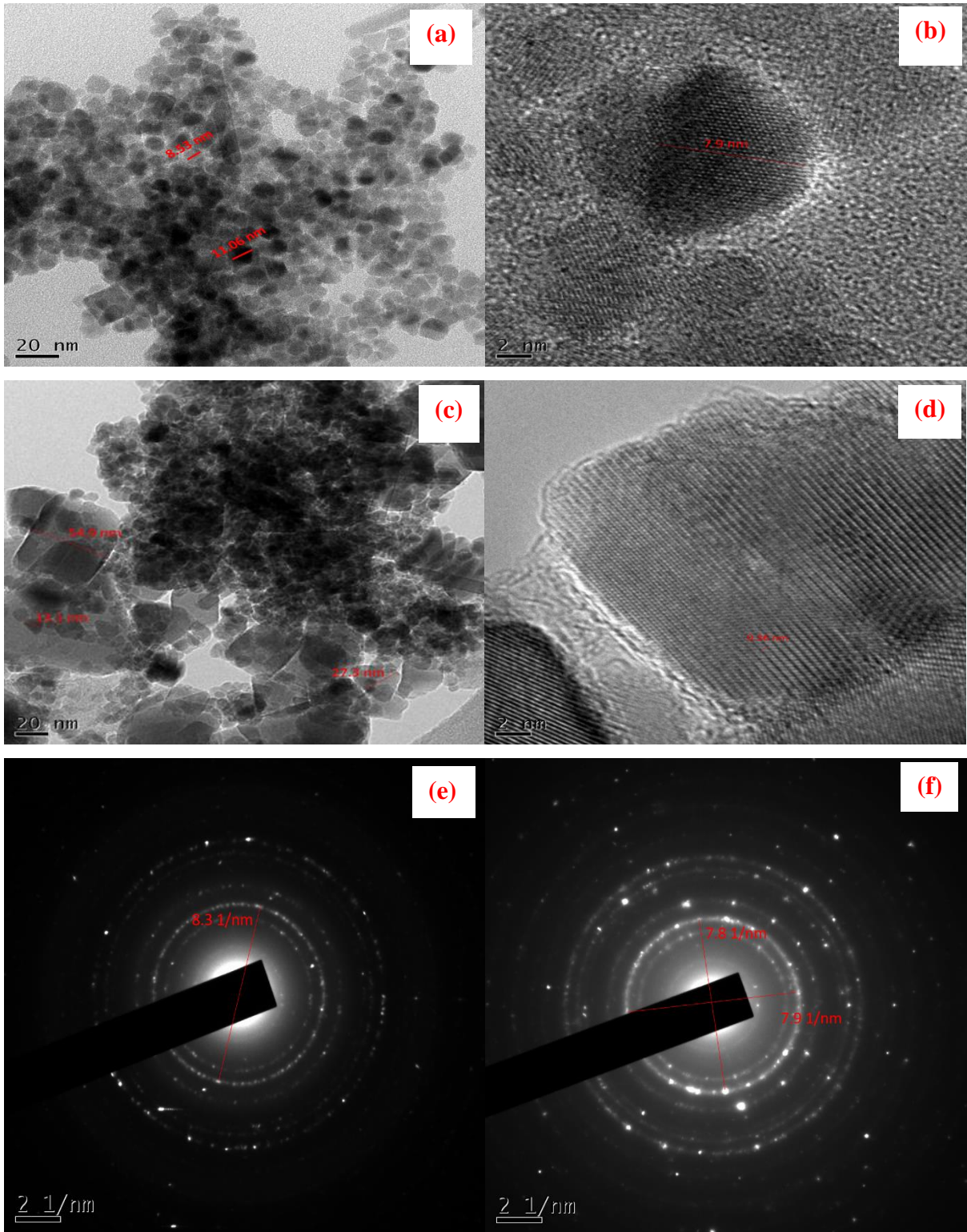


Figure 7.9. TEM images of the a,b) MF, e) SAED pattern of MF, d,e) Composite & f) SAED pattern of Composite

### 7.3.7 Vibrating-sample Magnetometry (VSM)

The magnetic properties of the MF and GO-Fe/CPTMS-SiO<sub>2</sub>@MF measured at room temperature with an applied magnetic field which mainly dependent on magnetization. The magnetic properties of the MF and GO-Fe/CPTMS-SiO<sub>2</sub>@MF are mainly varied due to the particle size, surface morphology and the microstructural defects. Figure 7.10 shows the hysteresis loop of the synthesized nanoparticle and nanocomposite which measured at 300K. Further, the saturation magnetization of MF and GO-Fe/CPTMS-SiO<sub>2</sub>@MF are 70.83 emu/g and 59.93 emu/g respectively given in table 7.1. At first, the Fe ions migrated from the tetrahedral site to the octahedral voids due to the presence of Zn ions during the synthesis process which lead to the increase in  $M_s$  values (Cao et al. 2016; Jia et al. 2017; Mansour et al. 2016). The decrease in saturation magnetization is due to substitution of Zn into ferrites during the synthesis or the redistribution of all cations among the lattice voids in the synthesized materials due to the involvement of Zn into the Fe<sup>3+</sup> metal ions (Ahmed et al. 2007; Bansal et al. 2015; Ikram et al. 2020; Zhao et al. 2006). Due to the substitution of Zn<sup>2+</sup> by Co<sup>2+</sup> ions, Zn<sup>2+</sup> cations are replaced in tetrahedral(A) sites and Fe<sup>3+</sup> ions in octahedral(B) sites with antiparallel moments which got reduced the A-B super-exchange interaction. Therefore, a competition held between the disordered surface as well as ordered core spins which affected the net magnetization value leading to a decrease in magnetization and monitored temperature in nanoparticle spinel (Bhowmik et al. 2003; Yousefi et al. 2010). The factors such as chemical composition, cation distribution, structure, grain size defects created surface effects whereas magnetic moments slanted by losing directionality and internal strain is greatly influenced the magnetic properties of spinel ferrites (Powar et al. 2018; Tatarchuk et al. 2017). A reduction in  $M_s$  is observed for composite is due to silica covering around the nanoparticle which further got improved silica functionalization with TEOS confirmed the presence of non-magnetic behavior of the silica and CPTMS (Arévalo-Cid et al. 2018; Mørup et al. 2013).

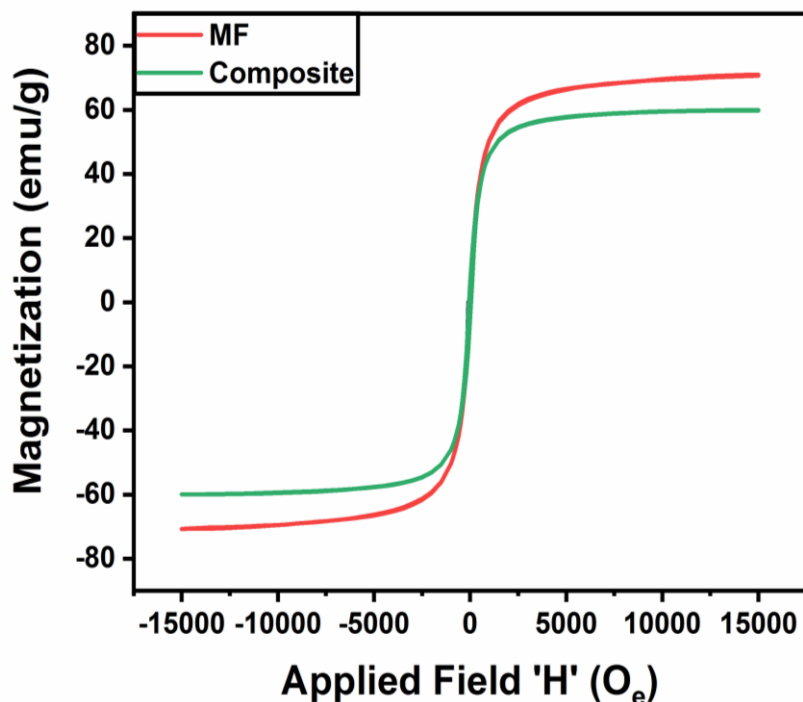


Figure 7.10. Applied magnetic field plot of MF & Composite (GO-Fe/CPTMS-SiO<sub>2</sub>@MF)

Table 7.1: M<sub>s</sub> and H<sub>c</sub> values of MF & GO-Fe/CPTMS-SiO<sub>2</sub>@MF

Type of Compounds	Magnetic properties	
	M <sub>s</sub>	H <sub>c</sub>
MF	70.83	130.40
GO-Fe/CPTMS-SiO <sub>2</sub> @MF	59.93	199.70

### 7.3.8 N<sub>2</sub> adsorption–desorption studies

BET is an effective and popular tool to measure the specific surface area and pore size distribution of the GO-Fe/CPTMS-SiO<sub>2</sub>@MF; hence N<sub>2</sub> adsorption-desorption isotherm experiments were performed at liquid N<sub>2</sub> temperature. Figure 7.11 shows the N<sub>2</sub> adsorption-desorption isotherm curve of GO-Fe/CPTMS-SiO<sub>2</sub>@MF, GO-Fe and MF nanoparticle together with their equivalent pore size curve distribution with the BJH method. From the graphs, the isotherm curves displayed type IV with H3 hysteresis loops representing the capillary condensation i.e., typical characteristics for the mesoporous material. Type H3 hysteresis describes the arbitrary dispersal of pores and interconnection between them (Tang et al. 2016; Zhao et al. 2016a). These properties of pores significantly controlled the desorption isotherm rather than adsorption process due to the difference in behavior of a pore network with a relative pressure of 0.4. The relative pressure (P/P<sub>0</sub>) of 0.42-0.98 showed the hysteresis loops of H3, attributed to the ink-bottle shaped mesopores originated in the primary MF nanoparticle present in magnetic GO nanosheets given in figure 7.12. It explained that the presence of mesopores

with narrow-slit shape which have formed through the assemblage of MF nanoparticle. The GO-Fe/CPTMS-SiO<sub>2</sub>@MF composite displayed characteristics similar to the MF nanoparticles, confirming the same pore structure as well as porosity. From the spectra, the specific surface area of GO-Fe/CPTMS-SiO<sub>2</sub>@MF, MF and GO-Fe were found to be 185 m<sup>2</sup>/g, 145.7 m<sup>2</sup>/g and 130 m<sup>2</sup>/g respectively given in table 7.2. Figure 7.12 shows the average pore diameter using Barrett-Joyner-Halenda (BJH) desorption for the GO-Fe/CPTMS-SiO<sub>2</sub>@MF was to be 7.8 nm with a varied pore size distribution corresponding to the total pore volume at P/P<sub>0</sub> is 0.98 is 0.55 cm<sup>3</sup>/g.

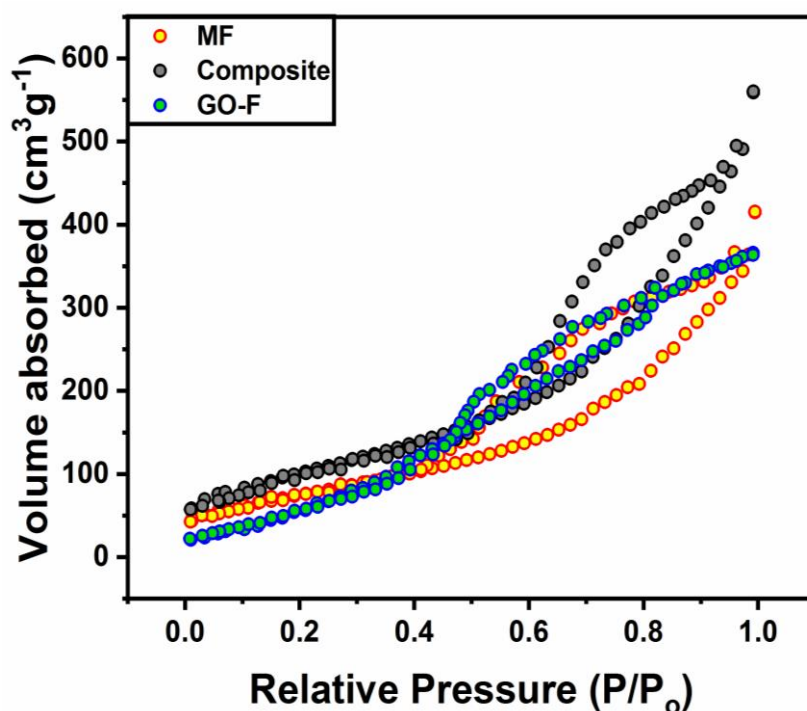
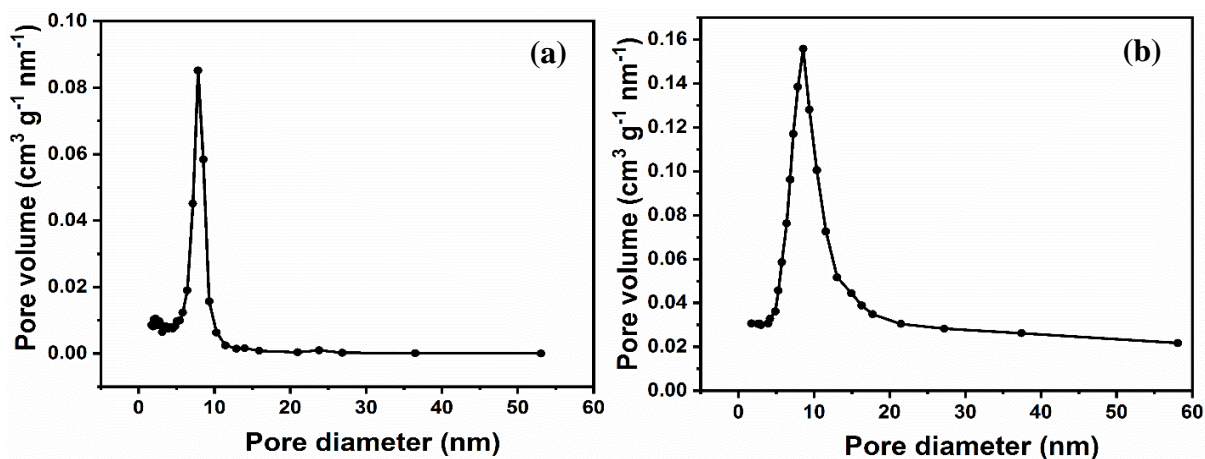


Figure 7.11. N<sub>2</sub> adsorption-desorption isotherms of MF, GO-Fe & Composite (GO-Fe/CPTMS-SiO<sub>2</sub>@MF)



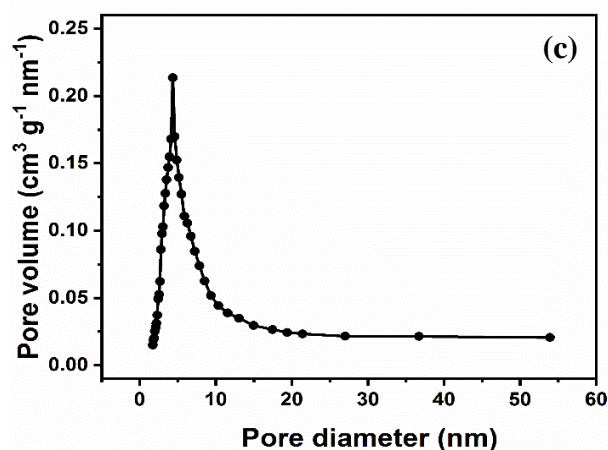


Figure 7.12. Pore size distribution of a) GO-Fe/CPTMS-SiO<sub>2</sub>@MF, b) GO-Fe & c)MF

Table 7.2: Pore characteristics for the GO-Fe/CPTMS-SiO<sub>2</sub>@MF, MF and GO-Fe

Samples	$S_{BET}$ (m <sup>2</sup> g <sup>-1</sup> )	$V_p$ (cm <sup>3</sup> g <sup>-1</sup> )	$d_p$ (nm)
GO-Fe	130	0.35	9.3
MF	145.7	0.41	5.2
GO-Fe/CPTMS-SiO <sub>2</sub> @MF	185	0.55	7.8

### 7.3.9 Zeta potential

Figure 7.13 shows the electronic charges on the surface of GO-Fe/CPTMS-SiO<sub>2</sub>@MF dispersed in water are characterized by using the zeta potential. Figure 7.13 shows the various charges of the zeta potential with measured average values of -40 mV to 38 mV respectively. The isoelectric point (IEP) of the graphene oxide reported to be 3-4 (Lin et al. 2016; Zheng et al. 2019). Usually the presence of various oxygen functionalities of GO-Fe upon the surface and edges exhibited the tendency to deprotonate and the surface of GO is negatively charged at pH-7 (Zhu et al. 2015). Furthermore, a class of materials, which possessed positive charge ferrite moieties with an IEP of 7.4, which enhanced the IEP of the composite to 5.6. Here, the surface of MF nanoparticles is positively charged at neutral condition. These composites, which possessed MF nanoparticles, do not completely cover the whole surface of the GO-Fe material. Therefore, the GO-Fe/CPTMS-SiO<sub>2</sub>@MF composites is lesser positive charged compared to that of the MF nanoparticle at pH-7, due to the presence of negative charge on its surface of GO-Fe. Due to the surface possessing positive charge on GO-Fe/CPTMS-SiO<sub>2</sub>@MF composite which can allure anionic species at lower pH and cationic species at higher pH through hydrogen-bonding, electrostatic and  $\pi$ - $\pi$  interactions which is commodious for the removal of pollutants (Lei et al. 2016; Wang et al. 2018).

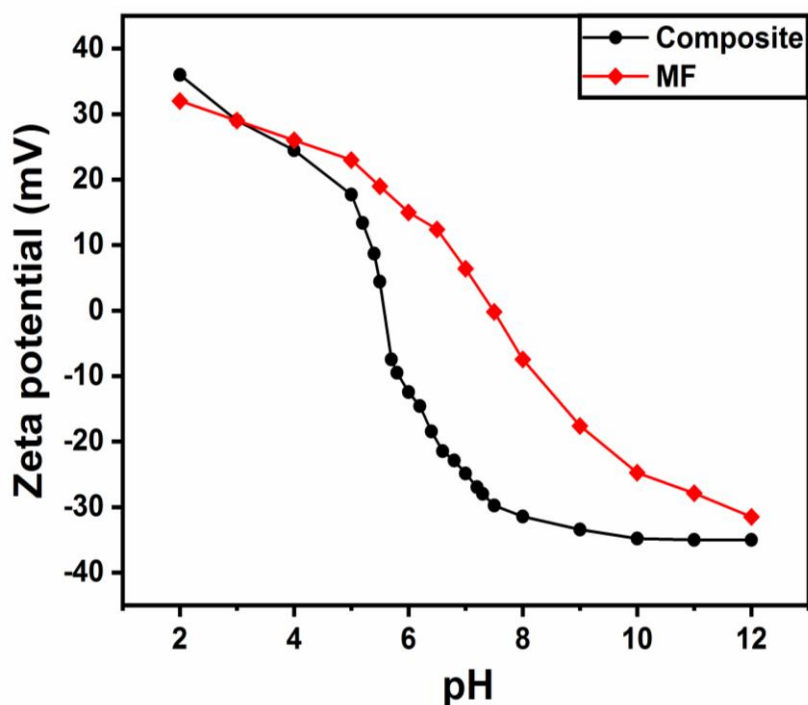


Figure 7.13. Zeta potential values of MF and Composite (GO-Fe/CPTMS-SiO<sub>2</sub>@MF) at different pH

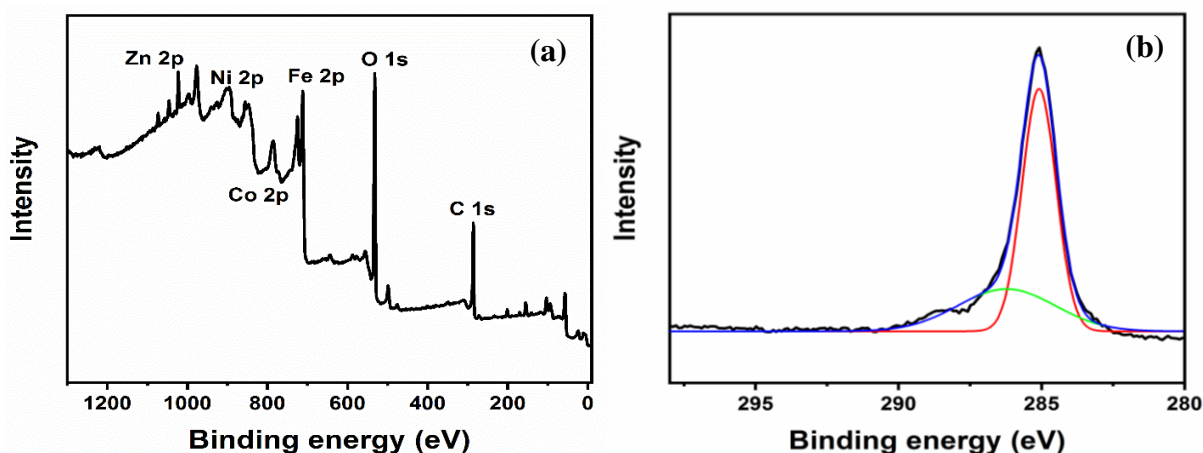
### 7.3.10 X-ray photoelectron Spectroscopy (XPS)

To justify the role of mixed ferrite/ GO-Fe nanocomposite on the adsorption of pollutants, XPS measurements were investigated to analyze and identify different chemical composition, oxidation states and the chemical functionality of the samples representing the full-survey spectrum of nanocomposite. The elements investigated in the full survey spectra are Cobalt, oxygen, carbon, silicon, nickel, zinc and Iron in composite in figure 7.15(a) and cobalt, oxygen, zinc, iron & nickel for the MF shown in figure 7.14(a). The ratio of Co 2p molar ratio was weak and it is in agreement with the percentage of raw cobalt materials used in experimental methodology.

Zn 2p spectra whose binding energies are in between 1021.3 eV and 1044.4 eV represented that the Zn atoms are in +2 oxidation state given in figure 7.15(h). The O 1s spectrum in figure 7.15(f) represented a single peak centered having a energy of 530.1 eV which is relevant to O<sup>2-</sup> ions and a shoulder peak at 532.6 eV which correlates to the adsorbed species (OH<sup>-</sup>, C-O) at the surface of the heterogeneous support i.e., graphene oxide (Beck et al. 2017; Kumar et al. 2014). The peak with binding energy 284.8 eV from figure 7.15(b) which is centered is the dominant one is corresponded to the sp<sup>2</sup> carbon of graphitic C-C bond and the additional peaks at the 286.8 eV and 287.6 eV represented to the oxide groups of both C-O and C=O respectively

(Haldorai et al. 2016; Nasser et al. 2020; Tran et al. 2016). The characteristic peaks of Co 2p present in figure 7.15(c) with binding energies of 780.4 eV and 795.6 eV which is represented to the Co 2p<sub>3/2</sub> and Co 2p<sub>1/2</sub> core levels which corresponded to the successful deposition of cobalt mixed ferrite onto the heterogeneous graphene support (Guo et al. 2019; Yang et al. 2020). The characteristic peaks of Co 2p with binding energy of 796.3 eV and 780.3 eV attributed to the Co 2p<sub>1/2</sub> and Co 2p<sub>3/2</sub> corresponded to the spin-orbit characteristic of Co<sup>3+</sup>, whereas the peaks at 799.7 eV and 781.7 eV associated with Co 2p<sub>1/2</sub> and Co 2p<sub>3/2</sub> with respect to Co<sup>2+</sup> respectively. However, in mixed ferrite shown in figure 7.14(c) the binding energy 779.4 eV represented the Co 2p<sub>3/2</sub> core level in Co<sup>3+</sup> (Wang et al. 2020b; Zhang et al. 2019a; b). The ratio of Co 2p molar ratio was weak because XPS is a surface sensitive technique and coating of SiO<sub>2</sub> and heterogeneous support onto the mixed ferrite nanoparticle.

The spin-orbit doublet present in figure 7.15(e) at 872.5 eV and 853.2 eV corresponded to the Ni 2p<sub>1/2</sub> and Ni 2p<sub>3/2</sub> are characteristic of Ni<sup>2+</sup>, while the second spin-orbit doublet at 873.8 eV and 855.5 eV related to the Ni 2p<sub>1/2</sub> and Ni 2p<sub>3/2</sub> are characteristic of Ni<sup>3+</sup> respectively (Wang et al. 2019, 2020). In case of mixed ferrite shown in figure 7.14(e), the Ni 2p<sub>3/2</sub> core level of Ni<sup>2+</sup> is stronger peak than nanocomposite. The peak at 103.4 eV binding energy in the nanocomposite indicate the Si 2p level which confirmed the formation of SiO<sub>2</sub> on MF nanoparticle during the preparation process represented in figure 7.15(a, g) (Briggs 1981). The O 1s spectra peak displayed peaks at 533 eV, 531.6 eV and 530.6 eV are attributed to C-O-C, O-C=O, M-O (Co, Ni, Zn/Fe-O) bonds respectively shown in figure 7.14(f) (Niu et al. 2020; Wang et al. 2018). Two peaks around 710.1 eV and 724.3 eV which corresponded to the Fe 2p<sub>3/2</sub> and 2p<sub>1/2</sub> of Fe<sup>3+</sup> ions gave the confirmation for the formation of MF nanoparticle and there are no structural changes in MF nanoparticle during the formation of nanocomposite in figure 7.15 (Fu et al. 2012).



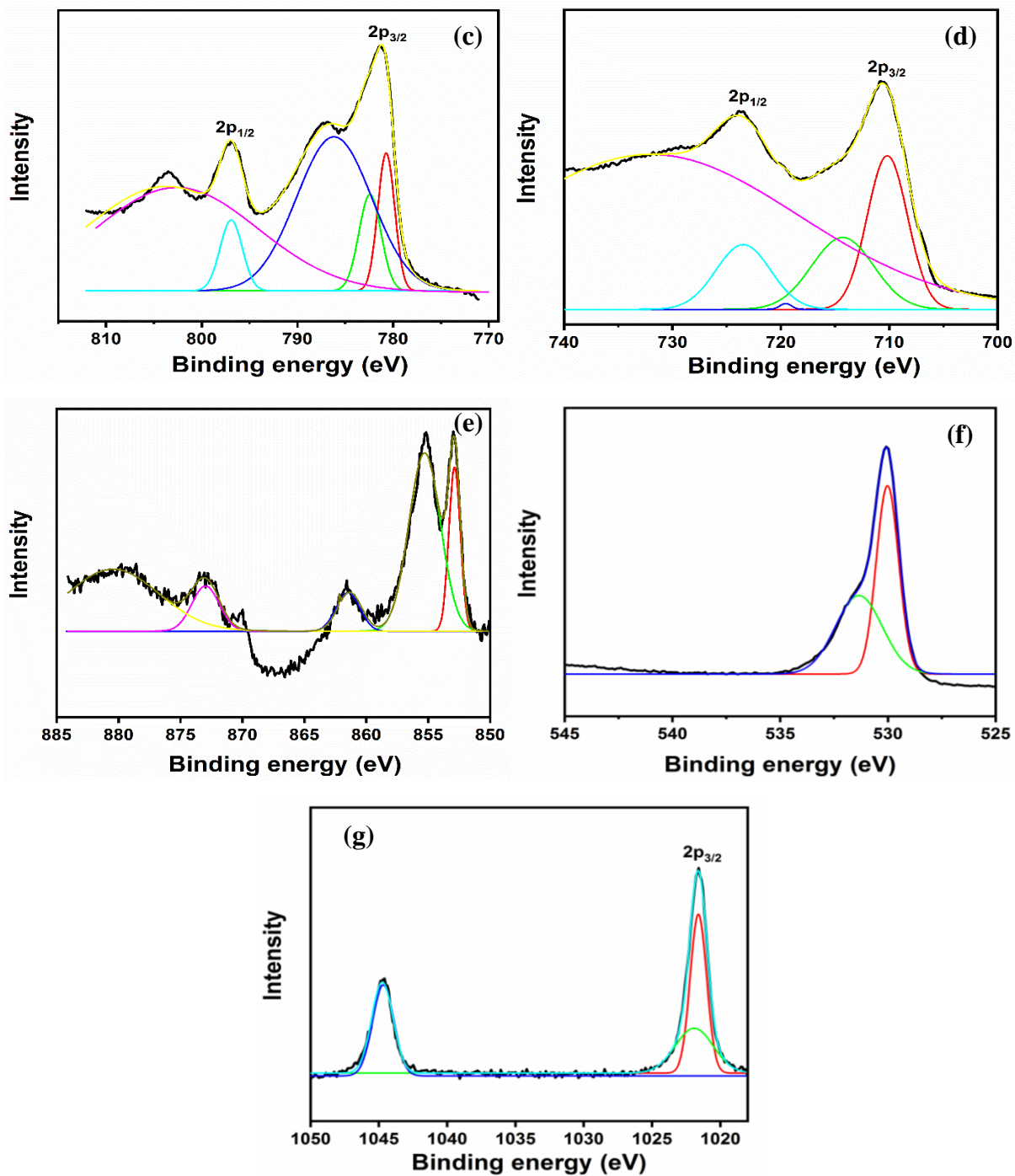
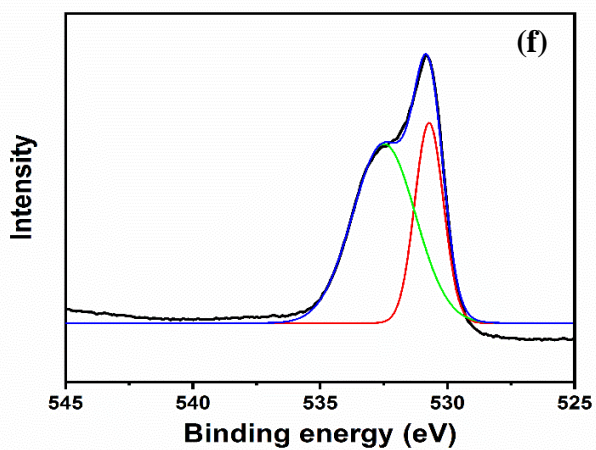
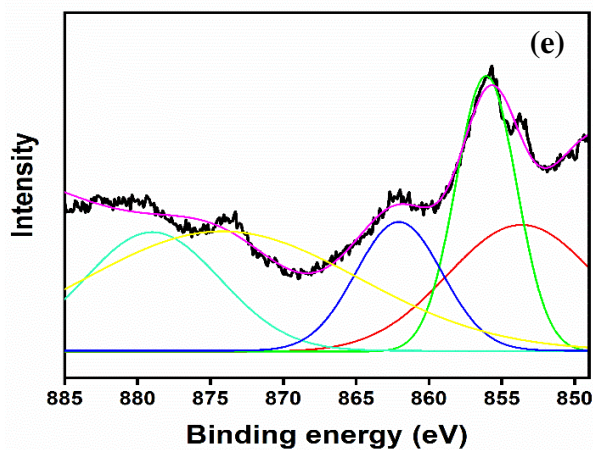
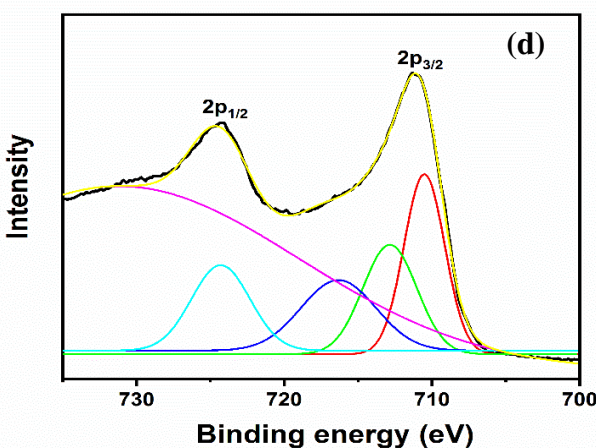
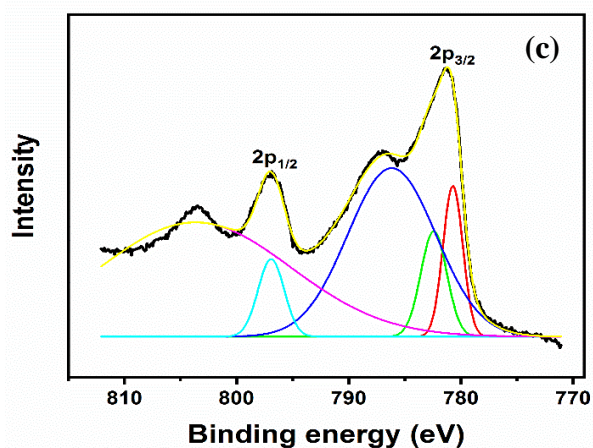
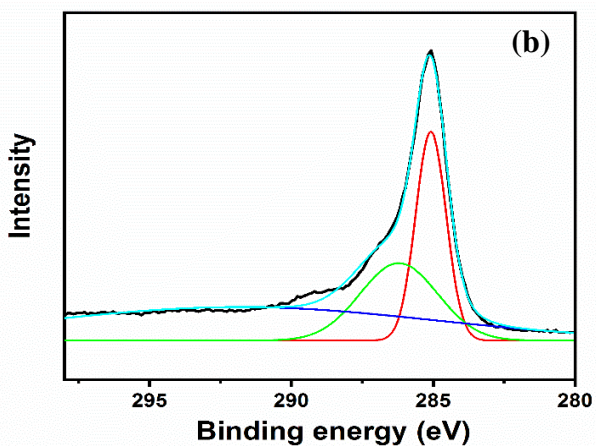
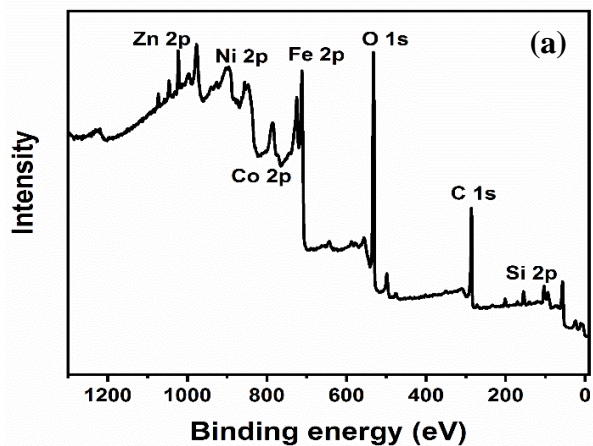


Figure 7.14. XPS Spectrum of MF a) Elemental survey, b) C 1s, c) Co 2p, d) Fe 2p, e) Ni 2p, f) O 1s & g) Zn 2p





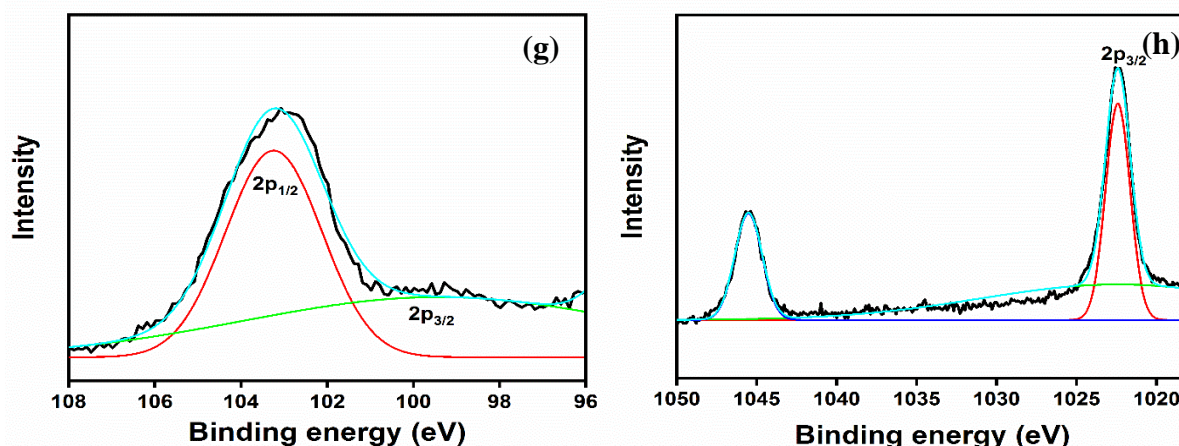


Figure 7.15. XPS spectrum of Composite (GO-Fe/CPTMS-SiO<sub>2</sub>@MF): a) Elemental survey, b) C 1s, c) Co 2p, d) Fe 2p, e) Ni 2p, f) O 1s, g) Si 2p & h) Zn 2p

### 7.3.11 Effect of initial solution pH of pollutants on adsorption

Protonation or deprotonation of functionalities, competitive adsorption between the pollutants and H<sup>+</sup> ions, solubility and precipitative in nature along with their existence form (i.e., dyes) were greatly influenced by pH. Here, the adsorption efficiency of GO-Fe/CPTMS-SiO<sub>2</sub>@MF towards MB, RB, CR, Pb(II) and Cd(II) pollutants at varied pH conditions were evaluated in batch adsorption process. However, a pH range of 2-10 was screened for the adsorbates in order to get the maximum adsorption capacity which played an important role for the elimination of harmful pollutants. The introduction of GO-Fe as well as silylation upon the MF nanoparticle which was explained by the availability of plentiful hydroxyl groups reduced the zeta potential movement towards the negative value in Figure 7.16 thus granted a good attractiveness towards the positive charged adsorbates in presence of electrostatic interactions. Further, a huge quantity of surface hydroxyl groups as well as carboxyl groups on the GO-Fe/CPTMS-SiO<sub>2</sub>@MF composite bounded with pollutants through hydrogen bonding and chelation effect. In case of cationic pollutants, at highly acidic conditions, pH less than 3.5, the removal rates and adsorption capacity are very low for the adsorbates. This process described with two factors: i) protonated functional groups such as OH & COOH groups made the active adsorption sites on GO-Fe/CPTMS-SiO<sub>2</sub>@MF mostly reduced due to low affinity between GO-Fe/CPTMS-SiO<sub>2</sub>@MF and the cationic dyes and metal ions ii) surface complexation theory, as a high amount of H<sup>+</sup> ions hampered the effective adsorption sites reserved for pollutants. In case of anionic dye CR, which is an acidic dye possessing the NH<sub>2</sub><sup>-</sup> and SO<sub>3</sub><sup>-</sup> groups with an isoelectric point approximately to 3. At low pH (1-3), it became more cationic which exhibited ammonium and azonium rich tautomer types,  $\lambda_{\max} = 576$  nm. This leads to  $\pi$ -

$\pi^*$  transition in azo group of CR driving the color changes from blue to red (Tran et al. 2017). In case of higher pH (>12) the stability of chromophore is lost which made CR to red color different from the native red color (Wu et al. 2014). The CR amino group undergoes protonation at pH 4-5.5 explained the removal efficiency of anionic dye higher at lower pH, leading to the augmentation of electrostatic interactions in the adsorbent and adsorbate molecules (Salleh et al. 2011).

In case of MB, the rate of removal and adsorption capacity of GO-Fe/CPTMS-SiO<sub>2</sub>@MF enhanced monotonously due to the uplift in solution pH with the rise in deprotonated functional groups further reduced the competition in hydrogen ions. At low pH, the cationic MB<sup>+</sup> ions compete with H<sup>+</sup> ions leading to reduction of sorption sites, thus decreasing the adsorption efficiency (Liu et al. 2019; Weng et al. 2018). In case of RB, at lower pH (< 4.2), the amine group of RB converted into tertiary ammonium cation although carboxylic acid remains neutral existed in the form of cationic and monomeric form. At higher pH greater than 4.2, it gains a net negative charge and it existed in zwitterionic form which led to the electrostatic attractions between xanthene and COOH group of a monomer to dimer formation and the removal rate increased 81 to 94% as the pH increased from 4.2-5.5 and it kept stable at 94% with the pH 5.4. For metal ions, a small decrease in composite adsorption capacity is observed at high pH values is because of the visibility in soluble nature in hydroxyl groups shown in figure 7.17. This adsorption capacity of pH-independent adsorbent explained that the composite used to treat a variety of pollutants wastewater under various pH range. This satisfactory adsorption performance in all pollutants at the acidic conditions explained by electrostatic interactions of carboxyl groups. For anionic CR, the maximum adsorption efficiency is at pH 5.4 with a maximum adsorption rate of 98.4. Based on the above explanation, the removal of pollutants at the solution pH are set to be at 7.3, 6.8, 5.4, 6.4 & 5.7 is the removal of cationic dyes i.e., MB, RB, anionic dye CR and heavy metal ions Pb(II), Cd(II) respectively.

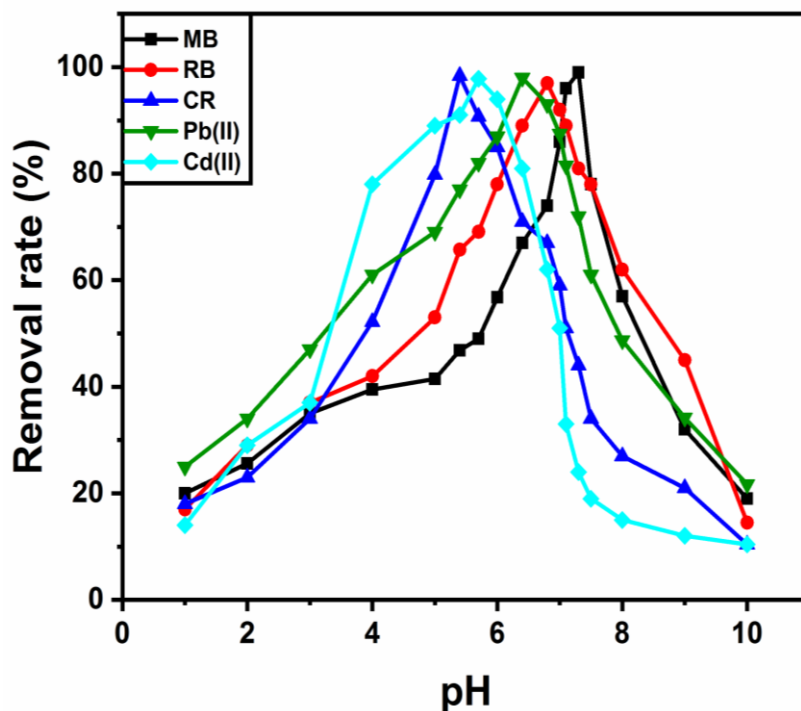


Figure 7.16. Effect of pH on the adsorption of the pollutants: MB, RB, CR, Pb(II) & Cd(II)

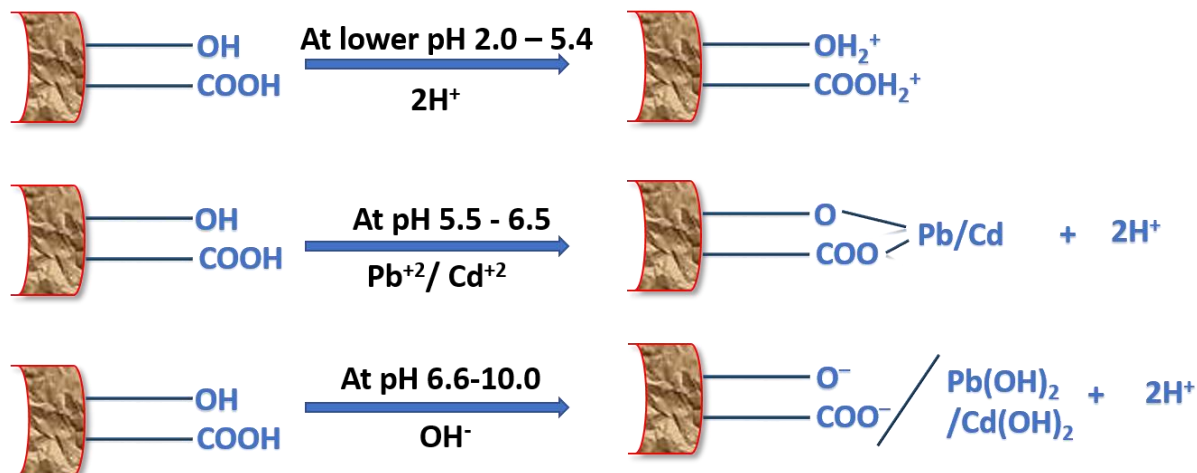


Figure 7.17. Proposed mechanism for the metal ions Pb(II) & Cd(II) ions

### 7.3.12 Effect of adsorbent dosage on adsorption

The adsorbent dosage effect upon adsorbates such as CR, MB, RB, Pb(II) and Cd(II) was studied by differing the concentration from  $0.005 \text{ g L}^{-1}$  to  $0.05 \text{ g L}^{-1}$  at a pH of 5.1, 7.8, 6.1, 5.7 and 6.2, respectively shown in figure 7.18(a-e). A vial of 50 mL of dye having  $300 \text{ mg L}^{-1}$  (RB),  $400 \text{ mg L}^{-1}$  (MB),  $400 \text{ mg L}^{-1}$  (CR),  $400 \text{ mg L}^{-1}$  Pb(II) &  $400 \text{ mg L}^{-1}$  Cd(II) of initial concentration were stirred with GO-Fe/CPTMS-SiO<sub>2</sub>@MF at vibrating speed of 200 rpm. From the figure 7.18, the percent of rate of removal for all the pollutants enhanced with the increase in dosage of adsorbent. The adsorption of RB marked a relative increase from 22% to

99%, MB with an increase of 40% to 98.6%, CR with an increase of 35% to 99%, Pb(II) with a maximum adsorption of 99%, and Cd(II) with a steadily increase of 98.5% was observed. The increase in the removal rate of all pollutants is due to the presence of more active sites of adsorbent. Further increase in the adsorbent led to the enhancement in collision rate between the composite and pollutants, later aggravated the flapping of active adsorption sites, resulting in the lack of free adsorption sites.

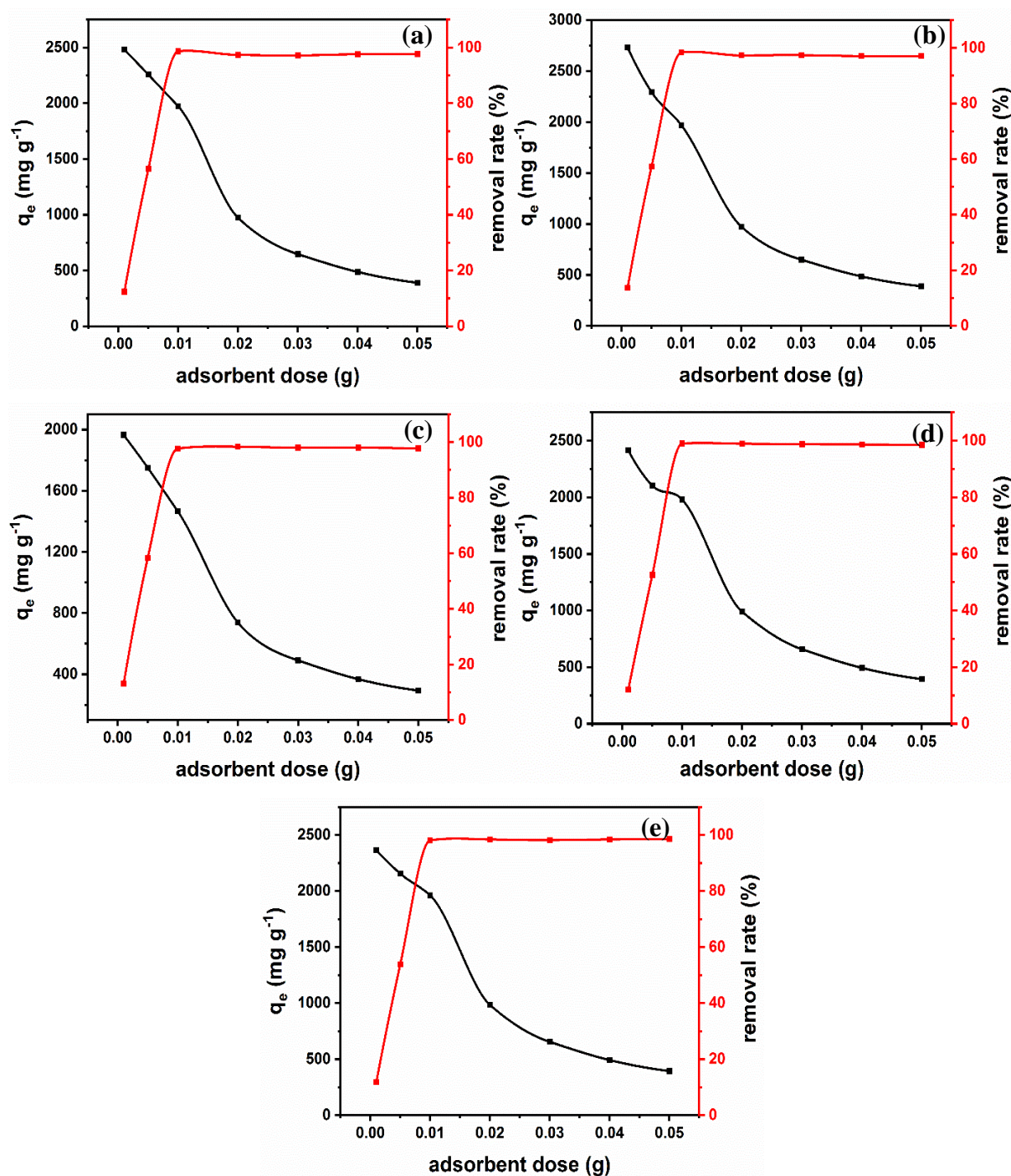


Figure 7.18. Effect on adsorbent dosage on adsorption capacity upon pollutants a) MB, b) RB, c) CR, d) Pb(II) & e) Cd(II)

### 7.3.13 Effect of capacity of adsorbate on adsorption capacity

The adsorbate dosage variation and their adsorption capacity shown in the figure 7.19(a-e). Further the removal rate of pollutants decreases with the increase in adsorbate dosage due to the absence of active sites on the fixed amount of GO-Fe/CPTMS-SiO<sub>2</sub>@MF. Hence, there is no surprising theory and as the initial concentration of adsorbate is higher, the adsorption efficiency will fall gradually.

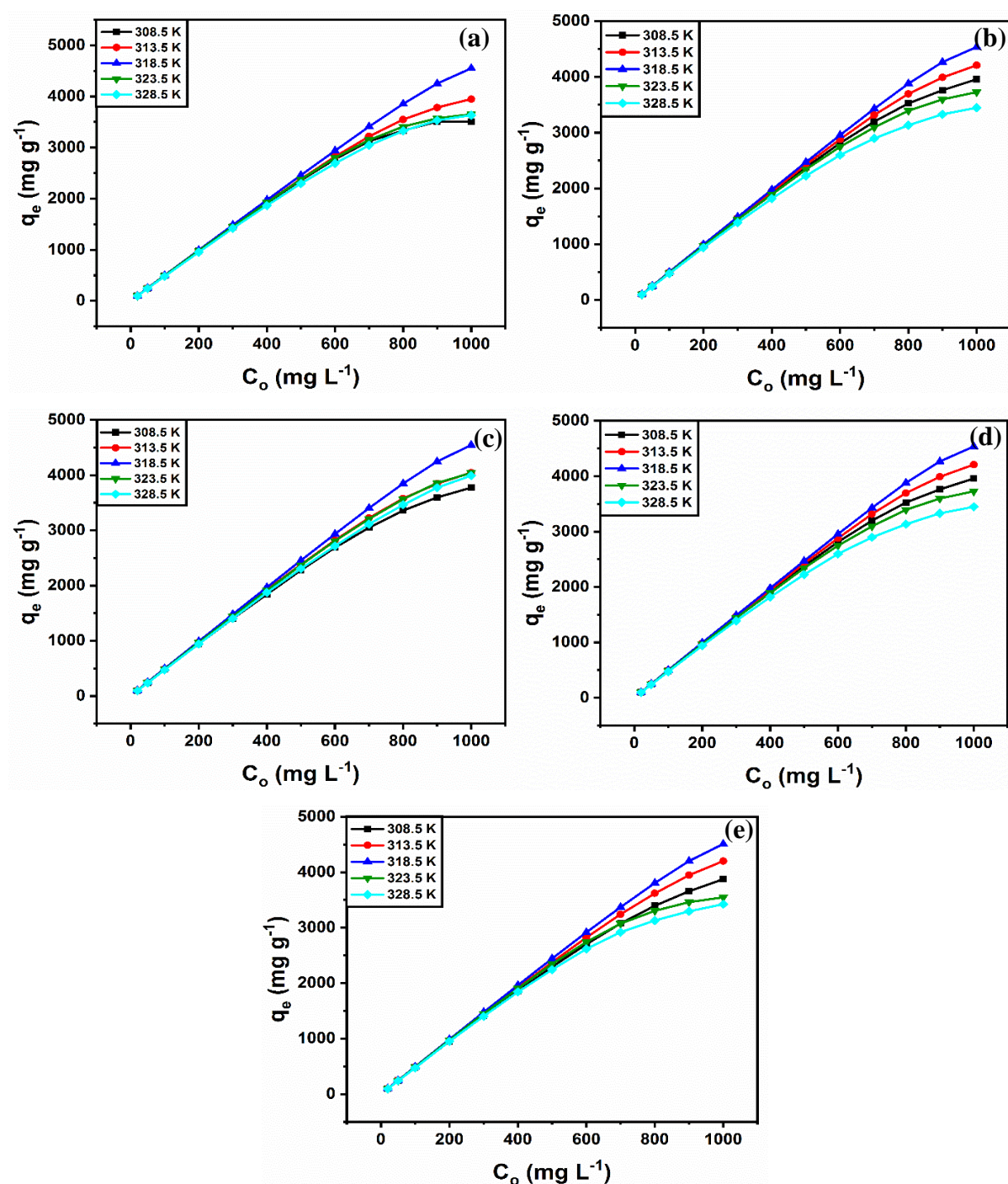


Figure 7.19. Adsorbent dosage on the adsorption of pollutants: a) MB, b) RB, c) CR, d) Pb(II) & e) Cd(II)

### 7.3.14 Effect of contact time on adsorption

The contact time effect on the pollutants adsorbed onto the composite examined at different time intervals shown in figure 7.20. In the first stage of adsorption, the capabilities of both CR, RB and Pb(II) (first 3h) exhibited faster rate of adsorption compared to MB and Cd(II). An increase in initial stage of adsorption is adjoined due to the presence of a greater number of active sites, increasingly occupied with the contact time, governing the stability in adsorption process.

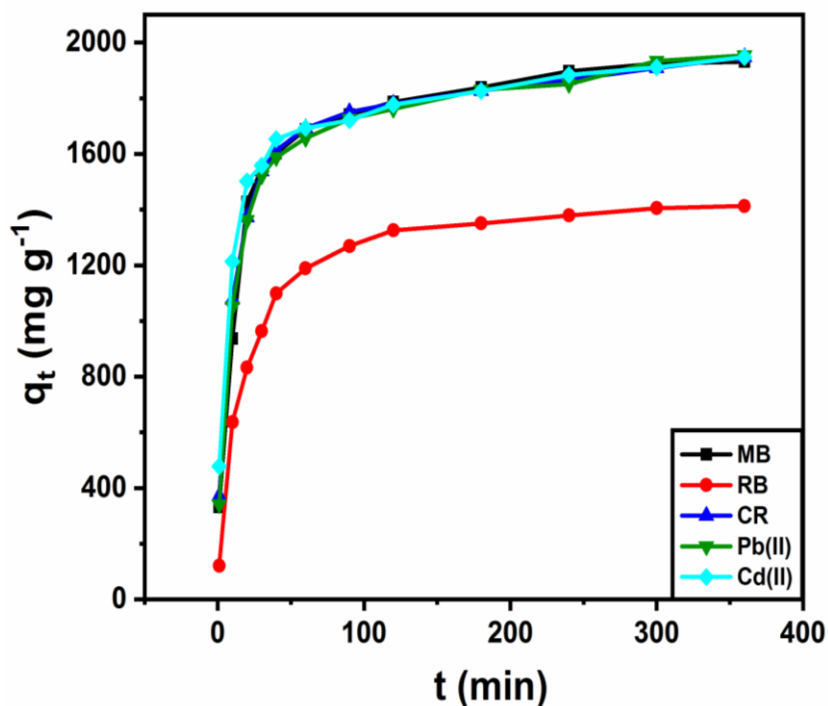


Figure 7.20. Effect of time on the adsorption of pollutants on adsorbent

### 7.3.15 Effect of Ionic strength

Due to the presence of various contaminants in the mainstream sewage effluents, ionic strength effect for the removal of pollutants was examined. NaCl is used as a characteristic pollutant and directly mixed with the existing synthetic wastewater of dyes and pollutants before the adsorption process. From the figure 7.21 & 7.22, the removal rates of pollutants reduced with the rise in ionic strength due to the presence of positive charged sodium ions not only frailer the electrostatic attraction between the pollutants and GO-Fe/CPTMS-SiO<sub>2</sub>@MF composite but also curtailed the charge on surface of composite and became more infuriated (He et al. 2018). Further, the competitive adsorption of Na<sup>+</sup> preoccupied already existed active sites, which hindered the process (Huang et al. 2018). Especially, the NaCl which was added 10 times more than the pollutants, the rate of removal for MB, RB, CR, Pb(II) & Cd(II) decreased

by 8.1%, 13.6%, 11.8%, 9.2% & 13.3% respectively. Due to the presence of impurity concentration relatively low in actual wastewater which contains pollutants i.e., dyes and metal ions, GO-Fe/CPTMS-SiO<sub>2</sub>@MF is considered as an efficient adsorbent for the elimination of pollutants in practical applications.

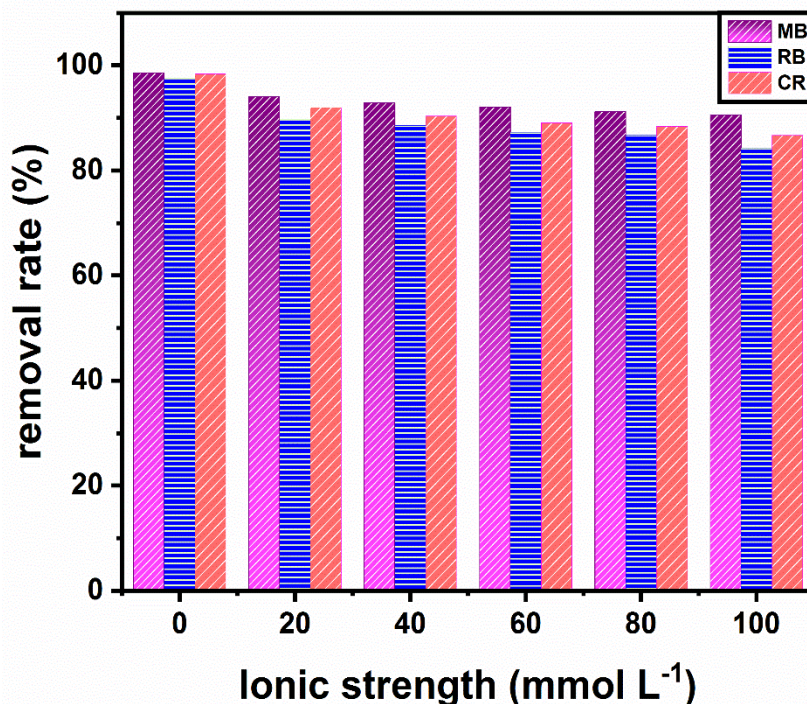


Figure 7.21. Ionic strength of dye adsorbed composite in synthetic wastewater

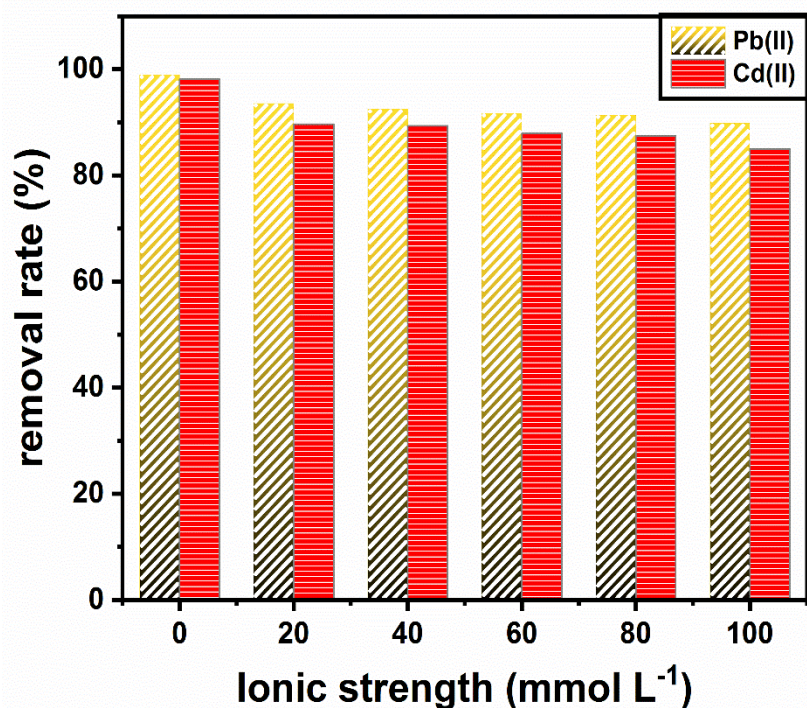


Figure 7.22. Ionic strength of metal adsorbed composite in synthetic wastewater



### 7.3.16 Adsorption Isotherm Studies

Adsorption isotherms can explain the association of nanocomposite equilibrium state with the pollutants initial concentration gave the experimental data on adsorption process and mechanism. Isotherms studies done at different temperature (i.e., 308.5 K, 312.5 K, 318.5 K, 323.5 K & 328.5 K), and the range of initial concentration of different pollutants such as MB, RB, CR, Pb(II) & Cd(II) were 0-1000 mg L<sup>-1</sup>, 0-600 mg L<sup>-1</sup>, 0-1000 mg L<sup>-1</sup>, 0-1000 mg L<sup>-1</sup> & 0-1000 mg L<sup>-1</sup> respectively. Here, four adsorption isotherm models have been studied to interpret the data obtained from adsorption phenomena, and also non-linear patterns represented in eq 7.5-7.8. The adsorption model i.e., Langmuir isotherm stated that all the active sites on GO-Fe/CPTMS-SiO<sub>2</sub>@MF are equivalent and monolayer adsorption on a homogeneity surface of nanocomposite with the adsorbate species; Freundlich model stated that it is multilayer adsorption onto a heterogenetic surface with a non-uniform distribution of heat across the nanocomposite; D-R model stated that the physical or chemical nature is predicted by this isotherm formula; Temkin model indicated the possible effects raised due to the interactions of pollutants with the adsorbent as well as the temperature effects were considered due to the assumption of linear relationship between the heat of adsorption and the analysis. Furthermore, these isotherms assumed the uniform distribution of adsorbate.

$$q_e = \frac{Q_m K_a C_e}{1 + K_a C_e} \quad (7.5)$$

$$q_e = K_f C_e^{1/n} \quad (7.6)$$

$$q_e = \frac{RT}{b_T} \ln A_T C_e \quad (7.7)$$

$$q_e = (q_s) \exp(-K_{DR} \varepsilon^2) \quad (7.8)$$

From the equation 7.5.,  $Q_m$  (mg g<sup>-1</sup>) corresponds to the highest adsorption capacity of GO-Fe/CPTMS-SiO<sub>2</sub>@MF that explained the monolayer for the pollutant per unit weight of the nanocomposite.  $K_L$  known to be Langmuir adsorption coefficient (L mg<sup>-1</sup>) in equipoise condition corresponding to the energy of adsorption. The constant  $K_f$  is an approximation factor for the adsorption capacity and the  $1/n$  denoted to the function of efficiency of adsorption strength. The term  $1/n$  if it is more than one then it corresponds to the surface having cooperative adsorption.  $K_f$  value can be directly linked to the adsorption capacity and the  $K_f$  value increases with an enhancement of its capacity. From Temkin model, where  $R$  represented Universal gas constant (8.314 J/mol/K),  $A_T$  termed to be residual binding constant (L g<sup>-1</sup>) attributed to the highest binding energy and  $b_T$  corresponds to the heat of adsorption (J mol<sup>-1</sup>).

$q_s$  ( $\text{mol g}^{-1}$ ) represented the highest adsorption capacity of D-R model applicable to measure the porous nature of GO-Fe/CPTMS-SiO<sub>2</sub>@MF and probable energy of the adsorption ( $E$ ),  $K_{DR}$  ( $\text{mol}^2/\text{k/J}^2$ ) termed as D–R isotherm constant, which is linked to the free energy required for adsorption per unit mass of the adsorbate,  $\varepsilon$  represented the Polanyi potential gave the following expression:

$$\varepsilon = RT \ln \left( 1 + \frac{1}{C_e} \right) \quad (7.9)$$

These formulas are helpful to measure the mean free energy of adsorption.

$$E = \frac{1}{(2B_D)^{1/2}} \quad (7.10)$$

The above given isotherms performed by non-linear graph plotting technique (Figure 7.23-7.27 respectively). The all four models were analyzed and optimized the results for determining the coefficients of determination (COD)  $R^2$  (equation) between these models and the experiment executed values, by non-linear graph plotting used from Origin Pro.

$$R^2 = \frac{(q_m - \bar{q}_e)^2}{(q_m - \bar{q}_e)^2 + (q_m - q_e)^2} \quad (7.11)$$

The graphs resembled to the adsorbates onto GO-Fe/CPTMS-SiO<sub>2</sub>@MF drawn by pollutants adsorbed per unit mole of the GO-Fe/CPTMS-SiO<sub>2</sub>@MF,  $q_e$  verses the pollutant concentration remained within the adsorbate wastewater,  $C_e$  shown in figure 7.23-7.27. The comparison of adjusted  $R^2$  values were given in Table 7.3 & 7.4 represented the adsorbates and the data along with their isotherms fit in the corresponding pattern i.e., Langmuir > Freundlich > Temkin > D-R. Various adsorption isotherms for the pollutants drawn and shown in figure 7.23-7.27.

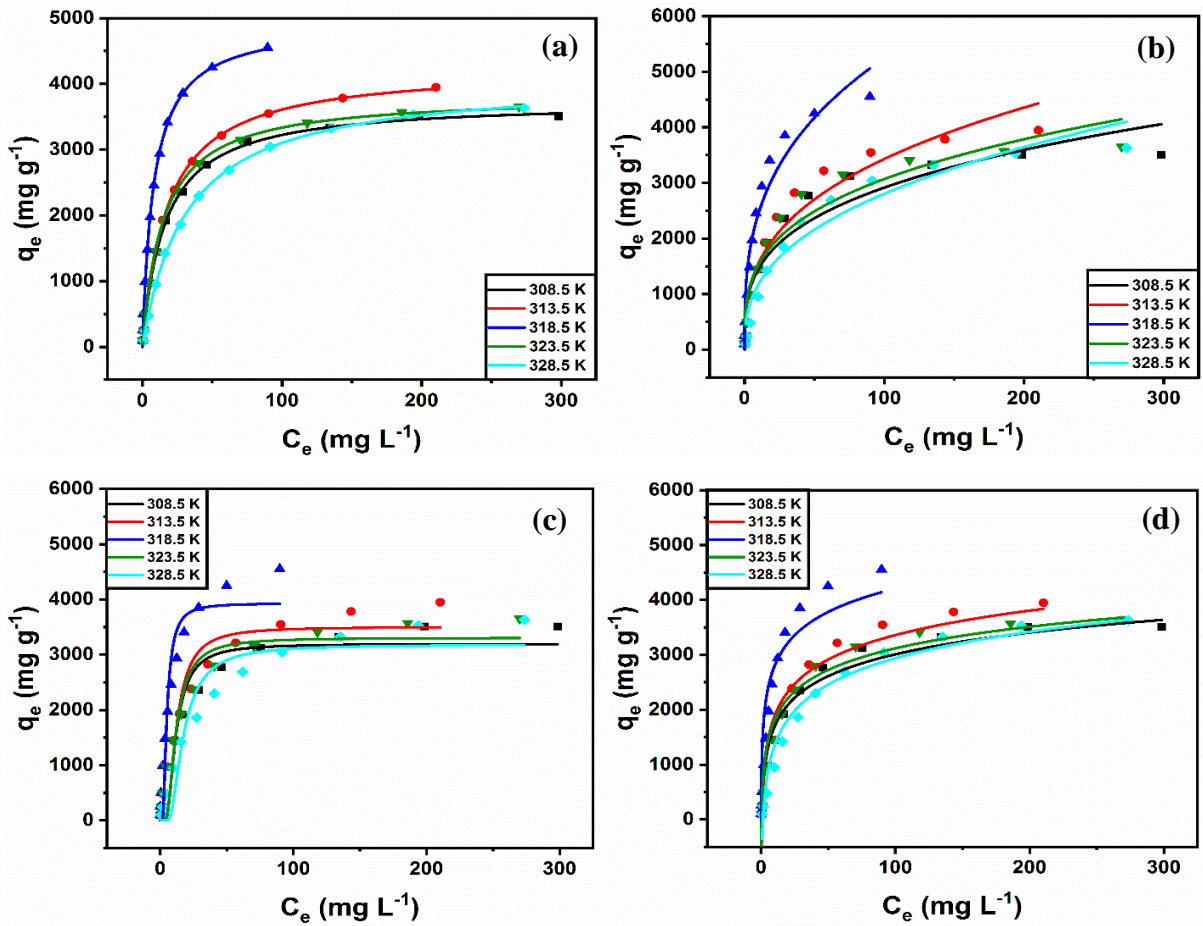
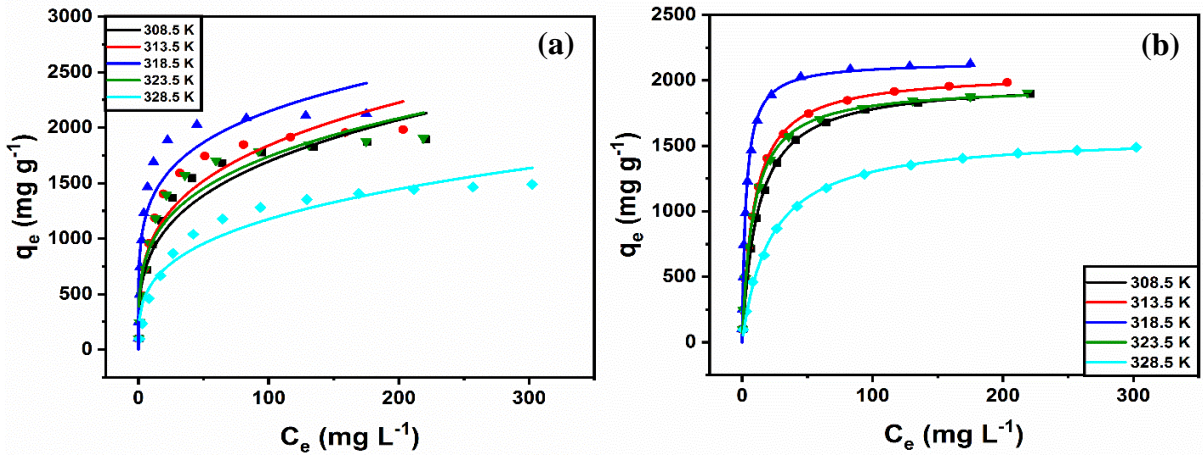


Figure 7.23. MB adsorption values for the four isotherms: a) Langmuir b) Freundlich c) DR & d) Temkin



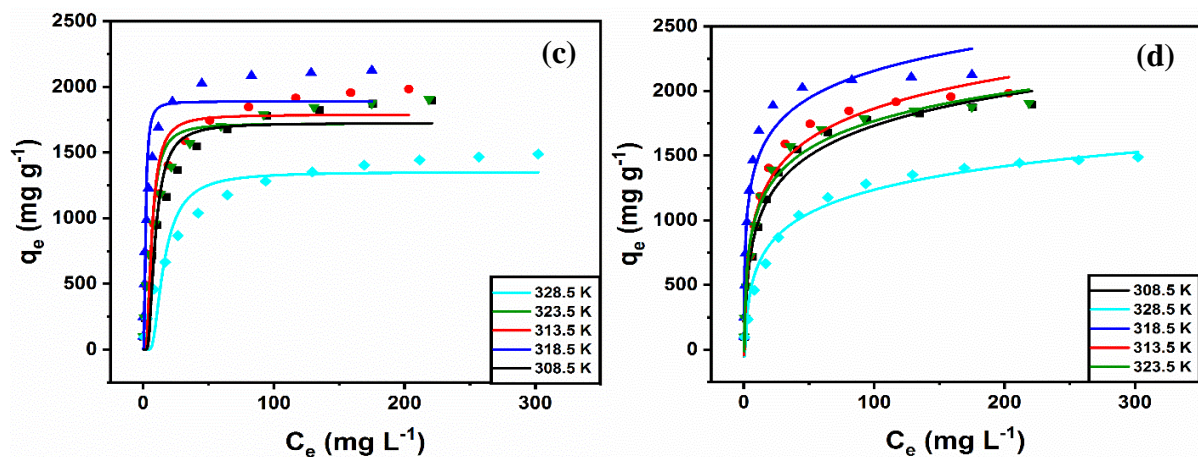


Figure 7.24. RB adsorption values for the four isotherms: a) Langmuir b) Freundlich c) DR & d) Temkin

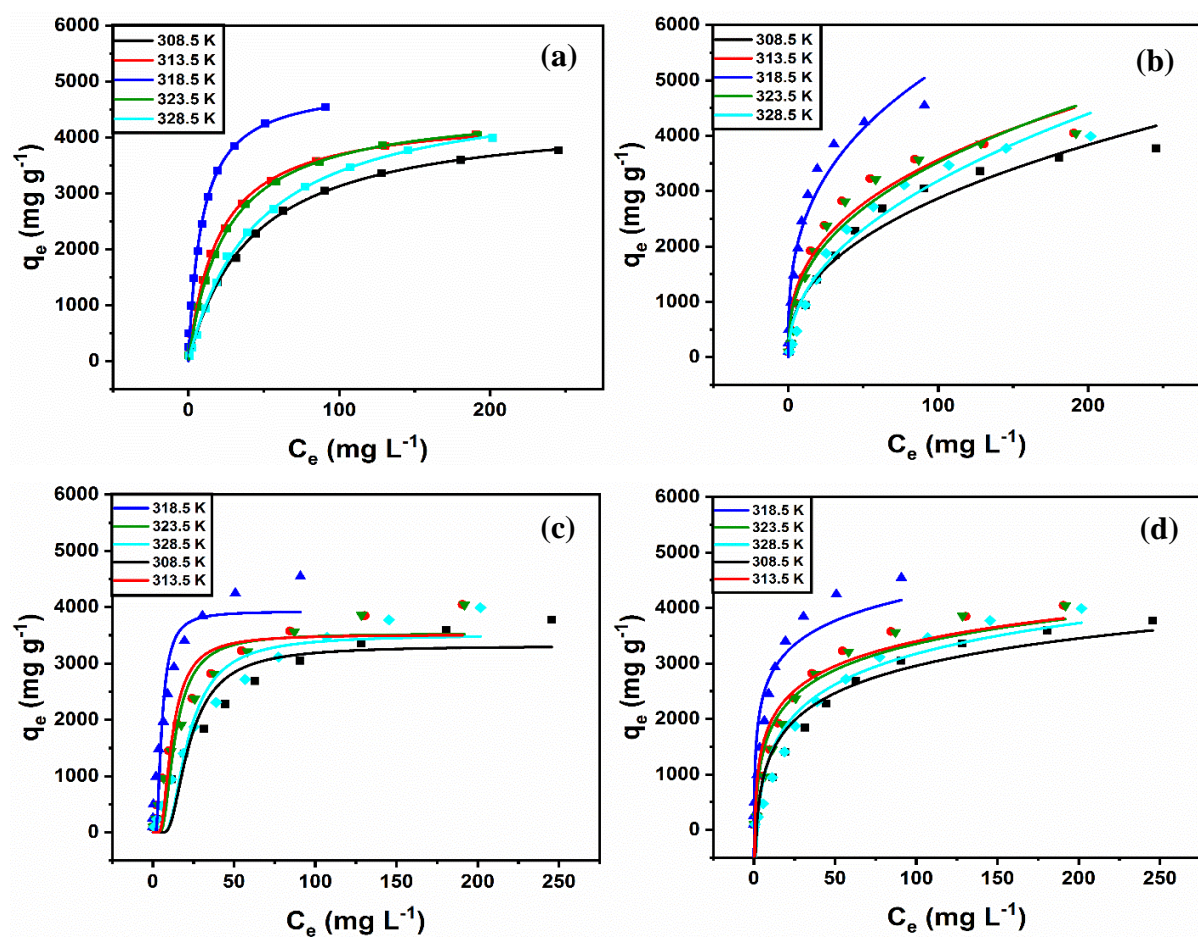


Figure 7.25. CR adsorption values for the four isotherms: a) Langmuir b) Freundlich c) DR & d) Temkin

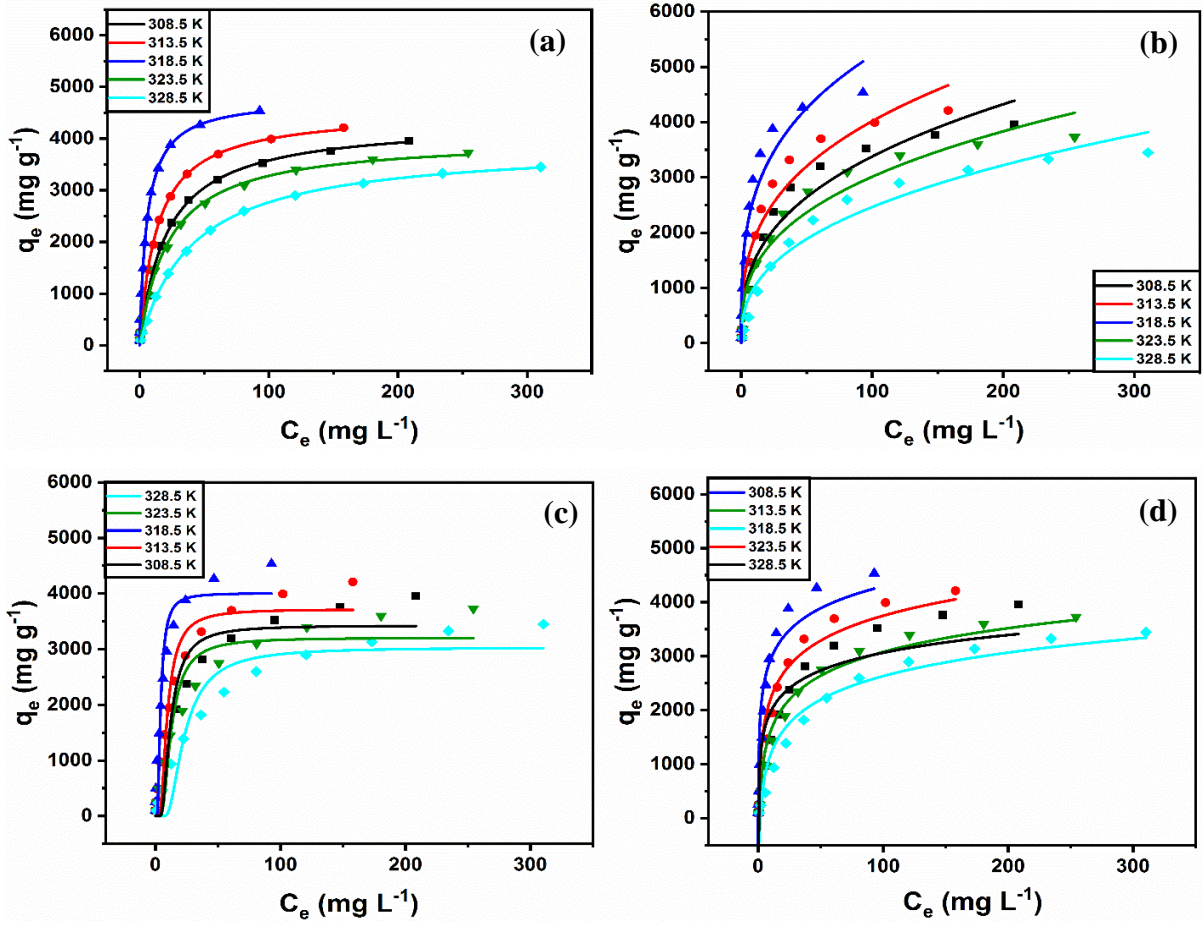
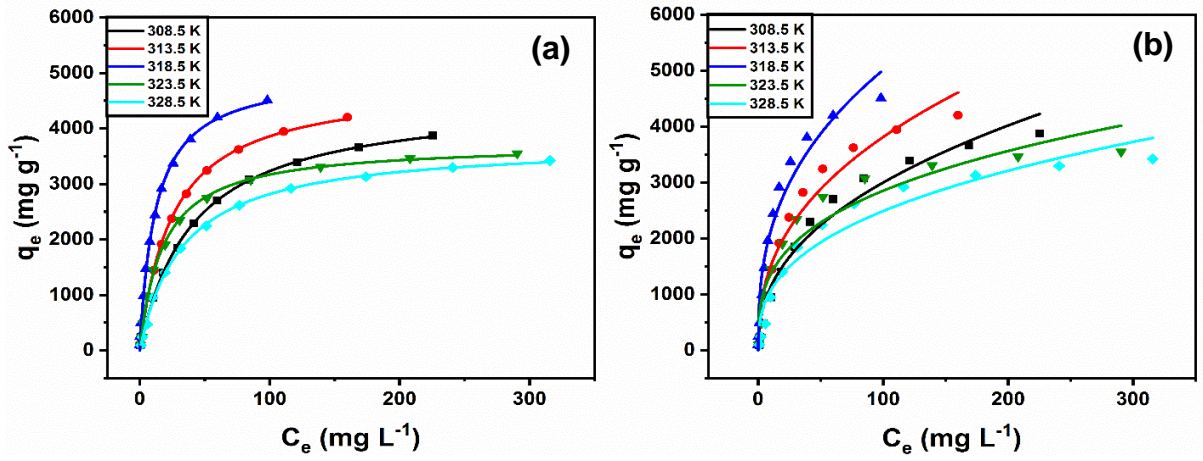


Figure 7.26. Pb(II) adsorption values for the four isotherms: a) Langmuir b) Freundlich c) DR & d) Temkin



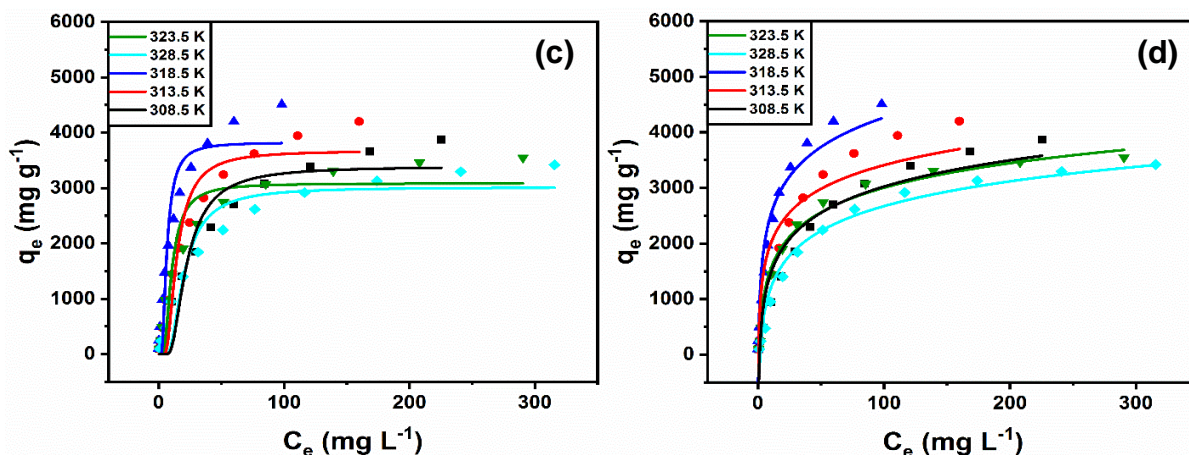


Figure 7.27. Cd(II) adsorption values for the four isotherms: a) Langmuir b) Freundlich c) DR & d) Temkin

Table 7.3: Langmuir & Freundlich Isotherm values for the pollutants adsorption: a) MB, b) RB, c) CR, d) Pb(II) & e) Cd(II)

Pollutants	Temp(K)	Langmuir				Freundlich			
		$Q_{max}$ $mg\ g^{-1}$	$K_a$ $L\ mg^{-1}$	Adj. $R^2$	$R^2$ (COD)	n	$K_F$ $(mg\ g^{-1})(L\ mg^{-1})^{1/n}$	Adj. $R^2$	$R^2$ (COD)
MB	308.5	3743.68630	0.06193	0.99897	0.99906	3.30702	724.29448	0.90741	0.91583
	313.5	4259.36540	0.07553	0.99921	0.99928	2.90224	701.81783	0.93428	0.94025
	318.5	4944.29910	0.09437	0.99524	0.99568	3.02546	1144.76525	0.95423	0.95839
	323.5	3829.76830	0.11837	0.99744	0.99768	3.30170	760.76620	0.92261	0.92965
	328.5	4081.00300	0.14317	0.99958	0.99962	2.64696	492.48819	0.93823	0.94385
RB	308.5	1993.49535	0.08337	0.99759	0.99779	3.46829	449.43708	0.90684	0.91460
	313.5	2058.95336	0.10804	0.99877	0.99887	3.63335	517.90778	0.89915	0.90756
	318.5	2142.85429	0.13578	0.99359	0.99412	4.97503	850.28837	0.89458	0.90336
	323.5	1958.74611	0.16968	0.99801	0.99812	3.83009	522.71791	0.90620	0.91402
	328.5	1585.05614	0.21596	0.99818	0.99833	3.33127	294.97473	0.93391	0.93942
CR	308.5	4434.80990	0.02391	0.99929	0.99936	2.38674	416.52180	0.95961	0.96082
	313.5	4434.87558	0.03788	0.99919	0.99927	2.74968	667.39394	0.94785	0.95259
	318.5	4980.20468	0.05681	0.99319	0.99381	2.97611	1108.11929	0.95996	0.96360
	323.5	4581.07370	0.08168	0.99908	0.99916	2.56029	582.52148	0.93844	0.94404
	328.5	4927.46753	0.12204	0.99868	0.9988	2.15425	375.58438	0.95757	0.96142
Pb	308.5	4331.79508	0.0474	0.99883	0.99893	2.81088	656.37278	0.93776	0.94342

	313.5	4534.92440	0.06362	0.99621	0.99656	3.05109	888.06298	0.95090	0.95536
	318.5	4788.94890	0.08378	0.99247	0.99316	3.41653	1352.84204	0.94149	0.94681
	323.5	4011.19956	0.10979	0.99846	0.9986	2.87147	605.74361	0.94237	0.94761
	328.5	3886.02988	0.14247	0.99963	0.99966	2.58836	415.82107	0.95163	0.95602
<b>Cd</b>	308.5	4550.82902	0.02452	0.99891	0.99901	2.36827	429.01262	0.96661	0.96964
	313.5	4827.64323	0.03528	0.99868	0.9988	2.47484	593.09644	0.96514	0.96831
	318.5	5022.35244	0.05066	0.99734	0.99758	2.69362	906.51007	0.96190	0.96536
	323.5	3732.28427	0.07137	0.99794	0.99813	3.11687	651.02628	0.91193	0.91994
	328.5	3746.48722	0.10033	0.99882	0.99882	2.72544	459.55148	0.93741	0.94310

Table 7.4: DR & Temkin Isotherm values for the pollutants adsorption: a) MB, b) RB, c) CR, d) Pb(II) & e) Cd(II)

Pollutants	Temp(K)	Dubinin-Radushkevich				Temkin			
		$q_s$	$K_{DR}$	Adj. $R^2$	$R^2$ (COD)	$A_T$	$B_T$	Adj. $R^2$	$R^2$ (COD)
		( $\text{mol g}^{-1}$ )	( $\text{mol}^2 \text{k}^{-1} \text{J}^{-2}$ )			( $\text{L g}^{-1}$ )	( $\text{J mol}^{-1}$ )		
<b>MB</b>	308.5	3197.12259	0.04317	0.90160	0.91055	1.91488	4.47430	0.94333	0.94848
	313.5	3503.95501	0.04566	0.90349	0.91226	1.86071	4.05000	0.92740	0.93400
	318.5	3931.08610	0.00841	0.90660	0.90969	9.52387	4.31388	0.87821	0.88438
	323.5	3306.11319	0.04172	0.89364	0.90331	2.44855	4.73965	0.94388	0.94898
	328.5	3181.97955	0.08631	0.90683	0.91530	0.69617	3.93807	0.96460	0.96782
<b>RB</b>	308.5	1352.59484	0.07213	0.88038	0.89034	1.66953	7.57021	0.97522	0.97728
	313.5	1721.44345	0.01310	0.88474	0.89435	2.27874	7.58233	0.97576	0.97778
	318.5	1889.25101	0.00144	0.88958	0.89878	11.5794	8.65404	0.96309	0.96616
	323.5	1788.34799	0.01418	0.88278	0.89255	3.0037	8.67026	0.97771	0.97957
	328.5	1724.85833	0.02650	0.88347	0.89318	1.08995	10.35320	0.97419	0.97634
<b>CR</b>	308.5	3313.88380	0.15405	0.90561	0.91419	0.63859	3.59987	0.94084	0.94622
	313.5	3512.51061	0.04332	0.90146	0.91042	1.97677	4.04932	0.90990	0.91809
	318.5	3926.47311	0.01008	0.89023	0.90021	8.35633	4.23537	0.88583	0.89621
	323.5	3534.39615	0.05592	0.90753	0.91594	1.36735	3.93821	0.88510	0.89554

	328.5	3509.25377	0.13693	0.91945	0.92677	0.53186	3.41536	0.92214	0.92922
<b>Pb</b>	308.5	3426.62806	0.04438	0.91188	0.91989	6.44993	5.40779	0.75525	0.77750
	313.5	3718.94363	0.02737	0.90095	0.90995	2.82564	3.91782	0.93010	0.93645
	318.5	4009.11515	0.00572	0.91098	0.91908	15.14230	4.50580	0.88945	0.89950
	323.5	3207.05453	0.04704	0.88872	0.89884	1.27364	4.22811	0.95448	0.95862
	328.5	3031.58475	0.15241	0.90319	0.91199	0.65897	4.34091	0.94800	0.95273
<b>Cd</b>	308.5	3391.81674	0.15031	0.90054	0.90958	0.83737	3.75060	0.92326	0.93023
	313.5	3675.59520	0.06380	0.89939	0.90853	2.52045	4.22150	0.84833	0.86212
	318.5	3825.64484	0.01342	0.89887	0.90806	2.63916	3.45665	0.93021	0.93655
	323.5	3086.18675	0.03204	0.88965	0.89968	1.10959	4.21189	0.97601	0.97819
	328.5	3015.56893	0.11661	0.89544	0.90495	0.63371	4.23614	0.96907	0.97188

Table 7.3 & 7.4 gives the data of prominent values of the isotherms at five different temperatures acquired with the non-linear plotting in origin software. The adsorption capacity of adsorbent is mainly dependent on temperature factor. The maximum adsorption capacity of GO-Fe/CPTMS-SiO<sub>2</sub>@MF for MB at 318.5 K was 4944.29 mg g<sup>-1</sup>, RB at 318.5 K was 2142.85 mg g<sup>-1</sup>, CR at 318.5 K was 4980.20 mg g<sup>-1</sup>, Pb(II) at 318.5 K was 4788.94 mg g<sup>-1</sup> and Cd(II) at 318.5 K was 5022.35 mg g<sup>-1</sup>. R<sub>L</sub> termed as dimensional separation factor is analyzed to determine the relationship between nanocomposite and pollutant molecules given by eq. 7.12.

$$R_L = \frac{1}{1 + K_a \times C_o} \quad (7.12)$$

The adsorption process divided into 4 types based on the values of R<sub>L</sub> is not favorable if is greater than 1, if it is above 0 to 1 then it is favorable, irreversible if it is zero and when it is equal to one it means linear. Figure 7.28 represented the R<sub>L</sub> values from 0-1, which indicated that they are robust interactions in between the adsorbent and the pollutants. Freundlich constant termed to be K<sub>f</sub> and their values for the dyes and metals i.e., 1144.76 (MB), 850.28 (RB), 1108.12 (CR), 1352.84 (Pb(II)) & 906.51 (Cd(II)) and n values are calculated from the plots that are 3.02, 4.97, 2.97, 3.41 & 2.69 which explained that it is beneficial nature of adsorption. This Temkin isotherm explains about the nanocomposite surface that have been enveloped with dyes and metal ions (MB, RB, CR, Pb(II) & Cd(II)) and temperature as a function for adsorption (heat of adsorption) reduces in a linear fashion compared to decreasing



logarithmic fashion neglecting the effectiveness of high to low concentration range. It is due to the interaction of adsorbents with the pollutants.

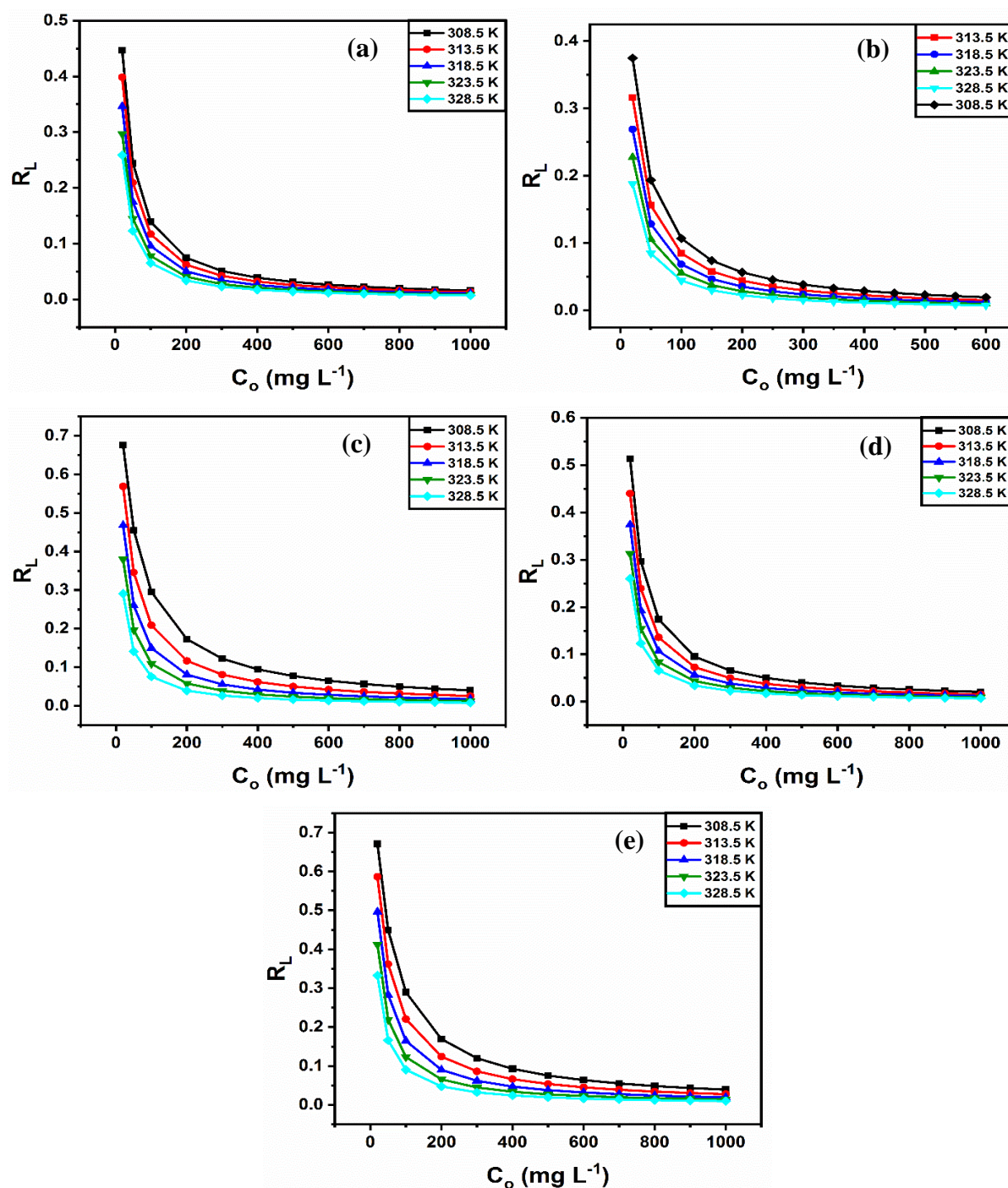


Figure 7.28.  $R_L$  values for the pollutants adsorption: a) MB, b) RB, c) CR, d) Pb(II) & e) Cd(II)

### 7.3.17 Van't Hoff plot (Thermodynamic studies)

Temperature is a prominent factor for the adsorption studies of GO-Fe/CPTMS-SiO<sub>2</sub>@MF, since most of the dyes released relatively high doses at high temperatures into the wastewater

from the industry. Langmuir adsorption studies is found to be well suited isotherm model for all the pollutants using non-linear method at five different temperatures and the values of  $K_a$  made dimensionless in order to calculate the thermodynamic parameters shown in figure 7.29(a-e). The parameters include Gibbs free energy ( $\Delta G^\circ$ , KJ mol<sup>-1</sup>), change on enthalpy ( $\Delta H^\circ$ , KJ mol<sup>-1</sup>) and change in entropy ( $\Delta S^\circ$ , J/mol/K) were measured via equations and given in the table 7.5. In this, the adsorption process is a unimolecular chemisorption and the data calibrated to know the expression for adsorption equilibrium constant  $K_e$  is given below eq.

$$K_e = \frac{1000 \times K_a \times M}{\gamma} \quad (7.13)$$

$$K_e = \frac{1000 \times K_a \times \text{mol. wt. of adsorbate} \times \text{standard conc. of adsorbate}}{\text{activity coefficient of adsorbate}}$$

$$\Delta G = -RT \ln(K_e) \quad (7.14)$$

From the thermodynamics 3<sup>rd</sup> law, the formula is as follows,

$$\Delta G = \Delta H - T\Delta S \quad (7.15)$$

By fitting the curve with equation (7.14) and (7.15) Van't Hoff Equation can be obtained by (Lima et al. 2015, 2019; Liu 2009; Xu and Liu 2008)

$$\ln K_e = \frac{\Delta S}{R} - \frac{\Delta H}{RT} \quad (7.16)$$

The term  $K_e$  represented equilibrium constant for adsorption,  $M$  (g/mol) refers to the pollutant molar mass,  $\gamma$  referred to the activity coefficient (dimensionless),  $R$  termed to the gas constant,  $T$  refers to the temperature in Kelvin (K). A graph plotted  $\ln K_e$  against  $1/T$  which allow slope and intercept to measure  $\Delta H$  as well as  $\Delta S$  (Panagopoulos et al. 2017). Van't Hoff plots for the adsorbates are given in figure 7.29(a-e). The thermodynamic parameters estimated from formula were given in the tabular form 7.5.

The negative values of  $\Delta G$  in all situations illustrated that the adsorption process of all pollutants was spontaneous in nature. Further, the decreasing trend in  $\Delta G$  values with the advancement of temperature that the pollutants removed more effectively by adsorbent at high temperatures. The  $\Delta H$  data was 7.7361 KJ mol<sup>-1</sup> for MB, 10.4537 KJ mol<sup>-1</sup> for RB, 17.7252 KJ mol<sup>-1</sup> for CR, 18.7632 KJ mol<sup>-1</sup> for Pb(II) and 22.5652 KJ mol<sup>-1</sup> for Cd(II) respectively confirmed the adsorption is endothermic process, chemisorptive nature as well as randomness increase of adsorbent/pollutant interface in adsorbate solution respectively. Due to the availability of various hydroxyl, carboxyl group functionalities assumed to further develop secondary forces of attraction led to the enhancement in rate of adsorption. The randomness in

the adsorbate molecules resulted in positive values of  $\Delta S$  and it also enhanced the interactions in solution/solid interface during this phenomena (Değermenci et al. 2019). These data also predicted that they will be possible structural changes in both pollutants and GO-Fe/CPTMS-SiO<sub>2</sub>@MF during the adsorption process. R<sup>2</sup> values measured from the plot which tends to unity determined the accurate values of achieved  $\Delta H$  and  $\Delta S$  values. At last, the increment in temperature is also beneficial to the adsorption process for the GO-Fe/CPTMS-SiO<sub>2</sub>@MF.

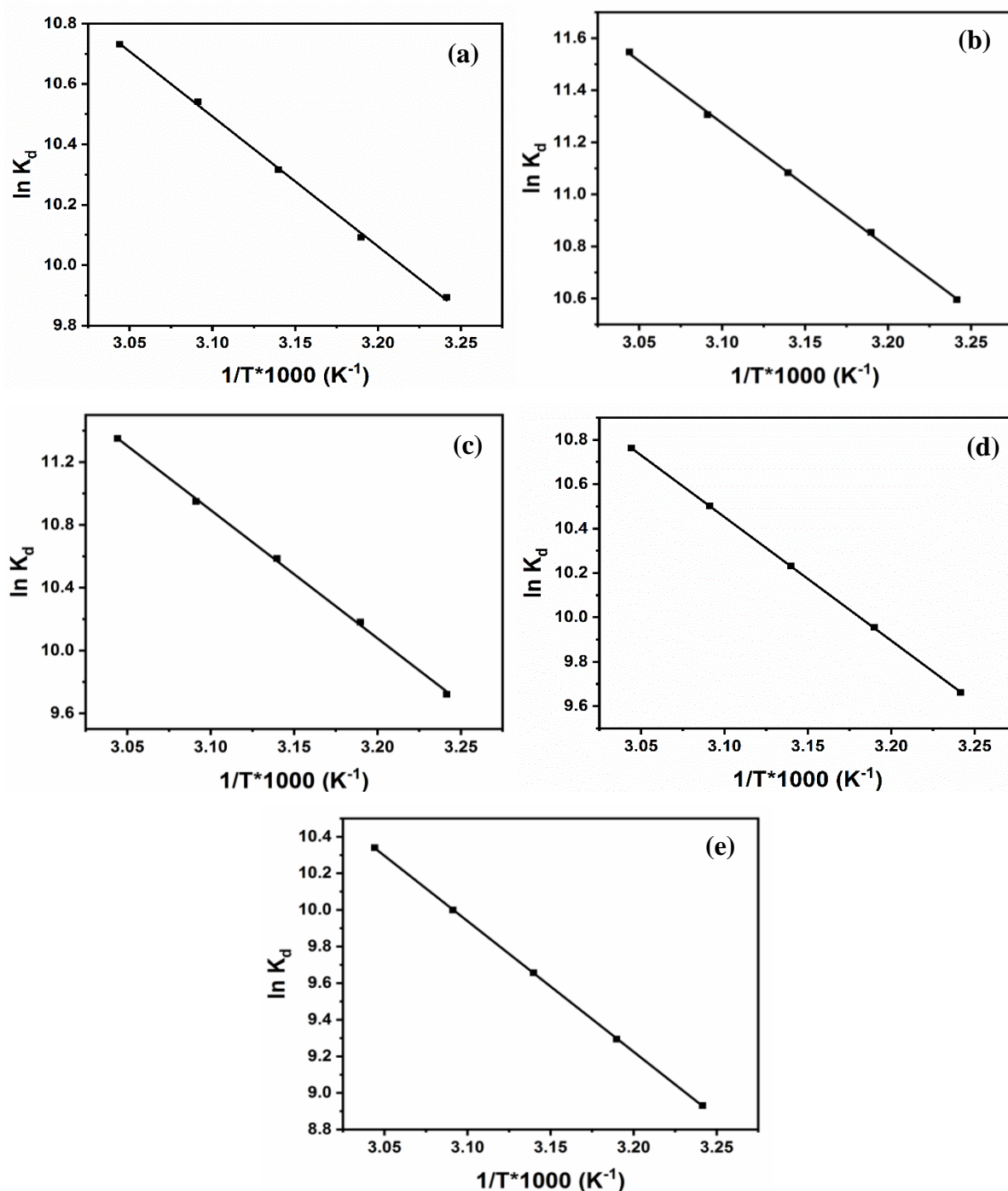


Figure 7.29. Van't hoff plot for the pollutants adsorption: a) MB, b) RB, c) CR, d) Pb(II) & e) Cd(II)

Table 7.5: Thermodynamic studies for the pollutants adsorption: a) MB, b) RB, c) CR, d) Pb(II) & e) Cd(II)

Thermodynamics parameters					
Pollutants	Temp(K)	$\Delta G$ (kJ mol <sup>-1</sup> )	$\Delta H$ (kJ mol <sup>-1</sup> )	$\Delta S$ (JK <sup>-1</sup> mol <sup>-1</sup> )	R <sup>2</sup>
MB	308.5	25.37645	7.7361	115.0475	0.99897
	313.5	26.30518			
	318.5	27.31441			
	323.5	28.37527			
	328.5	29.30867			
RB	308.5	27.1748	10.4537	133.6251	0.99957
	313.5	28.2909			
	318.5	29.3473			
	323.5	30.4074			
	328.5	31.5361			
CR	308.5	24.9321	17.7252	176.4006	0.99922
	313.5	26.5354			
	318.5	28.0318			
	323.5	29.4485			
	328.5	31.0003			
Pb	308.5	24.78	18.7632	188.8409	0.99997
	313.5	25.9487			
	318.5	27.0915			
	323.5	28.244			
	328.5	29.3922			
Cd	308.5	22.9072	22.5654	200.1838	0.99998
	313.5	24.225			
	318.5	25.5712			
	323.5	26.8945			
	328.5	28.2404			

---

### 7.3.18 Adsorption Kinetic Studies

The time dependence of pollutants adsorbed onto GO-Fe/CPTMS-SiO<sub>2</sub>@MF to evaluate the adsorption process better. All the kinetic curves revealed that the rate of uptake  $q_t$  is faster at the starting stages for all pollutants adsorption phenomena explained due to the presence of plentiful functional moieties on the adsorbent surface which indicated GO-Fe/CPTMS-SiO<sub>2</sub>@MF be used as an effective adsorbent in wastewater treatment. This is also due to the presence of huge amount of vacant adsorption sites feasible in initial period and then residual vacant sites become lesser with enhancing adsorption.

The processed data were measured for two kinetic models (i) Lagergren pseudo first order (PFO) & (ii) pseudo second order (PSO) employed to analyze the kinetic properties of adsorption of pollutants using adsorbent. The PFO equation kinetic model is given below:

$$\ln(q_e - q_t) = \ln q_e - k_1 t \quad (7.17)$$

The PSO kinetic model equation is as follows:

$$\frac{t}{q_t} = \frac{1}{k_2 q_e^2} + \frac{1}{q_e} \quad (7.18)$$

Where  $k_1$  (min<sup>-1</sup>) is the pseudo 1<sup>st</sup> order rate constant and  $k_2$  (g/mg/min) is the pseudo 2<sup>nd</sup> order rate constant;  $q_t$  &  $q_e$  are the adsorption capacities of the adsorbent at any time  $t$  and equilibrium respectively.

The pseudo first order kinetic model presumed that the adsorption process is predominated by diffusion path which is shown from figure 7.30(a-e). And the pseudo second order kinetic model presumed that rate of adsorption is monitored by chemical adsorption phenomenon in figure 7.31 (An et al. 2019; Zhao et al. 2019). This chemical adsorption describes about the electron deactivation, adsorption and desorption process of agile active sites on GO-Fe/CPTMS-SiO<sub>2</sub>@MF surface.

$R^2$  values justified that the calculated values not suitable for the PFO is due to the less  $q_e$  value which can be prognosticated significantly by this pseudo first order model as collated with experimental values, highlighted the inapplicability of the model. The pseudo 2<sup>nd</sup> order for all the pollutants gave better regression ( $R^2$ ) values close to 1. The  $q_{e(\text{calc})}$  values of the PSO for the pollutants MB, RB, CR, Pb(II) & Cd(II) was 1972.3, 1464.1, 1964.6, 1980.1, 1960.7 mg g<sup>-1</sup> almost close to the  $q_{e(\text{exp})}$  are 1972.1, 1464.8, 1965.8, 1979.1, 1961.4 mg g<sup>-1</sup> respectively.

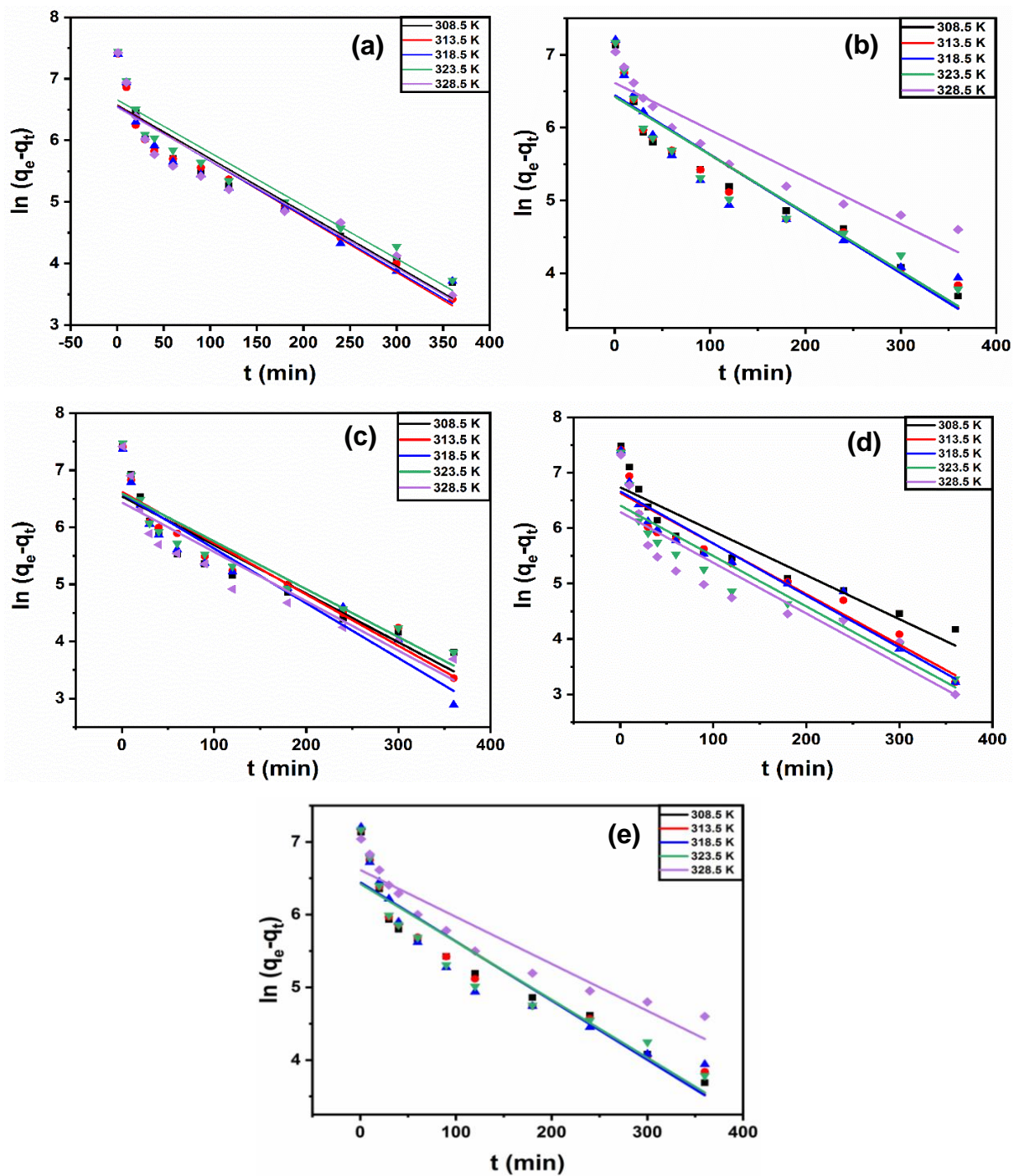


Figure 7.30. Pseudo first order values for the pollutants: a) MB, b) RB, c) CR, d) Pb(II) & e) Cd(II)

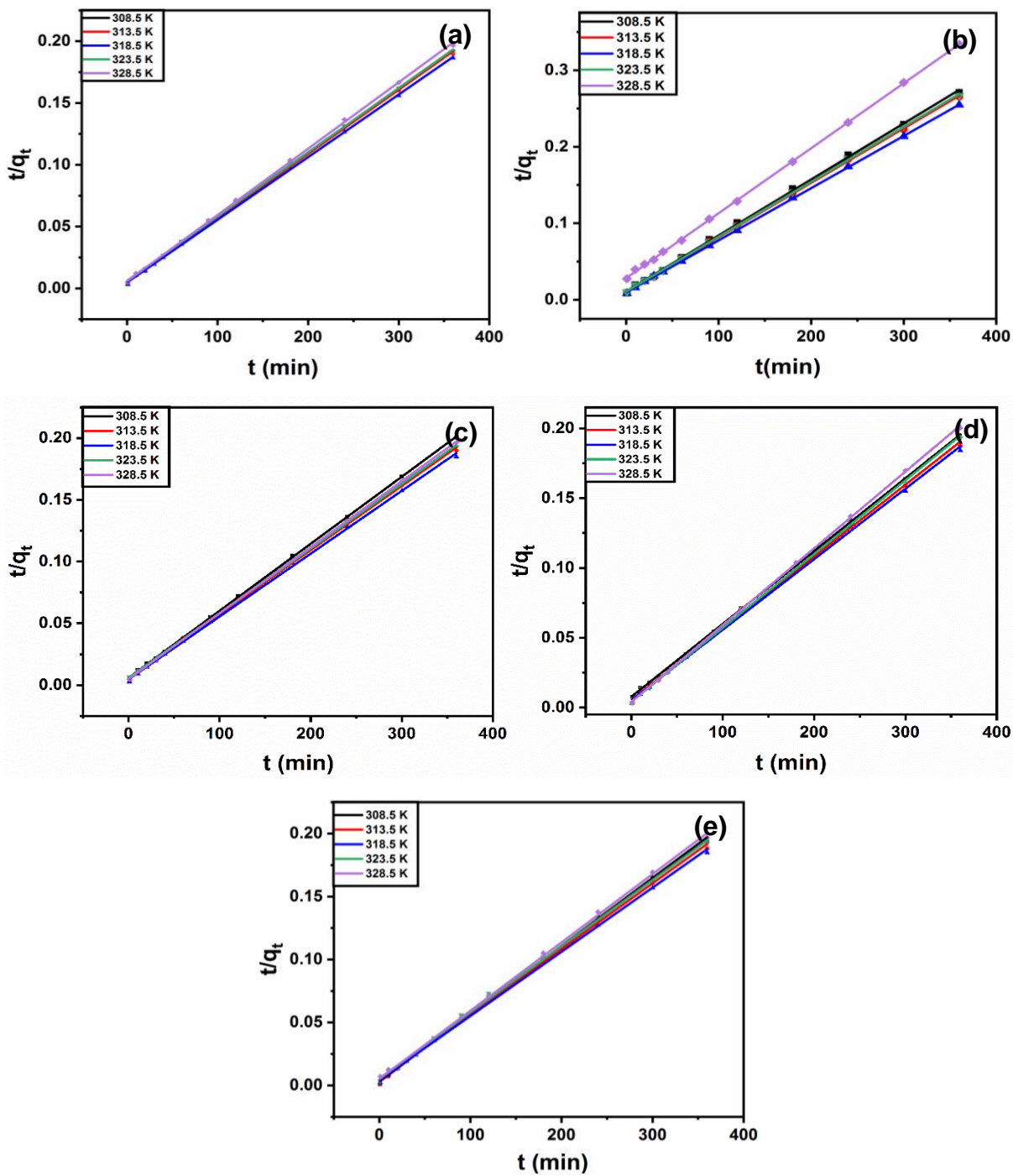


Figure 7.31. Pseudo second order values for the pollutants: a) MB, b) RB, c) CR, d) Pb(II) & e) Cd(II)

Table 7.6: Kinetic studies values for the pollutants adsorption: a) MB, b) RB, c) CR, d) Pb(II) & e) Cd(II)

Pollutants	Temp (K)	Pseudo-first-order				Pseudo-second-order			
		$q_{e(\text{exp})}$ ( $\text{mg g}^{-1}$ )	$q_{e(\text{calc})}$ ( $\text{mg g}^{-1}$ )	$k_1$ ( $\text{min}^{-1}$ )	$R^2$	$q_{e(\text{calc})}$ ( $\text{mg g}^{-1}$ )	$k_2$ ( $\text{g mg}^{-1} \text{min}^{-1}$ )	$R^2$	$E_a$ ( $\text{kJ mol}^{-1}$ )
MB	308.5	1916.6	622.20009	0.00873	0.89279	1915.7088	$5.018 \times 10^{-5}$	0.99966	30.8718
	313.5	1927.15	665.29173	0.00903	0.91059	1926.7822	$5.25 \times 10^{-5}$	0.99937	
	318.5	1972.10	610.23982	0.00891	0.89288	1972.3865	$5.366 \times 10^{-5}$	0.99961	
	323.5	1922.05	676.54421	0.0086	0.90527	1923.0769	$4.396 \times 10^{-5}$	0.99956	
	328.5	1862.70	570.7111	0.00869	0.87416	1862.1973	$5.068 \times 10^{-5}$	0.9996	
RB	308.5	1367.85	715.66593	0.0081	0.90463	1366.1202	$4.906 \times 10^{-5}$	0.99934	35.6922
	313.5	1404.3	704.7713	0.00809	0.89374	1404.4943	$4.84 \times 10^{-5}$	0.9997	
	318.5	1464.8	596.65871	0.00814	0.86944	1464.1288	$4.98 \times 10^{-5}$	0.99988	
	323.5	1392.75	629.88158	0.00798	0.87705	1392.7576	$4.83 \times 10^{-5}$	0.99976	
	328.5	1177.3	904.40445	0.00646	0.90951	1176.4705	$2.566 \times 10^{-5}$	0.99982	
CR	308.5	1842.75	558.31612	0.00852	0.86464	1841.6206	$4.988 \times 10^{-5}$	0.99983	37.8366
	313.5	1925.75	694.05886	0.00899	0.91659	1926.7822	$4.933 \times 10^{-5}$	0.99939	
	318.5	1965.8	621.50404	0.0096	0.90952	1964.6365	$5.547 \times 10^{-5}$	0.99934	
	323.5	1912.05	611.39643	0.00839	0.8813	1912.0458	$4.582 \times 10^{-5}$	0.99976	
	328.5	1872.9	511.69216	0.00865	0.86674	1872.6591	$5.843 \times 10^{-5}$	0.99985	
Pb	308.5	1916.65	1484.1486	0.00794	0.8743	1915.7088	$3.525 \times 10^{-5}$	0.99977	42.2671
	313.5	1945.6	1506.7502	0.00914	0.91137	1945.5253	$4.812 \times 10^{-5}$	0.99906	
	318.5	1979.15	1500.6002	0.0094	0.92256	1980.198	$4.876 \times 10^{-5}$	0.99897	
	323.5	1892.05	1559.6974	0.00912	0.88145	1890.3592	$6.60 \times 10^{-5}$	0.99978	
	328.5	1817.75	1588.9915	0.00914	0.8351	1818.1818	$7.506 \times 10^{-5}$	0.99979	
Cd	308.5	1852.75	1553.3739	0.0081	0.90463	1851.8518	$1.016 \times 10^{-4}$	0.99954	26.3098
	313.5	1915.9	1552.3852	0.00809	0.89374	1915.7088	$6.812 \times 10^{-5}$	0.99887	
	318.5	1961.45	1551.3930	0.00814	0.86944	1960.7843	$6.192 \times 10^{-5}$	0.99916	
	323.5	1902.75	1556.1562	0.00798	0.87705	1901.1406	$5.021 \times 10^{-5}$	0.99865	



### Intra-particle diffusion model

In the above specified models cannot identify the solution(diffusion) mechanism and the rate-determining strategy, intra-particle diffusion (ID) model was also examined. The uptake of pollutant mechanism by the GO-Fe/CPTMS-SiO<sub>2</sub>@MF consists of three steps: (i) film diffusion, (ii) intra-particle diffusion & (iii) mass action. This mechanism gave the equation 7.19 where the uptake of pollutant at regular time interval ( $q_t$ ) vs time  $t$ , where  $k_p$  ((mg/g) min<sup>1/2</sup>) is a intraparticle diffusion rate constant (Weber and Morris 1963).

$$q_t = k_p t^{1/2} + x_i \quad (7.19)$$

Where  $x_i$  represented the boundary layer thickness (Kavitha and Namasivayam 2007). The plots between  $q_t$  and  $t^{1/2}$  indicated the intercept positive values i.e.,  $x_i \neq 0$  shown in figure 7.32. If  $x_i = 0$ , the way, adsorption phenomena is monitored by this method(Wu et al. 2009), the positive value of intercept explained the spontaneous type that took at time  $t = 0$  initially through film diffusion. As shown in the figure 7.32, each multi-linear plot showed three linear regions which corresponded to the three steps of adsorption for all the pollutants. All fitting slant lines of this model could not get through this origin software, proved that the pollutants removal rate determined by intraparticle diffusion only (Xu et al. 2019). The initial step having the highest rate constant ( $k_p$ ) represented the surface adsorption. The huge amount of adsorption sites on the surface of GO-Fe/CPTMS-SiO<sub>2</sub>@MF gets engaged, the secondary step begin with the pollutants enters into pores and were adsorbed into the inner areas of adsorbent. The tertiary step referred to the equilibrium phase, rate constants gradually decreases because of the absence of free active sites and the residual concentration of adsorbate (Ahmad et al. 2019). Therefore, the adsorption is controlled by the quicker film and sluggish intra-particle diffusion for all pollutants.

The initial adsorption factor ( $R_i$ ) gave the formula where  $R_i$  is conveyed in terms of  $x_i$ :

$$R_i = 1 - \frac{x_i}{q_e} \quad (7.20)$$

The larger values of  $x_i$  for Cd(II), Pb(II) and CR than that of MB and RB proved that the film diffusion is primarily controlled by overall rate-limiting step shown in table 7.7.

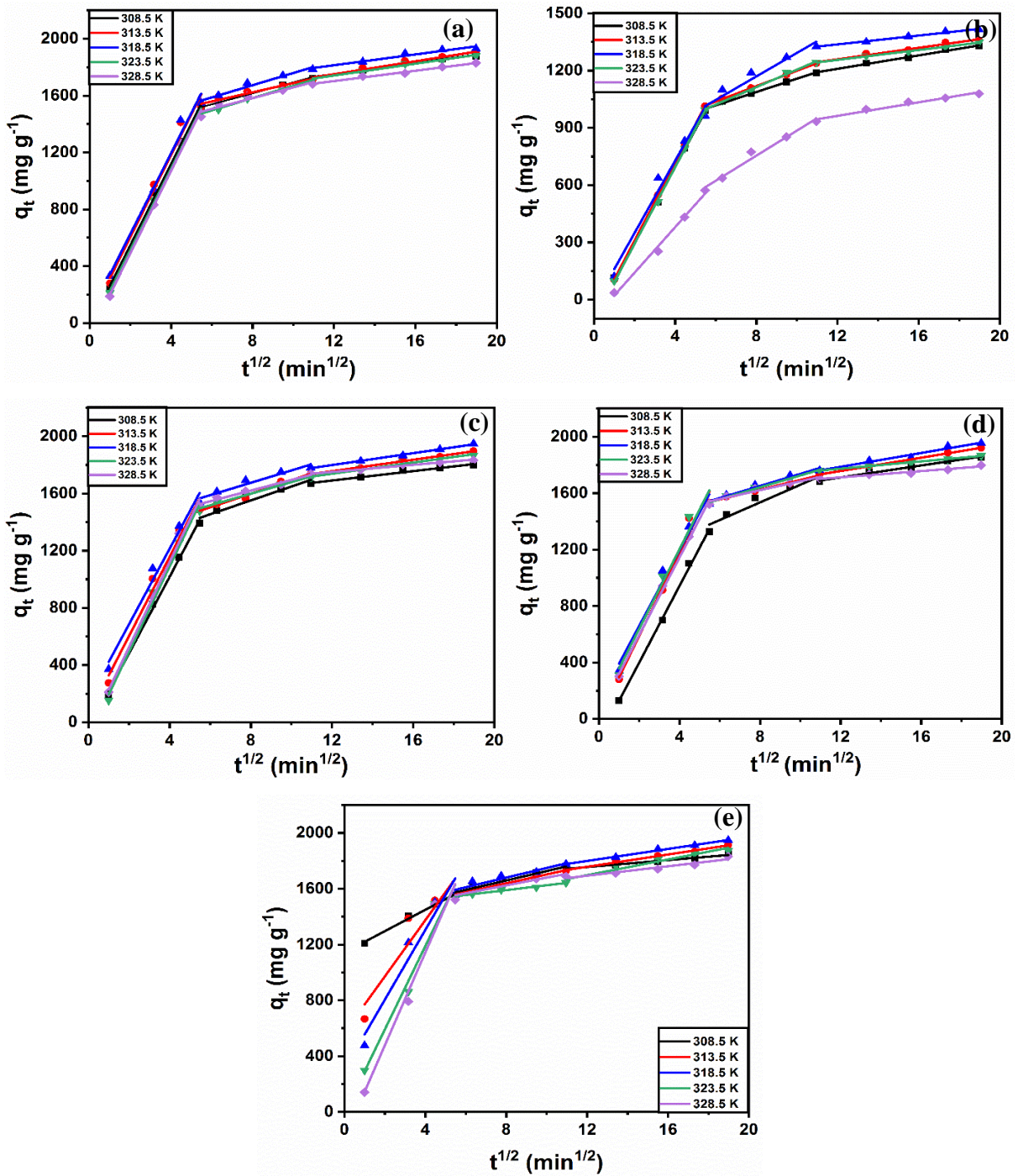


Figure 7.32. Intraparticle diffusion values for the pollutants: a) MB, b) RB, c) CR, d) Pb(II) & e) Cd(II)

Table 7.7: Intraparticle diffusion values for the pollutant adsorption on the GO-Fe/CPTMS-SiO<sub>2</sub>@MF

Intraparticle diffusion						
Pollutants	Temp (K)	K <sub>p</sub>	x <sub>i</sub>	q <sub>e</sub>	R <sub>i</sub>	R <sup>2</sup>
		mmol g <sup>-1</sup> min <sup>-1/2</sup>	(mmol g <sup>-1</sup> )	(mmol g <sup>-1</sup> )		
MB	308.5	114.52353	932.79118	1916.6	0.51331	0.98553
	313.5	114.35163	957.90741	1927.15	0.50294	0.96474
	318.5	115.31734	991.41498	1972.1	0.49727	0.97084
	323.5	116.76319	890.12852	1922.05	0.53688	0.99356
	328.5	115.33868	891.22024	1862.7	0.52154	0.96768
RB	308.5	82.93948	571.93661	1367.85	0.58187	0.99464
	313.5	86.19836	592.35737	1404.3	0.57818	0.99169
	318.5	87.50574	615.06728	1464.8	0.5801	0.96552
	323.5	86.42734	579.79586	1392.75	0.5837	0.99694
	328.5	67.56767	293.59039	1177.3	0.75062	0.97979
CR	308.5	110.90607	868.12248	1842.75	0.52889	0.95997
	313.5	114.64009	928.61521	1925.75	0.51779	0.98318
	318.5	109.34371	1012.44105	1965.8	0.48497	0.97335
	323.5	119.68454	890.65627	1912.05	0.53418	0.98158
	328.5	115.77015	951.84159	1872.9	0.49178	0.98257
Pb	308.5	118.3897	782.89283	1916.65	0.59153	0.96602
	313.5	117.30586	940.89091	1945.6	0.5164	0.99119
	318.5	111.83402	974.92899	1979.15	0.5074	0.9726
	323.5	112.28968	999.73672	1892.05	0.47161	0.98708
	328.5	105.76064	997.75718	1817.75	0.4511	0.96986
Cd	308.5	40.90706	1380.22725	1852.75	0.25503	0.97491
	313.5	85.12388	1149.27373	1915.9	0.40014	0.95048
	318.5	102.03077	1083.92842	1961.45	0.44738	0.94543
	323.5	114.71777	935.89373	1902.75	0.50813	0.96213

### 7.3.19 Activation energy of adsorption

The graphs plotted between  $\ln k_2$  vs  $1/T$  taken for examining the data of rate constants of pseudo second order ( $k_2$ ) at five distant temperatures given in figure 7.33. From the Arrhenius plot, the dyes and metal ions (MB, RB, CR, Pb(II) & Cd(II)) having activation energy ( $E_a$ ) data was found to be 30.87 KJ mol<sup>-1</sup>, 35.69 KJ mol<sup>-1</sup>, 37.83 KJ mol<sup>-1</sup>, 42.26 KJ mol<sup>-1</sup> and 26.31 KJ mol<sup>-1</sup>. The relatively smaller  $E_a$  values were favorable for the easy adsorption of pollutants.

$$\ln k_2 = -\frac{E_a}{2.303RT} + \text{constant} \quad (7.21)$$

Figure 7.33 indicated the  $q_e$  i.e., adsorption capacity for all the pollutants enhances with an increment in pollutant concentration. The shift explained that it can effectively remove pollutants from water. Therefore, GO-Fe/CPTMS-SiO<sub>2</sub>@MF was employed for the elimination of dyes and heavy metal ions from the waste effluents. The nanocomposite proved to have highest removal efficacy (97%) for the pollutants in synthetic effluents favored its advantage and a way to use in industrial wastewater treatment.

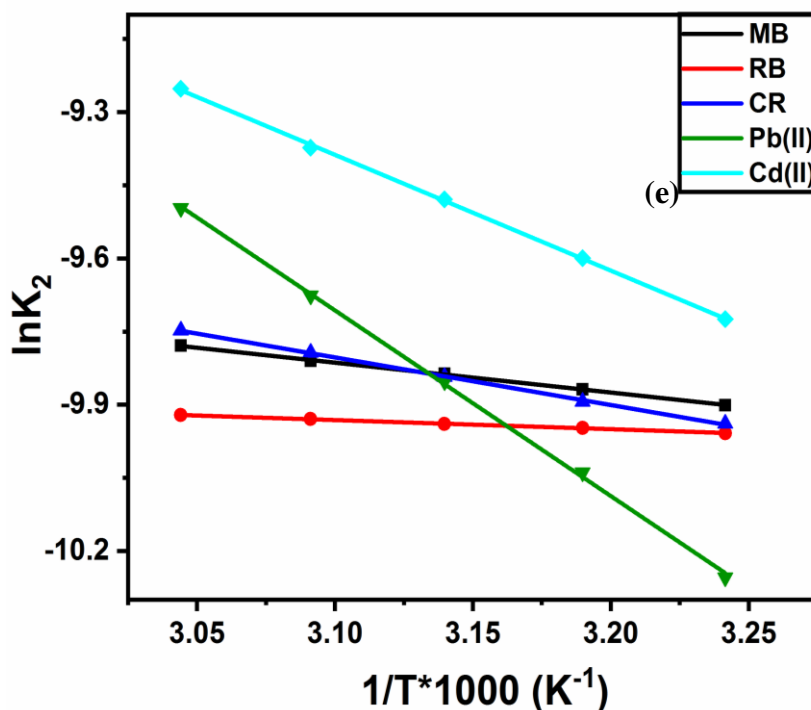


Figure 7.33. Activation energy of the pollutants adsorbed on composite: a) MB, b) RB, c) CR, d) Pb(II) & e) Cd(II)

### 7.3.20 Stability and reusability of adsorbent

The stability and reusability of GO-Fe/CPTMS-SiO<sub>2</sub>@MF is a crucial index for real life application. GO-Fe/CPTMS-SiO<sub>2</sub>@MF stability has been determined for the calibration of amount of Fe leached in solution at various pH range 0-10 in figure 7.34. Fe leaching is prevented in nanocomposite compared to plane Fe<sub>3</sub>O<sub>4</sub> nanoparticle at highly acidic solution (i.e., pH=0) because of the silylation process using SiO<sub>2</sub> and CPTMS during the nanocomposite synthesis. The Fe loss is negligibly detected in case of adsorbent for a given range of pH, which demonstrated that the adsorbent possesses outstanding stability.

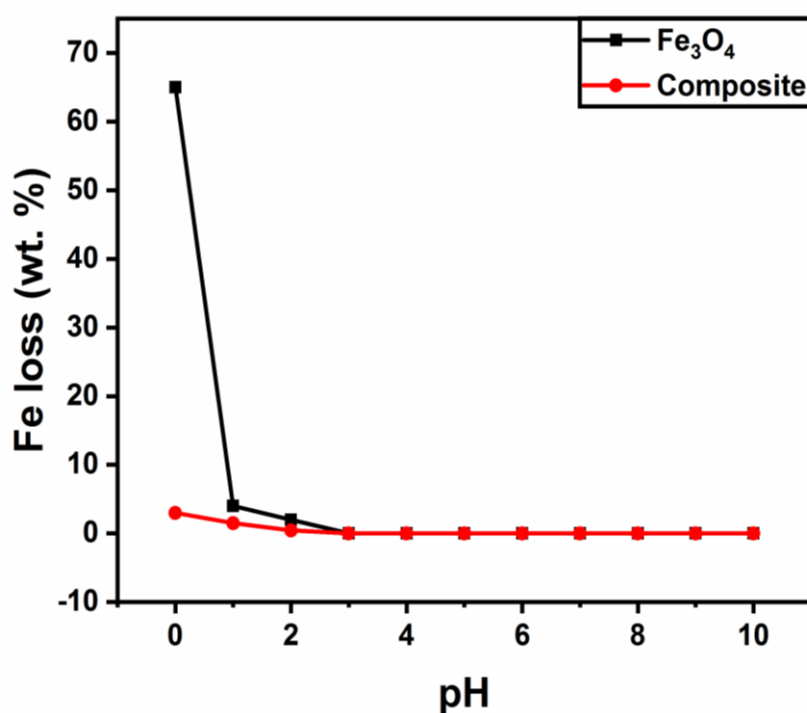


Figure 7.34. Stability of Fe's leaching on Fe<sub>3</sub>O<sub>4</sub> and GO-Fe/CPTMS-SiO<sub>2</sub>@MF Composite

After the dyes and heavy metals ions got adsorbed, saturated GO-Fe/CPTMS-SiO<sub>2</sub>@MF was recovered using various desorbing agents with their equivalent desorption values given in table 7.9a & 7.9b. In case of dyes, the desorption capacity enhanced with the rise in HCl concentration. Further, the maximum value was obtained with 1.0 M HCl concentration. In case of heavy metal ions, the desorption capacity monitored using both HCl and EDTA solutions separately. In case of HCl concentration, the desorption rate is lower i.e., 91% with 1.0 M HCl concentration. In case of EDTA, the desorption rates were 92% with 0.01 mol L<sup>-1</sup> EDTA regeneration due to the existence of few EDTA molecules in the mesoporous adsorbent even after desorption process. Due to the good desorption performance towards all the pollutants were satisfactory, when the HCl concentration 1.0 M utilized in the 1<sup>st</sup> cycle adsorption-desorption test, and it was similar for the selective desorption agent in the

corresponding six cycles. As shown in figure 7.35, a slight decline in regeneration rate is observed, but it is still higher than 90% for all the pollutants after five adsorption-desorption cycles. This was justified using the regeneration process showed no effect on the structural and functional(chemical) properties of GO-Fe/CPTMS-SiO<sub>2</sub>@MF composite. Figure 7.36 represented the desorption studies of various pollutants with 1.0 M HCl solution as eluent and it proved that the desorption rate gradually decreased due to the consecutive cycles which is effective for CR and Pb(II) when compared to MB, RB & Cd(II) pollutants. Figure 7.37 gave the adsorption capacity of the recycled studies up to 5 cycles with the desorption rate.

Table 7.8a: Percentage desorption efficiency of dyes over adsorbent using different HCl concentrations

Eluents	% desorption efficiency of dyes		
	MB	RB	CR
1.0 M HCl	89.24	83.63	91.72
0.1 M HCl	61.56	51.61	46.82
0.01 M HCl	34.65	21.72	10.67

Table 7.8b: Percentage desorption efficiency of metal ions over adsorbent using different eluents

Eluents	% desorption efficiency of heavy metal ions	
	Pb(II)	Cd(II)
1.0 M HCl	91.95	91.47
0.01 M EDTA	92.88	92.24
0.005 M EDTA	43.67	42.36

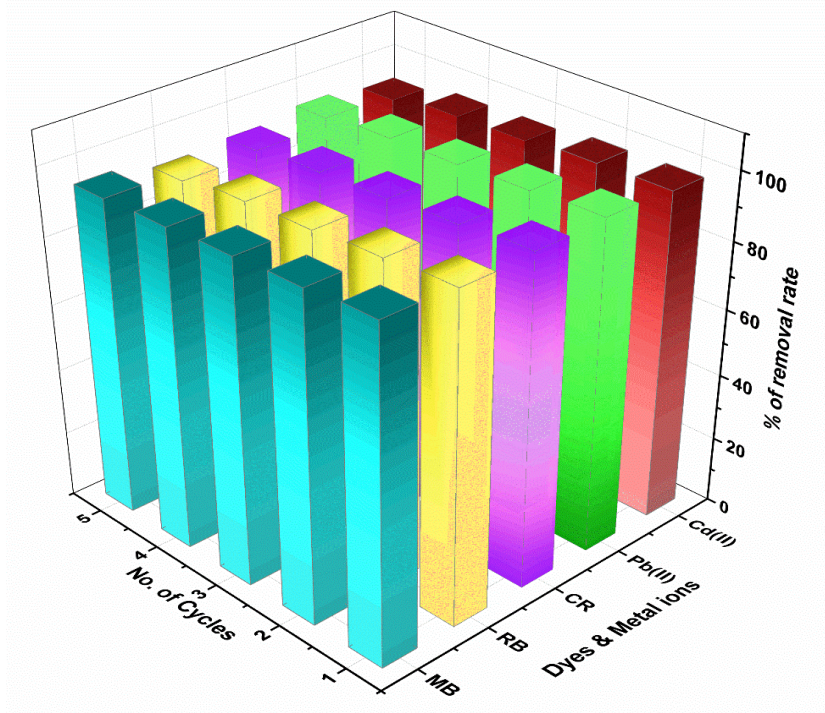


Figure. 7.35. Recyclability studies of synthetic wastewater with GO-Fe/CPTMS-SiO<sub>2</sub>@MF  
 The equation 7.22 is used for calculating the desorption studies given below:

$$\% \text{ Desorption efficiency} = \frac{100 \times C_D V_D}{q_e m_D} \quad (7.22)$$

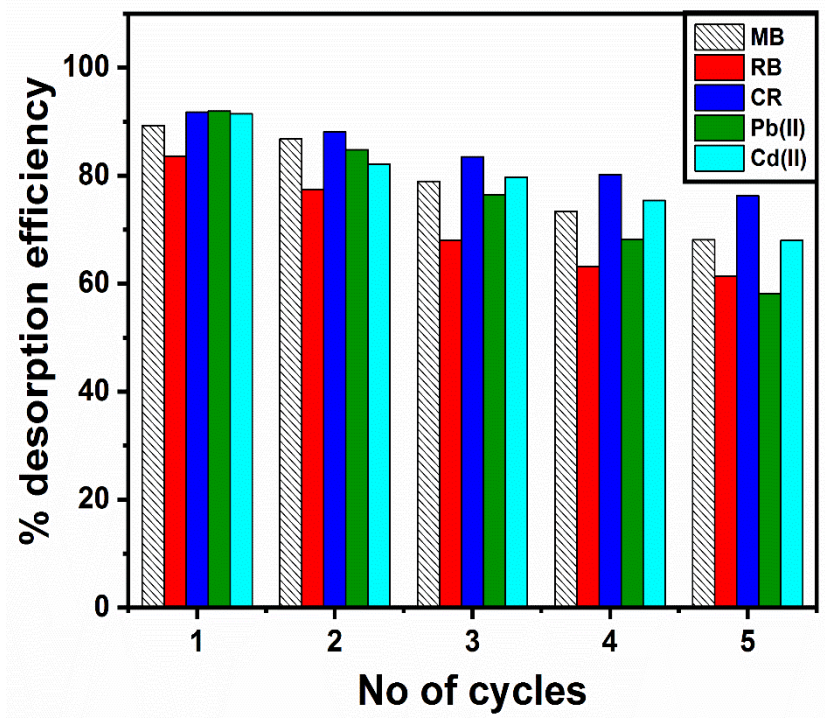


Figure. 7.36. Desorption studies of synthetic wastewater with GO-Fe/CPTMS-SiO<sub>2</sub>@MF

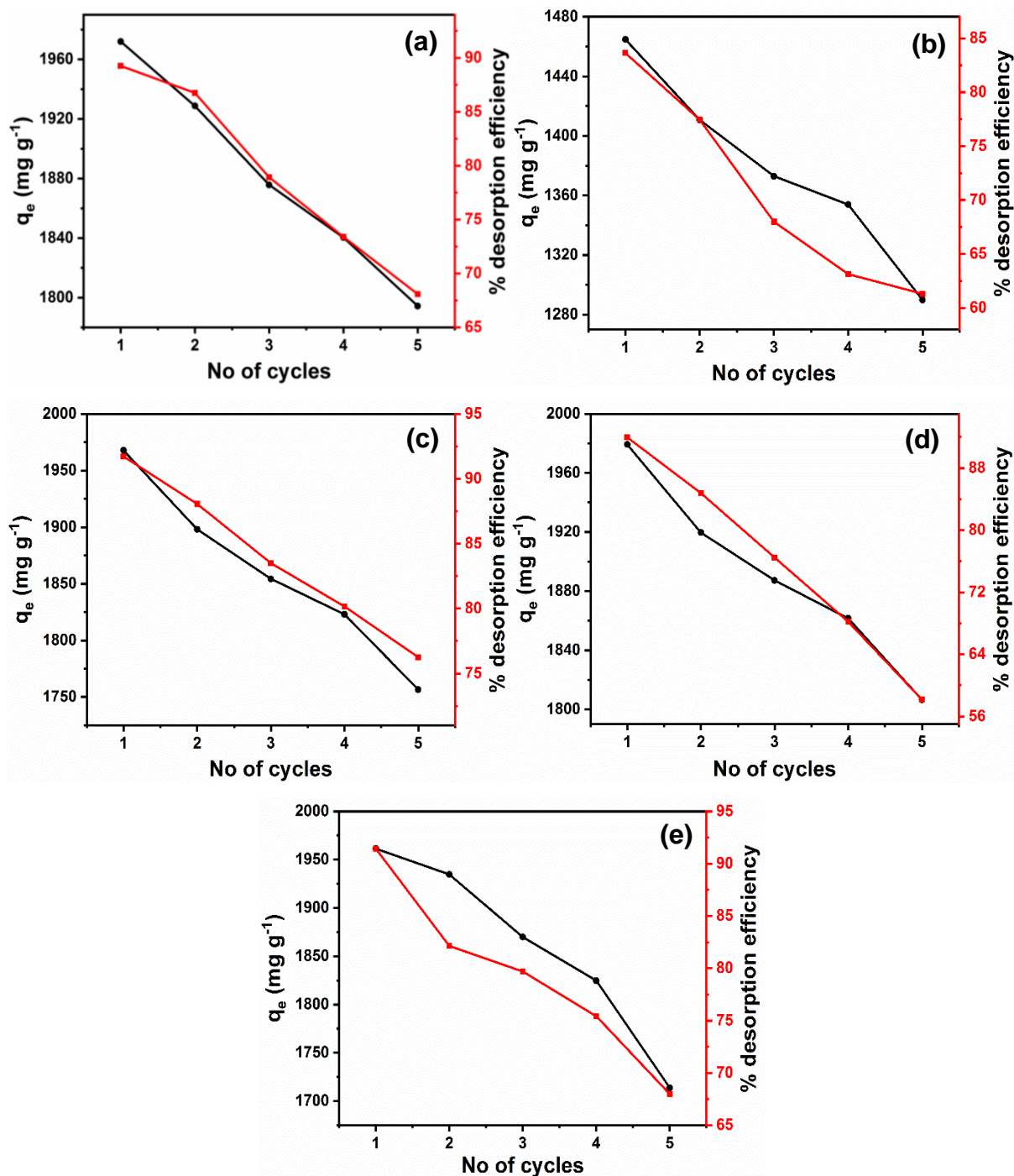


Figure. 7.37. Desorption studies of synthetic wastewater with adsorption capacity  $q_e$  of regeneration cycles: a) MB, b) RB, c) CR, d) Pb(II) & e) Cd(II)

### 7.3.21 Recycled graphs

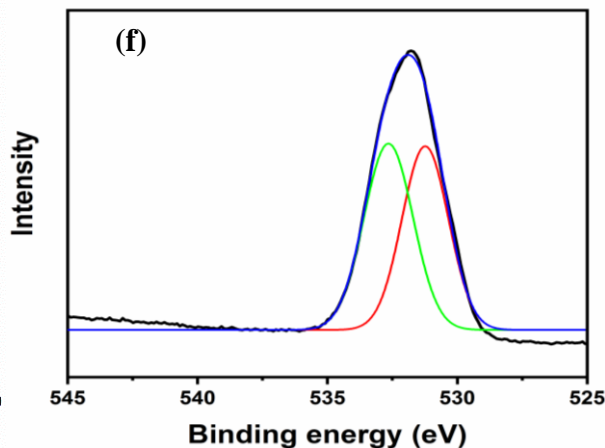
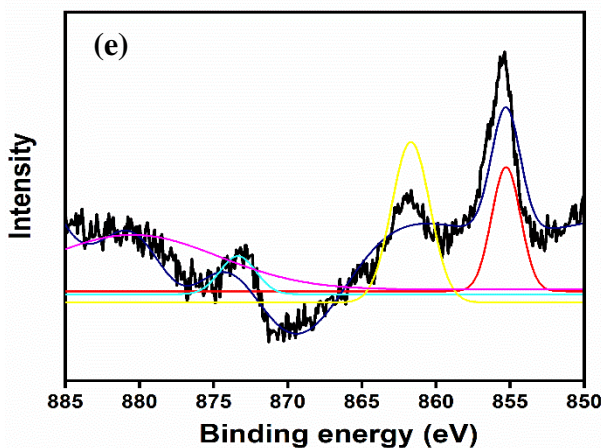
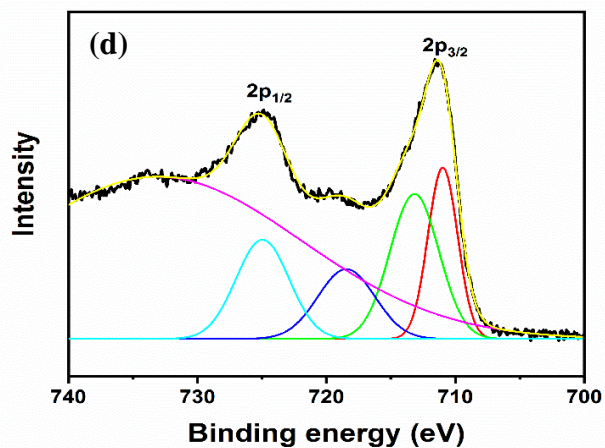
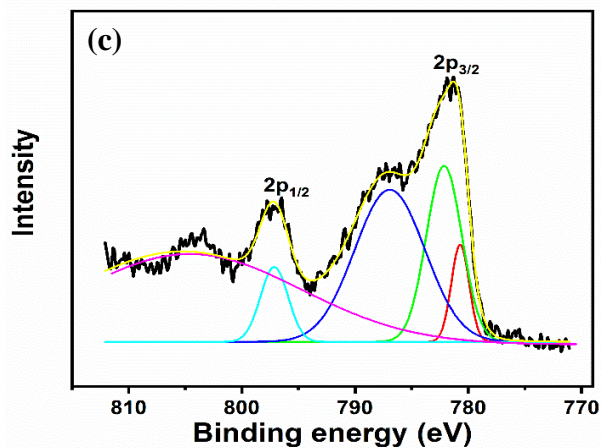
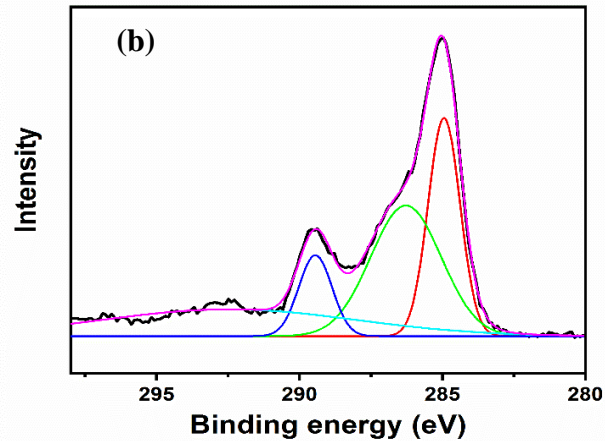
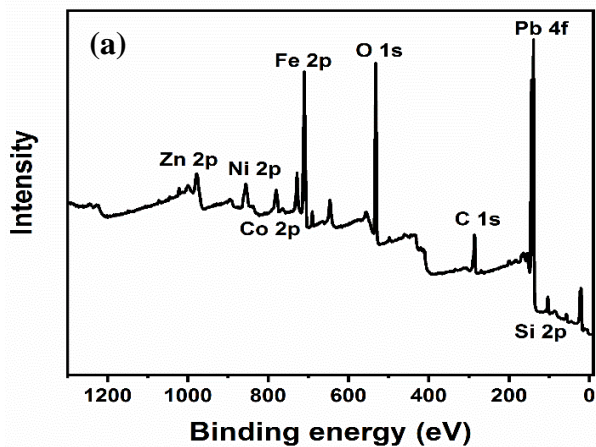
The high adsorption capacity for the adsorbates onto the nanocomposite can be explained; Fe<sub>3</sub>O<sub>4</sub> nanoparticles and MF nanoparticles grafted onto the GO nanosheets by silylation to form nano structural composites which not only provide rich functional groups as binding agents



with the pollutants but also possesses high surface area in order to increase the effective usage of functional moieties.

To further analyse Pb 2p adsorption mechanism, XPS studies were analyzed before and after adsorption are performed. Figures 7.15 & 7.38 showed the XPS Spectra before and after Pb(II) adsorption. It has been observed that the strong peaks at 143.5 eV and 136.8 eV which were ascribed to Pb 4f<sub>5/2</sub> and Pb 4f<sub>7/2</sub> respectively (Alqadami et al. 2020). It indicated that the Pb 2p is efficiently adsorbed on the adsorbent surface. The O 1s spectra after Pb(II) adsorption shifted to lower binding energy after Pb(II) uptake. In the C 1s spectra, except the C-C bond, shifting of carbon- related groups was investigated towards higher binding energy values after Pb 2p as well as Cd 3d adsorption. Meanwhile, Zn 2p spectra has been reduced to a lower binding energy after Pb 2p adsorption and in case of Co 2p and Ni 2p has been shifted to a higher binding energy. No changes observed in Fe 2p XPS spectra after Pb 2p and Cd 3d adsorption. It has been observed the Co 2p/ Ni-O groups have a strong tendency towards Pb 2p compared to the Fe-O group (Wu et al. 2019). Figure 7.39 which shows the binding energy values of Cd 3d<sub>5/2</sub> and Cd 3d<sub>3/2</sub> are at 405.5 eV as well as 412.25 eV which are attributed to the Cd(II) uptake happened on adsorbent after adsorption process (Chen et al. 2017; WANG et al. 2009). In case of Cd 3d adsorption, there is only 0.1 eV increase in binding energy values in case Co 2p spectra and there is a drastic shift in Ni 2p spectra towards higher values. The O 1s spectra in the Cd 3d adsorption has been shifted towards higher value, which indicated that the lead has been confirmed to get adsorbed more on its nanocomposite. Figure 7.41 represented the FTIR Spectra of nanocomposite and Pb(II) & Cd(II) adsorption. A peak around 3420 cm<sup>-1</sup> indicated ad O-H group is moved to lower frequency 3406 cm<sup>-1</sup> might have interacted with Pb 4f and Cd 3d which is due to the interaction of adsorbate with the nanocomposite surface (Hu et al. 2016; Yang et al. 2020). Besides this, the peak at C=O and C-O-C around 1630 and 1120 cm<sup>-1</sup> shifted to lower frequency 1620 and 1040 cm<sup>-1</sup> in case of Pb(II) adsorption and 1595 cm<sup>-1</sup> and 1025 cm<sup>-1</sup> for Cd(II) adsorption respectively (Liu et al. 2020; Maziarz et al. 2019). The characteristic peak at 566 cm<sup>-1</sup> indicated the Fe-O remains unaffected before and after adsorption process and it is in equable with the XPS analysis. After the CR adsorption shown in figure 7.40, the new peaks at 1086 cm<sup>-1</sup> which originated due to the stretching mode of S=O in sulfonate groups (-SO<sub>3</sub><sup>-</sup>) (Wang et al. 2020; Zheng et al. 2019). The two peaks which appeared at 1540 cm<sup>-1</sup> and 1605 cm<sup>-1</sup> confirmed to be N=N stretching vibration and aromatic skeletal vibration proved the adsorption of CR (Deng et al. 2018; Zhao et al. 2016). The stretching band of hydroxyl around 3420 cm<sup>-1</sup> reduced to 3406 cm<sup>-1</sup> is because of the interaction of hydroxyl group with anionic CR dye and as well as the effect of N=N stretching vibrations

in the adsorbate molecules. Removal of MB dye is improved with the increment in pH of the solution given in figure 7.40. The electrostatic repulsions between the positively charged adsorbent and the MB<sup>+</sup> species go weakened the adsorption capacity in pH lower than 2.4 (Pereira et al. 2003; Tang et al. 2007). However, as the pH increased, the adsorption efficiency improved and at a very low pH around 2, the adsorption efficiency is around 35%. These interactions are due to the wide availability of aromatic rings and  $\pi$ - $\pi$  interactions between the MB molecules and adsorbent (Ai et al. 2011; Hu et al. 2016). The peak around 1660 cm<sup>-1</sup> is shifted lower to 1620 cm<sup>-1</sup> after adsorption due to  $\pi$ - $\pi$  stacking interactions (Arasteh et al. 2010; Bradder et al. 2011). With the increase in pH, the electrostatic interactions between the negatively charged adsorbent and the cationic MB molecules which increased the adsorption capacity of MB (Xiong et al. 2010). The peak attributed to the -OH groups with 3420 cm<sup>-1</sup> shifted to lower frequency 3404 cm<sup>-1</sup> which explained the interaction between the dissociated hydroxyls group and MB<sup>+</sup> molecules (Kyzas et al. 2015). The adsorption of RhB dye onto adsorbent is observed due to the existence of novel peaks around 1586 cm<sup>-1</sup> and 1211 cm<sup>-1</sup> which confirmed RhB dye uptake on nanocomposite shown in figure 7.40 (Chouket et al. 2007; Zhang et al. 2011). Here the mechanism of adsorption through OH groups which shifted from 3420 cm<sup>-1</sup> to 3401 cm<sup>-1</sup> and the C=O group which shifted from 1620 cm<sup>-1</sup> to 1609 cm<sup>-1</sup> confirmed the mode of adsorption through electrostatic interactions (Hontoria-Lucas et al. 1995; Szabó et al. 2005).



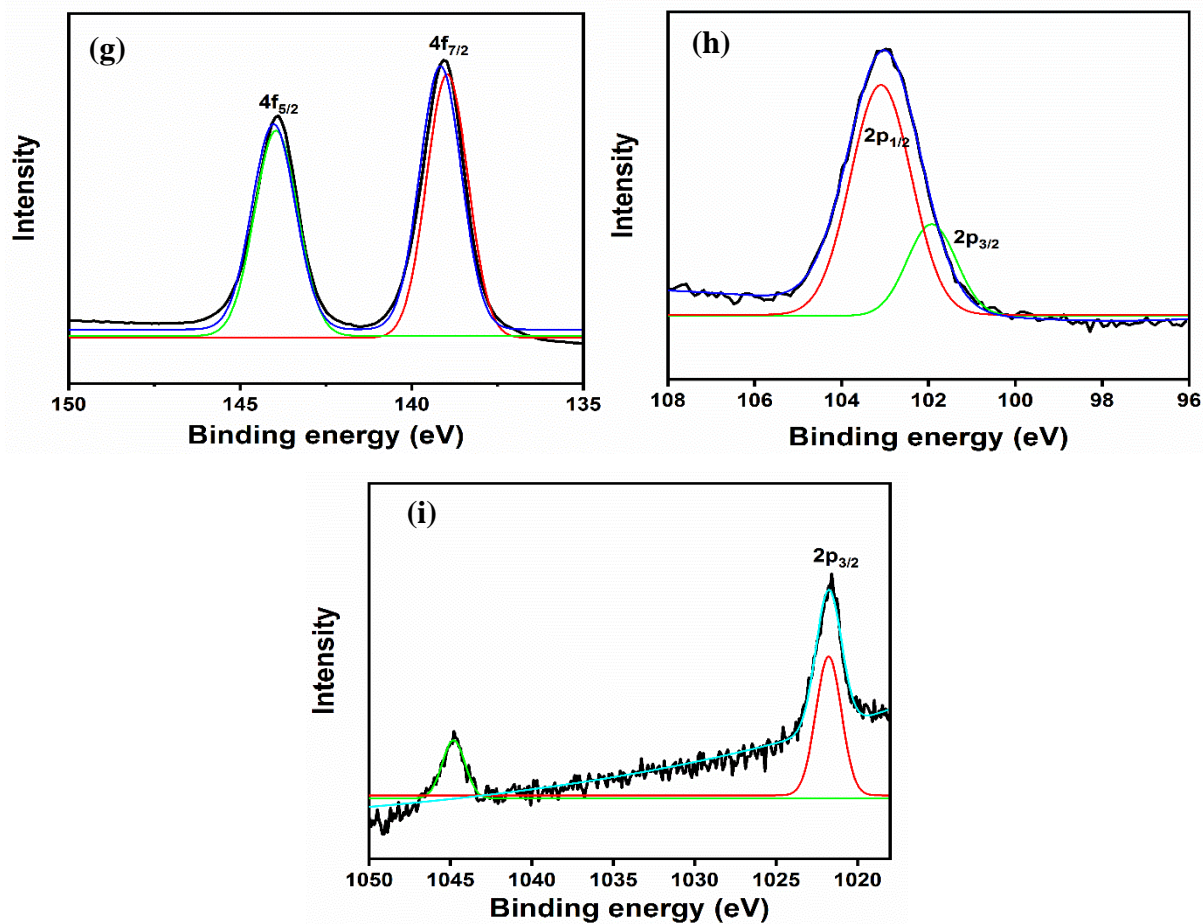
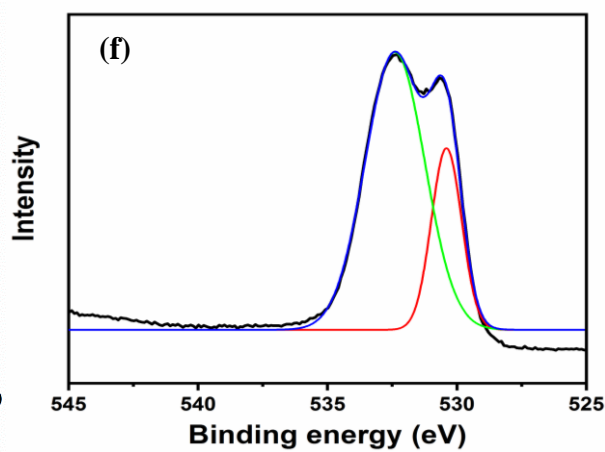
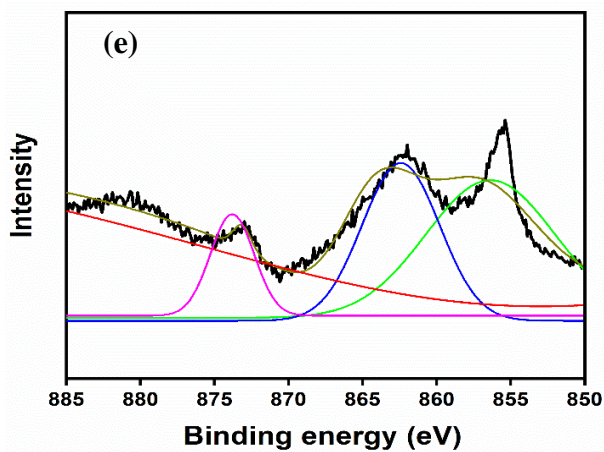
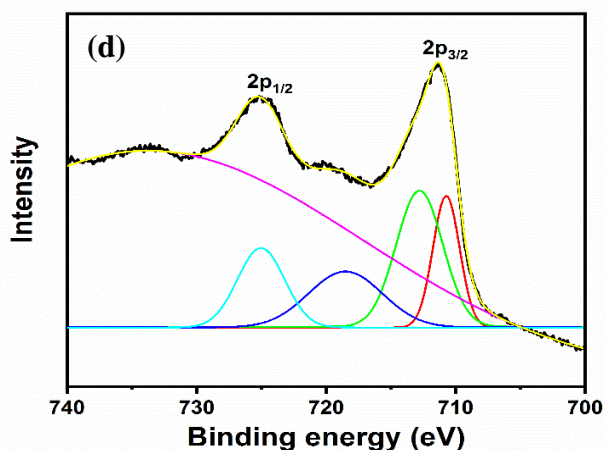
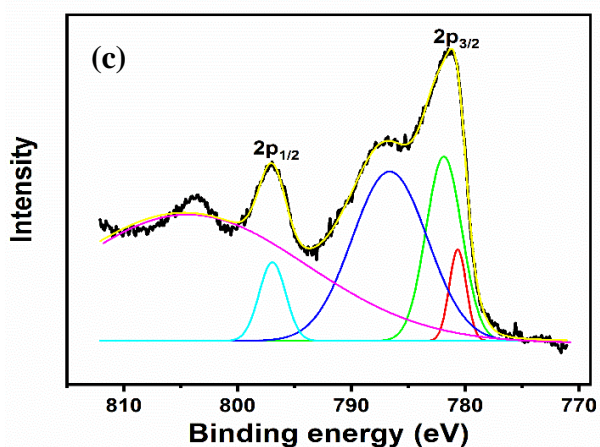
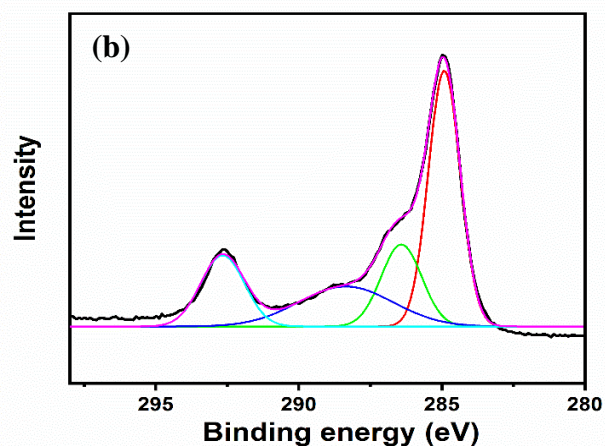
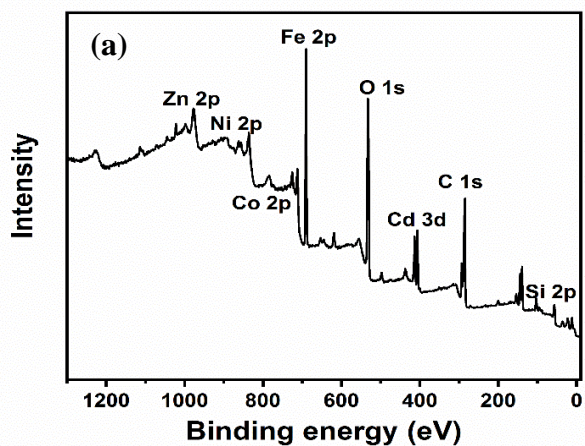


Figure 7.38. XPS Spectrum of Pb(II) adsorbed composite: a) Elemental survey, b) C 1s, c) Co 2p, d) Fe 2p, e) Ni 2p, f) O 1s g) Pb 4f, h) Si 2p & i) Zn 2p



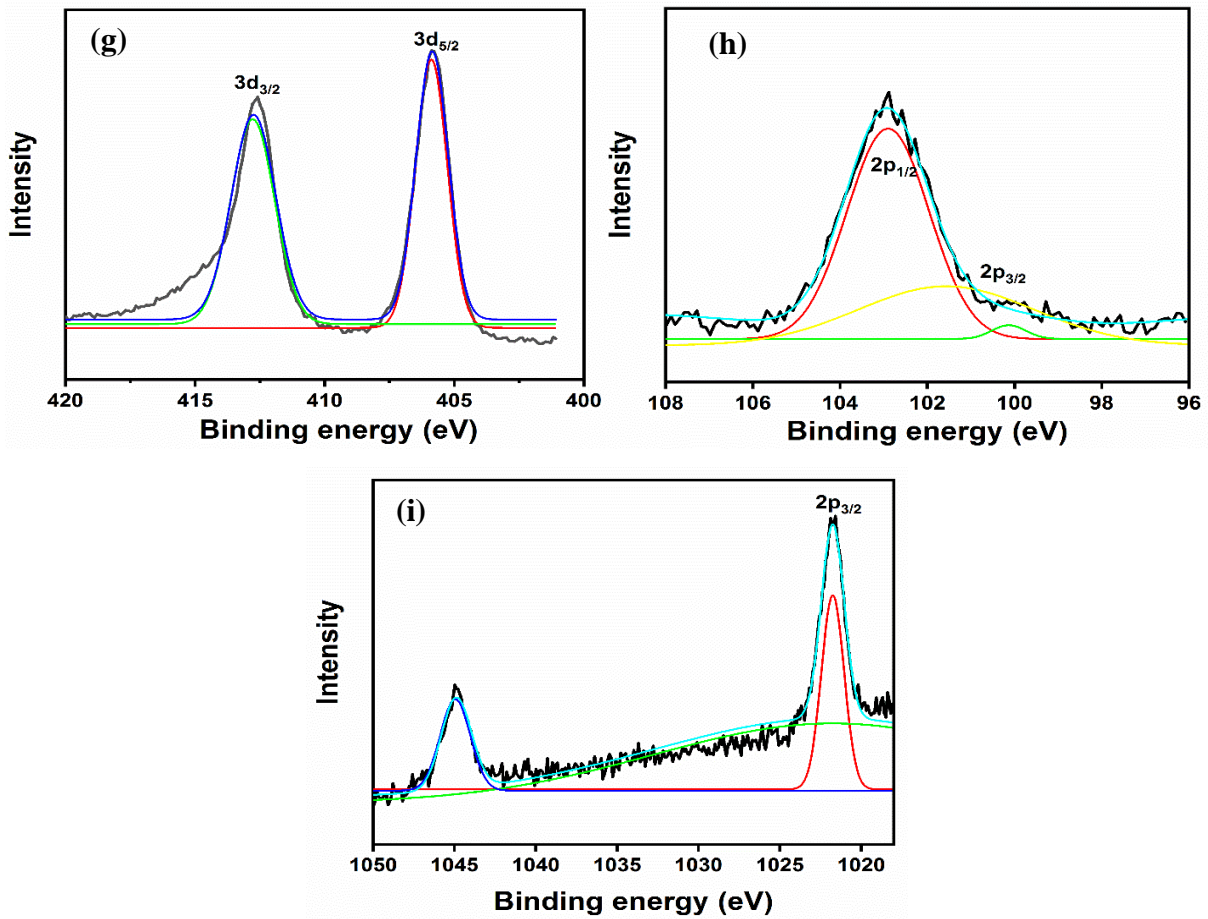


Figure 7.39. XPS Spectrum of Cd(II) adsorbed composite: a) Elemental Survey, b) C 1s, c) Co 2p, d) Fe 2p, e) Ni 2p, f) O 1s, g) Cd 3d, h) Si 2p & i) Zn 2p

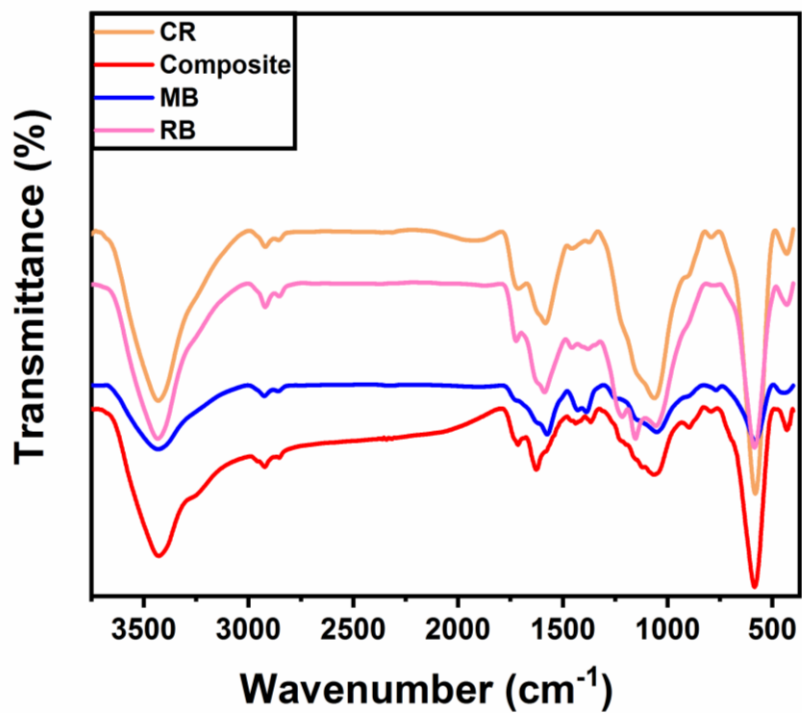


Figure 7.40. FTIR Spectra of Composite & dye adsorbed composite: MB, RB & CR

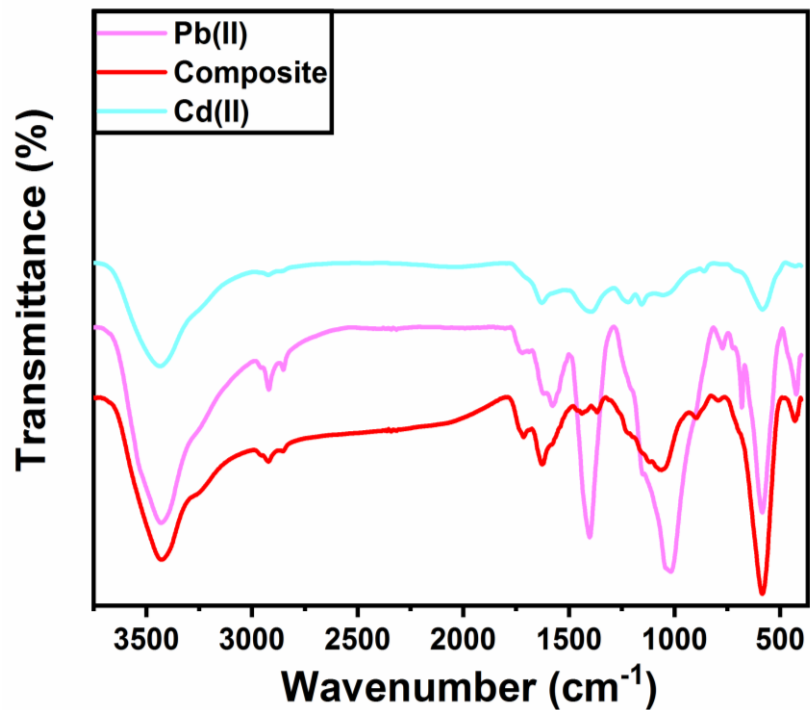
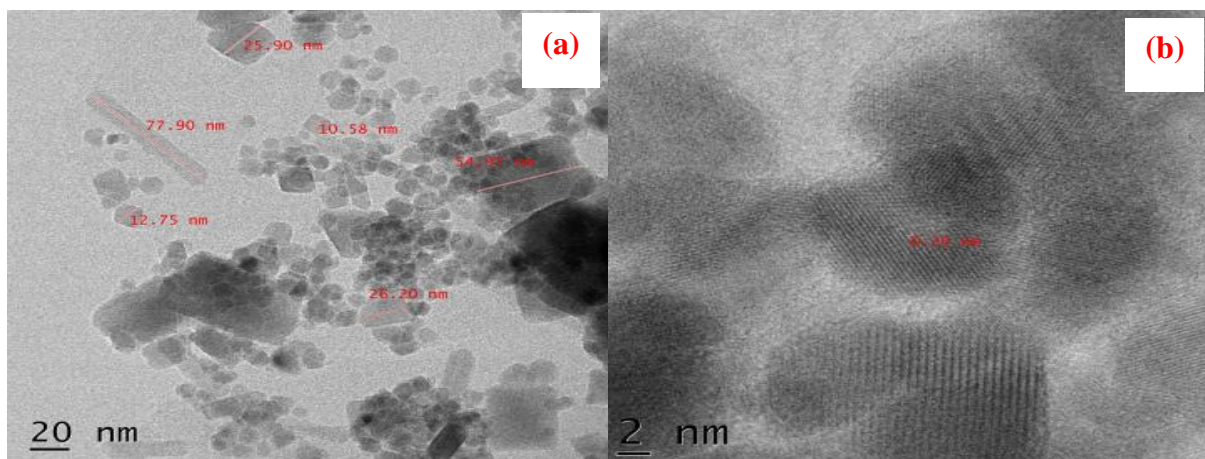
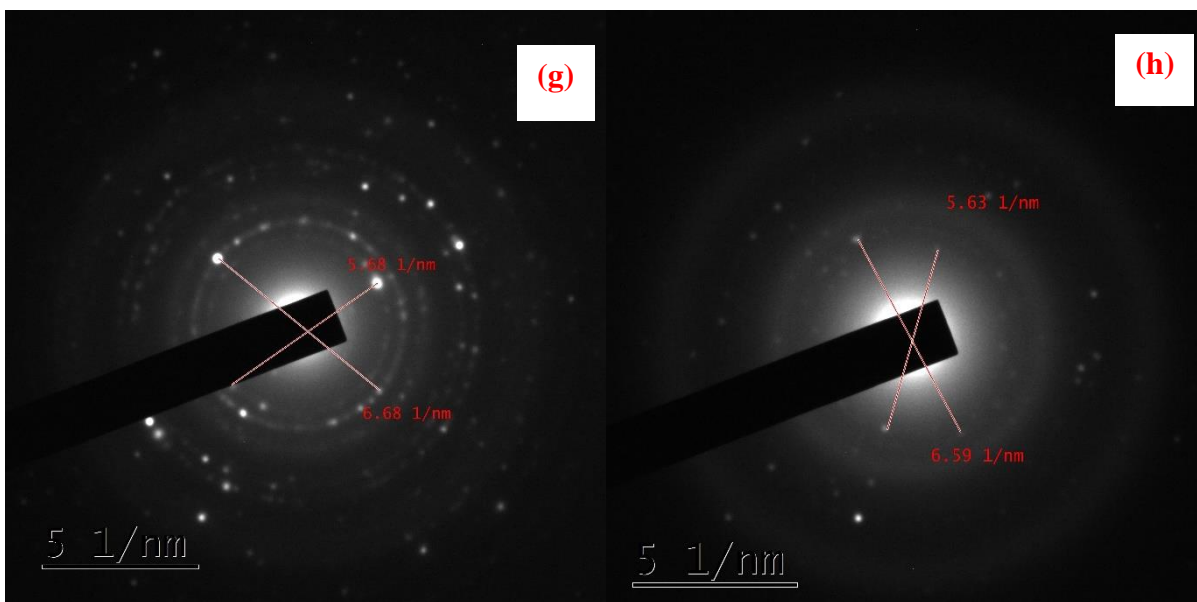
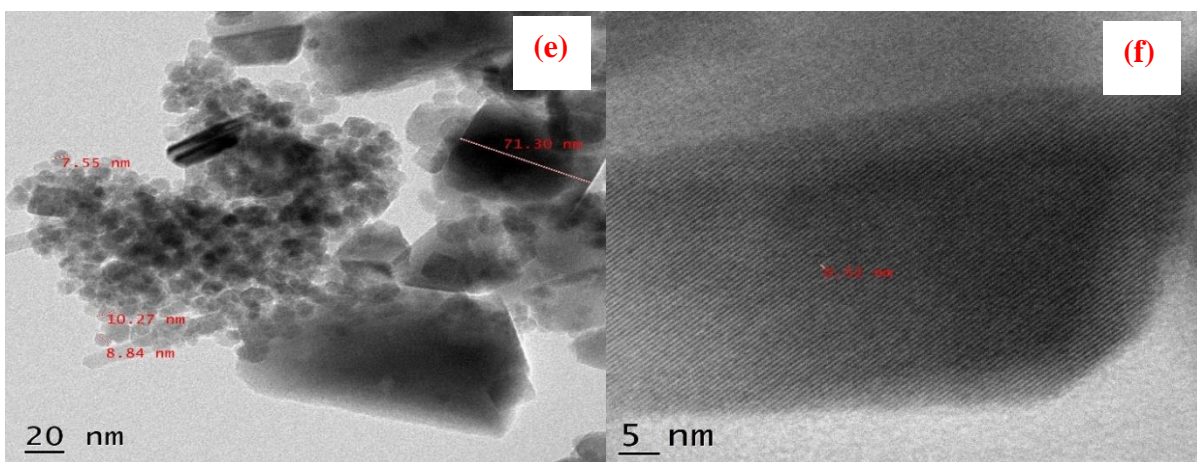
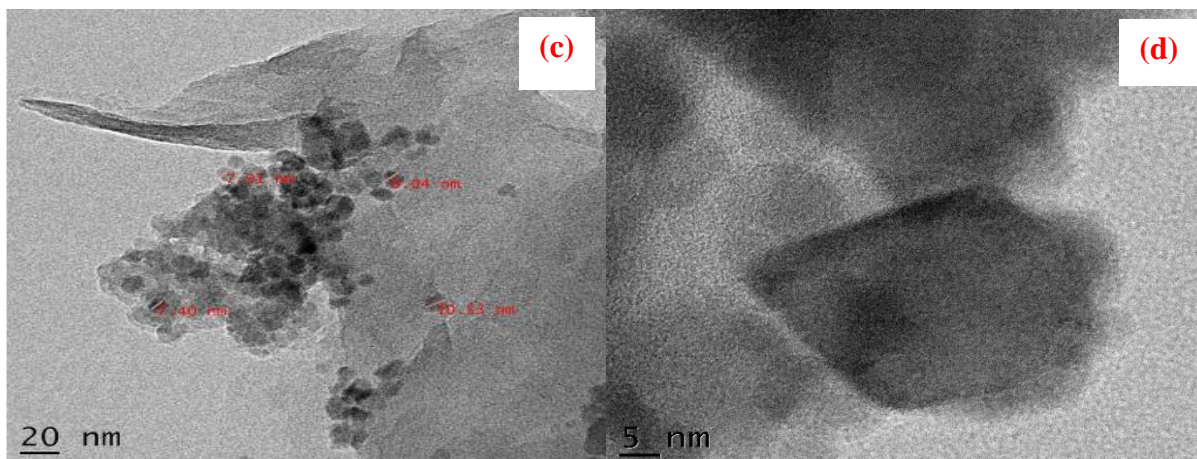


Figure 7.41. FTIR Spectra of Composite & metal adsorbed composite: Pb(II) & Cd(II)

The TEM images after the adsorption of cationic and anionic dyes confirmed the adsorption phenomena taken place on nanocomposite. The size of the nanocomposite varied in HR-TEM images before and after adsorption are given in figure 7.42(a-i). The SAED pattern also justified the loss of crystallinity after the adsorption of dyes due to repeated cycles.







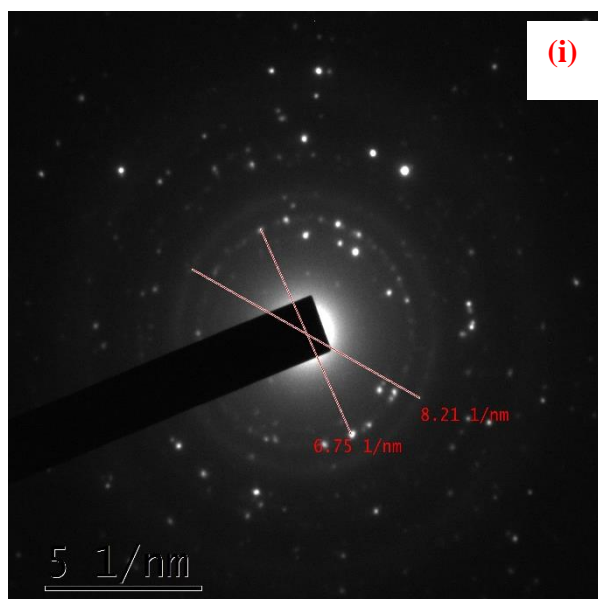


Figure 7.42. TEM images of dye adsorbed composite: a,b) MB, g) SAED pattern of MB d,e) RB, h) SAED pattern of RB & g,h) CR & i) SAED pattern of CR

### 7.3.22 Proposed mechanism for adsorption

Among the various adsorbents, magnetic spinel ferrites gained interest and attained a first choice for water treatment due to their nano-sized, superparamagnetic property and a huge surface to volume ratio. Graphene based nanocomposites effective for the fast contact and adsorption period, which helps in removal of pollutants from the wastewater. The difference in adsorption capacity of all pollutants were dependent on the type of ionic species, surface functional groups and the surface properties of the nanocomposites affected by the solution pH values. At higher pH value, the adsorption capacity of all pollutants reduced with the increasing pH due to the electrostatic interactions between the negatively charged surface of nanocomposite and the pollutants. In the model applications of nanocomposite for the heavy metal ions adsorption, the pH of the solution played a key role which is strongly dependent on the removal efficiency.

The influence of impurities in pollutants which affected their removal efficiency on GO-Fe/CPTMS-SiO<sub>2</sub>@MF shown in figure 7.43 is explained by (i) the strong affinity between the ionic species and the nanocomposite affected the binding nature of pollutant on to the solid support further it lead to the competitive ability of impurity in pollutants on the surface active sites on GO-Fe/CPTMS-SiO<sub>2</sub>@MF and the reduction in adsorption capacity (ii) the concentration of impurity significantly affected the electrostatic interactions, further having an impact on particle aggregation (iii) the presence of other pollutants showed the change in

activity coefficients of the dyes and metals ions in the wastewater, thereby limiting the transfer of dyes and metal ions onto the adsorbent surface. Generally, if the adsorption phenomena is affected by ionic strength strongly and the pH effect weakly, then the adsorption is controlled by outer-sphere surface complexation. If it is affected by pH strongly and very less ionic strength, then it is governed by inner-sphere surface interactions. Therefore, if the adsorption is strongly affected only by ionic strength irrespective of the solution pH, then the total concentration of different pollutants and ions in wastewater need to be considered for the real applications. The other way is to adjust the pH of wastewater and it is not required to consider other pollutants in real applications.

In order to understand the interactive mechanism between GO-Fe/CPTMS-SiO<sub>2</sub>@MF and dyes and heavy metal ions, the effective removal of pollutants is substantiated using the ion-exchange, surface complexion and precipitation which takes a major part in determining the removal process at the solid-liquid interfaces. The batch experiments and surface chemical analysis by using FTIR, XPS & TEM techniques which can determine the physicochemical interactions between the adsorbent-adsorbate played a prominent role in knowing the adsorption phenomena. Mostly it is predominated using the H<sub>2</sub> bonding,  $\pi$ - $\pi$  interactions, surface complexion, electrostatic interactions, ion exchange along with the chemisorption process. But in case of spinel GO composites, the presence of vast number of hydroxyl groups on its surface as well as surface charge play a pivotal role in the adsorption of different cationic and anionic pollutants. For the metal ion (M-OH, Fe-OH) interstices, the hydroxyl groups which are available on its surface could show the variations in the adsorption capacity for different pollutants. Due to the variation in pH of the solution for both cationic and anionic pollutants, the charge on the adsorbent may vary from a positively charged at lower pH to a negatively charged at higher pH.

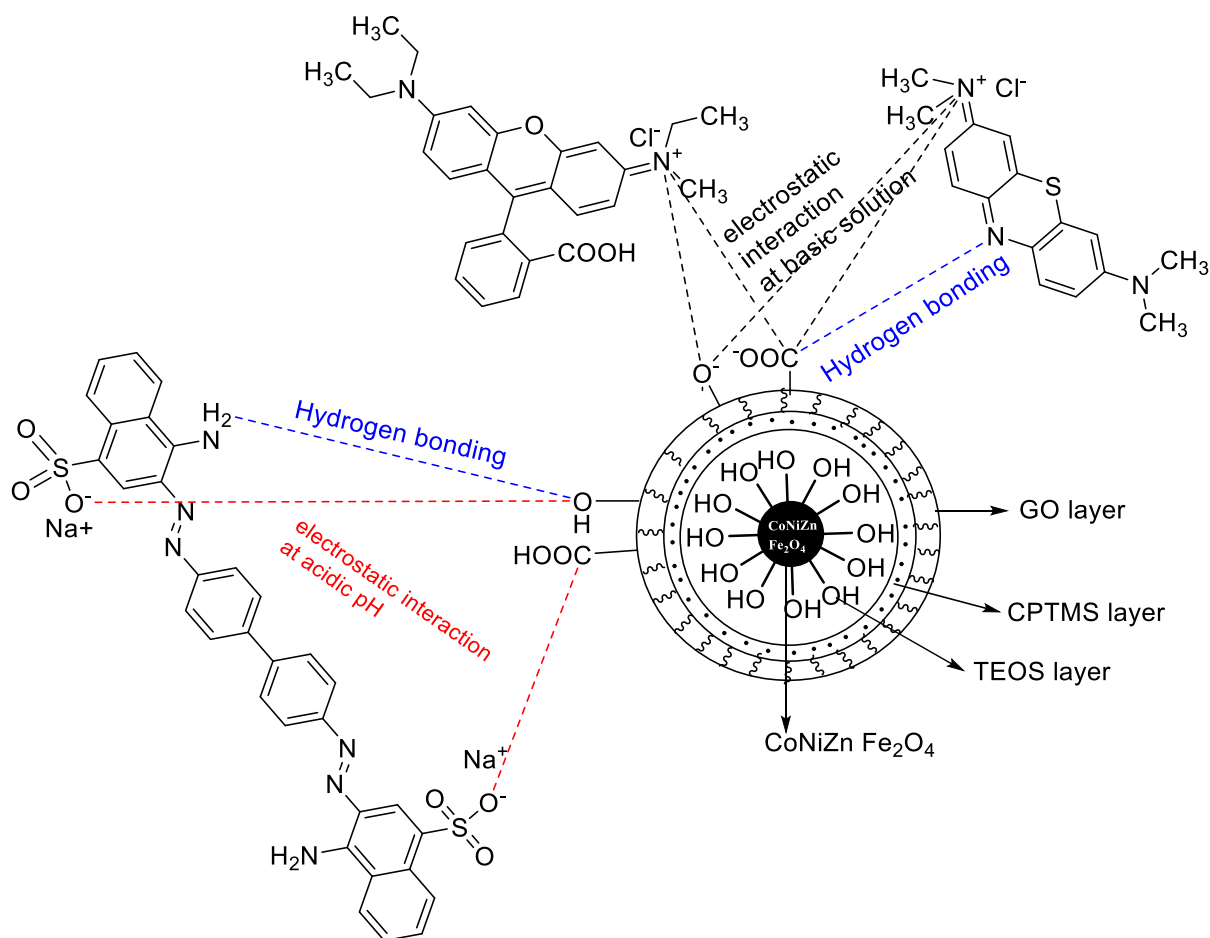


Figure 7.43. Proposed mechanism for the dyes MB, RB & CR.

### 7.3.23 Adsorption and recycling performances of GO-Fe/CPTMS-SiO<sub>2</sub>@MF in model waste water

To appraise the prospective for the GO-Fe/CPTMS-SiO<sub>2</sub>@MF in real life application, the performance and the number of cycles regenerated with the adsorbates MB, RB, CR, Pb(II) & Cd(II) are analyzed in model wastewater given in figure 7.44. For the nanocomposite, the removal rate of pollutants around 20 mg L<sup>-1</sup> in this wastewater were 96.67(MB), 93.45(RB), 95.8(CR), 97.4(Pb(II)) & 96.7(Cd(II)) respectively. The data obtained through adsorption phenomena were almost nearby to the synthetic wastewater removal rate (as mentioned in figure 7.35) further explained due to the existence of both chemical and biological medium in dissolved organic nitrogen form doesn't possess any significant impact in the pollutants adsorption. A minute reduction in the adsorbate removal rates is noticed after regeneration cycle, clarified that the nanoadsorbent GO-Fe/CPTMS-SiO<sub>2</sub>@MF having good stability as well as reusability factor in this model wastewater. From the above analysis, GO-Fe/CPTMS-SiO<sub>2</sub>@MF can be an efficient solicitant for the real wastewater treatment.

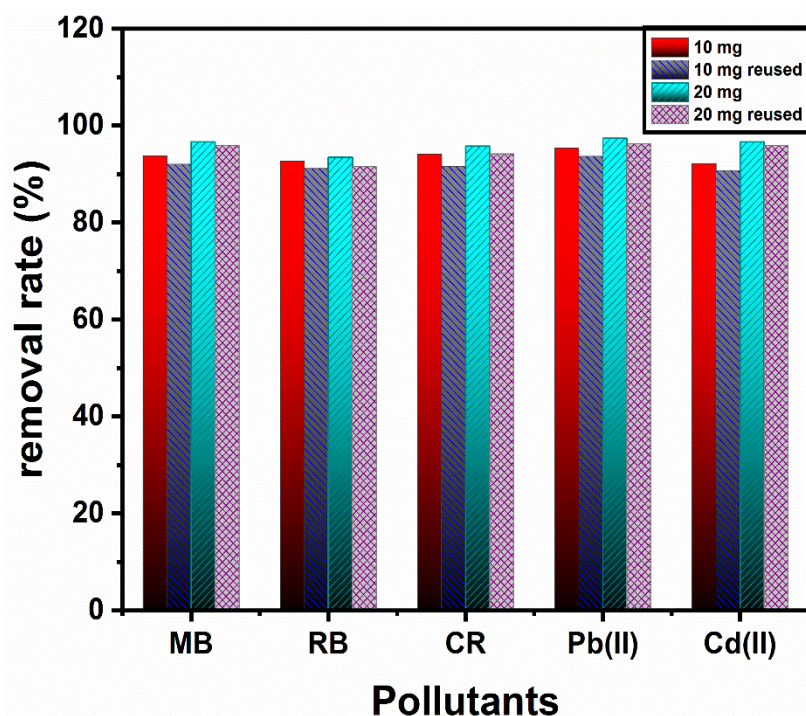


Figure 7.44. Recycling performances of GO-Fe/CPTMS-SiO<sub>2</sub>@MF in model waste water

### 7.3.24 Adsorption of real wastewater on GO-Fe/CPTMS-SiO<sub>2</sub>@MF

The real wastewater analysis has been carried out with all the adsorbates to investigate the efficacy of the nanocomposite in industrial waste effluents. This real wastewater then determined to find out its COD and turbidity values with reference to the nanocomposite given in table 7.8. The dye and heavy metal ion structure in the real wastewater are not known, and the declaration of any identification or structural data is stringently adhered from the purveyor. The experiments were conducted temperature 318.5 K & 323.5 K for the pollutants and the amount taken for the adsorption phenomena is same as that of the synthetic wastewater.

Chemical Oxygen Demand carried out by USEPA 2013 method in presence of Digital Reactor Block 2000 (Hack, Germany). Turbidimeter is used to find out turbidity in wastewater procured with Bante Instruments.

Table 7.9: Analysis of the real wastewater sample

Type of test	COD (mg L <sup>-1</sup> )	TOC	Turbidity	Temperature	Color
Value	703	237	27.4	25	Black

Table 7.10: Langmuir and Freundlich Isotherms of GO-Fe/CPTMS-SiO<sub>2</sub>@MF in real wastewater

Pollutants	Temp(K)	Langmuir				Freundlich			
		Q <sub>max</sub>	K <sub>a</sub>	Adj.	R <sup>2</sup>	n	K <sub>F</sub>	Adj.	R <sup>2</sup>
		mg g <sup>-1</sup>	L mg <sup>-1</sup>	R <sup>2</sup>	(COD)		(mg g <sup>-1</sup> ) (L mg <sup>-1</sup> ) <sup>1/n</sup>	R <sup>2</sup>	(COD)
MB	318.5	4185.2023	0.04808	0.99515	0.99559	2.86511	653.70600	0.95114	0.95558
	323.5	4262.542	0.02259	0.99887	0.99897	2.43038	402.41975	0.95180	0.95619
RB	318.5	1767.0344	0.05709	0.99471	0.99515	3.34836	350.56392	0.94299	0.94774
	328.5	1499.1189	0.05102	0.99519	0.99559	3.40213	290.48746	0.92883	0.93476
CR	318.5	3324.6017	0.02568	0.99852	0.99866	2.53384	350.82810	0.94557	0.95052
	323.5	4200.6350	0.01815	0.99765	0.99786	2.31774	333.00869	0.94834	0.95303
Pb	318.5	3924.6915	0.03041	0.99380	0.99437	2.73815	496.86952	0.96223	0.96567
	323.5	3924.9377	0.02186	0.99764	0.99785	2.51749	386.79556	0.96247	0.96588
Cd	318.5	3680.0201	0.02456	0.99428	0.99480	2.70888	425.58390	0.96704	0.97004
	323.5	3752.6797	0.01810	0.99903	0.99912	2.46603	330.014400	0.94381	0.94892

Table 7.11: DR and Temkin Isotherms of GO-Fe/CPTMS-SiO<sub>2</sub>@MF in real wastewater

Pollutants	Temp(K)	Dubinin-Radushkevich				Temkin			
		q <sub>s</sub>	K <sub>DR</sub>	Adj.	R <sup>2</sup>	A <sub>T</sub>	B <sub>T</sub>	Adj.	R <sup>2</sup>
		(mol g <sup>-1</sup> )	(mol <sup>2</sup> k <sup>-1</sup> J <sup>-2</sup> )	R <sup>2</sup>	(COD)	(L g <sup>-1</sup> )	(J mol <sup>-1</sup> )	R <sup>2</sup>	(COD)
MB	318.5	3413.876	0.06064	0.87885	0.88986	1.71931	4.19567	0.94659	0.95145
	323.5	3246.004	0.05490	0.90087	0.90988	0.60089	3.91556	0.93952	0.94502
RB	318.5	1507.859	0.04848	0.85735	0.86923	1.4448	9.14911	0.98111	0.98268
	323.5	1264.821	0.03600	0.86078	0.87239	0.98832	10.37579	0.98454	0.98583
CR	318.5	2537.293	0.03401	0.90911	0.91737	0.9002	5.34172	0.89420	0.90382
	323.5	3142.618	0.05872	0.92488	0.93171	0.50956	4.01745	0.90007	0.90916
Pb	318.5	3180.255	0.05211	0.87596	0.88723	1.31753	4.66102	0.92521	0.93201
	323.5	3105.587	0.08247	0.88789	0.89808	0.69867	4.42525	0.93417	0.94015
Cd	318.5	2985.495	0.08399	0.87555	0.88686	1.03365	4.91518	0.93234	0.93849

323.5    2888.449    0.07670    0.915    0.92273    0.42596    4.29304    0.94053    0.94594

### Kinetic studies

Table 7.12: Kinetic studies of GO-Fe/CPTMS-SiO<sub>2</sub>@MF in real wastewater

Pollutants	Temp (K)	Pseudo-first-order				Pseudo-second-order		
		q <sub>e(exp)</sub> (mg g <sup>-1</sup> )	q <sub>e(calc)</sub> (mg g <sup>-1</sup> )	k <sub>1</sub> (min <sup>-1</sup> )	R <sup>2</sup>	q <sub>e(calc)</sub> (mg g <sup>-1</sup> )	k <sub>2</sub> (g mg <sup>-1</sup> min <sup>-1</sup> )	R <sup>2</sup>
MB	318.5	1904	1038.012	0.16190	0.89059	1899.371	0.00517	0.99963
	323.5	1821	1109.378	0.15140	0.89836	1820.647	0.00645	0.99973
RB	318.5	1263	1212.931	0.13145	0.89047	1253.551	0.01673	0.99974
	323.5	1148	1108.647	0.15154	0.87661	1146.924	0.01551	0.99995
CR	318.5	1841.5	1180.882	0.14227	0.90448	1840.329	0.00753	0.99958
	323.5	1801.5	980.392	0.17144	0.87237	1797.268	0.00563	0.99984
Pb	318.5	1841.5	1088.050	0.15441	0.88888	1840.949	0.00711	0.99986
	323.5	1792.0	1521.894	0.11039	0.90941	1790.782	0.01739	0.99991
Cd	318.5	1785.5	1214.113	0.13838	0.91381	1785.099	0.00749	0.99914
	323.5	1751.5	813.008	0.20599	0.84278	1751.264	0.00446	0.99989

With respect to the above analysis, it displayed that the adsorption efficiency and adsorption capacity is less to that of the synthetic wastewater because of the existence of unlimited organic species and impurities percolated in the textile effluents. The performance of the nanocomposite and its experimental values represented in corresponding tables 7.9, 7.10 & 7.11.

### 7.3.25 Regeneration studies

The recyclability studies on the GO-Fe/CPTMS-SiO<sub>2</sub>@MF adsorbent revealed that the real wastewater removal rate is less compared to the simulated wastewater under the same parameters as shown in figure 7.45 and the table 7.12.

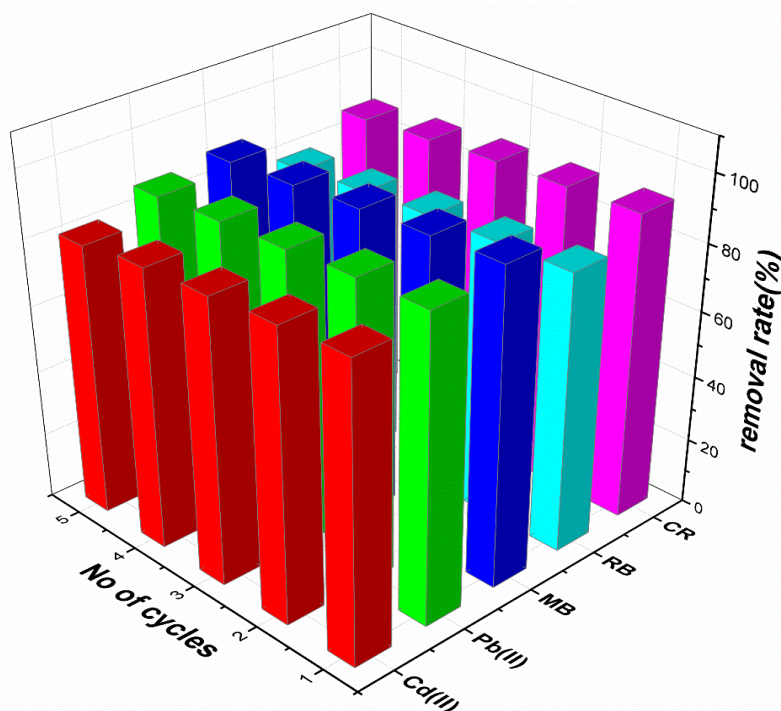


Figure. 7.45. Recyclability studies of real wastewater with GO-Fe/CPTMS-SiO<sub>2</sub>@MF

Table 7.13: The recyclability studies of pollutants such as MB, RB, CR, Pb(II) & Cd(II) over GO-Fe/CPTMS-SiO<sub>2</sub>@MF

No. of cycles	Removal rate of pollutants in real wastewater(%)				
	MB	RB	CR	Pb(II)	Cd(II)
1	95.2	84.2	92.07	92.02	89.2
2	94.1	83.7	91.4	91.4	87.8
3	92.9	82.9	90.7	90.1	86.1
4	91.4	81.6	89.3	89.2	84.8
5	90.1	80.1	87.9	87.9	82.1

## 7.4 CONCLUSIONS

In this study, GO-Fe/CPTMS-SiO<sub>2</sub>@MF nanohybrid was synthesized using hydrothermal methodology has been successfully developed. The synthesized nanocomposite acquired a high surface area with wrinkled morphology. GO-Fe/CPTMS-SiO<sub>2</sub>@MF efficiently removed the dyes like MB, RB, CR and the heavy metal ions Pb(II), Cd(II) in aqueous sewage effluents. GO-Fe/CPTMS-SiO<sub>2</sub>@MF being magnetic in nature, gets easily separated, is a beneficial aspect of adsorbent. With the increase in pH, the maximum adsorption capacity increases for the cationic pollutants correlated with the anionic pollutants. This hybrid composite which consist of supermagnetic ferrite found effective in real wastewater for a varied pH range. It can be recycled using desorption agents like HCl and EDTA. The results determine the

nanocomposite GO-Fe/CPTMS-SiO<sub>2</sub>@MF as a promising material for the removal of cationic and anionic dyes along with heavy metal ions from the real-life wastewater.



**CHAPTER-8**  
**CONCLUSIONS**

*Abstract: This chapter provides the summary of the thesis and important conclusions drawn from the undertaken research work.*

## **8.1 SUMMARY OF RESEARCH WORK**

In the present work, we synthesized 5 different types of metal nanoparticles using the hydrothermal methodology and they are functionalized using heterogeneous support GO using solvothermal process.

- The synthesized GO support which includes the Copper Schiff bases complexes and Cobalt oxide Schiff base complexes using APTMS, Cobalt oxide-Polypyrrole, Cobalt ferrite-nanoceria and mixed ferrite through silylation of TEOS and CPTMS upon iron oxide functionalized GO.
- GO was synthesized using improved Hummer's method using  $\text{KMnO}_4$  as oxidant and further solvothermal synthesis of nanocomposites using different silylation agents.
- FTIR analysis is performed to know the nature of bonding in the nanocomposite and the nanoparticles.
- X-ray Diffraction analysis is carried out to know the lattices points of nanoparticles and nanocomposites.
- Scanning electron microscopy and EDX analysis were utilized to know the surface morphology of the synthesized compounds their elemental composition can be estimated respectively. TEM & HR-TEM analysis is performed to know the morphology at the atomic level.
- Thermogravimetric analysis (TGA) was performed to measure the thermal stability of the synthesized compounds and X-ray photoelectron spectroscopic analysis (XPS) were done to know the elemental mapping of the synthesized nanocomposite and their bonding.
- Magnetic studies were done using Vibrating-Sample Magnetometry (VSM) and Electron Paramagnetic Resonance spectroscopy (EPR) to know the magnetic saturation point of the nanoparticles and synthesized nanocomposites and Raman spectroscopy is to know the vibration frequencies of the nanocomposite chemical bonding and symmetry.
- In case wastewater treatment application zeta potential was performed to know the surface charge of the nanocomposite and BET analysis to know the surface area and pore volume of the nanocomposite.

Table 8.1: Types of metal nanoparticles synthesized and their functionalization on GO support

Compounds code	Nano-additives	Coupling agent	Functionalized group	Nanoparticles synthesized
CAGO	Terephthalaldehyde, 2-amino phenol & Cu(Ac) <sub>2</sub> .H <sub>2</sub> O	APTMS	--	Copper Schiff base complex
CoASGO	SDS, urea, CoNO <sub>3</sub> .6H <sub>2</sub> O, Terephthalaldehyde & 2-amino ethanol	APTMS	--	Cobalt oxide Schiff base complex
COPYGO	Glycine, hydrazine hydrate, pyrrole monomer & FeCl <sub>3</sub>	--	Polypyrrole	Co <sub>3</sub> O <sub>4</sub>
GO-CeO <sub>2</sub> @CoFe <sub>2</sub> O <sub>4</sub>	PVP, ethylene glycol, NaOH, urea & Cerium nitrate	--	Cerium oxide	CoFe <sub>2</sub> O <sub>4</sub>
GO-Fe/CPTMS-SiO <sub>2</sub> @MF	2-pentanol, oleic acid, hydrazine hydrate, n-hexane, FeCl <sub>3</sub> & hydrazine	TEOS, CPTMS	Iron oxide	CoNiZnFe <sub>2</sub> O <sub>4</sub>

### Comparison of the recyclability studies of CoASGO and CAGO

The catalyst activity for the Suzuki cross-coupling reaction have been investigated and been given in the table 8.2. The highest yield of CoASGO is due to its ferromagnetic nature and it is highly stable to air and moisture.

Table 8.2: Highest yield obtained for the synthesized nanocomposites

Nanocomposite	Wt. %	Base	Reactants	Product	Product yield
CAGO	0.36%	K <sub>2</sub> CO <sub>3</sub>	Phenyl iodide	Phenylboronic acid	94%
CoASGO	0.32%	Cs <sub>2</sub> CO <sub>3</sub>	Phenyl iodide	Phenylboronic acid	97.4%

We reported a plausible mechanism for the CoASGO catalyst which facilitates a detailed study to comprehend the process of C-C coupling reaction. At first, the Co metal in CoASGO (Fig. 8.1 (a)) may be reduced to either Co (0) or Co (I) is just a possibility and determining the active species is quite difficult. Here, we tentatively speculate that the Co (0) (Fig. 8.1 (b)) might be formed by reaction with arylboronic acid ( $R_1B(OH)_2$ ) and  $Cs_2CO_3$  base. Then, the central Co (0) reacts with aryl halide ( $R_2-X$ ) affords to form an X-Co(II)- $R_2$  intermediate (Fig. 8.1 (c)) which is an oxidative addition and further nucleophilic substitution of halo group and followed by transmetallation between arylboronic acid and GOAS-Co- $R_2$ - $CO_3$  intermediate (Fig. 8.1 (d)) could results in biaryl  $R_1$ -GOAS-Co- $R_2$  species (Fig. 8.1 (e)). In the final step, reductive elimination takes place to form the target biaryl ( $R_1$ - $R_2$ ) (Fig. 8.1 (f)) product along with regeneration of CoASGO complex to complete the catalytic cycle.

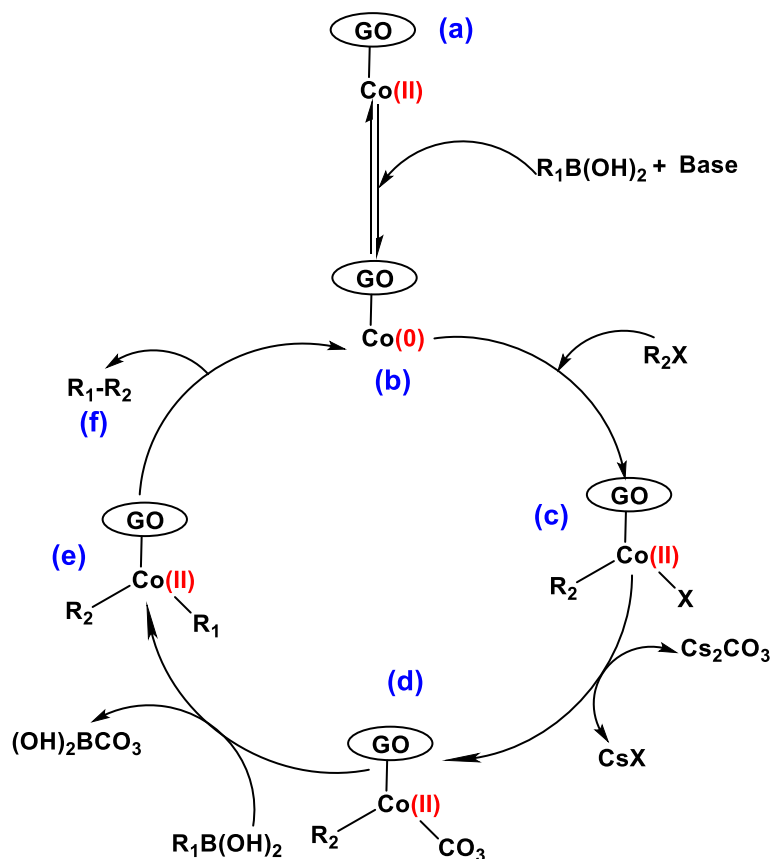


Figure 8.1. A plausible mechanism of CoASGO catalyst in Suzuki cross-coupling reaction

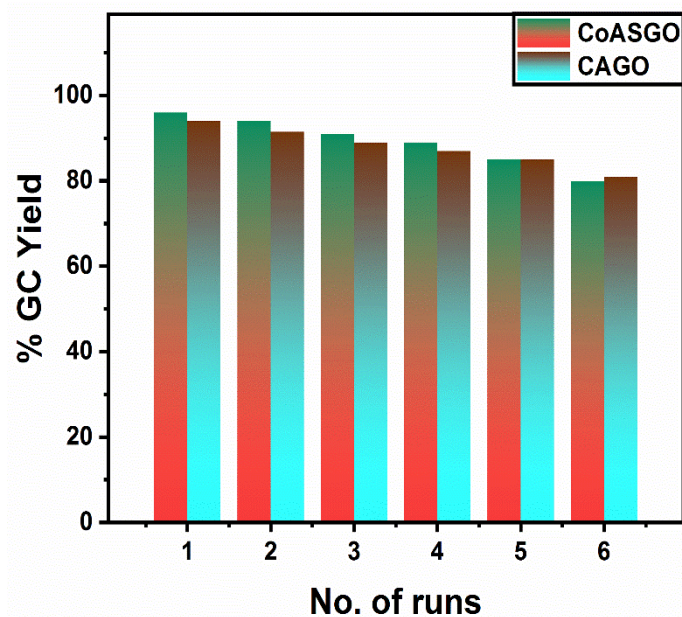


Figure 8.2. The recyclability studies of Suzuki cross-coupling reaction of CoASGO and CAGO

From the above figure 8.2, the recyclability studies of Suzuki coupling reaction in presence of catalysts such as CoASGO and CAGO which showed that CoASGO is more effective than CAGO in the synthesis of biphenyl derivatives. However, it is shown that the CoASGO is effective for the synthesis of simple aromatic biphenyls as products in presence of Iodobenzene and Bromobenzene with phenylboronic acid as reactants. Compared with both iodo and bromo functional groups, the iodo group (C-I) is a better leaving group due to low bond dissociation energy whereas C-Cl group has high bond dissociation energy (96 kcal/mol). From the studies, it is proved that 0.32 mol% of CoASGO under the optimized conditions is catalysed to form 97.4% biphenyl product in the 1<sup>st</sup> cycle of coupling reaction when compared to CAGO it is 0.36 mol% to form 94% biphenyl product using Iodobenzene as a reactant being a best leaving group. In CoASGO, the reactant is Bromobenzene whose bond dissociation energy is high compared to the Iodobenzene reactant. This result justified that the CoASGO is a better catalyst compared to CAGO in the Suzuki cross-coupling reactions.

## Comparison of the recyclability studies of simulated wastewater using adsorbents

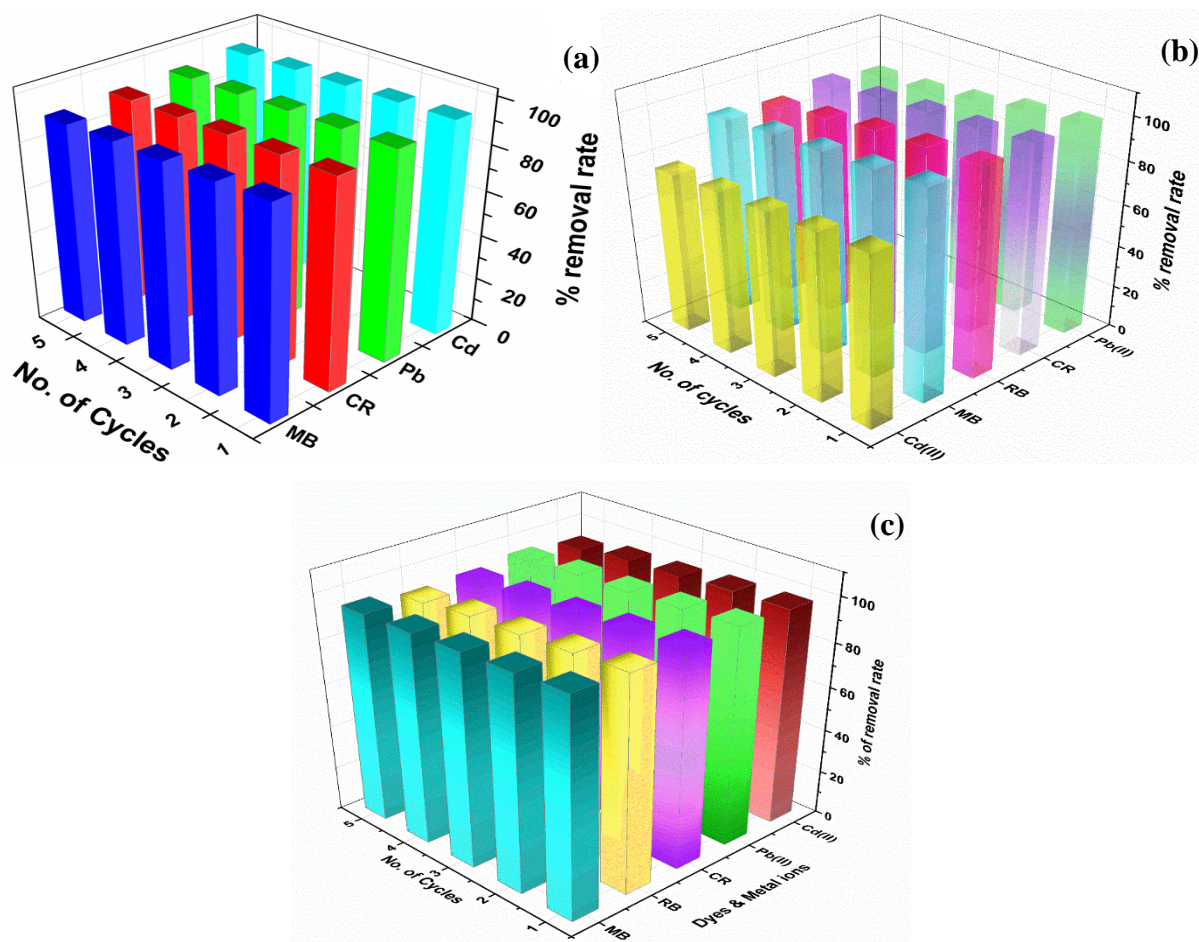


Figure 8.3. The recyclability studies of pollutants in simulated wastewater on adsorbents a) COPYGO, b) GO-CeO<sub>2</sub>@CoFe<sub>2</sub>O<sub>4</sub> & c) GO-Fe/CPTMS-SiO<sub>2</sub>@MF

The regenerative cycles of pollutants MB, CR, Pb(II) and Cd(II) over the nanocomposites such as COPYGO, GO-CeO<sub>2</sub>@CoFe<sub>2</sub>O<sub>4</sub> and GO-Fe/CPTMS-SiO<sub>2</sub>@MF in the adsorption process confirmed that the GO-Fe/CPTMS-SiO<sub>2</sub>@MF was effective in the removal of cationic and anionic dyes along with heavy metal ions. In case of COPYGO, the highest removal rate for the pollutants MB, CR, Pb(II) and Cd(II) were 92.8, 92.2, 93.08 & 95.28 in the first cycle of adsorption. From the figure 8.3b & 8.3c, the adsorption of cationic RB dye was carried out and the results of first adsorption cycles shows that the removal rate of adsorption of GO-Fe/CPTMS-SiO<sub>2</sub>@MF was effective in removing the RB from the aqueous solution along with other pollutants. The removal rate of first cycle of GO-Fe/CPTMS-SiO<sub>2</sub>@MF for the pollutants MB, RB, CR, Pb(II) and Cd(II) are 98.6, 97.65, 98.39, 98.96 & 98.07 and for the GO-CeO<sub>2</sub>@CoFe<sub>2</sub>O<sub>4</sub> the removal rate is 98.16, 98.12, 98.86, 98.87 & 80.27. This is due to the presence of abundant hydroxyl groups (M-OH, Fe-OH) on the surface of nanocomposite which

have enhanced the adsorption and also showed the variation of adsorption capacity for different pollutants. The strong affinity between the pollutant ionic species and the nanocomposite enhanced the binding capacity and reduced the competitive inhibition on the active sites of GO-Fe/CPTMS-SiO<sub>2</sub>@MF.

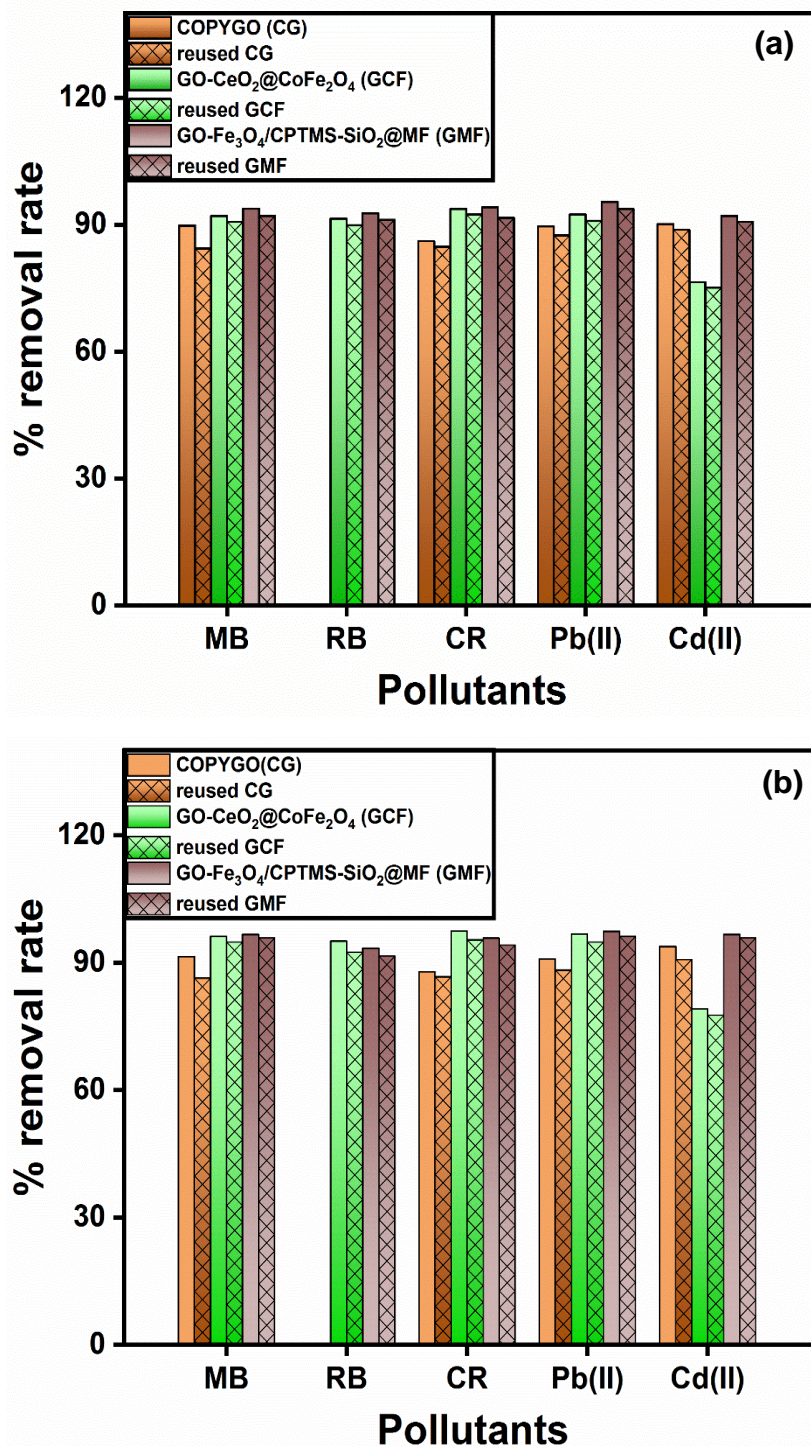


Figure 8.4. Removal rate of model wastewater in adsorbent dosages, a) 10 mg and b) 20 mg

Table 8.3: Removal rate of model wastewater of all pollutants in various adsorbents dosages

Adsorbents	Dosage	MB	RB	CR	Pb(II)	Cd(II)
<b>COPYGO(CG)</b>	<b>10 mgL<sup>-1</sup></b>	89.8	-	86.1	89.6	90.1
<b>Reused CG</b>		84.4	-	84.8	87.5	88.8
<b>GO-CeO<sub>2</sub>@CoFe<sub>2</sub>O<sub>4</sub>(GCF)</b>		92.1	91.4	93.7	92.4	76.4
<b>Reused GCF</b>		90.7	89.9	92.4	90.9	75.1
<b>GO-Fe/CPTMS-SiO<sub>2</sub>@MF (GMF)</b>		93.8	92.7	94.1	95.4	92.1
<b>Reused GMF</b>		92.1	91.2	91.6	93.7	90.7
<b>COPYGO(CG)</b>	<b>20 mgL<sup>-1</sup></b>	91.4	-	87.9	90.9	93.8
<b>Reused CG</b>		86.4	-	86.7	88.3	90.8
<b>GO-CeO<sub>2</sub>@CoFe<sub>2</sub>O<sub>4</sub>(GCF)</b>		96.2	95.1	97.46	96.82	79.1
<b>Reused GCF</b>		94.9	92.46	95.4	94.9	77.6
<b>GO-Fe/CPTMS-SiO<sub>2</sub>@MF (GMF)</b>		96.67	93.45	95.8	97.4	96.7
<b>Reused GMF</b>		95.91	91.57	94.2	96.2	95.9

To know the effectiveness of the nanoadsorbents, the evaluation studies were performed using the model synthetic wastewater, that can lead to its prospective in real life wastewater. The results with the adsorbents dosage 10 mg L<sup>-1</sup> and 20 mg L<sup>-1</sup> in model wastewater treatment were calculated and confirmed that they are bit little closer to the synthetic wastewater upon comparison were given in figure 4. The reduction in removal rate of pollutants is due to the presence of chemical and biological medium such as dissolved organic nitrogen which had some effect on the removal rates of pollutants. The results proved that the 20 mg L<sup>-1</sup> in model wastewater are having the removal rate for the COPYGO, GO-CeO<sub>2</sub>@CoFe<sub>2</sub>O<sub>4</sub> & GO-Fe/CPTMS-SiO<sub>2</sub>@MF are given in the table 2. Further, with the regeneration cycles, there is a decrease in removal rate is observed for the pollutants in all 3 nanoadsorbents. But the removal rate of pollutants on the GO-Fe/CPTMS-SiO<sub>2</sub>@MF adsorbent is higher and with the consecutive cycles, the decrease in removal rate is slightly less compared to the other adsorbents i.e., COPYGO & GO-CeO<sub>2</sub>@CoFe<sub>2</sub>O<sub>4</sub>. This adsorption experiments finally paved a way to further explore in real or actual wastewater systems.



## Adsorption studies in real wastewater

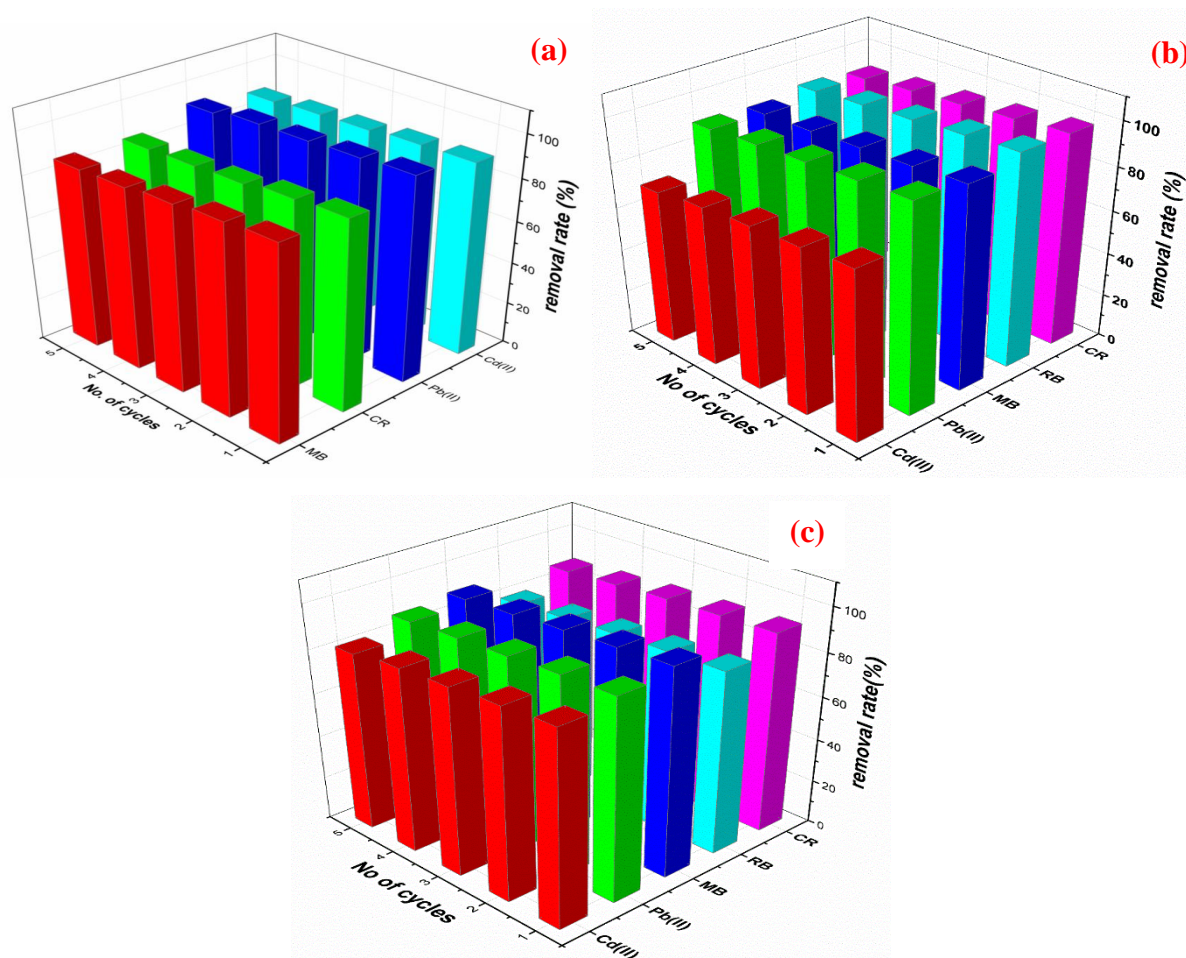


Figure 8.5. The recyclability studies of pollutants in real wastewater on adsorbents (a) COPYGO, (b) GO-CeO<sub>2</sub>@CoFe<sub>2</sub>O<sub>4</sub> & (c) GO-Fe/CPTMS-SiO<sub>2</sub>@MF

Table 8.4: The recyclability studies of pollutants such as MB, CR, Pb(II) & Cd(II) over COPYGO

No. of cycles	Removal rate of pollutants in real wastewater (%)			
	MB	CR	Pb(II)	Cd(II)
1	91.6	89.9	96.96	92.07
2	90.4	88.8	95.9	91.7
3	88.6	86.5	95.1	90.3
4	86.7	85.8	94.8	89.8
5	85.9	85.1	92.2	88.4

Table 8.5: The recyclability studies of pollutants such as MB, RB, CR, Pb(II) & Cd(II) over GO-CeO<sub>2</sub>@CoFe<sub>2</sub>O<sub>4</sub>

No. of cycles	Removal rate of pollutants in real wastewater (%)				
	MB	RB	CR	Pb(II)	Cd(II)
1	93.6	98.1	97.9	95.8	77.9
2	92.1	96.9	96.1	94.7	76.4
3	91.4	95.4	94.5	93.6	75.4
4	90.4	94.1	93.1	92.4	73.8
5	89.9	92.7	91.2	90.9	71.2

Table 8.6: The recyclability studies of pollutants such as MB, RB, CR, Pb(II) & Cd(II) over GO-Fe/CPTMS-SiO<sub>2</sub>@MF

No. of cycles	Removal rate of pollutants in real wastewater (%)				
	MB	RB	CR	Pb(II)	Cd(II)
1	95.2	84.2	92.07	92.02	89.2
2	94.1	83.7	91.4	91.4	87.8
3	92.9	82.9	90.7	90.1	86.1
4	91.4	81.6	89.3	89.2	84.8
5	90.1	80.1	87.9	87.9	82.1

The recyclability studies of pollutants in real wastewater over the adsorbents such as COPYGO, GO-CeO<sub>2</sub>@CoFe<sub>2</sub>O<sub>4</sub> & GO-Fe/CPTMS-SiO<sub>2</sub>@MF is given in the figure 5 and the tabular form 3, 4 & 5. In case of the GO-Fe/CPTMS-SiO<sub>2</sub>@MF adsorbent shown in table 5, the concentration of 400 mg L<sup>-1</sup> for the pollutants and for RB dye, the concentration is 300 mg L<sup>-1</sup> which showed that it is effective for the removal of dyes and metal ions compared to the other adsorbents. But the concentration of pollutants in real wastewater are MB, CR & Pb(II) is 150 mg L<sup>-1</sup> and the Cd(II) concentration is 100 mg L<sup>-1</sup> for the COPYGO adsorbent shown in table 3. In case of the adsorbent from table 4, GO-CeO<sub>2</sub>@CoFe<sub>2</sub>O<sub>4</sub> the concentration of pollutants such as RB, CR, Pb(II) & Cd(II) is 200 mg L<sup>-1</sup> and the MB dye is 400 mg L<sup>-1</sup>. The time period for the adsorption process is 360 min and the temperature for all adsorbents is 318.5 K remains same with respect to the recyclability studies of all the pollutants. Out of all the adsorbates, the dye MB and the metal ion Pb(II) have been effectively adsorbed onto the GO-Fe/CPTMS-SiO<sub>2</sub>@MF adsorbent with a high removal rate of 90.1 and 87.9 with a high initial concentration compared with other adsorbents with the 5<sup>th</sup> adsorptive cycle respectively. The high removal rate of pollutants on GO-Fe/CPTMS-SiO<sub>2</sub>@MF adsorbent is due to the strong affinity between the ionic species and the nanocomposite which led to the reduction of particle aggregation and the ionic strength of the aqueous wastewater along with the adjustable pH which matched with the pollutant and as well as the nanocomposite possessing functional groups.

## 8.2 CONCLUSIONS

Graphene oxide (GO), a derivative of graphene family created an interest to explore due to high surface area, conductivity and high thermal stability which led to investigate its applications in catalysis and adsorption process. The surface modification of GO using various materials such as silane agents like 3-aminopropyltrimethoxy silane (APTMS), Iron oxide nanoparticle, Tetraethyl orthosilicate (TEOS), 3-chloropropyltrimethoxy silane (CPTMS), polypyrrole and nanoceria respectively. These modifications enhanced the hydrophilicity on the GO and the mobility of ions over its surface. Further, the synthesis of nanoparticles such as Cobalt oxide nanoparticle, copper nanoparticle, ferrites i.e., cobalt ferrite, cobalt nickel zinc ferrite, Schiff base synthesis with metal nanoparticle and their immobilization onto the GO surface enhanced the nanocomposite for its application as catalyst in Suzuki cross-coupling reaction and the removal of dyes and metal ions from the wastewater by adsorption phenomena. The following are the key findings of the proposed investigation:

- ✓ Synthesis of Schiff base metal complexes onto graphene oxide using APTMS as a coupling agent using Cobalt and Copper metals as the catalyst utilized for the synthesis of biaryl product using aryl halides and phenylboronic acid in the Suzuki cross-coupling reaction.
- ✓ CoASGO is effective for the Suzuki cross-coupling reaction compared to CAGO due to its structural properties of cobalt nanoparticles in the nanocomposite.
- ✓ Addition of increased concentrations of hydrophilic inorganic nanoparticles onto the GO nanocomposite enhanced the surface morphology, magnetic property, charge factor and pore volume for having better efficiency in removal rate of adsorption.
- ✓ Induced surface charge on the nanocomposite surfaces because of the modifications may lead to the increased selectivity over the pollutants due to surface charge possessing hydrogen bonding and electrostatic interaction.
- ✓ As such the nanocomposites using cobalt oxide, cobalt ferrite and mixed ferrite derivatives exhibited enhanced surface charge positive charge at acidic pH and these are negatively charged at pH 7.0. So the cationic dyes and metal ions gets adsorbed on basic pH and anionic dyes at acidic pH in the aqueous wastewater.
- ✓ The good performed nanocomposites used in this study have been utilized for the separation of dyes and metal ions from aqueous wastewater and real wastewater under standard conditions with better results.

- ✓ Also the modified good performed nanocomposite GO-Fe/CPTMS-SiO<sub>2</sub>@MF utilized in this study can be employed for the removal rate of different dyes and metal ions from wastewater under standard conditions with better outcomes.

### **8.3 FUTURE WORK**

The principles of the properties exhibited by the nanocomposites are well known. However, the same cannot be said for graphene nanocomposites. Graphene nanocomposites in certain ways behave distinct of other nanocomposites. Although we can assume the cause for such behaviour, a thorough investigation in the atomic level is required to fully understand the behaviour of graphene nanocomposites. This would be an interesting research problem for the future work.

The applicability of graphene nanocomposites and specifically graphene oxide supported metal or metal oxides was found to be promising materials towards adsorption applications. However, the use of graphene nanocomposites in the catalytic applications for cross-coupling reactions is still at its infancy. The presented report over the use of graphene nanocomposites as a adsorbent in removal of pollutants and few works in literature reflects over the potential of the nanocomposites have in such areas. The 2D carbon nanostructures are also not utilized to its potential in other applications such as environmental and energy related devices. Therefore, the applicability of graphene nanocomposites and its derivative would be explored in future.

## REFERENCES:

- Abd El-Lateef, H. M., Sayed, A. R., and Adam, M. S. S. (2019). "Sulfonated salicylidene thiadiazole complexes with Co (II) and Ni (II) ions as sustainable corrosion inhibitors and catalysts for cross coupling reaction." *Appl. Organomet. Chem.*, 33(8), e4987.
- Abu-Dief, A. M., and Mohamed, I. M. A. (2015). "A review on versatile applications of transition metal complexes incorporating Schiff bases." *Beni-Suef Univ. J. Basic Appl. Sci.*, 4(2), 119–133.
- Acharya, J., Sahu, J. N., Mohanty, C. R., and Meikap, B. C. (2009). "Removal of lead(II) from wastewater by activated carbon developed from Tamarind wood by zinc chloride activation." *Chem. Eng. J.*, 149(1), 249–262.
- Adam, F., Osman, H., and Hello, K. M. (2009). "The immobilization of 3-(chloropropyl)triethoxysilane onto silica by a simple one-pot synthesis." *J. Colloid Interface Sci.*, 331(1), 143–147.
- Adhikari, S., Mandal, S., Sarkar, D., Kim, D.-H., and Madras, G. (2017). "Kinetics and mechanism of dye adsorption on WO<sub>3</sub> nanoparticles." *Appl. Surf. Sci.*, 420, 472–482.
- Ahmad, Z. U., Chao, B., Konggudinata, M. I., Lian, Q., Zappi, M. E., and Gang, D. D. (2018). "Molecular simulation and experimental validation of resorcinol adsorption on Ordered Mesoporous Carbon (OMC)." *J. Hazard. Mater.*, 354, 258–265.
- Ahmad, Z. U., Yao, L., Wang, J., Gang, D. D., Islam, F., Lian, Q., and Zappi, M. E. (2019). "Neodymium embedded ordered mesoporous carbon (OMC) for enhanced adsorption of sunset yellow: Characterizations, adsorption study and adsorption mechanism." *Chem. Eng. J.*, 359, 814–826.
- Ahmed, M. A., Okasha, N., and El-Sayed, M. M. (2007). "Enhancement of the physical properties of rare-earth-substituted Mn–Zn ferrites prepared by flash method." *Ceram. Int.*, 33(1), 49–58.
- Ahmed, N. S., Menzel, R., Wang, Y., Garcia-Gallastegui, A., Bawaked, S. M., Obaid, A. Y., Basahel, S. N., and Mokhtar, M. (2017). "Graphene-oxide-supported CuAl and CoAl layered double hydroxides as enhanced catalysts for carbon-carbon coupling via Ullmann reaction." *J. Solid State Chem.*, 246, 130–137.
- Ai, L., Zhang, C., and Chen, Z. (2011). "Removal of methylene blue from aqueous solution by a solvothermal-synthesized graphene/magnetite composite." *J. Hazard. Mater.*, 192(3), 1515–1524.

- Al Nafiey, A., Addad, A., Sieber, B., Chastanet, G., Barras, A., Szunerits, S., and Boukherroub, R. (2017). "Reduced graphene oxide decorated with Co<sub>3</sub>O<sub>4</sub> nanoparticles (rGO-Co<sub>3</sub>O<sub>4</sub>) nanocomposite: A reusable catalyst for highly efficient reduction of 4-nitrophenol, and Cr(VI) and dye removal from aqueous solutions." *Chem. Eng. J.*, 322, 375–384.
- Albornoz, C., Sileo, E. E., and Jacobo, S. E. (2004). "Magnetic polymers of maghemite ( $\gamma$ -Fe<sub>2</sub>O<sub>3</sub>) and polyvinyl alcohol." *Phys. B Condens. Matter*, 354(1), 149–153.
- Alqadami, A. A., Naushad, M., AlOthman, Z. A., Alsuhybani, M., and Algamdi, M. (2020). "Excellent adsorptive performance of a new nanocomposite for removal of toxic Pb(II) from aqueous environment: Adsorption mechanism and modeling analysis." *J. Hazard. Mater.*, 389, 121896.
- Alwan, S. H., Alshamsi, H. A. H., and Jasim, L. S. (2018). "Rhodamine B removal on A-rGO/cobalt oxide nanoparticles composite by adsorption from contaminated water." *J. Mol. Struct.*, 1161, 356–365.
- Alzari, V., Nuvoli, D., Scognamillo, S., Piccinini, M., Gioffredi, E., Malucelli, G., Marceddu, S., Sechi, M., Sanna, V., and Mariani, A. (2011). "Graphene-containing thermoresponsive nanocomposite hydrogels of poly (N-isopropylacrylamide) prepared by frontal polymerization." *J. Mater. Chem.*, 21(24), 8727–8733.
- An, Y., Zheng, H., Zheng, X., Sun, Q., and Zhou, Y. (2019). "Use of a floating adsorbent to remove dyes from water: A novel efficient surface separation method." *J. Hazard. Mater.*, 375, 138–148.
- Anastopoulos, I., Hosseini-Bandegharai, A., Fu, J., Mitropoulos, A. C., and Kyzas, G. Z. (2018). "Use of nanoparticles for dye adsorption: Review." *J. Dispers. Sci. Technol.*, 39(6), 836–847.
- Anuradha, Kumari, S., and Pathak, D. D. (2015). "Synthesis and development of Chitosan anchored copper(II) Schiff base complexes as heterogeneous catalysts for N-arylation of amines." *Tetrahedron Lett.*, 56(27), 4135–4142.
- Anuradha, Shweta Kumari, Devendra D. Pathak. (2015). "Synthesis and development of Chitosan anchored copper(II) Schiff base complexes as heterogeneous catalysts for N arylation of amines." *Receiv. 14 April 2015 Revis. 13 May 2015 Accept. 14 May 2015 Available Online 19 May 2015*, 56, 4135–4142.
- A.O, D., Olalekan, A., Olatunya, A., and Dada, A. O. (2012). "Langmuir, Freundlich, Temkin and Dubinin–Radushkevich Isotherms Studies of Equilibrium Sorption of Zn<sup>2+</sup> Unto Phosphoric Acid Modified Rice Husk." *J Appl Chem*, 3, 38–45.

- Appaturi, J. N., Pulingam, T., Muniandy, S., Dinshaw, I. J., Fen, L. B., and Johan, Mohd. R. (2019). "Supported cobalt nanoparticles on graphene oxide/mesoporous silica for oxidation of phenol and electrochemical detection of H<sub>2</sub>O<sub>2</sub> and Salmonella spp." *Mater. Chem. Phys.*, 232, 493–505.
- Arami, M., Limaee, N. Y., Mahmoodi, N. M., and Tabrizi, N. S. (2005). "Removal of dyes from colored textile wastewater by orange peel adsorbent: Equilibrium and kinetic studies." *J. Colloid Interface Sci.*, 288(2), 371–376.
- Arasteh, R., Masoumi, M., Rashidi, A. M., Moradi, L., Samimi, V., and Mostafavi, S. T. (2010). "Adsorption of 2-nitrophenol by multi-wall carbon nanotubes from aqueous solutions." *Appl. Surf. Sci.*, 256(14), 4447–4455.
- Arbabi, M., Hemati, S., and Amiri, M. (2015). "Removal of lead ions from industrial wastewater: A review of Removal methods." *Int. J. Epidemiol. Res.*, 2(2), 105–109.
- Arévalo-Cid, P., Isasi, J., and Martín-Hernández, F. (2018). "Comparative study of core-shell nanostructures based on amino-functionalized Fe<sub>3</sub>O<sub>4</sub>@SiO<sub>2</sub> and CoFe<sub>2</sub>O<sub>4</sub>@SiO<sub>2</sub> nanocomposites." *J. Alloys Compd.*, 766, 609–618.
- Arghan, M., Koukabi, N., and Kolvari, E. (2019). "Magnetic apple seed starch functionalized with 2, 2'-furyl as a green host for cobalt nanoparticles: Highly active and reusable catalyst for Mizoroki–Heck and the Suzuki–Miyaura reactions." *Appl. Organomet. Chem.*, 33(9), e5075.
- Associates, @ Sinauer Inc. (2001). "<http://www.columbia.edu/cu/biology/courses/c2005/purves6/figure06-14.jpg>."
- Asta, M., Kauzlarich, S. M., Liu, K., Navrotsky, A., and Osterloh, F. E. (2007). "Inorganic nanoparticles. Unique properties and novel applications." *Mater. Matters Milwaukee WI USA*, 2(1), 3–6.
- Astruc, D., Lu, F., and Aranzas, J. R. (2005). "Nanoparticles as recyclable catalysts: the frontier between homogeneous and heterogeneous catalysis." *Angew. Chem. Int. Ed.*, 44(48), 7852–7872.
- Babu, K. V., Sailaja, B., Jalaiah, K., Shibeshi, P. T., and Ravi, M. (2018). "Effect of zinc substitution on the structural, electrical and magnetic properties of nano-structured Ni<sub>0.5</sub>Co<sub>0.5</sub>Fe<sub>2</sub>O<sub>4</sub> ferrites." *Phys. B Condens. Matter*, 534, 83–89.
- Bahrami, K., and Kamrani, S. N. (2018). "Synthesis, characterization and application of graphene palladium porphyrin as a nanocatalyst for the coupling reactions such as: Suzuki–Miyaura and Mizoroki–Heck." *Appl. Organomet. Chem.*, 32(2), e4102.
- Bahrami, K., Khodaei, M. M., and Meibodi, F. S. (2017). "Suzuki and Heck cross-coupling reactions using ferromagnetic nanoparticle-supported palladium complex as an efficient and

recyclable heterogeneous nanocatalyst in sodium dodecylsulfate micelles.” *Appl. Organomet. Chem.*, 31(6), n/a-n/a.

Bai, G., Wang, J., Yang, Z., Wang, H., Wang, Z., and Yang, S. (2014). “Preparation of a highly effective lubricating oil additive – ceria/graphene composite.” *RSC Adv*, 4(87), 47096–47105.

Bai, S., and Shen, X. (2012). “Graphene –inorganic nanocomposites.” *RSC Adv.*, 2(1), 64–98.

Bailey, R. E., Smith, A. M., and Nie, S. (2004). “Quantum dots in biology and medicine.” *Phys. E Low-Dimens. Syst. Nanostructures*, 25(1), 1–12.

Bakhteeva, I. A., Medvedeva, I. V., Uimin, M. A., Byzov, I. V., Zhakov, S. V., Yermakov, A. E., and Shchegoleva, N. N. (2016). “Magnetic sedimentation and aggregation of Fe<sub>3</sub>O<sub>4</sub>@SiO<sub>2</sub> nanoparticles in water medium.” *Sep. Purif. Technol.*, 159, 35–42.

Bansal, M., Aghamkar, P., and Ahlawat, D. (2015). “Structural properties of CoFe<sub>2</sub>O<sub>4</sub>:SiO<sub>2</sub> nanocomposites prepared by sol-gel method and co-precipitation method: A comparative study.” *Int J Sci Technol Manag*, 871–877.

Bao, S., Yang, W., Wang, Y., Yu, Y., and Sun, Y. (2020). “One-pot synthesis of magnetic graphene oxide composites as an efficient and recoverable adsorbent for Cd(II) and Pb(II) removal from aqueous solution.” *J. Hazard. Mater.*, 381, 120914.

Baran, T., Sargin, İ., Kaya, M., Mulerčikas, P., Kazlauskaitė, S., and Menteş, A. (2018a). “Production of magnetically recoverable, thermally stable, bio-based catalyst: Remarkable turnover frequency and reusability in Suzuki coupling reaction.” *Chem. Eng. J.*, 331, 102–113.

Baran, T., Yılmaz Baran, N., and Menteş, A. (2018b). “Sustainable chitosan/starch composite material for stabilization of palladium nanoparticles: Synthesis, characterization and investigation of catalytic behaviour of Pd@chitosan/starch nanocomposite in Suzuki–Miyaura reaction.” *Appl. Organomet. Chem.*, 32(2), e4075.

Basila, M. R. (1961). “Hydrogen Bonding Interaction between Adsorbate Molecules and Surface Hydroxyl Groups on Silica.” *J. Chem. Phys.*, 35(4), 1151–1158.

Basso, A., and Serban, S. (2019). “Industrial applications of immobilized enzymes—A review.” *Mol. Catal.*, 479, 110607.

B. Bhat, P., and Ramachandra Bhat, B. (2015). “Nano Fe<sub>3</sub>O<sub>4</sub>@APTES@Ni(OH)<sub>2</sub> as a catalyst for alcohol oxidation.” *New J. Chem.*, 39(1), 273–278.

Beck, L., Gutiérrez, P. C., Miro, S., and Miserque, F. (2017). “Ion beam modification of zinc white pigment characterized by ex situ and in situ  $\mu$ -Raman and XPS.” *Nucl. Instrum. Methods Phys. Res. B*, 409, 96–101.

Bektar, M., Rasekh, H. [Ali, and Soltanianfard, M. [Jaafar. (2020). “Synthesis and characterization of CoFe<sub>2</sub>O<sub>4</sub>@SiO<sub>2</sub>-polyethyleneimine magnetic nanoparticle and its



application for ultrasonic-assisted removal of disulfine blue dye from aqueous solution.” *Arab. J. Chem.*, 13(5), 5430–5437.

Bell, A. T. (2003). “The impact of nanoscience on heterogeneous catalysis.” *Science*, 299(5613), 1688–1691.

Benaïssa, H., and Elouchdi, M. A. (2007). “Removal of copper ions from aqueous solutions by dried sunflower leaves.” *Chem. Eng. Process. Process Intensif.*, 46(7), 614–622.

Bensalah, N., Alfaro, M. A. Q., and Martínez-Huitle, C. A. (2009). “Electrochemical treatment of synthetic wastewaters containing Alphazurine A dye.” *Chem. Eng. J.*, 149(1), 348–352.

Berger, C., Song, Z., Li, T., Li, X., Ogbazghi, A. Y., Feng, R., Dai, Z., Marchenkov, A. N., Conrad, E. H., and First, P. N. (2004). “Ultrathin epitaxial graphite: 2D electron gas properties and a route toward graphene-based nanoelectronics.” *J. Phys. Chem. B*, 108(52), 19912–19916.

Bhatnagar, A., and Sillanpää, M. (2009). “Applications of chitin- and chitosan-derivatives for the detoxification of water and wastewater — A short review.” *Adv. Colloid Interface Sci.*, 152(1), 26–38.

Bhojane, J. M., Sarode, S. A., and Nagarkar, J. M. (2016). “Nickel–glycerol: an efficient, recyclable catalysis system for Suzuki cross coupling reactions using aryl diazonium salts.” *New J Chem*, 40(2), 1564–1570.

Bhowmik, R. N., Ranganathan, R., Sarkar, S., Bansal, C., and Nagarajan, R. (2003). “Magnetic enhancement of  $\text{Co}_{0.2}\text{Zn}_{0.8}\text{Fe}_2\text{O}_4$  spinel oxide by mechanical milling.” *Phys Rev B*, 68(13), 134433.

Blakely, J., Kim, J., and Potter, H. (1970). “Segregation of carbon to the (100) surface of nickel.” *J. Appl. Phys.*, 41(6), 2693–2697.

Boehm, H., Setton, R., and Stumpp, E. (1986). “Nomenclature and terminology of graphite intercalation compounds.”

Bogár, K., Vidal, P. H., Alcántara León, A. R., and Bäckvall, J.-E. (2007). “Chemoenzymatic dynamic kinetic resolution of allylic alcohols: A highly enantioselective route to acyloin acetates.” *Org. Lett.*, 9(17), 3401–3404.

Bommarius, A., and Riebel, B. (2005). “Biocatalysis, Fundamentals and Applications.” *Synth.-Stuttg.*, 2005, 338–338.

Bordoloi, A., Mathew, N. T., Lefebvre, F., and Halligudi, S. B. (2008). “Inorganic–organic hybrid materials based on functionalized silica and carbon: A comprehensive understanding toward the structural property and catalytic activity difference over mesoporous silica and carbon supports.” *Microporous Mesoporous Mater.*, 115(3), 345–355.

- Bose, S., Kuila, T., Uddin, Md. E., Kim, N. H., Lau, A. K. T., and Lee, J. H. (2010). "In-situ synthesis and characterization of electrically conductive polypyrrole/graphene nanocomposites." *Polymer*, 51(25), 5921–5928.
- Boyle, A., Geniès, E. M., and Lapkowski, M. (1989). "Application of the electronic conducting polymers as sensors: Polyaniline in the solid state for detection of solvent vapours and polypyrrole for detection of biological ions in solutions." *Proc. Int. Conf. Sci. Technol. Synth. Met.*, 28(1), 769–774.
- Bradder, P., Ling, S. K., Wang, S., and Liu, S. (2011). "Dye Adsorption on Layered Graphite Oxide." *J. Chem. Eng. Data*, 56(1), 138–141.
- Briggs, D. (1981). "Handbook of X-ray Photoelectron Spectroscopy C. D. Wanger, W. M. Riggs, L. E. Davis, J. F. Moulder and G. E. Muilenberg Perkin-Elmer Corp., Physical Electronics Division, Eden Prairie, Minnesota, USA, 1979. 190 pp. \$195." *Surf. Interface Anal.*, 3(4), v–v.
- Brodie, B. C. (1859). "XIII. On the atomic weight of graphite." *Philos. Trans. R. Soc. Lond.*, (149), 249–259.
- Brundle, C. R., Chuang, T. J., and Wandelt, K. (1977). "Core and valence level photoemission studies of iron oxide surfaces and the oxidation of iron." *Surf. Sci.*, 68, 459–468.
- Budiman, F., Bashir, N., Tan, W. K., Razak, K. A., Matsuda, A., and Lockman, Z. (2016). "Rapid nanosheets and nanowires formation by thermal oxidation of iron in water vapour and their applications as Cr(VI) adsorbent." *Proc. Int. Conf. Surf. Coat. Nanostructured Mater. NANOSMAT-10 Manch. UK*, 380, 172–177.
- Burroughs, P., Hamnett, A., Orchard, A. F., and Thornton, G. (1976). "Satellite structure in the X-ray photoelectron spectra of some binary and mixed oxides of lanthanum and cerium." *J Chem Soc Dalton Trans*, (17), 1686–1698.
- Buzea, C., Pacheco, I. I., and Robbie, K. (2007). "Nanomaterials and nanoparticles: Sources and toxicity." *Biointerphases*, 2(4), MR17–MR71.
- Cahiez, G., and Meyeux, A. (2010). "Cobalt-Catalyzed Cross-Coupling Reactions." *Chem. Rev.*, 110(3), 1435–1462.
- Cai, K., Shen, W., Ren, B., He, J., Wu, S., and Wang, W. (2017). "A phytic acid modified CoFe<sub>2</sub>O<sub>4</sub> magnetic adsorbent with controllable morphology, excellent selective adsorption for dyes and ultra-strong adsorption ability for metal ions." *Chem. Eng. J.*, 330, 936–946.
- Cai, Y., Tang, B., Bin, L., Huang, S., Li, P., and Fu, F. (2020). "Constructing a multi-layer adsorbent for controllably selective adsorption of various ionic dyes from aqueous solution by simply adjusting pH." *Chem. Eng. J.*, 382, 122829.

- Cao, D., Wang, X., Pan, L., Li, H., Jing, P., Wang, J., and Liu, Q. (2016). “Nonmetal sulfur-doped coral-like cobalt ferrite nanoparticles with enhanced magnetic properties.” *J Mater Chem C*, 4(5), 951–957.
- Cao, L., Rantwijk, F. van, and Sheldon, R. A. (2000). “Cross-linked enzyme aggregates: a simple and effective method for the immobilization of penicillin acylase.” *Org. Lett.*, 2(10), 1361–1364.
- CAO, Y., LIU, C., QIAN, J., CHEN, Z., and CHEN, F. (2017). “Novel 3D porous graphene decorated with Co<sub>3</sub>O<sub>4</sub>/CeO<sub>2</sub> for high performance supercapacitor power cell.” *J. Rare Earths*, 35(10), 995–1001.
- Carolin, C. F., Kumar, P. S., Saravanan, A., Joshiba, G. J., and Naushad, Mu. (2017). “Efficient techniques for the removal of toxic heavy metals from aquatic environment: A review.” *J. Environ. Chem. Eng.*, 5(3), 2782–2799.
- C. H. Woo. (2018). *Desalination and Water Treatment*. Intech Open.
- Chae, H. K., Siberio-Pérez, D. Y., Kim, J., Go, Y., Eddaoudi, M., Matzger, A. J., O’Keeffe, M., and Yaghi, O. M. (2004). “A route to high surface area, porosity and inclusion of large molecules in crystals.” *Nature*, 427(6974), 523.
- Chafai, H., Laabd, M., Elbariji, S., Bazzaoui, M., and Albourine, A. (2017). “Study of congo red adsorption on the polyaniline and polypyrrole.” *J. Dispers. Sci. Technol.*, 38(6), 832–836.
- Chandra, V., Park, J., Chun, Y., Lee, J. W., Hwang, I.-C., and Kim, K. S. (2010). “Water-Dispersible Magnetite-Reduced Graphene Oxide Composites for Arsenic Removal.” *ACS Nano*, 4(7), 3979–3986.
- Chandramohan, P., Srinivasan, M. P., Velmurugan, S., and Narasimhan, S. V. (2011). “Cation distribution and particle size effect on Raman spectrum of CoFe<sub>2</sub>O<sub>4</sub>.” *J. Solid State Chem.*, 184(1), 89–96.
- Chaouati, N., Soualah, A., and Chater, M. (2013). “Adsorption of phenol from aqueous solution onto zeolites Y modified by silylation.” *Comptes Rendus Chim.*, 16(3), 222–228.
- Chen, H., Zheng, Y., Cheng, B., Yu, J., and Jiang, C. (2018). “Chestnut husk-like nickel cobaltite hollow microspheres for the adsorption of Congo red.” *J. Alloys Compd.*, 735, 1041–1051.
- Chen, J., Duan, M., and Chen, G. (2012a). “Continuous mechanical exfoliation of graphene sheets via three-roll mill.” *J. Mater. Chem.*, 22(37), 19625–19628.
- Chen, J., Feng, J., and Yan, W. (2016). “Influence of metal oxides on the adsorption characteristics of PPy/metal oxides for Methylene Blue.” *J. Colloid Interface Sci.*, 475, 26–35.

Chen, K., He, J., Li, Y., Cai, X., Zhang, K., Liu, T., Hu, Y., Lin, D., Kong, L., and Liu, J. (2017). "Removal of cadmium and lead ions from water by sulfonated magnetic nanoparticle adsorbents." *J. Colloid Interface Sci.*, 494, 307–316.

Chen, R., Wang, W., Zhao, X., Zhang, Y., Wu, S., and Li, F. (2014). "Rapid hydrothermal synthesis of magnetic  $\text{Co}_x\text{Ni}_{1-x}\text{Fe}_2\text{O}_4$  nanoparticles and their application on removal of Congo red." *Chem. Eng. J.*, 242, 226–233.

Chen, S., Wu, Q., Mishra, C., Kang, J., Zhang, H., Cho, K., Cai, W., Balandin, A. A., and Ruoff, R. S. (2012b). "Thermal conductivity of isotopically modified graphene." *Nat. Mater.*, 11(3), 203–207.

Chen, X., Hou, Y., Wang, H., Cao, Y., and He, J. (2008). "Facile deposition of Pd nanoparticles on carbon nanotube microparticles and their catalytic activity for Suzuki coupling reactions." *J. Phys. Chem. C*, 112(22), 8172–8176.

Chen, X., Wright, J. V., Conca, J. L., and Peurrung, L. M. (1997). "Evaluation of heavy metal remediation using mineral apatite." *Water. Air. Soil Pollut.*, 98(1), 57–78.

Chen, Y.-H., Hung, H.-H., and Huang, M. H. (2009). "Seed-mediated synthesis of palladium nanorods and branched nanocrystals and their use as recyclable Suzuki coupling reaction catalysts." *J. Am. Chem. Soc.*, 131(25), 9114–9121.

Cheng, B., Le, Y., Cai, W., and Yu, J. (2011). "Synthesis of hierarchical  $\text{Ni}(\text{OH})_2$  and  $\text{NiO}$  nanosheets and their adsorption kinetics and isotherms to Congo red in water." *J. Hazard. Mater.*, 185(2), 889–897.

Chouket, A., Elhouichet, H., Oueslati, M., Koyama, H., Gelloz, B., and Koshida, N. (2007). "Energy transfer in porous-silicon/laser-dye composite evidenced by polarization memory of photoluminescence." *Appl. Phys. Lett.*, 91(21), 211902.

Chung, K.-T. (2016). "Azo dyes and human health: A review." *J. Environ. Sci. Health Part C*, 34(4), 233–261.

Coey, J. M. D., and Cass, S. (2000). "Magnetic water treatment." *J. Magn. Magn. Mater.*, 209(1), 71–74.

Compton, O. C., and Nguyen, S. T. (2010a). "Graphene oxide, highly reduced graphene oxide, and graphene: versatile building blocks for carbon-based materials." *small*, 6(6), 711–723.

Compton, O. C., and Nguyen, S. T. (2010b). "Graphene oxide, highly reduced graphene oxide, and graphene: versatile building blocks for carbon-based materials." *small*, 6(6), 711–723.

Corma, A., Gutiérrez-Puebla, E., Iglesias, M., Monge, A., Pérez-Ferreras, S., and Sánchez, F. (2006). "New Heterogenized Gold (i)-Heterocyclic Carbene Complexes as Reusable Catalysts in Hydrogenation and Cross-Coupling Reactions." *Adv. Synth. Catal.*, 348(14), 1899–1907.

- Cui, K., Yan, B., Xie, Y., Qian, H., Wang, X., Huang, Q., He, Y., Jin, S., and Zeng, H. (2018). “Regenerable urchin-like Fe<sub>3</sub>O<sub>4</sub>@PDA-Ag hollow microspheres as catalyst and adsorbent for enhanced removal of organic dyes.” *J. Hazard. Mater.*, 350, 66–75.
- Cullity, B.D. (1978). “Elements of X-Ray Diffraction.” 2nd Ed.
- Cwik, A., Hell, Z., and Figueras, F. (2005). “Suzuki–Miyaura cross-coupling reaction catalyzed by Pd/MgLa mixed oxide.” *Org. Biomol. Chem.*, 3(24), 4307–4309.
- Dąbrowski, A. (2001). “Adsorption — from theory to practice.” *Adv. Colloid Interface Sci.*, 93(1), 135–224.
- DE LA CRUZ, F. A., and COWLEY, J. M. (1962). “Structure of Graphitic Oxide.” *Nature*, 196(4853), 468–469.
- Değermenci, G. D., Değermenci, N., Ayvaoglu, V., Durmaz, E., Çakır, D., and Akan, E. (2019). “Adsorption of reactive dyes on lignocellulosic waste; characterization, equilibrium, kinetic and thermodynamic studies.” *J. Clean. Prod.*, 225, 1220–1229.
- Demim, S., Drouiche, N., Aouabed, A., Benayad, T., Dendene-Badache, O., and Semsari, S. (2013). “Cadmium and nickel: Assessment of the physiological effects and heavy metal removal using a response surface approach by *L. gibba*.” *Ecol. Eng.*, 61, 426–435.
- Deng, J.-H., Zhang, X.-R., Zeng, G.-M., Gong, J.-L., Niu, Q.-Y., and Liang, J. (2013). “Simultaneous removal of Cd(II) and ionic dyes from aqueous solution using magnetic graphene oxide nanocomposite as an adsorbent.” *Chem. Eng. J.*, 226, 189–200.
- Deng, L., Shi, Z., Peng, X., and Zhou, S. (2016). “Magnetic calcinated cobalt ferrite/magnesium aluminum hydrotalcite composite for enhanced adsorption of methyl orange.” *J. Alloys Compd.*, 688, 101–112.
- Deng, L., Zeng, H., Shi, Z., Zhang, W., and Luo, J. (2018). “Sodium dodecyl sulfate intercalated and acrylamide anchored layered double hydroxides: A multifunctional adsorbent for highly efficient removal of Congo red.” *J. Colloid Interface Sci.*, 521, 172–182.
- Dey, S., Dhal, G. C., Mohan, D., Prasad, R., and Gupta, R. N. (2018). “Cobalt doped CuMnOx catalysts for the preferential oxidation of carbon monoxide.” *Appl. Surf. Sci.*, 441, 303–316.
- Dikin, D. A., Stankovich, S., Zimney, E. J., Piner, R. D., Dommett, G. H., Evmenenko, G., Nguyen, S. T., and Ruoff, R. S. (2007). “Preparation and characterization of graphene oxide paper.” *Nature*, 448(7152), 457.
- Du, H., Xie, Y., Xia, C., Wang, W., and Tian, F. (2014). “Electrochemical capacitance of polypyrrole–titanium nitride and polypyrrole–titania nanotube hybrids.” *New J. Chem.*, 38(3), 1284–1293.

- Du, X., Jiang, D., Chen, S., Dai, L., Zhou, L., Hao, N., You, T., Mao, H., and Wang, K. (2017). “CeO<sub>2</sub> nanocrystallines ensemble-on-nitrogen-doped graphene nanocomposites: one-pot, rapid synthesis and excellent electrocatalytic activity for enzymatic biosensing.” *Biosens. Bioelectron.*, 89, 681–688.
- Du, X., Skachko, I., Barker, A., and Andrei, E. Y. (2008). “Approaching ballistic transport in suspended graphene.” *Nat. Nanotechnol.*, 3(8), 491–495.
- Dujardin, E., Thio, T., Lezec, H., and Ebbesen, T. W. (2001). “Fabrication of mesoscopic devices from graphite microdisks.” *Appl. Phys. Lett.*, 79(15), 2474–2476.
- Ebbesen, T. W., and Hiura, H. (1995). “Graphene in 3-dimensions: Towards graphite origami.”
- Einollahi Peer, F., Bahramifar, N., and Younesi, H. (2018). “Removal of Cd (II), Pb (II) and Cu (II) ions from aqueous solution by polyamidoamine dendrimer grafted magnetic graphene oxide nanosheets.” *J. Taiwan Inst. Chem. Eng.*, 87, 225–240.
- Elias, D. C., Nair, R. R., Mohiuddin, T. M. G., Morozov, S. V., Blake, P., Halsall, M. P., Ferrari, A. C., Boukhvalov, D. W., Katsnelson, M. I., Geim, A. K., and Novoselov, K. S. (2009). “Control of Graphene’s Properties by Reversible Hydrogenation: Evidence for Graphane.” *Science*, 323(5914), 610–613.
- Elmorsi, R. R., El-Wakeel, S. T., Shehab El-Dein, W. A., Lotfy, H. R., Rashwan, W. E., Nagah, M., Shaaban, S. A., Sayed Ahmed, S. A., El-Sherif, I. Y., and Abou-El-Sherbini, K. S. (2019). “Adsorption of Methylene Blue and Pb<sup>2+</sup> by using acid-activated *Posidonia oceanica* waste.” *Sci. Rep.*, 9(1), 3356.
- Eriksson, M., Lundström, I., and Ekedahl, L.-G. (1997). “A model of the Temkin isotherm behavior for hydrogen adsorption at Pd–SiO<sub>2</sub> interfaces.” *J. Appl. Phys.*, 82(6), 3143–3146.
- Facchi, D. P., Cazzetta, A. L., Canesin, E. A., Almeida, V. C., Bonafé, E. G., Kipper, M. J., and Martins, A. F. (2018). “New magnetic chitosan/alginate/Fe<sub>3</sub>O<sub>4</sub>@SiO<sub>2</sub> hydrogel composites applied for removal of Pb(II) ions from aqueous systems.” *Chem. Eng. J.*, 337, 595–608.
- Fan, L.-Q., Liu, G.-J., Wu, J.-H., Liu, L., Lin, J.-M., and Wei, Y.-L. (2014). “Asymmetric supercapacitor based on graphene oxide/polypyrrole composite and activated carbon electrodes.” *Electrochimica Acta*, 137, 26–33.
- Fan, X., Guan, J., Cao, X., Wang, W., and Mou, F. (2010). “Low-Temperature Synthesis, Magnetic and Microwave Electromagnetic Properties of Substoichiometric Spinel Cobalt Ferrite Octahedra.” *Eur. J. Inorg. Chem.*, 2010(3), 419–426.
- Fan, X., Yang, Z., and He, N. (2015a). “Hierarchical nanostructured polypyrrole/graphene composites as supercapacitor electrode.” *RSC Adv.*, 5(20), 15096–15102.

- Fan, X., Zhang, G., and Zhang, F. (2015b). "Multiple roles of graphene in heterogeneous catalysis." *Chem. Soc. Rev.*, 44(10), 3023–3035.
- Fan, X., Zhang, G., and Zhang, F. (2015c). "Multiple roles of graphene in heterogeneous catalysis." *Chem. Soc. Rev.*, 44(10), 3023–3035.
- Fareghi-Alamdari, R., Haqiqi, M. G., and Zekri, N. (2016). "Immobilized Pd (0) nanoparticles on phosphine-functionalized graphene as a highly active catalyst for Heck, Suzuki and N-arylation reactions." *New J. Chem.*, 40(2), 1287–1296.
- Farghali, A. A., Bahgat, M., ElRouby, W. M. A., and Khedr, M. H. (2013). "Decoration of multi-walled carbon nanotubes (MWCNTs) with different ferrite nanoparticles and its use as an adsorbent." *J. Nanostructure Chem.*, 3(1), 50.
- Farhadi, S., Javanmard, M., and Nadri, G. (2016). "Characterization of Cobalt Oxide Nanoparticles Prepared by the Thermal Decomposition of  $[\text{Co}(\text{NH}_3)_5(\text{H}_2\text{O})](\text{NO}_3)_3$  Complex and Study of Their Photocatalytic Activity." *Acta Chim. Slov.*, 63, 335–343.
- Feng, Y.-S., Lin, X.-Y., Hao, J., and Xu, H.-J. (2014). "Pd–Co bimetallic nanoparticles supported on graphene as a highly active catalyst for Suzuki–Miyaura and Sonogashira cross-coupling reactions." *Tetrahedron*, 70(34), 5249–5253.
- Ferrari, A. C., Meyer, J. C., Scardaci, V., Casiraghi, C., Lazzeri, M., Mauri, F., Piscanec, S., Jiang, D., Novoselov, K. S., Roth, S., and Geim, A. K. (2006). "Raman Spectrum of Graphene and Graphene Layers." *Phys. Rev. Lett.*, 97(18), 187401.
- Feynman, R. (1959). "There's plenty of room at the bottom: An invitation to enter a new physics." *First Present. Am. Phys. Soc. Calif. Inst. Technol. Dec.*, 29.
- Fihri, A., Cha, D., Bouhrara, M., Almana, N., and Polshettiwar, V. (2012). "Fibrous Nano-Silica (KCC-1)-Supported Palladium Catalyst: Suzuki Coupling Reactions Under Sustainable Conditions." *ChemSusChem*, 5(1), 85–89.
- Filipič, M. (2012). "Mechanisms of cadmium induced genomic instability." *Micronutr. Genomic Stab.*, 733(1), 69–77.
- F. Machado, B., and Serp, P. (2012). "Graphene -based materials for catalysis." *Catal. Sci. Technol.*, 2(1), 54–75.
- Freundlich, H. (1907). "Über die adsorption in lösungen." *Z. Für Phys. Chem.*, 57(1), 385–470.
- Fu, Y., Chen, H., Sun, X., and Wang, X. (2012). "Combination of cobalt ferrite and graphene: High-performance and recyclable visible-light photocatalysis." *Appl. Catal. B Environ.*, 111–112, 280–287.

- Gandhi, N., Singh, K., Ohlan, A., Singh, D. P., and Dhawan, S. K. (2011). “Thermal, dielectric and microwave absorption properties of polyaniline–CoFe<sub>2</sub>O<sub>4</sub> nanocomposites.” *Compos. Sci. Technol.*, 71(15), 1754–1760.
- Gangatharan, S., Chidambaram, V., and Sivakumar, K. (2010). “Synthesis, Structural and Dielectric Studies of Nickel Substituted Cobalt-Zinc Ferrite.” *Mater. Sci. Appl.*, 01.
- Gangopadhyay, S., Chung, S. W., Thiruvengadathan, R., Staley, C. S., Gangopadhyay, K., and Raymond, K. E. (2019). “Hierarchical self-assembled energetic materials and formation methods.”
- Gao, X., Yang, L., Petros, J. A., Marshall, F. F., Simons, J. W., and Nie, S. (2005). “In vivo molecular and cellular imaging with quantum dots.” *Curr. Opin. Biotechnol.*, 16(1), 63–72.
- Gawande, M. B., Goswami, A., Felpin, F.-X., Asefa, T., Huang, X., Silva, R., Zou, X., Zboril, R., and Varma, R. S. (2016). “Cu and Cu-based nanoparticles: synthesis and applications in catalysis.” *Chem. Rev.*, 116(6), 3722–3811.
- Geim, A. K. (2009). “Graphene: status and prospects.” *science*, 324(5934), 1530–1534.
- Geim, A. K., and Novoselov, K. S. (2010). “The rise of graphene.” *Nanosci. Technol. Collect. Rev. Nat. J.*, World Scientific, 11–19.
- Gemeay, A. H., El-Halwagy, M. E., El-Sharkawy, R. G., and Zaki, A. B. (2017). “Chelation mode impact of copper (II)-aminosilane complexes immobilized onto graphene oxide as an oxidative catalyst.” *J. Environ. Chem. Eng.*, 5(3), 2761–2772.
- Ghaemi, N., and Safari, P. (2018). “Nano-porous SAPO-34 enhanced thin-film nanocomposite polymeric membrane: Simultaneously high water permeation and complete removal of cationic/anionic dyes from water.” *J. Hazard. Mater.*, 358, 376–388.
- Gilman, J. W. (1999). “Flammability and thermal stability studies of polymer layered-silicate (clay) nanocomposites” This work was carried out by the National Institute of Standards and Technology (NIST), an agency of the U. S. government, and by statute is not subject to copyright in the United States.1.” *Appl. Clay Sci.*, 15(1), 31–49.
- Gisi, S. D., Lofrano, G., Grassi, M., and Notarnicola, M. (2016). “Characteristics and adsorption capacities of low-cost sorbents for wastewater treatment: A review.” *Sustain. Mater. Technol.*, 9, 10–40.
- González, J. A., Villanueva, M. E., Piehl, L. L., and Copello, G. J. (2015). “Development of a chitin/graphene oxide hybrid composite for the removal of pollutant dyes: Adsorption and desorption study.” *Chem. Eng. J.*, 280, 41–48.
- Gosetti, F., Gianotti, V., Angioi, S., Polati, S., Marengo, E., and Gennaro, M. C. (2004). “Oxidative degradation of food dye E133 Brilliant Blue FCF: Liquid chromatography–



electrospray mass spectrometry identification of the degradation pathway.” *Food Sci.*, 1054(1), 379–387.

Gosmini, C., Bégouin, J.-M., and Moncomble, A. (2008). “Cobalt-catalyzed cross-coupling reactions.” *Chem. Commun.*, (28), 3221.

Grant, J., and Haas, T. (1970). “A study of Ru (0001) and Rh (111) surfaces using LEED and Auger electron spectroscopy.” *Surf. Sci.*, 21(1), 76–85.

Guideline, P.-B. T. (2001). “OECD guideline for the testing of chemicals.” *The Hershberger*, 601, 858.

Guo, Y., Li, L., Song, L., Wu, M., Gao, Y., Chen, J., Mao, C., Song, J., and Niu, H. (2019). “Co<sup>2+</sup> induced phase transformation from  $\delta$ - to  $\alpha$ -MnO<sub>2</sub> and their hierarchical  $\alpha$ -MnO<sub>2</sub>@ $\delta$ -MnO<sub>2</sub> nanostructures for efficient asymmetric supercapacitors.” *J Mater Chem A*, 7(20), 12661–12668.

Guram, A. S., King, A. O., Allen, J. G., Wang, X., Schenkel, L. B., Chan, J., Bunel, E. E., Faul, M. M., Larsen, R. D., and Martinelli, M. J. (2006). “New air-stable catalysts for general and efficient Suzuki–Miyaura cross-coupling reactions of heteroaryl chlorides.” *Org. Lett.*, 8(9), 1787–1789.

H. M. F. Freundlich. (1906). “Over the adsorption in solution.” *J. Phys. Chem.*, 57, 385–471.

Haddad, M. E., Slimani, R., Mamouni, R., ElAntri, S., and Lazar, S. (2013). “Removal of two textile dyes from aqueous solutions onto calcined bones.” *J. Assoc. Arab Univ. Basic Appl. Sci.*, 14(1), 51–59.

Haldorai, Y., Giribabu, K., Hwang, S.-K., Kwak, C. H., Huh, Y. S., and Han, Y.-K. (2016). “Facile synthesis of  $\alpha$ -MnO<sub>2</sub> nanorod/graphene nanocomposite paper electrodes using a 3D precursor for supercapacitors and sensing platform to detect 4-nitrophenol.” *Electrochimica Acta*, 222, 717–727.

Hancock, Y. (2011). “The 2010 Nobel Prize in physics—ground-breaking experiments on graphene.” *J. Phys. Appl. Phys.*, 44(47), 473001.

Handa, S., Wang, Y., Gallou, F., and Lipshutz, B. H. (2015). “Sustainable Fe–ppm Pd nanoparticle catalysis of Suzuki–Miyaura cross-couplings in water.” *Science*, 349(6252), 1087–1091.

Harris, V. G. (2012). “Modern Microwave Ferrites.” *IEEE Trans. Magn.*, 48(3), 1075–1104.

Hass, J., De Heer, W., and Conrad, E. (2008). “The growth and morphology of epitaxial multilayer graphene.” *J. Phys. Condens. Matter*, 20(32), 323202.

Hassan, A., Khan, M. A., Shahid, M., Asghar, M., Shakir, I., Naseem, S., Riaz, S., and Warsi, M. F. (2015). “Nanocrystalline Zn<sub>1-x</sub>Co<sub>0.5x</sub>Ni<sub>0.5x</sub>Fe<sub>2</sub>O<sub>4</sub> ferrites: Fabrication via co-

precipitation route with enhanced magnetic and electrical properties.” *J. Magn. Magn. Mater.*, 393, 56–61.

He, S., Li, Y., Weng, L., Wang, J., He, J., Liu, Y., Zhang, K., Wu, Q., Zhang, Y., and Zhang, Z. (2018a). “Competitive adsorption of Cd<sup>2+</sup>, Pb<sup>2+</sup> and Ni<sup>2+</sup> onto Fe<sup>3+</sup>-modified argillaceous limestone: Influence of pH, ionic strength and natural organic matters.” *Sci. Total Environ.*, 637–638, 69–78.

He, Z., Jiang, Y., Li, Y., Zhu, J., Zhou, H., Meng, W., Wang, L., and Dai, L. (2018b). “Carbon layer-exfoliated, wettability-enhanced, SO<sub>3</sub>H-functionalized carbon paper: A superior positive electrode for vanadium redox flow battery.” *Carbon*, 127, 297–304.

Hernandez, Y., Nicolosi, V., Lotya, M., Blighe, F. M., Sun, Z., De, S., McGovern, I., Holland, B., Byrne, M., and Gun’Ko, Y. K. (2008). “High-yield production of graphene by liquid-phase exfoliation of graphite.” *Nat. Nanotechnol.*, 3(9), 563–568.

Hilpert, S. (1909). “Correspondence as to Structure and Origin in Magnetic properties of Ferrite and Iron Oxide.” *Ber Dtsch Chem Ges*, 42, 2248–2261.

Hontoria-Lucas, C., López-Peinado, A. J., López-González, J. de D., Rojas-Cervantes, M. L., and Martín-Aranda, R. M. (1995). “Study of oxygen-containing groups in a series of graphite oxides: Physical and chemical characterization.” *Carbon*, 33(11), 1585–1592.

Hou, X., Feng, J., Liu, X., Ren, Y., Fan, Z., Wei, T., Meng, J., and Zhang, M. (2011). “Synthesis of 3D porous ferromagnetic NiFe<sub>2</sub>O<sub>4</sub> and using as novel adsorbent to treat wastewater.” *J. Colloid Interface Sci.*, 362(2), 477–485.

Hou, X., Feng, J., Ren, Y., Fan, Z., and Zhang, M. (2010). “Synthesis and adsorption properties of spongelike porous MnFe<sub>2</sub>O<sub>4</sub>.” *Colloids Surf. Physicochem. Eng. Asp.*, 363(1), 1–7.

Hu, H., Liu, J., Xu, Z., Zhang, L., Cheng, B., and Ho, W. (2019). “Hierarchical porous Ni/Co-LDH hollow dodecahedron with excellent adsorption property for Congo red and Cr(VI) ions.” *Appl. Surf. Sci.*, 478, 981–990.

Hu, J., Shao, D., Chen, C., Sheng, G., Li, J., Wang, X., and Nagatsu, M. (2010). “Plasma-Induced Grafting of Cyclodextrin onto Multiwall Carbon Nanotube/Iron Oxides for Adsorbent Application.” *J. Phys. Chem. B*, 114(20), 6779–6785.

Hu, L., Yang, Z., Cui, L., Li, Y., Ngo, H. H., Wang, Y., Wei, Q., Ma, H., Yan, L., and Du, B. (2016). “Fabrication of hyperbranched polyamine functionalized graphene for high-efficiency removal of Pb(II) and methylene blue.” *Chem. Eng. J.*, 287, 545–556.

Huang, Q., Zhou, L., Jiang, X., Zhou, Y., Fan, H., and Lang, W. (2014). “Synthesis of Copper Graphene Materials Functionalized by Amino Acids and Their Catalytic Applications.” *ACS Appl. Mater. Interfaces*, 6(16), 13502–13509.

- Huang, Z., Huang, Z., Feng, L., Luo, X., Wu, P., Cui, L., and Mao, X. (2018). “Modified cellulose by polyethyleneimine and ethylenediamine with induced Cu(II) and Pb(II) adsorption potentialities.” *Carbohydr. Polym.*, 202, 470–478.
- Hummers Jr, W. S., and Offeman, R. E. (1958). “Preparation of graphitic oxide.” *J. Am. Chem. Soc.*, 80(6), 1339–1339.
- Iijima, S. (1991). “Helical microtubules of graphitic carbon.” *Nature*, 354(6348), 56–58.
- Ikram, S., Jacob, J., Mahmood, K., Mehboob, K., Maheen, M., Ali, A., Amin, N., Hussain, S., Ashraf, F., and Ilyas, S. Z. (2020). “A Kinetic study of Tb<sup>3+</sup> and Dy<sup>3+</sup> co-substituted CoFe<sub>2</sub>O<sub>4</sub> spinel ferrites using temperature dependent XRD, XPS and SQUID measurements.” *Ceram. Int.*, 46(10, Part B), 15943–15948.
- Inyang, M., Gao, B., Zimmerman, A., Zhang, M., and Chen, H. (2014). “Synthesis, characterization, and dye sorption ability of carbon nanotube–biochar nanocomposites.” *Chem. Eng. J.*, 236, 39–46.
- ISO, T. (2008). “27687.” *Nanotechnologies–Terminology Defin. Nano-Objects–nanoparticle Nanofibre Nanoplate.*
- Jana, S. K., Majumder, S., Satpati, B., Mishra, S. K., Srivastava, R. K., and Banerjee, S. (2015). “Enhancement of photoluminescence emission and anomalous photoconductivity properties of Fe<sub>3</sub>O<sub>4</sub>@SiO<sub>2</sub> core–shell microspheres.” *RSC Adv*, 5(47), 37729–37736.
- Jha, P., Jobby, R., and Desai, N. S. (2016). “Remediation of textile azo dye acid red 114 by hairy roots of *Ipomoea carnea* Jacq. and assessment of degraded dye toxicity with human keratinocyte cell line.” *J. Hazard. Mater.*, 311, 158–167.
- Jia, Y., Wu, C., Lee, B. W., Liu, C., Kang, S., Lee, T., Park, Y. C., Yoo, R., and Lee, W. (2017). “Magnetically separable sulfur-doped SnFe<sub>2</sub>O<sub>4</sub>/graphene nanohybrids for effective photocatalytic purification of wastewater under visible light.” *J. Hazard. Mater.*, 338, 447–457.
- Jiang, C., Wang, X., Qin, D., Da, W., Hou, B., Hao, C., and Wu, J. (2019). “Construction of magnetic lignin-based adsorbent and its adsorption properties for dyes.” *J. Hazard. Mater.*, 369, 50–61.
- Jiang, L., Yao, M., Liu, B., Li, Q., Liu, R., Lv, H., Lu, S., Gong, C., Zou, B., Cui, T., Liu, B., Hu, G., and Wågberg, T. (2012). “Controlled Synthesis of CeO<sub>2</sub>/Graphene Nanocomposites with Highly Enhanced Optical and Catalytic Properties.” *J. Phys. Chem. C*, 116(21), 11741–11745.
- Kabalka, G. W., Pagni, R. M., and Hair, C. M. (1999). “Solventless Suzuki coupling reactions on palladium-doped KF/Al<sub>2</sub>O<sub>3</sub>.” *Org. Lett.*, 1(9), 1423–1425.

- Kafshgari, L. A., Ghorbani, M., and Azizi, A. (2017). "Fabrication and investigation of MnFe<sub>2</sub>O<sub>4</sub>/MWCNTs nanocomposite by hydrothermal technique and adsorption of cationic and anionic dyes." *Appl. Surf. Sci.*, 419, 70–83.
- Kalavathy, M. H., and Miranda, L. R. (2010). "Comparison of copper adsorption from aqueous solution using modified and unmodified Hevea brasiliensis saw dust." *Desalination*, 255(1), 165–174.
- Kant, R. (2012). "Textile dyeing industry an environmental hazard." *Nat. Sci.*, 04.
- Kashinath, L., Namratha, K., and Byrappa, K. (2019). "Microwave mediated synthesis and characterization of CeO<sub>2</sub>-GO hybrid composite for removal of chromium ions and its antibacterial efficiency." *J. Environ. Sci.*, 76, 65–79.
- Kavitha, D., and Namasivayam, C. (2007). "Experimental and kinetic studies on methylene blue adsorption by coir pith carbon." *Bioresour. Technol.*, 98(1), 14–21.
- Kharisov, B. I., and Kharissova, O. V. (2019). *Carbon allotropes: metal-complex chemistry, properties and applications*. Springer.
- Khatri, P. K., Choudhary, S., Singh, R., Jain, S. L., and Khatri, O. P. (2014). "Grafting of a rhenium-oxo complex on Schiff base functionalized graphene oxide: an efficient catalyst for the oxidation of amines." *Dalton Trans.*, 43(21), 8054–8061.
- Khurana, I., Saxena, A., Bharti, Khurana, J. M., and Rai, P. K. (2017). "Removal of Dyes Using Graphene-Based Composites: a Review." *Water. Air. Soil Pollut.*, 228(5), 180.
- Kim, W. (2015). "Fabrication and characterization of graphene-based electronic devices."
- Kong, D., Zheng, X., Tao, Y., Lv, W., Gao, Y., Zhi, L., and Yang, Q.-H. (2016). "Porous graphene oxide-based carbon artefact with high capacity for methylene blue adsorption." *Adsorption*, 22(8), 1043–1050.
- Kong, J. (2003). *Carbon nanotubes: Synthesis, integration and properties*. Stanford University.
- Kong, S., Wang, Y., Zhan, H., Liu, M., Liang, L., and Hu, Q. (2014). "Competitive adsorption of humic acid and arsenate on nanoscale iron–manganese binary oxide-loaded zeolite in groundwater." *J. Geochem. Explor.*, 144, 220–225.
- Konicki, W., Hełminiak, A., Arabczyk, W., and Mijowska, E. (2018). "Adsorption of cationic dyes onto Fe@graphite core–shell magnetic nanocomposite: Equilibrium, kinetics and thermodynamics." *Chem. Eng. Res. Des.*, 129, 259–270.
- Kreuter, J. (2014). *Colloidal drug delivery systems*. CRC Press.
- Kroto, H. W., Allaf, A., and Balm, S. (1991). "C<sub>60</sub>: Buckminsterfullerene." *Chem. Rev.*, 91(6), 1213–1235.

Kuang, P., Zhu, B., Li, Y., Liu, H., Yu, J., and Fan, K. (2018). "Graphdiyne: a superior carbon additive to boost the activity of water oxidation catalysts." *Nanoscale Horiz.*, 3(3), 317–326.

Kuhlbusch, T. A., Asbach, C., Fissan, H., Göhler, D., and Stintz, M. (2011). "Nanoparticle exposure at nanotechnology workplaces: A review." *Part. Fibre Toxicol.*, 8(1), 22.

Kuila, T., Bose, S., Mishra, A. K., Khanra, P., Kim, N. H., and Lee, J. H. (2012). "Chemical functionalization of graphene and its applications." *Prog. Mater. Sci.*, 57(7), 1061–1105.

Kulandaivalu, S., Suhaimi, N., and Sulaiman, Y. (2019). "Unveiling high specific energy supercapacitor from layer-by-layer assembled polypyrrole/graphene oxide|polypyrrole/manganese oxide electrode material." *Sci. Rep.*, 9(1), 4884.

Kumar, G. P., Kumar, P. A., Chakraborty, S., and Ray, M. (2007a). "Uptake and desorption of copper ion using functionalized polymer coated silica gel in aqueous environment." *Sep. Purif. Technol.*, 57(1), 47–56.

Kumar, P. A., Ray, M., and Chakraborty, S. (2007b). "Hexavalent chromium removal from wastewater using aniline formaldehyde condensate coated silica gel." *J. Hazard. Mater.*, 143(1), 24–32.

Kumar, R., and Lal, S. (2014). "Synthesis of organic nanoparticles and their applications in drug delivery and food nanotechnology: a review. *J Nanomater Mol Nanotechnol* 3: 4." *of*, 11, 2.

Kumar, S., Ojha, A. K., Patrice, D., Yadav, B. S., and Materny, A. (2016). "One-step in situ synthesis of CeO<sub>2</sub> nanoparticles grown on reduced graphene oxide as an excellent fluorescent and photocatalyst material under sunlight irradiation." *Phys Chem Chem Phys*, 18(16), 11157–11167.

Kumar, V., Kumar, V., Som, S., Purohit, L. P., Ntwaeaborwa, O. M., and Swart, H. C. (2014). "Role of swift heavy ions irradiation on the emission of boron doped ZnO thin films for near white light application." *J. Alloys Compd.*, 594, 32–38.

Kumari, S., Shekhar, A., and Pathak, D. D. (2016). "Synthesis and characterization of a Cu(ii) Schiff base complex immobilized on graphene oxide and its catalytic application in the green synthesis of propargylamines." *RSC Adv*, 6(19), 15340–15344.

Kunde, G. B., Sehgal, B., and Ganguli, A. K. (2019). "Synthesis of mesoporous rebar MWCNT/alumina composite (RMAC) nodules for the effective removal of methylene blue and Cr (VI) from an aqueous medium." *J. Hazard. Mater.*, 374, 140–151.

Kuzminska, M., Carlier, N., Backov, R., and Gaigneaux, E. M. (2015). "Magnetic nanoparticles: Improving chemical stability via silica coating and organic grafting with silanes for acidic media catalytic reactions." *Appl. Catal. Gen.*, 505, 200–212.

- Kyzas, G. Z., Siafaka, P. I., Pavlidou, E. G., Chrissafis, K. J., and Bikiaris, D. N. (2015). "Synthesis and adsorption application of succinyl-grafted chitosan for the simultaneous removal of zinc and cationic dye from binary hazardous mixtures." *Chem. Eng. J.*, 259, 438–448.
- Lagergren, S. (1898). "Zur theorie der sogenannten adsorption geloster stoffe."
- Lamei, K., Eshghi, H., Bakavoli, M., and Rostamnia, S. (2017). "Highly dispersed copper/ppm palladium nanoparticles as novel magnetically recoverable catalyst for Suzuki reaction under aqueous conditions at room temperature." *Appl. Organomet. Chem.*, 31(11), n/a-n/a.
- Langmuir, I. (1916). "THE CONSTITUTION AND FUNDAMENTAL PROPERTIES OF SOLIDS AND LIQUIDS. PART I. SOLIDS." *J. Am. Chem. Soc.*, 38(11), 2221–2295.
- Leadbeater, N. E., and Marco, M. (2003). "Transition-metal-free Suzuki-type coupling reactions." *Angew. Chem. Int. Ed.*, 42(12), 1407–1409.
- Lee, A., Elam, J. W., and Darling, S. B. (2016a). "Membrane materials for water purification: design, development, and application." *Env. Sci Water Res Technol*, 2(1), 17–42.
- Lee, C., Wei, X., Kysar, J. W., and Hone, J. (2008). "Measurement of the elastic properties and intrinsic strength of monolayer graphene." *science*, 321(5887), 385–388.
- Lee, J. Y., Shin, J.-H., Lee, G.-H., and Lee, C.-H. (2016b). "Two-Dimensional Semiconductor Optoelectronics Based on van der Waals Heterostructures." *Nanomaterials*, 6(11).
- Lei, C., Pi, M., Cheng, B., Jiang, C., and Qin, J. (2018). "Fabrication of hierarchical porous ZnO/NiO hollow microspheres for adsorptive removal of Congo red." *Appl. Surf. Sci.*, 435, 1002–1010.
- Lei, C., Zhu, X., Le, Y., Zhu, B., Yu, J., and Ho, W. (2016a). "Hierarchically porous NiO–Al<sub>2</sub>O<sub>3</sub> nanocomposite with enhanced Congo red adsorption in water." *RSC Adv.*, 6(13), 10272–10279.
- Lei, C., Zhu, X., Zhu, B., Yu, J., and Ho, W. (2016b). "Hierarchical NiO–SiO<sub>2</sub> composite hollow microspheres with enhanced adsorption affinity towards Congo red in water." *J. Colloid Interface Sci.*, 466, 238–246.
- Li, J., Fan, Q., Wu, Y., Wang, X., Chen, C., Tang, Z., and Wang, X. (2016). "Magnetic polydopamine decorated with Mg–Al LDH nanoflakes as a novel bio-based adsorbent for simultaneous removal of potentially toxic metals and anionic dyes." *J Mater Chem A*, 4(5), 1737–1746.
- Li, J., Feng, J., and Yan, W. (2013a). "Excellent adsorption and desorption characteristics of polypyrrole/TiO<sub>2</sub> composite for Methylene Blue." *Appl. Surf. Sci.*, 279, 400–408.

- Li, W.-G., Gong, X.-J., Wang, K., Zhang, X.-R., and Fan, W.-B. (2014). “Adsorption characteristics of arsenic from micro-polluted water by an innovative coal-based mesoporous activated carbon.” *Bioresour. Technol.*, 165, 166–173.
- Li, Y., Hong, X. M., Collard, D. M., and El-Sayed, M. A. (2000). “Suzuki cross-coupling reactions catalyzed by palladium nanoparticles in aqueous solution.” *Org. Lett.*, 2(15), 2385–2388.
- Li, Y.-S., Church, J. S., Woodhead, A. L., and Moussa, F. (2010). “Preparation and characterization of silica coated iron oxide magnetic nano-particles.” *Spectrochim. Acta. A. Mol. Biomol. Spectrosc.*, 76(5), 484–489.
- Li, Z., Wu, S., Ding, H., Zheng, D., Hu, J., Wang, X., Huo, Q., Guan, J., and Kan, Q. (2013b). “Immobilized Cu (II) and Co (II) salen complexes on graphene oxide and their catalytic activity for aerobic epoxidation of styrene.” *New J. Chem.*, 37(5), 1561–1568.
- Li, Z., Wu, S., Ding, H., Zheng, D., Hu, J., Wang, X., Huo, Q., Guan, J., and Kan, Q. (2013c). “Immobilized Cu( ii ) and Co( ii ) salen complexes on graphene oxide and their catalytic activity for aerobic epoxidation of styrene.” *New J. Chem.*, 37(5), 1561–1568.
- Liang, H., Meng, F., Cabán-Acevedo, M., Li, L., Forticaux, A., Xiu, L., Wang, Z., and Jin, S. (2015). “Hydrothermal Continuous Flow Synthesis and Exfoliation of NiCo Layered Double Hydroxide Nanosheets for Enhanced Oxygen Evolution Catalysis.” *Nano Lett.*, 15(2), 1421–1427.
- Lima, É. C., Adebayo, M. A., and Machado, F. M. (2015). “Kinetic and Equilibrium Models of Adsorption.” *Carbon Nanomater. Adsorbents Environ. Biol. Appl.*, C. P. Bergmann and F. M. Machado, eds., Cham: Springer International Publishing, 33–69.
- Lima, E. C., Hosseini-Bandegharaei, A., Moreno-Piraján, J. C., and Anastopoulos, I. (2019). “A critical review of the estimation of the thermodynamic parameters on adsorption equilibria. Wrong use of equilibrium constant in the Van’t Hoof equation for calculation of thermodynamic parameters of adsorption.” *J. Mol. Liq.*, 273, 425–434.
- Lin, R., Yue, W., Niu, F., and Ma, J. (2016). “Novel strategy for the preparation of graphene-encapsulated mesoporous metal oxides with enhanced lithium storage.” *Electrochimica Acta*, 205, 85–94.
- Liu, B., Reddy, C. D., Jiang, J., Baimova, J. A., Dmitriev, S. V., Nazarov, A. A., and Zhou, K. (2012). “Morphology and in-plane thermal conductivity of hybrid graphene sheets.” *Appl. Phys. Lett.*, 101(21), 211909.

- Liu, G., Liao, L., Dai, Z., Qi, Q., Wu, J., Ma, L. Q., Tang, C., and Xu, J. (2020). “Organic adsorbents modified with citric acid and Fe<sub>3</sub>O<sub>4</sub> enhance the removal of Cd and Pb in contaminated solutions.” *Chem. Eng. J.*, 395, 125108.
- Liu, S., Li, J., Xu, S., Wang, M., Zhang, Y., and Xue, X. (2019). “A modified method for enhancing adsorption capability of banana pseudostem biochar towards methylene blue at low temperature.” *Bioresour. Technol.*, 282, 48–55.
- Liu, T., Zhang, L., You, W., and Yu, J. (2018). “Core–Shell Nitrogen-Doped Carbon Hollow Spheres/Co<sub>3</sub>O<sub>4</sub> Nanosheets as Advanced Electrode for High-Performance Supercapacitor.” *Small*, 14(12), 1702407.
- Liu, W., Bao, J., Guan, M., Zhao, Y., Lian, J., Qiu, J., Xu, L., Huang, Y., Qian, J., and Li, H. (2017). “Nickel–cobalt-layered double hydroxide nanosheet arrays on Ni foam as a bifunctional electrocatalyst for overall water splitting.” *Dalton Trans.*, 46(26), 8372–8376.
- Liu, X., and Deng, M. (2002). “Remarkable co-catalysis by copper (I) oxide in the palladium catalyzed cross-coupling of arylboronic acids with ethyl bromoacetate.” *Chem. Commun.*, (6), 622–623.
- Liu, Y. (2009). “Is the Free Energy Change of Adsorption Correctly Calculated?” *J. Chem. Eng. Data*, 54(7), 1981–1985.
- Liu, Y., Khemtong, C., and Hu, J. (2004). “Synthesis and catalytic activity of a poly(N,N-dialkylcarbodiimide)/palladium nanoparticle composite: a case in the Suzuki coupling reaction using microwave and conventional heating.” *Chem Commun*, (4), 398–399.
- Liu, Y., Zhou, J., Tang, J., and Tang, W. (2015). “Three-Dimensional, Chemically Bonded Polypyrrole/Bacterial Cellulose/Graphene Composites for High-Performance Supercapacitors.” *Chem. Mater.*, 27(20), 7034–7041.
- Lobato, N. C. C., Ferreira, A. [de M., Weidler, P. G., Franzreb, M., and Mansur, M. B. (2019). “Improvement of magnetic solvent extraction using functionalized silica-coated Fe<sub>3</sub>O<sub>4</sub> nanoparticles.” *Sep. Purif. Technol.*, 229, 115839.
- Lu, L., Li, J., Yu, J., Song, P., and Ng, D. H. L. (2016). “A hierarchically porous MgFe<sub>2</sub>O<sub>4</sub>/γ-Fe<sub>2</sub>O<sub>3</sub> magnetic microspheres for efficient removals of dye and pharmaceutical from water.” *Chem. Eng. J.*, 283, 524–534.
- Lu, X., Yu, M., Huang, H., and Ruoff, R. S. (1999). “Tailoring graphite with the goal of achieving single sheets.” *Nanotechnology*, 10(3), 269.
- Lv, D., Sung, H.-S., Li, X., Zhang, X., Li, Z., and Chen, D. (2020). “Effects of single layer graphene and graphene oxide modification on the properties of phthalocyanine blue pigments.” *Dyes Pigments*, 180, 108449.



- Ma, F., Zhang, D., Zhang, N., Huang, T., and Wang, Y. (2018a). "Polydopamine-assisted deposition of polypyrrole on electrospun poly(vinylidene fluoride) nanofibers for bidirectional removal of cation and anion dyes." *Chem. Eng. J.*, 354, 432–444.
- Ma, F., Zhang, D., Zhang, N., Huang, T., and Wang, Y. (2018b). "Polydopamine-assisted deposition of polypyrrole on electrospun poly(vinylidene fluoride) nanofibers for bidirectional removal of cation and anion dyes." *Chem. Eng. J.*, 354, 432–444.
- Ma, J., Fu, K., Shi, J., Sun, Y., Zhang, X., and Ding, L. (2016). "Ultraviolet-assisted synthesis of polyacrylamide-grafted chitosan nanoparticles and flocculation performance." *Carbohydr. Polym.*, 151, 565–575.
- Ma, L., Islam, S. M., Liu, H., Zhao, J., Sun, G., Li, H., Ma, S., and Kanatzidis, M. G. (2017). "Selective and Efficient Removal of Toxic Oxoanions of As(III), As(V), and Cr(VI) by Layered Double Hydroxide Intercalated with MoS<sub>4</sub>2-." *Chem. Mater.*, 29(7), 3274–3284.
- Maegawa, T., Kitamura, Y., Sako, S., Udzu, T., Sakurai, A., Tanaka, A., Kobayashi, Y., Endo, K., Bora, U., and Kurita, T. (2007). "Heterogeneous Pd/C-catalyzed ligand-free, room-temperature Suzuki–Miyaura coupling reactions in aqueous media." *Chem. Eur. J.*, 13(20), 5937–5943.
- Magasinski, A., Dixon, P., Hertzberg, B., Kvit, A., Ayala, J., and Yushin, G. (2010). "High-performance lithium-ion anodes using a hierarchical bottom-up approach." *Nat. Mater.*, 9(4), 353–358.
- Magdy, Y. H., and Altaher, H. (2018). "Kinetic analysis of the adsorption of dyes from high strength wastewater on cement kiln dust." *J. Environ. Chem. Eng.*, 6(1), 834–841.
- Mahmoodi, N. M. (2013). "Magnetic ferrite nanoparticle–alginate composite: Synthesis, characterization and binary system dye removal." *J. Taiwan Inst. Chem. Eng.*, 44(2), 322–330.
- Mahmoud, M. E., Amira, M. F., Seleim, S. M., and Mohamed, A. K. (2020). "Amino-decorated magnetic metal-organic framework as a potential novel platform for selective removal of chromium (VI), cadmium (II) and lead (II)." *J. Hazard. Mater.*, 381, 120979.
- Malard, L. M., Pimenta, M. A., Dresselhaus, G., and Dresselhaus, M. S. (2009). "Raman spectroscopy in graphene." *Phys. Rep.*, 473(5), 51–87.
- Mansour, S. F., Hemedat, O. M., El-Dek, S. I., and Salem, B. I. (2016). "Influence of La doping and synthesis method on the properties of CoFe<sub>2</sub>O<sub>4</sub> nanocrystals." *J. Magn. Magn. Mater.*, 420, 7–18.
- Mao, J., Guo, J., Fang, F., and Ji, S.-J. (2008). "Highly efficient copper (0)-catalyzed Suzuki–Miyaura cross-coupling reactions in reusable PEG-400." *Tetrahedron*, 64(18), 3905–3911.

- Marcano, D. C., Kosynkin, D. V., Berlin, J. M., Sinitskii, A., Sun, Z., Slesarev, A., Alemany, L. B., Lu, W., and Tour, J. M. (2010a). "Improved Synthesis of Graphene Oxide." *ACS Nano*, 4(8), 4806–4814.
- Marcano, D. C., Kosynkin, D. V., Berlin, J. M., Sinitskii, A., Sun, Z., Slesarev, A., Alemany, L. B., Lu, W., and Tour, J. M. (2010b). "Improved synthesis of graphene oxide." *ACS Nano*, 4(8), 4806–4814.
- Marcano, D. C., Kosynkin, D. V., Berlin, J. M., Sinitskii, A., Sun, Z., Slesarev, A. S., Alemany, L. B., Lu, W., and Tour, J. M. (2018). "Correction to Improved Synthesis of Graphene Oxide." *ACS Nano*, 12(2), 2078–2078.
- Marinescu, C., Ben Ali, M., Hamdi, A., Cherifi, Y., Barras, A., Coffinier, Y., Somacescu, S., Raditoiu, V., Szunerits, S., and Boukherroub, R. (2018a). "Cobalt phthalocyanine-supported reduced graphene oxide: A highly efficient catalyst for heterogeneous activation of peroxymonosulfate for rhodamine B and pentachlorophenol degradation." *Chem. Eng. J.*, 336, 465–475.
- Marinescu, C., Ben Ali, M., Hamdi, A., Cherifi, Y., Barras, A., Coffinier, Y., Somacescu, S., Raditoiu, V., Szunerits, S., and Boukherroub, R. (2018b). "Cobalt phthalocyanine-supported reduced graphene oxide: A highly efficient catalyst for heterogeneous activation of peroxymonosulfate for rhodamine B and pentachlorophenol degradation." *Chem. Eng. J.*, 336, 465–475.
- Martin, Y. E., and Johnson, E. A. (2012). "Biogeosciences survey: Studying interactions of the biosphere with the lithosphere, hydrosphere and atmosphere." *Prog. Phys. Geogr. Earth Environ.*, 36(6), 833–852.
- Martínez-Klimov, M. E., Hernández-Hipólito, P., Martínez-García, M., and Klimova, T. E. (2018). "Pd catalysts supported on hydrogen titanate nanotubes for Suzuki-Miyaura cross-coupling reactions." *Catal. Today*, 305, 58–64.
- Masindi, V., and Muedi, K. L. (2018). "Environmental contamination by heavy metals." *Heavy Met.*, 10, 115–132.
- Mastalir, M., Stöger, B., Pittenauer, E., Allmaier, G., and Kirchner, K. (2016). "Air-Stable Triazine-Based Ni(II) PNP Pincer Complexes As Catalysts for the Suzuki–Miyaura Cross-Coupling." *Org. Lett.*, 18(13), 3186–3189.
- Mattevi, C., Kim, H., and Chhowalla, M. (2011). "A review of chemical vapour deposition of graphene on copper." *J. Mater. Chem.*, 21(10), 3324–3334.

Mauricio, M. R., Barros, H. R. [de, Guilherme, M. R., Radovanovic, E., Rubira, A. F., and Carvalho, G. M. [de. (2013). "Synthesis of highly hydrophilic magnetic nanoparticles of Fe<sub>3</sub>O<sub>4</sub> for potential use in biologic systems." *Colloids Surf. Physicochem. Eng. Asp.*, 417, 224–229.

Maziarz, P., Matusik, J., and Radziszewska, A. (2019). "Halloysite-zero-valent iron nanocomposites for removal of Pb(II)/Cd(II) and As(V)/Cr(VI): Competitive effects, regeneration possibilities and mechanisms." *J. Environ. Chem. Eng.*, 7(6), 103507.

McClure, J. W. (1956). "Diamagnetism of Graphite." *Phys Rev*, 104(3), 666–671.

McConville, C., Woodruff, D., Kevan, S., Weinert, M., and Davenport, J. (1986). "Electronic structure of the (2× 2) C p<sub>4</sub>g carbidic phase on Ni {100}." *Phys. Rev. B*, 34(4), 2199.

McGivern, W. S., Derecskei-Kovacs, A., North, S. W., and Francisco, J. S. (2000). "Computationally Efficient Methodology to Calculate C–H and C–X (X = F, Cl, and Br) Bond Dissociation Energies in Haloalkanes." *J. Phys. Chem. A*, 104(2), 436–442.

McNaught, A. D., and Wilkinson, A. (1997). *Compendium of chemical terminology*. Blackwell Science Oxford.

Metin, Ö., Ho, S. F., Alp, C., Can, H., Mankin, M. N., Gültekin, M. S., Chi, M., and Sun, S. (2013). "Ni/Pd core/shell nanoparticles supported on graphene as a highly active and reusable catalyst for Suzuki-Miyaura cross-coupling reaction." *Nano Res.*, 6(1), 10–18.

Meyer, J. C., Kisielowski, C., Erni, R., Rossell, M. D., Crommie, M. F., and Zettl, A. (2008). "Direct Imaging of Lattice Atoms and Topological Defects in Graphene Membranes." *Nano Lett.*, 8(11), 3582–3586.

Mirabedini, M., Motamedi, E., and Kassae, M. Z. (2015). "Magnetic CuO nanoparticles supported on graphene oxide as an efficient catalyst for A<sub>3</sub>-coupling synthesis of propargylamines." *Chin. Chem. Lett.*, 26(9), 1085–1090.

Miyaura, N., Ishiyama, T., Sasaki, H., Ishikawa, M., Sato, M., and Suzuki, A. (1989). "Palladium-catalyzed inter- and intramolecular cross-coupling reactions of B-alkyl-9-borabicyclo[3.3.1]nonane derivatives with 1-halo-1-alkenes or haloarenes. Syntheses of functionalized alkenes, arenes, and cycloalkenes via a hydroboration-coupling sequence." *J. Am. Chem. Soc.*, 111(1), 314–321.

Miyaura, N., and Suzuki, A. (1995). "Palladium-catalyzed cross-coupling reactions of organoboron compounds." *Chem. Rev.*, 95(7), 2457–2483.

Miyaura, N., Yamada, K., and Suzuki, A. (1979). "A new stereospecific cross-coupling by the palladium-catalyzed reaction of 1-alkenylboranes with 1-alkenyl or 1-alkynyl halides." *Tetrahedron Lett.*, 20(36), 3437–3440.

- Miyaura, N., Yanagi, T., and Suzuki, A. (1981). "The palladium-catalyzed cross-coupling reaction of phenylboronic acid with haloarenes in the presence of bases." *Synth. Commun.*, 11(7), 513–519.
- Mkhoyan, K. A., Contryman, A. W., Silcox, J., Stewart, D. A., Eda, G., Mattevi, C., Miller, S., and Chhowalla, M. (2009). "Atomic and electronic structure of graphene-oxide." *Nano Lett.*, 9(3), 1058–1063.
- Mohammadinezhad, A., and Akhlaghinia, B. (2017). "Fe<sub>3</sub>O<sub>4</sub>@ Boehmite-NH<sub>2</sub>-Co II NPs: an inexpensive and highly efficient heterogeneous magnetic nanocatalyst for the Suzuki–Miyaura and Heck–Mizoroki cross-coupling reactions." *Green Chem.*, 19(23), 5625–5641.
- Mohit, K., Gupta, V. R., Gupta, N., and Rout, S. K. (2014). "Structural and microwave characterization of Ni<sub>0.2</sub>CoxZn<sub>0.8-x</sub>Fe<sub>2</sub>O<sub>4</sub> for antenna applications." *Ceram. Int.*, 40(1, Part B), 1575–1586.
- Molnár, Á., and Papp, A. (2017). "Catalyst recycling—A survey of recent progress and current status." *Coord. Chem. Rev.*, 349, 1–65.
- More, S., Jadhav, S., Salunkhe, R., and Kumbhar, A. (2017). "Palladium supported ionic liquid phase catalyst (Pd@SILP-PS) for room temperature Suzuki-Miyaura cross-coupling reaction." *Mol. Catal.*, 442, 126–132.
- Mori, Y., and Seki, M. (2003). "Pd(OH)<sub>2</sub>/C (Pearlman's Catalyst): A Highly Active Catalyst for Fukuyama, Sonogashira, and Suzuki Coupling Reactions." *J. Org. Chem.*, 68(4), 1571–1574.
- Mørup, S., Brok, E., and Frandsen, C. (2013). "Spin Structures in Magnetic Nanoparticles." *J. Nanomater.*, (W. Kleemann, ed.), 2013, 720629.
- Moussavi, G., and Mahmoudi, M. (2009). "Removal of azo and anthraquinone reactive dyes from industrial wastewaters using MgO nanoparticles." *J. Hazard. Mater.*, 168(2), 806–812.
- Mouzdahir, Y. E., Elmchaouri, A., Mahboub, R., Gil, A., and Korili, S. A. (2010). "Equilibrium modeling for the adsorption of methylene blue from aqueous solutions on activated clay minerals." *Desalination*, 250(1), 335–338.
- Muhammad Shariq Vohra, Dhahran (SA). (2016). "METHOD OF DYE REMOVAL FROM WASTEWATER." Dhahran.
- Mukherjee, A., Chakrabarty, S., Su, W.-N., and Basu, S. (2018). "Nanostructured nickel ferrite embedded in reduced graphene oxide for electrocatalytic hydrogen evolution reaction." *Mater. Today Energy*, 8, 118–124.

- Mungse, H. P., Verma, S., Kumar, N., Sain, B., and Khatri, O. P. (2012a). "Grafting of oxovanadium Schiff base on graphene nanosheets and its catalytic activity for the oxidation of alcohols." *J. Mater. Chem.*, 22(12), 5427–5433.
- Mungse, H. P., Verma, S., Kumar, N., Sain, B., and Khatri, O. P. (2012b). "Grafting of oxovanadium Schiff base on graphene nanosheets and its catalytic activity for the oxidation of alcohols." *J Mater Chem*, 22(12), 5427–5433.
- Nandan, B., and Bhatnagar, M. C. (2015). "Structural, vibrational and magnetic properties of Ni<sub>1-x</sub>Co<sub>x</sub>Fe<sub>2</sub>O<sub>4</sub> ferrites." *AIP Conf. Proc.*, 1675(1), 030072.
- Nandan, B., Bhatnagar, M. C., and Kashyap, S. C. (2019). "Cation distribution in nanocrystalline cobalt substituted nickel ferrites: X-ray diffraction and Raman spectroscopic investigations." *J. Phys. Chem. Solids*, 129, 298–306.
- Nasser, R., Zhang, G.-F., and Song, J.-M. (2020). "Facile and low-cost synthesis of cobalt-doped MnO<sub>2</sub> decorated with graphene oxide for high performance 2.3 V aqueous asymmetric supercapacitors." *Electrochimica Acta*, 345, 136198.
- Nasseri, M. A., Allahresani, A., and Raissi, H. (2014). "Grafting of a chiral Mn(III) complex on graphene oxide nanosheets and its catalytic activity for alkene epoxidation." *RSC Adv.*, 4(50), 26087–26093.
- Natale, F. D., Erto, A., and Lancia, A. (2013). "Desorption of arsenic from exhaust activated carbons used for water purification." *J. Hazard. Mater.*, 260, 451–458.
- Nethravathi, C., Rajamathi, C. R., Rajamathi, M., Wang, X., Gautam, U. K., Golberg, D., and Bando, Y. (2014). "Cobalt Hydroxide/Oxide Hexagonal Ring–Graphene Hybrids through Chemical Etching of Metal Hydroxide Platelets by Graphene Oxide: Energy Storage Applications." *ACS Nano*, 8(3), 2755–2765.
- Ni, S.-Q., Ni, J., Yang, N., and Wang, J. (2013). "Effect of magnetic nanoparticles on the performance of activated sludge treatment system." *Bioresour. Technol.*, 143, 555–561.
- Nie, R., Shi, J., Du, W., and Hou, Z. (2014). "Ni<sub>2</sub>O<sub>3</sub>-around-Pd hybrid on graphene oxide: an efficient catalyst for ligand-free Suzuki–Miyaura coupling reaction." *Appl. Catal. Gen.*, 473, 1–6.
- Niu, Z., Feng, W., Huang, H., Wang, B., Chen, L., Miao, Y., and Su, S. (2020). "Green synthesis of a novel Mn–Zn ferrite/biochar composite from waste batteries and pine sawdust for Pb<sup>2+</sup> removal." *Chemosphere*, 252, 126529.
- Novoselov, K. S., Fal'ko, V. I., Colombo, L., Gellert, P. R., Schwab, M. G., and Kim, K. (2012). "A roadmap for graphene." *Nature*, 490(7419), 192–200.

Novoselov, K. S., Geim, A. K., Morozov, S. V., Jiang, D., Zhang, Y., Dubonos, S. V., Grigorieva, I. V., and Firsov, A. A. (2004). “Electric Field Effect in Atomically Thin Carbon Films.” *Science*, 306(5696), 666.

Nuvoli, D., Valentini, L., Alzari, V., Scognamillo, S., Bon, S. B., Piccinini, M., Illescas, J., and Mariani, A. (2011). “High concentration few-layer graphene sheets obtained by liquid phase exfoliation of graphite in ionic liquid.” *J. Mater. Chem.*, 21(10), 3428–3431.

Ohashi, Y., Hironaka, T., Kubo, T., and Shiiki, K. (2000). “Magnetoresistance effect of thin films made of single graphite crystals.” *Tanso*, 2000(195), 410–413.

Ohashi, Y., Koizumi, T., Yoshikawa, T., Hironaka, T., and Shiiki, K. (1997). “Size effect in the in-plane electrical resistivity of very thin graphite crystals.” *Tanso*, 1997(180), 235–238.

Okamoto, M., and Ray, S. S. (2004). “Polymer/clay nanocomposites.” *Encycl. Nanosci. Nanotechnol.*, 8, 791–843.

Organisation mondiale de la santé, WHO--Work programme, Światowa Organizacja Zdrowia, World Health Organization, and World Health Organisation Staff. (2004). *Guidelines for drinking-water quality*. World Health Organization.

Ornelas, C., Ruiz, J., Salmon, L., and Astruc, D. (2008). “Sulphonated ‘Click’ Dendrimer-Stabilized Palladium Nanoparticles as Highly Efficient Catalysts for Olefin Hydrogenation and Suzuki Coupling Reactions Under Ambient Conditions in Aqueous Media.” *Adv. Synth. Catal.*, 350(6), 837–845.

Osuna, J., Caro, D. de, Amiens, C., Chaudret, B., Snoeck, E., Respaud, M., Broto, J.-M., and Fert, A. (1996). “Synthesis, Characterization, and Magnetic Properties of Cobalt Nanoparticles from an Organometallic Precursor.” *J. Phys. Chem.*, 100(35), 14571–14574.

Panagopoulos, D., Jahnke, A., Kierkegaard, A., and MacLeod, M. (2017). “Temperature Dependence of the Organic Carbon/Water Partition Ratios (KOC) of Volatile Methylsiloxanes.” *Environ. Sci. Technol. Lett.*, 4(6), 240–245.

Pandey, P. C., Shukla, S., and Pandey, Y. (2016). “3-Aminopropyltrimethoxysilane and graphene oxide/reduced graphene oxide-induced generation of gold nanoparticles and their nanocomposites: electrocatalytic and kinetic activity.” *RSC Adv.*, 6(84), 80549–80556.

Park, C. M., Kim, Y. M., Kim, K.-H., Wang, D., Su, C., and Yoon, Y. (2019). “Potential utility of graphene-based nano spinel ferrites as adsorbent and photocatalyst for removing organic/inorganic contaminants from aqueous solutions: A mini review.” *Chemosphere*, 221, 392–402.

Parveen SAINI, New Delhi (IN);, Manju ARORA, New Delhi (IN);, Ravinder Kumar KOTNALA, New, Delhi (IN); Sunil Kumar BARALA, New Delhi (IN); Rajendra Prasad,

PANT, New Delhi (IN); Chandni PURI, New Delhi (IN), COUNCIL OF SCIENTIFIC & INDUSTRIAL RESEARCH, New, and Delhi (IN). (2016). "MAGNETIC NANOPARTICLES DECORATED ACTIVATED CARBON NANOCOMPOSITES FOR PURIFICATION OF WATER." New Delhi.

Parwaiz, S., Bhunia, K., Das, A. K., Khan, M. M., and Pradhan, D. (2017). "Cobalt-Doped Ceria/Reduced Graphene Oxide Nanocomposite as an Efficient Oxygen Reduction Reaction Catalyst and Supercapacitor Material." *J. Phys. Chem. C*, 121(37), 20165–20176.

Peng, L., Qin, P., Lei, M., Zeng, Q., Song, H., Yang, J., Shao, J., Liao, B., and Gu, J. (2012). "Modifying Fe<sub>3</sub>O<sub>4</sub> nanoparticles with humic acid for removal of Rhodamine B in water." *J. Hazard. Mater.*, 209–210, 193–198.

Pereira, M. F. R., Soares, S. F., Órfão, J. J. M., and Figueiredo, J. L. (2003). "Adsorption of dyes on activated carbons: influence of surface chemical groups." *Carbon*, 41(4), 811–821.

Petcharoen, K., and Sirivat, A. (2012). "Synthesis and characterization of magnetite nanoparticles via the chemical co-precipitation method." *Mater. Sci. Eng. B*, 177(5), 421–427.

Petitto, S. C., and Langell, M. A. (2004). "Surface composition and structure of Co<sub>3</sub>O<sub>4</sub>(110) and the effect of impurity segregation." *J. Vac. Sci. Technol. A*, 22(4), 1690–1696.

Philippova, O., Barabanova, A., Molchanov, V., and Khokhlov, A. (2011). "Magnetic polymer beads: Recent trends and developments in synthetic design and applications." *Eur. Polym. J.*, 47(4), 542–559.

Pinto, V. H. A., Rebouças, J. S., Ucoski, G. M., Faria, E. H. [de, Ferreira, B. F., Gil, R. A. [Silva S., and Nakagaki, S. (2016). "Mn porphyrins immobilized on non-modified and chloropropyl-functionalized mesoporous silica SBA-15 as catalysts for cyclohexane oxidation." *Appl. Catal. Gen.*, 526, 9–20.

Pokropivny, V. V., and Skorokhod, V. V. (2007). "Classification of nanostructures by dimensionality and concept of surface forms engineering in nanomaterial science." *Mater. Sci. Eng. C*, 27(5), 990–993.

Ponnusami, V., Vikram, S., and Srivastava, S. N. (2008). "Guava (*Psidium guajava*) leaf powder: Novel adsorbent for removal of methylene blue from aqueous solutions." *J. Hazard. Mater.*, 152(1), 276–286.

Powar, R. R., Phadtare, V. D., Parale, V. G., Park, H.-H., Pathak, S., Kamble, P. R., Piste, P. B., and Zambare, D. N. (2018). "Structural, morphological, and magnetic properties of Zn<sub>x</sub>Co<sub>1-x</sub>Fe<sub>2</sub>O<sub>4</sub> (0 ≤ x ≤ 1) prepared using a chemical co-precipitation method." *Ceram. Int.*, 44(17), 20782–20789.

- Pradeep, A., Priyadharsini, P., and Chandrasekaran, G. (2008). "Production of single phase nano size NiFe<sub>2</sub>O<sub>4</sub> particles using sol-gel auto combustion route by optimizing the preparation conditions." *Mater. Chem. Phys.*, 112(2), 572–576.
- Pullar, R. C. (2012). "Hexagonal ferrites: A review of the synthesis, properties and applications of hexaferrite ceramics." *Prog. Mater. Sci.*, 57(7), 1191–1334.
- Qiao, D., Li, Z., Duan, J., and He, X. (2020). "Adsorption and photocatalytic degradation mechanism of magnetic graphene oxide/ZnO nanocomposites for tetracycline contaminants." *Chem. Eng. J.*, 400, 125952.
- Qin, L., Lv, W., Wei, W., Kang, F., Zhai, D., and Yang, Q.-H. (2019). "Oxygen-enriched carbon nanotubes as a bifunctional catalyst promote the oxygen reduction/evolution reactions in Li-O<sub>2</sub> batteries." *Carbon*, 141, 561–567.
- Qu, X., Alvarez, P. J. J., and Li, Q. (2013). "Applications of nanotechnology in water and wastewater treatment." *Nanotechnol. Water Wastewater Treat.*, 47(12), 3931–3946.
- Rahsepar, M., Pakshir, M., Piao, Y., and Kim, H. (2012). "Synthesis and electrocatalytic performance of high loading active PtRu multiwalled carbon nanotube catalyst for methanol oxidation." *Electrochimica Acta*, 71, 246–251.
- RAI, H. S., BHATTACHARYYA, M. S., SINGH, J., BANSAL, T. K., VATS, P., and BANERJEE, U. C. (2005). "Removal of Dyes from the Effluent of Textile and Dyestuff Manufacturing Industry: A Review of Emerging Techniques With Reference to Biological Treatment." *Crit. Rev. Environ. Sci. Technol.*, 35(3), 219–238.
- Rajabzadeh, M., Khalifeh, R., Eshghi, H., and Bakavoli, M. (2018). "A facile hydrothermal synthesis of novel hollow triple-shell CuNiFe<sub>2</sub>O<sub>4</sub> nanospheres with robust catalytic performance in the Suzuki–Miyaura coupling reaction." *J. Catal.*, 360, 261–269.
- Raju, K., G., V., and Yoon, D.-H. (2014). "Effect of Zn substitution on the structural and magnetic properties of Ni–Co ferrites." *Ceram. Int.*, 40.
- Ramesh, S., Haldorai, Y., Kim, H. S., and Kim, J.-H. (2017). "A nanocrystalline Co<sub>3</sub>O<sub>4</sub>@polypyrrole/MWCNT hybrid nanocomposite for high performance electrochemical supercapacitors." *RSC Adv.*, 7(58), 36833–36843.
- Rashad, M. M., Elsayed, E. M., Moharam, M. M., Abou-Shahba, R. M., and Saba, A. E. (2009). "Structure and magnetic properties of Ni<sub>x</sub>Zn<sub>1-x</sub>Fe<sub>2</sub>O<sub>4</sub> nanoparticles prepared through co-precipitation method." *J. Alloys Compd.*, 486(1), 759–767.
- Read, S. A., Jiménez, A. S., Ross, B. L., Aitken, R. J., and Tongeren, M. van. (2014). "Nanotechnology and exposure scenarios." *Handb. Nanosafety Meas. Expo. Toxicol.*, Elsevier BV, 17–58.



- Redlich, O., and Peterson, D. L. (1959). "A Useful Adsorption Isotherm." *J. Phys. Chem.*, 63(6), 1024–1024.
- Reetz, M. T., and Westermann, E. (2000). "Phosphane-Free Palladium-Catalyzed Coupling Reactions: The Decisive Role of Pd Nanoparticles." *Angew. Chem. Int. Ed.*, 39(1), 165–168.
- Ren, C., Ding, X., Fu, H., Meng, C., Li, W., and Yang, H. (2016). "Preparation of amino-functionalized CoFe<sub>2</sub>O<sub>4</sub>@SiO<sub>2</sub> magnetic nanocomposites for potential application in absorbing heavy metal ions." *RSC Adv*, 6(76), 72479–72486.
- Ren, F., Li, Z., Tan, W.-Z., Liu, X.-H., Sun, Z.-F., Ren, P.-G., and Yan, D.-X. (2018). "Facile preparation of 3D regenerated cellulose/graphene oxide composite aerogel with high-efficiency adsorption towards methylene blue." *J. Colloid Interface Sci.*, 532, 58–67.
- Ren, G., Li, Y., Guo, Z., Xiao, G., Zhu, Y., Dai, L., and Jiang, L. (2015). "A bio-inspired Co<sub>3</sub>O<sub>4</sub>-polypyrrole-graphene complex as an efficient oxygen reduction catalyst in one-step ball milling." *Nano Res.*, 8(11), 3461–3471.
- Rida, K., Bouraoui, S., and Hadnine, S. (2013). "Adsorption of methylene blue from aqueous solution by kaolin and zeolite." *Appl. Clay Sci.*, 83–84, 99–105.
- Rodriguez-Reinoso, F. (1998). "The role of carbon materials in heterogeneous catalysis." *Carbon*, 36(3), 159–175.
- Rosei, R., De Crescenzi, M., Sette, F., Quaresima, C., Savoia, A., and Perfetti, P. (1983). "Structure of graphitic carbon on Ni (111): A surface extended-energy-loss fine-structure study." *Phys. Rev. B*, 28(2), 1161.
- S, L., and A-H, M. (2012). "Removal of Copper (II) from Aqueous Solution by Agricultural By-Products-Sawdust." *Energy Procedia*, 18, 915–923.
- Sabarish, R., and Unnikrishnan, G. (2018). "Novel biopolymer templated hierarchical silicalite-1 as an adsorbent for the removal of rhodamine B." *J. Mol. Liq.*, 272, 919–929.
- Sabatier, P. A. (1986). "Top-Down and Bottom-Up Approaches to Implementation Research: a Critical Analysis and Suggested Synthesis." *J. Public Policy*, 6(1), 21–48.
- Safarpour, M., and Khataee, A. (2019). "Chapter 15 - Graphene-Based Materials for Water Purification." *Nanoscale Mater. Water Purif.*, Micro and Nano Technologies, S. Thomas, D. Pasquini, S.-Y. Leu, and D. A. Gopakumar, eds., Elsevier, 383–430.
- Salleh, M. A. M., Mahmoud, D. K., Karim, W. A. W. A., and Idris, A. (2011). "Cationic and anionic dye adsorption by agricultural solid wastes: A comprehensive review." *Desalination*, 280(1), 1–13.

- Sánchez-Arenillas, M., Oujja, M., Moutinho, F., Figuera, J. de la, Cañamares, M. V., Quesada, A., Castillejo, M., and Marco, J. F. (2019). “Bulk and surface characterisation of micrometer-thick cobalt ferrite films grown by IR PLD.” *Appl. Surf. Sci.*, 470, 917–922.
- Santhosh, C., Daneshvar, E., Kollu, P., Peräniemi, S., Grace, A. N., and Bhatnagar, A. (2017a). “Magnetic SiO<sub>2</sub>@CoFe<sub>2</sub>O<sub>4</sub> nanoparticles decorated on graphene oxide as efficient adsorbents for the removal of anionic pollutants from water.” *Chem. Eng. J.*, 322, 472–487.
- Santhosh, C., Daneshvar, E., Kollu, P., Peräniemi, S., Grace, A. N., and Bhatnagar, A. (2017b). “Magnetic SiO<sub>2</sub>@CoFe<sub>2</sub>O<sub>4</sub> nanoparticles decorated on graphene oxide as efficient adsorbents for the removal of anionic pollutants from water.” *Chem. Eng. J.*, 322, 472–487.
- Santhosh, C., Kollu, P., Felix, S., Velmurugan, V., Jeong, S. K., and Grace, A. N. (2015). “CoFe<sub>2</sub>O<sub>4</sub> and NiFe<sub>2</sub>O<sub>4</sub>@graphene adsorbents for heavy metal ions – kinetic and thermodynamic analysis.” *RSC Adv*, 5(37), 28965–28972.
- Satilmis, B., and Budd, P. M. (2017). “Selective dye adsorption by chemically-modified and thermally-treated polymers of intrinsic microporosity.” *J. Colloid Interface Sci.*, 492, 81–91.
- Sawai, K., Tatumi, R., Nakahodo, T., and Fujihara, H. (2008). “Asymmetric Suzuki–Miyaura coupling reactions catalyzed by chiral palladium nanoparticles at room temperature.” *Angew. Chem.*, 120(36), 7023–7025.
- Saygılı, G. A. (2015). “Synthesis, characterization and adsorption properties of a novel biomagnetic composite for the removal of Congo red from aqueous medium.” *J. Mol. Liq.*, 211, 515–526.
- Schafhaeutl, C. (1840). “LXXXVI. On the combinations of carbon with silicon and iron, and other metals, forming the different species of cast iron, steel, and malleable iron.” *Lond. Edinb. Dublin Philos. Mag. J. Sci.*, 16(106), 570–590.
- Scheuermann, G. M., Rumi, L., Steurer, P., Bannwarth, W., and Mülhaupt, R. (2009a). “Palladium Nanoparticles on Graphite Oxide and Its Functionalized Graphene Derivatives as Highly Active Catalysts for the Suzuki–Miyaura Coupling Reaction.” *J. Am. Chem. Soc.*, 131(23), 8262–8270.
- Scheuermann, G. M., Rumi, L., Steurer, P., Bannwarth, W., and Mülhaupt, R. (2009b). “Palladium nanoparticles on graphite oxide and its functionalized graphene derivatives as highly active catalysts for the Suzuki–Miyaura coupling reaction.” *J. Am. Chem. Soc.*, 131(23), 8262–8270.
- Schiff, U. (1866). “Sopra una nova serie di basi organiche (On a new series of organic bases).” *G. Sci. Nat. Ed Econ.*, 2, 201–257.

Schönfelder, D., Fischer, K., Schmidt, M., Nuyken, O., and Weberskirch, R. (2005). "Poly(2-oxazoline)s Functionalized with Palladium Carbene Complexes: Soluble, Amphiphilic Polymer Supports for C–C Coupling Reactions in Water." *Macromolecules*, 38(2), 254–262.

Schweizer, S., Becht, J.-M., and Drian, C. L. (2010). "Highly efficient reusable polymer-supported Pd catalysts of general use for the Suzuki reaction." *Tetrahedron*, 66(3), 765–772.

Seibert, K., Cho, G., Kütt, W., Kurz, H., Reitze, D., Dadap, J., Ahn, H., Downer, M., and Malvezzi, A. (1990). "Femtosecond carrier dynamics in graphite." *Phys. Rev. B*, 42(5), 2842.

Semenoff, G. W. (1984). "Condensed-matter simulation of a three-dimensional anomaly." *Phys. Rev. Lett.*, 53(26), 2449.

Šetka, M., Drbohlavová, J., and Hubálek, J. (2017). "Nanostructured Polypyrrole-Based Ammonia and Volatile Organic Compound Sensors." *Sensors*, 17(3).

Shahabuddin, S., Sarih, N. M., Mohamad, S., and Atika Baharin, S. N. (2016). "Synthesis and characterization of Co<sub>3</sub>O<sub>4</sub> nanocube-doped polyaniline nanocomposites with enhanced methyl orange adsorption from aqueous solution." *RSC Adv.*, 6(49), 43388–43400.

Shahane, G. S., Kumar, A., Arora, M., Pant, R. P., and Lal, K. (2010). "Synthesis and characterization of Ni–Zn ferrite nanoparticles." *J. Magn. Magn. Mater.*, 322(8), 1015–1019.

Sham, A. Y. W., and Notley, S. M. (2018). "Adsorption of organic dyes from aqueous solutions using surfactant exfoliated graphene." *J. Environ. Chem. Eng.*, 6(1), 495–504.

Shan, C., Ma, Z., Tong, M., and Ni, J. (2015). "Removal of Hg(II) by poly(1-vinylimidazole)-grafted Fe<sub>3</sub>O<sub>4</sub>@SiO<sub>2</sub> magnetic nanoparticles." *Water Res.*, 69, 252–260.

Shang, N., Feng, C., Zhang, H., Gao, S., Tang, R., Wang, C., and Wang, Z. (2013). "Suzuki–Miyaura reaction catalyzed by graphene oxide supported palladium nanoparticles." *Catal. Commun.*, 40(Supplement C), 111–115.

Shao, M., Ning, F., Zhao, J., Wei, M., Evans, D. G., and Duan, X. (2012). "Preparation of Fe<sub>3</sub>O<sub>4</sub>@SiO<sub>2</sub>@Layered Double Hydroxide Core–Shell Microspheres for Magnetic Separation of Proteins." *J. Am. Chem. Soc.*, 134(2), 1071–1077.

Sharma, H., Sharma, S., Sharma, C., Paul, S., and Clark, J. H. (2019). "Magnetically recoverable graphene oxide supported Co@ Fe<sub>3</sub>O<sub>4</sub>/L-dopa for CC cross-coupling and oxidation reactions in aqueous medium." *Mol. Catal.*, 469, 27–39.

Shebanova, O. N., and Lazor, P. (2003). "Raman spectroscopic study of magnetite (FeFe<sub>2</sub>O<sub>4</sub>): a new assignment for the vibrational spectrum." *J. Solid State Chem.*, 174(2), 424–430.

Shields, J. D., Gray, E. E., and Doyle, A. G. (2015). "A modular, air-stable nickel precatalyst." *Org. Lett.*, 17(9), 2166–2169.

Shimizu, K., Koizumi, S., Hatamachi, T., Yoshida, H., Komai, S., Kodama, T., and Kitayama, Y. (2004). "Structural investigations of functionalized mesoporous silica-supported palladium catalyst for Heck and Suzuki coupling reactions." *J. Catal.*, 228(1), 141–151.

Shobana, M. K., Rajendran, V., Jeyasubramanian, K., and Kumar, N. [Suresh. (2007). "Preparation and characterisation of NiCo ferrite nanoparticles." *Mater. Lett.*, 61(13), 2616–2619.

Siamaki, A. R., Abd El Rahman, S. K., Abdelsayed, V., El-Shall, M. S., and Gupton, B. F. (2011). "Microwave-assisted synthesis of palladium nanoparticles supported on graphene: A highly active and recyclable catalyst for carbon–carbon cross-coupling reactions." *J. Catal.*, 279(1), 1–11.

Sing, K. S. W. (1982). "Reporting physisorption data for gas/solid systems with special reference to the determination of surface area and porosity (Provisional)." *Pure Appl. Chem.*, 54(11), 2201–2218.

Singer, P. C., and Bilyk, K. (2002). "Enhanced coagulation using a magnetic ion exchange resin." *Water Res.*, 36(16), 4009–4022.

Sivashankar, R., Sathya, A. B., Vasantharaj, K., and Sivasubramanian, V. (2014). "Magnetic composite an environmental super adsorbent for dye sequestration – A review." *Environ. Nanotechnol. Monit. Manag.*, 1–2, 36–49.

Smith, M. D., Stepan, A. F., Ramarao, C., Brennan, P. E., and Ley, S. V. (2003). "Palladium-containing perovskites: recoverable and reuseable catalysts for Suzuki couplings." *Chem. Commun.*, (21), 2652–2653.

Sobhani, S., Moghadam, H. H., Skibsted, J., and Sansano, J. M. (2020). "A hydrophilic heterogeneous cobalt catalyst for fluoride-free Hiyama, Suzuki, Heck and Hirao cross-coupling reactions in water." *Green Chem.*, 22(4), 1353–1365.

Sofo, J. O., Chaudhari, A. S., and Barber, G. D. (2007). "Graphane: A two-dimensional hydrocarbon." *Phys Rev B*, 75(15), 153401.

Song, S., Wang, D., Di, L., Wang, C., Dai, W., Wu, G., Guan, N., and Li, L. (2018). "Robust cobalt oxide catalysts for controllable hydrogenation of carboxylic acids to alcohols." *Chin. J. Catal.*, 39(2), 250–257.

Song, Z. J., Ran, W., and Wei, F. Y. (2016). "One-step approach for the synthesis of CoFe<sub>2</sub>O<sub>4</sub>@rGO core-shell nanocomposites as efficient adsorbent for removal of organic pollutants." *Water Sci. Technol.*, 75(2), 397–405.

- Stankovich, S., Dikin, D. A., Dommett, G. H. B., Kohlhaas, K. M., Zimney, E. J., Stach, E. A., Piner, R. D., Nguyen, S. T., and Ruoff, R. S. (2006). "Graphene-based composite materials." *Nature*, 442(7100), 282–286.
- Stankovich, S., Dikin, D. A., Piner, R. D., Kohlhaas, K. A., Kleinhammes, A., Jia, Y., Wu, Y., Nguyen, S. T., and Ruoff, R. S. (2007). "Synthesis of graphene-based nanosheets via chemical reduction of exfoliated graphite oxide." *carbon*, 45(7), 1558–1565.
- Staudenmaier, L. (1898). "Verfahren zur darstellung der graphitsäure." *Berichte Dtsch. Chem. Ges.*, 31(2), 1481–1487.
- Stergiou, C. (2017). "Magnetic, dielectric and microwave absorption properties of rare earth doped Ni–Co and Ni–Co–Zn spinel ferrites." *J. Magn. Magn. Mater.*, 426, 629–635.
- Stevens, P. D., Fan, J., Gardimalla, H. M. R., Yen, M., and Gao, Y. (2005). "Superparamagnetic Nanoparticle-Supported Catalysis of Suzuki Cross-Coupling Reactions." *Org. Lett.*, 7(11), 2085–2088.
- Su, H., Li, Z., Huo, Q., Guan, J., and Kan, Q. (2014a). "Immobilization of transition metal (Fe<sup>2+</sup>, Co<sup>2+</sup>, VO<sup>2+</sup> or Cu<sup>2+</sup>) Schiff base complexes onto graphene oxide as efficient and recyclable catalysts for epoxidation of styrene." *RSC Adv.*, 4(20), 9990.
- Su, H., Li, Z., Huo, Q., Guan, J., and Kan, Q. (2014b). "Immobilization of transition metal (Fe<sup>2+</sup>, Co<sup>2+</sup>, VO<sup>2+</sup> or Cu<sup>2+</sup>) Schiff base complexes onto graphene oxide as efficient and recyclable catalysts for epoxidation of styrene." *RSC Adv.*, 4(20), 9990–9996.
- Sujandi, Prasetyanto, E. A., Lee, S.-C., and Park, S.-E. (2009). "Microwave synthesis of large pored chloropropyl functionalized mesoporous silica with p6mm, Ia-3d, and Im3m structures." *Microporous Mesoporous Mater.*, 118(1), 134–142.
- Sun, W., Wang, Y., Wu, X., and Yao, X. (2013). "Palladium-, ligand-, and solvent-free synthesis of ynones by the coupling of acyl chlorides and terminal alkynes in the presence of a reusable copper nanoparticle catalyst." *Green Chem.*, 15(9), 2356–2360.
- Szabó, T., Berkesi, O., and Dékány, I. (2005). "DRIFT study of deuterium-exchanged graphite oxide." *Carbon*, 43(15), 3186–3189.
- Tadjarodi, A., Imani, M., and Salehi, M. (2015). "ZnFe<sub>2</sub>O<sub>4</sub> nanoparticles and a clay encapsulated ZnFe<sub>2</sub>O<sub>4</sub> nanocomposite: synthesis strategy, structural characteristics and the adsorption of dye pollutants in water." *RSC Adv.*, 5(69), 56145–56156.
- Tang, D., Zheng, Z., Lin, K., Luan, J., and Zhang, J. (2007). "Adsorption of p-nitrophenol from aqueous solutions onto activated carbon fiber." *J. Hazard. Mater.*, 143(1), 49–56.

- Tang, J., Huang, Y., Gong, Y., Lyu, H., Wang, Q., and Ma, J. (2016). "Preparation of a novel graphene oxide/Fe-Mn composite and its application for aqueous Hg(II) removal." *J. Hazard. Mater.*, 316, 151–158.
- Tang, Z.-Y., and Hu, Q.-S. (2004). "Room-temperature Ni (0)-catalyzed cross-coupling reactions of aryl arenesulfonates with arylboronic acids." *J. Am. Chem. Soc.*, 126(10), 3058–3059.
- Tao, B., and Boykin, D. W. (2002). "Pd (OAc)<sub>2</sub>-aryl-2-oxazolines catalyzed Suzuki coupling reactions of aryl bromides and arylboronic acids." *Tetrahedron Lett.*, 43(28), 4955–4957.
- Tao, B., and Boykin, D. W. (2004). "Simple Amine/Pd(OAc)<sub>2</sub>-Catalyzed Suzuki Coupling Reactions of Aryl Bromides under Mild Aerobic Conditions." *J. Org. Chem.*, 69(13), 4330–4335.
- Tatarchuk, T. R., Bououdina, M., Paliychuk, N. D., Yaremiy, I. P., and Moklyak, V. V. (2017). "Structural characterization and antistructure modeling of cobalt-substituted zinc ferrites." *J. Alloys Compd.*, 694, 777–791.
- Thathagar, M. B., Beckers, J., and Rothenberg, G. (2002). "Copper-catalyzed Suzuki cross-coupling using mixed nanocluster catalysts." *J. Am. Chem. Soc.*, 124(40), 11858–11859.
- Thathagar, M. B., Beckers, J., and Rothenberg, G. (2003). "Combinatorial Design of Copper-Based Mixed Nanoclusters: New Catalysts for Suzuki Cross-Coupling." *Adv. Synth. Catal.*, 345(8), 979–985.
- Thomas, B., and Alexander, L. K. (2020). "Removal of Pb<sup>2+</sup> and Cd<sup>2+</sup> toxic heavy metal ions driven by Fermi level modification in NiFe<sub>2</sub>O<sub>4</sub>-Pd nano hybrids." *J. Solid State Chem.*, 288, 121417.
- Thommes Matthias, Kaneko Katsumi, Neimark Alexander V., Olivier James P., Rodriguez-Reinoso Francisco, Rouquerol Jean, and Sing Kenneth S.W. (2015). "Physisorption of gases, with special reference to the evaluation of surface area and pore size distribution (IUPAC Technical Report)." *Pure Appl. Chem.*, 87(9–10), 1051.
- Thota, S., Kashyap, S. C., Sharma, S. K., and Reddy, V. R. (2016). "Cation distribution in Ni-substituted Mn<sub>0.5</sub>Zn<sub>0.5</sub>Fe<sub>2</sub>O<sub>4</sub> nanoparticles: A Raman, Mössbauer, X-ray diffraction and electron spectroscopy study." *Mater. Sci. Eng. B*, 206, 69–78.
- Tikish, T. A., Kumar, A., and Kim, J. Y. (2018). "Study on the miscibility of Polypyrrole and polyaniline polymer blends." *Adv. Mater. Sci. Eng.*, 2018.

- Tong, J., Su, L., Bo, L., Cai, X., Zhang, Q., and Wang, Q. (2016). “Mesoporous palladium–copper ferrites as highly efficient and magnetically separable catalysts for Suzuki coupling reaction.” *Mater. Res. Bull.*, 73, 240–246.
- Tran, H. N., You, S.-J., Hosseini-Bandegharaei, A., and Chao, H.-P. (2017). “Mistakes and inconsistencies regarding adsorption of contaminants from aqueous solutions: A critical review.” *Water Res.*, 120, 88–116.
- Tran, T. P. N., Thakur, A., Trinh, D. X., Dao, A. T. N., and Taniike, T. (2018). “Design of Pd@Graphene oxide framework nanocatalyst with improved activity and recyclability in Suzuki-Miyaura cross-coupling reaction.” *Appl. Catal. Gen.*, 549, 60–67.
- Tran, T. S., Park, S. J., Yoo, S. S., Lee, T.-R., and Kim, T. (2016). “High shear-induced exfoliation of graphite into high quality graphene by Taylor–Couette flow.” *RSC Adv*, 6(15), 12003–12008.
- Turhan, K., and Turgut, Z. (2009). “Decolorization of direct dye in textile wastewater by ozonization in a semi-batch bubble column reactor.” *Desalination*, 242(1), 256–263.
- Vahidhabanu, S., Abideen Idowu, A., Karuppasamy, D., Ramesh Babu, B., and Vineetha, M. (2017). “Microwave Initiated Facile Formation of Sepiolite-Poly(dimethylsiloxane) Nanohybrid for Effective Removal of Congo Red Dye from Aqueous Solution.” *ACS Sustain. Chem. Eng.*, 5(11), 10361–10370.
- Van Lier, G., Van Alsenoy, C., Van Doren, V., and Geerlings, P. (2000). “Ab initio study of the elastic properties of single-walled carbon nanotubes and graphene.” *Chem. Phys. Lett.*, 326(1–2), 181–185.
- Vanitha, M., Keerthi, Cao, P., and Balasubramanian, N. (2015). “Ag nanocrystals anchored CeO<sub>2</sub>/graphene nanocomposite for enhanced supercapacitor applications.” *J. Alloys Compd.*, 644, 534–544.
- Velusamy, S., Roy, A., Sundaram, S., and Kumar Mallick, T. (2021). “A Review on Heavy Metal Ions and Containing Dyes Removal Through Graphene Oxide-Based Adsorption Strategies for Textile Wastewater Treatment.” *Chem. Rec.*, 21(7), 1570–1610.
- Verma, S., Aila, M., Kaul, S., and Jain, S. L. (2014). “Immobilized oxo-vanadium Schiff base on graphene oxide as an efficient and recyclable catalyst for the epoxidation of fatty acids and esters.” *RSC Adv.*, 4(58), 30598–30604.
- Wallace, P. R. (1947). “The band theory of graphite.” *Phys. Rev.*, 71(9), 622.
- Wan, C., Jiao, Y., and Li, J. (2017). “Flexible, highly conductive, and free-standing reduced graphene oxide/polypyrrole/cellulose hybrid papers for supercapacitor electrodes.” *J. Mater. Chem. A*, 5(8), 3819–3831.

Wang, C., and Astruc, D. (2018). “Recent developments of metallic nanoparticle-graphene nanocatalysts.” *Prog. Mater. Sci.*, 94, 306–383.

WANG, F., WANG, L., LI, J., SUN, X., and HAN, W. (2009). “Adsorption behavior and mechanism of cadmium on strong-acid cation exchange resin.” *Trans. Nonferrous Met. Soc. China*, 19(3), 740–744.

Wang, H., Hao, Q., Yang, X., Lu, L., and Wang, X. (2010). “Effect of Graphene Oxide on the Properties of Its Composite with Polyaniline.” *ACS Appl. Mater. Interfaces*, 2(3), 821–828.

Wang, H., Maiyalagan, T., and Wang, X. (2012a). “Review on Recent Progress in Nitrogen-Doped Graphene: Synthesis, Characterization, and Its Potential Applications.” *ACS Catal.*, 2(5), 781–794.

Wang, H., Yuan, X., Wu, Y., Chen, X., Leng, L., Wang, H., Li, H., and Zeng, G. (2015a). “Facile synthesis of polypyrrole decorated reduced graphene oxide-Fe<sub>3</sub>O<sub>4</sub> magnetic composites and its application for the Cr(VI) removal.” *Chem. Eng. J.*, 262, 597–606.

Wang, J.-Q., Huang, L., Xue, M., Wang, Y., Gao, L., Zhu, J. H., and Zou, Z. (2008). “Architecture of a Hybrid Mesoporous Chemosensor for Fe<sup>3+</sup> by Covalent Coupling Bis-Schiff Base PMBA onto the CPTES-Functionalized SBA-15.” *J. Phys. Chem. C*, 112(13), 5014–5022.

Wang, L., Hu, D., Kong, X., Liu, J., Li, X., Zhou, K., Zhao, H., and Zhou, C. (2018a). “Anionic polypeptide poly( $\gamma$ -glutamic acid)-functionalized magnetic Fe<sub>3</sub>O<sub>4</sub>-GO-(o-MWCNTs) hybrid nanocomposite for high-efficiency removal of Cd(II), Cu(II) and Ni(II) heavy metal ions.” *Chem. Eng. J.*, 346, 38–49.

Wang, L., Li, J., Wang, Y., Zhao, L., and Jiang, Q. (2012b). “Adsorption capability for Congo red on nanocrystalline MFe<sub>2</sub>O<sub>4</sub> (M=Mn, Fe, Co, Ni) spinel ferrites.” *Chem. Eng. J.*, 181–182, 72–79.

Wang, L., and Wang, A. (2008). “Adsorption properties of Congo Red from aqueous solution onto surfactant-modified montmorillonite.” *J. Hazard. Mater.*, 160(1), 173–180.

Wang, P., Qi, J., Li, C., Chen, X., Luo, J., Li, W., Shi, X., Olivet, L., Wang, T., and Liang, C. (2019). “In-situ surface selective removal: An efficient way to prepare water oxidation catalyst.” *Int. J. Hydrog. Energy*, 44(29), 14955–14967.

Wang, P., Qi, J., Li, C., Chen, X., Wang, T., and Liang, C. (2020a). “N-Doped Carbon Nanotubes Encapsulating Ni/MoN Heterostructures Grown on Carbon Cloth for Overall Water Splitting.” *ChemElectroChem*, 7(3), 745–752.



- Wang, P., Qi, J., Li, C., Li, W., Wang, T., and Liang, C. (2020b). “Hierarchical CoNi<sub>2</sub>S<sub>4</sub>@NiMn-layered double hydroxide heterostructure nanoarrays on superhydrophilic carbon cloth for enhanced overall water splitting.” *Electrochimica Acta*, 345, 136247.
- Wang, T., Jiang, Z., An, T., Li, G., Zhao, H., and Wong, P. K. (2018b). “Enhanced Visible-Light-Driven Photocatalytic Bacterial Inactivation by Ultrathin Carbon-Coated Magnetic Cobalt Ferrite Nanoparticles.” *Environ. Sci. Technol.*, 52(8), 4774–4784.
- Wang, W., Cai, K., Wu, X., Shao, X., and Yang, X. (2017). “A novel poly(m-phenylenediamine)/reduced graphene oxide/nickel ferrite magnetic adsorbent with excellent removal ability of dyes and Cr(VI).” *J. Alloys Compd.*, 722, 532–543.
- Wang, W., Ding, Z., Cai, M., Jian, H., Zeng, Z., Li, F., and Liu, J. P. (2015b). “Synthesis and high-efficiency methylene blue adsorption of magnetic PAA/MnFe<sub>2</sub>O<sub>4</sub> nanocomposites.” *Appl. Surf. Sci.*, 346, 348–353.
- Wang, X., Wu, S., Li, Z., Yang, X., Su, H., Hu, J., Huo, Q., Guan, J., and Kan, Q. (2016a). “Cu(II), Co(II), Fe(III) or VO(II) Schiff base complexes immobilized onto CMK-3 for styrene epoxidation.” *Microporous Mesoporous Mater.*, 221(Supplement C), 58–66.
- Wang, Y., Du Pasquier, A., Li, D., Atanassova, P., Sawrey, S., and Oljaca, M. (2018c). “Electrochemical double layer capacitors containing carbon black additives for improved capacitance and cycle life.” *Carbon*, 133, 1–5.
- Wang, Y., and Huang, L. (2014). “Chapter Five - Composite Nanoparticles for Gene Delivery.” *Nonviral Vectors Gene Ther.*, Advances in Genetics, L. Huang, D. Liu, and E. Wagner, eds., Academic Press, 111–137.
- Wang, Y., Li, L., Luo, C., Wang, X., and Duan, H. (2016b). “Removal of Pb<sup>2+</sup> from water environment using a novel magnetic chitosan/graphene oxide imprinted Pb<sup>2+</sup>.” *Int. J. Biol. Macromol.*, 86, 505–511.
- Wang, Y., Xiao, N., Wang, Z., Tang, Y., Li, H., Yu, M., Liu, C., Zhou, Y., and Qiu, J. (2018d). “Ultrastable and high-capacity carbon nanofiber anodes derived from pitch/polyacrylonitrile for flexible sodium-ion batteries.” *Carbon*, 135, 187–194.
- Wang, Y., Xie, X., Chen, X., Huang, C., and Yang, S. (2020c). “Biochar-loaded Ce<sup>3+</sup>-enriched ultra-fine ceria nanoparticles for phosphate adsorption.” *J. Hazard. Mater.*, 396, 122626.
- Wang, Y., Zhou, R., Wang, C., Zhou, G., Hua, C., Cao, Y., and Song, Z. (2020d). “Novel environmental-friendly nano-composite magnetic attapulgite functionalized by chitosan and EDTA for cadmium (II) removal.” *J. Alloys Compd.*, 817, 153286.

- Wang, Y., Zhu, L., Wang, X., Zheng, W., Hao, C., Jiang, C., and Wu, J. (2018e). "Synthesis of aminated calcium lignosulfonate and its adsorption properties for azo dyes." *J. Ind. Eng. Chem.*, 61, 321–330.
- Waranusantigul, P., Pokethitiyook, P., Kruatrachue, M., and Upatham, E. S. (2003). "Kinetics of basic dye (methylene blue) biosorption by giant duckweed (*Spirodela polyrrhiza*)." *Environ. Pollut.*, 125(3), 385–392.
- Weber, W. J., and Morris, J. C. (1963). "Kinetics of adsorption on carbon from solution." *J. Sanit. Eng. Div.*, 89(2), 31–60.
- Wei, S., Hu, X., Liu, H., Wang, Q., and He, C. (2015). "Rapid degradation of Congo red by molecularly imprinted polypyrrole-coated magnetic TiO<sub>2</sub> nanoparticles in dark at ambient conditions." *J. Hazard. Mater.*, 294, 168–176.
- Weng, X., Lin, Z., Xiao, X., Li, C., and Chen, Z. (2018). "One-step biosynthesis of hybrid reduced graphene oxide/iron-based nanoparticles by eucalyptus extract and its removal of dye." *J. Clean. Prod.*, 203, 22–29.
- Witek-Krowiak, A., Szafran, R. G., and Modelski, S. (2011). "Biosorption of heavy metals from aqueous solutions onto peanut shell as a low-cost biosorbent." *Desalination*, 265(1), 126–134.
- Wolfe, J. P., and Buchwald, S. L. (1999). "A highly active catalyst for the room-temperature amination and Suzuki coupling of aryl chlorides." *Angew. Chem. Int. Ed.*, 38(16), 2413–2416.
- Wu, D., Wang, Y., Li, Y., Wei, Q., Hu, L., Yan, T., Feng, R., Yan, L., and Du, B. (2019a). "Phosphorylated chitosan/CoFe<sub>2</sub>O<sub>4</sub> composite for the efficient removal of Pb(II) and Cd(II) from aqueous solution: Adsorption performance and mechanism studies." *J. Mol. Liq.*, 277, 181–188.
- Wu, F., Xie, A., Sun, M., Wang, Y., and Wang, M. (2015a). "Reduced graphene oxide (RGO) modified spongelike polypyrrole (PPy) aerogel for excellent electromagnetic absorption." *J. Mater. Chem. A*, 3(27), 14358–14369.
- Wu, F.-C., Tseng, R.-L., and Juang, R.-S. (2009). "Initial behavior of intraparticle diffusion model used in the description of adsorption kinetics." *Chem. Eng. J.*, 153(1), 1–8.
- Wu, W., Qi, W., Zhao, Y., Tang, X., Qiu, Y., Su, D., Fan, H., and Wang, G. (2019b). "Hollow CeO<sub>2</sub> spheres conformally coated with graphitic carbon for high-performance supercapacitor electrodes." *Appl. Surf. Sci.*, 463, 244–252.
- Wu, W., Yang, L., Chen, S., Shao, Y., Jing, L., Zhao, G., and Wei, H. (2015b). "Core-shell nanospherical polypyrrole/graphene oxide composites for high performance supercapacitors." *RSC Adv.*, 5(111), 91645–91653.

- Wu, X.-L., Wang, L., Chen, C.-L., Xu, A.-W., and Wang, X.-K. (2011). “Water-dispersible magnetite-graphene-LDH composites for efficient arsenate removal.” *J Mater Chem*, 21(43), 17353–17359.
- Wu, Y., Luo, H., and Wang, H. (2014). “Efficient Removal of Congo Red from Aqueous Solutions by Surfactant-Modified Hydroxo Aluminum/Graphene Composites.” *Sep. Sci. Technol.*, 49(17), 2700–2710.
- Xia, W., Chen, X., Kundu, S., Wang, X., Grundmeier, G., Wang, Y., Bron, M., Schuhmann, W., and Muhler, M. (2007). “Chemical vapor synthesis of secondary carbon nanotubes catalyzed by iron nanoparticles electrodeposited on primary carbon nanotubes.” *Surf. Coat. Technol.*, 201(22), 9232–9237.
- Xiang, B., Ling, D., Lou, H., and Gu, H. (2017). “3D hierarchical flower-like nickel ferrite/manganese dioxide toward lead (II) removal from aqueous water.” *J. Hazard. Mater.*, 325, 178–188.
- Xiao, J., Lu, Z., and Li, Y. (2015). “Carboxymethylcellulose-Supported Palladium Nanoparticles Generated in Situ from Palladium(II) Carboxymethylcellulose: An Efficient and Reusable Catalyst for Suzuki–Miyaura and Mizoroki–Heck Reactions.” *Ind. Eng. Chem. Res.*, 54(3), 790–797.
- Xie, Y., Yan, B., Xu, H., Chen, J., Liu, Q., Deng, Y., and Zeng, H. (2014). “Highly Regenerable Mussel-Inspired Fe<sub>3</sub>O<sub>4</sub>@Polydopamine-Ag Core–Shell Microspheres as Catalyst and Adsorbent for Methylene Blue Removal.” *ACS Appl. Mater. Interfaces*, 6(11), 8845–8852.
- Xie, Y.-C., and Tang, Y.-Q. (1990). “Spontaneous monolayer dispersion of oxides and salts onto surfaces of supports: applications to heterogeneous catalysis.” *Adv. Catal.*, Elsevier, 1–43.
- Xiong, L., Yang, Y., Mai, J., Sun, W., Zhang, C., Wei, D., Chen, Q., and Ni, J. (2010). “Adsorption behavior of methylene blue onto titanate nanotubes.” *Chem. Eng. J.*, 156(2), 313–320.
- Xiong, S., Yuan, C., Zhang, X., Xi, B., and Qian, Y. (2009). “Controllable Synthesis of Mesoporous Co<sub>3</sub>O<sub>4</sub> Nanostructures with Tunable Morphology for Application in Supercapacitors.” *Chem. – Eur. J.*, 15(21), 5320–5326.
- Xu, H., and Liu, Y. (2008). “Mechanisms of Cd<sup>2+</sup>, Cu<sup>2+</sup> and Ni<sup>2+</sup> biosorption by aerobic granules.” *Sep. Purif. Technol.*, 58(3), 400–411.
- Xu, J., Cao, Z., Zhang, Y., Yuan, Z., Lou, Z., Xu, X., and Wang, X. (2018a). “A review of functionalized carbon nanotubes and graphene for heavy metal adsorption from water: Preparation, application, and mechanism.” *Chemosphere*, 195, 351–364.

- Xu, J., Cao, Z., Zhang, Y., Yuan, Z., Lou, Z., Xu, X., and Wang, X. (2018b). "A review of functionalized carbon nanotubes and graphene for heavy metal adsorption from water: Preparation, application, and mechanism." *Chemosphere*, 195, 351–364.
- Xu, Q., Cheng, B., Yu, J., and Liu, G. (2017a). "Making co-condensed amorphous carbon/g-C<sub>3</sub>N<sub>4</sub> composites with improved visible-light photocatalytic H<sub>2</sub>-production performance using Pt as cocatalyst." *Carbon*, 118, 241–249.
- Xu, T., Xue, J., Zhang, X., He, G., and Chen, H. (2017b). "Ultrafine cobalt nanoparticles supported on reduced graphene oxide: Efficient catalyst for fast reduction of hexavalent chromium at room temperature." *Appl. Surf. Sci.*, 402, 294–300.
- Xu, W., Song, Y., Dai, K., Sun, S., Liu, G., and Yao, J. (2018c). "Novel ternary nanohybrids of tetraethylenepentamine and graphene oxide decorated with MnFe<sub>2</sub>O<sub>4</sub> magnetic nanoparticles for the adsorption of Pb(II)." *J. Hazard. Mater.*, 358, 337–345.
- Xu, Y., Bao, J., Zhang, X., Li, W., Xie, Y., Sun, S., Zhao, W., and Zhao, C. (2019). "Functionalized polyethersulfone nanofibrous membranes with ultra-high adsorption capacity for organic dyes by one-step electrospinning." *J. Colloid Interface Sci.*, 533, 526–538.
- Yam, K. M., Guo, N., Jiang, Z., Li, S., and Zhang, C. (2020). "Graphene-Based Heterogeneous Catalysis: Role of Graphene." *Catalysts*, 10(1).
- Yamada, N., Kowalski, D., Koyama, A., Zhu, C., Aoki, Y., and Habazaki, H. (2019). "High dispersion and oxygen reduction reaction activity of Co<sub>3</sub>O<sub>4</sub> nanoparticles on platelet-type carbon nanofibers." *RSC Adv.*, 9(7), 3726–3733.
- Yan, J., Wei, T., Shao, B., Fan, Z., Qian, W., Zhang, M., and Wei, F. (2010). "Preparation of a graphene nanosheet/polyaniline composite with high specific capacitance." *Carbon*, 48(2), 487–493.
- Yan, Q.-L., Gozin, M., Zhao, F.-Q., Cohen, A., and Pang, S.-P. (2016). "Highly energetic compositions based on functionalized carbon nanomaterials." *Nanoscale*, 8(9), 4799–4851.
- Yang, J., Wu, J.-X., Lü, Q.-F., and Lin, T.-T. (2014a). "Facile Preparation of Lignosulfonate–Graphene Oxide–Polyaniline Ternary Nanocomposite as an Effective Adsorbent for Pb(II) Ions." *ACS Sustain. Chem. Eng.*, 2(5), 1203–1211.
- Yang, L., Zhang, Y., Liu, X., Jiang, X., Zhang, Z., Zhang, T., and Zhang, L. (2014b). "The investigation of synergistic and competitive interaction between dye Congo red and methyl blue on magnetic MnFe<sub>2</sub>O<sub>4</sub>." *Chem. Eng. J.*, 246, 88–96.
- Yang, Q., Lu, R., Ren, S., Chen, C., Chen, Z., and Yang, X. (2018). "Three dimensional reduced graphene oxide/ZIF-67 aerogel: Effective removal cationic and anionic dyes from water." *Chem. Eng. J.*, 348, 202–211.

- Yang, Q., Ma, S., Li, J., Xiao, F., and Xiong, H. (2006). "A water-compatible, highly active and reusable PEG-coated mesoporous silica-supported palladium complex and its application in Suzuki coupling reactions." *Chem. Commun.*, (23), 2495–2497.
- Yang, X., Peng, W., Fu, K., Mao, L., Jin, J., Yang, S., and Li, G. (2020a). "Nanocomposites of honeycomb double-layered MnO<sub>2</sub> nanosheets /cobalt doped hollow carbon nanofibers for application in supercapacitor and primary zinc-air battery." *Electrochimica Acta*, 340, 135989.
- Yang, Y., Tian, C., Sun, L., Lü, R., Zhou, W., Shi, K., Kan, K., Wang, J., and Fu, H. (2013a). "Growth of small sized CeO<sub>2</sub> particles in the interlayers of expanded graphite for high-performance room temperature NO<sub>x</sub> gas sensors." *J Mater Chem A*, 1(41), 12742–12749.
- Yang, Z., Chen, X., Li, S., Ma, W., Li, Y., He, Z., Hu, H., and Wang, T. (2020b). "Effective removal of Cd(II) from aqueous solution based on multifunctional nanoporous silicon derived from solar kerf loss waste." *J. Hazard. Mater.*, 385, 121522.
- Yang, Z., Ji, S., Gao, W., Zhang, C., Ren, L., Tjiu, W. W., Zhang, Z., Pan, J., and Liu, T. (2013b). "Magnetic nanomaterial derived from graphene oxide/layered double hydroxide hybrid for efficient removal of methyl orange from aqueous solution." *J. Colloid Interface Sci.*, 408, 25–32.
- Yang, Z. L., Gao, B. Y., Li, C. X., Yue, Q. Y., and Liu, B. (2010). "Synthesis and characterization of hydrophobically associating cationic polyacrylamide." *Chem. Eng. J.*, 161(1), 27–33.
- Yano, K., Usuki, A., Okada, A., Kurauchi, T., and Kamigaito, O. (1993). "Synthesis and properties of polyimide–clay hybrid." *J. Polym. Sci. Part Polym. Chem.*, 31(10), 2493–2498.
- Yao, Y., Miao, S., Liu, S., Ma, L. P., Sun, H., and Wang, S. (2012). "Synthesis, characterization, and adsorption properties of magnetic Fe<sub>3</sub>O<sub>4</sub>@graphene nanocomposite." *Chem. Eng. J.*, 184, 326–332.
- Yao, Y., Xu, C., Qin, J., Wei, F., Rao, M., and Wang, S. (2013). "Synthesis of Magnetic Cobalt Nanoparticles Anchored on Graphene Nanosheets and Catalytic Decomposition of Orange II." *Ind. Eng. Chem. Res.*, 52(49), 17341–17350.
- Ye, Y.-M., Wang, B.-B., Ma, D., Shao, L.-X., and Lu, J.-M. (2010). "CuO-2, 2'-Diamino-6, 6'-Dimethylbiphenyl Catalyzed Suzuki–Miyaura Coupling Reactions of Arylboronic Acids with Aryl Iodides and Bromides." *Catal. Lett.*, 139(3), 141–144.
- Yin, P., Xu, Q., Qu, R., and Zhao, G. (2009). "Removal of transition metal ions from aqueous solutions by adsorption onto a novel silica gel matrix composite adsorbent." *J. Hazard. Mater.*, 169(1), 228–232.

- Yorimitsu, H., and Oshima, K. (2006). "New synthetic reactions catalyzed by cobalt complexes." *Pure Appl. Chem.*, 78(2), 441–449.
- Yousefi, M. H., Manouchehri, S., Arab, A., Mozaffari, M., Amiri, G. R., and Amighian, J. (2010). "Preparation of cobalt–zinc ferrite (Co<sub>0.8</sub>Zn<sub>0.2</sub>Fe<sub>2</sub>O<sub>4</sub>) nanopowder via combustion method and investigation of its magnetic properties." *Mater. Res. Bull.*, 45(12), 1792–1795.
- Yussuf, A., Al-Saleh, M., Al-Enezi, S., and Abraham, G. (2018). "Synthesis and Characterization of Conductive Polypyrrole: The Influence of the Oxidants and Monomer on the Electrical, Thermal, and Morphological Properties." *Int. J. Polym. Sci.*, (H. Roghani-Mamaqani, ed.), 2018, 4191747.
- Zamaro, J. M., Pérez, N. C., Miró, E. E., Casado, C., Seoane, B., Téllez, C., and Coronas, J. (2012). "HKUST-1 MOF: A matrix to synthesize CuO and CuO–CeO<sub>2</sub> nanoparticle catalysts for CO oxidation." *Chem. Eng. J.*, 195–196, 180–187.
- Zarnegaryan, A., Moghadam, M., Tangestaninejad, S., Mirkhani, V., and Mohammadpoor-Baltork, I. (2016). "A graphene oxide immobilized Cu (II) complex of 1, 2-bis (4-aminophenylthio) ethane: an efficient catalyst for epoxidation of olefins with tert-butyl hydroperoxide." *New J. Chem.*, 40(3), 2280–2286.
- Zhang, C., Huang, J., Trudell, M. L., and Nolan, S. P. (1999). "Palladium–Imidazol-2-ylidene Complexes as Catalysts for Facile and Efficient Suzuki Cross-Coupling Reactions of Aryl Chlorides with Arylboronic Acids." *J. Org. Chem.*, 64(11), 3804–3805.
- Zhang, G., Wang, B., Li, L., and Yang, S. (2019a). "Phosphorus and Yttrium Codoped Co(OH)F Nanoarray as Highly Efficient and Bifunctional Electrocatalysts for Overall Water Splitting." *Small*, 15(42), 1904105.
- Zhang, L., Luo, L., and Zhang, S. (2011a). "Adsorption of phenanthrene and 1,3-dinitrobenzene on cation-modified clay minerals." *Colloids Surf. Physicochem. Eng. Asp.*, 377(1), 278–283.
- Zhang, P., O'Connor, D., Wang, Y., Jiang, L., Xia, T., Wang, L., Tsang, D. C. W., Ok, Y. S., and Hou, D. (2020a). "A green biochar/iron oxide composite for methylene blue removal." *J. Hazard. Mater.*, 384, 121286.
- Zhang, R., Hummelgård, M., Lv, G., and Olin, H. (2011b). "Real time monitoring of the drug release of rhodamine B on graphene oxide." *Carbon*, 49(4), 1126–1132.
- Zhang, R., Wan, W., Qiu, L., Wang, Y., and Zhou, Y. (2017). "Preparation of hydrophobic polyvinyl alcohol aerogel via the surface modification of boron nitride for environmental remediation." *Appl. Surf. Sci.*, 419, 342–347.

- Zhang, X. and Bai. (2003). "Surface Electric Properties of Polypyrrole in Aqueous Solutions." *Langmuir*, 19(26), 10703–10709.
- Zhang, X., Zhang, S., Chen, B., Wang, H., Wu, K., Chen, Y., Fan, J., Qi, S., Cui, X., Zhang, L., and Wang, J. (2016). "Direct synthesis of large-scale hierarchical MoS<sub>2</sub> films nanostructured with orthogonally oriented vertically and horizontally aligned layers." *Nanoscale*, 8(1), 431–439.
- Zhang, Y., Qiu, Y., Ji, X., Ma, T., Ma, Z., and Hu, P. A. (2019b). "Direct Growth of CNTs@CoS<sub>x</sub>Se<sub>2</sub>(1-x) on Carbon Cloth for Overall Water Splitting." *ChemSusChem*, 12(16), 3792–3800.
- Zhang, Y., Su, P., Weathersby, D., Zhang, Q., Zheng, J., Fan, R., Zhang, J., and Dai, Q. (2020b). "Synthesis of  $\gamma$ -Fe<sub>2</sub>O<sub>3</sub>-ZnO-biochar nanocomposites for Rhodamine B removal." *Appl. Surf. Sci.*, 501, 144217.
- Zhang, Y., Yan, L., Xu, W., Guo, X., Cui, L., Gao, L., Wei, Q., and Du, B. (2014). "Adsorption of Pb(II) and Hg(II) from aqueous solution using magnetic CoFe<sub>2</sub>O<sub>4</sub>-reduced graphene oxide." *J. Mol. Liq.*, 191, 177–182.
- Zhao, B., Jiang, H., Lin, Z., Xu, S., Xie, J., and Zhang, A. (2019). "Preparation of acrylamide/acrylic acid cellulose hydrogels for the adsorption of heavy metal ions." *Carbohydr. Polym.*, 224, 115022.
- Zhao, D., Gao, X., Wu, C., Xie, R., Feng, S., and Chen, C. (2016a). "Facile preparation of amino functionalized graphene oxide decorated with Fe<sub>3</sub>O<sub>4</sub> nanoparticles for the adsorption of Cr(VI)." *Appl. Surf. Sci.*, 384, 1–9.
- Zhao, F., Repo, E., Yin, D., Meng, Y., Jafari, S., and Sillanpää, M. (2015). "EDTA-Cross-Linked  $\beta$ -Cyclodextrin: An Environmentally Friendly Bifunctional Adsorbent for Simultaneous Adsorption of Metals and Cationic Dyes." *Environ. Sci. Technol.*, 49(17), 10570–10580.
- Zhao, H., Fan, S., Chen, Y., Feng, Z., Zhang, H., Pang, W., Zhang, D., and Zhang, M. (2017). "Oxygen Plasma-Treated Graphene Oxide Surface Functionalization for Sensitivity Enhancement of Thin-Film Piezoelectric Acoustic Gas Sensors." *ACS Appl. Mater. Interfaces*, 9(46), 40774–40781.
- Zhao, H., Liu, X., Cao, Z., Zhan, Y., Shi, X., Yang, Y., Zhou, J., and Xu, J. (2016b). "Adsorption behavior and mechanism of chloramphenicols, sulfonamides, and non-antibiotic pharmaceuticals on multi-walled carbon nanotubes." *J. Hazard. Mater.*, 310, 235–245.

Zhao, L., Yang, H., Yu, L., Cui, Y., Zhao, X., and Feng, S. (2006). "Study on magnetic properties of nanocrystalline La-, Nd-, or Gd-substituted Ni–Mn ferrite at low temperatures." *J. Magn. Magn. Mater.*, 305(1), 91–94.

Zhao, Q., Bai, C., Zhang, W., Li, Y., Zhang, G., Zhang, F., and Fan, X. (2014a). "Catalytic Epoxidation of Olefins with Graphene Oxide Supported Copper (Salen) Complex." *Ind. Eng. Chem. Res.*, 53, 4232–4238.

Zhao, X., Wang, W., Zhang, Y., Wu, S., Li, F., and Liu, J. P. (2014b). "Synthesis and characterization of gadolinium doped cobalt ferrite nanoparticles with enhanced adsorption capability for Congo Red." *Chem. Eng. J.*, 250, 164–174.

Zheng, H., Ma, J., Zhu, C., Zhang, Z., Liu, L., Sun, Y., and Tang, X. (2014). "Synthesis of anion polyacrylamide under UV initiation and its application in removing dioctyl phthalate from water through flocculation process." *Sep. Purif. Technol.*, 123, 35–44.

Zheng, X., Zheng, H., Zhou, Y., Sun, Y., Zhao, R., Liu, Y., and Zhang, S. (2019a). "Enhanced adsorption of Orange G from aqueous solutions by quaternary ammonium group-rich magnetic nanoparticles." *Colloids Surf. Physicochem. Eng. Asp.*, 580, 123746.

Zheng, Y., Cheng, B., You, W., Yu, J., and Ho, W. (2019b). "3D hierarchical graphene oxide-NiFe LDH composite with enhanced adsorption affinity to Congo red, methyl orange and Cr(VI) ions." *J. Hazard. Mater.*, 369, 214–225.

Zheng, Y., Zhu, B., Chen, H., You, W., Jiang, C., and Yu, J. (2017). "Hierarchical flower-like nickel(II) oxide microspheres with high adsorption capacity of Congo red in water." *J. Colloid Interface Sci.*, 504, 688–696.

Zhou, T., Chen, F., Liu, K., Deng, H., Zhang, Q., Feng, J., and Fu, Q. (2010). "A simple and efficient method to prepare graphene by reduction of graphite oxide with sodium hydrosulfite." *Nanotechnology*, 22(4), 045704.

Zhu, B., Xia, P., Ho, W., and Yu, J. (2015). "Isoelectric point and adsorption activity of porous g-C<sub>3</sub>N<sub>4</sub>." *Appl. Surf. Sci.*, 344, 188–195.

Zhu, T., Chen, J. S., and Lou, X. W. (2010a). "Shape-controlled synthesis of porous Co<sub>3</sub>O<sub>4</sub> nanostructures for application in supercapacitors." *J. Mater. Chem.*, 20(33), 7015–7020.

Zhu, Y., Murali, S., Cai, W., Li, X., Suk, J. W., Potts, J. R., and Ruoff, R. S. (2010b). "Graphene and graphene oxide: synthesis, properties, and applications." *Adv. Mater.*, 22(35), 3906–3924.

Zou, H., He, B., Kuang, P., Yu, J., and Fan, K. (2018). "NixSy Nanowalls/Nitrogen-Doped Graphene Foam Is an Efficient Trifunctional Catalyst for Unassisted Artificial Photosynthesis." *Adv. Funct. Mater.*, 28(13), 1706917.



## PUBLICATIONS

### LIST OF PUBLICATIONS

1. Anuma Saroja and B. Ramachandra Bhat (2018) “Nanographene sheet immobilized transition metal complexes for C-C coupling reactions”, *International Journal of Engineering and Technology* (UAE) Scopus indexed, 7(4.5), 431-434; DOI: 10.14419/ijet.v7i4.5.20199
2. Anuma Saroja, Praveen Mishra and B. Ramachandra Bhat (2019) “Copper complex with N-, O- architecture grafted graphene oxide nanosheet as a heterogeneous catalyst for Suzuki Cross Coupling Reaction” *Journal of Taiwan Institute of Chemical Engineers*, 95, 643-651; DOI: 10.1016/j.jtice.2018.09.029
3. Anuma Saroja and B. Ramachandra Bhat (2019) “Cobalt Schiff Base immobilized on Graphene nanosheet with N, O linkage for Cross-Coupling reaction” *ACS Industrial and Engineering Chemistry Research*, 58, 2, 590-601; DOI: 10.1021/acs.iecr.8b02979
4. Anuma Saroja and B. Ramachandra Bhat (2019) “Synthesis of Copper Graphene by amino functionalization and their catalytic applications” *Materials Today: Proceedings*, 18, 7, 4942-4951; DOI:10.1016/j.matpr.2019.07.486
5. Anuma Saroja, Praveen Mishra and B. Ramachandra Bhat (2021) “Polypyrrole functionalized Cobalt oxide Graphene (COPYGO) nanocomposite for the efficient removal of dyes and heavy metal pollutants from aqueous effluents” *Journal of Hazardous Materials*, 416, 15, 125959; DOI: 10.1016/j.jhazmat.2021.125929
6. Anuma Saroja and B. Ramachandra Bhat (2021) “Synthesis of GO-CeO<sub>2</sub>@CoFe<sub>2</sub>O<sub>4</sub> nanocomposite by hydrothermal method for the effective adsorption of cationic and anionic pollutants from textile wastewater” (**communicated**).
7. Anuma Saroja and B. Ramachandra Bhat (2021) “Synthesis of GO-CeO<sub>2</sub>@CoFe<sub>2</sub>O<sub>4</sub> nanocomposite by hydrothermal method for the effective adsorption of cationic and anionic pollutants from textile wastewater” (**Patent pending**).

### LISTS OF CONFERENCES

1. Anuma Saroja and Badekai Ramachandra Bhat (2017). “Grafting of Copper complexes onto Graphene oxide Nanosheets and its Catalytic Study in Suzuki Cross Coupling Reaction” 4<sup>th</sup> International Conference on Nanoscience and Nanotechnology (ICONN 2017). 9<sup>th</sup>-11<sup>th</sup> August 2017, SRM University, Kattankulathur, Tamil Nadu, India.
2. Anuma Saroja and Badekai Ramachandra Bhat (2017). “Nickel complex grafted on Graphene oxide Nanosheet and its catalytic activity in Suzuki cross coupling reaction”

- 2<sup>nd</sup> International Conference on Advances in Material Science and Technology (ICAMST 2017). 9<sup>th</sup>-11<sup>th</sup> October 2017, VIT University, Vellore, Tamil Nadu, India.
3. Anuma Saroja and Badekai Ramachandra Bhat (2018). "Nickel Schiff base complex grafted on Graphene oxide Nanosheet and its catalytic activity in Suzuki cross coupling reaction" International conference on Science and Engineering of Materials (ICSEM 2018). 6<sup>th</sup>-8<sup>th</sup> January 2018, Sharda University, Greater Noida, Uttar Pradesh, India.
  4. Anuma Saroja and Badekai Ramachandra Bhat (2018). "Nanographene sheet immobilized transition metal complexes for C-C coupling reaction" International Conference on Recent Trends in Engineering and Sciences (ICRTES 2018). 20<sup>th</sup>-21<sup>st</sup> February 2018, Visakhapatnam, Andhra Pradesh, India.
  5. Anuma Saroja and Badekai Ramachandra Bhat (2018). "Cobalt Schiff base immobilized on Graphene nanosheet with N,O linkage for Cross-Coupling reaction" 4<sup>th</sup> International Conference of Chemical Engineering & Industrial Biotechnology (ICCEIB 2018). 1<sup>st</sup>-2<sup>nd</sup> August 2018, Kuala Lumpur, Malaysia.
  6. Anuma Saroja and Badekai Ramachandra Bhat (2018). "Nickel complex immobilized on functionalized graphene oxide as an efficient and recyclable catalyst for the Suzuki cross coupling" 37<sup>th</sup> National Conference on Indian Council of Chemists (ICC 2018). 12<sup>th</sup>-14<sup>th</sup> December 2018, NITK Surathkal, Mangalore, Karnataka, India.
  7. Anuma Saroja and Badekai Ramachandra Bhat (2019). "Functionalized Graphene oxide-Schiff base Nickel complex with (N, O) linkage as an efficient and recyclable catalyst for the Suzuki cross coupling reaction" 5<sup>th</sup> International Conference of Nanoscience and Nanotechnology (ICONN 2019). 28<sup>th</sup>-30<sup>th</sup> January 2019, SRM University, Kattankulathur, Tamil Nadu, India.
  8. Anuma Saroja and Badekai Ramachandra Bhat (2019). "Synthesis of Copper Graphene nanocomposites by amino functionalization and their catalytic applications" 9<sup>th</sup> International Conference on Material Processing and Characterizations (ICMPC 2019). 8<sup>th</sup>-10<sup>th</sup> March 2019, Gokaraju Rangaraju Institute of Engineering and Technology, Hyderabad, Telangan, India.
  9. Anuma Saroja and Badekai Ramachandra Bhat (2019). "Cobalt Ferrite Nanoparticle by hydrothermal Synthesis for the efficient removal of cationic dyes from Wastewater" 38<sup>th</sup> National Conference on Indian Council of Chemists (ICC 2019). 26<sup>th</sup>-28<sup>th</sup> December 2019, Jaipur National University, Jaipur, Rajasthan, India.

## **LIST OF WORKSHOPS**

1. GIAN workshop on “Novel Functional Materials for Energy Conversion”. 4<sup>th</sup> -7<sup>th</sup> October 2016, NITK Surathkal, Karnataka, India.
2. GIAN workshop on “Modern Perspectives on Renewable Energy and Biorefinery”. 6<sup>th</sup> -10<sup>th</sup> November 2017, NITK Surathkal, Karnataka, India.
3. Faculty development program workshop on “Recent Trends in Chemical Sciences” 21<sup>st</sup> -25<sup>th</sup> September 2020, Nitte Meenakshi Institute of Technology, Bangalore, Karnataka, India.

# CURRICULUM VITAE

**A SAROJA**

**Present Address:**

Lab No: 413

Catalysis and Materials laboratory,

National Institute of Technology,

Surathkal, Mangalore,

Karnataka-575025, India

Mobile: +91-8867946863

Email: [saru2032@gmail.com](mailto:saru2032@gmail.com), [cy14f03@nitk.edu.in](mailto:cy14f03@nitk.edu.in)

**Sex and Marital Status:** Female and Single

**Nationality:** Indian

**Date of Birth:** 23-12-1988



**Permanent Address:**

H: No:-3-155, Kannala,

Basantnagar, Kamanpur(M),

Karimnagar, PIN-505187,

Telangana, INDIA

---

## RESEARCH EXPERIENCE

- Project Assistant on the CSIR sponsored network project “INDUS MAGIC” at CSIR-CSMCRI, Gujarat, India from August 2013 – Oct 2014.
- Worked as a summer project trainee at Indian Institute of Technology, Gandhinagar, on “small molecule synthesis” from May 2012 - July 2012.

## RESEARCH KEYWORDS

- Heterogeneous catalysis, Designing nanomaterials and composites for Dye adsorption and heavy metal ion rejection.

## ACADEMIC DETAILS

**PhD**

**Chemistry (2014)** pursuing

National Institute of Technology, Surathkal, Karnataka, India.

**M. Sc.**

**Chemistry (2010 - 2012)**

Specialization:

(6.89 CGPA), Organic Chemistry, from National Institute of Technology, Warangal Telangana, India

**B. Sc.**

**Chemistry, Microbiology, Biotechnology (2006-2009)**

(83.4%), Vaagdevi Degree & PG College, Kakatiya University, Warangal, Telangana, India.

**Intermediate** (12<sup>th</sup>) Botany, Zoology, **Chemistry & Physics (2004-2006)**  
(87%) Trinity Junior College, Peddapalli, Telangana, India

**SSC** (10<sup>th</sup>) **2004** (78.9%)  
Oxford Creativity High School, CCC Naspur, Mancherial, Telangana, India

## **SOFTWARE KNOWLEDGE**

- Have acquired knowledge in using chemistry utility programs like Chem draw, Scifinder, Origin.
- Thoroughly trained in Windows operating systems and application software: Chem windows, MS Office and Adobe Photoshop

## **PRESENTATIONS AT CONFERENCES**

- Anuma Saroja and Kannan Srinivasan (2013), "Dehydration of 2-octanol to 1-octene over heterogeneous acid catalysts in Continuous flow reactor" in Workshop on intensification and upscaling of continuous processes, 13<sup>th</sup> -14<sup>th</sup> Dec 2013, CSIR-National Chemical Laboratory, Pune, India.
- Anuma Saroja and Badekai Ramachandra Bhat (2017). "Grafting of Copper complexes onto Graphene oxide Nanosheets and its Catalytic Study in Suzuki Cross Coupling Reaction" 4<sup>th</sup> International Conference on Nanoscience and Nanotechnology (ICONN 2017). 9<sup>th</sup>-11<sup>th</sup> August 2017, SRM University, Kattankulathur, Tamil Nadu, India.
- Anuma Saroja and Badekai Ramachandra Bhat (2017). "Nickel complex grafted on Graphene oxide Nanosheet and its catalytic activity in Suzuki cross coupling reaction" 2<sup>nd</sup> International Conference on Advances in Material Science and Technology (ICAMST 2017). 9<sup>th</sup>-11<sup>th</sup> October 2017, VIT University, Vellore, Tamil Nadu, India.
- Anuma Saroja and Badekai Ramachandra Bhat (2018). "Nickel Schiff base complex grafted on Graphene oxide Nanosheet and its catalytic activity in Suzuki cross coupling reaction" International conference on Science and Engineering of Materials (ICSEM 2018). 6<sup>th</sup>-8<sup>th</sup> January 2018, Sharda University, Greater Noida, Uttar Pradesh, India.
- Anuma Saroja and Badekai Ramachandra Bhat (2018). "Nanographene sheet immobilized transition metal complexes for C-C coupling reaction" International Conference on Recent Trends in Engineering and Sciences (ICRTES 2018). 20<sup>th</sup>-21<sup>st</sup> February 2018, Visakhapatnam, Andhra Pradesh, India.
- Anuma Saroja and Badekai Ramachandra Bhat (2018). "Cobalt Schiff base immobilized on Graphene nanosheet with N,O linkage for Cross-Coupling reaction" 4<sup>th</sup> International Conference of Chemical Engineering & Industrial Biotechnology (ICCEIB 2018). 1<sup>st</sup>-2<sup>nd</sup> August 2018, Kuala Lumpur, Malaysia.
- Anuma Saroja and Badekai Ramachandra Bhat (2018). "Nickel complex immobilized on functionalized graphene oxide as an efficient and recyclable catalyst for the Suzuki cross coupling" 37<sup>th</sup> National Conference on Indian Council of Chemists (ICC 2018). 12<sup>th</sup>-14<sup>th</sup> December 2018, NITK Surathkal, Mangalore, Karnataka, India.
- Anuma Saroja and Badekai Ramachandra Bhat (2019). "Functionalized Graphene oxide-Schiff base Nickel complex with (N, O) linkage as an efficient and recyclable catalyst for the Suzuki cross coupling reaction" 5<sup>th</sup> International Conference of Nanoscience and Nanotechnology (ICONN 2019). 28<sup>th</sup>-30<sup>th</sup> January 2019, SRM University, Kattankulathur, Tamil Nadu, India.
- Anuma Saroja and Badekai Ramachandra Bhat (2019). "Synthesis of Copper Graphene nanocomposites by amino functionalization and their catalytic applications" 9<sup>th</sup> International

Conference on Material Processing and Characterizations (ICMPC 2019). 8<sup>th</sup>-10<sup>th</sup> March 2019, Gokaraju Rangaraju Institute of Engineering and Technology, Hyderabad, Telangan, India.

- Anuma Saroja and Badekai Ramachandra Bhat (2019). “Cobalt Ferrite Nanoparticle by hydrothermal Synthesis for the efficient removal of cationic dyes from Wastewater” 38<sup>th</sup> National Conference on Indian Council of Chemists (ICC 2019). 26<sup>th</sup>-28<sup>th</sup> December 2019, Jaipur National University, Jaipur, Rajasthan, India.

## RESEARCH JOURNALS

- 1) Anuma Saroja and B. Ramachandra Bhat (2018) “Nanographene sheet immobilized transition metal complexes for C-C coupling reactions”, *International Journal of Engineering and Technology* (UAE) Scopus indexed, 7(4.5), 431-434; DOI: 10.14419/ijet.v7i4.5.20199
- 2) Anuma Saroja, Praveen Mishra and B. Ramachandra Bhat (2019) “Copper complex with N-, O-architecture grafted graphene oxide nanosheet as a heterogeneous catalyst for Suzuki Cross Coupling Reaction” *Journal of Taiwan Institute of Chemical Engineers*, 95, 643-651; DOI: 10.1016/j.jtice.2018.09.029
- 3) Anuma Saroja and B. Ramachandra Bhat (2019) “Cobalt Schiff Base immobilized on Graphene nanosheet with N, O linkage for Cross-Coupling reaction” *ACS Industrial and Engineering Chemistry Research*, 58, 2, 590-601; DOI: 10.1021/acs.iecr.8b02979
- 4) Anuma Saroja and B. Ramachandra Bhat (2019) “Synthesis of Copper Graphene by amino functionalization and their catalytic applications” *Materials Today: Proceedings*, 18, 7, 4942-4951; DOI:10.1016/j.matpr.2019.07.486
- 5) Anuma Saroja, Praveen Mishra and B. Ramachandra Bhat (2021) “Polypyrrole functionalized Cobalt oxide Graphene (COPYGO) nanocomposite for the efficient removal of dyes and heavy metal pollutants from aqueous effluents” *Journal of Hazardous Materials*, 416, 15, 125959; DOI: 10.1016/j.jhazmat.2021.125929

## INSTRUMENTATION HANDLED

- Experienced with the handling of **JEOL NMR ECS 400** Magnet Console instrumentation. More than 100 samples collected and analyzed.
- Well acquainted with the operation and analysis of IR & UV –analysis.
- Column chromatography using silica-gel and neutral alumina, preparative thin layer chromatography (preparative TLC), Thin layer chromatography.
- Distillation techniques, High pressure autoclave reactors and Continuous flow reactors.
- Skilled in handling Gas Chromatography.

## PERSONAL COMPETENCE

- Well experienced to execute the synthesis of carbon composites as well as nanoparticle
- Hands on experience in the calibration of Gas chromatography data and catalysis applications.
- **Chromatography:** Purification of compounds using Gravitational Column Chromatography.
- **Spectroscopy:** Well versed with analysis of compounds by <sup>1</sup>H NMR, <sup>13</sup>C NMR. Interpretation of data obtained from UV, IR, Raman Spectroscopy, GC-MS and XPS and various diffraction methods i.e., XRD, SEM and TEM as well as Magnetic studies using VSM and EPR analysis
- Positive attitude to create pleasant work environment.
- Project execution and management.

## LANGUAGE PROFICIENCY

- English (Good speaking and writing knowledge), Telugu: (Native Language) and Hindi.